Geographia Technica

Technical Geography
an International Journal for the Progress of Scientific Geography

Volume 20, Geographia Technica No. 2/2025

www.technicalgeography.org

Cluj University Press

Editorial Board

Okke **Batelaan**, Flinders University Adelaide, Australia
Yazidhi **Bamutaze**, Makerere University, Kampala, Uganda
Valerio **Baiocchi**, Sapienza University of Rome, Italy
Gabriela **Biali**, "Gh. Asachi" University of Iasi, Romania
Habib **Ben Boubaker**, University of Manouba, Tunisia
Gino **Dardanelli**, University of Palermo, Italy
Qingyun **Du**, Wuhan University, China
Renata **Dulias**, University of Silesia, Poland
Massimiliano **Fazzini**, University of Ferrara, Italy
Muhammad **Helmi,** Diponegoro University, Indonesia
Edward **Jackiewicz**, California State University, Northridge CA, USA
Shadrack **Kithiia**, University of Nairobi, Kenya
Jaromir **Kolejka**, Masaryk University Brno, Czech Republic
Jelena **Kovačević-Majkić,** Geographical Institute "Jovan Cvijić", Belgrade, Serbia
František **Križan**, Comenius University in Bratislava, Slovakia
Muh Aris **Marfai**, Universitas Gadjah Mada, Yogyakarta, Indonesia
Béla **Márkus**, University of West Hungary Szekesfehervar, Hungary
Jean-Luc **Mercier**, Université de Strasbourg, France
Yuri Sandoval **Montes,** Universidad Mayor de San Andrés, La Paz, Bolivia
Igor **Patrakeyev**, Kyiv University of Construction and Architecture, Ukraine
Cristian Valeriu **Patriche**, Romanian Academy, Iasi, Romania
Dušan **Petrovič**, University of Lujubjana, Slovenia
Claudia **Pipitone,** National Institute of Geophysics and Volcanology, Naples, Italy
Hervé **Quénol**, Université de Rennes 2 et CNRS, France
Sanda **Roșca**, Babes-Bolyai University of Cluj-Napoca, Romania
José J. de **Sanjosé Blasco**, University of Extremadura, Spain
Lucian **Sfîcă,** "Al.I.Cuza" University of Iasi, Romania
Richard R. **Shaker**, Reyson University, Toronto, Canada
Sarintip **Tantanee**, Naresuan University, Phitsanulok, Thailand
Gábor **Timár**, Eötvös University Budapest, Hungary
Kinga **Temerdek-Ivan**, Babes-Bolyai University of Cluj-Napoca, Romania
Yuri **Tuchkovenko**, Odessa State Environmental University, Ukraine
Kamila **Turečková,** Silesian University in Opava, Czech Republic
Eugen **Ursu**, Université de Bordeaux, France
Changshan **Wu**, University of Wisconsin-Milwaukee, USA
Chong-yu **Xu**, University of Oslo, Norway

Editor-in-chief

Ionel **Haidu**, University of Lorraine, France

Editorial Secretary

Marcel Mateescu, Airbus Group Toulouse, France
George Costea, Yardi Systemes, Cluj-Napoca, Romania

Online Publishing

Magyari-Sáska Zsolt, "Babes-Bolyai" University of Cluj-Napoca, Romania

Geographia Technica

Technical Geography

an International Journal for the Progress of Scientific Geography

2025 – No. 2

Cluj University Press

ISSN: 1842 - 5135 (Printed version)
ISSN: 2065 - 4421 (Online version)

© 2025. All rights reserved. No part of this publication may be reproduced or transmitted in any form or by any means, electronic or mechanical, including photocopy, recording or any information storage and retrieval system, without permission from the editor.

Babeș-Bolyai University
Cluj University Press
Director: Codruța Săcelean
Str. Hașdeu nr. 51
400371 Cluj-Napoca, România
Tel./fax: (+40)-264-597.401
E-mail: editura@editura.ubbcluj.ro
http://www.editura.ubbcluj.ro/

Asociatia Geographia Technica
2, Prunilor Street
400334 Cluj-Napoca, România
Tel. +40 744 238093
editorial-secretary@technicalgeography.org
http://technicalgeography.org/

Cluj University Press and Asociatia Geographia Technica
assume no responsibility for material, manuscript, photographs or artwork.

C o n t e n t

Geographia Technica

Volume 20, Issue 2, autumn 2025

An International Journal of Technical Geography

ISSN 2065-4421 (Online); ISSN 1842-5135 (printed)

DEVELOPMENT AND ASSESSMENT OF LANDSLIDE SUSCEPTIBILITY IN THE PROVINCE OF CHEFCHAOUEN, NORTH-WEST MOROCCO, USING REMOTE SENSING AND GIS: A WEIGHTED OVERLAY ANALYSIS APPROACH

Lahcen DAHMANI, Said LAARIBYA, Hafida NAIM & Turgay DINDAROGLU 1

DOI: 10.21163/GT_2025.202.01

STUDY OF THE IMPACT OF CLIMATE CHANGE ON TOURISM ACTIVITIES USING REMOTE SENSING IN THE CARPATHIAN REGION

Mykola DEPUTAT, Khrystyna TERLETSKA, Vasyl ZHUPNYK, Pavlo HORISHEVSKYI & Dmytro KASIYANCHUK 15

DOI: 10.21163/GT_2025.202.02

HYDRODYNAMIC MODELING OF POLLUTANT DISTRIBUTIONS FROM THE BERA WATERSHED AND ITS IMPACT TO THE COASTAL AREA OF SALEH BAY, WEST NUSA TENGGARA, INDONESIA

Amar Malikal RAHMAN, Dini PURBANI, Syamsul B. AGUS, Taslim ARIFIN, Yulius YULIUS, Aprizon PUTRA, Aida HERIATI, Joko PRIHANTONO, Rudhy AKHWADY, Agus SUFYAN, Eva MUSTIKASARI, Sri Endah PURNAMANINGTYAS, Rinny RAHMANIA, Muhammad RAMDHAN, Arya NINGSIH, Sadad SADAD & Didik Wahju HENDRO TJAHJO 31

DOI: 10.21163/GT_2025.202.03

HABITAT ASSESSMENT OF WHALE SHARKS (RHINCODON TYPUS) IN SALEH BAY, INDONESIA: LINKING CHLOROPHYLL-A AND SEA SURFACE TEMPERATURE USING AQUA MODIS DATA

Thalia Putri HERDIANTI, Yulius YULIUS, Syamsul B. AGUS, Taslim ARIFIN, Aprizon PUTRA, Joko PRIHANTONO, Aida HERIATI, Sri Turni HARTATI, Rudhy AKHWADY, Devi D. SURYONO, Rinny RAHMANIA, Muhammad RAMDHAN, Arif HILMAWAN, Arya NINGSIH, Sadad SADAD, Mudjijono MUDJIJONO & Abdul ASYIRI 52

DOI: 10.21163/GT_2025.202.04

CREATION OF TECHNIQUE FOR ASSESSING ABOVE GROUND BIOMASS AND CARBON SEQUESTRATION USING UNMANNED AERIAL VEHICLES

Teerawong LAOSUWAN, Tanutdech ROTJANAKUSOL, Wutthisat CHOKKUEA, Mehsa SINGHARATH & Jumpol ITSARAWISU 65

DOI : 10.21163/GT_2025.202.05

USING GEOSPATIAL TECHNOLOGY TO ANALYSE VEGETATION VULNERABILITY: APPLICATION TO PRISHTINA, KOSOVO
Albert BERILA, Florim ISUFI & Ferat KRASNIQI 79
DOI : 10.21163/GT_2025.202.06

THE EFFECT OF LAND USE PATTERNS ON FLOOD VULNERABILITY LEVELS. CASE STUDY: WEST LOMBOK REGENCY, WEST NUSA TENGGARA PROVINCE, INDONESIA
I Wayan YASA, Heri SULISTIYONO, Muhajirah MUHAJIRAH, Dewandha Mas AGASTYA & Unsila T. ARTAWAN 97
DOI: 10.21163/GT_2025.202.07

GIS AND AHP-BASED FLOOD ZONING AND CONSERVATION STRATEGIES IN THE TARUSAN WATERSHED, INDONESIA
Eri BARLIAN, Iswandi UMAR, Indang DEWATA, Triyatno TRIYATNO, Aprizon PUTRA, Eva MUSTIKASARI, Sri Endah PURNAMANINGTYAS, Erfan Andi HENDRAJAT, Serly Mutia SARI, Yulius YULIUS & Dewi Rahmadani SIREGAR 114
DOI: 10.21163/GT_2025.202.08

ASSESSING THE SUSTAINABILITY OF LAGOON-BASED ENVIRONMENTAL WATERFRONT IN THE COASTAL ZONE OF PARIAMAN CITY, INDONESIA
Olivia OKTORIE, Indang DEWATA, Eri BARLIAN, Dedi HERMON & Aprizon PUTRA 134
DOI: 10.21163/GT_2025.202.09

PREDICTING FOREST FIRE HOTSPOTS IN KALIMANTAN USING BEST SUBSET VARIABLE SELECTION, REGULARIZED REGRESSION MODEL, AND BAYESIAN MODEL AVERAGING
Sri NURDIATI, I Wayan MANGKU, Isnayni Feby HAWARI & Mohamad Khoirun NAJIB 150
DOI : 10.21163/GT_2025.202.10

FORECASTING REGIONAL TOURISM FLOWS IN ALBANIA USING ARIMA AND SPATIAL ANALYSIS: A DATA-DRIVEN APPROACH BASED ON NATIONAL ACCOMMODATION STATISTICS
Medjon HYSENAJ & Ditmira TAHIRI 179
DOI: 10.21163/GT_2025.202.11

PREDICTING EARTHQUAKE POTENTIAL THROUGH MORPHODEFORMATION MODELING USING SENTINEL-1A IMAGERY IN THE SINGKARAK SEGMENT, INDONESIA
Triyatno TRIYATNO, Dipo CAESARIO, Febriandi FEBRIANDI, Beni AULIA & Azhari SYARIEF 190
DOI: 10.21163/GT_2025.202.12

A COMPARATIVE EVALUATION OF GEOREFERENCING TECHNIQUES IN UAV PHOTOGRAMMETRY: A CASE STUDY FROM THE CZECH REPUBLIC
Velile MOYO & Michal KAČMAŘÍK 204
DOI: 10.21163/GT_2025.202.13

AN ANALYSIS OF ECONOMIC CROP PLANTING CALENDAR USING DATA FROM THE MODERATE RESOLUTION IMAGING SPECTRORADIOMETER ON THE TERRA SATELLITE

Jumpol ITSARAWISUT, Tanutdech ROTJANAKUSOL, Chaiphat PLYBOUR, Mehsa SINGHARATH & Teerawong LAOSUWAN 218
DOI: 10.21163/GT_2025.202.14

GEOGRAPHICALLY WEIGHTED REGRESSION (GWR) MODEL FOR ANALYZING FACTORS OF LAND SUBSIDENCE IN JAKARTA PROVINCE

Cahyadi SETIAWAN, Fauzi Ramadhoan A'RACHMAN, Ode Sofyan HARDI, Ika Muti RAHMAH, Muhammad DEFFRY, Zidan FURQON, Nabilah Firdha KHAIRUNNISA & Muhammad Wahyu WARDANA . 229
DOI: 10.21163/GT_2025.202.15

SPATIO-TEMPORAL MODELING FOR THE ANALYSIS OF HYDROLOGICAL DROUGHT AND ITS IMPACT ON RICE PRODUCTION IN THE UPPER BENGAWAN SOLO BASIN, CENTRAL JAVA, INDONESIA

Santhyami SANTHYAMI, Jumadi JUMADI, Kuswaji Dwi PRIYONO, Triastuti RAHAYU, Dewi Novita SARI, Murnira OTHMAN & Rudiyanto RUDI 253
DOI: 10.21163/GT_2025.202.16

LINKING TROPHIC STATE INDEX TO HIGH RESOLUTION SATELLITE IMAGERY DATA OF MRICA RESERVOIR, BANJARNEGARA – CENTRAL JAVA

Yoga Candra DITYA, Muhammad RAMDHAN, Siswanta KABAN, Gema WAHYUDEWANTORO, Suryo KUSUMO, Agus Djoko UTOMO, Sigid HARIYADI, Majariana KRISANTI & Luky ADRIANTO 269
DOI: 10.21163/GT_2025.202.17

PREDICTION OF SPATIAL LAND USE LAND COVER CHANGES IN BOVEN DIGOEL, SOUTH PAPUA IN 2031 AND 2041 USING LCM AND CA-MARKOV MODELS

Dewi Novita SARI, Muhammad Hafizh Fadhl MUTASHIM, Frichelia Varadhita RESTUVICA, Kusuma Prayoga Basuki PUTRA, Aziz Akbar MUKASYAF, Nirma Lila ANGGANI & Ayodya Rido NUGRAGA ... 283
DOI: 10.21163/GT_2025.202.18

GIS-BASED PREDICTION OF WATER QUALITY INDEX USING MACHINE LEARNING: A CASE STUDY OF THE THA CHIN RIVER, THAILAND

Pasin PROMHAN & Sitang PILAILAR 303
DOI: 10.21163/GT_2025.202.19

COMPARISON OF Triple-Dip LA NIÑA IN 2020-2023 WITH STRONG AND WEAK LA NIÑA EVENTS ON INDONESIAN RAINFALL AND SST

Gangga Dara DESTYANO, Anindya WIRASATRIYA, Muhammad ZAINURI, Yusuf Jati WIJAYA, Bayu MUNANDAR & Muhammad HELMI 319
DOI: 10.21163/GT_2025.202.20

GIS-BASED ANALYSIS OF SLOPE, LANDSLIDE AND FLOOD HAZARDS, AND LAND USE INTEGRATED WITH INDIGENOUS KNOWLEDGE IN NAGARI SIJUNJUNG, INDONESIA

HARYANI, Eri BARLIAN, I Nengah TELA, Ezra ADITIA & Aprizon PUTRA 336
DOI: 10.21163/GT_2025.202.21

DEVELOPMENT AND ASSESSMENT OF LANDSLIDE SUSCEPTIBILITY IN THE PROVINCE OF CHEFCHAOUEN, NORTH-WEST MOROCCO, USING REMOTE SENSING AND GIS: A WEIGHTED OVERLAY ANALYSIS APPROACH

Lahcen DAHMANI [1*], Said LAARIBYA[1], Hafida NAIM [2], Turgay DINDAROGLU [3]

DOI: 10.21163/GT_2025.202.01

ABSTRACT

This study maps landslide susceptibility in the Chefchaouen region of northwestern Morocco using remote sensing and Geographic Information Systems (GIS) with a weighted overlay analysis approach. Key environmental factors considered include slope, aspect, elevation, vegetation cover, and soil characteristics. The results show a Kappa coefficient of 0.72, indicating substantial agreement between observed and expected accuracies. The user's and producer's accuracy for low susceptibility areas is 75%, for medium susceptibility areas is 85%, and for high susceptibility areas is 80%. These findings indicate a good match between the model's predictions and actual field conditions. Validation of the Landslide Susceptibility Zoning (LSZ) map revealed that most high-risk areas are located on steep slopes in the northern and western regions of Chefchaouen. Nine major landslide-prone zones were identified, providing crucial information for stakeholders to formulate effective mitigation measures. Despite several limitations, such as the temporal scope of data and the resolution of satellite imagery, this research offers significant insights into landslide risk management in the Chefchaouen region. Future perspectives include integrating long-term climate change scenarios and improving methodology to better capture local geological complexity. This study emphasizes the importance of sustainable land and vegetation management practices to reduce landslide risks.

Key-words: *Landslide Susceptibility Assessment, Remote Sensing Analysis, LULC, Chefchaouen, Weighted Overlay Analysis.*

1. INTRODUCTION

Landslides, considered ordinary natural disasters, pose a threat to human life. Various factors, such as slope, altitude, precipitation, and more, can influence landslide incidence (Marín-Rodríguez et al. 2024). In our study region, satellite imagery is employed to recognize and assess the impact of these elements on landslide occurrences (Ali et al., 2023; Arumugam et al., 2023). The Rif mountains are located in the north-western part of Morocco. Chefchaouen considered a captivating geographical landscape marked by intricate topographical features (**Fig. 1**) and a variety of climatic conditions (Cheddadi et al. 2015; Muller et al. 2015).

Chefchaouen's susceptibility to various geomorphological processes, especially landslides, underscores the necessity of unraveling intricate interactions shaped by human activities (Bukhari et

[1] *Faculty of Humanities and Social Sciences, Laboratory of Territories, Environment, and Development, Ibn Tofail University, Kenitra, Morocco.* [*] *Corresponding author (LD) lahcen.dahmani@uit.ac.ma; (SL) said.laaribya1@uit.ac.ma.*

[2] *Faculty of Humanities and Social Sciences, Geosciences Laboratory, Ibn Tofail University, Kenitra, Morocco. (HN) Naim.hafida@uit.ac.ma*

[3] *Faculty of Forestry, Department of Forest Engineering, Karadeniz Technical University, Trabzon, Türkiye. (TD) turgay.dindaroglu@ktu.edu.tr*

al. 2023; Obda et al. 2024). Urbanization, agriculture, and deforestation affect land use, vegetation, and slope stability.

Geospatial data and GIS techniques were used to map and assess landslide susceptibility in Chefchaouen. (Laaribya et al. 2021; Arumugam et al. 2023). These technologies serve as indispensable tools, providing a comprehensive view of the spatial allocation and intensity of landslides.

The selection of Chefchaouen as the focal point of this study was grounded in its susceptibility to natural disasters, particularly landslides. Factors such as local slope, orientation, curvature, lithology, geology, and drainage characteristics accentuate the heightened risk of landslides in this region (Chebli et al. 2021; Ali et al. 2023). Moreover, Chefchaouen's complex topography and climatic variability present a distinctive challenging terrain, necessitating comprehensive research on landslides (El Amiri et al. 2024; Ghallab et al. 2024).

As natural disasters, including landslides, continue to pose imminent threats to lives, economic assets, and environmental sustainability (Sharma et al. 2024; Tayebi et al. 2024), this study aims to contribute invaluable insights into effective disaster preparedness, mitigation, and sustainable land management in Chefchaouen.

This research aims to investigate the relationship between physiographic characteristics and landslide vulnerability in Chefchaouen using advanced remote sensing and GIS technologies. The dual objectives are to create a detailed landslide susceptibility map and assess how integrating remote sensing and GIS parameters can refine vulnerability cartography. The results will help identify high-risk areas and develop targeted conservation and restoration strategies.

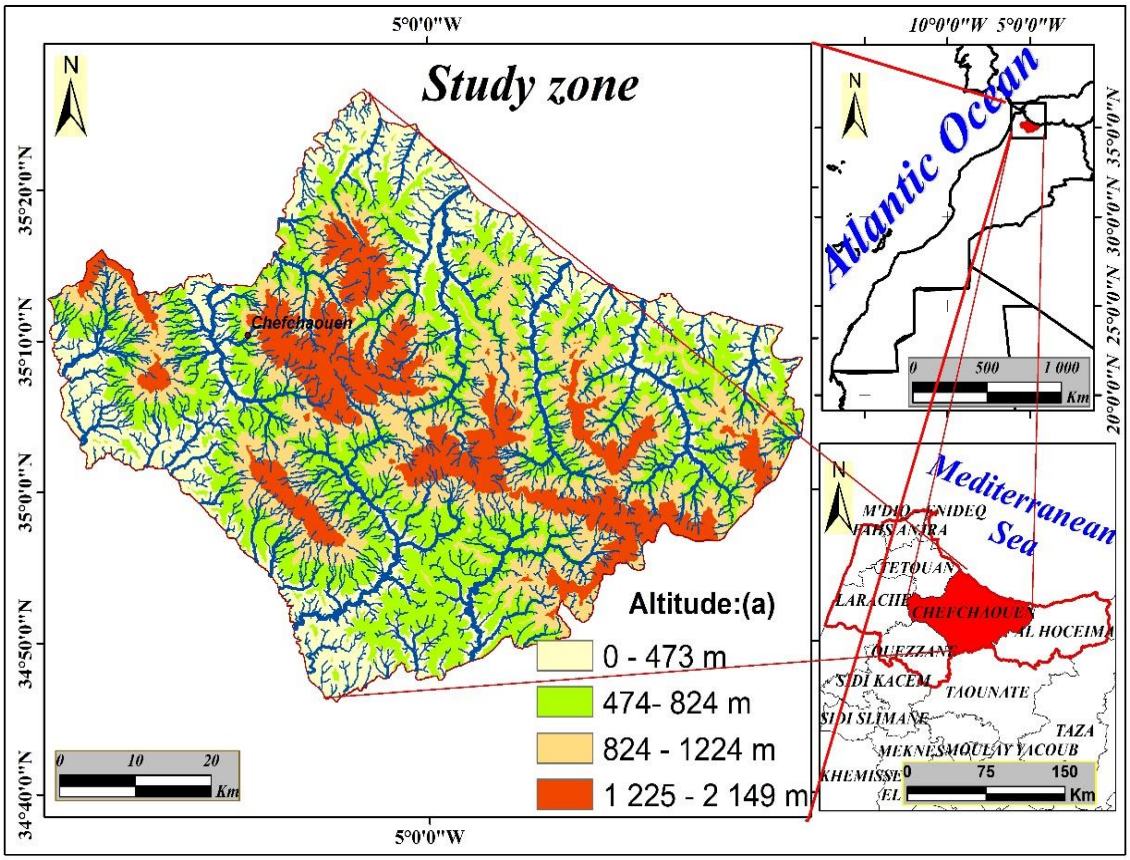

Fig. 1. Provides a visual representation of the study area, highlighting its geographical features and spatial extent.

2. STUDY AREA

Unsupervised classification using the ISODATA algorithm identified LULC categories like settlements, forests, agriculture, and water bodies in 2022. The results will be validated through field visits (**Fig. 2**). Thus, we have measured flows of different nature. **Table 1** shows an example of indicators of material and energy flows of urban environment for subsystem of city economy, which includes 16 indicators.

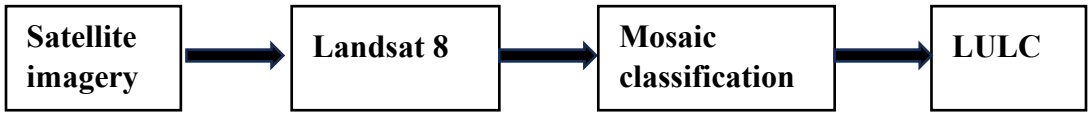

Fig. 2. Visually represents the unsupervised classification process, outlining the steps involved in identifying changes in LULC patterns as proposed by Lu et al. (2019) and Verma and Jana (2019).

3. COLLECTION AND ANALYSIS OF DATA

3.1. Lithology

Chefchaouen, situated in the Rif Mountains of Morocco, has a geological landscape primarily composed of sedimentary rocks and flysch formations. The combination of this geological makeup, rugged terrain, rock weathering, clay layers, tectonic activity, and heavy rainfall contribute to the region's susceptibility to landslides. These factors lead to slope instability, posing significant risks to infrastructure and the local population (Chalouan et al. 2008; Morino, Coratza & Soldati 2022) (**Fig. 3a**).

3.2. Precipitation

The northern and western parts of Chefchaouen have altitudes of over 825 meters and are considered the areas most affected by landslides. Rainfall in the Chefchaouen region generally increases from south to north (**Fig. 3b**). This rainfall distribution makes the northern and slightly western parts of the region more prone to landslides. The rainy season extends from November to March, when it rains the most is most intense. Heavy rainfall during this period increases water pressure on the ground, weakening the slope and increasing the danger of landslides. As a result, regions with a higher risk are more prone to landslides. Rainfall data show that the Chefchaouen region in northern Morocco receives its heaviest rainfall in December January, February, and March. This period corresponds to the main rainy season within a specified locality (El Kharim et al., 2021a; Salhi et al., 2019).

3.3. Lineament density

The geologically complex Chefchaouen region is characterized by a dense network of linear features known as lineaments, which play a significant role in influencing landslides (Ramli et al. 2010a; Obda et al. 2024). These features create weaknesses in the rock formation, enhance water infiltration and erosion, and can potentially act as slip planes. Moreover, lineaments serve as pathways for groundwater flow, which contributes to soil saturation (Wu et al. 2021). Therefore, it is essential to map and analyze these features to effectively assess risk areas and guide geological hazard management in Chefchaouen's mountainous terrain (El Kharim et al., 2021c; Ramli et al., 2010b; Sadiq et al., 2022b) (**Fig. 3c**).

3.4. Land Use and Land Cover (LULC)

Landslides are generally influenced by land use and land cover (LULC) (Dahmani et al., 2024; Laaribya et al., 2024). the map depicting LULC in the study area, shown in **figure 3d**, classifies the whole area into seven distinct categories using unsupervised classification. These are urban areas (12%), dense forests (19%), plantations (14%), agriculture (21%), mixed residential and agricultural areas (11%), other (17%), and water bodies (7%) (**Fig. 4**).

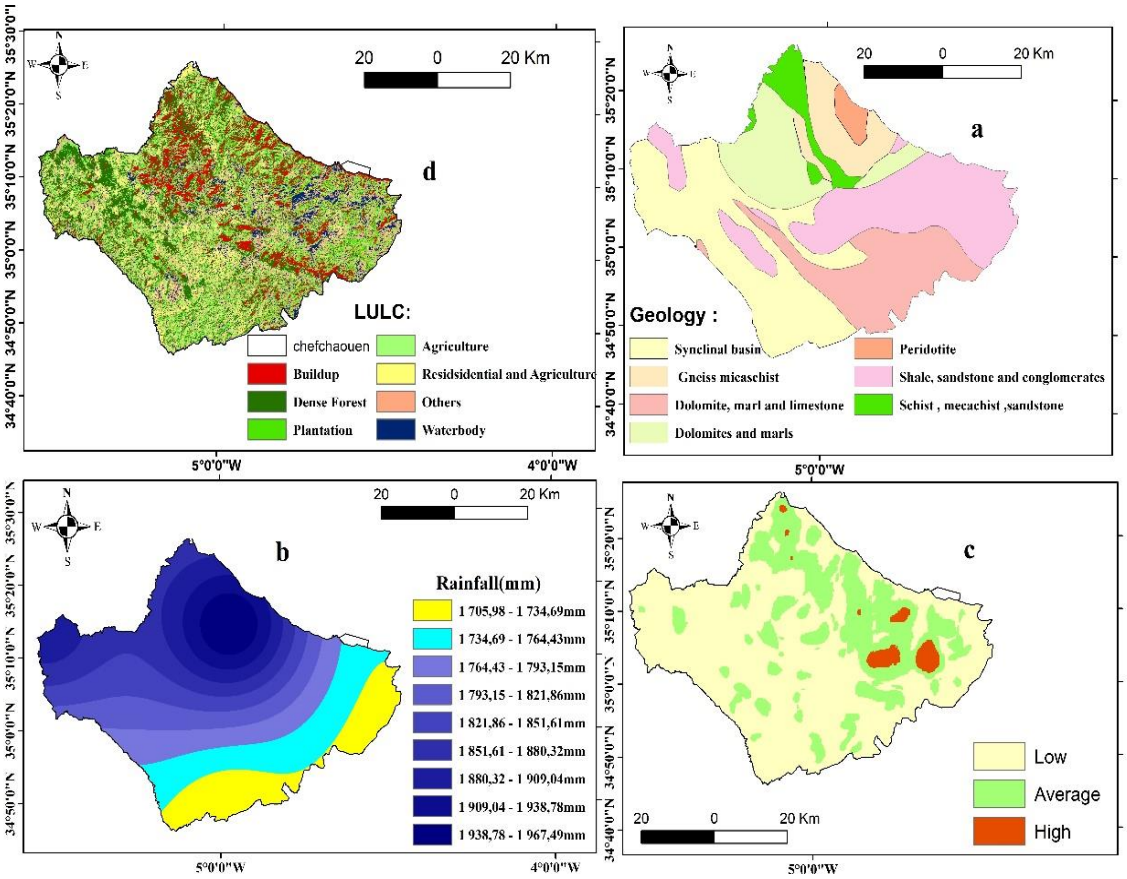

Fig. 3. a**)** Lithology Map of Chefchaouen, Morocco (Mastere, Van Vliet-Lanoë & Brahim 2013; Obda et al. 2024) (*Modified and Simplified*); b**)** illustrates the rainfall map of the Chefchaouen study area, depicting the spatial distribution of precipitation and its potential impact on landslide susceptibility; c**)** dense network of linear features; d**)** LULC.

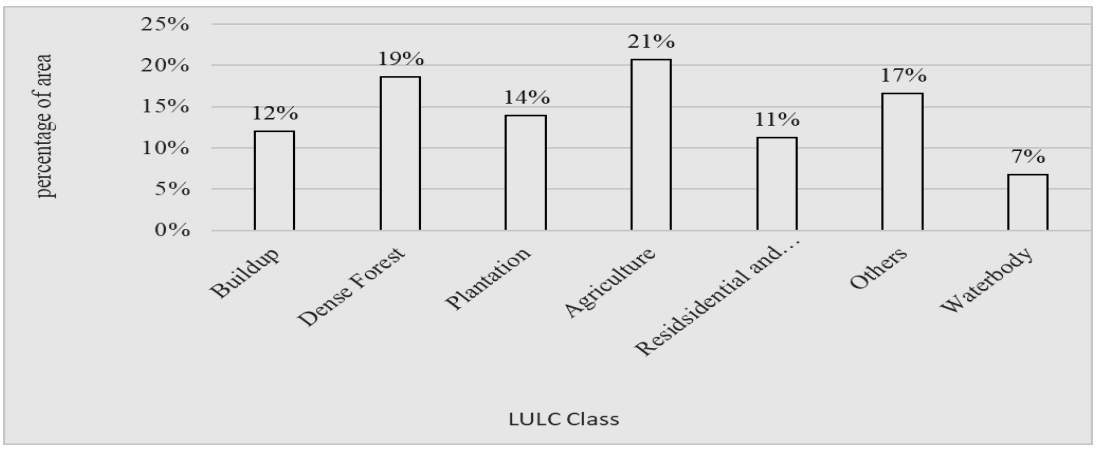

Fig. 4. Exploring the graph showing the percentage of land use and occupation by zone in the Chefchaouen study area, providing insights into spatial variations in human-environment interactions.

3.5. Elevation

Large-scale landslides are crucial factors influencing landslides (El Jazouli, Barakat & Khellouk 2019; Wu et al. 2023). An elevation model with a precision of 30 m was created using ArcGIS technology. **Figure 1** a depicts the geographical setting of the research region on the elevation map is created using DEM (digital terrain model) and exists classified into four types: 0-473 m, 474-824 m, 825-1224 m, and 1225-2149 m. The altitude of Chefchaouen and its rainfall distribution highlight the vulnerability of the northern and western regions, emphasizing the interplay between high rainfall, altitude, and landslide risk. The distribution of altitudes in the Chefchaouen region is shown in **figure 5-a1**.

3.6. Slope

The incline, which represents the steepness of a surface, is generally acknowledged that more inclined slopes are prone to landslides because of gravitational factors. (Maleika 2020; Zhao, Liu & Xu 2021). In this study, slope data were extensively utilized to create a landslide vulnerability map. The incline map, generated from Digital Terrain Model (DTM) data, is divided into four categories: 0-14, 15-34, 35-54, and 55-75 degrees (**Fig. 5b**). As the slope increases, the peak stress at the base of the slope inclines, steeper slopes become more likely to experience distortion and collapse According to the classification, the study area, particularly the northern regions, features steep slopes ranging from 54 to 74 degrees. Notably, the city of Chefchaouen and the northern and northeast regions exhibit slopes steeper than 35° (El Kharim et al., 2021a; Jin et al., 2022). Landslides within the study region are concentrated on slopes in mountainous areas exceeding 10°, with the 0 to 14° slope areas experiencing no landslide events (Dahmani et al., 2024), map and graphical data in the **figure 5-b1**.

3.7. Aspect

The terrain slope is generally measured in degrees and varies from 0 to 360 degrees. This is an important variable in landslide research, because it influences solar radiation, wind, precipitation, and instability conditions (Auflič et al. 2023). According to Somnath and colleagues (2019), the ground experiences varying amounts of solar radiation depending on its slope, which affects vegetation cover, surface evaporation and the landslides that occur

In **figure 5c**, an aspect maps the segmentation derived from the DEM data for the region under analysis.is illustrated, categorized into segments oriented towards the northeast, southeast, southwest, and northwest directions. This division is attributed to the influence of solar radiation, landslides occur more frequently in the west, northwest, and southwest than in the east, according to the data from the aspect map and **figure 5-c1**, North-East (N-E): 25%, East-South (E-S): 23%, Southwest (S-W): 26%, West-North (W-N): 25%.

Table 1.

Slope classes and their percentage distribution in the study area.

Slope (degree)	Percentage distribution	Where
0 - 14	38%	predominantly in the south and west.
15 – 34	55%	mainly in the southwest, west, and east
35 - 54	6%	primarily in the north, northeast, and southeast.
55 - 75	1%	mainly in the north near the city of Chefchaouen

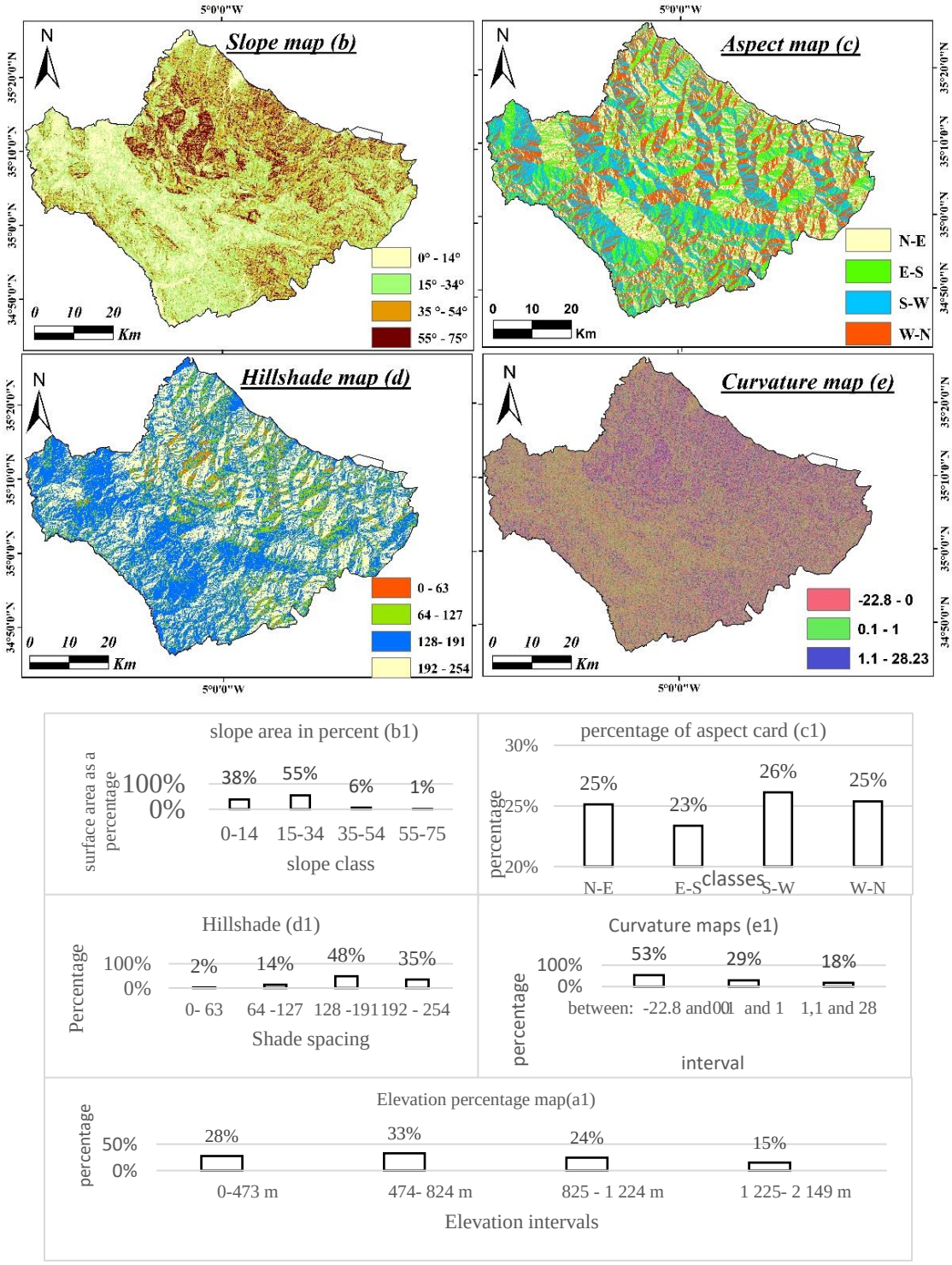

Fig. 5. Percentage distribution of factors: slope map (b); aspect map (c); hillslope map (d); curvature map (c); slope area in percentage (b1); percentage of aspect card (c1); hillshade percentage (d1); cuvature map percentage (e1); elevation percentage (a1).

3.8. Hillshade

Chefchaouen shadow map provides information about solar radiation on different mountain slopes, the intensity of shadows and changes in solar radiation in the region. It can also be used to assess the effects of shading on phenomena such as sunlight availability, soil temperature, and plant growth. (**Fig. 5**). A more detailed analysis of the shade map of the Chefchaouen Mountains requires, in addition to the map itself, information on the method of map creation, the shade parameters, and the specific objective of the study (**Fig. 5d**) (Qi et al. 2021). **Figure 5-d1** are shown the distribution in percentage of each class.

3.9. Curvature

The orientation of slopes concerning topographic slopes is typically measured in north latitude and ranges from 0 degrees to 360 degrees. This factor is pivotal in landslide occurrence research as it influences slope radiation, wind direction, precipitation, and failure conditions (Pacheco Quevedo et al. 2023) impact of solar radiation on the ground varies with slope, affecting vegetation density, soil erosion the process of evaporation, leading to landslides. Solar slopes retain less water due to the process of evaporation by solar radiation, as explored by various researchers (Arumugam et al. 2023). Consequently, plants located on sunlit slopes, including grasses, survive drought and radiation better. For the specific case of Chefchaouen province in northern Morocco, this study shows that the slope orientation map obtained from DEM data comprises segments northeast, southeast, southwest, and northeast. to the west (**Fig. 5e**) (Liu et al. 2021).

Under the influence of solar radiation, landslides occur more often in the west, northwest, and southwest directions than in the probable directions, and a smaller curvature indicates an effect (Jerez et al. 2021; Jin et al. 2022). Analysis of the curvature map reveals significant variations that could influence landslide susceptibility. **Figure 5e** and **figure 5-e1** show the distribution of curvature in the study area.

4. METHODS

4.1. Inverse Distance Weighting Approach (IDW)

The IDW method performs spatial interpolation by assigning values to points based on their distance, with closer points having greater influence than distant ones. (Li et al. 2020; Maleika 2020). IDW can effectively manage evenly distributed points with a more uniform weight distribution among neighboring points because of its lower power requirement (Arumugam et al., 2023; Kinattinkara, et al., 2020). We collected DGM precipitation data from 1992 to 2022 and interpolated them using the IDW method. A precipitation map was created to display the average precipitation.

4.2. Analyzing with Weighted Overlay Analysis (WOA)

The statistical technique known as Weighted Overlay Analysis (WOA) is frequently employed to allocate weights derived from the interaction incorporating causal factors of landslides considering the occurrence frequency of landslides. This method follows an overlay principle where values are assigned according to the overlay, and this process can be easily expanded to include additional criteria. Each stratum illustrated on the thematic map receives a numerical value based on its significance across all corresponding layers. Subsequently, these weighted layers are overlaid, resulting in the creation of a comprehensive map. Landslide Hazard Zoning Map (LHZ) is produced by overlaying thematic maps using the weighted overlay method. **Figure 6** depicts the comprehensive steps of the preparation procedure.

This method, known as Weighted Overlay Analysis, is a statistical approach used to merge thematic maps. It assigns weights to each map based on its significance, creating a composite map representing an aggregated risk or value. The weight assignment involves allocating weights to each map (e.g., slope, vegetation, proximity to water bodies) based on their presumed impact on the target phenomenon.

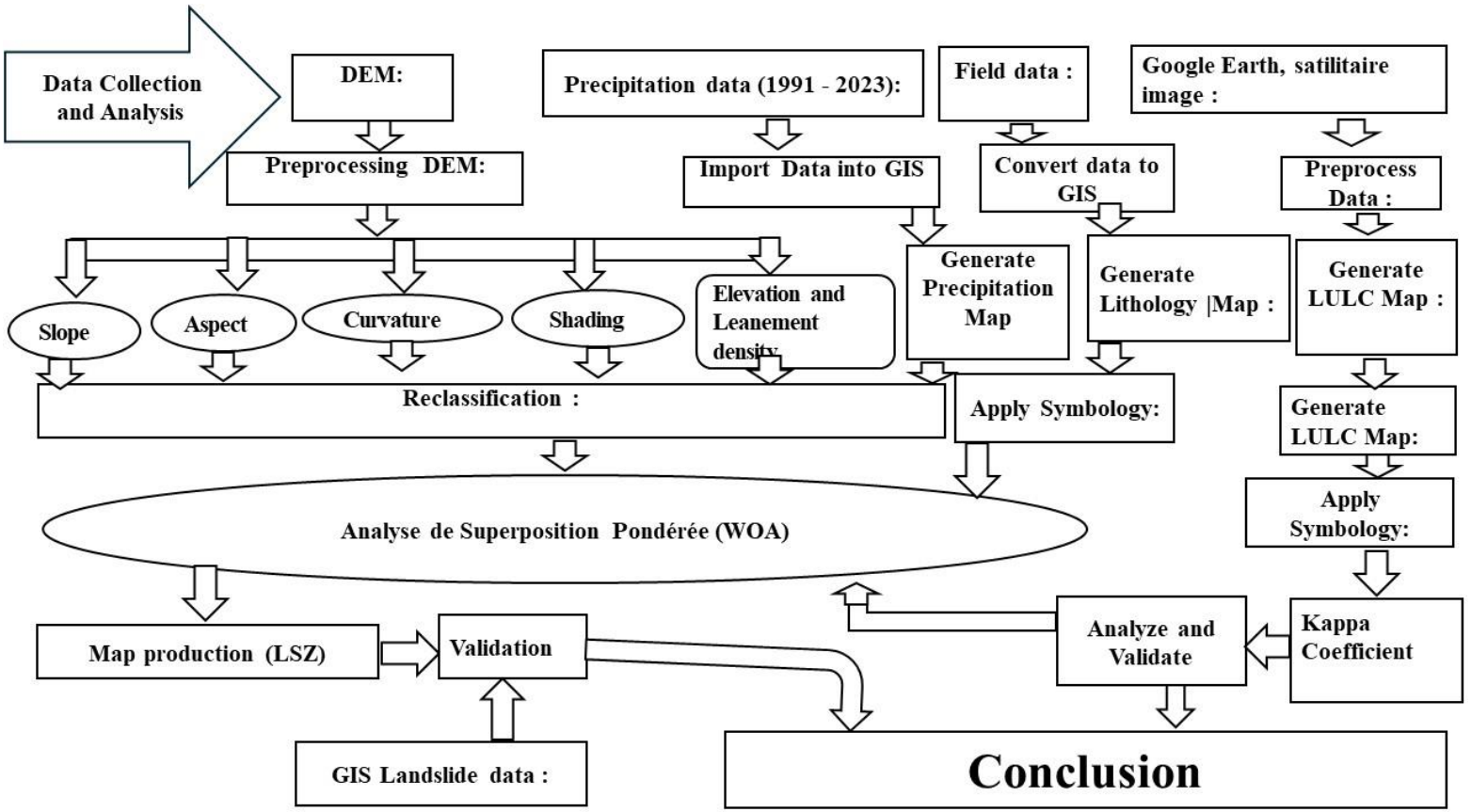

Fig. 6. Workflow for the preparation of landslide zooning map.

Numerical values are then assigned to each map based on specific characteristics, such as a higher slope receiving a higher assigned value. The weighted sum calculation involves multiplying the values of each map by their respective weights and combining the results. The calculation relationship within the WOA can be summarized by the following formula:

Composite Value *= (Map Value 1 × Map Weight 1) + (Map Value 2 × Map Weight 2) +*
+ (Map Value 3 × Map Weight 3) + (Map Value 4 × Map Weight 4+ ... (1)

Composite Value *= (slope value × slope weight) + (aspect value × aspect weight) +*
+ (elevation value × elevation weight) + (lithology value × lithology weight)
+ (land use value × land use weight) + (precipitation value × precipitation weight) +
+ (distance to faults value × distance to faults weight)

Higher values on the composite map indicate a higher level of the studied phenomenon, such as an increased risk of landslides. In summary, WOA combines information from diverse maps, considering their relative importance, to generate a synthetic map highlighting areas of elevated risk. **Figure 6** illustrates the workflow for the preparation of landslide zoning maps.

5. RESULTS AND DISCUSSION

Different types of factors were assigned ordered weights, with larger weights signifying greater impacts on the incidence of landslides (Basharat et al., 2016). The Landslide Susceptibility Zoning (LSZ) map for the study area was constructed, factoring in key elements such as slope, elevation, rainfall and land use and land cover (**Fig. 7**).

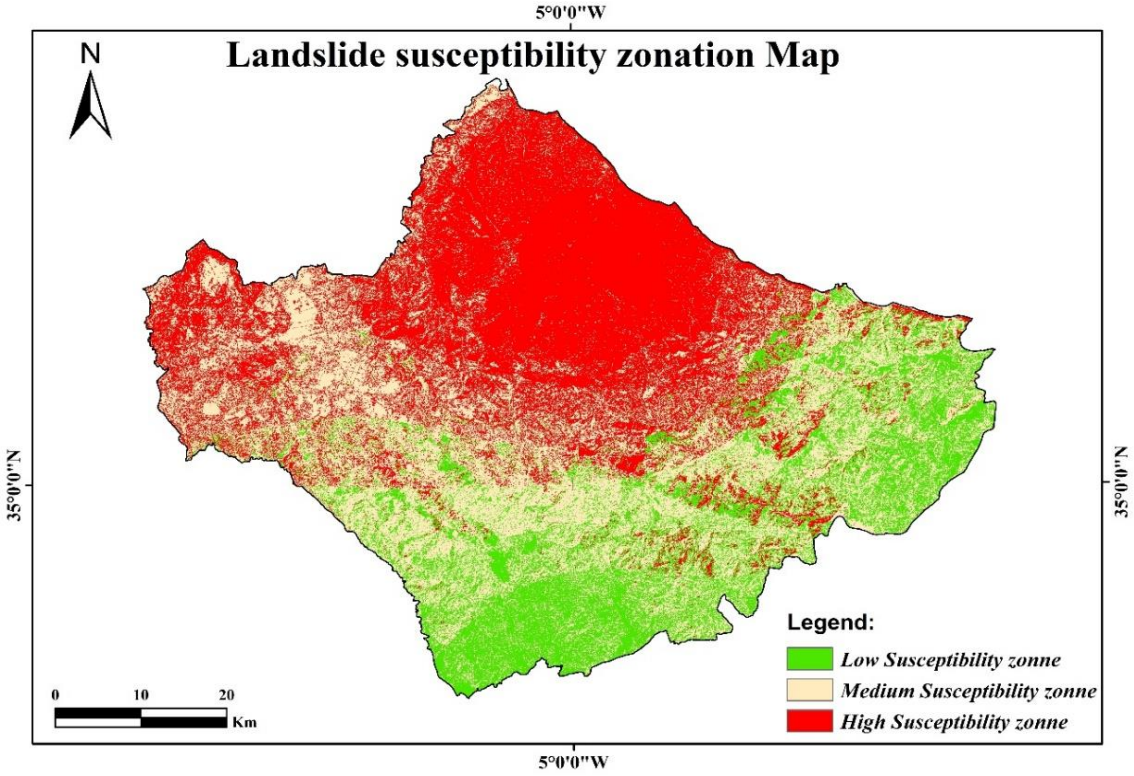

Fig. 7. Illustrates the landslide susceptibility zoning map of the Chefchaouen study area, highlighting different zones based on their susceptibility to landslides.

Using a weighted analysis technique with ArcGIS tools, the LSZ map was created by defining an index map layer for these features. **Table 2** shows the percentage of indicating landslide susceptibility as a function of land use and land cover (LULC). The analysis can be summarized as follows: in areas with low landslide susceptibility (LSZ), dense forests and plantations were the highest proportions (6% and 5%, respectively). Agricultural, mixed, other and water areas have a proportion of 2%. For average landslide susceptibility (LSZ), agricultural and other zones had the highest proportions (9% each), followed by dense forests (8%) and mixed zones (6%). Built-up areas, plantations and water areas have a lower proportion (2%, 5% and 2% respectively). In terms of high landslide susceptibility (LSZ), built-up and agricultural areas represent the highest proportion (10% each), followed by other areas (6%) and dense forests (5%). Plantations, mixed zones and water areas have a lower proportion (4%, 3% and 1% respectively), suggesting that built-up agricultural areas are more likely to be affected by landslides, while water areas are the least likely (**Table 2**).

Table 2.

The distribution of LULC types according to LSZs in the Chefchaouen study area, providing insights into the spatial variation of land cover within different susceptibility zones.

LSZ	LULC						
	Buildup	**Dense Forest**	**Plantation**	**Agriculture**	**Mixed**	**Others**	**Water**
Low	0%	6%	5%	2%	2%	2%	4%
Medium	2%	8%	5%	9%	6%	9%	2%
High	10%	5%	4%	10%	3%	6%	1%

5.1. Accuracy Assessment of Geological Factors Influencing Landslides

The evaluation of precision in land use was conducted using 140 control points (**Table 3**).

Table 3

The accuracy assessment results of land use classification for different land use categories, providing insights into the reliability of classification results for each category.

Land use	Buildup	Dense Forest	Plantation	Agriculture	Mixed	Others	Water	Total	User's accuracy (%)
Buildup	15	1	1	1	1	1	0	20	0,75
Dense Forest	1	16	1	0	1	1	0	20	0,80
Plantation	0	1	16	1	1	1	0	20	0,80
Agriculture	0	0	1	14	0	5	0	20	0,70
Mixed	2	0	0	1	15	2	0	20	0,75
Others	2	2	1	3	2	10	0	20	0,50
Water	0	0	0	0	0	0	20	20	1,00
Total	20	20	20	20	20	20	20	140	0,76
Producer's accuracy (%)	0,75	0,80	0,80	0,70	0,75	0,50	1,00	0,76	
Kappa									0,72

The Kappa coefficient of 0.72 indicates substantial agreement between observed and expected accuracies. The accuracy assessment of landslide susceptibility mapping (LSZ) was carried out with 60 control points. The results show a user and producer accuracy of 75% for low susceptibility areas, 85% for medium susceptibility areas, and 80% for high susceptibility areas. These accuracy measures provide an evaluation of how well the LSZ map corresponds to the actual distribution of landslide susceptibility categories, demonstrating satisfactory agreement between observed and expected accuracy (**Table 4**).

Table 4.

Agreement between observed and expected accuracy for different land use categories.

Land Use Type	Built-up Areas	Dense Forest Areas	Plantations	Agricultural Areas	Mixed Areas	Other Areas	Water Areas
User' Accuracy	75%	80%	80%	70%	75%	50%	100%
Producer's Accuracy	75%	80%	80%	70%	75%	50%	100%

5.2. Validation of the Landslide Susceptibility Zonation Map

To Field validation at five sites in Chefchaouen confirmed the LSZ map's accuracy (**Fig. 8**). Observations matched predicted susceptibility levels, with minor discrepancies analyzed. This process improved the map's reliability and future mapping techniques.

Fig. 8. Landslides in northern Chefchaouen: recent events and local testimonies (20/07/2024 - 01/08/2024).

5.3. Limitation of The Study

Our landslide susceptibility study in Chefchaouen faces limitations, including restricted temporal data, moderate image resolution, and limited validation sites. Rapid urbanization, climate change scenarios, and geological complexity are not fully captured. The lack of detailed historical landslide data also affects model validation, requiring careful result interpretation and future research.

6. CONCLUSIONS

The results of the association between the Land Use and Land Cover (LULC) maps and landslides reveal crucial information about the susceptibility of different areas.

In the context of the study focused on severe natural disasters, especially landslides, it revealed distinctive geological and climatic conditions leading to frequent occurrences in the northwest region. Factors such as slope, orientation, curvature, hillshade and height are considered to minimize slope stability. This study identified high-risk landslide zones in the north and west regions, mainly on steep slopes. Nine major landslide-prone zones were identified, assisting stakeholders in formulating effective mitigation measures based on Landslide Susceptibility Zone (LSZ) maps.

This study emphasized the importance of comprehensive information from risk areas, providing insights into current and potential landslides. This information proves valuable in mitigating construction challenges related to landslides, and benefits the public, engineers, and urban planners. Effective modeling and implementation of mitigation measures are crucial to addressing landslide risks in the northwest region of Morocco.

According to maps and field visits, deforestation in the northwest and the presence of a water body in the north, due to heavy precipitation from the northern regions as opposed to the southern ones, play a part in shaping the present landscape. This research identified high-risk landslide zones in the north and west regions, mainly on steep slopes. Nine major landslide-prone zones are identified, assisting stakeholders in formulating effective mitigation measures based on Landslide Susceptibility Zone (LSZ) map.

REFERENCES

Ali, S.A., Mohajane, M., Parvin, F., Varasano, A., Hitouri, S., Łupikasza, E., Pham, Q.B., 2023. Mass movement susceptibility prediction and infrastructural risk assessment (IRA) using GIS-based Meta classification algorithms. Appl Soft Comput 145, 110591. https://doi.org/10.1016/j.asoc.2023.110591

Arumugam, T., Kinattinkara, S., Velusamy, S., Shanmugamoorthy, M., Murugan, S., 2023. GIS based landslide susceptibility mapping and assessment using weighted overlay method in Wayanad: A part of Western Ghats, Kerala. Urban Clim 49, 101508. https://doi.org/10.1016/j.uclim.2023.101508

Auflič, M.J., Herrera, G., Mateos, R.M., Poyiadji, E., Quental, L., Severine, B., Peternel, T., Podolszki, L., Calcaterra, S., Kociu, A., Warmuz, B., Jelének, J., Hadjicharalambous, K., Becher, G.P., Dashwood, C., Ondrus, P., Minkevičius, V., Todorović, S., Møller, J.J., Marturia, J., 2023. Landslide monitoring techniques in the Geological Surveys of Europe. Landslides 20, 951–965. https://doi.org/10.1007/s10346-022-02007-1

Bukhari, M.H., da Silva, P.F., Pilz, J., Istanbulluoglu, E., Görüm, T., Lee, J., Karamehic-Muratovic, A., Urmi, T., Soltani, A., Wilopo, W., Qureshi, J.A., Zekan, S., Koonisetty, K.S., Sheishenaly, U., Khan, L., Espinoza, J., Mendoza, E.P., Haque, U., 2023. Community perceptions of landslide risk and susceptibility: a multi-country study. Landslides 20, 1321–1334. https://doi.org/10.1007/S10346-023-02027-5/METRICS

Chalouan, A., Michard, A., Kadiri, K. El, Negro, F., Frizon de Lamotte, D., Soto, J.I., Saddiqi, O., 2008. The Rif Belt. Lecture Notes in Earth Sciences 116, 203–302. https://doi.org/10.1007/978-3-540-77076-3_5

Chebli, Y., Otmani, E., National, I., Agronomique, D.R., Mohamed, B., Abdellah, B., 2021. du Rif occidental (Chefchaouen) 180–200.

Cheddadi, R., Nourelbait, M., Bouaissa, O., Tabel, J., Rhoujjati, A., López-Sáez, J.A., Alba-Sánchez, F., Khater, C., Ballouche, A., Dezileau, L., Lamb, H., 2015. A History of Human Impact on Moroccan Mountain Landscapes. African Archaeological Review 32, 233–248. https://doi.org/10.1007/S10437-015-9186-7/METRICS

Dahmani, Lahcen, Laaribya, S., Naim, H., Dindaroglu, T., 2024. Landslide hazard mapping in Chefchaouen, Morocco: AHP-GIS integration. International Journal of Environmental Studies. https://doi.org/10.1080/00207233.2024.2412483

Dahmani, L., Laaribya, S., Naim, H., Tunguz, V., Dindaroglu, T., 2024. Assessing landslide susceptibility in Chefchaouen, Morocco: An application of the landslide numerical risk factor method for sustainable urban development and disaster risk management. Biosyst Divers 32, 389–397. https://doi.org/10.15421/012442

El Amiri, B., Azmi, R., Laaribya, S., Dani, B., Sibaoueih, M., Omar, B., 2024. The Drought Resilience of Vast Livestock Reared in Agropastoral Versus Sylvo-Agro-Pastoral Systems in Morocco 99–110. https://doi.org/10.1007/978-3-031-59603-2_7

El Jazouli, A., Barakat, A., Khellouk, R., 2019. GIS-multicriteria evaluation using AHP for landslide susceptibility mapping in Oum Er Rbia high basin (Morocco). Geoenvironmental Disasters 6. https://doi.org/10.1186/s40677-019-0119-7

El Kharim, Y., Bounab, A., Ilias, O., Hilali, F., Ahniche, M., 2021a. Landslides in the urban and suburban perimeter of Chefchaouen (Rif, Northern Morocco): inventory and case study. Natural Hazards 107, 355–373. https://doi.org/10.1007/S11069-021-04586-Z/METRICS

El Kharim, Y., Bounab, A., Ilias, O., Hilali, F., Ahniche, M., 2021b. Landslides in the urban and suburban perimeter of Chefchaouen (Rif, Northern Morocco): inventory and case study. Natural Hazards 107, 355–373. https://doi.org/10.1007/S11069-021-04586-Z/METRICS

Ghallab, A., Boubekraoui, H., Laaribya, S., Ben-Said, M., 2024. Potential natural vegetation pattern based on major tree distribution modeling in the western Rif of Morocco. IForest 17, 405. https://doi.org/10.3832/IFOR4602-017

Jerez, S., Palacios-Peña, L., Gutiérrez, C., Jiménez-Guerrero, P., María López-Romero, J., Pravia-Sarabia, E., Montávez, J.P., 2021. Sensitivity of surface solar radiation to aerosol-radiation and aerosol-cloud interactions over Europe in WRFv3.6.1 climatic runs with fully interactive aerosols. Geosci Model Dev 14, 1533–1551. https://doi.org/10.5194/gmd-14-1533-2021

Jin, H., Wang, S., Yan, P., Qiao, L., Sun, L., Zhang, L., 2022. Spatial and temporal characteristics of surface solar radiation in China and its influencing factors. Front Environ Sci 10, 1–15. https://doi.org/10.3389/fenvs.2022.916748

Kinattinkara, S., Arumugam, T., Poongodi, K.S., 2020. Surveillance of groundwater quality of selected rural and industrial areas of Coimbatore: A GIS Approach. IOP Conf Ser Mater Sci Eng 955. https://doi.org/10.1088/1757-899X/955/1/012083

Laaribya, S., Alaoui, A., Ayan, S., Benabou, A., Labbaci, A., Ouhaddou, H., Bijou, M., 2021. Prediction by maximum entropy of potential habitat of the cork oak (Quercus suber L.) in Maamora Forest, Morocco. Forestist 71, 63–69. https://doi.org/10.5152/forestist.2021.20059

Laaribya, S., Alaoui, A., Ayan, S., Dindaroglu, T., 2023. Changes in the Potential Distribution of Atlas Cedar in Morocco in the Twenty-First Century According to the Emission Scenarios of RCP 4,5 and RCP 8,5. Forestist. https://doi.org/10.5152/forestist.2023.0004

Li, Z., Zhang, X., Zhu, R., Zhang, Z., Weng, Z., 2020. Integrating data-to-data correlation into inverse distance weighting. Comput Geosci 24, 203–216. https://doi.org/10.1007/s10596-019-09913-9

Liu, C., Huang, Y., Wu, F., Liu, W., Ning, Y., Huang, Z., Tang, S., Liang, Y., 2021. Plant adaptability in karst regions. J Plant Res 134, 889–906. https://doi.org/10.1007/s10265-021-01330-3

Maleika, W., 2020. Inverse distance weighting method optimization in the process of digital terrain model creation based on data collected from a multibeam echosounder. Applied Geomatics 12, 397–407. https://doi.org/10.1007/s12518-020-00307-6

Marín-Rodríguez, N.J., Vega, J., Zanabria, O.B., González-Ruiz, J.D., Botero, S., 2024. Towards an understanding of landslide risk assessment and its economic losses: a scientometric analysis. Landslides 1–17. https://doi.org/10.1007/S10346-024-02272-2/FIGURES/12

Mastere, M., Van Vliet-Lanoë, B., Brahim, L.A., 2013. Cartographie de l'occupation des sols en relation avec les mouvements gravitaires et le ravinement dans le Rif nord-occidental (Maroc). http://journals.openedition.org/geomorphologie 335–352. https://doi.org/10.4000/GEOMORPHOLOGIE.10328

Mohamed Mastere, B.V.V.-L. et L.A.B., n.d. Cartographie de l'occupation des sols en relation avec les mouvements gravitaires et le ravinement dans le Rif nord-occidental (Maroc).

Morino, C., Coratza, P., Soldati, M., 2022. Landslides, a Key Landform in the Global Geological Heritage. Front Earth Sci (Lausanne) 10, 864760. https://doi.org/10.3389/FEART.2022.864760/BIBTEX

Muller, S.D., Rhazi, L., Andrieux, B., Bottollier-Curtet, M., Fauquette, S., Saber, E.R., Rifai, N., Daoud-Bouattour, A., 2015. Vegetation history of the western Rif mountains (NW Morocco): origin, late-Holocene dynamics and human impact. Veg Hist Archaeobot 24, 487–501. https://doi.org/10.1007/S00334-014-0504-9/METRICS

Obda, O., El Kharim, Y., Obda, I., Ahniche, M., Sahrane, R., 2024. Landslide Susceptibility Assessment and Factors' Selection Using the GIS Matrix Method (GMM) in Chefchaouen Province (Northern Morocco). Advances in Science, Technology and Innovation 197–199. https://doi.org/10.1007/978-3-031-43218-7_46

Pacheco Quevedo, R., Velastegui-Montoya, A., Montalván-Burbano, N., Morante-Carballo, F., Korup, O., Daleles Rennó, C., 2023. Land use and land cover as a conditioning factor in landslide susceptibility: a literature review. Landslides 20, 967–982. https://doi.org/10.1007/s10346-022-02020-4

Qi, X., Li, Q., Jiao, Y., Tan, F., 2021. Experimental study on response law and failure process of slopes in fully weathered granites under precipitation infiltration. Environ Earth Sci 80, 685. https://doi.org/10.1007/s12665-021-09995-8

Ramli, M.F., Yusof, N., Yusoff, M.K., Juahir, H., Shafri, H.Z.M., 2010a. Lineament mapping and its application in landslide hazard assessment: a review. Bulletin of Engineering Geology and the Environment 2009 69:2 69, 215–233. https://doi.org/10.1007/S10064-009-0255-5

Ramli, M.F., Yusof, N., Yusoff, M.K., Juahir, H., Shafri, H.Z.M., 2010b. Lineament mapping and its application in landslide hazard assessment: a review. Bulletin of Engineering Geology and the Environment 2009 69:2 69, 215–233. https://doi.org/10.1007/S10064-009-0255-5

RGPH, 2014a. RGPH. CHEFCHAOUEN PROVINCE. https://doi.org/http://www.hcp.ma/

RGPH, 2014b. RGPH. CHEFCHAOUEN PROVINCE. https://doi.org/http://www.hcp.ma/

Sadiq, S., Muhammad, U., Fuchs, M., 2022. Investigation of landslides with natural lineaments derived from integrated manual and automatic techniques applied on geospatial data. Natural Hazards 110, 2141–2162. https://doi.org/10.1007/S11069-021-05028-6/METRICS

Salhi, A., Martin-Vide, J., Benhamrouche, A., Benabdelouahab, S., Himi, M., Benabdelouahab, T., Casas Ponsati, A., 2019. Rainfall distribution and trends of the daily precipitation concentration index in northern Morocco: a need for an adaptive environmental policy. SN Appl Sci 1, 277. https://doi.org/10.1007/s42452-019-0290-1

Sharma, A., Sajjad, H., Roshani, Rahaman, M.H., 2024. A systematic review for assessing the impact of climate change on landslides: research gaps and directions for future research. Spatial Information Research 32, 165–185. https://doi.org/10.1007/S41324-023-00551-Z/METRICS

Tayebi, S., Jabed, M.A., Ruano, A.L., Lee, G.O., da Silva, P.F., Ahmed, S., G, E.V.A., Dahal, R.K., Soltani, A., Imran Khan, M., Rahman, M.A., Islam, M.A., Haque, U., 2024. Stakeholder perspectives on landslide triggers and impacts in five countries. Landslides 1–11. https://doi.org/10.1007/S10346-024-02270-4/TABLES/3

Wu, J., Zhang, Ya, Yang, L., Zhang, Yongxian, Lei, J., Zhi, M., Ma, G., 2023. Identifying the essential influencing factors of landslide susceptibility models based on hybrid-optimized machine learning with different grid resolutions: a case of Sino-Pakistani Karakorum Highway. Environmental Science and Pollution Research 30, 100675–100700. https://doi.org/10.1007/s11356-023-29234-w

Wu, X., Meng, Z., Dang, X., Wang, J., 2021. Effects of rock fragments on the water infiltration and hydraulic conductivity in the soils of the desert steppes of Inner Mongolia, China. https://swr.agriculturejournals.cz/doi/10.17221/107/2020-SWR.html 16, 151–163. https://doi.org/10.17221/107/2020-SWR

Zhao, Z., Liu, Z. yuan, Xu, C., 2021. Slope Unit-Based Landslide Susceptibility Mapping Using Certainty Factor, Support Vector Machine, Random Forest, CF-SVM and CF-RF Models. Front Earth Sci (Lausanne) 9, 1–16. https://doi.org/10.3389/feart.2021.589630

STUDY OF THE IMPACT OF CLIMATE CHANGE ON TOURISM ACTIVITIES USING REMOTE SENSING IN THE CARPATHIAN REGION

***Mykola DEPUTAT*[1], *Khrystyna TERLETSKA*[1], *Vasyl ZHUPNYK*[1], *Pavlo HORISHEVSKYI*[1], *Dmytro KASIYANCHUK*[2*]**

DOI: 10.21163/GT_2025.202.02

ABSTRACT

Climate change is having a significant impact on the tourism and recreational potential of the Ukrainian Carpathians, particularly in mountainous regions that rely on winter sports, hiking and ecotourism. Rising temperatures, decreasing snow cover and changing precipitation patterns threaten the viability of ski resorts and winter tourism. This study aims to assess the impact of climate change on tourism development in the Carpathians through remote sensing, GIS modelling and analysis of long-term climate data. The research is based on a comparative analysis of historical climate trends, satellite imagery and mathematical modelling of temperature and precipitation dynamics. Using Google Earth Engine and remote sensing techniques, key indicators such as snow cover area, albedo index and normalised difference snow index (NDSI) were analysed to assess changes in seasonal conditions. The results show a significant decrease in snow depth (approximately 4.4 mm per year) and snow-covered area (0.21% per year). The data indicate a shift in seasonality, a shortening of the winter season and an increase in climate-related risks to tourism infrastructure. Despite the negative impacts on winter tourism, climate change may increase opportunities for summer and autumn tourism, such as hiking and cycling. To mitigate these challenges, adaptation strategies need to be developed, including snowmaking technologies, diversification of tourism services, and sustainable environmental management. This study provides critical insights into the long-term dynamics of climate change in the Carpathians and supports strategic planning for sustainable tourism development.

Key-words: *Climate; Tourism; Snow cover; Geostatistics; Spatial analysis; GIS; Remote Sensing; Carpathians; Forecast.*

1. INTRODUCTION

Climate change is having a significant impact on winter tourism in the Carpathian region, especially in the context of decreasing snowfall, which makes ski resorts less attractive to tourists and less competitive. Winter tourism, and ski resorts in particular, are highly dependent on snowfall as it is the main natural resource that sustains the resorts during the winter season. Reduced precipitation in the form of snow leads to a shorter ski season, and in some places, there is not enough snow at all. Research shows that mountain landscapes and communities are particularly vulnerable to climate change, which has a direct impact on tourism.

In the Carpathian Mountains, an important mountainous region for Ukraine, rich in biodiversity, climate change is causing the winter tourist season to shrink, affecting infrastructure development and recreational opportunities. Climate change makes it impossible to plan new infrastructure facilities

[1]*Department of Tourism, Hotel and Restaurant Business, King Danylo University,Ivano-Frankivsk, Ukraine. (MK) mykola.m.deputat@ukd.edu.ua; (KT) khrystyna.m.terletska@ukd.edu.ua; (VZ) vasyl.v.zhupnyk@ukd.edu.ua; (PH) pavlo.gorishevskyy@ukd.edu.ua.*

[2]*Department of Geodesy and Land Management, Ivano-Frankivsk National Technical University of Oil and Gas, Ivano-Frankivsk, Ukraine. * Corresponding author: (DK) dima_kasiyanchuk@ukr.net*

for snow sports, and only two of the existing snow slopes (Bukovel and Dragobrat) are currently operating steadily. Resorts such as Bukovel and Dragobrat are focusing their efforts on using artificial snow to compensate for the lack of natural cover. Smaller resorts that do not have sufficient financial resources to provide artificial snowmaking cannot operate at full capacity, leading to less competition in the market. The introduction of snowmaking technologies makes it possible to extend the winter season even in the absence of natural snow, but requires significant capital expenditures, energy and water, which may pose additional environmental threats in the context of a shortage of natural resources due to climate change.

Tourism itself is also a significant source of greenhouse gas emissions, further exacerbating the problem of climate change. The impact of artificial snow on the ecosystem, including changes in soil and water resources, can have a negative impact on local biodiversity. In addition, artificial snowmaking is not only economically costly, but also changes the natural landscape of mountainous areas, which can have long-term consequences for environmental sustainability.

In light of these challenges, the question arises: how suitable will the climatic conditions remain for winter tourism in the Carpathian region in the coming decades? To address this question, it is necessary to develop effective adaptation strategies that take into account long-term climate projections. An important step in this direction is to analyse the impact of climate change on the seasonality of tourism and the quality of tourism services.

For this purpose, modern methods of geospatial analysis and satellite image processing are used. Modern geographic information systems (GIS) provide accurate information on the dynamics of snow cover, albedo and other climatic indicators, which allows us to create mathematical models to assess spatial and temporal changes in climatic factors and their impact on various aspects of human activity, including tourism. A large number of available remote sensing images are widely used to map snow cover in mountainous regions. This opens up new opportunities for a detailed assessment of the impact of climate change on the tourism potential of the Carpathian region and the development of strategies for the sustainable development of the tourism industry in the face of climate change.

The Carpathian tourist region (**Fig. 1**) consists of four districts in western Ukraine: Lviv, Ivano-Frankivsk, Zakarpattia and Chernivtsi. The Carpathian tourist region covers an area of 56,600 km^2, which is 9.4% of Ukraine's territory.

Reducing precipitation in the form of snow is an important aspect of ski tourism. Snow is the main natural resource that keeps ski resorts open in winter. However, the Carpathians, as an important mountain region rich in biodiversity, are increasinglay threatened by climate change (Turnock, 2001). Rising temperatures caused by climate change are leading to shorter ski season, and in some areas there is no snow at all. Research (Steiger et al., 2022) shows that mountain landscapes and communities are particularly vulnerable to climate change, which has a direct impact on tourism, and this is the basis for assessing the suitability of weather conditions, organising and planning tourism activities for outdoor recreation using the Holiday Climate Index (HCI) (Magyari-Sáska et al., 2023). Decreasing snow cover has a negative impact on winter tourism, while the impact on summer tourism may fluctuate. This can make ski resorts less attractive to tourists and less competitive. In addition, tourism itself is a significant source of greenhouse gas emissions, further exacerbating the problem of climate change (Steiger et al., 2023). One way to address these issues is to introduce snowmaking technology. This extends the skiing season even in the absence of natural snow. However, in order to develop effective adaptation strategies, it is important to analyse whether climatic conditions will remain suitable for tourism in certain regions and how they may change over time (Nistor et al., 2018; Kovács, Király, 2021).

The process of artificial snowmaking requires significant capital and energy costs and consumes large amounts of water, which can pose a threat to the environment, especially as natural resources become increasingly scarce due to climate change. The development of aerospace remote sensing and computer modelling of energy and mass transfer processes in the Earth's geosphere plays a crucial role in tracking these environmental changes and achieving sustainable development (Lyalko et al., 2022). Artificial snow can have several environmental impacts, including changes in soil composition and water resources, which can affect local ecosystems and biodiversity.

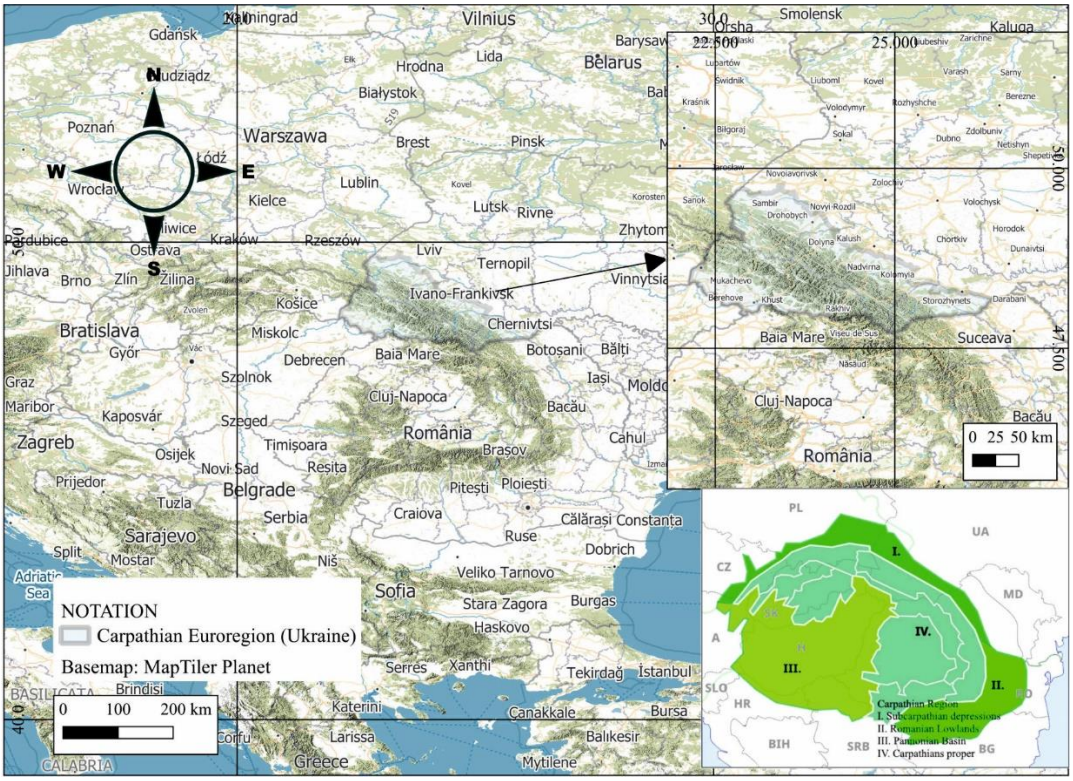

Fig. 1. Map of the Carpathian Euroregion study area within Ukraine (Basemap MapTiler, n.d.).

Remote sensing studies by Kulemin et al (2001) have shown that snow properties, including microwave backscattering properties, depend on many environmental parameters. A large number of available remote sensing images are widely used for snow cover mapping in mountainous regions. However, most studies have focused on quantifying the uncertainty inherent in snow mapping algorithms based on Landsat observations, especially in the context of snowline establishment, which is a key parameter for understanding the spatial and temporal dynamics of snow cover. The study (Xiongxin & Shuang, 2024) provides a comprehensive guide for selecting appropriate snow mapping algorithms and contributes to effective Landsat-based snow monitoring in mountainous regions. It is also worth noting that artificial snowmelt is not only economically costly, but also alters the natural landscape of mountainous areas and may undermine the sustainability of the ecosystem in the long term.

Climate change, changes in the regime of tourist complexes due to insufficient precipitation in winter, and human impact on landscapes are the main issues that require in-depth analysis and research. A detailed analysis of long-term observations of climatic parameters (air temperature, precipitation, duration of snow cover) should be carried out to identify key trends and their impact on tourism activities in the region. This allows us to assess the impact of climate change on the seasonality and quality of tourism services. Modern GIS technologies make it possible to interpret satellite image data for climate change analysis (Burrough, 2001; Odiljon, 2022). They provide accurate information on the dynamics of snow cover, the surface reflectivity index (Albedo) and other indicators that are important for developing mathematical models that allow assessing spatial and temporal changes in climate factors and their impact on various aspects of human activity.

The aim of this study is to quantify the impact of climate change on winter tourism in the Carpathian region of Ukraine, using geospatial analysis of satellite data and statistical modelling to assess changes in snow cover and predict long-term impacts on the tourism industry.

2. STUDY AREA DATA

2.1. Temperature and precipitation

The capabilities of the Google Earth engine, mainly satellite imagery data, allow us to cover a wide range of data that differ in their characteristics in our analysis. In recent decades, the impact on the environment of global temperature fluctuations has been increasingly associated with changes in the seasonality of the seasons. It is important to analyse long-term data of the main meteorological indicators at the initial stage. The period from 1980 to 2024 was chosen as the basis for the analysis. GEE is one of the most widely used methods for modelling.

Coding in JavaScript enables the analysis of available information based on satellite image decryption data.

The average monthly temperature changes fully characterise the main seasons – spring (+1.0 – +12.0ºC), summer (+15.7 – +17.1ºC), autumn (+12.4 – +1.2ºC), winter (-2.3 – -3.0ºC). However, if we look at the dynamic multi-month values, we actually have a situation where the seasons are not so distinct, and seasonal factors can change.

Along with temperature (T), precipitation (P) must be considered. It is an integral part of the climate, especially in mountainous areas. As with temperature, we consider a series of monthly data averaged over many years of observations. Traditionally, the rainiest months are May (300mm), June (317mm) and July (256mm).

But it is important not only to consider seasonality, but also to identify the points of change between temperature and precipitation. According to the analysis, two points can be identified in the summer (first decade of June: T=+15.7° C, P=317mm) and autumn (second half of October: T=4.0 ° C, P=114mm). The rainy period clearly correlates with precipitation during the snowmelt period until June, and from the first half of the year in an opposite phase. July, August, and September de facto become a continuation of the summer season, and are characterised by low precipitation, which has a very negative impact on the hydrological balance of the region's rivers. This is confirmed by other studies (Pona et al, 2016; Kasiyanchuk, 2022). Mid-October becomes the second variable stage between the short autumn period and the onset of cold weather. However, the decrease in air temperature does not lead to the active development of cyclones, and the amount of precipitation is insignificant. This dynamic has been particularly noticeable in recent decades.

Obviously, climate change is one of the main tasks for assessing the impact on the development of the region's tourism and recreational potential. Let's consider the basic seasonal characteristics, allocating summer (June, July, August), autumn (September, October, November), winter (December, January, February) and spring (March, April, May) in the traditional division (**Fig. 2**) with regression equations presented. The linear trend provides a simple and straightforward model for analysing long-term changes, estimating average annual growth and facilitating future forecasts.

Figure 3 shows the results of running a code that represents the long-term average of temperature and precipitation data from 1980 to 2024.

Air temperature as a basis for reflecting global trends is quite characteristic of them, as can be seen from the figure. All seasons show a clear increase in average annual temperature. The average annual temperature increase for spring is +0.041° C, summer – +0.075° C, autumn – +0.051° C, winter – +0.073° C.

Frequent anticyclones that linger in Ukraine cause a decrease in precipitation in the form of rain and a slight increase in the form of snow (mainly sleet), as shown in the graphs in **Figure 3**.

Analysing the trend lines for the seasons, it can be concluded that precipitation decreases in spring, summer, and autumn, and slightly increases in winter. Reduced precipitation in the spring and summer, during the active growing season, negatively affects the microclimate of the region (Ivanyshyn, 2024).

The average annual precipitation is -1.1 mm in spring, -2.2 mm in summer, -0.2 mm in autumn, and +0.9 mm in winter.

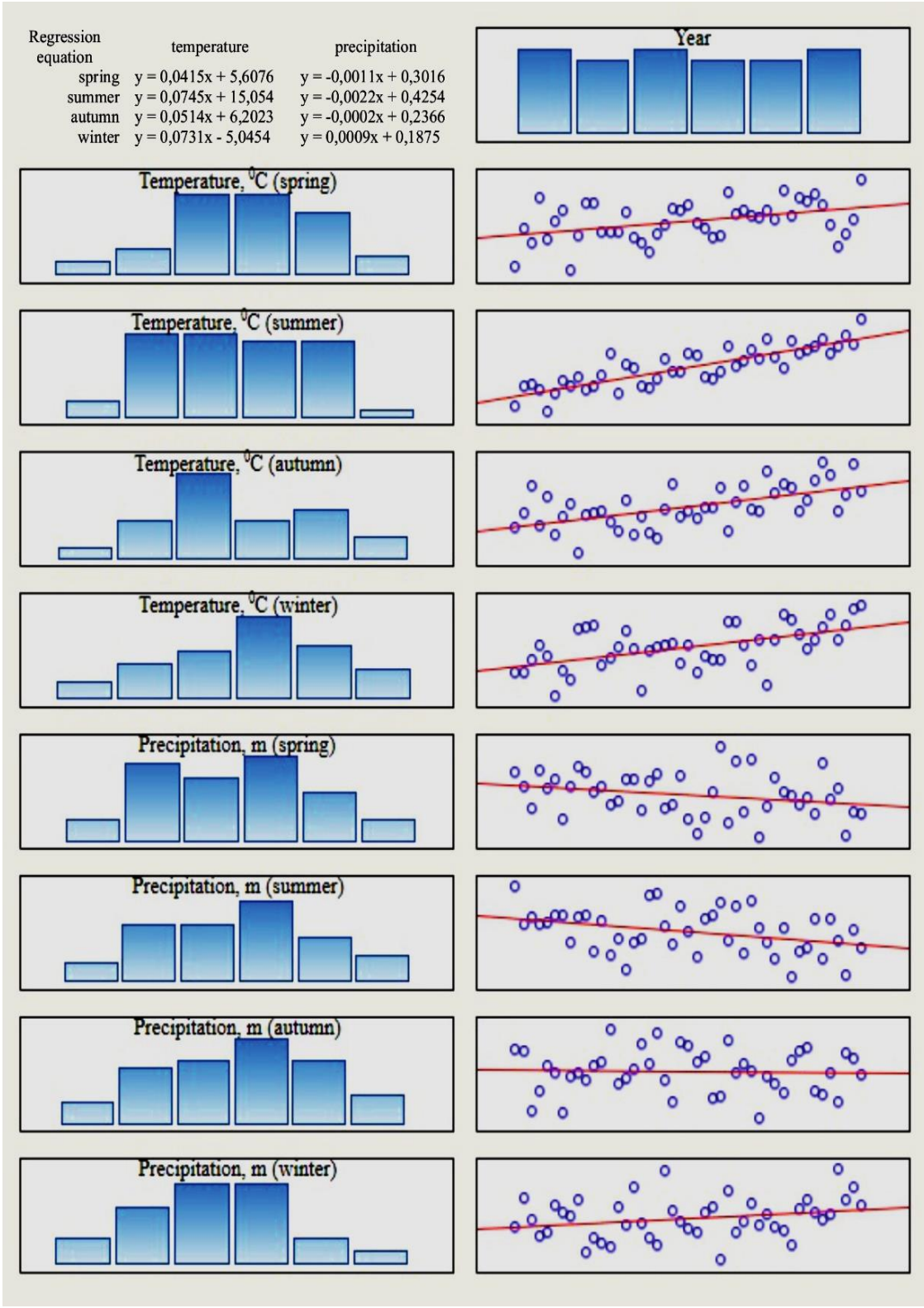

Fig. 2. Average long-term data from 1980 to 2024 by temperature and precipitation.

2.2. Snow parameters

The spatial and temporal variability of seasonal snow cover in mountainous regions is considered a significant knowledge gap in terms of climate, ecosystems and water resources (Gascoin et al., 2024). Three main elements where recent advances in remote sensing of snow and data accumulation promise to deliver significant gains include long-term observations of snow cover, including snow water equivalent, high-resolution snow cover and snow albedo. Various datasets have been used for analysis using the open-source Java Script, including ERA5-Land (Muñoz Sabater, 2019).

ERA5-Land is a reanalysed global atmospheric data set (climate and meteorological data) that has increased resolution compared to ERA5 and provides a consistent view of the evolution of land change over several decades. ERA5-Land was created by replicating the terrestrial component of the ECMWF ERA5 climate analysis. Reanalysis uses the laws of physics to combine model data with observational data from around the world to create a globally complete and consistent dataset. The reanalysis creates data spanning several decades, giving an accurate description of the climate of the past. This dataset includes all 50 variables available in the CDS.

2.3. Snow cover and NDSI

Matson's (1991) research includes comprehensive satellite studies since 1966 on snow cover. In the same year, NOAA satellites were used to produce weekly snow cover maps in the Northern Hemisphere. This 24-year database is available as a digital feed and is updated annually. The digital data can be used to calculate snow cover and create maps of snow frequency and anomalies. In (Wang & Wang, 2024) a new approach for snow mapping was developed using spectral feature fusion and correlation by integrating and analysing the Normalised Forest Snow Difference Index (NDFSI). Normalised Difference Vegetation Index (NDVI) and NDSI indices. High resolution OLI images from Landsat 8 were used to assess the accuracy of the snow maps. Experimental results show that the combination of NDFSI and NDVI indices has great potential for determining the distribution of snow cover in forested areas.

Table 1.

Bands of the ERA5-Land Daily Aggregated - ECMWF Climate Reanalysis.

Name	Units	Description
temperature_2m	*K*	The 2m air temperature is the interpolated temperature at 2 meters above land, sea, or inland waters, considering atmospheric conditions.
snow_cover	*%*	It represents the fraction (0-1) of a grid cell covered by snow, similar to ERA5 cloud cover fields.
snow_density	kg/m^3	Snow density represents the mass of snow per cubic meter in the snow layer, modeled in ECMWF IFS as a single layer over the uppermost soil level, covering all or part of the grid box.
snow_depth	*m*	Snow depth represents the instantaneous grid-box average of snow thickness on the ground, excluding snow on the canopy.
total_precipitation_sum	*m*	Accumulated precipitation includes liquid and frozen water, such as rain and snow, that reaches the Earth's surface. It consists of large-scale precipitation from weather patterns and convective precipitation caused by rising warm air. Precipitation is measured in meters as the depth it would have if evenly spread over the grid box, but observations may differ as they are often localized rather than averaged over a model grid.

2.4. Albedo

Another parameter is albedo, which is an important element in snow cover studies (Calleja, 2019; Laurin, 2022; Feng, 2023). MCD43A3.061 (Schaaf, 2021) is a MODIS (Moderate Resolution Imaging Spectroradiometer) satellite data product that provides daily land surface albedo data with a spatial resolution of 500 m. It is based on combined observations from the Terra and Aqua satellites. **Table 1** provides a list and description of the bands that will be used when writing the code.

3. METHODS

To achieve the main goal, namely modelling the impact of global climate change on tourism and resource potential, a number of steps need to be taken.

1. Determination of the area of the Carpathian Euroregion within the territory of Ukraine, which will serve as the basis for cartographic research:

- use of official geographic data (administrative boundaries, DEM models) to delineate the Ukrainian part of the Carpathian Euroregion;
- loading the relevant layers into QGIS and preparing the basic mapping material.

2. The analysis of the main groups of publicly available data in order to select the optimal ones in terms of factors and duration of observations should focus on:

- availability (NASA, ESA, Copernicus).
- duration of observations (minimum 20-30 years for climate trends).
- spatial resolution (optimally 250 m-1 km for regional analysis).

3. Formation of file data and further programming in the Google Earth Engine in JavaScript:

- uploading satellite data (Landsat, MODIS, Sentinel-2);
- using GEE to automate data collection, filtering, and pre-processing (scaling, normalisation, region cropping);
- creating JavaScript code to calculate time trends.

4. Analysis of meteorological and climatic parameters of the region:

- work with data from ground-based weather stations and reanalysis (ERA5);
- determining trends in temperature, precipitation, humidity and aridity index;
- creation of climate maps in QGIS.

5. Construction of mathematical models to assess the dynamics of temperature (T) and precipitation (P):

- using STATISTICA for cluster analysis;
- create a trend equation (1)

$$T(t) = a \cdot t + b \quad (1)$$

where:

T(t) – the temperature in year t,
a – the slope coefficient (corresponding to the average annual temperature increase),
b – is a constant that determines the temperature level at the beginning of the period;

6. Study of snow cover indicators in the region and check the consistency of trends between different data groups:

- evaluation of MODIS (MOD10A1) and Sentinel-2 satellite data;
- checking the consistency of trends between different data sets.

7. Calculation of the Albedo reflectivity index and snow layer for areas with intensive development of winter sports:

- using Landsat-8 and Sentinel-2 data to calculate Albedo;
- analysis of changes in areas with a high concentration of winter resorts.

8. Comparison of the relationship between snow cover and the Albedo reflectivity index using STATISTICA (correlation analysis).

9. Determination of the normalised differential snow index (formula 2):

$$NDSI = (B3+B11) / (B3-B11) \quad (2)$$

where:

B3 (Green, 560 nm) – reflects snow well,
B11 (SWIR, 1610 nm) – is strongly absorbed by snow;

10. Building maps of dynamic snow layer assessment with comparison of snow cover data and Albedo index:

- creating maps in QGIS with comparison of snow cover and Albedo data;
- analysing changes in the territory over the decades.

4. RESULTS AND DISCUSSIONS

The Carpathian region is quite gradient in terms of climate and is characterised by altitude zonation. Given the main content of the paper, we decided not to divide it according to the stratigraphic basis, since long-term temporal changes will be the same for each zone, which is, in particular, summarised in Ivanyshyn (2024) and Shtohryn (2020). Changes in the seasonality of the seasons are extremely important, especially in reference regions that are important for the sustainable development of communities. The de facto shift, or rather reduction, of seasons from four to three (Kasiyanchuk, 2022), leads to sharp drops and sharp rises in temperature, and a clear division between seasons in long-term analysis is lost.

Analysing geospatial data using Google Earth Engine (GEE) (Gorelick et al., 2017) is done by writing code in JavaScript or Python to work with satellite images.

Code execution involves, first of all, a clear structuring of the main steps that will ensure the correct output:

1) Region Cropping. At the initial stage, all satellite images were cropped outside the study region to ensure that the analysis was carried out exclusively on the territory of interest. For this purpose, the `.clip()` function was used, which cropped the image according to the geometry of the selected area.

2) Image scaling (Scaling). Since data with different resolutions are used (Sentinel-2 with a resolution of 10-20 metres and MODIS with a resolution of 500 metres), the appropriate scaling was used to coordinate the calculations. The scale is set when calculating average index values.

3) Cloud Filtering. This step is described in detail below.

4) Normalisation of data. The Normalised Difference Snow Index (NDSI) was used to estimate the snow cover (formula 2). NDSI is calculated using normalised channel difference methods, such as normalisedDifference ().

5) Along with climatic parameters, it is important *to analyse the depth, area, and volume* of precipitation when studying snow cover. The software code uses ERAS-LAND data. Remote sensing capabilities are broad, but most limited by the level of cloud cover, which should always be taken into account when analysing for the purpose of correct interpretation. **Figure 3** shows the results of three characteristics - ‘snow_cover’, ‘snow_density’, ‘snow_depth’. Their detailed description is given in **Table 1**. As the results of the climate change study showed, with a clear increase in temperature and a decrease in precipitation, the most tourist-loaded mountainous area was chosen as the basis for further analysis in order to reduce the amount of additional calculations and detail the results within the tourist zones. The village of Polianytsia, the village of Verkhovyna, the city of Yaremche and the resort of Bukovel are known among a wide range of holidaymakers as the centre of active development of ski tourism and other recreational activities. The territory within these territorial units is defined as an active recreation area (ARA).

6) Analysis and removal of anomalies: During the results validation phase, additional analysis is performed to identify anomalous values (e.g., too low or high NDSI or albedo values that may be caused by residual clouds or other factors). Anomalies can be filtered out or corrected.

In contrast to the snow cover parameters, we calculated above, we will analyse two important indices, the 8-day average of snow area and Albedo (**Fig. 4**). The latter is an extremely important element of the study of snow cover, water bodies or any other objects with high reflectivity.

Figure 4 shows a graph that clearly indicates that both parameters are dependent, which is typical for the winter period. However, the data sample should be with 0% cloud cover within the study area (we do not exclude satellite images with a higher percentage of cloud cover).

Reducing the thickness of the snow cover changes the temperature regime of the soil, which affects the local flora and fauna, and reduces the supply of meltwater needed for aquatic ecosystems and river basins. This leads to the drying up of springs and disruption of natural hydrological cycles. In addition, snow plays an important stabilizing role, and a lack of it contributes to increased soil erosion.

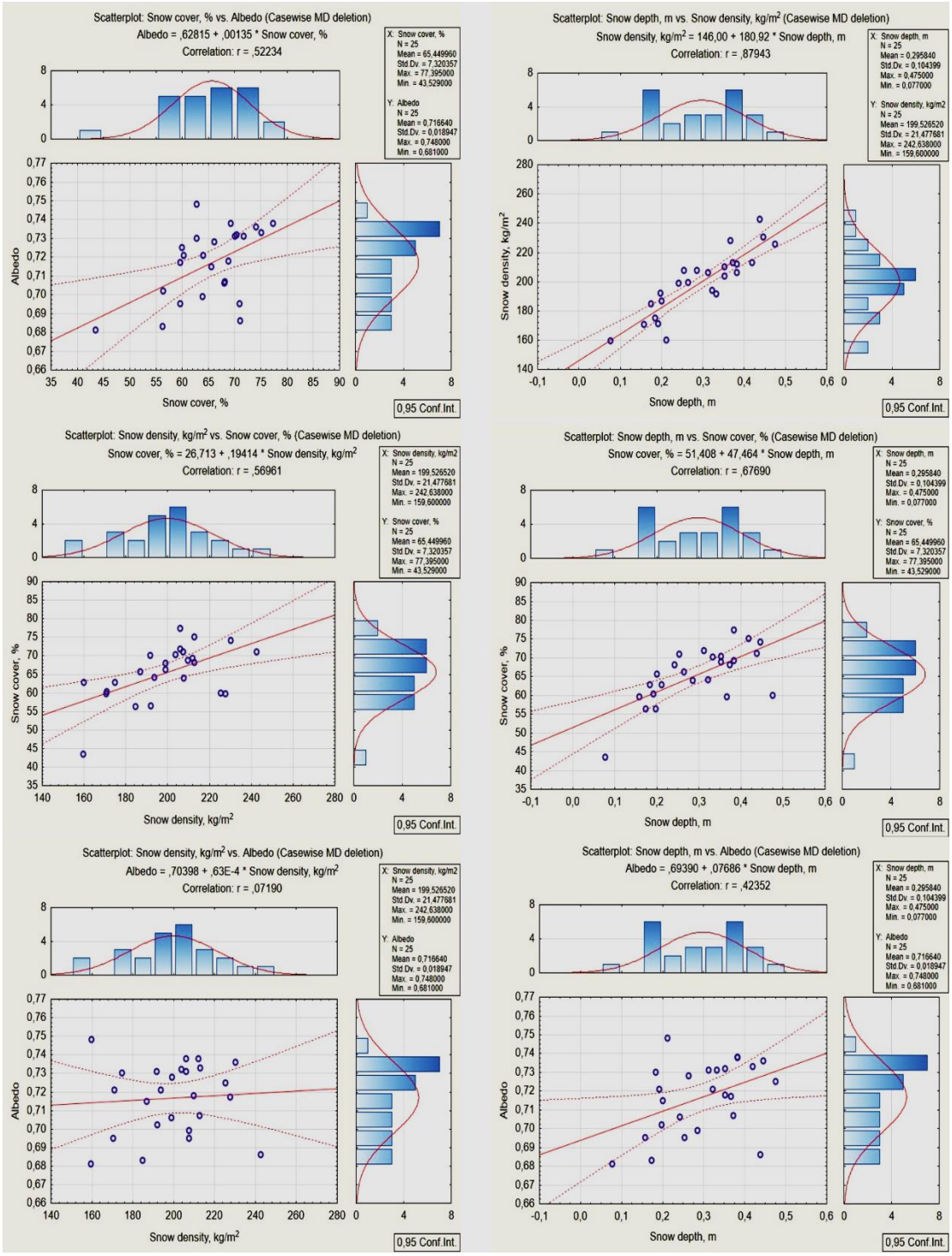

Fig. 3. Statistic of snow parameters from 2000 to 2024.

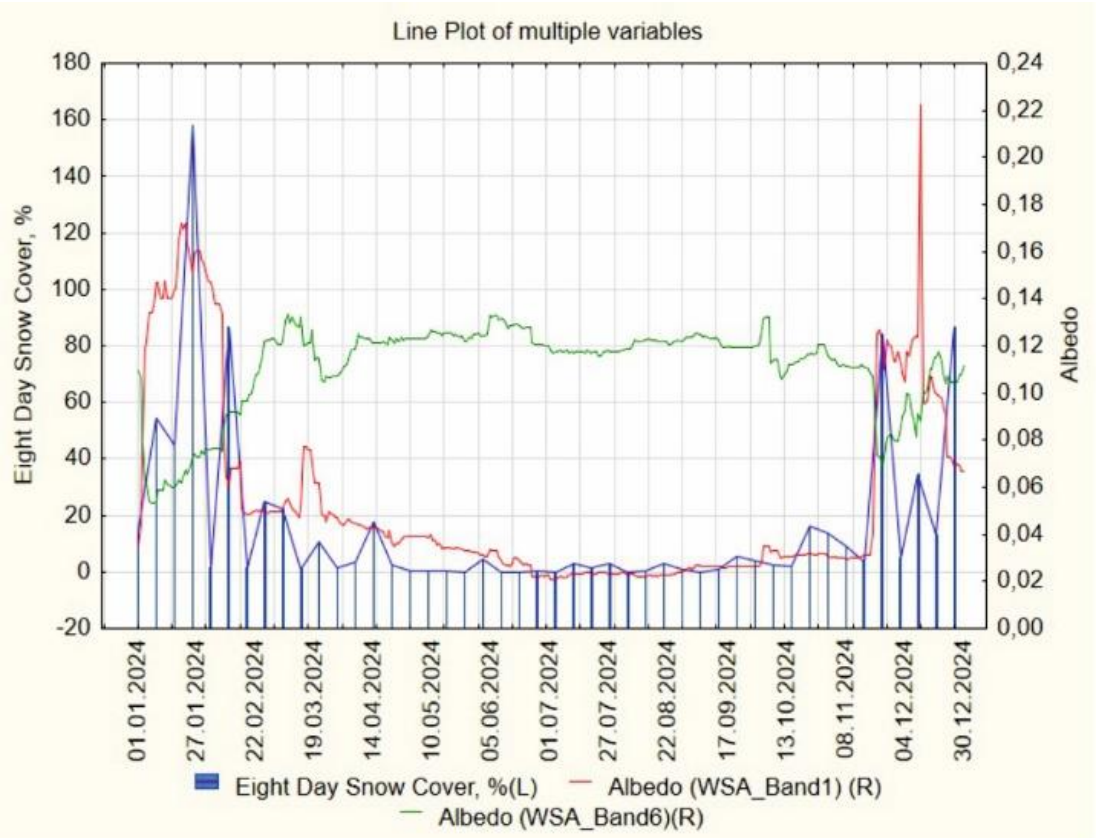

Color map of correlations
N=46 (Casewise deletion of missing data)
r>= -1 -0,80 -0,60 -0,40 -0,20 0 0,20 0,40 0,60 0,80 1

Variable	Eight Day Snow Cover, %	Albedo (WSA_Band1)	Albedo (WSA_Band6)
Eight Day Snow Cover, %	1,000000	0,628590	-0,642249
Albedo (WSA_Band1)	0,628590	1,000000	-0,881005
Albedo (WSA_Band6)	-0,642249	-0,881005	1,000000

Fig. 4. The 8-day average of snow area and Albedo.

In the tourism sector, a decrease in snow cover directly affects winter sports such as skiing and snowboarding. A shorter snow season reduces the profits of tourist complexes and affects local communities that depend on winter tourism revenues. In addition, deteriorating snow conditions may force tourists to choose other regions for their holidays, which will reduce the flow of visitors. In addition, changes in the structure of the snow layer may increase the risk of avalanches, which poses an additional threat to visitors and infrastructure. Thus, the decline in snow cover has a complex negative impact on both the environment and the economic stability of the region.

The resulting correlation coefficient of -0.64 between NDSI and albedo indicates a moderately strong inverse relationship between these indicators. This means that as snow cover decreases (lower NDSI), albedo also decreases, leading to greater solar energy absorption and accelerated snowmelt. This trend may contribute to a further reduction in snow cover in mountainous regions, which will affect the length of the winter season and the quality of the snow cover. For the future of tourism, this could mean a shorter period of winter sports, the need for artificial snowmaking and a general decline in the attractiveness of mountain resorts.

The European Space Agency has a wide range of Sentinel data. The most common way to analyse snow cover today is to estimate the Normalised Differential Snow Index (NDSI) (**Formula 2**). As mentioned above, the main thing in analysing satellite images is the absence of clouds. To compare the relationship between the NDSI and Albedo, the corresponding snow index maps were constructed (**Figure 5**).

In **Figure 5**, **Table 2**, we see the results of snow index decoding for two dates - 26.11.2024 and 28.12.2024. The average NDSI for the ARA is -0.079 and 0.03. On the map, the corresponding colours are interpreted as: black (-1) → no snow, blue (0) → partially snowy surface (coniferous forest zone), white (1) → snow.

For most of the bands (Band1-Band4), albedo significantly decreased from 26.11.2024 to 28.12.2024, Band5 remained almost unchanged, Band6 decreased significantly, and Band7 decreased slightly, but not significantly. While the first one gives us an idea of the vegetation, dense coniferous forests (Ivanyshyn, 2024), channel 6 clearly shows a change in reflectivity that has increased, which corresponds to an increase in snow mass, as shown in **Figure 5**.

The index map for the two dates gives us a clear spatial representation of the snow cover. The decoding allowed us to clearly show the differences between the indices and estimate that as of 28.12.2024, the snow cover was more significant, covering not only the tops of the mountains, but also the areas where ski resorts are located (central part of the ARA). This is where Bukovel is located, as well as some ski lifts in Yablunytsia and Vorokhta.

Data uncertainty is one of the most important limitations in satellite imagery, and the resolution, atmospheric conditions and time interval of the survey can affect the accuracy of the study. When generating the code using the methods described above, these uncertainties were minimised in order to accurately calculate the indices. The only drawback is that the limited frequency of image acquisition does not allow for the assessment of short-term changes in snow cover, which is important for detailed local monitoring and would require additional ground observations.

The importance of understanding the relationship between the parameters defined above is the main element that allows machine learning methods to be used for snow cover assessment. The written code implements a comprehensive approach to satellite image analysis using the Google Earth Engine (GEE) platform. The aim of the work is to classify the land cover in a given study area using Sentinel-2 multispectral data, MODIS temperature data, and the SRTM digital elevation model for snow cover assessment. The main classification tool is the Random Forest algorithm, which allows to effectively take into account various spectral and geophysical characteristics of the surface.

Table 2.

Average albedo value for each band and NDSI by date.

Albedo (Bands) / NDSI	**Date**	
	28.12.2024	**26.11.2024**
Band 1 (Visible Red, 620-670 nm) – displays the red part of the visible spectrum, which is important for studying vegetation	76,111	132,977
Band 2 (NIR, 841-876 nm) – reflects the near-infrared part of the spectrum, which is often used to study water stress and vegetation indices	219,268	263,218
Band 3 (Blue, 459-479 nm) – is used to assess water and atmospheric quality	62,512	126,887
Band 4 (Green, 545-565 nm) – important for studying vegetation	80,692	138,316
Band 5 (NIR, 1230-1250 nm) – helps to assess soil moisture and plant health	195,954	190,526
Band 6 (SWIR, 1628-1652 nm) – used to study snow cover and soil moisture	122,902	89,930
Band 7 (SWIR, 2105-2155 nm) is sensitive to water, important for monitoring glaciers and the water cycle	47,595	43,073
NDSI	0,030	-0,079

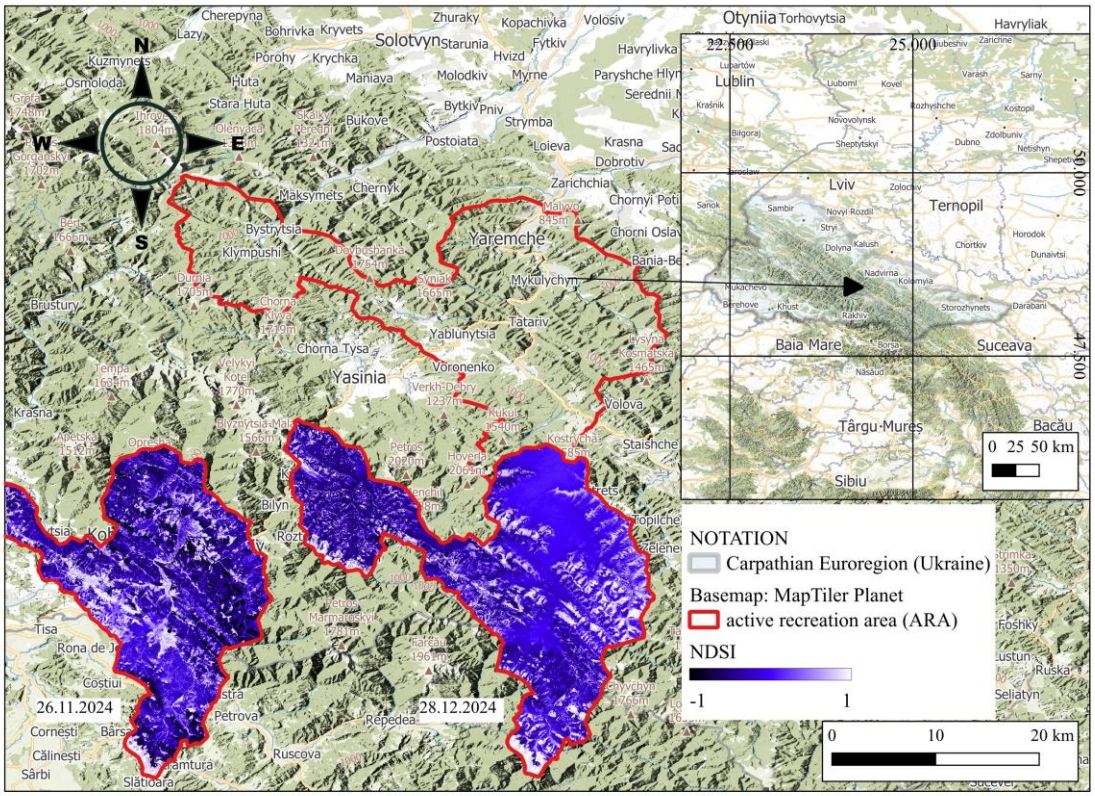

Fig. 5. NDSI map of the active recreation area (ARA) (Basemap MapTiler, n.d.)

At the first stage of the work, the study area is loaded, which is represented as a vector layer (FeatureCollection). This area is used to filter satellite images by geographic boundaries. Sentinel-2 data is loaded for a specific date, namely 28.12.2024, with the percentage of cloud cover taken into account to ensure the quality of the analysis. In addition, MODIS data is loaded to obtain the daily average surface temperature (LST) and SRTM data to obtain information on the height above sea level.

The next step is to calculate spectral indices that allow us to identify key characteristics of the land cover. In particular, we calculate such indices as NDSI (Normalised Difference Snow Index) to detect snow cover, NDVI (Normalised Difference Vegetation Index) to assess vegetation, and NDWI (Normalised Difference Water Index) to detect water bodies. Surface albedo from MODIS data is also loaded, which allows to take into account the reflectivity of the study area. Based on the calculated indices, masks for water bodies and healthy vegetation are created and used for further analysis.

To classify the land cover, a data stack is formed, which includes Sentinel-2 spectral channels, calculated indices, MODIS temperature data and elevation data. This stack is used to prepare the training data, which is generated by sampling pixels from a given geographic area. The Random Forest model is trained using 100 trees and 10 variables for each split. After the model is trained, the image is classified and the results are visualised on the map (**Fig. 6**).

The Random Forest model provides several important additional insights for analysing snow cover and land cover in general. Firstly, it allows to effectively take into account multidimensional spectral and geophysical characteristics, which improves classification accuracy. Secondly, the model provides an assessment of the importance of each feature (e.g., spectral channels, height, temperature), which makes it possible to understand which parameters have the greatest impact on the final classification.

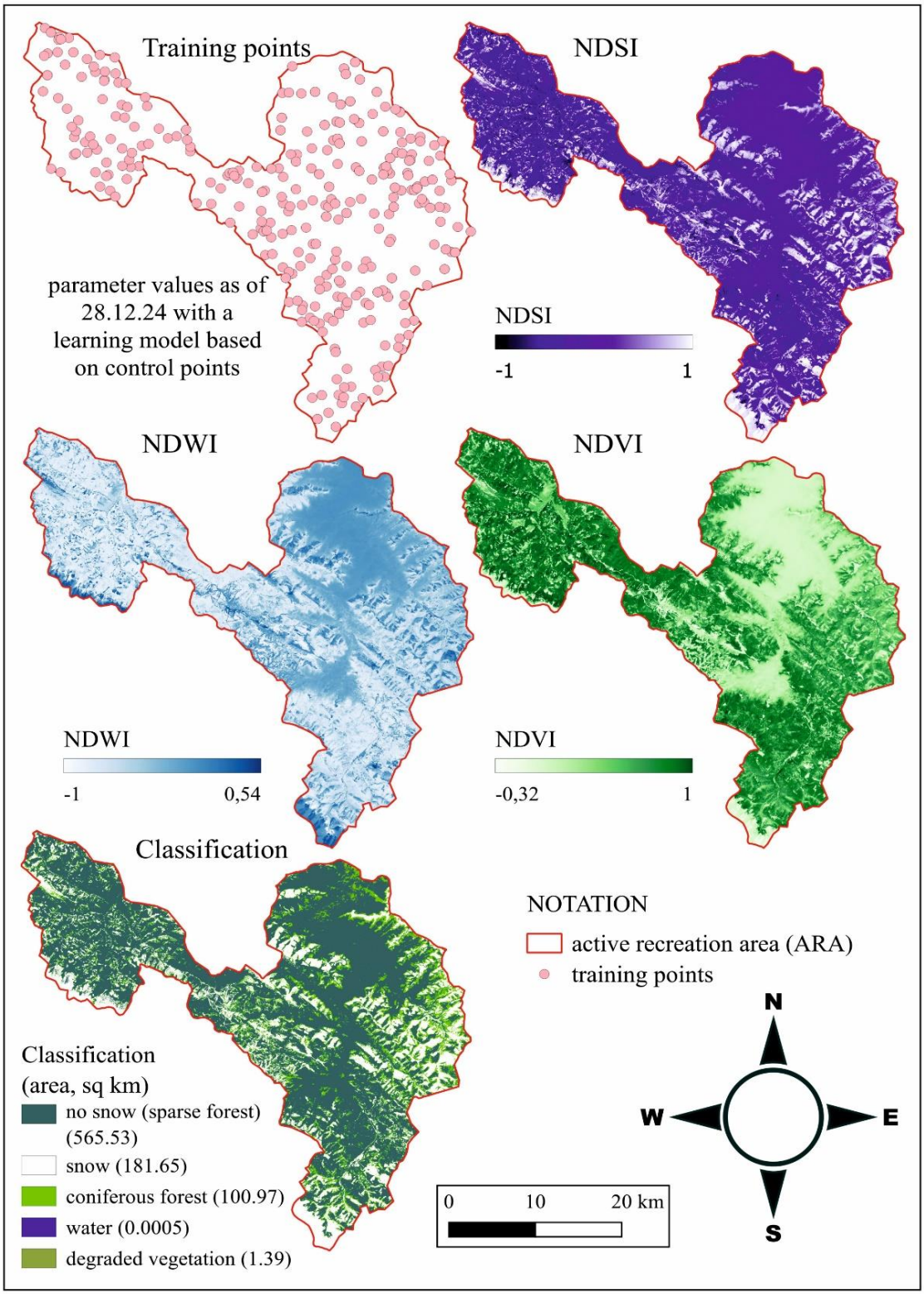

Fig. 6. Machine learning model based on Random Forest (RF).

Thirdly, Random Forest makes it possible to evaluate the accuracy of the model through Out-of-Bag (OOB) errors, which provides an independent measure of model quality. It is also possible to model the change in accuracy when each variable is changed, which helps to optimise the choice of parameters for classification.

In order to assess the quality of the model, a feature importance analysis was performed to determine the contribution of each variable to classification accuracy. In addition, the Out-of-Bag (OOB) error was estimated, which is a measure of the model's accuracy based on data that was not used during training. For a more detailed analysis of the impact of each feature on the model's accuracy, we implemented a simulation of the Mean Decrease in Accuracy method. This method allows you to assess how changing each variable affects the overall classification accuracy.

Based on the results of training a model that included 100 points divided into 10 subclasses, the generated sample allowed us to achieve a high level of training accuracy. More than 72% of the training points were correctly classified and showed good results, as we not only estimated the snow area, which is more than 21% of the study area, but also found that there are clearcuts on the study area of 1.39 km^2 (0.2%).

5. CONCLUSIONS

Climate change will have a significant impact on the tourism and recreational potential of the Carpathian Mountains, especially on winter tourism, eco‑trails and water tourism. Rising temperatures and changing climatic conditions may shorten winter seasons, reduce snow cover, alter ecosystems, and reduce the attractiveness of recreational destinations and eco-trails. To sustainably develop the region's tourism potential, it is necessary to adapt infrastructure, protect natural ecosystems, and develop and invest in new forms of tourism.

The capabilities of Google earth engine, and especially satellite image data, allow us to cover a wide range of data in the analysis, which are different in their features.

The main results of the work include:

1) The increase in average annual temperatures (0.73 degrees per decade) and the decrease in snowfall have a negative impact on winter tourism, particularly on ski resorts.
2) Climate change is causing a decrease in snow cover by ≈4.4 mm annually, and the area of snowy areas is shrinking by 0.21% per year, making winter tourism in the Carpathians, especially in lowland resorts, increasingly less sustainable and could make ski tourism impractical over the next 40 years without appropriate adaptation measures.
3) Changes in climatic conditions lead to a decrease in the clear separation of seasons, which affects the periods of tourist activity. A gradual shift in seasonality and a reduction in the length of winter have been identified.
4) Satellite imagery and indices (NDSI, Albedo) have proven to be highly effective in monitoring climate change. The use of Google Earth Engine data allowed for a detailed assessment of the dynamics of temperature, precipitation and snow cover.
5) The use of the Random Forest algorithm allows to effectively take into account various surface characteristics, which makes this approach useful for solving a wide range of tasks in the field of remote sensing, accurately classifying more than 72% of the training points.

Although winter tourism is experiencing negative changes, the growing popularity of activities such as hiking and cycling may partially offset the losses. To maintain the Carpathian Mountains' tourist attractiveness, it is important to develop adaptation measures, including investments in alternative types of tourism, sustainable water and ecosystem management practices, and the development of artificial snowmaking. This will help to ensure a balance between environmental sustainability and economic development, as well as preserve the attractiveness of the Carpathians as a tourist and recreational region in the face of climate change.

REFERENCES

Burrough, P. A. (2001) In Environmental and Ecological Statistics. *Springer Science and Business Media LLC* 8 (4), 361–377. DOI: 10.1023/a:1012734519752

Calleja, J. F., Corbea-Pérez, A., Fernández, S., Recondo, C., Peón, J., & De Pablo, M. Á. (2019) Snow Albedo Seasonality and Trend from MODIS Sensor and Ground Data at Johnsons Glacier, Livingston Island, Maritime Antarctica. *Sensors*, 19(16), 3569. DOI: 10.3390/s19163569

Feng, S., Cook, J. M., Onuma, Y., Naegeli, K., Tan, W., Anesio, A. M., Benning, L. G., & Tranter, M. (2023) Remote sensing of ice albedo using harmonized Landsat and Sentinel 2 datasets: validation. *International Journal of Remote Sensing*, 45(19–20), 7724–7752. DOI: 10.1080/01431161.2023.2291000

Gascoin, S., Luojus, K., Nagler, T., Lievens, H., Masiokas, M., Jonas, T., Zheng, Z. & De Rosnay, P. (2024) Remote sensing of mountain snow from space: status and recommendations. Front. *Earth Sci*, 12:1381323. DOI: 10.3389/feart.2024.1381323

Gorelick, N., Hancher, M., Dixon, M., Ilyushchenko, S., Thau, D., & Moore, R. (2017) Google Earth Engine: Planetary-scale geospatial analysis for everyone. *Remote Sensing of Environment*, 202, 18-27. DOI: 10.1016/j.rse.2017.06.031

Hablovska N., Hablovskyi B., Shtohryn L., Kasiyanchuk D. (2022) Analysis of natural factors and prediction of landslide activation processes in the Folded Carpathians. Monitoring of Geological Processes and Ecological Condition of the Environment 2022 – XVI International Scientific Conference. DOI: 10.3997/2214–4609.2022580129.

Hablovskyi, B., Hablovska, N., Shtohryn, L., Kasiyanchuk, D., & Kononenko, M. (2023) The Long–Term Prediction of Landslide Processes within the Precarpathian Depression of the Cernivtsi Region of Ukraine. *Journal of Ecological Engineering*, 24(7), 254–262. DOI: 10.12911/22998993/164753

Hall, D.K. and G.A. Riggs. (2021) MODIS/Terra Snow Cover 8–Day L3 Global 500m SIN Grid, Version 61. Boulder, Colorado USA. *NASA National Snow and Ice Data Center Distributed Active Archive Center*. DOI: 10.5067/MODIS/MOD10A2.061. (10/01/2025)

Ivanyshyn, V., & Kasiyanchuk, D. (2024) Analysis of the impact of climate change on the vegetation of the Perehinsk Territorial Community in Ukraine. *Grassroots Journal of Natural Resources*, 7(2): 199–215. DOI: 10.33002/nr2581.6853.070210

Jianfeng, L., Chunyu, D., Kairong, L., Xiaohong, C., Liqiang, Z., Lucas, M. (2022) Mapping snow cover in forests using optical remote sensing, machine learning and time–lapse photography. *Remote Sensing of Environment*, 275, 113017. DOI: 10.1016/j.rse.2022.113017

Kasiyanchuk, D. (2022) Study of temporary climate change within the boundaries of the Carpathian region and their relationship with global temperature fluctuations. *Ecological Sciences*, 42(3), 131–135. DOI: 10.32846/2306–9716/2022.eco.3–42.21

Kovács A., & Király A. (2021) Assessment of climate change exposure of tourism in Hungary using observations and regional climate model data. *Hungarian Geographical Bulletin*, 70(3), 215–231. DOI: 10.15201/hungeobull.70.3.2

Kulemin, G.P., Lukin, V.V., Zelensky, A.A., & Alekseyev, L.Y. (2001) Evaluation of snow cover characteristics in Ukraine from the radar images of Ocean satellite. *In Remote Sensing for Agriculture, Ecosystems, and Hydrology II* , 4171, 261–270. DOI: 10.1117/12.413934

Laurin, G.V., Francini, S., Penna, D., Zuecco, G., Chirici, G., Berman, E., Coops, N. C., Castelli, G., Bresci, E., Preti, F., & Valentini, R. (2022) SnowWarp: An open science and open data tool for daily monitoring of snow dynamics. *Environmental Modelling & Software*, 156, 105477. DOI: 10.1016/j.envsoft.2022.105477

Lyalko, V., Popov, M., Sedlerova, O., Fedorovskyi, O., Stankevich, S., Yelistratova, L., Filipovych, V., & Khyzhniak, A. (2022) On the development of remote sensing methods and technologies in Ukraine. *Ukrainian Journal of Remote Sensing*, 9(2), 43–53. DOI: 10.36023/ujrs.2022.9.2.214

Magyari-Sáska, Z., & Magyari-Sáska, A. (2023) Changes and trends in ideal holiday period based on Holiday climate index applied to the Carpathian basin. *Geographia Technica*, 18(2/2023), 225–237. DOI: 10.21163/gt_2023.182.17

MapTiler. (n.d.). *MapTiler Planet* [Map]. Retrieved January 3, 2025, from https://www.maptiler.com/

Matson, M. (1991) NOAA satellite snow cover data. Global and Planetary Change, 4(1–3), 213–218. DOI: 10.1016/0921–8181(91)90095–E

Muñoz Sabater, J., (2019) ERA5–Land monthly averaged data from 1981 to present. *Copernicus Climate Change Service (C3S) Climate Data Store (CDS)*. (10.01.2025), doi:10.24381/cds.68d2bb30

Nedostrelova, L., & Nedostrelov, M. (2024) Analysis of spatio–temporal allocation of snow cover on the territory of Vinnytsia region. *Visnyk of V. N. Karazin Kharkiv National University*, Series "Geology. Geography. Ecology, (60), 240–251. DOI: 10.26565/2410–7360–2024–60–17

Nistor, M. M., Nicula, A. S., Cervi, F., Man, T. C., Irimuş, I. A., & Surdu, I. (2018). Groundwater vulnerability GIS models in the Carpathian Mountains under climate and land cover changes. *In Applied Ecology and Environmental Research*, 16(4), 5095–5116. doi: 10.15666/aeer/1604_50955116

Odiljon, T. (2022) Methodology for Assessing the Tourist Potential of the Nature of the Fergana Valley using GIS Technologies and Experimental Methods. *MDPI AG*. DOI: 10.20944/preprints202209. 0181.v1

Pona, O., Shtogryn, L., & Kasianchuk, D. (2016) The analysis of the relationship between the phases of the Moon and the occurrence of landslides. Geoinformatics 2016 – XVth International Conference on Geoinformatics – Theoretical and Applied Aspects. DOI: 10.3997/2214–4609.201600486.

Schaaf, C., Wang, Z. (2021) MODIS/Terra+Aqua BRDF/Albedo Daily L3 Global – 500m V061. NASA EOSDIS Land Processes Distributed Active Archive Center. Accessed 2025–01–11. DOI: 10.5067/MODIS/MCD43A3.061

Scherer, D., Hall, D.K., Hochschild, V., König, M., Winther J.G., Duguay, C.R., Pivot, F., Mätzler, C., Rau, F., Seidel, K., Solberg, R., Walker, A.E. (2005) Remote Sensing in Northern Hydrology: Measuring Environmental Change. Chapter 2. *Remote Sensing of Snow Cover*. DOI: 10.1029/163GM03

Shtohryn L., Kasiyanchuk D., Kuzmenko E. (2020) The problem of long–term prediction of landslide processes within the Transcarpatian inner depression of the Carpatian region of Ukraine. *Carpathian Journal of Earth and Environmental Sciences*, 15(1): 157–166. DOI: 10.26471/cjees/2020/015/118

Shtohryn, L. V., & Kasiynchuk, D. V. (2024) Analysis of natural and man–made factors of landslide development in the Carpathian region using GIS. *Naukovyi Visnyk Natsionalnoho Hirnychoho Universytetu*, 5: 93–98. DOI: 10.33271/nvngu/2024–5/093

Steiger, R., Demiroglu, O. C., Pons, M., & Salim, E. (2023) Climate and carbon risk of tourism in Europe. *Journal of Sustainable Tourism*, 32(9): 1893–1923. DOI: 10.1080/09669582.2022.2163653

Steiger, R., Knowles, N., Pöll, K., & Rutty, M. (2022) Impacts of climate change on mountain tourism: a review. *Journal of Sustainable Tourism*, 32(9): 1984–2017. DOI: 10.1080/09669582.2022.2112204

Tymkiv, M., Kasiyanchuk, D. (2019) Research of data sequences of groundwater levels with gaps. *Journal of Ecological Engineering*, 20(3), 141–151. DOI: 10.12911/22998993/99744.

Turnock, D. (2001) East Central Europe and the Former Soviet Union: Environment and Society (1st ed.). *Routledge*. DOI: 10.4324/9781003571926

Xiongxin, X., Shuang, L. (2024) Assessment of snow cover mapping algorithms from Landsat surface reflectance data and application to automated snowline delineation. *Remote Sensing of Environment*, 307, 114163. DOI: 10.1016/j.rse.2024.114163.

HYDRODYNAMIC MODELING OF POLLUTANT DISTRIBUTIONS FROM THE BERA WATERSHED AND ITS IMPACT TO THE COASTAL AREA OF SALEH BAY, WEST NUSA TENGGARA, INDONESIA

Amar Malikal RAHMAN [1*], ***Dini PURBANI*** [2], ***Syamsul B. AGUS*** [1], ***Taslim ARIFIN*** [2], ***Yulius YULIUS*** [2], ***Aprizon PUTRA*** [2], ***Aida HERIATI*** [2], ***Joko PRIHANTONO*** [2], ***Rudhy AKHWADY*** [2], ***Agus SUFYAN*** [2], ***Eva MUSTIKASARI*** [2], ***Sri Endah PURNAMANINGTYAS*** [2], ***Rinny RAHMANIA*** [2], ***Muhammad RAMDHAN*** [3], ***Arya NINGSIH*** [4], ***Sadad SADAD*** [4], ***Didik Wahju HENDRO TJAHJO*** [2]

DOI: 10.21163/GT_2025.202.03

ABSTRACT

Pollutant distribution from the Bera Watershed may impacts the coastal environment of Saleh Bay. This study aims to map pollutant distribution and assess its ecological effects using a hydrodynamic modeling approach in the coastal waters of Saleh Bay, particularly around the estuaries of the Bera Watershed. The MIKE 21 software with the EcoLab module was used to simulate hydrodynamics and pollutant dispersion. The hydrodynamic model was validated using tidal data from Nao Tide Model, which had been previously compared with observed tidal measurements and showed good agreement. This validation showed a Root Mean Square Error (RMSE) of 0.19423 in April and 0.27589 in September, confirming the model's reliability in simulating pollutant dispersion. Pollutant data, including Biochemical Oxygen Demand (BOD), Chemical Oxygen Demand (COD), Nitrate (NO_3-N), and Phosphate (PO_4-P), were collected from the Brang Bera, Brang Maronge, and Brang Kolong Rivers in the Bera Watershed during April and September. Simulations were conducted for both periods. Since discharge data were unavailable, the Manning equation was applied to estimate river discharge at the mouths of these three rivers based on cross-sectional area, hydraulic radius, wetted perimeter, and a consistent roughness coefficient (n = 0.045). Bathymetric analysis revealed depth variations ranging from, 5 to 500 m, while wind data indicated stronger winds in September (5.70–8.80 m/s). Pollutant concentration modeling indicated fluctuating levels, with BOD ranging from 1.2 to 1.8 mg/L, COD from 18 to 28 mg/L, NO_3-N from 3 to 5 mg/L, and PO_4-P from 1.2 to 1.8 mg/L. Peak concentrations occurred during high tides, while localized accumulation was observed during low tides. These findings emphasize the urgent need for effective pollutant management and mariculture to ensure the long-term ecological stability of Saleh Bay.

Key-words: *Pollutant, Hydrodynamic modeling, Bera watershed, Environmental quality, Saleh Bay.*

[1]*Department of Marine Science and Technology, Faculty of Fisheries and Marine Sciences, IPB University (Bogor Agricultural University), Bogor, Indonesia. (AMR) amarmalikal@apps.ipb.ac.id; (SBA) mycacul@gmail.com.*

[2]*National Research and Innovation Agency, KST Soekarno, Cibinong, West Java, Indonesia. (DP) dini017@brin.go.id; (TA) tasl003@brin.go.id; (YY) yuli058@brin.go.id; (AP) apri024@brin.go.id; (AH) aida002@brin.go.id; (JP) joko043@brin.go.id; (RA) Akhwady2012@gmail.com; (AS) agus181@brin.go.id; (EM) evam002@brin.go.id; (SEP) srie005@brin.go.id; (RR) rinny.rahmania@brin.go.id.*

[3]*National Research and Innovation Agency, KST Samaun Samadikun, Bandung, Indonesia. (MR) muha307@brin.go.id.*

[4]*Agency for Local Research and Development, Government of Sumbawa, Sumbawa, Indonesia. (AN) ningsiharya67@gmail.com; (SS) sadadmagrabi@gmail.com; (DWHT) didi029@brin.go.id.*

[*] *Corresponding author: (AMR) amarmalikal@apps.ipb.ac.id*

1. INTRODUCTION

Saleh Bay is a semi-enclosed water body directly connected to the Flores Sea and located in the northeastern part of Sumbawa Island, West Nusa Tenggara Province, Indonesia. The bay falls under the jurisdiction of two administrative regencies: Sumbawa and Dompu (Yulius et al., 2019). It is renowned for its rich marine biodiversity and mariculture, making it both ecologically and economically significant (Marzuki et al., 2014; Yulius, et al., 2018; Efendi et al., 2020;). Due to its favorable physicochemical properties, including optimal salinity, temperature, and water circulation (Purwanto et al., 2021), Saleh Bay has been identified as a potential site for mariculture development, particularly for seaweed and fish farming (Kusumawati et al., 2019; Arifin et al., 2025).

However, despite its suitability for aquaculture, the bay is increasingly affected by environmental stressors such as sedimentation, eutrophication, and chemical contamination, primarily due to pollutants carried by riverine inputs from urban, industrial, and agricultural activities (Darmawan et al., 2023). These environmental issues vary both spatially and temporally, meaning that while some areas remain viable for aquaculture, others require adaptive management strategies to mitigate adverse effects. For instance, during the dry season, seaweed farming is conducted at the estuary of the Bera Watershed, where stable salinity and nutrient levels support optimal growth. Conversely, during the rainy season, the farming location is relocated to avoid excessive runoff, which increases turbidity and nutrient loading, potentially compromising seaweed productivity and quality (Arifin et al., 2025). This dynamic interaction between environmental conditions and aquaculture practices highlights the need for a comprehensive assessment of water quality and its implications for sustainable mariculture development in Saleh Bay.

Saleh Bay is also increasingly exposed to significant pollution threats, particularly from phosphates and nitrates, which are primary contributors to eutrophication, a process that promotes excessive algal growth, ultimately deteriorating water quality and disrupting marine life (Smith et al., 2006). Two critical parameters for assessing water pollution levels are Chemical Oxygen Demand (COD) and Biochemical Oxygen Demand (BOD). COD quantifies the total concentration of oxidizable substances, encompassing both organic and inorganic matter present in the water, while BOD measures the oxygen consumed by microorganisms in breaking down organic pollutants (Chen et al., 2022). These parameters are vital indicators of water quality and overall aquatic ecosystem health. Phosphate (PO_4-P) contamination commonly originates from detergent residues and fertilizers, while elevated nitrate (NO_3-N) concentrations are predominantly associated with wastewater discharge from domestic and agricultural activities (Carpenter, 2005; Putra et al., 2024). Both COD and BOD are crucial metrics for monitoring water pollution, as they provide insights into contamination levels and their direct impacts on ecosystem health and water quality (Di et al., 2019).

The coastal waters of Saleh Bay are heavily influenced by the Bera Watershed, which discharges into the bay and serves as a major pathway for pollutants. Three major rivers Brang Bera, Brang Maronge, and Brang Kolong act as primary conduits for pollutant transport. Human activities within the watershed, including agriculture, residential settlements, and industrial operations, introduce various contaminants such as sediment, household waste, pesticides, and heavy metals. These pollutants are transported by river flow into the coastal waters of Saleh Bay, leading to water quality degradation and posing threats to coastal ecosystems (Risna et al., 2022). Addressing this environmental challenge requires comprehensive pollution source mapping within the Bera Watershed. Harianto & Efendi (2017) emphasize that such an approach would facilitate the identification of pollutant distribution patterns, pinpoint major contamination sources, and evaluate their impact on the coastal waters of Saleh Bay.

Manning's theory is a valuable tool for simulating river and watershed hydrodynamics, providing critical insights into water flow behavior within the Bera Watershed. This is particularly useful for modeling the flow characteristics of Brang Bera, Brang Maronge, and Brang Kolong, allowing for better prediction of river discharge variations (Benedini, 2011). Implementing Manning's theory in pollution mapping provides a deeper understanding of discharge patterns, which is essential for designing effective river management strategies to mitigate pollution in Saleh Bay’s coastal area

(Ansari et al., 2024). Furthermore, the use of Manning's equation aligns with geospatial analytical techniques, as it integrates hydrodynamic modeling, a fundamental component of Geographic Information Systems (GIS) used in water resource management studies. Pollution from human activities, including domestic and industrial waste disposal, poses significant environmental challenges to Saleh Bay's coastal area. To assess the impact of this pollution on marine ecosystems and water quality, pollutant modeling serves as an essential analytical tool. One promising approach is the application of Modeling Interface for Knowledge-based Engineering (MIKE) 21 EcoLab software, which simulates interactions between pollutant concentrations and hydrodynamic processes in aquatic environments (Basheer et al., 2024; Xu et al., 2023). This technique is particularly effective for estuaries affected by anthropogenic activities, as it visualizes the spatial distribution of key water quality indicators such as COD, BOD, NO_3-N, and PO_4-P (Nugroho et al., 2016). The use of computational models in pollution analysis is crucial for identifying environmental trends over time and supports technical geography studies by integrating spatial data with hydrodynamic modeling techniques. Pollution modeling offers critical insights into the current state of water quality, enabling the development of targeted pollution control measures to safeguard Saleh Bay's ecosystem.

This study aims to map pollutant distribution across the Bera Watershed, assess its impact on the coastal waters of Saleh Bay, and evaluate its ecological consequences using a hydrodynamic modeling approach. This method aligns with technical geography studies by leveraging hydrodynamic simulations to analyze pollutant dispersion patterns, a key component in understanding spatial water dynamics. By providing a detailed analysis of pollution dispersion, this research aims to enhance the understanding of its ecological effects on the Saleh Bay marine environment. The novelty of this study lies in its integration of hydrodynamic models to analyze pollution dynamics, enabling more accurate predictions of pollutant transport behavior and its environmental repercussions in an area heavily influenced by human activities.

2. STUDY AREA

The study was conducted in the coastal area of Saleh Bay in latitudes 8°33'30" to 8°43'30" South and longitudes 117°44'0" to 117°51'0" East (see **Fig. 1**).

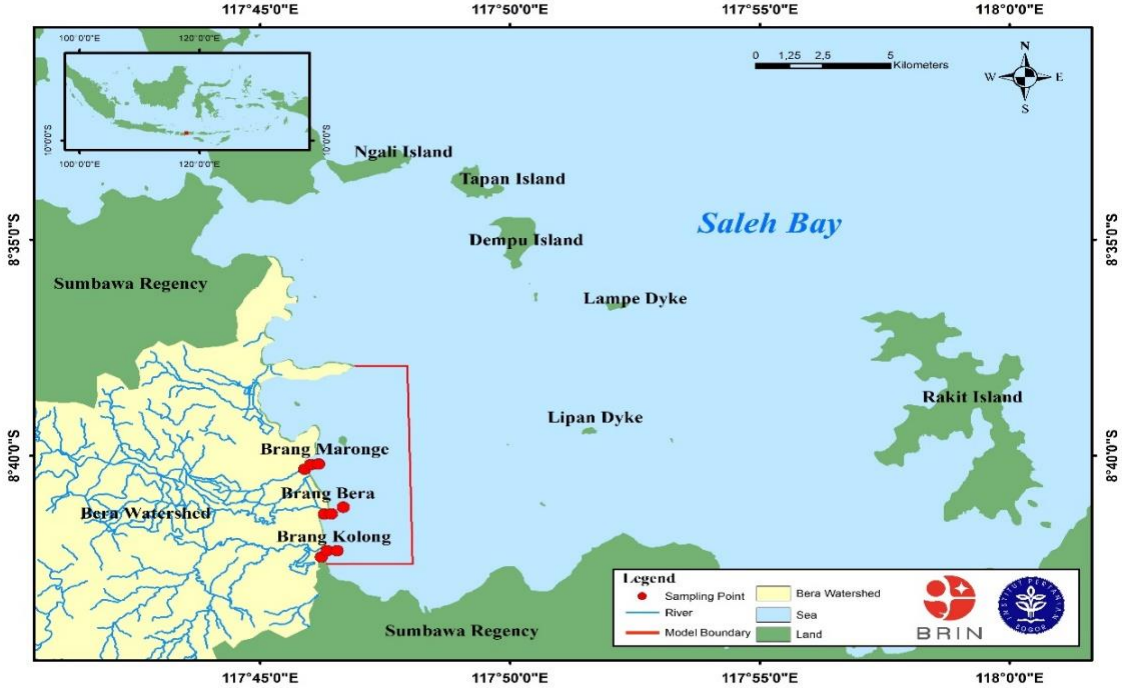

Fig. 1. Map of study area and sampling points in the Bera Watershed and the coastal area of Saleh Bay.

The study area was chosen due to their proximity to the three main rivers within the Bera Watershed, namely Brang Bera, Brang Maronge, and Brang Kolong which serve as the primary sources of pollutants in the areas. The bay features a diverse range of depths, from shallow coastal zones to deeper areas towards the center. This study focuses on pollutant distribution within the bay, with sampling carried out at three strategically selected sites along the rivers and shoreline, where pollutants tend to accumulate and are significantly influenced by tidal fluctuations.

3. DATA AND METHODS

3.1. Data collection, processing, and water quality analysis

To enhance the accuracy of the analysis, bathymetric data from the National Digital Elevation Model (DEMNAS) were utilized to generate a bathymetric map using TIF data acquired in 2024, and processed through Ocean Data View (ODV) software. Wind data were obtained from the European Centre for Medium-Range Weather Forecasts (ECMWF), while tidal data were sourced from the Naotide Model and validated with Geospatial Information Agency (BIG). A structured and systematic approach was employed to collect and process various data sources essential for examining pollutant dispersion and its impact on marine ecosystems. The compiled data serves as a key input for hydrodynamic modeling and ecological assessments, enhancing the understanding of environmental dynamics in the Bera Watershed and the coastal area of Saleh Bay. This dataset includes bathymetric, wind, tidal, and watershed discharge data, along with water quality parameters such as COD, BOD, NO_3-N, and PO_4-P, which are essential for evaluating pollution levels in the bay. The data sources, processing techniques, and measurement tools can be seen in **table 1** below.

Table 1.

Data collection, processing, and analysis methods.

Parameter	Unit	Data Source/Processing	Measurement Tools	Purpose
Bathymetry Data	-	DEMNAS(https://tanahair.indonesia.go.id/demnas), processed Ocean Data View (ODV) (2024)	GIS Software	Understanding depth variations for hydrodynamic modeling and pollutant analysis
Wind Data	-	ECMWF(https://www.ecmwf.int/), analyzed using Microsoft Excel and visualized with WRPLOT software	Weather Modeling Software	Evaluating wind-driven transport mechanisms affecting pollutant distribution
Tidal Data	-	Naotide Model and BIG (https://srgi.big.go.id/) analyzed using Microsoft Excel	Tidal Prediction	Determining how tidal fluctuations influence pollutant concentration in coastal zones
Watershed Discharge	m^3/s	Calculated using Manning equation	Hydraulic Modeling Software	Understanding freshwater inputs affecting Saleh Bay
Water quality parameters				
COD	mg/L	Sample Testing	Agilent 7890B GC System	Assessing the presence of organic and inorganic pollutants affecting water quality and determining the water contamination
Biological Oxygen Demand(BOD)	mg/L	Sample Testing	Hach HQ440D Multi-Parameter Meter	Measuring the amount of oxygen required by microorganisms to decompose organic matter
Nitrate (NO_3-N)	mg/L	Sample Testing	YSI ProDSS Digital Sampling System	Evaluating nitrogen pollution from agricultural runoff, domestic wastewater, and its contribution to eutrophication
Phosphate (PO_4-P)	mg/L	Sample Testing	Hach DR3900 Spectrophotometer	Monitoring nutrient pollution levels from agricultural and industrial sources, which contribute to water quality degradation

Field data pollutant concentration can be seen in **table 2** below. By integrating water quality parameters with hydrodynamic and oceanographic data, this study establishes a comprehensive framework for analyzing pollutant dynamics in Saleh Bay. The systematic integration of these datasets improves scientific assessments, supporting the conservation and sustainable management of the bay.

Table 2.

Field Data Pollutant Concentration.

Sampling Point	Time	BOD (mg/L)	COD (mg/L)	NO_3-N (mg/L)	PO_4-P (mg/L)
Brang Bera	Apr-22	0.66	3	0.5	0.12
	Sep-22	1.52	21	0.5	0.13
Brang Maronge	Apr-22	0.9	11	0.5	0.13
	Sep-22	2.07	2	0.6	0.19
Brang Kolong	Apr-22	0.6	3	0.5	0.02
	Sep-22	1.77	18	0.5	0.16

3.2. Manning theory for discharge calculation

The Manning equation is applied to estimate water flow discharge. The roughness coefficient (n) varies depending on the channel surface material (Benedini, 2011). As direct discharge data was unavailable, Manning equation served as an alternative method for estimating discharge. The equation applied is as follows:

$$Q = \frac{1}{n} \times A \times R \left(\frac{A}{P}\right)^{\frac{2}{3}} \times S^{\frac{1}{2}} \quad (1)$$

where: Q = Flow discharge (m^3/s); n = Manning roughness coefficient; A = Cross-sectional flow area (m^2); R = Hydraulic radius (A/P, where P is the wetted perimeter); P = Wetted perimeter of the channel; S = Hydraulic slope of the river.

3.3. Data analysis and modeling

The hydrodynamic and pollutant distribution modeling in this study was carried out using the MIKE 21 integrated model. The pollutant modeling process began with the development of a domain based on Flexible Mesh within the MIKE 21 software. The model consists of three main modules, namely Hydrodynamic (HD), Transport, and Ecolab, which together simulate pollutant dispersion to illustrate the distribution pattern in the coastal area of Saleh Bay (Prihantono et al., 2018). **Table 3** below provides a summary of the different components of the modeling process and their respective functions. The simulation incorporated data from various tidal conditions, specifically the highest and lowest tides observed in April and September 2022. These datasets were utilized to model and predict the dispersion of organic and chemical pollutants within the coastal area of Saleh Bay.

3.4. Data validation

The reliability of the pollutant distribution model was assessed by comparing the simulated tide by Naotide model against actual field measurements (https://srgi.big.go.id/tides/clbi). **Table 4** below outlines the validation process steps along with the corresponding techniques employed.

The integration of on-site measurements with numerical modeling strengthens the reliability of the modeling approach, enabling a more precise assessment of the model and improving the accuracy of hydrodynamics model. This methodology, which aligns with validating model principles, combines by integrating field measurements and numerical modeling to develop a comprehensive understanding of hydrodynamics in the coastal area of Saleh Bay. The Naotide Model is utilized for model validation due to the limited availability of tidal data within the study area. This validation process aims to determine the RMSE, which will be employed to assess the accuracy of the MIKE 21 Integrated Model FM in simulating pollutant dispersion dynamics.

Table 3.

Hydrodynamic and pollutant distribution modeling components.

Parameter	Applied in simulation
HD Model	
Simulation time	30 days (1 – 30 April 2022 and 1-30 September 2022)
Mesh and Bathymetry	Mesh interpolation results
Time step	1 Hours
Tides	Naotide Model (1 – 30 April 2022 and 1-30 September 2022)
Wind data	ECMWF (1 – 30 April 2022 and 1-30 September 2022)
River discharge	Brang Bera = 32.70 m^3/s Brang Maronge = 13.14 m^3/s Brang Kolong = 15.93 m^3/s
Transport Model	
Advection Scheme	Semi-Lagrangian
COD Concentration	Brang Bera = 3 mg/L (April 2022), 21 mg/L (September 2022) Brang Maronge = 11 mg/L (April 2022), 2 mg/L (September 2022) Brang Kolong = 3 mg/L (April 2022), 18 mg/L (September 2022)
Ecolab Model	
BOD Concentration	Brang Bera = 0.66 mg/L (April 2022), 1.52 mg/L (September 2022) Brang Maronge = 0.9 mg/L (April 2022), 2.07 mg/L (September 2022) Brang Kolong = 0.6 mg/L (April 2022), 1.77 mg/L (September 2022)
NO_3-N Concentration	Brang Bera = 0.5 mg/L (April 2022), 0.5 mg/L (September 2022) Brang Maronge = 0.5 mg/L (April 2022), 0.6 mg/L (September 2022) Brang Kolong = 0.5 mg/L (April 2022), 0.5 mg/L (September 2022)
PO_4-P Concentration	Brang Bera = 0.12 mg/L (April 2022), 0.13 mg/L (September 2022) Brang Maronge = 0.13 mg/L (April 2022), 0.19 mg/L (September 2022) Brang Kolong = 0.02 mg/L (April 2022), 0.16 mg/L (September 2022)

Table 4.

Data validation methods.

Validation Step	Data Source/Tools Used
Model Calibration	Field data, tide measurements
Model Simulation	Naotide Model and MIKE 21 FM Integrated Model

The validation of tidal simulations at Calabai Station (08° 12’ 50.94” S, 117° 42’ 33.408” E) in Saleh Bay was conducted using observational tidal data and Naotide model outputs. Due to the limited availability of in situ tidal records, model validation was performed by comparing Naotide-derived tidal predictions with the available station measurements. The results indicate that the Naotide model exhibits a reasonable representation of tidal variations, with RMSE values of 0.107 in April and 0.228 in September (**Fig. 2**). These validation metrics suggest that, despite data constraints, the Naotide model can be reliably utilized for tidal simulations in Saleh Bay, providing a valuable tool for hydrodynamic analysis and coastal management.

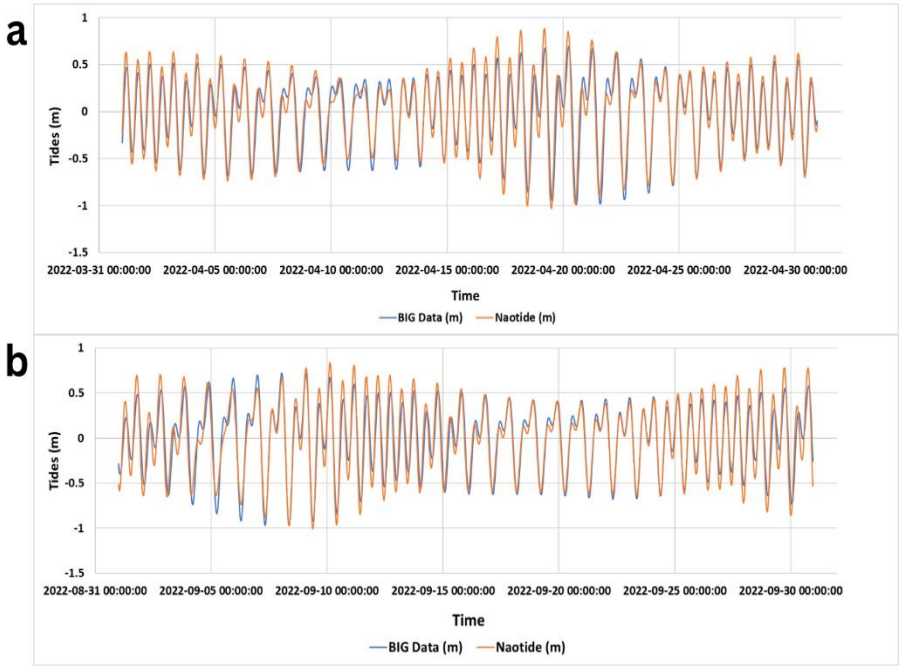

Fig. 2. Tide Comparasion of Naotide Model and BIG Station measurement: a) April 2022, b) September 2022.

4. RESULTS AND DISCUSSION

4.1. Analysis results for bathymetric data

Saleh Bay features a diverse bathymetric profile that plays a crucial role in hydrodynamic processes and ecological sustainability. The submarine topography significantly influences sediment transport, nutrient distribution, and water circulation, with depths varying from shallow coastal areas to nearly 300 m in the central area. The Bera Watershed, which encompasses the Brang Bera, Brang Maronge, and Brang Kolong, has a significant impact on water quality and sedimentation patterns in the coastal area of Saleh Bay. These rivers carry freshwater, sediments, and pollutants from inland areas to the coastal zone, thereby influencing nutrient distribution and marine habitat conditions. The interaction between river discharge and bathymetric variations governs the extent of pollutant dispersion and the formation of sediment deposition zones within the bay. The bathymetric heterogeneity directly affects ecosystems and habitats, influencing biodiversity and the availability of marine resources. The depth variations in Saleh Bay, as shown in f**igure 3** below.

The bathymetric characteristics of Saleh Bay significantly influence its suitability for mariculture development, particularly in terms of site selection, species compatibility, and environmental sustainability. Depth plays a critical role in determining water exchange, nutrient availability, and oxygen dynamics factors essential for the success of aquaculture practices. Shallow zones ranging from 5 to 50 m are considered optimal for the cultivation of species such as finfish and shellfish, as these areas provide adequate light penetration and facilitate infrastructure installation (Bath et al., 2023). However, these zones are also more vulnerable to pollutant accumulation and reduced water circulation, which may lead to eutrophication and compromise the health of cultured organisms. Effective bathymetric mapping is therefore crucial for identifying areas with sufficient hydrodynamic flushing to disperse organic waste from mariculture activities (Iglesias et al., 2020). In contrast, the central region of Saleh Bay reaches depths of approximately 400 to 500 m (as shown in **Fig. 3**), presenting distinct hydrodynamic conditions that may be less favorable for traditional aquaculture systems due to logistical challenges and limited vertical mixing.

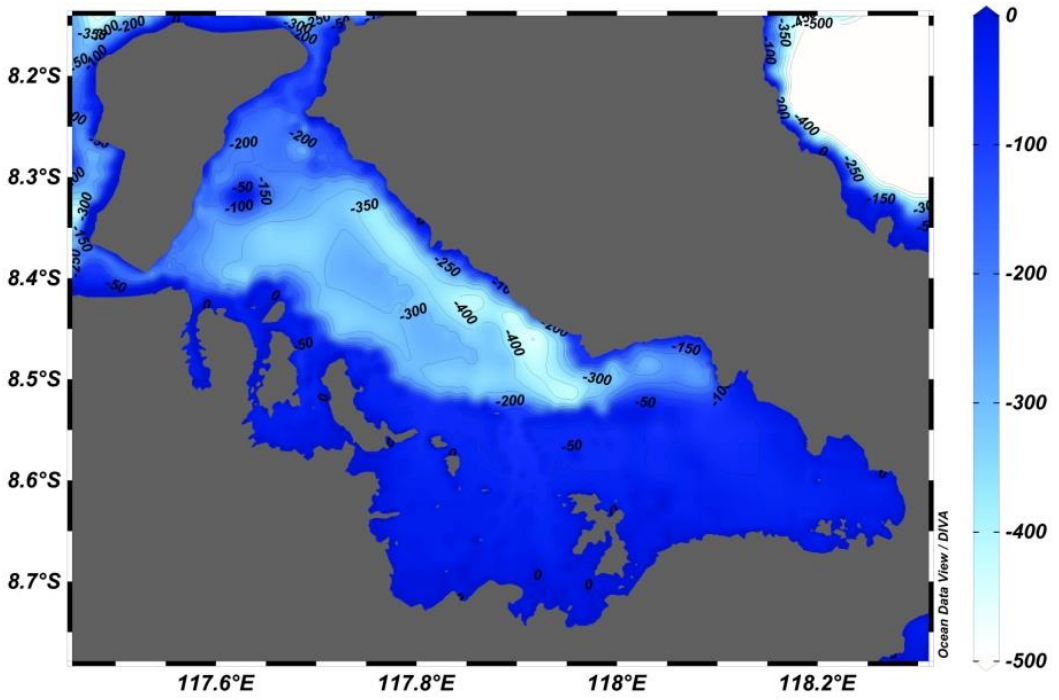

Fig. 3. Analysis results for the bathymetric map of Saleh Bay using ODV 2024.

Nonetheless, these deeper areas could support offshore aquaculture technologies or serve as buffer zones for ecosystem carrying capacity assessments. A comprehensive understanding of the interplay between bathymetry, water circulation, and nutrient cycling is essential for sustainable mariculture planning, ensuring both productivity and ecological integrity in Saleh Bay (Ferreira et al., 2023).

4.2. Model validation from tide data

Tidal fluctuations impact hydrodynamic and ecological processes, including water circulation, sediment transport, and pollutant distribution (Bilal et al., 2020). The Naotide model was used to validate these tidal dynamics by providing hydrodynamic simulations that assess tidal variations and their influence on pollutant transport (Rachman et al., 2023). For a more thorough hydrodynamic analysis, tidal data can be compared with predictions from other models, such as those provided by BIG, analyzed using the Admiralty Method. If the error margin between Naotide and BIG tidal data is minimal, Naotide data can serve as a reliable reference. However, if substantial discrepancies are found, alternative hydrodynamic models should be considered to enhance prediction accuracy and validation reliability.

The tidal model was validated by comparing its outputs with Naotide-derived tidal predictions to assess its accuracy in simulating tidal dynamics within the study area (**Fig. 4**). The root mean square error (RMSE) values were calculated as 0.194 in April and 0.276 in September, providing a quantitative measure of the model's performance. While these RMSE values indicate a moderate level of agreement between the model and Naotide data, some discrepancies remain, particularly in September, where the higher error suggests increased deviations. These variations could be attributed to hydrodynamic complexities, model assumptions, or external influences such as atmospheric forcing and boundary condition limitations. Despite these differences, the model demonstrates a reasonable capability in capturing tidal patterns, though further refinements may be needed to improve its predictive reliability.

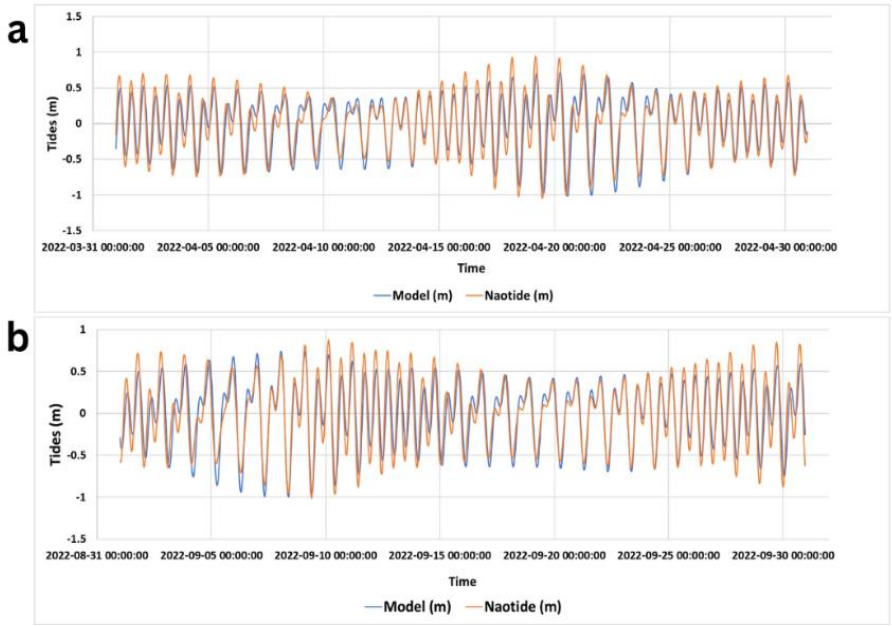

Fig. 4. Tide Comparasion of Result Model and Naotide Model:
a) April 2022, b) September 2022

4.3. Current Pattern Dynamics

The hydrodynamic conditions of the study area are strongly influenced by tidal fluctuations and seasonal wind variations. As illustrated in **figure 5**, the windrose diagrams depict dominant wind directions and speeds during **April 2022 (Fig. 5a)** and **September 2022 (Fig. 5b)**. In April, the prevailing winds originated predominantly from the north-northwest sector with moderate speeds ranging between 0.50–5.70 m/s, as represented by the dominant green, yellow, and red sectors. The resultant wind vector shows a northwesterly direction (334°) with a frequency of 67%, indicating a relatively moderate and variable wind regime. Conversely, in September, stronger wind speeds (3.60–8.80 m/s) were more frequently observed, with a dominant westerly component (323°) and higher resultant vector magnitude (94%). This shift reflects the transition to drier conditions and a more intense wind regime, likely influenced by the southeast monsoon period.

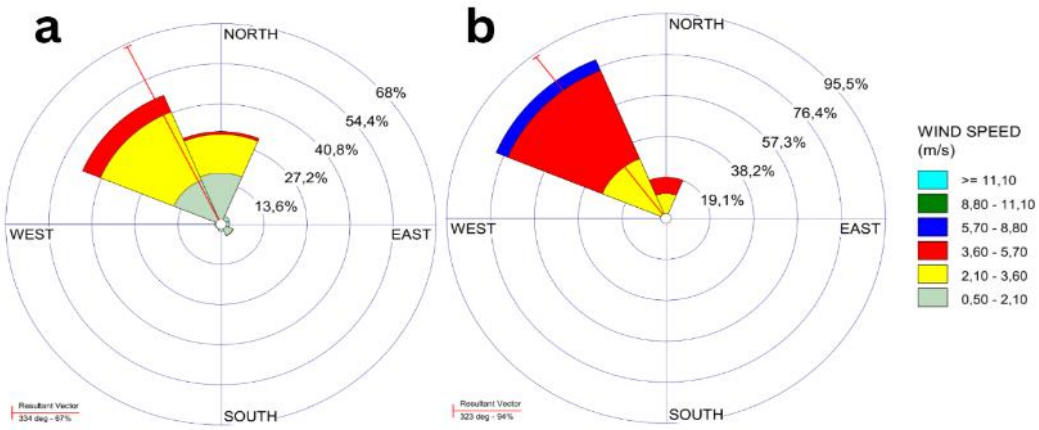

Fig. 5. Windrose in the months: a) April 2022, b) September 2022.

Correspondingly, the tidal current distribution patterns are visualized in **figure 6**, which presents the results of a hydrodynamic model simulation under different tidal conditions and time intervals.

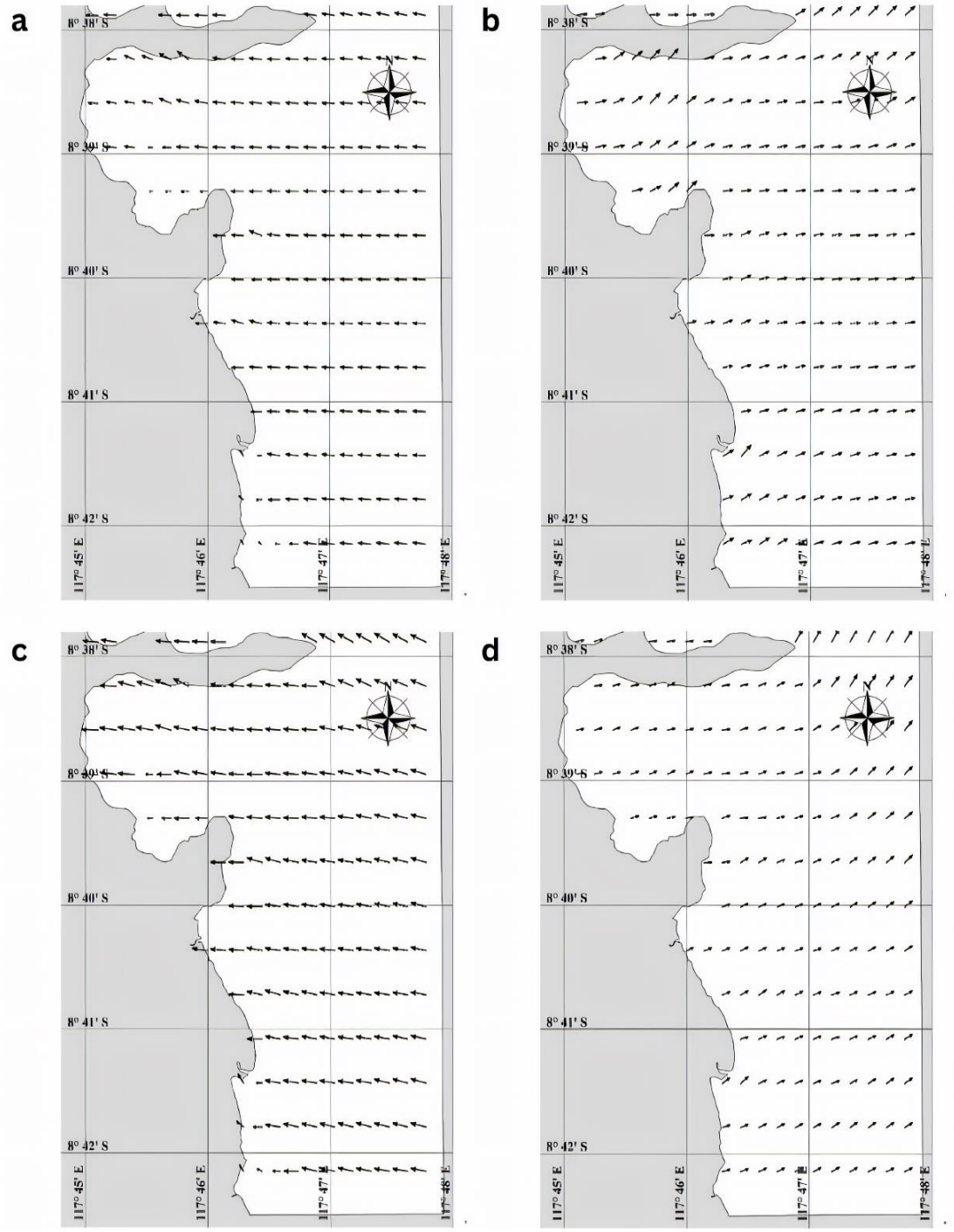

Fig. 6. Hydrodynamic model of current distribution patterns at different tidal conditions and time intervals: a) Highest Tide–April 2022, b) Lowest Tide–April 2022, c) Highest Tide–September 2022 and d) Lowest Tide–September 2022.

During the highest tidal condition in April 2022 **(Fig. 6a)**, the current vectors indicate a moderate eastward flow pattern across the coastal region, consistent with the influence of tidal forcing and wind-driven surface currents. At the lowest tide in April **(Fig. 6b)**, current intensity diminishes significantly, and flow directions exhibit greater spatial variability, particularly near the coastline, suggesting the formation of localized eddies and weaker circulation cells.

In contrast, during September 2022, a noticeable intensification of current velocities is observed. The highest tide scenario **(Fig. 6c)** exhibits stronger and more organized current vectors flowing predominantly east-northeastward, likely enhanced by the increased wind stress observed in the windrose analysis. Meanwhile, during the lowest tide in September **(Fig. 6d)**, although the flow velocity decreases, the directional consistency of current movement remains more structured compared to April. This indicates a higher wind-driven influence on current dynamics in September, aligning with the windrose pattern that shows stronger and more unidirectional winds.

These changes altered rainfall patterns, impacted temperature-sensitive marine organisms, and influenced coastal hydrodynamics, potentially affecting mariculture. Stronger monsoonal winds also amplified wave activity, leading to shoreline changes and increased sedimentation. As Marganingrum & Santoso (2019) highlight, wind-driven transport mechanisms play a crucial role in pollutant dispersion, underscoring the importance of seasonal wind analysis for environmental monitoring and coastal resource management.

4.4. Analysis results for discharge calculation (Manning theory)

The outcomes of manning theory calculations, presented in Table 2, illustrate the influence of the cross-sectional area (A), hydraulic radius (R), and wetted perimeter (P) on river discharge (Q) for the three primary rivers in the Bera Watershed. The calculations reveal that all three rivers share a consistent roughness coefficient (n = 0.045), indicating similar riverbed characteristics. These results emphasize that river discharge is primarily influenced by the cross-sectional area and hydraulic characteristics of the riverbed, as outlined by manning equation. The discharge values used for the simulation represent the average values from April and September. The calculated results for the three watersheds, you can see at **table 5** below.

Table 5.

River discharge based on manning calculation.

River Names	n	A (m²)	R (m)	S	P	Q (m³/s)
Brang Bera	0.045	24	0.48	0.01	50	32.70
Brang Maronge	0.045	10	0.45	0.01	22	13.14
Brang Kolong	0.045	12	0.46	0.01	26	15.93

Based on calculations, the Brang Bera River exhibits the largest cross-sectional area (A = 24 m²) and wetted perimeter (P = 50 m), resulting in the highest discharge rate of 32.70 m³/s compared to the other two rivers. This makes the Brang Bera River the most significant contributor to water flow within the Bera Watershed, playing a critical role in hydrodynamic processes and pollutant transport to Saleh Bay. In contrast, the Brang Maronge River, with the smallest cross-sectional area (A = 10 m²) and wetted perimeter (P = 22 m), records the lowest discharge of 13.14 m³/s. This indicates a lower capacity for transporting water and sediment, potentially leading to a reduced impact on estuarine hydrodynamics when compared to Brang Bera. Meanwhile, the Brang Kolong River, which has an intermediate cross-sectional area (A = 12 m²) and wetted perimeter (P = 26 m), produces a moderate discharge of 15.93 m³/s, reflecting its relative contribution to the overall flow regime in the watershed.

The variations in river discharge among these three rivers highlight their differing capacities to convey water and transport pollutants into Saleh Bay. Rivers with higher discharge rates, such as the Brang Bera River, can carry a larger volume of sediments, nutrients, and potential contaminants, significantly influencing water quality, sedimentation patterns, and pollutant dispersion in coastal and estuarine areas.

4.5. Analysis results for water quality parameters (pollutant)

4.5.1 BOD Pollutant Distribution Modeling

The BOD modeling over two months demonstrates variations in pollutant concentration under different tidal conditions. During the highest tide in April 2022 (**Figure 7a**), BOD concentrations peaked at 1.5 mg/L in the central coastal area, indicating a significant accumulation of organic pollutants. In contrast, during the lowest tide in April 2022 (**Figure 7b**), BOD levels decreased to approximately 1.2 mg/L, with pollutant concentrations remaining localized near major discharge sources. A similar trend was observed in September 2022, where BOD concentrations increased to 1.8 mg/L during the highest tide (**Figure 7c**), with the western coastal zone experiencing the most significant pollutant accumulation. However, during the lowest tide in September 2022 (**Figure 7d**), BOD levels decreased to around 1.4 mg/L, with pollutants remaining concentrated near contamination sources. For more details see the model in **figure 7** below. The findings further emphasize the impact of tidal fluctuations on BOD spatial allocation: intensified tidal phases encourage widespread contaminant distribution, while attenuated tides lead to localized aggregation. The interplay between tidal flows and contaminant origins is vital in shaping water quality and influencing potential ecological outcomes along the coast.

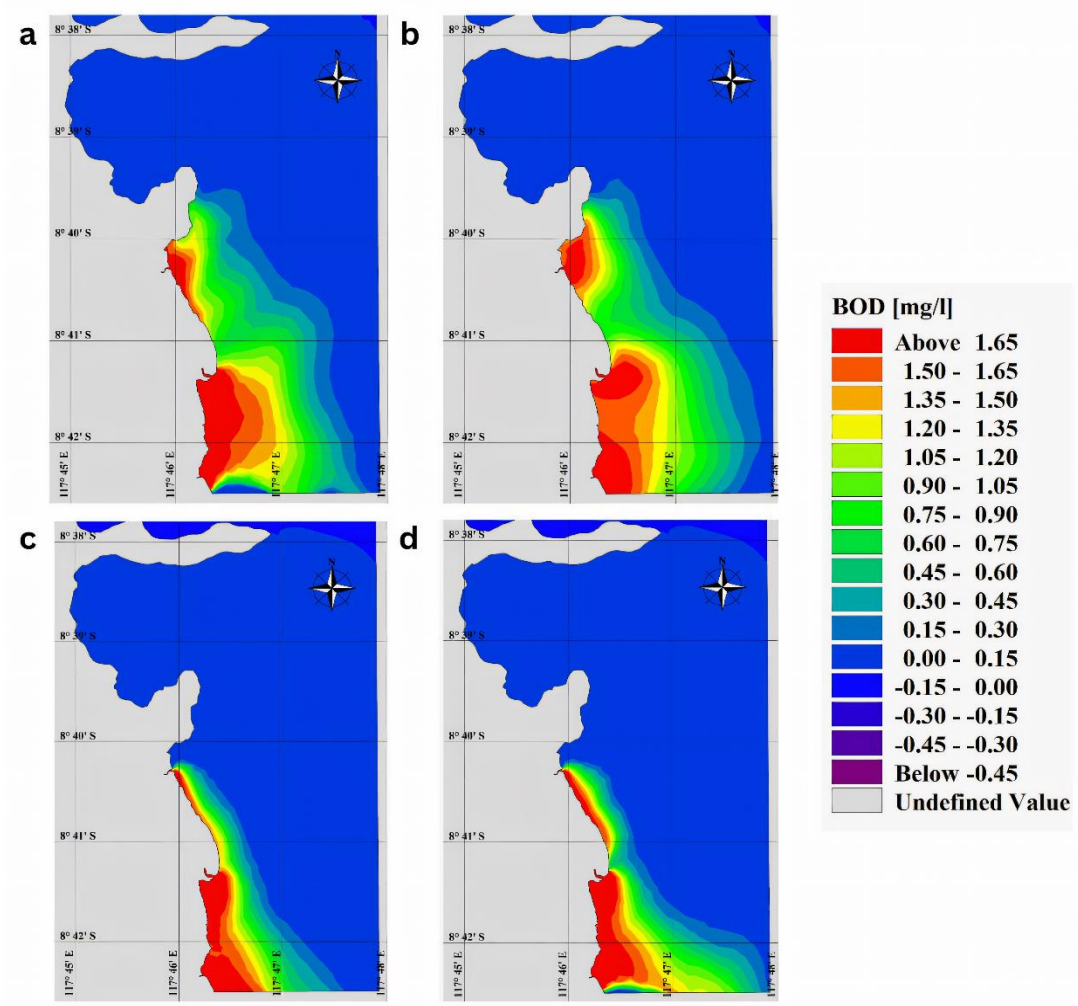

Fig. 7. BOD pollutant distribution modeling at different tidal conditions and time intervals: a) Highest Tide–April 2022, b) Lowest Tide–April 2022, c) Highest Tide–September 2022 and d) Lowest Tide–September 2022.

4.5.2. COD pollutant distribution modeling

The COD modeling over two months demonstrates variations in pollutant concentration under different tidal conditions. During the highest tide in April 2022 (**Fig. 8a**), COD concentrations peaked at approximately 25 mg/L in the central coastal area, indicating the presence of non-biodegradable chemical pollutants transported by tidal currents. In contrast, during the lowest tide in April 2022 (**Fig. 8b**), COD levels dropped to around 18 mg/L, but pollutants remained concentrated near discharge points, as reduced water movement limited dispersion. A similar trend was observed in September 2022, where COD concentrations reached 28 mg/L during the highest tide (**Fig. 8c**), particularly in the southern coastal area, likely due to industrial and agricultural runoff. During the lowest tide in September 2022 (**Fig. 8d**), COD levels decreased to approximately 20 mg/L, but remained elevated near pollution hotspots, as restricted tidal circulation prevented further dilution.

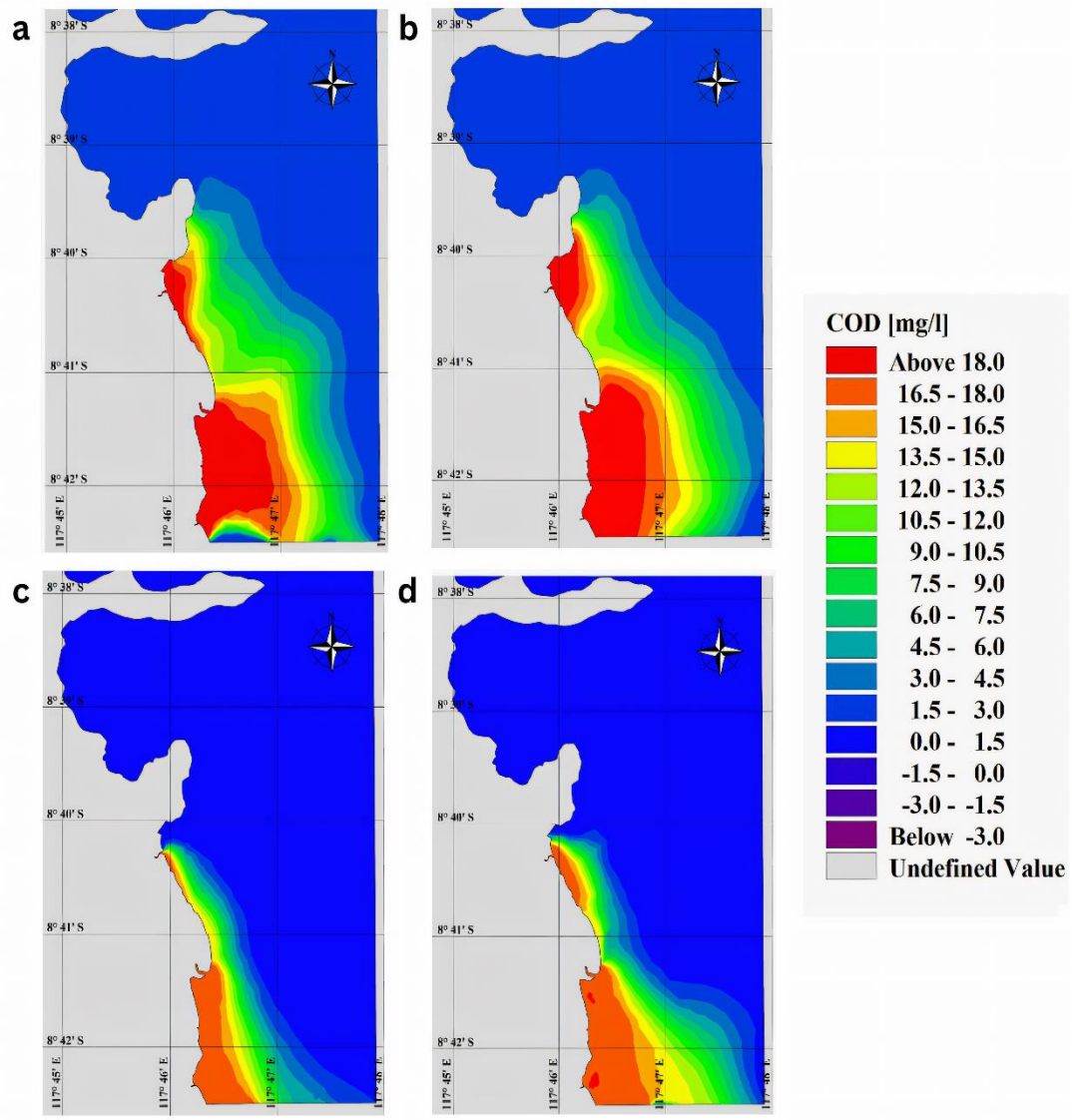

Fig. 8. COD pollutant distribution modeling at different tidal conditions and time intervals: a) Highest Tide–April 2022, b) Lowest Tide–April 2022, c) Highest Tide–September 2022 and d) Lowest Tide–September 2022.

The COD pollutant distribution modeling reveals a strong interaction between tidal variations and pollutant dispersion in Saleh Bay. As demonstrated in **figure 8**, tidal fluctuations significantly influence the spread and accumulation of chemical pollutants, affecting water quality and marine ecosystems. During the highest tides (**Fig. 8a** and **Fig. 8c**), COD concentrations peaked at 25 mg/L in April 2022 and 28 mg/L in September 2022, indicating wider pollutant dispersion due to stronger tidal currents. These findings align with Lee et al. (2020), who state that high tides facilitate the transport of pollutants over larger areas, which may contribute to dissolved oxygen depletion and further degrade water quality. The higher COD levels observed in September 2022 correlate with increased anthropogenic activities, such as agricultural runoff and industrial waste discharge, leading to more severe pollution impacts (Abdelmongy & El-Moselhy, 2015).

Conversely, during low tides (**Fig. 8b** and **Fig. 8d**), COD concentrations decreased but remained localized near major pollutant sources, with values around 18 mg/L in April and 20 mg/L in September. According to Zhang & Li (2010), low tides restrict pollutant dispersion, causing higher concentrations near discharge points and exacerbating oxidative stress on marine life. The limited water circulation during low tide periods intensifies COD accumulation, further threatening coastal biodiversity.

4.5.3 NO_3-N pollutant distribution modeling

The NO_3-N modeling over two months demonstrates variations in pollutant concentration under different tidal conditions. The highest tide in April 2022 (**Fig. 9a**) recorded NO_3-N concentrations peaking at approximately 4 mg/L in the eastern coastal area, likely due to agricultural runoff transported by strong surface currents. In contrast, during the lowest tide in April 2022 (**Fig. 9b**), NO_3-N concentrations decreased to around 3 mg/L, remaining concentrated near major agricultural discharge points, as weaker tidal flows limited dispersion. A similar pattern was observed in September 2022, where NO_3-N levels reached nearly 5 mg/L during the highest tide (**Fig. 9c**), particularly in the western coastal zone, indicating an increase in agricultural activity and runoff during the rainy season. However, during the lowest tide in September 2022 (**Fig. 9d**), NO_3-N concentrations dropped to approximately 3.5 mg/L, although higher levels persisted near pollution sources. For more details see the model in **figure 9** below.

The NO_3-N pollutant distribution modeling in Saleh Bay reveals a strong correlation between tidal dynamics and NO_3-N dispersion patterns. As shown in **figure 9**, the highest NO_3-N concentrations are influenced by tidal variations, hydrodynamic forces, and seasonal changes in pollutant input. During the highest tides in April and September 2022 (**Fig. 9a** and **Fig. 9c**), NO_3-N concentrations peaked at 4 mg/L and 5 mg/L, respectively, particularly in the eastern and western coastal areas. This pattern aligns with Russo et al. (2016); Arroyo-Ortega et al. (2019) who found that high tides enhance NO_3-N distribution, increasing the risk of eutrophication. Conversely, during the lowest tides (**Fig. 9b** and **Fig. 9d**), NO_3-N concentrations dropped to 3 mg/L in April and 3.5 mg/L in September, with pollutants remaining highly concentrated near major agricultural and wastewater discharge points.

According to Islam & Tanaka (2004), reduced water movement during low tides leads to localized NO_3-N accumulation, increasing the risk of hypoxic conditions. As supported by Liu et al. (2023), implementing ecosystem-based pollutant control strategies, such as improved wastewater treatment and sustainable agricultural practices, is critical to mitigating NO_3-N accumulation and protecting water quality in Saleh Bay.

4.5.4. PO_4-P pollutant distribution modeling

The PO_4-P modeling over two months demonstrates variations in pollutant concentration under different tidal conditions. PO_4-P concentrations were notably affected by industrial discharge, household waste, and agricultural runoff, particularly during high tide and rainy seasons. During the highest tide in April 2022 (**Fig. 10a**), PO_4-P levels peaked at approximately 1.5 mg/L, particularly in the central coastal zone, suggesting an increased input from industrial effluents and domestic waste.

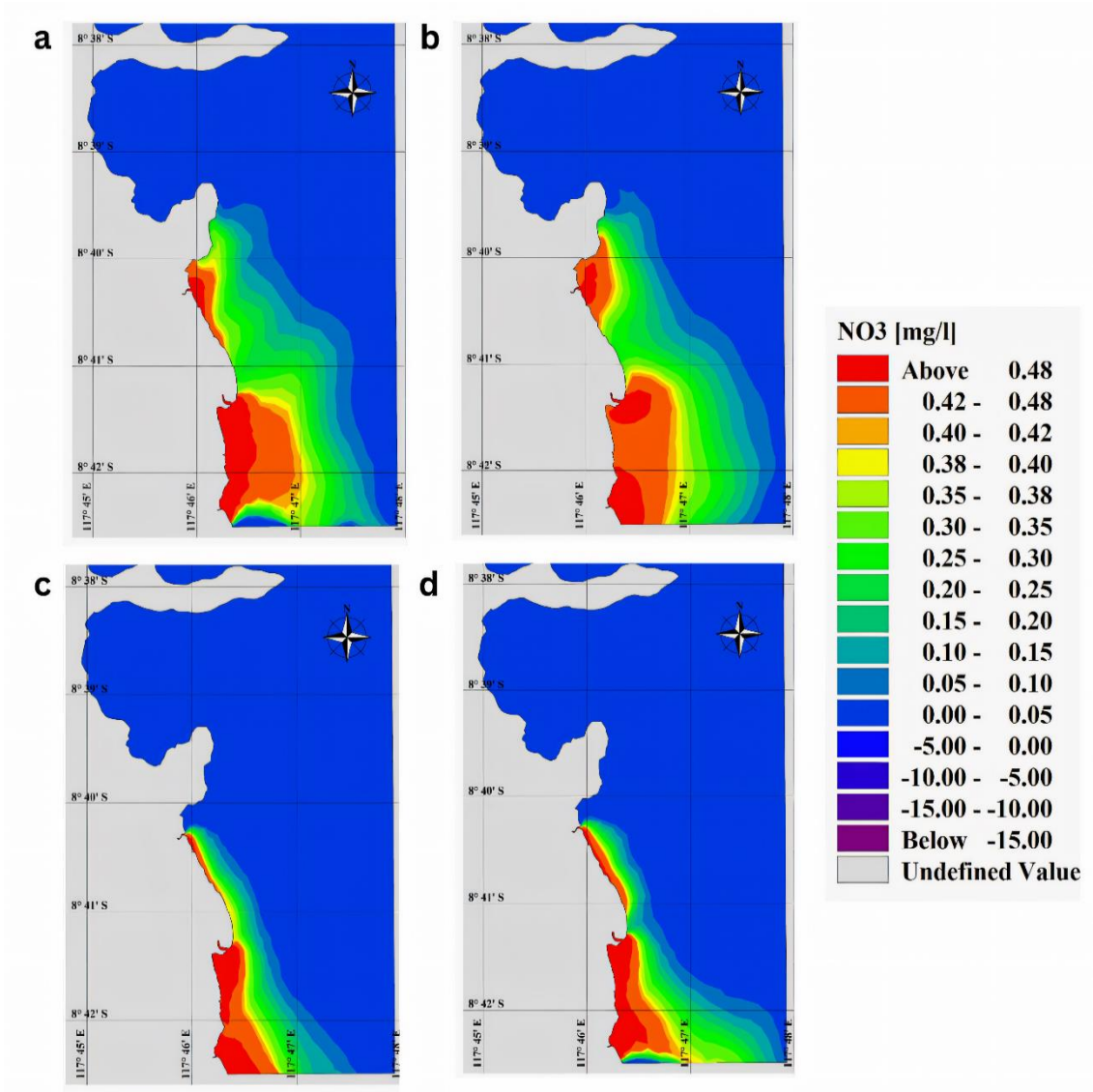

Fig. 9. NO_3 pollutant distribution modeling at different tidal conditions and time intervals: a) Highest Tide–April 2022, b) Lowest Tide–April 2022, c) Highest Tide–September 2022 and d) Lowest Tide–September 2022.

In contrast, during the lowest tide in April (**Fig. 10b**), PO_4-P concentrations dropped to 1.2 mg/L, remaining concentrated near major industrial discharge points due to reduced tidal circulation limiting pollutant dispersal. A similar pattern was observed in September 2022, where PO_4-P concentrations reached 1.8 mg/L during the highest tide (**Fig. 10c**), especially in the southern coastal area. During the lowest tide in September (**Fig. 10d**), PO_4-P levels declined to 1.4 mg/L, though elevated concentrations persisted near industrial sites, highlighting restricted transport during low tide conditions. For more details see the model in **figure 10** below. The PO_4-P pollutant distribution modeling in Saleh Bay highlights the significant impact of anthropogenic activities and tidal variations on nutrient dispersion and accumulation patterns. As observed in **figure 10**, PO_4-P concentrations fluctuate in response to tidal forces, industrial discharges, and agricultural runoff, affecting water quality and the risk of eutrophication.

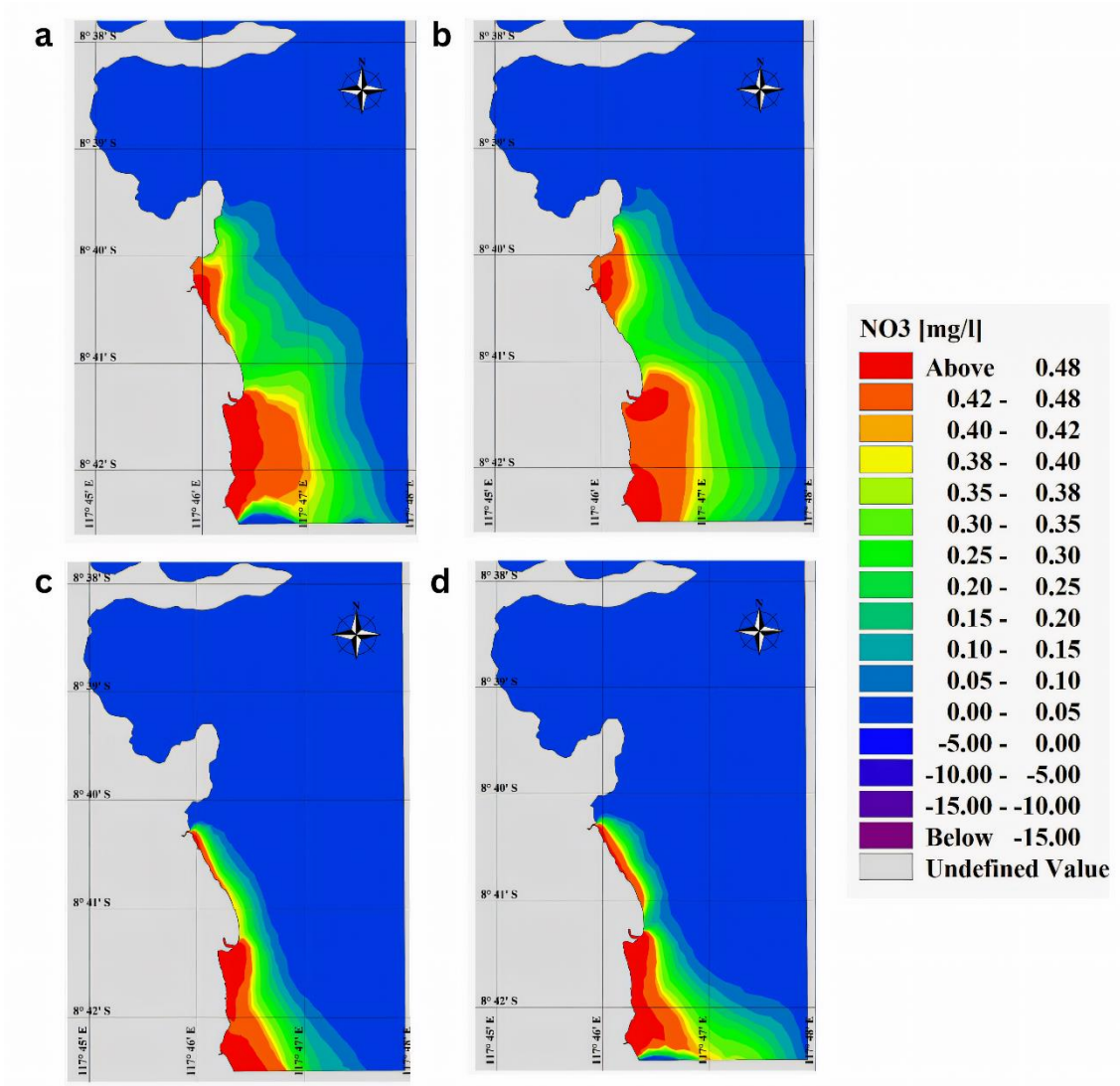

Fig. 10. PO_4-P pollutant distribution modeling at different tidal conditions and time intervals: a) Highest Tide–April 2022, b) Lowest Tide–April 2022, c) Highest Tide–September and d) Lowest Tide–September 2022

During the highest tides in April and September 2022 (**Fig. 10a** and **Fig. 10c**), PO_4-P concentrations peaked at 1.5 mg/L and 1.8 mg/L, respectively, with a wider spatial dispersion facilitated by stronger tidal currents.

This trend aligns with Lee et al. (2020), who emphasized that high tides promote broader phosphate transport, increasing eutrophication potential across coastal waters. The elevated phosphate levels in September suggest a greater influence of seasonal runoff and increased pollutant loading from industrial and agricultural sources. Conversely, during lowest tides (**Fig. 10b** and **Fig. 10d**), PO_4-P levels dropped to 1.2 mg/L in April and 1.4 mg/L in September, but remained highly concentrated near major discharge zones. According to Cheng et al. (2023), restricted tidal movement during low tides enhances pollutant accumulation near source areas, increasing the risk of localized eutrophication and water quality degradation.

4.6. Mariculture site selection and the pollutant distribution

The identification of suitable mariculture zones is a critical step in ensuring the sustainability and productivity of marine aquaculture activities. **Figure 1**1 illustrates the spatial distribution of mariculture suitability in Saleh Bay, which was derived from a digitized map based on the research of Arifin et al. (2025). The assessment considered multiple parameters, including water quality characteristics, ecological sensitivity, and technical feasibility for marine cultivation. The suitability classification was delineated into two categories, Suitable and Very Suitable, represented spatially in different shades. The categorization reflects integrated biophysical assessments encompassing nutrient concentrations, hydrodynamics, and proximity to pollutant sources primarily influenced by the surrounding watershed activities, such as those from the Bera Watershed area.

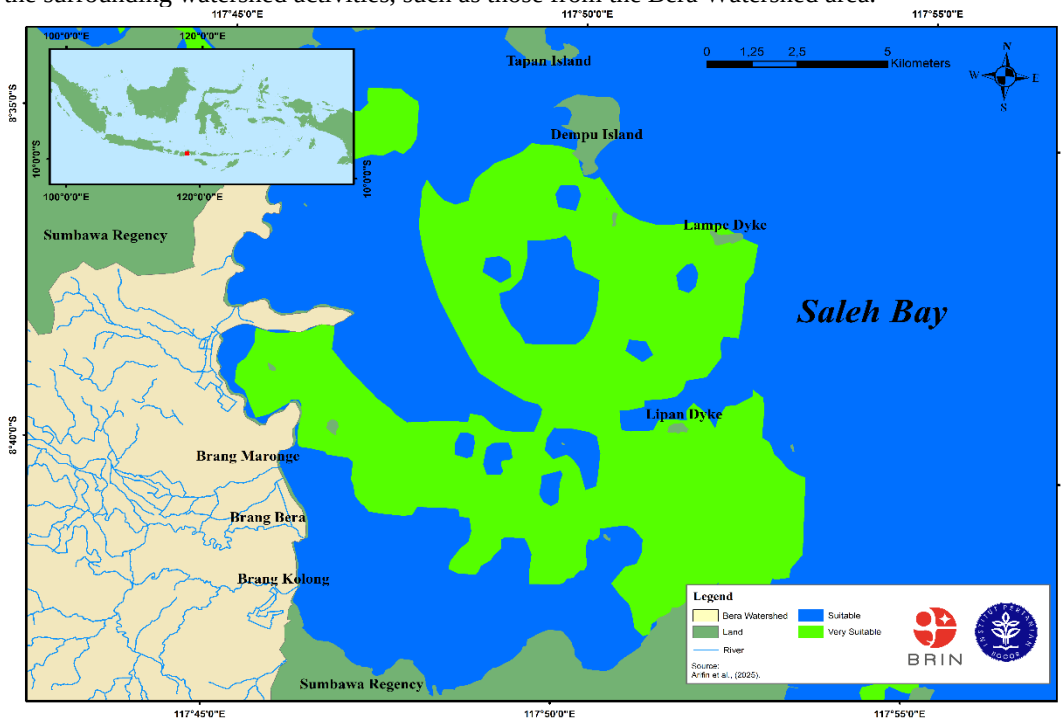

Fig. 11. Digitized map of mariculture suitability in Saleh Bay.

To further assess the potential environmental risks to mariculture, it is essential to examine the spatial distribution of water quality parameters that influence ecosystem health (Arifin et al., 2025). **Figure 12** presents the spatial distribution of key pollutant parameters, including BOD, COD, PO_4-P, and NO_3, during two monitoring periods which is April 2022 (wet season) and September 2022 (dry season). The results show that elevated concentrations of BOD and COD are consistently found near the river estuaries namely Brang Maronge, Brang Bera, and Brang Kolong indicating significant input of organic matter and oxidizable pollutants from upstream sources. Similarly, PO_4-P and NO_3 levels are higher in coastal zones during the wet season due to agricultural runoff and domestic waste discharge, with slightly lower concentrations in the dry season. These seasonal variations highlight the influence of land-based activities and hydrological dynamics on coastal water quality.

Overlaying the mariculture suitability map with the pollutant distribution layers underscores the importance of spatial planning in aquaculture development. While the central offshore areas of Saleh Bay remain highly suitable for mariculture due to low pollutant concentrations (Arifin et al., 2025), the coastal “Suitable” zones are more exposed to land-based pollution, especially during the wet season. Therefore, mariculture operations should be strategically located in “Very Suitable” areas to minimize exposure to pollutants and ensure better growth conditions for cultured species.

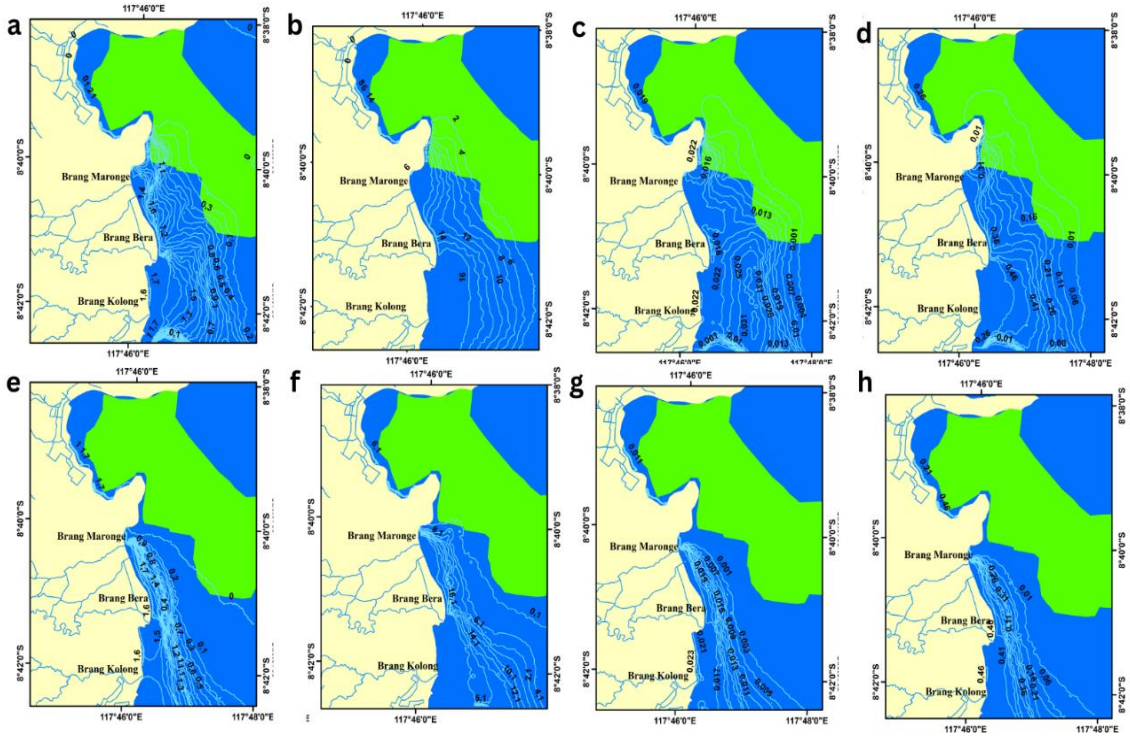

Fig. 12. Contour maps of pollutant parameter distributions of: a) BOD-April 2022, b) COD-April 2022, c) PO_4-P-April 2022, d) NO_3-April 2022, e) BOD-September 2022, f) COD-September 2022, g) PO_4-P-September 2022 and h) NO_3-September 2022.

Additionally, implementing integrated watershed management is essential to control nutrient and organic matter input from upstream areas, thereby maintaining the ecological integrity of Saleh Bay and supporting the long-term sustainability of mariculture activities concentrations (Freeman et al., 2019).

6. CONCLUSIONS

This study elucidates the dynamic interplay between bathymetry, hydrodynamics, and pollutant dispersion in the coastal waters of Saleh Bay and its implications for mariculture sustainability. The findings reveal that shallow coastal zones (5–50 m) are particularly vulnerable to pollutant accumulation due to limited water circulation and seasonal variability in wind and tidal regimes. Key pollutants, including BOD, COD, NO_3-N, and PO_4-P, were identified as primary contributors to eutrophication and ecological degradation in the bay.

The Brang Bera River was found to be the dominant source of freshwater inflow and pollutant transport, owing to its highest discharge capacity among the studied tributaries. The application of MIKE 21 modeling demonstrated that pollutant concentrations were significantly influenced by tidal dynamics, with higher dispersion during peak tides and more localized accumulation during low tides. These hydrodynamic behaviors underscore the importance of integrating spatial and temporal factors in coastal water quality assessments.

To mitigate the adverse effects of pollutant loading, the implementation of robust pollution control strategies is essential. These should include improved wastewater treatment systems, sustainable land-use practices, and integrated watershed management, particularly in the upstream catchment areas of the Bera Watershed. Additionally, continuous monitoring of physicochemical water quality parameters and pollutant concentrations is crucial for early detection and mitigation of environmental threats.

Furthermore, the establishment of Marine Protected Areas (MPAs), coupled with environmentally sustainable mariculture practices, can enhance ecological resilience and support long-term productivity. Advanced hydrodynamic and pollutant dispersion modelling should be further utilized to inform evidence-based coastal management strategies. Lastly, fostering active stakeholder and community participation remains vital for the successful implementation of conservation initiatives and the sustainable development of coastal ecosystems in Saleh Bay.

ACKNOWLEDGEMENT

This study was funded by RIIM G-2/2022, BRIN- Indonesia Endowment Fund for Education Agency [LPDP]. National Research and Innovation Agency [Grant number 82/II.7/HK/2022]; Contract Number: B-1740/II.7.5/FR/11/2022 dan B-15177/III.4/KS.00/11/2022. The authors also thanks to the Research Center for Conservation of Marine and Inland Water Resources, BRIN; Sumbawa Regency Government (PEMDA), Department of Marine Science and Technology, FPIK-IPB University, and Coastal Dynamics Laboratory, Directorate of Laboratory Management Research Facilities, and Science Parks and Science and Technology Parks, National Research and Innovation Agency BRIN.

REFERENCES

Abdelmongy, A.S. & El-Moselhy, K.M. (2015). Seasonal variations of the physical and chemical properties of seawater at the Northern Red Sea, Egypt. *Open Journal of Ocean and Coastal Sciences*, 2(1), 1–17. DOI: 10.1007/s10661-020-8134-4.

Ansari, M.S., Sharma, S., Armstrong, F.P., Delisio, M., & Ehsani, S. (2024). Exploring PCSWMM for large mixed land-use watershed by establishing monitoring sites to evaluate stream water quality. *Hydrology*, 11(7), 104. DOI: 10.3390/hydrology11070104

Arifin, T., Yulius., Ramdhan, M., Johan, O., Gunawan, D.P., Heriati, A., Mustikasari, E., Rahmania, R., Purbani, D., Dillenia, I., Agus, S.B., Asaf, R., Hatta, M., Marzuki, I., Akhwady, R., Sufyan, A., Fihrin, H., Septiningsih, E., Wahyono, A., & Athirah, A. (2025). Mariculture site selection based on water quality, cultivation, and ecological condition. *Global Journal of Environmental Science and Management, 11*(1), 129–146. DOI: 10.22034/gjesm.2025.01.08

Arroyo-Ortega, I., Chavarin-Pineda, Y. & Torres, E. (2024). Assessing contamination in transitional waters using geospatial technologies: A review. *ISPRS International Journal of Geo-Information*, 13(6), 196. DOI: 10.3390/ijgi13060196

Basheer, M., Abutaleb, K., Mekawy, A., & Abed, N. (2024). Simulation of Water Quality and Pollution Reduction of Qarun Lake, Egypt using 2D Hydrodynamic Ecological Modelling. *Egyptian Journal of Aquatic Biology and Fisheries*, *28*(6), 1975-2002

Bath, G.E., Price, C.A., Riley, K.L. and Morris Jr, J.A. (2023). A global review of protected species interactions with marine aquaculture. *Reviews in Aquaculture*, *15*(4), 1686-1719.

Benedini, M. (2011). Water quality models for rivers and streams: State of the art and future perspectives. *European Water*, 34(1), 27–40.

Bilal, A., Xie, Q., & Zhai, Y. (2020). Flow, sediment, and morpho-dynamics of river confluence in tidal and non-tidal environments. *Journal of Marine Science and Engineering*, *8*(8), 591. DOI: 10.3390/jmse8080591

Carlson, R.R., Foo, S.A. & Asner, G.P. (2019). Land use impacts on coral reef health: A ridge-to-reef perspective. *Frontiers in Marine Science*, 6, 562. DOI: 10.3389/fmars.2019.00562

Carpenter, S.R. (2005). Eutrophication of aquatic ecosystems: bistability and soil phosphorus. Proceedings of the National Academy of Sciences, 102(29), 10002–10005. DOI: 10.1073/pnas.0503959102

Chen, S.S., Kimirei, I.A., Yu, C., Shen, Q. & Gao, Q. (2022). Assessment of urban river water pollution with urbanization in East Africa. *Environmental Science and Pollution Research*, 29(27), 40812–40825. DOI: 0.1007/s11356-021-18082-1

Cheng, Z., Hong, G., Li, Q., Liu, S., Wang, S. & Ma, Y. (2023). Seasonal dynamics of coastal pollution migration in open waters with intensive marine ranching. *Marine Environmental Research*, 190, 106101. DOI: 10.1016/j.marenvres.2023.106101

Di, Z., Chang, M. & Guo, P. (2019). Water quality evaluation of the Yangtze River in China using machine learning techniques and data monitoring on different time scales. *Water*, 11(2), 339. DOI: 10.3390/w11020339

Ferreira, J.G., Bernard-Jannin, L., Cubillo, A., e Silva, J.L., Diedericks, G.P., Moore, H., Service, M. and Nunes, J.P. (2023). From soil to sea: An ecological modelling framework for sustainable aquaculture. *Aquaculture*, *577*, 739920.

Freeman, S., Angel, D. and Freeman, S. (2019). Integrated aquaculture (INTAQ) as a tool for an ecosystem approach to the marine farming sector in the Mediterranean Sea. *Integr. Maric*, *529*, 133-183.

Harianto, E., & Efendi, I. (2017). Analisis fisika kimia perairan untuk pemilihan lokasi budidaya ikan kerapu (*Serranidae*) di Teluk Saleh Kabupaten Sumbawa, Nusa Tenggara Barat dengan metode STORET dan analisis multivariat. *Jurnal Akuakultur Sungai dan Danau*, 2(1), 25–42.

Iglesias, I., Almeida, C.M.R., Teixeira, C., Mucha, A.P., Magalhães, A., Bio, A. and Bastos, L. (2020). Linking contaminant distribution to hydrodynamic patterns in an urban estuary: The Douro estuary test case. *Science of The Total Environment, 707*, 135792.

Islam, M.S. & Tanaka, M. (2004). Impacts of pollution on coastal and marine ecosystems including coastal and marine fisheries and approach for management: A review and synthesis. *Marine Pollution Bulletin*, 48(7-8), 624–649. DOI: 10.1016/j.marpolbul.2003.12.004

Kusumawati, E., Susilo, S.B, Agus, S.B., Arifin, A., Yulius. (2019). Analysis of Determination of Chlorophyll Concentration and Primary Productivity in the Saleh Bay Using Landsat OLI 8 Imagery. Journal of Natural Resources and Environmental Management 9(3): 671-679. http://dx.doi.org/10.29244/jpsl.9.3.671-679.

Lee, S.A., Lee, J., Han, Y. & Kim, G. (2020). Biogeochemical alteration and fluxes of dissolved organic matter and nutrients in coastal bays. Estuarine, *Coastal and Shelf Science*, 245, 106992. DOI: 10.1016/j.ecss.2020.106992

Liu, L., Ouyang, W., Wang, Y., Lian, Z., Pan, J., Liu, H., Chen, J. & Niu, S. (2023). Paddy water management for diffuse nitrogen and phosphorus pollution control in China: A comprehensive review and emerging prospects. *Agricultural Water Management*, 277, 108102. DOI: 10.1016/j.agwat.2022.108102

Marganingrum, D. & Santoso, H. (2019). Evapotranspiration of Indonesia tropical area. *Jurnal Presipitasi: Media Komunikasi dan Pengembangan Teknik Lingkungan*, 16(3), 106–116. DOI: 10.14710/presipitasi.v16i3.106-116

Marzuki, M., Nurjaya, I.W., Purbayanto, A., Budiharso, S. &Supriyono, E. (2014). Sustainability analysis of mariculture management in Saleh Bay, Sumbawa District. *Environmental Management and Sustainable Development*, 3(2), 127-137. DOI: 10.5296/emsd.v3i2.6427

Nalley, E.M., Tuttle, L.J., Barkman, A.L., Conklin, E.E., Wulstein, D.M., Richmond, R.H. and Donahue, M.J. (2021). Water quality thresholds for coastal contaminant impacts on corals: a systematic review and meta-analysis. *Science of the Total Environment, 794*, 148632.

Nugroho, A.R., Akhwady, R., Metakaryanto, D., & Yahya, F. (2016). Studi model distribusi pencemaran di pantai utara Jawa Tengah menggunakan model MIKE 21 ECOLab. *Jurnal Sains dan Teknologi Lingkungan*, 8(2), 89–100. DOI: 10.5296/emsd.v3i2.6427

Prihantono, J., Fajrianto, I.A. & Kurniadi, Y.N. (2018). Hydrodynamic and sediment transport modeling in coastal waters around Tanjung Pontang, Serang Regency-Banten. *Jurnal Kelautan Nasional*, 13(2), 75–88.

Purwanto., Sugianto, D. N., Zainuri, M., Permatasari, G., Atmodjo, W., Rochaddi, B., Ismanto, A., Wetchayont, P., & Wirasatriya, A. (2021). Seasonal variability of waves within the Indonesian seas and its relation with the monsoon wind. *Indonesian Journal of Marine Sciences*, 26(3), 189–196. DOI: 10.14710/ij.ijms.26.3.189-196

Putra, A., Hermon, D., Priakriesan, W., Syarief, A., Ridwan, N. N. H., Arifin, T., Febriandi, H., Damanhuri, H., Widodo, T., & Dermawan, A. (2024). Assessment of seawater quality and environmental sustainability for shipwreck diving tourism: A case study of MV Boelongan Nederland in Mandeh Bay, Indonesia. *Geography, Environment, Sustainability*, *4*(17), 171–182. DOI: 10.24057/2071-9388-2024-3469

Rachman, R. A., Armono, H. D., Wardani, K. S., Khoirunnisa, H., & Wijayanti, R. (2023). Study of Hydrodynamic Patterns of Tanjung Pasir Banten Waters to Support the NCICD Sea Wall Development Plan. *Journal of Geoscience, Engineering, Environment, and Technology*, *8*(1), 1-9. DOI: 10.25299/jgeet.2023.8.1.10801

Risna, W.O., Safilu, M.S. & Sirih, M. (2022). Analysis of water pollution levels in Kendari Bay based on gastropod (Prosobranchia) diversity. *Jurnal Alumni Pendidikan Biologi*, 7(2), 92–98. DOI: 10.36709/ampibi.v7i2.24486

Russo, A., Gouveia, C., Levy, I., Dayan, U., Jerez, S., Mendes, M. & Trigo, R. (2016). Coastal recirculation potential affecting air pollutants in Portugal: The role of circulation weather types. *Atmospheric Environment*, 135, 9–19. DOI: 10.1016/j.atmosenv.2016.03.039

Schlaefer, J. A., Tebbett, S. B., & Bellwood, D. R. (2021). The study of sediments on coral reefs: a hydrodynamic perspective. *Marine Pollution Bulletin*, *169*, 112580. DOI: 10.1016/j.marpolbul.2021.112580

Smith, V.H., Joye, S.B. & Howarth, R.W. (2006). Eutrophication of freshwater and marine ecosystems. *Limnology and Oceanography*, 51(1 part 2), 351–355. DOI: 10.4319/lo.2006.51.1_part_2.0351

Sobha, T. R., Vibija, C. P., & Fahima, P. (2023). Coral reef: A hot spot of marine biodiversity. *Sustainable development and biodiversity conservation and sustainable utilization of bioresources*. 171–194. DOI: 10.1007/978-981-19-5841-0_8

Xu, C., Ren, Z., Huang, S., Li, J., Zi, Y., & Hu, X. (2023). Simulation Study on the Impact of Water Flow Regulation Based on the MIKE 21 Model in a River Water Environment. *Sustainability*, *15*(13), 10313. DOI: 10.3390/su151310313

Yulius, Y., Aisyah, A., Prihantono, J., & Gunawan, D. (2018). Kajian Kualitas Perairan untuk Budidaya Laut di Teluk Saleh, Kabupaten Dompu. Jurnal Segara, 14(1), 57–68. DOI: 10.15578/segara.v14i1.7108

Zhang, H. & Li, S. (2010). Effects of physical and biochemical processes on the dissolved oxygen budget for the Pearl River Estuary during summer. *Journal of Marine Systems*, 79(1-2), 65–88. DOI: 10.1016/j.jmarsys.2009.07.002

HABITAT ASSESSMENT OF WHALE SHARKS (*RHINCODON TYPUS*) IN SALEH BAY, INDONESIA: LINKING CHLOROPHYLL-A AND SEA SURFACE TEMPERATURE USING AQUA MODIS DATA

Thalia Putri HERDIANTI[1], Yulius YULIUS[2]*, Syamsul B. AGUS[1], Taslim ARIFIN[2], Aprizon PUTRA[2], Joko PRIHANTONO[2], Aida HERIATI[2], Sri Turni HARTATI[2], Rudhy AKHWADY[2], Devi D. SURYONO[2], Rinny RAHMANIA[2], Muhammad RAMDHAN[3], Arif HILMAWAN[4], Arya NINGSIH[5], Sadad SADAD[5], Mudjijono MUDJIJONO[4], Abdul ASYIRI[6]

DOI: 10.21163/GT_2025.202.04

ABSTRACT

Saleh Bay is between Sumbawa Regency and Dompu Regency in Nusa Tenggara Barat (NTB) Province, Indonesia. It is spanning approximately 2,123 km². This semi-enclosed marine environment, designated as a protected marine area, connects directly to the Flores Sea and serves as a critical habitat for whale sharks (*Rhincodon typus*), an endangered species fully protected in Indonesia since 2013. This study aims to assess whale shark habitats by investigating their appearances and analyzing the relationship between Sea Surface Temperature (SST), Chlorophyll-a (Chl-a) concentration, and whale shark occurrences using Aqua Moderate Resolution Imaging Spectroradiometer (Aqua MODIS) data in the marine waters of Saleh Bay. The Inverse Distance Weighting (IDW) interpolation method in Quantum Geographic Information System (QGIS) was applied to process Chl-a and SST data, while field surveys provided records of whale shark sightings. From February, March, and April 2024, a total of 36 whale shark sightings were documented, corresponding to Chl-a concentrations ranging from 0.20 to 3.45 mg/m³ and SST values between 29.47-33.85°C. The analysis revealed significant relationships between whale shark occurrences and environmental factors, with coefficients of determination (R^2) of 0.9055 for February, 0.8959 for March, and 0.4638 for April. These results emphasize the importance of food availability (indicated by Chl-a) and SST in shaping whale shark distribution and behavior. The study underscores the importance of integrating SST and Chl-a monitoring into conservation and management strategies. By identifying key environmental drivers that shape whale shark habitats, this research offers valuable insights to support sustainable ecotourism initiatives and ensure the long-term protection of whale sharks in Saleh Bay.

Key-words: *Aqua MODIS; Chlorophyll-a (Chl-a); Saleh Bay; Sea Surface Temperature (SST); Whale Shark.*

[1]Department of Marine Science and Technology, IPB University, Bogor, Indonesia. (TPH) thaliaputri@apps.ipb.ac.id, (SBA) mycacul@gmail.com

[2]National Research and Innovation Agency, KST Soekarno, Cibinong, West Java, Indonesia. (YY) yuli058@brin.go.id, (TA) tasl003@brin.go.id, (AP) apri024@brin.go.id, (JP) joko043@brin.go.id, (AH) aida002@brin.go.id, (STH) srit002@brin.go.id, (RA) rudh002@brin.go.id, (DDS) devi022@brin.go.id, (RR) rinny.rahmania@brin.go.id

[3]National Research and Innovation Agency, KST Samaun Samadikun, Bandung, Indonesia. (MR) muha307@brin.go.id

[4]National Research and Innovation Agency, Gatot Subroto, Jakarta, Indonesia. (AH) arif032@brin.go.id, (AH) mudj004@brin.go.id

[5]Agency for Local Research and Development, Government of Sumbawa, Sumbawa, Indonesia. (AN) ningsiharya166@gmail.com, (SS) sadadmagrabi@gmail.com

[6]Center for Data and Information, Bearau of Organization and Human Resources, Cibinong, Indonesia. (AA) abdu009@brin.go.id

**Corresponding author: (YY) yuli058@brin.go.id*

1. INTRODUCTION

Saleh Bay is between Sumbawa Island and lies within the administrative territories of Sumbawa Regency and Dompu Regency in the Nusa Tenggara Barat (NTB) Province, Indonesia. It spans approximately 2,123 km² (Asrial et al., 2021). Designated as a protected marine area, the marine waters of Saleh Bay are developing to enhance its fisheries potential, particularly through cultivating reef fish and promoting marine fishing activities (Yulius et al., 2018; Kusumawati et al., 2019). The bay has gained national recognition as a prime location for observing whale sharks which inhabit the area year-round due to their distinctive home range movement patterns. This behavior positions the marine waters of Saleh Bay as a crucial congregation site for whale sharks throughout the year, distinguishing it as the only area in Indonesia to exhibit such a unique phenomenon (Faridet al., 2021).

Whale sharks or Rhincodon typus are classified as endangered on the International Union for Conservation of Nature and Natural Resources (IUCN) Red List (Djunaidi et al., 2020). Since 2002, they have been listed in Appendix II of the Convention on International Trade in Endangered Species of Wild Fauna and Flora (CITES) (Gallimore et al., 2024). The Convention on Migratory Species (CMS) also identifies whale sharks as migratory species requiring international protection due to their ability to traverse national boundaries (Fowler et al., 2021; Rumisha et al., 2024). In Indonesia, whale sharks have been fully protected since 2013 under Ministerial Decree No. 18/KEPMEN-KP/2013, issued by the Ministry of Marine Affairs and Fisheries (Lelono et al., 2024; Yasir et al., 2024).

Farid et al. (2021); Womersley et al. (2024) highlighted that the marine waters of Saleh Bay offer optimal conditions for whale shark visitation, largely due to its plentiful food resources. This is evident from the frequent annual sightings of whale sharks in the area, supported by the high biological productivity of the waters, which include abundant plankton, fish spawning grounds, and increased concentrations of Chlorophyll-a (Chl-a). Sianipar (2019); Adhitia (2023) reported that whale shark movement patterns vary depending on the unique environmental features of different water bodies. Sea Surface Temperature (SST) also plays a role in influencing the metabolism of marine organisms as well as the distribution of plankton, which is the main food source for whale sharks (Yunus et al., 2019; Reinero et al., 2024).

This study prioritizes two environmental parameters for SST and Chl-a. Both parameters are crucial for coastal and marine ecosystems as they play an essential role in sustaining fisheries and facilitating the growth of marine aquaculture (Doydee et al., 2010; Putri et al., 2025). Furthermore, these parameters are instrumental in identifying areas where fish are likely to be found (Enita et al., 2017).

Remote sensing technology offers an effective approach to obtaining data on SST and Chl-a concentration. Aqua Moderate Resolution Imaging Spectroradiometer (Aqua MODIS), a satellite equipped with an imaging spectroradiometer sensor, can detect and map SST and Chl-a concentrations in specific areas. This satellite provides high-resolution data that enables continuous and periodic monitoring of trends and variations in SST and Chl-a concentrations (Yulius et al., 2021). A critical aspect of this effort is understanding the occurrence and distribution of whale sharks, which depend on factors such as movement patterns, food availability, and favorable SST.

This study aims to assess whale shark habitats by investigating their appearances and analyzing the relationship between SST, Chl-a concentration, and whale shark occurrences using Aqua MODIS data in the marine waters of Saleh Bay. As part of this research, the focus is on mapping whale shark appearances alongside the distribution of phytoplankton abundance, SST, and Chl-a concentration in the marine waters of Saleh Bay, with a novelty in revealing a strong relationship between environmental parameters and whale shark habitat preferences through spatial overlay and linear regression analysis highlighted by R^2 values which demonstrates the potential use of these variables as predictors of whale shark distribution in the future.

2. STUDY AREA

The study area is situated within the marine waters of Saleh Bay, which is administratively shared between Sumbawa Regency and Dompu Regency in NTB Province, Indonesia. Saleh Bay is a semi-enclosed water body that directly connects to the Flores Sea. The bay is geographically positioned at coordinates 117°–118° East Longitude and 8.8°–8.1° South Latitude. The marine waters of Saleh Bay cover an area of approximately 2,123 km² and span a length of about 282 km, encompassing the waters of Empang, Plampang, Lape/Lopok, and Moyo Hilir in Sumbawa Regency. This area coverage was determined through spatial analysis using Geographic Information System (GIS) techniques, which involved digitizing the bay boundary and calculating the water surface area. Parts of Saleh Bay also fall within the Manggelewa and Kempo Districts of Dompu Regency. Several small islands within the bay, including Gili Panjang, Gili Meriam Besar, Gili Tapan, Gili Lipan, Gili Dompo, Gili Sentigi, and Gili Dangar Ode, have recently gained popularity among tourists. Coral reefs fringe nearly the entire bay and can be found at depths up to 15 meters below sea level. A map illustrating the distribution of whale shark sighting locations is provided for better understanding. For a more detailed visualization, refer to **Figure 1** below.

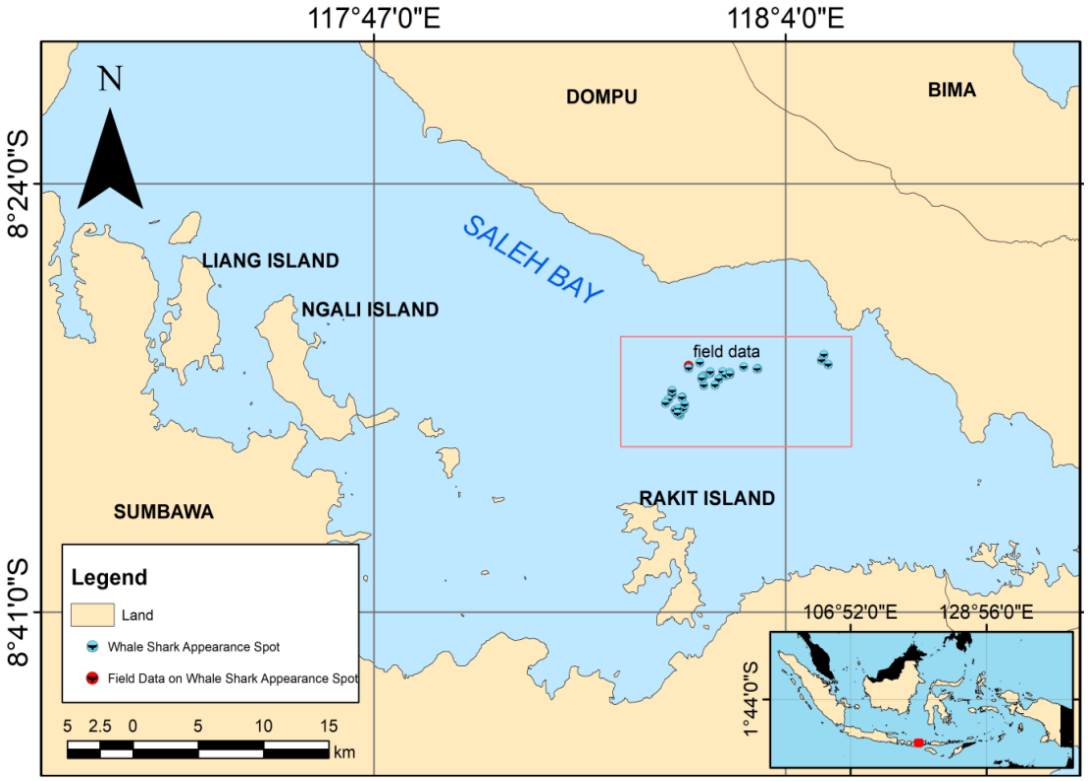

Fig. 1. Location map of Saleh Bay for whale shark sightings

3. DATA AND METHODS

3.1. Data Collections

This study employed Level-3 Aqua MODIS data, which provided information on SST and Chl-a concentrations for the period from February, March, and April 2024. The data was obtained from NASA's Ocean Color website (https://oceancolor.gsfc.nasa.gov/l3/) and processed using Quantum Geographic Information System (QGIS).

Bathymetry data was sourced from the Tanah Air Indonesia platform (https://tanahair.indonesia.go.id/) and processed using QGIS. Additionally, whale shark sighting data was collected through field surveys, recorded in MS Excel, and later converted into a format suitable for integration with QGIS.

3.2. Data Analysis Techniques

3.2.1. Processing of SST Data

The initial step in processing SST data involves cropping the research area from the Aqua MODIS dataset using Ocean Data View (ODV) software. The next phase involves interpolating the data using the Inverse Distance Weighting (IDW) method with the support of QGIS software. The IDW interpolation technique offers the advantage of giving greater weight to nearby input points, resulting in a more detailed surface. However, it has a limitation: it cannot estimate values beyond the maximum or below the minimum of the input sample points (Yudanegaraet al., 2021).

3.2.2. Processing of Chl-a Data

The method applied to process Chl-a data closely mirrors the approach used for SST data. Initially, the Chl-a data is cropped to focus on the research area using ODV software and then exported for further processing. Interpolation is subsequently conducted using the IDW method in QGIS software. This map serves as an indicator of primary productivity, a crucial element in marine ecosystems, which can significantly impact the occurrence of whale sharks.

3.2.3. Processing Whale Shark Sightings Data

Whale shark occurrence data from the study area was initially gathered through field surveys, organized using Excel software, and subsequently processed in QGIS. The occurrence points were mapped and overlaid onto spatial layers representing SST variability and Chl-a concentrations. SST and Chl-a values corresponding to each mapped occurrence point were then extracted, creating a dataset that linked environmental parameters to whale shark sightings.

3.2.4. Processing Bathymetry Data

In addition to SST and Chl-a, bathymetry data (sea depth) was processed using QGIS. This data was obtained from platform (https://tanahair.indonesia.go.id/) to create a detailed map of the underwater depth in the study area.

3.3. Data Analysis

After compiling data on SST, Chl-a, bathymetry, and whale shark sightings, a simple linear regression analysis was performed using Excel software. This analysis evaluated the strength and significance of the relationship between environmental variables, specifically SST and Chl-a, and whale shark occurrences. This analysis provided deeper insights into the environmental factors shaping whale shark habitat preferences.

4. RESULTS AND DISCUSSION

The photos in **Figure 2** capture whale shark sightings recorded during field observations conducted in July 2024. These observations emphasize the interaction between whale sharks and their surrounding environment, demonstrating their consistent presence in the marine waters of Saleh Bay.

Fig. 2. Photos of whale shark activity at the water surface 1) Whale sharks are observed near the platform, interacting mainly for feeding or observation; and 2) Whale sharks are seen farther away, positioned vertically, with their tails more visible.

Figure 2 above depicts whale shark activity near shallow platforms, suggesting that these areas identified on the bathymetry map at a depth of approximately -400 m may function as preferred zones for feeding or resting. By combining field observations, as depicted in the photographs, with the detailed seabed topography provided by the bathymetry map (**Figure 3**), this study underscores the importance of environmental factors such as sea depth and seabed structure in influencing whale shark behavior and habitat preferences within the marine waters of Saleh Bay.

The observed interactions between humans and whale sharks in these shallow areas highlight the urgency of implementing sustainable tourism practices and robust conservation strategies to protect the species natural environment. As illustrated in **Figure 1** (see Methods), a map showing whale shark appearance spots recorded 36 sightings of whale sharks between February, March, and April 2024. These sightings were based on field surveys, with additional data points collected in July 2024. The link between whale sharks and surface-feeding activities is supported by the findings of Mottaet al. (2010); Syahet al. (2018); Dove & Pierce (2022), who report that whale sharks' surface to feed on zooplankton, including sergestids, copepods, arrow worms, crab larvae, mollusks, crustaceans, coral eggs, and fish larvae.

Observations conducted between 05:00-09:00 AM documented whale sharks actively feeding, likely attracted by the strong scent of pelagic fish. It is hypothesized that the frequent sightings during these morning hours are due to the availability of abundant food resources (Suruanet al., 2024). As the day progresses, whale sharks are no longer observed near the surface, likely diving to greater depths in search of food. This behavior aligns with findings by Suprapti (2015), who highlights that whale sharks prefer deeper waters but surface when feeding.

Bathymetry data, which provides information on ocean depth, is essential for understanding oceanographic dynamics such as currents, navigation, habitat analysis, temperature variations, and plankton distribution. These factors indirectly influence the distribution of large marine species, including whale sharks (Almaret al., 2021). **Figure 3** presents the bathymetry map of Saleh Bay and its surrounding waters, derived from the National Bathymetry Database in platform https://tanahair.indonesia.go.id/ and processed using QGIS software. Analysis of the bathymetry data reveals that the marine waters of Saleh Bay reach a maximum depth of -400 m. This aligns with previous research showing that whale sharks are often found in nutrient-rich productive zones. Such zones are shaped by seabed topography and upwelling currents, which bring nutrients from the deep ocean to the surface, creating favorable feeding grounds for whale sharks (Ryanet al., 2017).

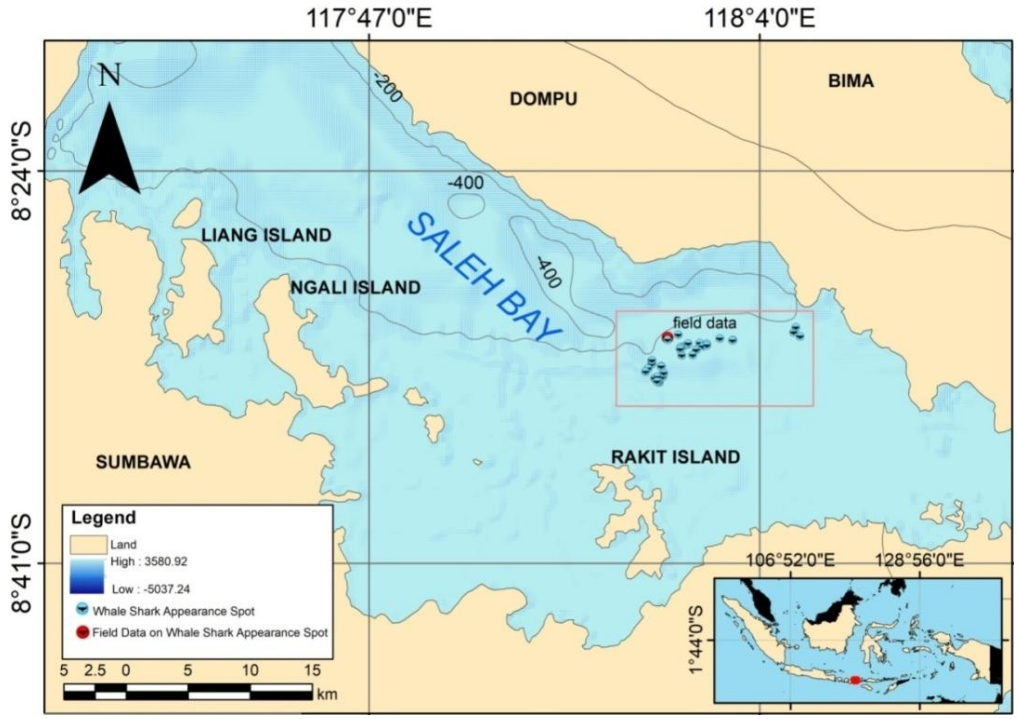

Fig. 3. Bathymetry map of Saleh Bay for whale shark sightings.

4.1. Chl-a Distributions and Whale Shark Sightings

The maps presented in **Figure 4** show the spatial distributions of Chl-a concentrations in the marine waters of Saleh Bay during different periods. The highlighted whale shark appearance spots, marked in blue, correspond to areas with varying levels of Chl-a concentration, as indicated by the gradient from low (light green) to high (dark green) values. Additionally, red markers indicate field data points where whale shark sightings were recorded. For more details see **Figure 4** below.

Figure 4 shows the distributions of Chl-a concentrations in the marine waters of Saleh Bay, which range from 0.20 to 3.45 mg/m³, alongside recorded whale shark appearance spots. The data reveals that whale shark sightings are concentrated in areas with elevated Chl-a levels, indicating high marine productivity. This correlation suggests that environmental factors, such as the availability of zooplankton and fish larvae, significantly influence whale shark presence in these areas (Foxet al., 2013). As McKinney (2012) notes, Chl-a is a critical indicator of marine productivity, closely linked to phytoplankton abundance. An increase in Chl-a levels leads to higher phytoplankton concentrations, which subsequently support greater densities of zooplankton and fish larvae in the water column. This trophic cascade directly aligns with whale shark sightings, as these organisms form their primary diet.

While whale sharks are generally solitary creatures, Cruzet al. (2013) observe that they tend to aggregate in areas abundant with food resources. As migratory species, they traverse areas in search of food, often following plankton concentrations in marine ecosystems. In the marine waters of Saleh Bay, whale shark surface appearances, as documented by Farid (2021), are frequently associated with the presence of small fish near the water's surface. The presence of small fish serves as a reliable indicator of plankton abundance, highlighting the interdependence of these organisms and the ecological dynamics at play. The patterns presented in **Figure 4** underscore the pivotal role of Chl-a concentrations in shaping whale shark distributions, emphasizing the importance of high-productivity zones in the marine waters of Saleh Bay. This relationship further highlights the ecological significance of plankton distributions, which initiates cascading effects across trophic levels, sustaining the dynamic marine ecosystem observed in the bay.

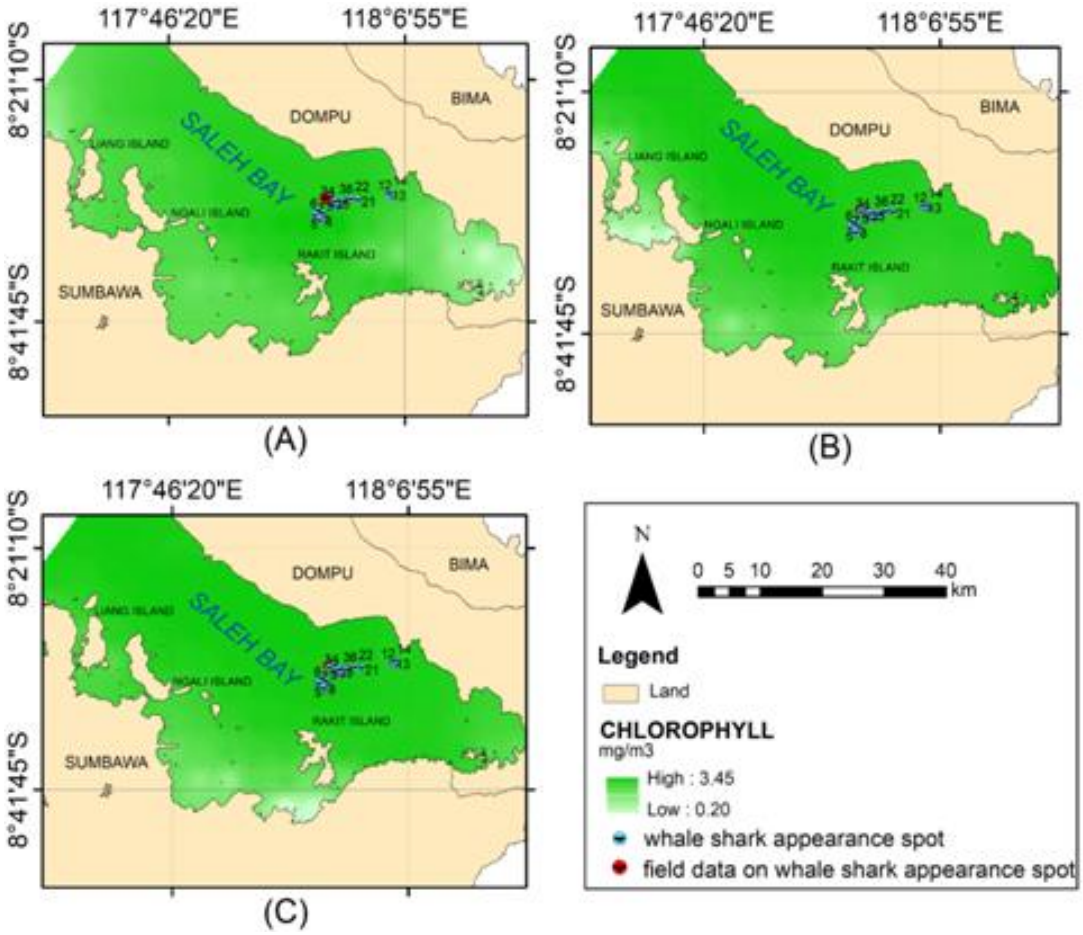

Fig 4. Chl-a distributions and whale shark sighting locations (A, B, C)

4.2 Sea Surface Temperature (SST) Distributions and Whale Shark Sightings

The maps presented in **Figure 5** show the spatial distributions of SST in the marine waters of Saleh Bay during different periods. The SST gradient ranges from low (blue) to high (red), reflecting variations in temperature across the area. The highlighted whale shark appearance spots, marked in blue, indicate locations where whale sharks were observed, while the red markers represent field data points confirming these sightings. These maps provide critical insights into the relationship between SST variability and the spatial patterns of whale shark appearances. For more details, refer to **Figure 5** below.

Figure 5 shows the distributions of SST in the marine waters of Saleh Bay, ranging from 29.47°C (blue) to 33.85°C (red), along with whale shark sighting locations (blue) and field observation data points (red). The variation in SST highlighted in **Figure 5** underscores its crucial role in influencing physical conditions within the water, which, in turn, can significantly impact marine organisms. As noted by Richmond (2011), SST affects metabolic rates, behavior, reproduction, and even broader meteorological patterns. Furthermore, temperature variability directly impacts oxygen solubility, with higher temperatures leading to increased oxygen consumption in aquatic organisms. Rahmanet al. (2017) reported that whale sharks typically inhabit waters with temperatures ranging from 18-30°C, while Murdaniet al. (2018) identified their preference for waters within 28-32°C.

The consistency between these ranges and the observed SST in the marine waters of Saleh Bay suggests that the area provides optimal thermal conditions for whale sharks, enabling them to thrive in these waters over extended periods.SST variability also plays a pivotal role in whale shark distribution and migration. According to Binderet al. (2011), temperature influences migratory behavior as part of thermoregulation, a process that organisms use to maintain their body temperature. Stewart (2011) emphasized that whale sharks avoid surface temperatures exceeding those in deeper waters, favoring habitats with warm but moderate SST.

Additionally, Staceyet al. (2008) noted that whale sharks are frequently observed in surface waters with SSTs above 29°C, with 90% of solitary sightings occurring in waters where SST ranges between 25-35°C. Interestingly, whale sharks demonstrate the ability to tolerate extreme temperatures during deep dives and tolerances as low as 10°C. Conversely, these sharks have also been observed in exceptionally high SSTs, such as in Fundy Bay on the eastern coast of North America, where SST reached 44°C. Nevertheless, the preferred temperature range of 28-32°C observed in the marine waters of Saleh Bay supports their metabolic processes and ensures sufficient food availability, making the bay an ideal habitat for these migratory giants.

The findings presented in **Figure 5** highlight the critical role of SST in influencing whale shark habitat preferences, migratory behavior, and thermoregulatory adaptations. By offering optimal thermal conditions, the marine waters of Saleh Bay sustain a dynamic ecosystem that attracts whale sharks, linking SST variability to broader ecological processes affecting marine life in the area.

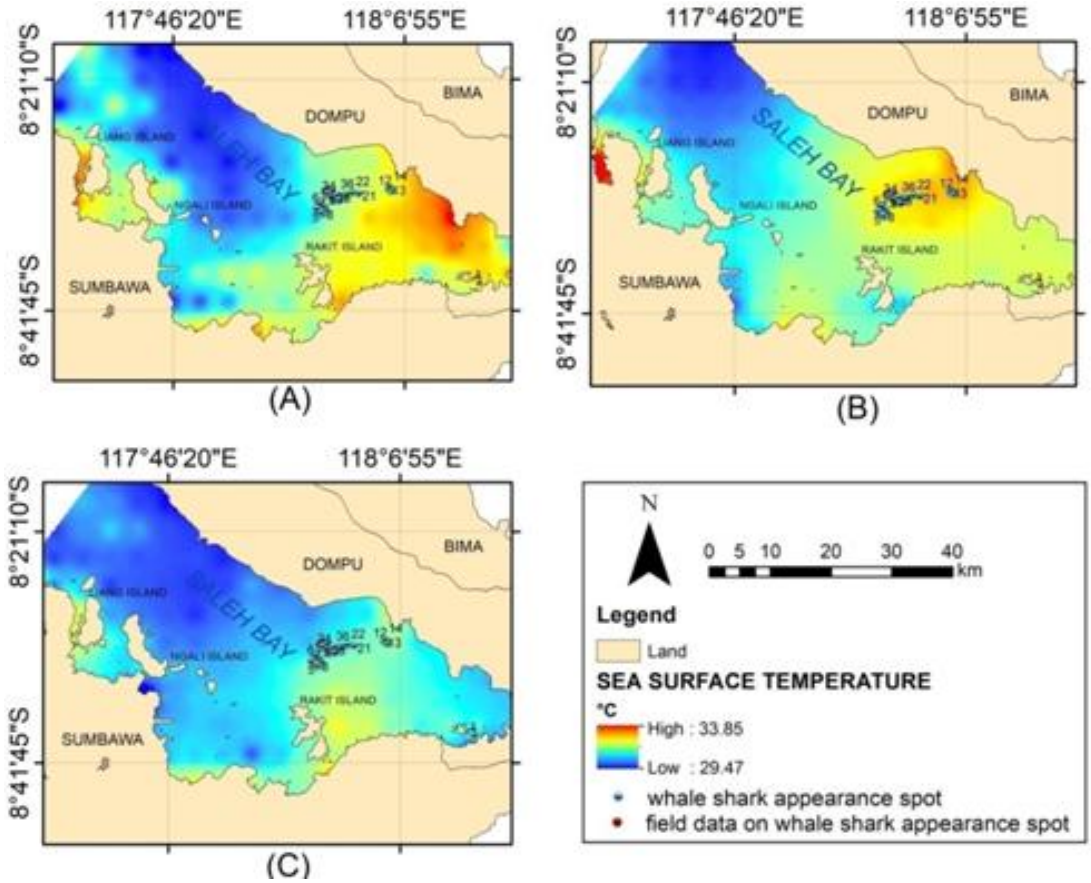

Fig. 5. SST distributions and whale shark sighting locations (A, B, C).

4.3 Linear Relationship (SST and Chl-a) Concentration in February, March, and April 2024

The relationship between SST and Chl-a concentration for February, March, and April 2024 in the marine waters of Saleh Bay was analyzed using linear regression.

The analysis revealed variations in the positive relationship between SST and Chl-a for each month, as indicated by the regression coefficients and R^2 values presented in the graphs. The findings highlight month-to-month differences in the strength and direction of the relationship. These variations may reflect changes in environmental conditions, such as nutrient availability, seasonal patterns, or phytoplankton dynamics within the Saleh Bay ecosystem. For more details, refer to **Figure 6** below.

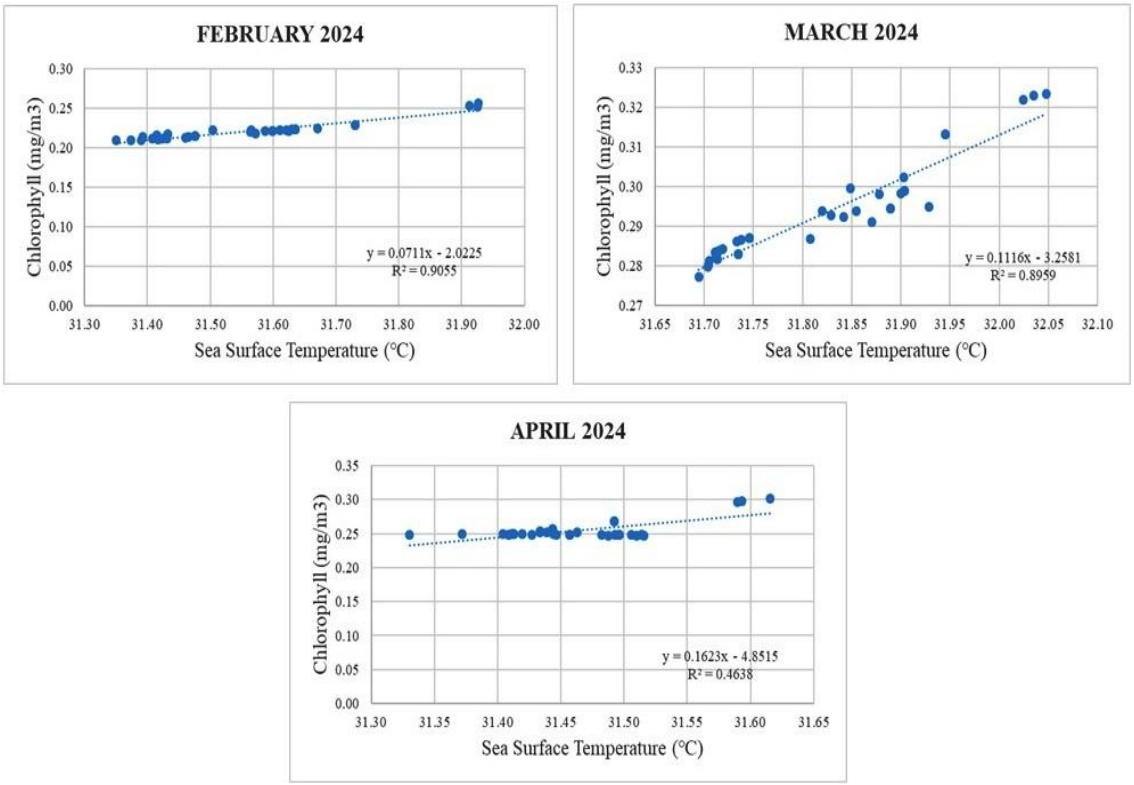

Fig. 6. Relationship between and Chl-a concentrations (February, March, and April 2024).

The graphs in **Figure 6** above show simple linear regression results between Chl-a concentrations and SST with the observed occurrence of whale sharks from February, March, and April 2024. The coefficient of determination (R^2) serves as a measure of how well the variability in whale shark occurrences can be explained by these environmental factors.

- February 2024: The R^2 value of 0.9055 indicates a very strong relationship, where nearly 90.55% of the variability in whale shark occurrences can be explained by Chl-a and SST. This suggests that the model provides a highly accurate representation of the factors influencing whale shark habitat preferences during this period.
- March 2024: The R^2 value of 0.8959 represents a similarly high correlation between Chl-a, SST, and whale shark occurrences. This finding supports research by Sequeiraet al. (2012), which identified temperature and productivity gradients as key determinants in whale shark aggregation sites globally.
- April 2024: The R^2 value of 0.4638 indicates a moderate relationship, suggesting that while Chl-a and SST still influence whale shark occurrences, additional factors may play a more significant

role during April. This aligns with observations by Normanet al. (2017), who noted that whale sharks might adapt their movements based on temporal prey availability or changes in water quality.

Chl-a acts as a proxy for primary productivity, representing the abundance of phytoplankton that forms the base of the marine food chain and serves as a primary food source for whale sharks. Taylor & Pearce (1999) highlight that higher Chl-a concentrations often correlate with increased prey density, attracting megafauna like whale sharks.

Similarly, SST influences metabolic rates, plankton activity, and the suitability of feeding and breeding conditions for whale sharks. Optimal SST ranges between 28-32°C are preferred for foraging and migration (Arrowsmith et al., 2021), as supported by Colman (1997), who reported that whale sharks frequently inhabit warm, productive waters where food availability is maximized.These findings emphasize the predictive potential of SST and Chl-a as key environmental indicators in identifying suitable whale shark habitats, particularly during peak aggregation periods. The consistency of high R^2 values in February and March also supports the integration of remote sensing data in ecological monitoring and habitat modeling, enabling more targeted conservation and ecotourism management strategies in regions like Saleh Bay.

5. CONCLUSIONS

In conclusion, the marine waters of Saleh Bay, located in NTB, Indonesia, serve as a vital habitat for whale sharks and hold significant ecological and economic importance. The observed Chl-a concentrations (0.20–3.45 mg/m³) and SST ranges (29.47–33.85°C) align closely with the ecological preferences of whale sharks, ensuring a consistent environment for feeding and aggregation. The regression analysis conducted in this study reveals a strong relationship between environmental variables and whale shark occurrences. The high R^2 values recorded in February (0.9055) and March (0.8959) indicate a robust predictive correlation, while the moderate value in April (0.4638) suggests the influence of additional ecological or oceanographic factors. These findings highlight the importance of considering both primary drivers and supplementary environmental variables when analyzing whale shark habitat preferences.

This study provides a novel insight by demonstrating that satellite-derived SST and Chl-a data, combined with bathymetric information and field observations, can serve as reliable indicators for predicting whale shark distribution in semi-enclosed tropical marine ecosystems. The practical implications of this research are significant.

First, in terms of marine conservation, the strong correlation between environmental variables and whale shark occurrences supports the integration of remote sensing data into conservation planning. This can assist authorities in identifying and prioritizing critical habitats for protection, especially in areas facing increasing human activity.

Second, for sustainable marine ecotourism, the identification of aggregation zones can inform the spatial regulation of tourism activities to ensure that interactions with whale sharks occur in ecologically appropriate areas while minimizing anthropogenic disturbances.

Third, the methodology used in this study offers potential for real-time habitat monitoring and the development of early warning systems based on SST and Chl-a variability. Such systems could help forecast seasonal whale shark presence, optimize tourism management, and detect environmental threats such as habitat degradation. Based on these implications, it is recommended that marine resource management agencies incorporate satellite-based oceanographic data into their monitoring and planning frameworks.

Further research should expand upon these findings by integrating additional environmental variables such as current patterns, salinity, or prey abundance and applying advanced modeling techniques to improve prediction accuracy. Collaboration between scientists, policymakers, and local communities will be essential to ensure the long-term conservation and sustainable utilization of whale shark habitats in Indonesia.

ACKNOWLEDGEMENTS

This study was funded by RIIM G-2/2022, the National Research and Innovation Agency (BRIN) ‑ Indonesia Endowment Fund for Education (LPDP) [Grant number: 82/II.7/HK/2022; Contract Numbers: B-1740/II.7.5/FR/11/2022 and B-15177/III.4/KS.00/11/2022], and Rumah Program Purwarupa, Research Organization for Earth Sciences [Grant number: DIPA-124.01.1.690501/2024]. The authors also thank the Research Center for Conservation of Marine and Inland Water Resources, BRIN; the Sumbawa Regency Government (PEMDA); and the Department of Marine Science and Technology, FPIK-IPB University.

REFERENCES

Adhitia, R. (2023). Deskripsi umum, fenomena menarik dan rencana pengembangan di Teluk Saleh dan laut sekitarnya. *Journal of Oceanography and Aquatic Science, 1*(3), 54-65. https://doi.org/10.56855/v1i3.820 (in Indonesian)

Almar, R., Bergsma, E.W.J., Thoumyre, G., Baba, M.W., Cesbron, G., Daly, C., Garlan, T., & Lifermann, A. (2021). Global satellite-based coastal bathymetry from waves. *Remote Sensing, 13*(22), 4628. https://doi.org/10.3390/rs13224628

Arrowsmith, L.M., Sequeira, A.M.M., Pattiaratchi, C.B., & Meekan, M.G. (2021). Water temperature is a key driver of horizontal and vertical movements of an ocean giant, the whale shark *Rhincodon typus*. *Marine Ecology Progress Series*, 679, 101–114. https://doi.org/10.3354/meps13899

Asrial, E., Marzuki, M., Hamid, & Khasanah, R.I. (2021). Sustainability analysis of tomato jellyfish (Crambione mastigophora) fisheries resources management in Saleh Bay Waters, Sumbawa Island, Indonesia. *Biodiversitas Journal of Biological Diversity, 22*(2), 512-520. https://doi.org/10.13057/biodiv/d220202

Binder, T.R., Cooke, S.J., & Hinch, S.G. (2011). The biology of fish migration. In A.P. Farrell (Ed.), *Encyclopedia of Fish Physiology: From Genome to Environment* (Vol. 3, pp. 1921-1927). Academic Press.

Colman, J.G. (1997). A review of the biology and ecology of the whale shark. *Journal of Fish Biology, 51*(6), 1219-1234. https://doi.org/10.1111/j.1095-8649.1997.tb01138.x

Cruz, F.A., Shoou-Jeng, J., Kwang-Ming, L., Hua-Hsun, H., & Tzu-Chi, H. (2013). A preliminary study on the feasibility of whale shark (*Rhincodon typus*) ecotourism in Taiwan. *Ocean & Coastal Management, 80*, 100-106. https://doi.org/10.1016/J.OCECOAMAN.2013.03.017

Djunaidi, A., Jompa, J., Kadir, N.N., Bahar, A., Tilahunga, S.D., Lilienfeld, D., & Hani, M.S. (2020). Analysis of two whale shark watching destinations in Indonesia: Status and ecotourism potential. *Biodiversitas Journal of Biological Diversity, 21*(10), 4911-4923. https://doi.org/10.13057/biodiv/d211058

Dove, A.D.M., & Pierce, S.J. (Eds.). (2022). *Whale sharks: Biology, ecology, and conservation* (1st ed.). CRC Press.

Doydee, P., Saitoh, S., & Matsumoto, K. (2010). Variability of chlorophyll-a and SST at regional sea levels in Thai waters using satellite data. *Journal of Fisheries and Environment, 34*(3), 35-44.

Enita, S.Y., Kunarso, & Wirasatriya, A. (2017). Identifikasi faktor oseanografi terhadap kemunculan hiu paus (*Rhincodon typus*) di perairan Kwatisore, Kabupaten Nabire, Papua. *Journal of Oceanography, 6*(4), 564-572. (in Indonesian)

Farid, M.F., Hariyadi, S., Kamal, M.M., & Susanto, H.A. (2021). Evidence of residential area of whale sharks in Saleh Bay, West Nusa Tenggara. *IOP Conference Series: Earth and Environmental Science, 744*. https://doi.org/10.1088/1755-1315/744/1/012018

Fowler, S., Bräutigam, A., Okes, N., & Sant, G. (2021). *Conservation, Fisheries, Trade and Management Status of CITES-listed Sharks*. BfN-Skripten 607. Federal Agency for Nature Conservation.

Fox, S., Foisy, I., De La Parra Venegas, R., Galván Pastoriza, B.E., Graham, R.T., Hoffmayer, E.R., Holmberg, J., & Pierce, S.J. (2013). Population structure and residency of whale sharks (*Rhincodon typus*) at Utila, Bay Islands, Honduras. *Journal of Fish Biology*, 1-14. https://doi.org/10.1111/jfb.12195

Gallimore,C.G., Walton, C., Nugent, R., Fradkin, M., Poppell, L., Schreiber, C., Coco, C., Grober, M., Carlson, B., Dove, D.M., & Black, M.P. (2024). A longitudinal behavioral analysis of aquarium whale sharks (*Rhincodon typus*): Insights into anticipatory cues, individual variation, and social interaction. *Frontiers in Marine Science*, 11, Article 1418002. https://doi.org/10.3389/fmars.2024.1418002

Kusumawati, E., Susilo, S.B., Agus, S.B., Arifin, T., & Yulius. (2019). Analisis penentuan sebaran konsentrasi klorofil-A dan produktivitas primer di perairan Teluk Saleh menggunakan citra satelit Landsat OLI 8. *Jurnal Pengelolaan Sumberdaya Alam dan Lingkungan, 9*(3), 671-679. https://doi.org/10.29244/jpsl.9.3.671-679. (in Indonesian)

Lelono, T.D., Bintoro, G., Setyanto, A., Setyahadi, D., Sutjipto, D.O., Adhihapsari, W., Aliviyanti, D., & Isdianto, A. (2024). [RETRACTED] Conservation status of sharks and rays caught in Indonesian Fisheries Management Area 712. *Biodiversitas Journal of Biological Diversity, 25*(6), 2603-2614. https://doi.org/10.13057/biodiv/d250631

McKinney, J.A., Fulford, R.S., Wu, W., Hoffmayer, E.R., & Hedon, J.M. (2012). Feeding habitat of the whale shark (*Rhincodon typus*) in the Northern Gulf of Mexico determined using species distribution modelling. *Marine Ecology Progress Series, 458*, 199-211. https://doi.org/10.3354/meps09777

Motta, P.J., Maslanka, M., Hueter, RE., Davis, RL., R de la Parra, Mulvany, SL., Habegger, M.L., Stother, J.A., Mara, K.R., Gardiner, J.M., Tyminski, J.P., & Zeigler, L.D. (2010). Feeding anatomy, filter-feeding rate, and diet of whale sharks (Rhicodon typus) during surface ram filter feeding off the yucatan peninsula, Mexico. *Zoology* 113: 199-212. https://doi.org/10.1016/j.zool.2009.12.001

Murdani, N.H., Masyud, B., & Yulianda, F. (2018). Bioecology and ecotourism development strategies of whale sharks (*Rhincodon typus*) in Cenderawasih Bay National Park. *Conservation Media, 23*(1), 77-84. https://doi.org/10.29243/medkon.23.1.77-84

Norman, B.M., Whitty, J.M., Beatty, S.J., Reynolds, S.D., & Morgan, D.L. (2017). Do they stay or do they go? Acoustic monitoring of whale sharks at Ningaloo Marine Park, Western Australia. *Journal of Fish Biology, 91*(6), 1713-1720. https://doi.org/10.1111/jfb.13461

Putri, D., Yulius., Rosalia, A.A., Arifin, T., Putra, A., Heriati, A., Prihantono, J., Purbani, D., Salim, H.L., Hartati, S.T., Ramdhan, M., Wahyono, A., & Rahmania, R. (2025). Influence of sea surface temperature and chlorophyll-a on mackerel productivity in Banten Bay, Indonesia: Analysis using Aqua MODIS data (2014–2023). *Geographia Technica*, 20(1), 44–63. https://doi.org/10.21163/GT_2025.201.05

Rahman, A., Haryadi, J., Sentosa, A.A., & Mujiyanto. (2017). Kajian awal kemunculan hiu paus (Rhyncodon typus, Smith 1828) di Teluk Tomini dihubungkan dengan faktor fisik dan biologi perairan. *Jurnal Akuatika Indonesia, 2*(2), 128-136. https://doi.org/10.24198/jaki.v2i2.23425. (in Indonesian)

Reinero, F.R., Marsella, A., Pacifico, A., Vicariotto, C., Maule, L., Mahrer, M., & Micarelli, P. (2024). Influence of environmental factors on the surface feeding behaviour of immature male whale sharks in the Gulf of Tadjoura (Djibouti). *Conservation*, 4(4), 792–811. https://doi.org/10.3390/conservation4040047

Richmond, M.D. (2011). *A Field Guide to the Seashores of Eastern Africa and Western Indian Ocean Islands*. Sida/WIOMSA.

Rumisha, C., Barongo, D., Saiperaki, J.L., Materu, S.F., & Mdegela, R.H. (2024). Threatening the endangered: Uncovering endangered elasmobranchs and factors perpetuating the Tanzanian shark-fin trade. *African Journal of Ecology*, e13275. https://doi.org/10.1111/aje.13275

Ryan, J.P., Green, J.R., Espinoza, E., & Hearn, A.R. (2017). Association of whale sharks (*Rhincodon typus*) with thermo-biological frontal systems of the eastern tropical Pacific. *PLOS ONE, 12*(8). https://doi.org/10.1371/journal.pone.0196443

Sequeira, A., Mellin, C., Rowat, D., Meekan, M.G., & Bradshaw, C.J. (2012). Ocean-scale prediction of whale shark distribution. *Diversity and Distributions, 18*(5), 504-518. https://doi.org/10.1111/j.1472-4642.2011.00853.x

Sianipar, A. (2019). *International Whale Shark (Rhincodon typus) Conference*. Exmouth, Western Australia, 28-31 May.

Stacey, E.N., Karam, J., Dwyer, C., Speed, C., & Meekan, M. (2008). Assessing traditional ecological knowledge of whale sharks (*Rhincodon typus*) in Eastern Indonesia: A pilot study with fishing communities in Nusa Tenggara Timur. Casuarina (AU): Charles Darwin University.

Stewart, B.S. (2011). *Workshop and monitoring training for whale sharks in Cenderawasih Bay National Park, West Papua, 2-7 May 2011, Nabire, Papua*. Hubbs-SeaWorld Research Institute Technical Report 2011-375: 1-27.

Suprapti, D. (2015). Marine Species Conservation Coordinator. WWF Indonesia.

Suruan, S.S., Manangkalangi, E., Simatauw, F.F.C., & Tebaiy, S. (2024). Distribution and behavior of whale sharks (*Rhincodon typus*) in Kwatisore waters, Cenderawasih Bay National Park, Central Papua Province. *Jurnal Sumberdaya Aquatik Indopasifik, 8*(1), 65-78. https://doi.org/10.46252/jsai-fpik-unipa.2024.Vol.8.No.1.341

Syah, A.F., Musrifah, & Cahyono, H. (2018). Pemodelan daerah potensial kemunculan hiu paus (*Rhincodon typus*) menggunakan data penginderaan jauh di perairan Probolinggo, Jawa Timur. *Jurnal Penelitian Perikanan Indonesia, 24*(3), 209-216. https://doi.org/10.15578/jppi.24.3.2018.209-216. (in Indonesian)

Taylor, J.G., & Pearce, A.F. (1999). Ningaloo Reef currents: Implications for coral spawn dispersal, zooplankton and whale shark abundance. *Journal of the Royal Society of Western Australia, 82*, 57.

Womersley, F.C., Rohner, C.A., Abrantes, K., Afonso, P., Arunrugstichai, S., Bach, S.S., Bar, S., Barash, A., Barnes, P., Barnett, A., Boldrocchi, G., Buffat, N., Canon, T., Canovas Perez, C., Chuangcharoendee, M., Cochran, J.E.M., de la Parra, R., Diamant, S., Driggers, W., Dudgeon, C.L., & Araujo, G. (2024). Identifying priority sites for whale shark ship collision management globally. *Science of The Total Environment*, 934, Article 172776. https://doi.org/10.1016/j.scitotenv.2024.172776

Yasir, M., Hartati, R., Indrayanti, E., Amar, F., & Tarigan, A.I. (2024). Seasonal constellation of juvenile whale sharks in Gorontalo Bay Coastal Park. *ILMU KELAUTAN: Indonesian Journal of Marine Sciences, 29*(2), 241-253. https://doi.org/10.14710/ik.ijms.29.2.241-253

Yudanegara, RA., D., Astutik, A., Hernandi, TP., Soedarmodjo &E., Alexander. (2021). The use of the Inverse Distance Weighted (IDW) method for mapping land value zones (case study: Gedong Meneng Village, Bandar Lampung). ELIPSOIDA 4(2): 85-90. DOI: https://doi.org/10.14710/elipsoida.2021.12534.

Yulius., Aidina, V., Ramdhan, M., & Daulat, A. (2021). Fishing ground mapping based on chlorophyll-a distribution using Aqua MODIS satellite imagery in the fisheries management area (FMA) 712. *MaCiFIC, 324*. https://doi.org/10.1051/e3sconf/202132401007

Yunus, F., Zainuddin, M., & Farhum, S. (2019). Pemetaan daerah potensial penangkapan ikan tongkol (Euthynnus sp) di Perairan Selat Makassar. *Jurnal Ipteks Pemanfaatan Sumberdaya Perikanan, 6*(11). https://doi.org/10.20956/jipsp.v6i11.6273. (in Indonesian)

Yulius., Ramdhan, M., & Ardiansyah, Y. (2018). Characteristic of Saleh Bay coastline. *Jurnal Segara*, 14(2), 117–125. https://doi.org/10.15578/segara.v14i2.6609

CREATION OF TECHNIQUE FOR ASSESSING ABOVE GROUND BIOMASS AND CARBON SEQUESTRATION USING UNMANNED AERIAL VEHICLES

***Teerawong LAOSUWAN*[1,2], *Tanutdech ROTJANAKUSOL*[1, 2], *Wutthisat CHOKKUEA*[1]**
***Mehsa SINGHARATH*[3], *Jumpol ITSARAWISUT*[1,2*]**

DOI: 10.21163/GT_2025.202.05

ABSTRACT
This study aims to develop a method for assessing above ground bimass and carbon sequestration using data obtained from unmanned aerial vehicle (UAV) imagery. The research focuses on analyzing above ground biomass and estimating carbon storage by examining the correlation between carbon sequestration and vegetation indices through regression analysis. Field survey data revealed a total of 336 trees and 22 plant species. The total above ground biomass in the study area was found to be 86.214 tons, with a corresponding carbon sequestration of 40.520 tons of carbon. Vegetation index (VI) analysis employed three modeling approaches—NDVI_FC, SAVI_FC, and MSAVI2_FC—using an area block method. The estimated carbon sequestration values were 6.90388, 6.90388, and 6.83419 tons, respectively. Using the grid block method, the carbon sequestration values derived from NDVI_FC, SAVI_FC, and MSAVI2_FC were 32.47310, 32.48533, and 34.17078 tons, respectively. This study demonstrates the effectiveness of UAV imagery in estimating carbon sequestration, which can be effectively applied in natural resource management and environmental planning.

Key-words: *UAV imagery, Above Ground Bimass, Carbon Sequestration, Vegetation Index.*

1. INTRODUCTION

Carbon is a fundamental element of all living organisms and plays a crucial role in maintaining balance within ecosystems. It is stored in various environmental components and circulates through the carbon cycle (Earthobservatory, 2025). In nature, carbon exists in different forms depending on the storage reservoirs, including terrestrial, aquatic, atmospheric, and biological systems. It can be found in solid, liquid, and gaseous states, with the majority of natural carbon stored in plants as hydrocarbon compounds that form part of plant tissues (Ngthai, 2025). Human activities have increasingly contributed to the release of carbon from natural reservoirs into the atmosphere in large quantities. These activities include the combustion of fossil fuels, transportation, and industrial production (Laosuwan et al., 2023; Laosuwan et al., 2025). Moreover, human-induced destruction of carbon sinks, such as deforestation, has diminished the natural capacity to absorb atmospheric carbon dioxide. This reduction weakens the effectiveness of the carbon removal process and leads to higher concentrations of carbon dioxide in the atmosphere, which contributes to the greenhouse effect—a phenomenon that increases the Earth's average temperature, known as global warming (Liu & Liang, 2017; Saengpradit et al., 2024; Vattanavongsiri et al., 2024). Carbon dioxide absorbs heat radiation from both the sun and the Earth's surface, intensifying this warming effect. A sustainable approach to mitigating global warming is to convert atmospheric carbon into carbon stored within living organisms, particularly through tree planting.

[1]*Department of Physics, Faculty of Science, Mahasarakham University, Maha Sarakham, Thailand, (TL) teerawong@msu.ac.th, (TR) tanutdech.r@msu.ac.th, (WC) wutthisat.c@msu.ac.th, (JI) drjumpol.i@gmail.com*
[2]*Space Technology and Geo-Informatics Research Unit, Faculty of Science, Mahasarakham University, Maha Sarakham, Thailand*
[3]*Nampapa Nakhoneluang, Vientiane Capital Water Supply State Enterprise, Kaisone Road, Xaysettha District, Vientiane City, Lao P.D.R., (MS) mesha_coltd@yahoo.com*
**Corresponding author: drjumpol.i@gmail.com*

Trees play a vital role as carbon sinks by absorbing carbon dioxide during photosynthesis. This carbon is then stored in various parts of the tree—such as the stem, branches, and leaves—in the form of biomass. Therefore, tree planting is an effective method for reducing atmospheric carbon and addressing the challenges of global warming (Lewis et al., 2009; Pandey et al., 2014; Yadav et al., 2017; Uttaruk & Laosuwan 2019; Lal & Singh, 2020). Typically, the amount of carbon sequestered in trees is directly related to biomass, which represents the total mass of all tree components, including the stem, branches, leaves, roots, and others (Chopra et al., 2023; Uttaruk et al., 2024). Therefore, anatomical characteristics of trees—such as height, trunk diameter, and crown width—can be used to estimate the amount of carbon stored in trees through the application of allometric equations. These equations describe the relationship between biomass and tree structural attributes. Such structural data can be obtained through field surveys (Uttaruk & Laosuwan 2020; Huynh et al., 2022; Oumasst et al., 2024). Although field surveys provide highly accurate data on tree structure and form, they require skilled personnel and can be time-consuming and costly. In densely vegetated or remote areas, field data collection can be inconvenient and prone to error (Uttaruk et al., 2024). As a result, remote sensing technology has been increasingly applied for large-scale spatial studies to reduce survey time (Auntarin et al., 2021; **Jomsrekrayom** et al., 2021; Ounrit et al., 2022; Samdaengchai et al., 2022; Nakapan & Hongthong, 2022; Uttaruk et al., 2022; Hongthong & Nakapan, 2023; Jumadi et al., 2024).

While satellite imagery is already available, its limitations in terms of resolution, area coverage, or cost may prevent it from being suitable for detailed carbon estimation. Currently, there is a growing demand for high-resolution data for site-specific studies, leading to the adoption of unmanned aerial vehicle (UAV) imagery. UAVs offer several advantages, including affordability, environmental friendliness, and high-resolution data acquisition, making them widely applicable in various fields (Mendes et al., 2023; Angkahad et al., 2024). However, a review of related literature indicates that the use of UAVs specifically for estimating above-ground biomass carbon sequestration remains limited. Most UAV applications focus on broader spatial analyses, such as land cover classification and land use change detection (Pepe et al., 2021; Lu et al., 2023; Alfio, 2024). This study aims to develop a method for surveying above-ground carbon sequestration using UAV imagery, with a case study conducted at SC1 and SC2 buildings of Mahasarakham University.

2. MATERIALS AND METHODS

2.1 Study Area

The study area includes the SC1 and SC2 buildings of the Faculty of Science, Mahasarakham University, located in Kham Riang Subdistrict, Kantharawichai District, Maha Sarakham Province, Thailand. The total area of the study site is 21,392.4198 square meters, as shown in **Fig. 1**.

2.2. Tree Physical Data Collection

In this study, the researcher measured the circumference of all trees with a minimum circumference of 4.5 centimeters at a height of 130 centimeters above ground level (approximately breast height). Tree height, measured from the ground to the top of the canopy, was recorded using a laser range finder.

2.3. UAV-Based Multispectral Image Acquisition

UAV-based imagery was collected using a multispectral camera system that captured data across multiple spectral bands, including Green, Red, Red Edge (RE), and Near Infrared (NIR). The collected data were used to calculate three types of Vegetation Indices (VIs): the Normalized Difference Vegetation Index (NDVI) (Tucker, 1979), the Soil-Adjusted Vegetation Index (SAVI) (Huete, 1988), and the Modified Soil-Adjusted Vegetation Index (MSAVI2) (Qi et al., 1994), as shown in Equations 1 to 3.

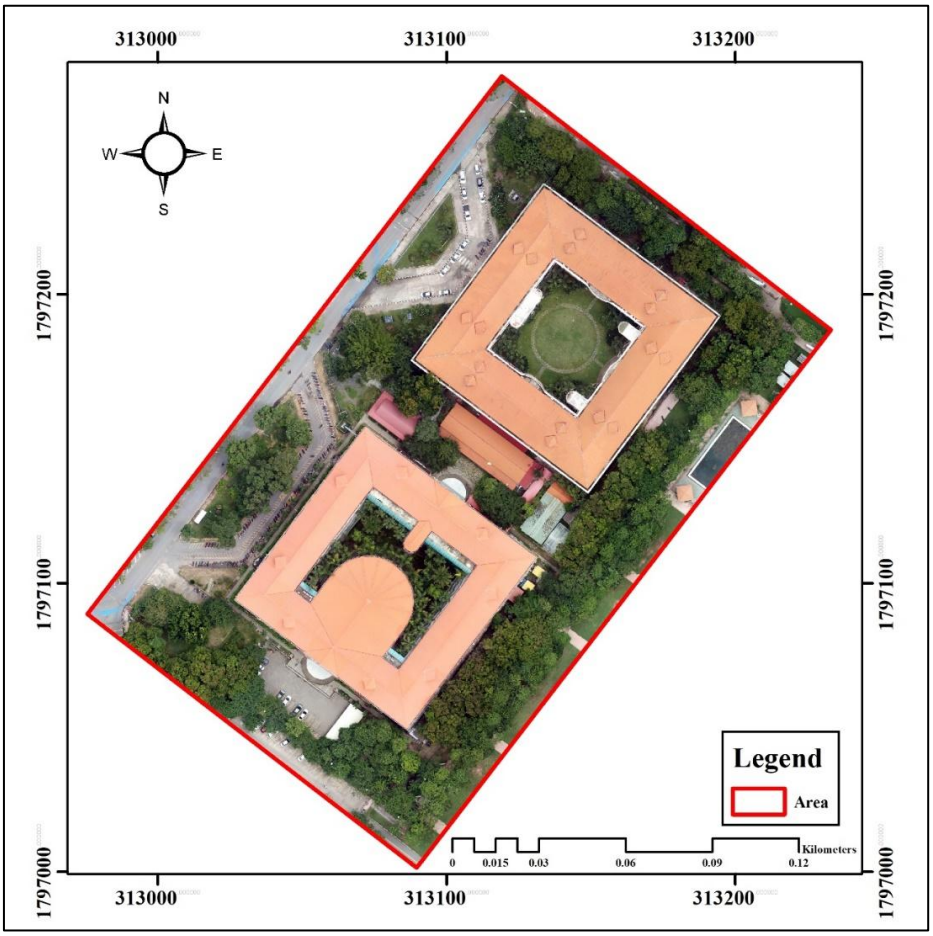

Fig. 1 Study area.

These indices were subsequently used to analyze the Fractional Green Vegetation Cover (FC), as shown in Equation 4.

$$NDVI = \frac{NIR - RED}{NIR + RED} \tag{1}$$

VIS and NIR refer to the spectral reflectance measurements obtained in the visible red and near-infrared regions, respectively.

$$SAVI = \frac{(L+1)\ x\ (NIR - RED)}{NIR + RED + L} \tag{2}$$

NIR and Red denote the bands linked to their respective wavelengths. The L value fluctuates based on the extent of green vegetative cover present. Typically, in regions devoid of green vegetation, L is equal to 1; in areas with moderate green cover, L is 0.5; and in regions with dense vegetation, L reaches 0, which aligns with the NDVI method. This index produces values ranging from -1.0 to 1.0.

$$MSAVI2 = \frac{(2NIR+1) - \sqrt{(2NIR+1)^2 - 8(NIR - RED)}}{2} \quad (3)$$

The Modified Soil Adjusted Vegetation Index 2 (MSAVI2) improves the dynamic range of vegetation signals and more effectively mitigates the influence of soil background effects compared to the Soil Adjusted Vegetation Index (SAVI). This characteristic is especially advantageous in areas with limited vegetation. VIS and NIR denote the spectral reflectance measurements captured in the visible red and near-infrared wavelengths, respectively.

Subsequently, utilize the results from the analysis of the three Index methods to evaluate the Fractional Green Vegetation Cover (FC) using Equation 4.

$$FC = \frac{VI - VI_{soil}}{VI_{forest} - VI_{soil}} \quad (4)$$

VIsoil represents the VI value of a pixel with 0% vegetation cover, while VIveg denotes the VI value of a pixel with 100% vegetation cover.

2.4. Field Survey for Tree Physical Measurement

2.4.1. Tree Physical Data Collection

Field data collection involved measuring the diameter at breast height (DBH) at 130 centimeters above ground level, with a minimum DBH of 4.5 centimeters. Tree height (H) was also measured. The geographic coordinates (X, Y) of each tree were recorded using GPS. Additional information including species name, trunk circumference (in centimeters), and tree height (in meters) was documented using a data recording form. Data were collected for all trees within the study area. In this study, data collection was conducted in the vicinity of the SC1 and SC2 buildings without defining sample plots; thus, all standing trees within the area were measured.

2.4.2. Above Ground Biomass and Carbon Sequestration

Once data such as height (H) and diameter at breast height (DBH) were collected from the field survey, these values were substituted into the allometric equation developed by Ogawa (Ogawa et al., 1965) (Equation 5), which is commonly used for dry dipterocarp and mixed deciduous forests, to estimate above ground biomass. The resulting biomass values were then used to calculate carbon sequestration using Equation 6 .

$$\begin{aligned} Ws &= 0.0396\, D^2 H\ 0.9326 \\ Wb &= 0.003487\, D^2 H\ 1.0270 \\ Wl &= \left(28.0 / wtc + 0.025\right)^{-1} \\ Wtc &= Ws + Wb \end{aligned} \quad (5)$$

where:

Ws represents the biomass of the trunk (in kilograms), Wb denotes the biomass of the branches (in kilograms), Wl indicates the biomass of the leaves (in kilograms), Wtc refers to the combined biomass of the trunk and branches (in kilograms), D signifies the diameter measured at a height of approximately 130 centimeters, and H represents the height of the tree up to the crown (in meters).

$$CS = AGB * 0.47 \quad (6)$$

In this context, CS represents the carbon stock measured in tonnes, above ground bimass denotes the above-ground biomass, and 0.47 (IPCC, 2006) serves as the conversion factor or the carbon fraction found in above ground bimass.

2.5. UAV Data Analysis Methods

In this research, three methods were employed for UAV data analysis: Crown Cover Generation, Area Block Generation, and Grid Block Generation, as illustrated in **Fig. 2**.

Fig. 2 (a) Crown Cover Generation, (b) Area Block Generation and (c) Grid Block Generation.

- Crown Cover Generation: This method involves generating crown covers by expanding the XY coordinates of each tree to create a buffer area representing the tree's canopy. The average vegetation index values within each crown cover area are calculated and used to determine the correlation with carbon sequestration values at the same coordinates. Only trees with clearly visible canopies in the UAV imagery were selected for this analysis.

- Area Block Generation: Area blocks were created to extract vegetation index values from each defined block. These values were then used to analyze their correlation with the total carbon content within each area block. This method provides spatially distributed data.

- Grid Block Generation: Grid blocks were created to extract vegetation index values from each block. These values were used to analyze the correlation with total carbon content per block. Grid blocks offer equal-sized areas and provide higher spatial resolution than the area block method.

2.6. Relationship Between Carbon Sequestration & Vegetation Indices Using the Crown Cover

The average vegetation index values derived from the crown cover method—limited to locations where tree canopies were clearly visible—were analyzed using Microsoft Excel. In this analysis, Y represents the amount of carbon sequestered (in tons of carbon) at coordinates corresponding to the vegetation index values, and X represents the average values of NDVI_FC, SAVI_FC, and MSAVI2_FC from 107 crown cover points.

2.7. Relationship Between Carbon Sequestration and Vegetation Indices Using the Area Block

The Area Block method involves calculating the sum of vegetation index values within each block, which are then used to analyze the correlation with the total carbon content in the corresponding block. In this analysis, Y represents the amount of carbon sequestered (in tons of carbon) in each block, and X represents the total values of NDVI_FC, SAVI_FC, and MSAVI2_FC within each block. A total of 11 Area Blocks (or 11 Area Block IDs) were randomly selected for analysis.

2.8. Relationship Between Carbon Sequestration and Vegetation Indices Using the Grid Block

The Grid Block method involves summing the vegetation index values within each grid block, which are then used to calculate the correlation with the total carbon content per block. In this analysis, Y represents the total carbon sequestered (in tons of carbon) within each grid block, and X represents the total NDVI_FC, SAVI_FC, and MSAVI2_FC values within each respective grid block.

3. RESULTS AND DISCUSSION

In this study, data obtained from unmanned aerial vehicle (UAV) imagery were utilized alongside physical measurements of individual trees surrounding the buildings. These data were used to calculate above-ground biomass and estimate the amount of carbon sequestered by each tree. Remote sensing technology was applied based on the principle of reflectance and absorption of electromagnetic energy at different wavelengths by vegetation. This enabled the calculation of vegetation indices, including NDVI, SAVI, and MSAVI2, as well as the fractional green vegetation cover (FC). The vegetation index values were then analyzed for their correlation with the carbon content of individual trees. The derived regression equations from these correlations were subsequently used to estimate spatial carbon values across the study area. The results of the implementation are presented as follows:

3.1. Above Ground Biomass

Based on the field survey, a total of 336 trees representing 22 different species were identified. The eight most frequently occurring species in the study area were: *Pterocarpus indicus Willd.*(119 trees), *Dalbergia cochinchinensis Pierre* (52 trees), *Cassia fistula Linn.* (38 trees), *Peltophorum pterocarpum (DC.) K.Heyne* (36 trees), *Peltophorum dasyrachis (Miq.) Kurz* (19 trees), *Lagerstroemia speciosa (L.) Pers.* (17 trees), *Sindora siamensis Teijsm. ex Miq.* (15 trees), and *Ficus benjamina L.* (8 trees), along with several other species. The total above ground biomass (AGB) estimated from this research is presented in **Table 1**.

Table 1.

Above Ground Biomass

Weight	Tons
The weight of the stem (Ws)	68.57863323 tons
The weight of the branch section (Wb)	15.56469544 tons
The weight of the leaf section (Wl)	2.07146152 tons
The total above ground biomass (AGB)	86.21479019 tons

Table 1 presents the weights of various components of aboveground biomass, which include the weight of the stem (Ws) at 68.57863323 tons, the weight of the branches (Wb) at 15.56469544 tons, and the weight of the leaves (Wl) at 2.07146152 tons. In total, the aboveground biomass (AGB) amounts to 86.21479019 tons. This data collection is crucial for studying the carbon cycle within ecosystems, as these biomass components can sequester carbon dioxide from the atmosphere through photosynthesis, converting it into organic matter within plants. Assessing biomass quantities enhances our understanding of forests' capacity to store carbon, which is vital for mitigating global warming and climate change. Furthermore, it facilitates more effective management of natural resources. Therefore, studies on biomass play a significant role in developing models and environmental management policies.

3.2. Carbon Sequestration from Field Data

The amount of carbon sequestration was calculated by using the above-ground biomass values to estimate the carbon content. According to the formula for carbon sequestration of trees (Cs) = above-ground biomass × 0.47, the total amount of carbon sequestered by the trees was 40.52095139 tons of carbon.

3.3 Vegetation Index Analysis Results

UAV imagery was analyzed using NDVI, SAVI, MSAVI2 models, along with the fractional green vegetation cover (FC). The analysis results are as follows:

3.3.1. NDVI Analysis Results

NDVI is a vegetation index derived from the ratio between the reflectance values of near-infrared and red wavelengths, normalized to a scale ranging from -1 to 1. The NDVI analysis results are shown in **Fig. 3** and can be described as follows:

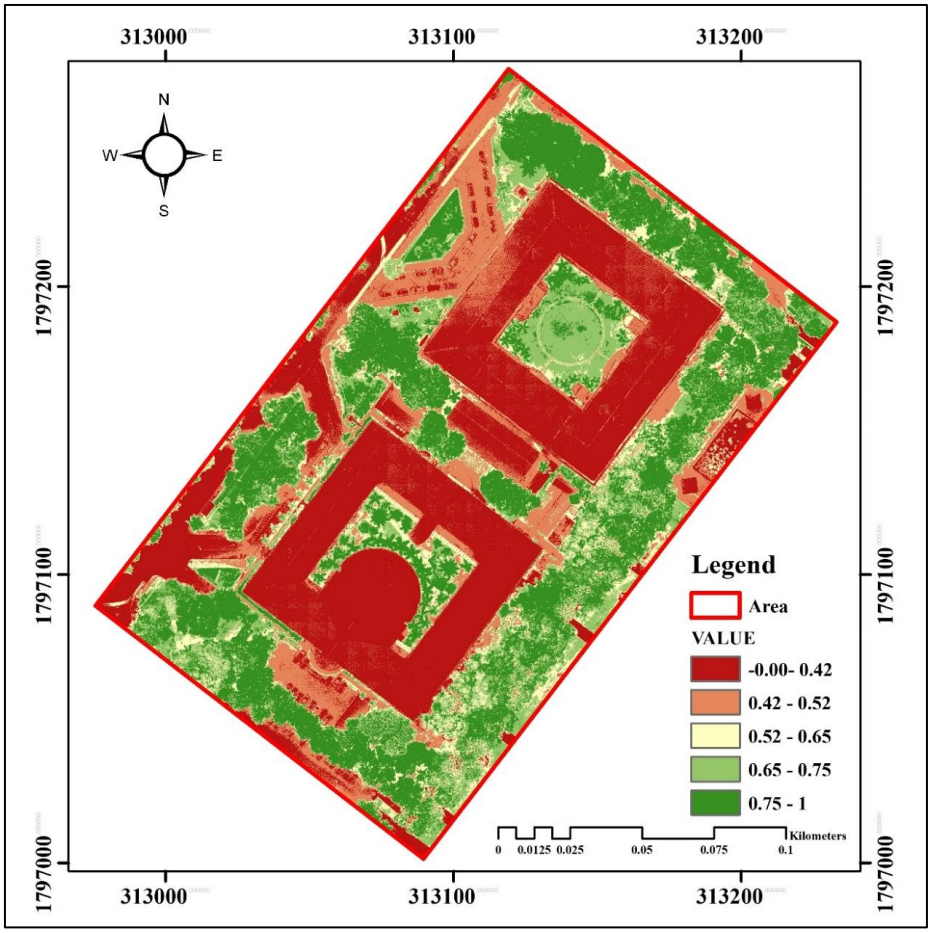

Fig. 3. NDVI Analysis Results.

According to **Fig. 3**, the calculated NDVI_FC value at coordinates 313121 1797057 was the lowest at 0.5147, while the highest NDVI_FC value was 0.8887 at coordinates 313217 1797182. On average, areas shaded in red and orange, with NDVI_FC values ranging from -0 to 0.5215,

represented areas with no vegetation cover, such as academic buildings and paved roads. Yellow to light green areas, with values ranging from 0.5215 to 0.7490, represented areas with moderate vegetation cover, such as grass patches. Dark green areas, with values ranging from 0.7490 to 1.0000, represented areas with dense vegetation cover, typically large trees with clearly visible canopies.

3.3.2. SAVI Analysis Results

SAVI (Soil-Adjusted Vegetation Index) is a vegetation index calculated from the difference in reflectance between near-infrared and red wavelengths, normalized by the sum of the two, with a correction factor applied to minimize the influence of soil brightness—particularly in areas with sparse vegetation. This method is commonly used in arid regions where vegetation cover is low. The SAVI analysis results are shown in **Fig. 4** and can be described as follows:

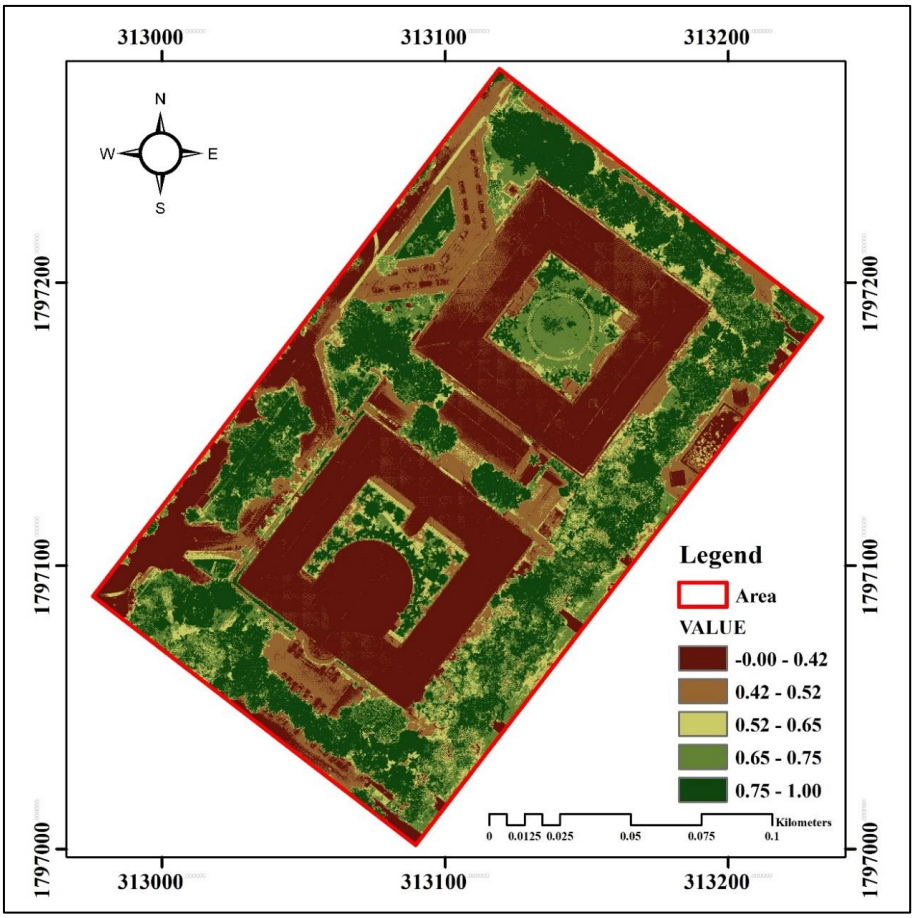

Fig. 4. SAVI Analysis Results.

According to **Fig. 4**, the SAVI_FC value at coordinates 313121 1797057 was the lowest at 0.5147, while the highest SAVI_FC value was 0.8887 at coordinates 313217 1797182. Areas with values between 0 and 0.5215 represent locations with no vegetation cover, such as academic buildings and paved roads. Areas with values between 0.5215 and 0.7490, typically shown in green shades, represent regions with moderate vegetation cover, such as grassy areas. Areas with values between 0.7490 and 1.0000, typically shown in dark green, represent regions with dense vegetation cover or large trees with prominent canopies.

3.3.3. MSAVI2 Analysis Results

MSAVI2 (Modified Soil-Adjusted Vegetation Index) is a vegetation index modified to reduce the influence of soil reflectance in areas with sparse vegetation cover. It incorporates both soil adjustment and vegetation weighting factors. The MSAVI2 analysis results are shown in **Fig. 5**. According to **Fig. 5**, the MSAVI2_FC value at coordinates 313095 1797105 was the lowest at 0.1912, while the highest value of 0.8543 was found at coordinates 313023 1797134. Areas with values between 0 and 0.2392 represent regions with no vegetation cover, such as academic buildings and paved roads. Yellow to orange shaded areas with values from 0.3725 to 0.6039 indicate regions with moderate vegetation cover, such as grass patches. Red shaded areas (excluding buildings and cemented surfaces), with values ranging from 0.6039 to 1.0000, represent areas with dense vegetation cover or large trees with well-defined canopies.

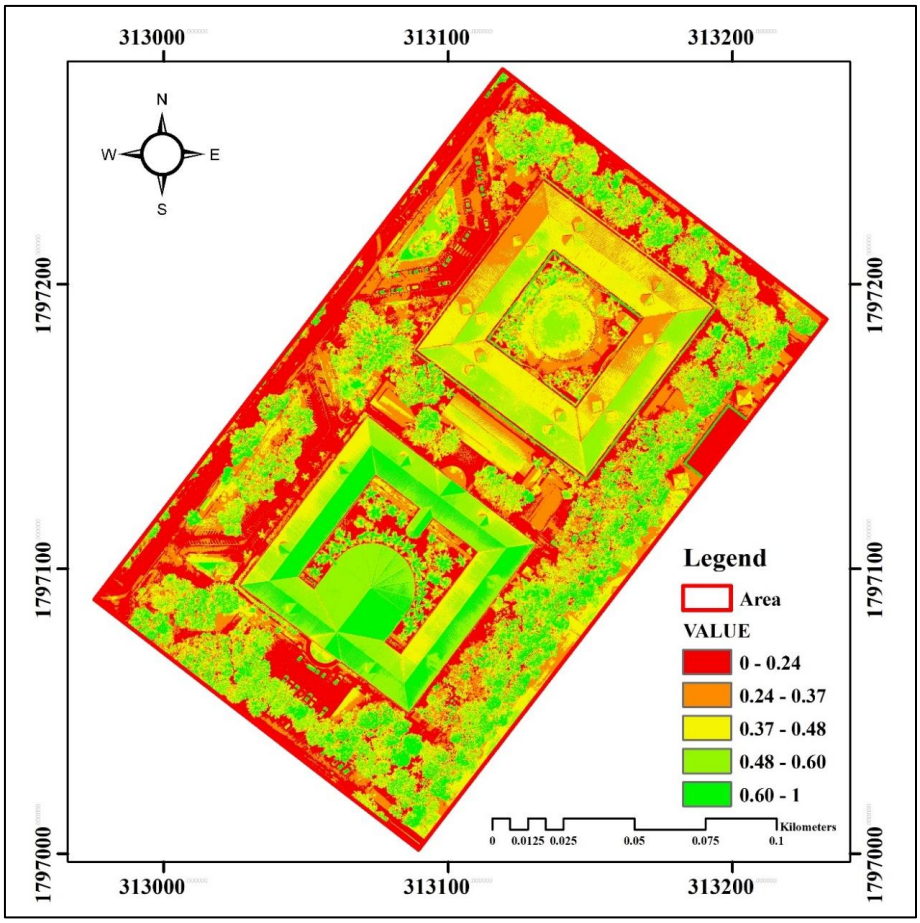

Fig. 5. MSAVI2 Analysis Results.

3.4. Correlation Analysis Results

3.4.1. Correlation Analysis Using the Crown Cover Method

The correlation analysis between carbon sequestration and vegetation indices using the Crown Cover method involved expanding the XY coordinates of each tree to define the radius of the crown cover area. The average vegetation index values within the crown cover were then calculated and paired with the carbon sequestration values of the corresponding trees. NDVI_FC, SAVI_FC, and

MSAVI2_FC values from 107 crown cover points at matching XY coordinates were used to perform regression analysis.

The results are as follows: the coefficient of determination (R^2) values for NDVI_FC, SAVI_FC, and MSAVI2_FC were found to be 0.0721, 0.0635, and 0.0639, respectively. These R^2 values indicate a low level of correlation. Therefore, it can be concluded that NDVI_FC, SAVI_FC, and MSAVI2_FC show weak relationships with carbon sequestration and are not suitable for accurately predicting carbon sequestration using this method, as the strength of the correlation is low.

3.4.2. Correlation Analysis Using the Area Block Method

The correlation analysis between carbon sequestration and vegetation indices using the Area Block method involved defining areas to calculate the total vegetation index values and total carbon sequestration within each Area Block. The carbon sequestration values (in tons of carbon) and the total values of NDVI_FC, SAVI_FC, and MSAVI2_FC within each of the 11 randomly selected Area Blocks (11 Area Block IDs) were used to perform regression analysis.

The results are as follows: from the vegetation indices NDVI_FC, SAVI_FC, and MSAVI2_FC, the derived regression equations were $y = 0.5966e^{0.0667x}$, $y = 0.5966e^{0.0667x}$ and $y = 0.5904e^{0.1068x}$, respectively, and the corresponding R^2 values were 0.8924, 0.8924, and 0.8940, respectively. It can be seen that the coefficient of determination (R^2) values for NDVI_FC, SAVI_FC, and MSAVI2_FC are high, indicating that the relationships between carbon sequestration and vegetation indices can be effectively predicted.

3.4.3. Correlation Analysis Using the Grid Block Method

The correlation analysis between carbon sequestration and vegetation indices using the Grid Block method involved creating areas to calculate the average vegetation index values and the total carbon sequestration within each Grid Block. The carbon sequestration values (in tons of carbon) and the total NDVI_FC, SAVI_FC, and MSAVI2_FC values from all 61 Grid Blocks were used to perform regression analysis.

The results are as follows: from the vegetation indices NDVI_FC, SAVI_FC, and MSAVI2_FC, the derived regression equations were $y = 0.2655e^{0.1847x}$, $y = 0.2656e^{0.1847x}$, and $y = 0.2814e^{0.2534x}$, respectively, and the corresponding R^2 values were 0.8526, 0.8526, and 0.7965, respectively. It can be seen that the R^2 values for the vegetation index models NDVI_FC, SAVI_FC, and MSAVI2_FC are relatively high, indicating that these models can be effectively used to predict the relationship between carbon sequestration and vegetation indices.

3.5. Carbon Estimation Results Using Modeling

3.5.1. Results from the Area Block Modeling Method

The carbon estimation results using the model based on the regression equations between total carbon sequestration and vegetation indices derived from the Area Block method are presented in **Table 2**. Table 2 shows a comparison of carbon values between field survey data and UAV imagery processed using the Area Block method. Among the 11 Area Blocks, differences were observed between carbon estimates obtained from vegetation indices (NDVI_FC, SAVI_FC, and MSAVI2_FC) and those from field data.

Two vegetation indices—NDVI_FC and SAVI_FC—produced identical carbon sequestration estimates: 6.90388 tC, 25.31424 tCO_2e, and 0.00432 tCO_2/m^2. In contrast, MSAVI2_FC estimated carbon sequestration at 6.83419 tC, 25.05868 tCO_2e, and 0.00427 tCO_2/m^2. When compared to the field survey data, which reported significantly higher values of 23.7047 tC and 86.91723 tCO_2e with a carbon per square meter ratio of 0.01482 tCO_2/m^2, clearly highlighting the discrepancy between carbon measurement using vegetation indices and field-based data. It can be concluded that estimating carbon sequestration using vegetation indices through the Area Block method tends to yield significantly lower results compared to field measurements.

Table 2.

Results from the Area Block Modeling Method.

Carbon volume	Area sq.m. (m^2)	Tons of carbon (tC)	Tons of carbon dioxide equivalent (tCO_2)	Tons of carbon dioxide/sq.m. (tCO_2/m^2)
RS_NDVI_FC	5,864.17956	6.90388	25.31424	0.00432
RS_SAVI_FC	5,864.17956	6.90388	25.31424	0.00432
RS_MSAVI2_FC	5,864.17956	6.83419	25.05868	0.00427
Field data	5,864.17956	23.7047	86.91723	0.01482

3.5.2. Results from the Grid Block Modeling Method

The carbon estimation results using the model based on the regression equations between total carbon sequestration and vegetation indices from the Grid Block method are presented in **Table 3**. Table 3 provides a comparison of carbon values obtained using the Grid Block method, highlighting differences in the amount of carbon measured through various techniques, including NDVI_FC, SAVI_FC, MSAVI2_FC, and field-based data collection. This comparison focuses on an area of 33,853.16369 square meters, with varying results in terms of total carbon (tC) and carbon dioxide equivalent (tCO_2). According to the data in **Table 3**, RS_NDVI_FC and RS_SAVI_FC produced similar results in terms of total carbon and carbon dioxide equivalents. RS_NDVI_FC yielded 32.47310 tC and 119.06804 tCO_2e, while RS_SAVI_FC recorded 32.48533 tC and 119.11288 tCO_2e. Both methods resulted in the same average carbon dioxide per square meter, at 0.00352 tCO_2/m^2. In contrast, RS_MSAVI2_FC produced slightly higher values, with 34.17078 tC and 125.29286 tCO2e, resulting in a higher average carbon dioxide per square meter of 0.00370 tCO_2/m^2. When compared with field data, a clear difference is observed. The field survey reported the highest carbon value at 40.52095 tC and 148.57682 tCO2e, resulting in the highest average carbon dioxide per square meter of 0.00439 tCO_2/m^2. From this comparison, it can be concluded that carbon estimation using various Grid Block techniques yields differing results, with variation in the level of accuracy and spatial detail. While field data remains the most accurate source, the use of emerging techniques may offer greater convenience and efficiency for future carbon assessments.

Table 3.

Results from the Grid Block Modeling Method.

Carbon volume	Area sq.m. (m^2)	Tons of carbon (tC)	Tons of carbon dioxide equivalent (tCO_2)	Tons of carbon dioxide/sq.m. (tCO_2/m^2)
RS_NDVI_FC	33853.16369	32.47310	119.06804	0.00352
RS_SAVI_FC	33853.16369	32.48533	119.11288	0.00352
RS_MSAVI2_FC	33853.16369	34.17078	125.29286	0.00370
Field data	33853.17307	40.52095	148.57682	0.00439

4. CONCLUSION

This research studied the relationship between carbon sequestration and vegetation indices using various spatial analysis methods. In the Crown Cover method, the R^2 values representing the relationship between carbon sequestration and vegetation indices were found to be low. Specifically,

the R^2 values for NDVI_FC, SAVI_FC, and MSAVI2_FC were approximately 0.0721, 0.0635, and 0.0639, respectively, indicating a weak predictive capability. In contrast, the Area Block method demonstrated stronger correlations, with R^2 values for NDVI_FC, SAVI_FC, and MSAVI2_FC reaching 0.8924, 0.8924, and 0.8940, respectively. These results indicate that the relationship between carbon sequestration and vegetation indices can be effectively predicted. The regression equations obtained from this study can be applied to spatial carbon analysis. For the Grid Block method, the R^2 values for NDVI_FC, SAVI_FC, and MSAVI2_FC were 0.8526, 0.8526, and 0.7965, respectively, which also demonstrate a good level of correlation and predictive capability. Regarding the carbon estimation results using the models, it was found that both the Area Block and Grid Block methods produced significantly different results compared to field data. Carbon estimation using vegetation indices with the Area Block method tended to yield lower values than field measurements. In contrast, the Grid Block method produced values closer to those obtained from field data, although differences still remained. Field data continues to serve as the most accurate reference. However, the application of new techniques such as Area Block and Grid Block methods may offer increased efficiency and convenience in carbon assessment in the future. These methods represent promising approaches that can be further developed and refined to enhance accuracy and practical value in carbon estimation across various areas.

ACKNOWLEDGMENTS

This research project was financially supported by Mahasarakham University.

REFERENCES

Alfio, V. S. (2024). UAV Photogrammetry as a Multidisciplinary Approach in Engineering Design and Sustainable Land Management. *Geographia Technica*, 19(2), 78–90.

Angkahad, T., Laosuwan, T., Sangpradid, S., Prasertsri, N., Uttaruk, Y., Phoophathong, T., & Nuchthapho, J. (2024). An empirical analysis of above ground biomass and carbon sequestration utilizing UAV photogrammetry and machine learning techniques. *IEEE Access*, 1.

Auntarin, C., Chunpang, P., Chokkuea, W., & Laosuwan, T. (2021). Using a Split-window Algorithm for the Retrieval of The Land Surface Temperature via Landsat-8 OLI/TIRS. *Geographia Technica*, 16 (Special Issue), 30–42.

Earthobservatory. (2005). The Carbon Cycle. Available online: https://earthobservatory.nasa.gov/features/CarbonCycle (accessed on 02 February 2025).

Chopra, N., Tewari, L. M., Tewari, A., Wani, Z. A., Asgher, M., Pant, S., Siddiqui, S., & Siddiqua, A. (2023). Estimation of Biomass and Carbon Sequestration Potential of Dalbergia latifolia Roxb. and Melia composita Willd. Plantations in the Tarai Region (India). *Forests*, 14(3), 646.

Hongthong, A., & Nakapan, S. (2023). Assessing the impact of a waste incinerator on the environment using the MAIAC-AOD and AERMOD models. *Frontiers in Environmental Science*, 11, 1240705.

Huete, A.R. (1988) A Soil Adjusted Vegetation Index (SAVI). *Remote Sensing of Environment*, 25, 295-309.

Huynh, T., Lewis, T., Applegate, G., Pachas, A. N. A., & Lee, D. J. (2022). Allometric Equations to Estimate Aboveground Biomass in Spotted Gum (*Corymbia citriodora* Subspecies *variegata*) Plantations in Queensland. *Forests*, *13*(3), 486.

IPCC. (2006). IPCC Guidelines for National Greenhouse Gas Inventories. Volume 4 Agriculture, Forestry and Other Land Use. Available online: https://www.ipcc-nggip.iges.or.jp/public/2006gl/pdf/4_Volume4/V4_04_Ch4_Forest_Land.pdf (accessed on 07 February 2025).

Jomsrekrayom, N., Meena, P., & Laosuwan, T. (2021). Spatiotemporal analysis of vegetation drought variability in the middle of the northeast region of Thailand using Terra/Modis satellite data. *Geographia Technica*, 16(Special Issue), 70–81.

Jumadi, J., Sari, D. N., Umrotun, U., Musiyam, M., Nurmantyo, C., Muhammad, S. F., & Ibrahim, M. H. (2024). Remote Sensing and GIS-Driven Model For Flood Susceptibility Assessment in the Upper Solo River Watershed. *Geographia Technica*, *19*(2/2024), 33–45.

Lal, M., & Singh, R. (2000). Carbon sequestration potential of Indian forests. *Environmental Monitoring and Assessment*, 60(3), 315–327.

Laosuwan, T., Uttaruk, Y., Sangpradid, S., Butthep, C., & Leammanee, S. (2023). The carbon sequestration potential of Silky Oak (*Grevillea robusta* A.Cunn. ex R.Br.), a high-value economic wood in Thailand. *Forests*, 14(9), 1824.

Laosuwan, T., Uttaruk, Y., Nakapan, S., Itsarawisut, J., & Plybour, C. (2025). Evaluation of Tree Biomass and Carbon Sequestration through Remote Sensing and Field Methods. *Geographia Technica*, 33–43. https://doi.org/10.21163/gt_2025.201.04

Lewis, S. L., Lopez-Gonzalez, G., Sonke, B., Affum-Baffoe, K., Baker, T. R., Ojo, L. O., & Phillips, O. L. (2009). Increasing carbon storage in intact African tropical forests. *Nature*, 457,1003–1007.

Liu, L. J., & Liang, Q. M. (2017). Changes to pollutants and carbon emission multipliers in China 2007-2012: An input-output structural decomposition analysis. *Journal of Environmental Management*, 203, 76.

Lu, T., Wan, L., Qi, S., & Gao, M. (2023). Land Cover Classification of UAV Remote Sensing Based on Transformer–CNN Hybrid Architecture. *Sensors*, *23*(11), 5288.

Mendes, P. A., Coimbra, A. P., & de Almeida, A. T. (2023). Forest vegetation detection using deep learning object detection models. *Forests*, *14*(9), 1787.

Nakapan, S., & Hongthong, A. (2022). Applying surface reflectance to investigate the spatial and temporal distribution of PM2.5 in Northern Thailand. *ScienceAsia*, 48, 75–81.

Ngthai. What is the carbon cycle? Available online: https://ngthai.com/science/31560/carbon-cycle/ (accessed on 03 February 2025).

Ogawa, H., Yoda, K., Ogino, K., & Kira, T. (1965). Comparative ecological studies on three main types of forest vegetation in Thailand II. Plant biomass. *Nature and Life in Southeast Asia*, 4, 49–80.

Oumasst, A., Tiouidji, F. E., Tabi, S., Zahidi, A., El Mousadik, A., El Finti, A., Aitlhaj, A., & Hallam, J. (2024). Development of Allometric Equations to Determine the Biomass of Plant Components and the Total Storage of Carbon Dioxide in Young Mediterranean Argan Trees. *Sustainability*, *16*(11), 4592.

Ounrit, I., Sinnung, S., Meena, P., & Laosuwan, T. (2022). Flash Flood Mapping based on Data from Landsat-8 Satellite and Water Indices. *International Journal on Technical and Physical Problems of Engineering*, 14 (2), 130–135.

Pandey, S. S., Maraseni, T. N., & Cockfield, G. (2014). Carbon stock dynamics in different vegetation dominated community forests under REDD+: A case from Nepal. *Forest Ecology and Management*, 327, 40–47.

Pepe, M., Costantino, D., Alfio, V. S., & Zannotti, N. (2021). 4D Geomatics Monitoring of a Quarry for the Calculation of Extracted Volumes by Tin and Grid Model: Contribute of UAV Photogrammetry. *Geographia Technica*, 16 (Special Issue), 1–14.

Qi, J., Chehbouni, A., Huete, A.R., Kerr, Y.H. and Sorooshian, S. (1994) A Modified Soil Adjusted Vegetation Index. *Remote Sensing of Environment*, 48, 119-126.

Saengpradit, P., Sangpradid, S., T. Laosuwan, T. (2024). Estimation of Above-Ground Biomass using Hybrid Machine Learning Based on Satellite Imagery. *International Journal on Technical and Physical Problems of Engineering*, 16 (4), 7–13.

Samdaengchai, B., Sinnung, S., Meena, P., & Laosuwan, T. (2022). An Analysis on Disasters Caused by Flood Via Data from Sentinel-1 Satellite. *International Journal on Technical and Physical Problems of Engineering*, 14 (2), 21–26.

Tucker, C.J. (1979) Red and Photographic Infrared Linear Combinations for Monitoring Vegetation. Remote Sensing of Environment, 8, 127–150.

Uttaruk, Y., & Laosuwan, T. (2019). Development of Prototype Project for Carbon Storage and Greenhouse Gas Emission Reduction from Thailand's Agricultural Sector. *Sains Malaysiana*, 48(10), 2083–2092.

Uttaruk, Y., Laosuwan, T., Sangpradid, S., Butthep, C., Rotjanakusol, T., Sittiwong, W., & Nilrit, S. (2024). Thailand's urban forestry programs are assisted by calculations of their ecological properties and economic values. *Land*, 13(9), 1440.

Uttaruk, Y., & Laosuwan, T. (2020). Methods of estimation for above ground carbon stock in Nongbua-nonmee community forest, Maha Sarakham Province, Thailand. Agriculture and Forestry, 66(3), 183–195.

Uttaruk, Y., Rotjanakusol, T., & Laosuwan, T. (2022). Burned Area Evaluation Method for Wildfires in Wildlife Sanctuaries Based on Data from Sentinel-2 Satellite. *Polish Journal of Environmental Studies*, *31*(6). 5875–5885.

Uttaruk, Y., Khoa, P.V., & Laosuwan, T. (2024). A Guideline for Greenhouse Gas Emission Reduction and Carbon Sequestration in Forest Sector Based on Thailand Voluntary Emission Reduction Programme. *Sains Malaysiana*, 53(3), 477–486.

Vattanavongsiri, W., Sangpradid, S., Chokkuea, W., Laosuwan, T. (2024). Estimation of Above-ground Carbon Sequestration in the National Reserved Forest using Vegetation Indices and Gradient Boosting Machine Learning. *International Journal on Technical and Physical Problems of Engineering*, 16 (3), 361–366.

Yadav, R. P., Bisht, J. K., & Bhatt, J. C. (2017). Biomass, carbon stock under different production systems in the mid hills of Indian Himalaya. *Tropical Ecology*, 58(1), 15–21.

USING GEOSPATIAL TECHNOLOGY TO ANALYSE VEGETATION VULNERABILITY: APPLICATION TO PRISHTINA, KOSOVO

***Albert BERILA*[1], *Florim ISUFI*[1*], *Ferat KRASNIQI*[1]**

DOI: 10.21163/GT_2025.202.06

ABSTRACT

The vulnerability of vegetation, influenced by factors of different levels, is a growing concern in Kosovo, particularly in the Municipality of Prishtina. This study investigates the extent and causes of vegetation vulnerability by analyzing key factors: roads, land use, slope, and settlements. Using GIS and Remote Sensing, the pairwise comparison method was applied to calculate the weight of each factor's impact. A weighted overlay method was employed to create a risk map of vegetation vulnerability. Results reveal that areas near roads, with gentle slopes, and unplanned land use are most vulnerable to vegetation degradation. Conversely, regions with steep slopes, planned land use, and distance from roads show lower vulnerability. Population density further exacerbates vegetation risk, emphasizing the need for proper planning and sustainable natural resource management. This research highlights the importance of positive land use practices and proactive measures to mitigate the adverse effects of rapid urbanization on natural vegetation.

Key-words: *Vegetation vulnerability; Geospatial Technology; Vegetation analysis; Factors weighting.*

1. INTRODUCTION

Contemporary lifestyle changes, coupled with the rapid and often uncontrolled expansion of settlements, have become increasingly prominent. Rapid population growth generates numerous challenges related to spatial organization and infrastructure development. Unplanned urbanization frequently results in critical issues, particularly where development occurs without prior planning, rendering the realization of comprehensive urban strategies virtually impossible. Consequently, this leads to multiple complications—both in the construction process and the management of built environments. Residential complexes are often constructed hastily, placing a high number of households within limited spatial confines. As a result, individuals experience a significant disconnection from the natural environment. The pace and scale of such urban development constitute a substantial burden on the population, frequently contributing to the onset of various health problems, including hypertension, neuroses, respiratory disorders, and arteriosclerosis. When these health issues are mapped spatially, it becomes evident that they are more prevalent in densely urbanized areas than in regions that maintain closer proximity to natural environments.

The natural world is shaped by a multitude of dynamic forces that act, to varying degrees, on vegetation. The cumulative effects of these forces—both natural and anthropogenic—constitute what is referred to as vegetation vulnerability. A wide array of factors contributes to vegetation degradation, including but not limited to human activities, armed conflict, both natural and deliberate fires, pests, natural disasters, and disease outbreaks (Tsegaye, 2019; Ganaie, Jamal & Ahmad, 2021; Badmaev & Bazarov, 2022; Maurya et al., 2020; Tsymbarovich et al., 2020). Among these, human activities have been identified as the most detrimental to vegetation health and sustainability (Badmaev & Bazarov, 2022; Maurya et al., 2020; Tsymbarovich et al., 2020; Minale & Gelaye, 2021). In this regard, people do a series of harmful actions that cause repairable damage (Nair & Tieguhong, 2021). Anthropogenic pressures—such as poor land management, expansion of road networks, proximity to settlements, and terrain accessibility—play a decisive role in the degradation of vegetation (Dien, 2004).

[1]*Department of Geography, Faculty of Mathematics and Natural Sciences, University of Prishtina, Prishtina, Republic of Kosovo, albert.berila@uni-pr.edu, florim.isufi@uni-pr.edu, ferat.krasniqi@uni-pr.edu*
[*]*Corresponding author*: florim.isufi@uni-pr.edu*

Consequently, areas that are remote or topographically inaccessible tend to be less exposed to human-induced threats. On the contrary, regions that are easily accessible are more susceptible to exploitation and ecological degradation (Minale & Gelaye, 2021). Furthermore, an increase in human population density and technological advancement correlates directly with environmental pressure and subsequent vegetation loss (EPA, 2021). The demand for agricultural land and forest products has further intensified the transformation of natural vegetation, often accelerated by technological innovations in agriculture.

Natural vegetation is essential not only for ecological stability but also for socio-economic wellbeing (Minale & Gelaye, 2021, Schröter et al., 2005). The connection of the earth's surface with the vegetation is extraordinary. Vegetation plays a vital role in reducing soil erosion and enhancing fertility by stabilizing soil surfaces (Minale & Gelaye, 2021; Sun, Hou & Chen, 2021; Berendse et al., 2015; Jin et al., 2021; Hou et al., 2020; North et al., 2021; El Kateb et al., 2013; Novara et al., 2018; Yu & Jia, 2014). Conversely, the absence or degradation of vegetative cover increases the risk of soil erosion and land degradation (Hou et al., 2020; Vieira et al., 2018; Moody & Martin, 2001; Morgan, 1986; Shakesby, Doerr & Walsh, 2000). In Kosovo, deforestation remains a principal driver of land degradation. A significant portion of the country's economy relies on agriculture, resulting in the conversion of vegetated lands into arable land. These transformations have led to significant alterations in vegetation cover over the decades. The degradation of natural vegetation in Kosovo poses a major threat to the sustainability of essential natural resources, such as water and soil (Wang & Stephenson, 2018; Wu et al., 2020; Huang, Van Den Dool & Georgakakos, 1996; Gebrehiwetk, 2004; Niu, Chen & Sun, 2015). Key contributors to vegetation degradation in Kosovo include rapid population growth, escalating demand for natural resources, illegal logging, and anthropogenic forest fires. Migration patterns, particularly from rural to urban areas in search of better livelihoods, have led to an intensification of construction, infrastructure development, and resource exploitation. These activities are particularly evident in Prishtina—the capital city—where post-conflict development has significantly impacted natural vegetation.

Although geoinformatics offers robust tools to assess vegetation vulnerability, their application remains underutilized, especially in Kosovo. Several studies have successfully employed geospatial technologies to analyze the impact of natural disasters on vegetation across the globe (Yin et al., 2020; Dashpurev et al., 2021; Gemitzi & Koutsias, 2021; Dutta et al., 2015; Gonçalves et al., 2015; Dindaroglu et al., 2021; Hislop et al., 2020). Due to human activities, the climate has changed, and such a change endangers the composition and distribution of vegetation by decreasing/destroying biodiversity and weakening the ecosystem (Bowler et al., 2020; Buizer, Humphreys & De Jong, 2014; Coomes et al., 2014; Hanewinkel et al., 2014; Khosravi et al., 2017; Lin, Xia & Wan, 2010; Lindner, 2010; Paterson & Newell, 2010; Ripple, 2013; Way & Oren, 2010; Wiens, 2011; Zhu et al., 2014). As a result of all this, the atmosphere will be threatened to cause the degradation of the living environment to increase—fragmentation and loss of vegetation (Buizer, Humphreys & De Jong, 2014; Awono et al., 2014; Evans, Murphy & De Jong, 2013; Hanski et al., 2015; Luttrell et al., 2014; Matthews, Cottee-Jones & Whittaker, 2014). Compared to traditional methods, the continuous monitoring of vegetated areas through the use of satellite data has tremendous advantages (Pei et al., 2018; Zhang et al., 2017). To analyze vegetative drought, one of the most widely applied indices is NDVI (Gomes, Bernardo & Alcântara, 2017; Kundu, Dwivedi & Dutta, 2016). Gomes, Bernardo and Alcântara (2017) identified that the areas with the highest level of vegetation change were those put under tremendous amount of stress. Such areas had high Land Surface Temperature (LST) values and low Vegetation Health Index (VHI) values. This work was carried out in southeastern Brazil for 14 years (2000-2014). Bhuiyan et al. (2017) for 29 years (1981-2010), examined the impact that thermal stress has on vegetation. The results clearly showed that heat stress damages vegetation to a great extent. Schröter et al. (2005) reported that the impacts of socio-economic activities on changes in vegetation distribution are evident. Berendse et al. (2015) concluded that the soil surface will be much more damaged if the vegetative cover layer is lost. Despite the global progress in geospatial vegetation studies, a significant gap remains in the scientific literature regarding the systematic mapping of vegetation vulnerability. A key limitation has been the lack of a coherent, standardized

methodological framework that can guide such research. Existing studies tend to focus primarily on identifying current vegetation status, underlying causes of degradation, and general ecological consequences. However, they often omit spatially explicit analyses that assess vulnerability and rank contributing factors according to their relative importance. This study aims to address these gaps by developing a detailed methodological workflow for mapping vegetation vulnerability using geospatial tools. The approach includes data acquisition (e.g., satellite imagery and elevation data) (**Tab. 1**), integration of environmental and socio-economic variables (slope, land use, proximity to roads and settlements), and the application of multi-criteria evaluation techniques, specifically the weighted linear combination method. The final output is a spatially explicit map of vegetation vulnerability, which can support both researchers and policymakers in environmental management efforts.

Although similar methodologies have been applied in other regions of the world, no such studies have been conducted in Kosovo. This absence is largely due to the lack of clear methodological standards. Therefore, this research not only fills a scientific gap but also proposes a replicable model for the application of geospatial technologies in vegetation vulnerability assessment.

In summary, the objectives of this study are threefold:

1. To design a replicable geospatial methodology for vegetation vulnerability mapping,
2. To identify and evaluate the key drivers of vegetation degradation in Prishtina, and
3. To generate a spatial vulnerability model that supports sustainable natural resource management.

This research is intended to serve as a reference point for future studies in the field of geoinformatics and environmental planning, contributing to more sustainable development practices in Kosovo and beyond.

2. STUDY AREA

Prishtina, the capital and largest city of the Republic of Kosovo, is situated in the northeastern region of the country, occupying a strategically significant position within the Balkan Peninsula (**Fig. 1**). The municipality is geographically bordered by Kastriot (Obiliq) to the west, Besiana (Podujeva) to the north, Graçanica and Lipjan to the south, Fushë Kosova to the southwest, Dardana (Kamenica) to the east, and Artana (Novobërdë) to the southeast.

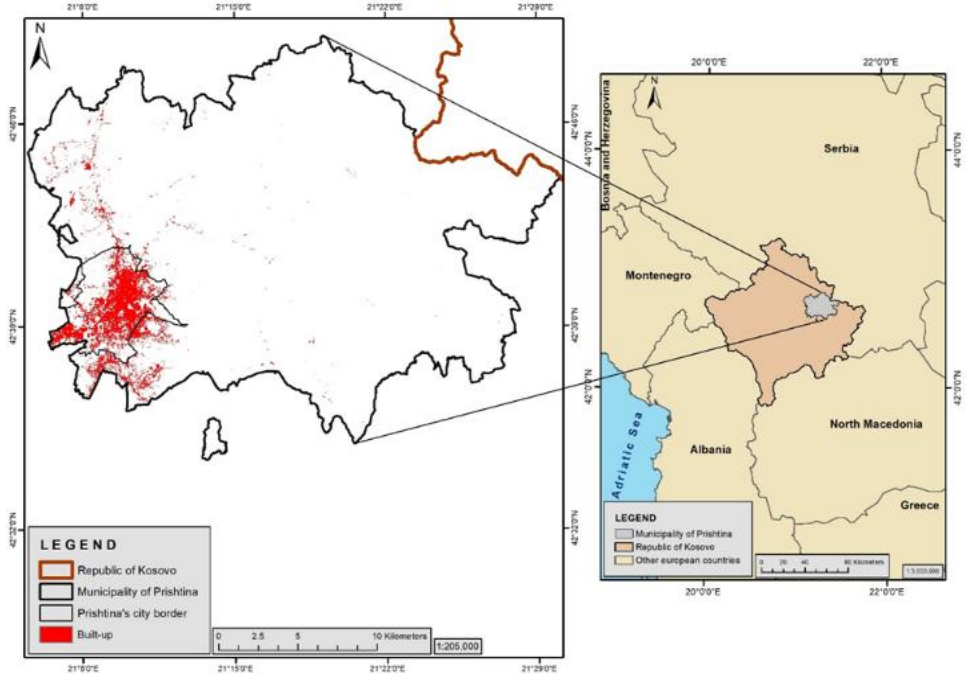

Fig. 1. Location of the study area (Berila & Dushi, 2021).

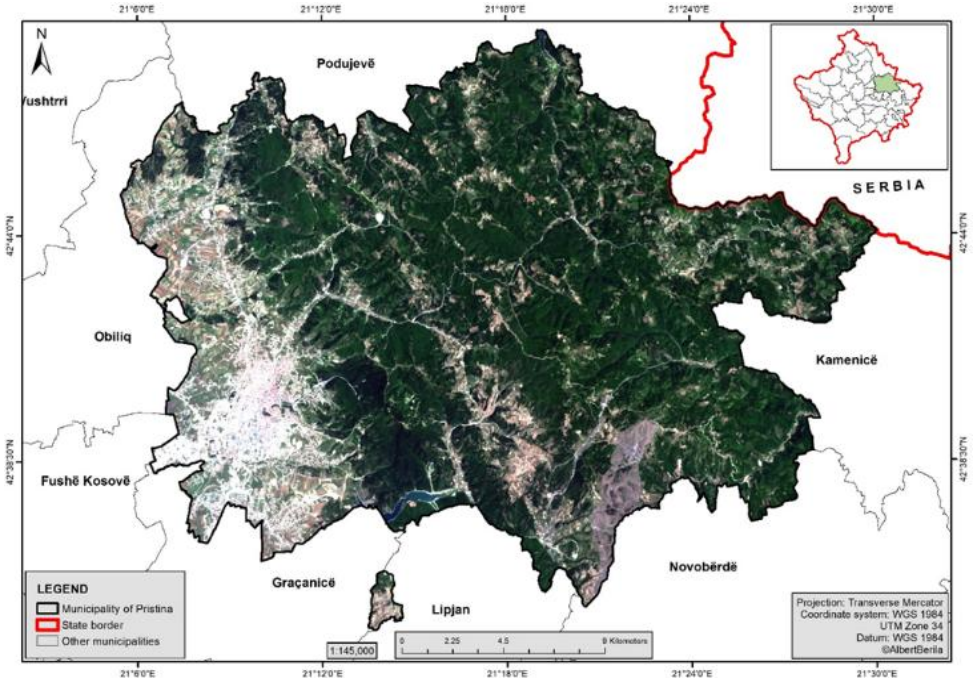

Fig. 2. Landsat 8 OLI RGB – composite (R = 0.6542 μm, G = 0.5609 μm, B = 0.4828 μm) of the study area (Berila & Isufi, 2021a).

Additionally, it shares a boundary with the Republic of Serbia along its northeastern frontier (**Fig. 2**) (Berila & Isufi, 2021a). The total area of the Municipality of Prishtina spans approximately 523 km². Geomorphologically, the municipality is part of the Kosovo Plain and is primarily composed of alluvial deposits originating from ancient lake sediments. Geologically, the region is characterized as a tectonic depression that formed during Oligo-Miocene tectonic activity, which has since shaped the contemporary landforms (Isufi & Berila, 2021; Berila & Isufi, 2021b; Municipality of Prishtina, 2021). The area experiences a continental climate, typified by cold winters and hot summers, with an average annual precipitation of approximately 600 mm (Isufi & Berila, 2021; Berila & Isufi, 2021b; Municipality of Prishtina, 2021).

Despite the global advancement in research on vegetation degradation and environmental vulnerability, Kosovo remains underrepresented in such investigations. The absence of localized studies is primarily due to a lack of clear, standardized scientific methodologies. Consequently, research in this domain has remained limited in scope and depth. To address this gap, there is a critical need for the application of advanced geospatial technologies—namely Geographic Information Systems (GIS) and Remote Sensing (RS)—which enable the integration and analysis of multiple environmental and anthropogenic variables (Minale & Gelaye, 2021).

In the context of Prishtina, the application of geospatial tools is particularly essential due to the rapid and unregulated environmental transformations observed in recent decades. These changes have largely been driven by the overexploitation of natural vegetation, primarily resulting from intensified human activities. Post-conflict urban expansion, infrastructure development, and the increasing demand for natural resources have significantly altered the landscape and degraded vegetative cover. To date, no comprehensive study has been conducted to evaluate the vulnerability of vegetation in this specific area using geospatial methodologies. Therefore, this research seeks to fill that gap by identifying the key environmental and anthropogenic drivers contributing to vegetation vulnerability and by producing detailed spatial maps that depict these patterns.

3. RESEARCH METHODOLOGY

The primary objective of this study is to assess the degree of vegetation degradation through the identification and spatial analysis of key contributing factors. To achieve this, we employed a multi-criteria geospatial approach that integrates several variables influencing vegetation vulnerability, as identified in relevant literature (Minale & Gelaye, 2021). Specifically, the following parameters were selected: slope, proximity to settlements, land use, and proximity to roads. Among these variables, terrain slope was considered particularly significant due to its direct influence on vegetation accessibility and susceptibility to human activities. To extract topographic information, we utilized a Digital Elevation Model (DEM) with a spatial resolution of 12.5 meters, obtained from the Alaska Satellite Facility (https://asf.alaska.edu/). This DEM was processed using ArcGIS 10.5, allowing for precise slope calculations at the cell level. The slope data were then classified into five distinct categories to reflect variations in terrain steepness across the study area (Berila & Dushi, 2021; Berila & Isufi, 2021c, 2021d).

The slope of the terrain is a significant factor influencing vegetation vulnerability, as steeper areas are generally less accessible and therefore less exposed to anthropogenic activities. Using ArcGIS 10.5, we derived the slope from the DEM through the ArcToolbox "Slope" function (**Fig. 3**). This output was then classified into five categories, each representing different degrees of slope steepness. This classification served as a basis for vulnerability analysis, with flatter areas typically indicating higher risk due to greater accessibility. The second variable analyzed was the proximity to roads. Road networks were manually digitized from existing maps of the study area using ArcGIS 10.5. Spatial analysis tools within the software were used to calculate Euclidean distances between vegetation and roads. These distances were categorized into four classes. Areas closer to roads were assigned lower values, indicating higher vegetation vulnerability, whereas areas further away were considered less vulnerable due to limited accessibility.

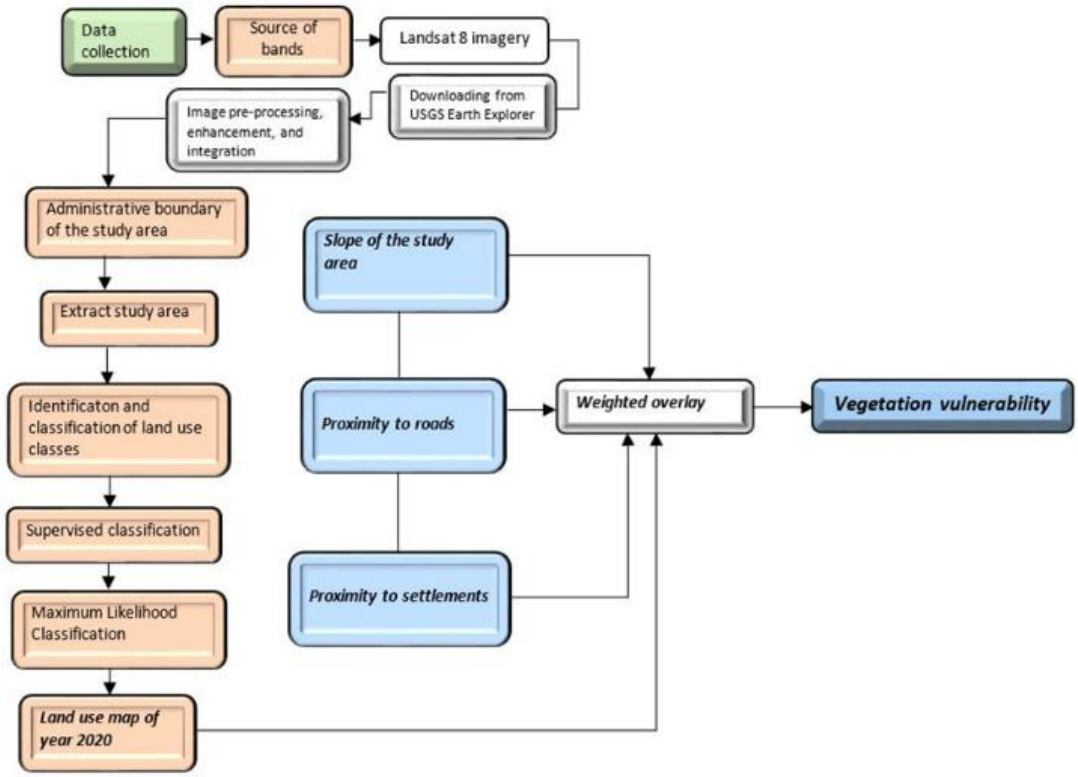

Fig. 3. Flowchart depicting methodology – general steps (compiled by authors).

To proceed further, it is necessary to scale the parameters that we will use, evenly (uniformly) according to Saaty (1987). To obtain the most accurate information on each option/variable, we had to know and consider the usefulness of each option or parameter entered so that, in the end, our decision-making was as rational as possible. For such a thing we have used multi-criteria evaluation using the weighted linear combination. For our study area, to determine the vulnerability of vegetation, we made comparisons of all variables included in the study, determining their importance according to our assessment. To have a clearer picture of the methodology used, we have presented such a thing in **Fig. 3**—general steps.

Table 1.

Data used in this study for compiling the land use map (compiled by authors).

Sensor type	Date	Path/Row	Cloud cover	Spatial resolution	Format	Source
Landsat 8 OLI	2020/09/06	185/30	0%	30m	Tiff	https://earthexplorer.usgs.gov/

Saaty (1987), in 1987, compiled a table called "The fundamental scale", in which are given a total of 9 points as a scale for assessing the importance of each variable under consideration—this is presented in **Tab. 2**. In the Analytic Hierarchical Process (AHP), we used the scale given by Saaty (Saaty, 1987) (**Tab. 3**). Through this scale, we have determined the values which we have compared for each variable considered.

Table 2.

Saaty's scale – the fundamental scale (Saaty, 1987).

Intensity of importance on an absolute scale	Definition	Explanation
1	Equal importance	Two activities contribute equally to the objective
3	Moderate importance of one over another	Experience and judgment strongly favor one activity over another
5	Essential or strong importance	Experience and judgment strongly favor one activity over another
7	Very strong importance	An activity is strongly favored and its dominance demonstrated in practice
9	Exteme importance	The evidence favoring one activity over another is of the highest possible order of affirmation
2,4,6,8	Intermediate values between the two adjacent judgments	When compromise is needed
Reciprocals	If activity i has one of the above numbers assigned to it when compared with activity j, then j has the reciprocal value when compared with i	
Rationals	Ratios arising from the scale	If consistency were to be forced by obtaining n numerical values to spam the matrix

For each pair, the weight was categorized—according to the importance of participating in the process—each of them was compared and, finally, they were recorded in a pairwise comparison matrix (Minale & Gelaye, 2021) (**Tab. 4**). The following constraint is met by a_{ji} and a_{ij} (Minale & Gelaye, 2021):

$$a_{ji} \times a_{ij} = 1 \quad (1)$$

in column j of the matrix, the element of row i, is a_{ij} (Minale & Gelaye, 2021).

Following the establishment of weights, each factor layer was reclassified and integrated using the Weighted Linear Combination (WLC) method within ArcGIS. In this overlay process, each raster cell's value was multiplied by the corresponding weight of its parameter. The final vegetation vulnerability model was produced by summing the weighted values of all cells. Higher cumulative values represent areas with greater susceptibility to degradation, while lower values indicate areas of relative ecological stability.

The overall methodological framework—illustrated in **Fig. 3**—ensures an objective and replicable approach to vegetation vulnerability assessment. By combining environmental and anthropogenic indicators within a geospatial context, this method supports the development of informed, spatially targeted conservation and land management strategies.

Table 3.

Saaty's scale – the fundamental scale (Saaty, 1987).

Scale	Definition	
9	Extremely	More important
7	Very strong	
5	Strong	
3	Moderately	
1	Equally important	
1/3	Moderately	
1/5	Strong	
1/7	Very strong	Less important
1/9	Extremely	

Table 4.

Saaty's scale – the fundamental scale (Saaty, 1987).

Factors	S	Pr	Ps	Lua	Weight
Slope (S)	1	1/2	1/2	5	0.24
Proximity to road (Pr)	2	1	2	3	0.40
Proximity to settlement (Ps)	2	1/2	1	3	0.28
Land use administration (Lua)	1/5	1/3	1/3	1	0.08

4. RESULTS AND DISCUSSIONS

4.1. Slope

The spatial distribution of vegetation is historically shaped by ecological conditions, natural evolution, and anthropogenic pressures. Among the primary physical factors influencing vegetation structure and vulnerability is terrain slope. Topography not only guides ecological processes but also exerts socio-economic implications, determining the suitability of land for settlement, agriculture, and infrastructure. Sloped terrains enhance erosion processes and constrain human activities, whereas flat lands are more accessible, favoring development and intensive land use.

Globally, more than 90% of the population resides in areas below 400 meters above sea level, typically lowland zones where economic activities are most intensive. These areas are preferred for mechanized agriculture, urban expansion, and infrastructure development. Human modification of natural landscapes—driven by technological advancement and socio-economic needs—intensifies degradation. Flattened areas with high accessibility are particularly vulnerable to these modifications, while steep and elevated regions remain more preserved.

Topographic characteristics, particularly terrain slope, play a fundamental role in shaping the spatial distribution, density, and structure of vegetation. The slope of the land not only influences ecological processes but also governs the extent to which an area is accessible and suitable for human activities.

Numerous studies have demonstrated a strong correlation between slope gradients and vegetation patterns, affirming that steeper terrains tend to preserve their natural cover due to reduced human interference (Giroux, Bergeron & Veillette, 2001; Lin et al., 2014; Simard et al., 2007; Wang et al., 2014). Furthermore, slope and altitude are known to affect forest diversity, contributing to variations in vegetative composition and ecosystem resilience (Fu et al., 2004). In the context of the Municipality of Prishtina, our slope analysis—derived from a 12.5-meter resolution Digital Elevation Model (DEM) obtained from the Alaska Satellite Facility—reveals a distinct spatial pattern. The eastern, northeastern, and southeastern regions exhibit higher slope values, whereas the western areas are predominantly flat.

This topographic configuration has direct implications for land use. Flat terrains, due to their accessibility and suitability for agricultural activities, are more prone to urban expansion and infrastructure development. Consequently, these areas are at a higher risk of vegetation degradation. The slope values within the study area range from 0 degrees (indicating flat land) to a maximum of 47 degrees (**Fig. 4**). Areas characterized by higher slope values are generally less affected by anthropogenic pressures, as the steepness poses significant challenges for construction, mechanized farming, and other land-altering activities. This natural inaccessibility serves as a protective factor, preserving vegetation and reducing ecological disturbance.

Given the critical role of terrain slope in shaping vegetation vulnerability, its inclusion as a core variable in this study was essential. However, it is important to acknowledge a methodological limitation: the use of a DEM with a 12.5-meter resolution, while adequate for regional-scale assessments, may not capture micro-topographic variations. Future studies are encouraged to utilize higher-resolution DEMs to enhance spatial precision and improve the granularity of terrain analysis. Terrain slope emerges as a key determinant of vegetation vulnerability. Steeper areas remain relatively intact due to natural constraints, while flat, low-lying areas are increasingly exposed to anthropogenic threats. These findings underscore the importance of integrating topographic variables into environmental planning and land-use decision-making processes.

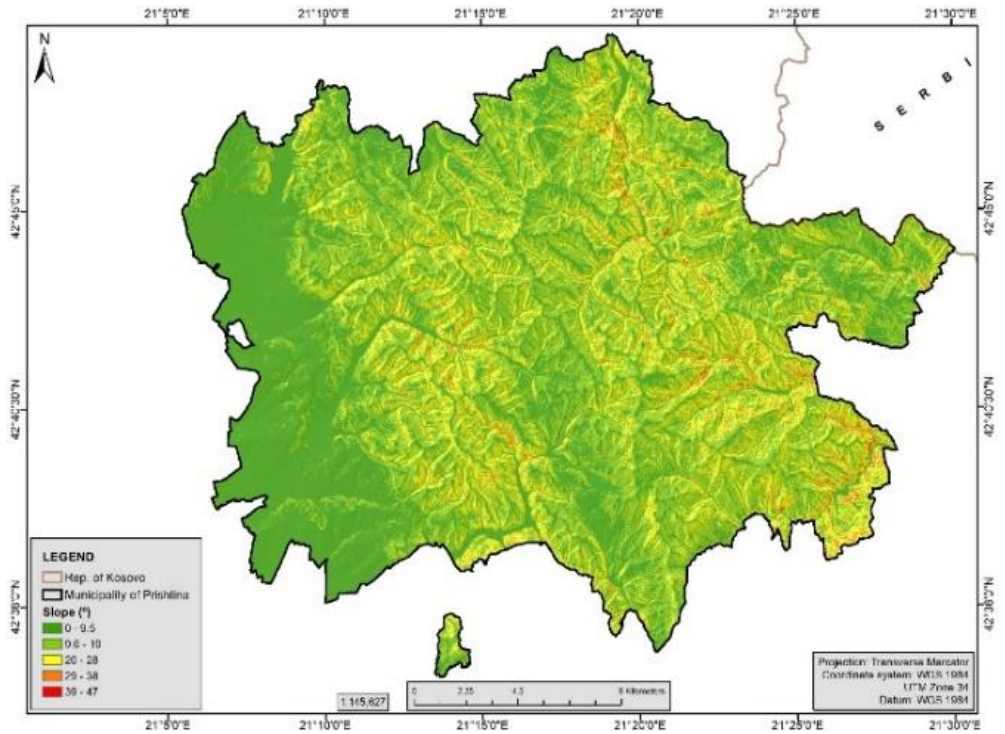

Fig. 4. Slope of the study area (compiled by authors).

4.2. Nearness to road

Road networks are among the most influential anthropogenic factors driving landscape transformation and vegetation degradation. As populations grow and economic activities expand, the demand for connectivity and mobility increases. Roads enable the movement of goods and people, but they also serve as vectors for ecological disturbance, facilitating access to previously undisturbed areas and accelerating processes such as deforestation, habitat fragmentation, and soil erosion.

The impact of roads on vegetation extends beyond the physical footprint of the infrastructure itself. Although roads occupy a relatively small proportion of land surface, their influence radiates into the surrounding environment. A variety of associated activities—such as increased vehicular traffic, emission of pollutants, noise, dust deposition, and land compaction—collectively contribute to the degradation of vegetation in adjacent areas. Numerous studies have documented the adverse ecological effects of roads, noting significant changes in vegetation composition and structure near road corridors (Findlay & Bourdages, 2000; Shakesby, Doerr & Walsh, 2000).

Vegetation located in close proximity to roads is particularly vulnerable due to its increased exposure to anthropogenic disturbances. In contrast, areas that are difficult to access due to the absence of road infrastructure tend to remain relatively intact, protected by natural barriers such as terrain slope, elevation, and remoteness. For this reason, proximity to roads was selected as a key variable in our study to assess vegetation vulnerability. Using ArcGIS 10.5, we digitized all road segments within the study area as line features and conducted a proximity analysis. The distances from roads to vegetated areas were categorized into eight distance intervals, ranging from 0 km (indicating immediate adjacency) to 4.8 km (**Fig. 5**). The spatial pattern of road density in Prishtina reveals a concentration of roads in the western region of the municipality, which also corresponds to zones of higher urbanization.

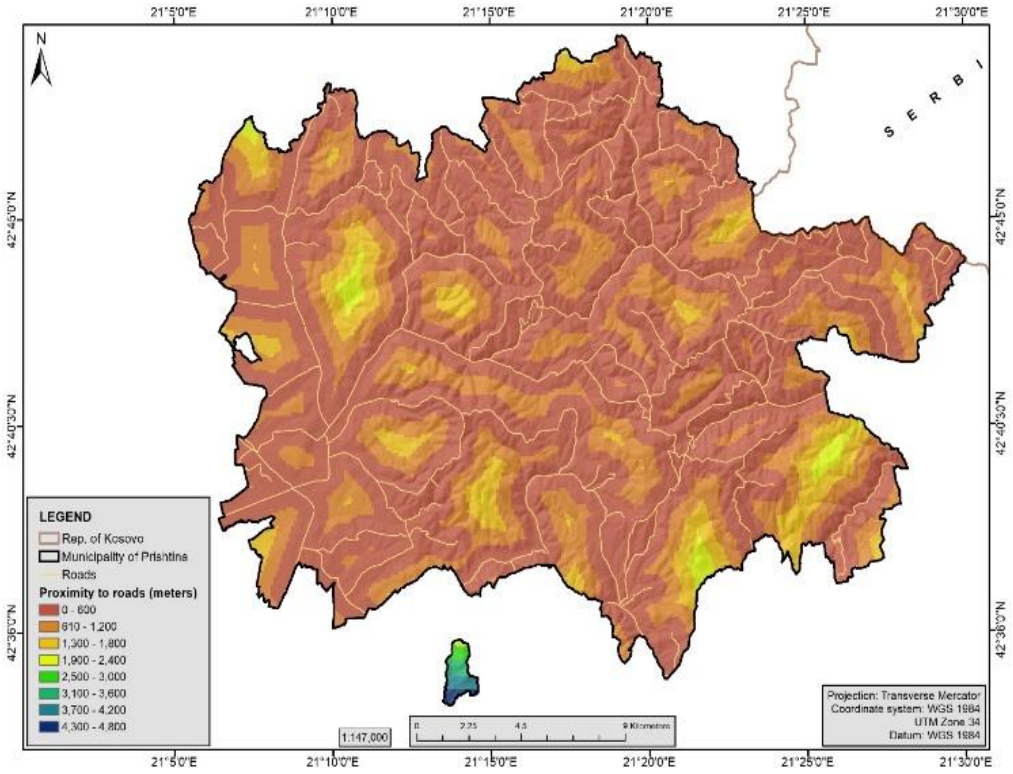

Fig. 5. Proximity to roads of the study area (compiled by authors).

This spatial correlation confirms that human activities are more intense in areas with greater road accessibility. In pursuit of minimal costs and maximum utility, individuals and communities tend to settle near roads, thereby increasing the likelihood of land conversion for agriculture, infrastructure, housing, and other uses. Consequently, vegetation near roads is subjected to heightened levels of disturbance through deforestation, logging, soil cultivation, and the expansion of the built environment. The general pattern indicates that the greater the accessibility, the higher the level of vegetation vulnerability—and vice versa.

While the methodology employed effectively illustrates the relationship between road proximity and vegetation degradation, certain limitations must be acknowledged. The accuracy of road digitization could have been improved through the use of high-resolution topographic maps or official road network datasets. The reliance on general base maps may reduce spatial precision. Moreover, the high density of road features can lead to cartographic clutter, complicating the process of spatial analysis. Future studies should consider using more detailed geospatial data and carefully manage map symbology to avoid overlapping features and visual confusion.

4.3. Proximity to settlements

Human settlements have historically evolved from rudimentary structures into complex urban systems, significantly reshaping natural landscapes and exerting continuous ecological pressure. The unregulated expansion of settlements and inefficient land use have contributed to the transformation of fertile agricultural areas and native vegetation into built-up environments, particularly in rapidly urbanizing regions.

The proximity of vegetation to human settlements is a critical factor influencing its vulnerability. Areas situated near settlements are frequently exploited for various socio-economic purposes, including the extraction of energy resources, construction materials, agricultural expansion, and other development-driven activities. For this reason, settlement proximity was included as a key variable in assessing vegetation vulnerability in this study. As noted by Dien (2004), the presence and expansion of settlements have a particularly strong and often detrimental impact on vegetation, especially in peri-urban zones.

Vegetation near settlements is more susceptible to degradation due to intensive land-use pressures, while areas located further from populated zones—particularly those that are difficult to access—tend to remain better preserved. To analyze this relationship, we employed ArcGIS 10.5, utilizing the Euclidean Distance tool from the Spatial Analyst toolbox to calculate the linear distance between vegetated areas and the nearest settlements. The resulting proximity values in the study area range from 0 km (immediate adjacency) to 6.3 km (maximum distance), as illustrated in **Fig. 6**.

The spatial distribution of settlements in Prishtina reveals a notable concentration in the western part of the municipality. This area, characterized by a higher density of built-up zones, also exhibits more significant vegetation degradation. The analysis confirms a direct correlation between settlement density and vegetation vulnerability: as settlement presence increases, so does the pressure on adjacent vegetated areas. This relationship underscores the impact of urban sprawl on the ecological stability of the region.

Settlements were digitized as point features using existing base maps of the study area. While this method proved effective for general proximity analysis, a limitation of the study lies in the absence of higher-resolution topographic maps, which could have improved the accuracy of settlement delineation. Overlapping features and excessive point density may also create visual clutter in cartographic outputs and analytical challenges in spatial modeling.

To enhance future research, it is recommended to utilize higher-scale and more detailed topographic or cadastral datasets, which allow for more precise settlement mapping. Additionally, selecting study areas with manageable settlement density can reduce spatial complexity and improve the clarity of vulnerability assessments.

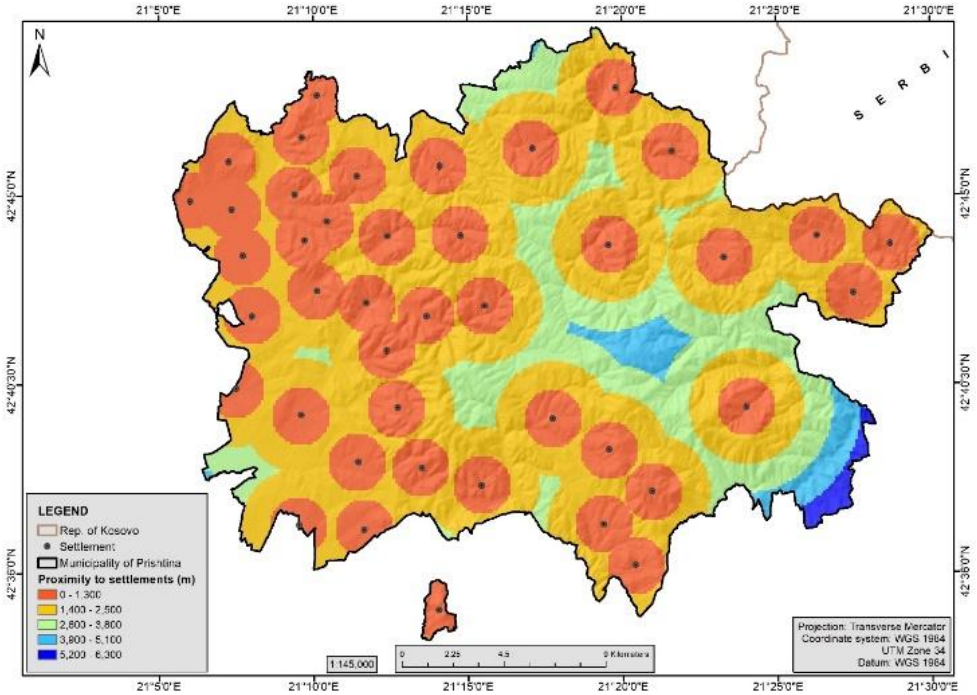

Fig. 6. Proximity to roads of the study area (compiled by authors).

4.4. Administration of the land

Land is a finite and multifunctional resource that plays a central role in sustaining ecological balance, supporting biodiversity, and enabling economic productivity. The manner in which land is utilized—and more importantly, how it is administered—has a direct and significant impact on the integrity of surrounding ecosystems, particularly vegetation. Poor land administration, characterized by unregulated urban sprawl, unsustainable agricultural expansion, and lack of environmental oversight, is one of the principal drivers of vegetation degradation and land cover transformation.

Effective land management is critical for maintaining the resilience of vegetated areas. Where land use is guided by sustainable planning and regulatory frameworks, vegetation is better preserved. Conversely, poorly managed land often experiences accelerated degradation. Land management practices are influenced by a wide array of local and global factors, including socio-economic development, governance, environmental policies, and population pressures (Minale & Gelaye, 2021; Pfaff et al., 2007).

In this study, land use within the Municipality of Prishtina was categorized into five major classes based on the type, intensity, and spatial distribution of land cover (**Fig. 7**). These classes were subsequently reclassified to reflect varying degrees of vegetation vulnerability. The analysis reveals that Prishtina has experienced substantial land mismanagement, particularly following the 1999 conflict. The rapid and often unregulated migration to the capital city has intensified land consumption without adherence to planning standards (Isufi & Berila, 2021). Large areas of vegetation have been cleared to accommodate residential developments, transportation infrastructure, and expanded agricultural fields. The phenomenon of deforestation, combined with poorly enforced environmental policies, has further exacerbated the situation.

As illustrated in **Fig. 7**, the western part of the municipality is almost entirely occupied by built-up areas and, in some zones, agricultural land. The dense settlement pattern and the rising demand for land resources in this region suggest that vegetation degradation is both ongoing and intensifying. The results of this study, supported by empirical evidence and existing literature, clearly indicate that poor land administration is a major contributor to environmental vulnerability in Prishtina.

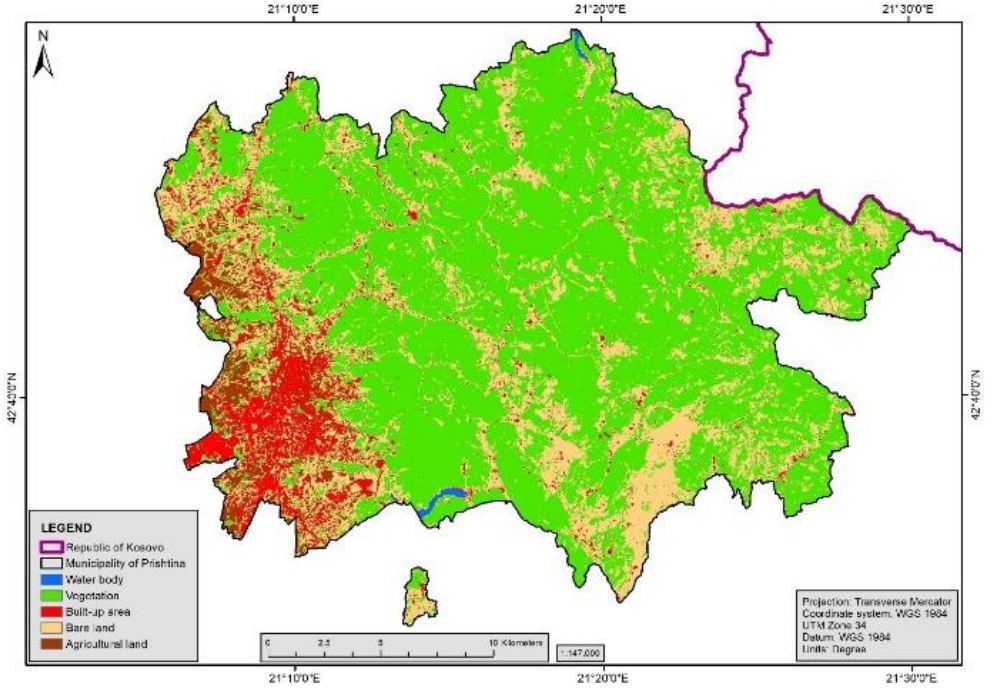

Fig. 7. Land use administration of the study area (compiled by authors).

The final variable analyzed in this study was land use, derived from a 2020 satellite image obtained from Landsat 8, accessed through the official United States Geological Survey (USGS) platform. The classification of land use plays a fundamental role in identifying high-risk zones for vegetation loss. However, the use of a 30-meter spatial resolution image imposes certain limitations on the granularity and precision of the analysis. In particular, pixel-based classification at this resolution may not accurately capture small-scale variations in land use, which are critical for fine-tuned environmental assessment. To enhance the reliability and accuracy of future research, it is recommended that satellite images with higher spatial resolution be employed. High-quality imagery allows for more precise delineation of land cover classes and supports more detailed monitoring of land use changes. Special attention should also be paid to pixel clarity and spectral definition during image processing to minimize classification errors and improve interpretability.

4.5. Compilation of the vegetation vulnerability map

Vegetation regeneration is most likely to occur in areas with limited human access—typically regions distant from roads and settlements. Consequently, dense vegetation is predominantly found in remote and topographically challenging areas, while vegetation in flat, accessible regions faces greater degradation. However, with the accelerated pace of global development and the expansion of infrastructure networks, such undisturbed areas have become increasingly rare. Modern transportation systems have drastically reduced the isolation of once-remote landscapes, increasing anthropogenic pressures even in previously inaccessible zones.

This pattern is also evident when analyzing altitudinal variations. Vegetation in elevated terrains and steeper slopes is generally less disturbed due to limited agricultural viability, erosion risks, and construction challenges. Conversely, flat and low-lying areas are often targeted for urban expansion, agriculture, and infrastructure development, making them more susceptible to vegetation loss.

In the context of the Prishtina municipality, four vegetation vulnerability classes were delineated using geospatial analysis tools (**Fig. 8**). These classes reflect varying levels of risk based on a combination of environmental and anthropogenic variables.

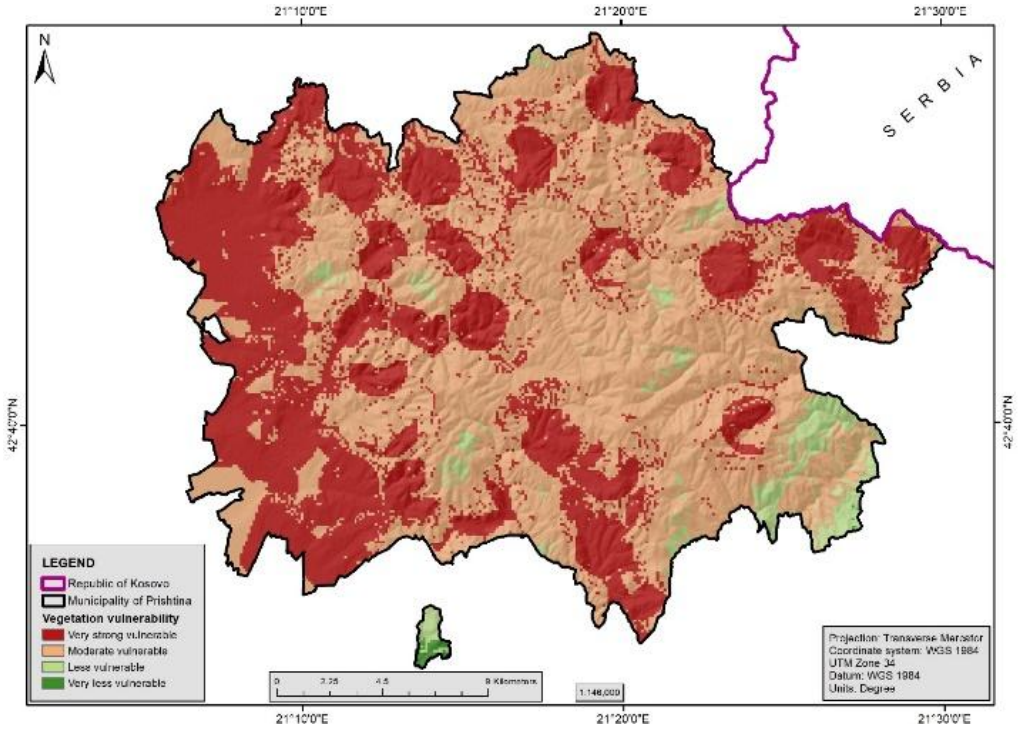

Fig. 8. Vegetation vulnerability map of the study area (compiled by authors).

Areas identified as highly vulnerable are predominantly located in flat terrains, near dense settlement clusters, and adjacent to road networks. In contrast, zones exhibiting lower vulnerability are situated on steeper slopes, at greater distances from built environments, and in regions where land use is managed more sustainably.

Our findings indicate that vegetation in Prishtina is under increasing threat, primarily due to population growth and the associated rise in demand for housing, energy, and agricultural land. The northeastern portion of the municipality, along with scattered patches across and a notable area in the south, were identified as the least vulnerable. These zones benefit from natural barriers and/or better land administration practices, which mitigate direct human impact.

A particularly noteworthy observation is the significant role of terrain slope in buffering against vegetation degradation. Steeper terrains are not only less accessible but also less suitable for cultivation due to poor soil fertility and high erosion potential. As a result, such areas tend to preserve their vegetative cover more effectively. Conversely, forested zones located near road infrastructure are highly susceptible to deforestation, emphasizing the compounded effect of accessibility and economic exploitation. The compiled vegetation vulnerability map thus serves as a critical spatial tool for environmental planning, enabling policymakers and land managers to prioritize conservation efforts in the most threatened areas while reinforcing protective strategies in ecologically stable zones.

5. CONCLUSIONS

Assessing vegetation vulnerability is critical for ensuring sustainable land use and for implementing targeted environmental protection strategies. Vegetation serves as a vital ecological component, regulating climate, supporting biodiversity, and maintaining soil quality. In this context, the present study offers a detailed spatial analysis of vegetation vulnerability within the Municipality of Prishtina, emphasizing the need for integrative geospatial approaches in understanding landscape dynamics and environmental degradation.

The findings of the study reveal that Prishtina, although rich in vegetative cover, faces serious degradation risks. Uncontrolled expansion of settlements, intensification of agriculture, and continuous development of road networks are key drivers of vulnerability. Our results confirm that vegetation is most threatened in areas with flat terrain, which are highly suitable for cultivation and construction due to their gentle slope and accessibility. Conversely, regions with steeper slopes demonstrate reduced vulnerability, as their topographic complexity limits human interference and discourages intensive land use.

The role of terrain slope is particularly significant: areas with low slope values are under greater pressure due to their agricultural potential and ease of access, while steeper terrains, often prone to erosion and less fertile, tend to remain less exploited. Similarly, proximity to roads and settlements emerged as strong determinants of vegetation degradation. Vegetation located near road infrastructure or within rapidly urbanizing zones faces increased risks due to human encroachment, pollution, and fragmentation of natural habitats.

Furthermore, poor land administration practices in Prishtina have exacerbated the situation. The post-war period has witnessed an accelerated transformation of vegetated land into urban and agricultural areas, often without adherence to sustainable planning or environmental regulation. Areas with effective land governance and environmental oversight exhibit better preservation of vegetation, underscoring the importance of institutional capacity and regulatory frameworks in conservation efforts.

This research provides a scientifically grounded vegetation vulnerability map that categorizes areas into four distinct risk levels, enabling policymakers, urban planners, and environmental managers to identify priority zones for conservation and rehabilitation. The methodology employed—based on the integration of GIS, Remote Sensing, and multi-criteria evaluation via the Analytic Hierarchy Process (AHP)—demonstrates the robustness and replicability of geospatial tools in environmental analysis. While limitations exist due to the moderate spatial resolution of the DEM and satellite imagery used, the study presents a strong foundation for future work that can incorporate finer-resolution data and temporal dynamics.

An equally important contribution of this study lies in addressing the existing gap in the literature regarding geospatial analyses of vegetation vulnerability. The methodological framework proposed here can serve as a template for similar studies in other regions facing comparable environmental pressures. By detailing every step—from data collection and factor weighting to spatial modeling and vulnerability mapping—this study encourages the adoption of best practices and fosters interdisciplinary research across geography, environmental science, and spatial planning.

Ultimately, this study reinforces the indispensable role of geospatial technology in assessing environmental vulnerability and guiding sustainable development. It urges decision-makers in Prishtina and beyond to prioritize the integration of spatial data and environmental intelligence into land use policy. Moreover, it calls on researchers to further explore and refine geospatial methods, ensuring their broader application in regional and global environmental assessments.

The degradation of vegetation is not only an ecological concern but a socio-economic challenge that requires coordinated efforts, informed by scientific data and implemented through evidence-based policies. This research contributes meaningfully to that endeavor by offering both a diagnostic tool and a roadmap for sustainable landscape management.

REFERENCES

Awono, A., Somorin, O. A., Eba'a Atyi, R., Levang, P. (2014). Tenure and participation in local REDD+ projects: Insights from southern Cameroon. *Environmental Science & Policy*, *35*, 76-86. https://doi.org/10.1016/j.envsci.2013.01.017

Badmaev, N., Bazarov, A. (2020). Correlation analysis of terrestrial and satellite meteodata in the territory of the Republic of Buryatia (Eastern Siberia, Russian Federation) with forest fire statistics. *Agricultural and Forest Meteorology*, *297*, 1. https://doi.org/10.1016/j.agrformet.2020.108245

Berendse, F., Van Ruijven, J., Jongejans, E., Keesstra, S.D. (2015). Loss of plant species diversity reduces soil erosion resistance of embankments that are crucial for the safety of human societies in low-lying areas. *Ecosystems*, *18*(5), 881-888. https://doi.org/10.1007/s10021-015-9869-6

Berila, A., Dushi, M. (2021). Measuring Surface Urban Heat Island in response to population density based on Remote Sensing data and GIS techniques: Application to Prishtina, Kosovo. *Folia Geographica*, *63*(2), 38-57.

Berila, A., Isufi, F. (2021a). Two Decades (2000-2020) Measuring Urban Sprawl Using GIS, RS and Landscape Metrics: a Case Study of Municipality of Prishtina (Kosovo). *Journal of Ecological Engineering*, *22*(6), 114-125. https://doi.org/10.12911/22998993/137078

Berila, A., Isufi, F. (2021b). "Mapping summer SUHI and its impact on the environment using GIS and Remote Sensing techniques: A case study on Municipality of Prishtina (Kosovo)". *European Journal of Geography*, *12*(3), 113-129. https://doi.org/10.48088/ejg.a.ber.12.3.113.129

Berila, A., Isufi F. (2021c). Application of GIS in the determination of vertical relief fragmentation: A case study on Drenica river basin (Kosovo). *Geographia Technica*, *16*(1), 39-47. https://doi.org/10.21163/GT_2021.161.04

Berila, A., Isufi, F. (2021d). Determination of Dissection Index (DI) using GIS & RS techniques: A case study on drenica river basin. *Folia Geographica*, *63*(1), 5-18.

Bhuiyan, C., Saha, A.K., Bandyopadhyay, N., Kogan, F.N. (2017). Analyzing the impact of thermal stress on vegetation health and agricultural drought – a case study from Gujarat, India. *GIScience & Remote Sensing*, *54*(5), 678-699. https://doi.org/10.1080/15481603.2017.1309737

Bowler, D.E., Bjorkman, A.D., Dornelas, M., Myers-Smith, I. H., Navarro, L.M., Niamir, A., Supp, S.R., Waldock, C., Winter, M., Vellend, M., Blowes, SH.A., Böhning-Gaese, K., Bruelheide, H., Elahi, R., Antão, L.H., Hines, J., Isbell, F., Jones, H.P., Magurran, A.E., Cabral, J.S., Bates, A.E. (2020). Mapping human pressures on biodiversity across the planet uncovers anthropogenic threat complexes. *People and Nature*, *2*(2), 380-394. https://doi.org/10.1002/pan3.10071

Buizer, M., Humphreys, D., De Jong, W. (2014). Climate change and deforestation: The evolution of an intersecting policy domain. *Environmental Science & Policy*, *35*, 1-11. https://doi.org/10.1016/j.envsci.2013.06.001

Coomes, D.A., Flores, O., Holdaway, R., Jucker, T., Lines, E.R., Vanderwel, M.C. (2014). Wood production response to climate change will depend critically on forest composition and structure. *Global Change Biology*, *20*(12), 3632-3645. https://doi.org/10.1111/gcb.12622

Dashpurev, B., Wesche, K., Jäschke, Y., Oyundelgerk., Phan, T.N., Bendix, J., Lehnert, L.W. (2021). A cost-effective method to monitor vegetation changes in steppes ecosystems: A case study on remote sensing of fire and infrastructure effects in eastern Mongolia. *Ecological Indicators*, *132*, 1-22. https://doi.org/10.1016/j.ecolind.2021.10833

Dien, V. T. (2004). *Susceptibility to forest degradation: A case study of the application of remote sensing and GIS in Bach Ma National Park, Thua-Thien Hue Province, Vietnam* [Master's thesis, International Institution for Geo-Information and Earth Observation]. Enschede.

Dindaroglu, T., Babur, E., Yakupoglu, T., Rodrigo-Comino, J., Cerdà, A. (2021). Evaluation of geomorphometric characteristics and soil properties after a wildfire using Sentinel-2 MSI imagery for future fire-safe forest. *Fire Safety Journal*, *122*, 103318. https://doi.org/10.1016/j.firesaf.2021.103318

Dutta, D., Kundu, A., Patel, N.R., Saha, S.K., Siddiqui, A.R. (2015). Assessment of agricultural drought in Rajasthan (India) using remote sensing derived Vegetation Condition Index (VCI) and Standardized Precipitation Index (SPI). T*he Egyptian Journal of Remote Sensing and Space Science*, *18*(1), 53-63. https://doi.org/10.1016/j.ejrs.2015.03.006

El Kateb, H., Zhang, H., Zhang, P., Mosandl, R. (2013). Soil erosion and surface runoff on different vegetation covers and slope gradients: A field experiment in Southern Shaanxi Province, China. *CATENA*, *105*, 1-10. https://doi.org/10.1016/j.catena.2012.12.012

EnvironmentaL Protection Authority (EPA). (2012). *National Report of Ethiopia. United Nations Conference on Sustainable Development (Rio+20)*. Federal Democratic Republic of Ethiopia, Addis Ababa. Retrieved January 25, 2023, from: https://sustainabledevelopment.un.org/content/documents/973ethiopia.pdf

Evans, K., Murphy, L., De Jong, W. (2013). Global versus local narratives of REDD: a case study from Peru's Amazon. *Environmental Science and Policy*, *35*, 98-108. https://doi.org/10.1016/j.envsci.2012.12.013

Findlay, C.S., Bourdages, J. (2000). Response time of wetland biodiversity to road construction on adjacent lands. *Conservation Biology*, *14*(1), 86-94.

Fu, B., Liu, S., Ma, K., Zhu, Y. (2004). Relationships between soil characteristics, topography and plant diversity in a heterogeneous deciduous broad-leaved forest near Beijing, China. *Plant and Soil*, *261*(1), 47-54. https://doi.org/10.1023/B:PLSO.0000035567.97093.48

Ganaie, T.A., Jamal, S., Ahmad, W.S. (2021). Changing land use/land cover patterns and growing human population in Wular catchment of Kashmir Valley, India. *GeoJournal*, *86*(4), 1589-1606. https://doi.org/10.1007/s10708-020-10146-y

Gebrehiwetk, B. (2004). *Land use land cover changes in the central highlands of Ethiopia: The case of Yerer mountains and its surroundings.* [Master's thesis, Addis Ababa University]. Addis Ababa.

Gemitzi, A., Koutsias, N. (2021). Assessment of properties of vegetation phenology in fire-affected areas from 2000 to 2015 in the Peloponnese, Greece. *Remote Sensing Applications: Society and Environment*, *23*, 100535. https://doi.org/10.1016/j.rsase.2021.100535

Giroux, J.-F., Bergeron, Y., Veillette, J.J. (2001). Dynamics and morphology of giant circular patterns of low tree density in black spruce stands in northern Quebec. *Canadian Journal of Botany*, *79*(4), 420-428. https://doi.org/10.1139/b01-022

Gomes, A.C.C., Bernardo, N., Alcântara, E. (2017). Accessing the southeastern Brazil 2014 drought severity on the vegetation health by satellite image. *Journal of Natural Hazards*, *89*(3), 1401-1420. https://doi.org/10.1007/s11069-017-3029-6

Gonçalves, N. B., Lopes, A.P., Dalagnol, R., Wu, J., Pinho, D.M., Nelson, B.W. (2020). Both near-surface and satellite remote sensing confirm drought legacy effect on tropical forest leaf phenology after 2015/2016 ENSO drought. *Remote Sensing of Environment*, *237*, 111489. https://doi.org/10.1016/j.rse.2019.111489

Hanewinkel, M., Cullmann, D.A., Schelhaas, M.-J., Nabuurs, G.-J., Zimmermann, N.E. (2012). Climate change may cause severe loss in the economic value of European forest land. *Nature Climate Change*, *3*(3), 203-207. https://doi.org/10.1038/nclimate1687

Hanski, I. (2015). Habitat fragmentation and species richness. *Journal of Biogeography*, *42*(5), 989-993. https://doi.org/10.1111/jbi.12478

Hislop, S., Haywood, A., Jones, S., Soto-Berelov, M., Skidmore, A., Nguyen, T.H. A (2020). Satellite data driven approach to monitoring and reporting fire disturbance and recovery across boreal and temperate forests. *International Journal of Applied Earth Observation and Geoinformation*, *87*, 102034. https://doi.org/10.1016/j.jag.2019.102034

Hou, G., Bi, H., Huo, Y., Wei, X., Zhu, Y., Wang, X., Liao, W. (2020). Determining the optimal vegetation coverage for controlling soil erosion in Cynodon dactylon grassland in North China. *Journal of Cleaner Production*, *244*(4), 118771. https://doi.org/10.1016/j.jclepro.2019.118771

Huang, J., Van Den Dool, H.M., Georgakakos, K.P. (1996). Analysis of model-calculated soil moisture over the United States (1931–1999) and applications to longrange temperature forecasts. *Journal of Climate*, *9*(6), 1350-1362. https://doi.org/10.1175/1520-0442(1996)009<1350:AOMCSM>2.0.CO;2

Isufi, F., Berila, A. (2021). Using geospatial technology to analyse land use/cover changes in Prishtina, Kosovo (2000-2020). *GeoJournal*, *87*, 3639–3653. https://doi.org/10.1007/s10708-021-10452-z

Jin, F., Yang, W., Fu, J., Li, Z. (2021). Effects of vegetation and climate on the changes of soil erosion in the Loess Plateau of China. *Science of The Total Environment*, *773*(3235), 145514. https://doi.org/10.1016/j.scitotenv.2021.145514

Khosravi, H., Haydari, E., Shekoohizadegan, S., Zareie, S. (2017). Assessment the Effect of Drought on Vegetation in Desert Area using Landsat Data. *The Egyptian Journal of Remote Sensing and Space Science*, *20*, 3-12. https://doi.org/10.1016/j.ejrs.2016.11.007

Kosovo Agency of Statistics (KAS). (2024). *Population and housing census in Kosovo: Preliminary results*. Retrieved October 1, 2024, from https://askapi.rks-gov.net/Custom/1d268e37-5934-4bd5-bbd1-34a9965cff92.pdf

Kundu, A., Dwivedi, S., Dutta, D. (2016). Monitoring the vegetation health over India during contrasting monsoon years using satellite remote sensing indices. *Arabian Journal of Geosciences*, *9*(2), 144. https://doi.org/10.1007/s12517-015-2185-9

Lin, D., Xia, J., Wan, S. (2010). Climate warming and biomass accumulation of terrestrial plants: a meta-analysis. *New Phytologist*, *188*(1), 187-198. https://doi.org/10.1111/j.1469-8137.2010.03347.x

Lin, Y., Cui, P., Ge, Y., Chen, C., Wangd., Wu, C-Zh., Li, J., Yu, W., Zhang, G-Sh., Lin, H. (2014). The succession characteristics of soil erosion during different vegetation succession stages in dry-hot river valley of Jinsha River, upper reaches of Yangtze River. *Ecological Engineering*, *62*, 13-26. https://doi.org/10.1016/j.ecoleng.2013.10.020

Lindner, M., Maroschek, M., Netherer, S., Kremer, A., Barbati, A., Garcia-Gonzaloj., Sedl, R., Delzon, S., Corona, P., Kolström, M., Lexer, M.J., Marchetti, M. (2010). Climate change impacts, adaptive capacity, and vulnerability of European forest ecosystems. *Forest Ecology and Management*, *259*(4), 698-709. https://doi.org/10.1016/j.foreco.2009.09.023

Luttrell, C., Resosudarmo, I.A.P., Muharrom, E., Brockhaus, M., Seymour, F. (2014). The political context of REDD+ in Indonesia: Constituencies for change. *Environmental Science & Policy*, *35*, 67-75. https://doi.org/10.1016/j.envsci.2012.10.001

Matthews, T.J., Cottee-Jones, H.E., Whittaker, R.J. (2014). Habitat fragmentation and the species–area relationship: a focus on total species richness obscures the impact of habitat loss on habitat specialists. *Diversity and Distributions*, *20*(10), 1136-1146. https://doi.org/10.1111/ddi.12227

Maurya, P. K., Ali, S. A., Ahmad, A., Zhou, Q., Da Silva Castro, J., Khan, E., & Ali, H. (2020). An introduction to environmental degradation: Causes, consequences, and mitigation. In V. Kumar, J. Singh, & P. Kumar (Eds.), *Environmental degradation: Causes and remediation strategies* (1st ed., pp. 227). Agro Environ Media. https://doi.org/10.26832/aesa-2020-edcrs-01

Minale, A.S., Gelaye, S. (2021). Vegetation vulnerability analysis by using GIS and remote sensing techniques: a case study of Sensawuha Watershed, Ethiopia. *GeoJournal*, *86*(1), 475-488. https://doi.org/10.1007/s10708-019-10082-6

Moody, J.A., Martin, D.A. (2001). Post-fire, rainfall intensity-peak discharge relations for three mountainous watersheds in the western USA. *Hydrological Processes*, *15*(15), 2981-2993. https://doi.org/10.1002/hyp.386

Morgan, R. P. C. (1986). *Soil erosion and conservation* (3rd ed.). Longman.

Municipality of Prishtina. (2013). *Municipal development plan of Prishtina 2012–2022*. Retrieved January 22, 2023, from https://prishtinaonline.com/uploads/prishtina_pzhk_2012-2022_shqip%20(1).pdf

Nair, C. T. S., & Tieguhong, J. (2004). *African forests and forestry: An overview*. African Forest Forum: Nairobi, Kenya. Retrieved January 18, 2023, from https://afforum.org/oldaff/sites/default/files/English/English_36.pdf

Niu, J., Chen, J., Sun, L. (2015). Exploration of drought evolution using numerical simulations over the Xijiang (West River) basin in South China. *Journal of Hydrology*, *526*, 68-77. https://doi.org/10.1016/j.jhydrol.2014.11.029

North, H., Amies, A., Dymond, J., Belliss, S., Pairman, D., Drewry, J., Schindler, J., Shepherd, J. (2021). Mapping bare ground in New Zealand hill-country agriculture and forestry for soil erosion risk assessment: An automated satellite remote-sensing method. *Journal of Environmental Management*, *301*(4), 113812. https://doi.org/10.1016/j.jenvman.2021.113812

Novara, A., Pisciotta, A., Minacapilli, M., Maltese, A., Capodici, F., Cerdà, A., Gristina, L. (2018). The impact of soil erosion on soil fertility and vine vigor. A multidisciplinary approach based on field, laboratory and remote sensing approaches. *Science of The Total Environment*, *622-623*, 474-480. https://doi.org/10.1016/j.scitotenv.2017.11.272

Paterson, M., & Newell, P. (2010). *Climate capitalism: Global warming and the transformation of the global economy* (1st ed.). Cambridge University Press.

Pei, F., Wu, C., Liu, X., Li, X., Yang, K., Zhou, Y., Wang, K., Li, X., Xia, G. (2018). Monitoring the vegetation activity in China using vegetation health indices. *Agricultural and Forest Meteorology*, *248*, 215-227. https://doi.org/10.1016/j.agrformet.2017.10.001

Pfaff, A., Robalino, J., Walker, R., Aldrich, S., Caldas, M., Reis, E., Perz, S., Bohrer, C., Arima, E., Laurence, W., Kirby, K. (2007). Road investments, spatial spill overs, and deforestation in the Brazilian Amazon. *Journal of Regional Science*, *47*(1), 109-123. https://doi.org/10.1111/j.1467-9787.2007.00502.x

Richards, J. A. (1995). *Remote sensing digital image analysis: An introduction* (5th ed.). Springer.

Ripple, W.J., Smith, P., Haberl, H., Montzka, S.A., Mcalpine, C., Boucher, D.H. (2013). Ruminants, climate change and climate policy. *Nature Climate Change*, *4*(1), 2-5. https://doi.org/10.1038/nclimate2081

Saaty, R.W. (1987). The analytic hierarchy process—what it is and how it is used. *Mathematical Modelling*, *9*(3-5), 161-176. https://doi.org/10.1016/0270-0255(87)90473-8

Schröter, D., Cramer, W., Leemans, R., Prentice, I. C., Araújo, M. B., Arnell, N. W., Bondeau, A., Bugmann, H., Carter, T. R., Gracia, C. A., de la Vega-Leinert, A. C., Erhard, M., Ewert, F., Glendining, M., House, J. I., Kankaanpää, S., Klein, R. J. T., Lavorel, S., Lind-Ner, M., Metzger, M. J., Meyer, J., Mitchell, T. D., Reginster, I., Rounsevell, M., Sabaté, S., Sitch, S., Smith, B., Smith, J., Smith, P., Sykes, M. T., Thonicke,

K., Thuiller, W., Tuck, G., Zaehle, S., & Zierl, B. (2005). Ecosystem service supply and vulnerability to global change in Europe. *Science*, *310*(5752), 1333–1337. https://doi.org/10.1126/science.1115233

Shakesby, R.A., Doerr, S.H., Walsh, R.P.D. (2000). The erosional impact of soil hydrophobicity: current problems and future research directions. *Journal of Hydrology*, *231-232*, 178-191. https://doi.org/10.1016/S0022-1694(00)00193-1

Simard, M., Lecomte, N., Bergeron, Y., Bernier, P.Y., PARÉ, D. (2007). Forest productivity decline caused by successional paludification of boreal soils. *Ecological Applications*, *17*(6), 1619-1637. https://doi.org/10.1890/06-1795.1

Sun, C., Hou, H., Chen, W. (2021). Effects of vegetation cover and slope on soil erosion in the Eastern Chinese Loess Plateau under different rainfall regimes. *PeerJ*, *9*(3-4), 1. https://doi.org/10.7717/peerj.11226

Tsegaye, B. (2019). Effect of Land Use and Land Cover Changes on Soil Erosion in Ethiopia. *International Journal of Agricultural Science and Food Technology*, *5*(1), 26-34. http://doi.org/10.17352/2455-815X.000038

Tsymbarovich, P., Kust, G., Kumani, M., Golosov, V., Andreeva, O. (2020). Soil erosion: An important indicator for the assessment of land degradation neutrality in Russia. *International Soil and Water Conservation Research*, *8*(4), 418-429. https://doi.org/10.1016/j.iswcr.2020.06.002

Vieira, D.C.S., Malvar, M.C., Martins, M.A.S., Serpa, D., & Keizer, J.J. (2018). Key factors controlling the post-fire hydrological and erosive response at micro-plot scale in a recently burned Mediterranean forest. *Geomorphology*, *319*, 161-173. https://doi.org/10.1016/j.geomorph.2018.07.014

Wang, H., Stephenson, S.R. (2018). Quantifying the impacts of climate change and land use/cover change on runoff in the lower Connecticut River Basin. *Hydrological Processes*, *32*(9), 1301-1312. https://doi.org/10.1002/hyp.11509

Wang, Z., Jiao, J., Su, Y., Chen, Y. (2014). The efficiency of large-scale afforestation with fish-scale pits for revegetation and soil erosion control in the steppe zone on the hillgully Loess Plateau. *CATENA*, *115*, 159-167. https://doi.org/10.1016/j.catena.2013.11.012

Way, D.A., Oren, R. (2010). Differential responses to changes in growth temperature between trees from different functional groups and biomes: a review and synthesis of data. *Tree Physiology*, *30*(6), 669-688. https://doi.org/10.1093/treephys/tpq015

Wiens, J.J. (2011). The niche, biogeography and species interactions. *Philosophical Transactions of the Royal Society B: Biological Sciences*, *366* (1576), 2336-2350. https://doi.org/10.1098/rstb.2011.0059

Wu, J., Ma, W., Li, G., Alhassan, A.-R.M., Wang, H., Chen, G. (2020). Vegetation degradation along water gradient leads to soil active organic carbon loss in Gahai wetland. *Ecological Engineering*, *145*, 105666. https://doi.org/10.1016/j.ecoleng.2019.105666

Yin, C., He, B., Quan, X., Yebra, M., Lai, G. (2020). Remote Sensing of Burn Severity Using Coupled Radiative Transfer Model: A Case Study on Chinese Qinyuan Pine Fires. *Remote Sensing*, *12*(21), 3590. https://doi.org/10.3390/rs12213590

Yu, Y., Jia, Z.Q. (2014). Changes in soil organic carbon and nitrogen capacities of Salix cheilophila Schneid along a revegetation chronosequence in semi-arid degraded sandy land of the Gonghe Basin, Tibet Plateau. *Solid Earth*, *5*(2), 1045-1054. https://doi.org/10.5194/se-5-1045-2014

Zhang, L., Jiao, W., Zhang, H., Huang, C., Tong, Q. (2017). Studying drought phenomena in the Continental United States in 2011 and 2012 using various drought indices. *Remote Sensing of Environment*, *190*, 96-106. https://doi.org/10.1016/j.rse.2016.12.010

Zhu, K., Woodall, C.W., Ghosh, S., Gelfand, A.E., Clark, J.S. (2013). Dual impacts of climate change: forest migration and turnover through life history. *Global Change Biology*, *20*(1), 251-264. https://doi.org/10.1111/gcb.12382

THE EFFECT OF LAND USE PATTERNS ON FLOOD VULNERABILITY LEVELS. CASE STUDY: WEST LOMBOK REGENCY, WEST NUSA TENGGARA PROVINCE, INDONESIA

I Wayan YASA [1], Heri SULISTIYONO [1], Muhajirah MUHAJIRAH [1], Dewandha Mas AGASTYA [1], Unsila T. ARTAWAN [1]*

DOI: 10.21163/GT_2025.202.07

ABSTRACT

Uncontrolled changes in land use patterns are one of the main factors causing increased levels of flood vulnerability in several areas. To overcome flooding problems, integrated planning is needed related to the suitability of the regional land use plan. However, inconsistencies still often occur in its implementation due to the emergence of various interests. This study aims to analyze the relationship between land conversion into built-up areas and increased flood risk, map the distribution of flood areas, and estimate the level of flood vulnerability. The methods used include spatial analysis, multicriteria analysis, and descriptive analysis using the Hierarchy Process (AHP) and Geographic Information Systems (GIS) applications. The input factors forming flood risk used in the analysis include rainfall intensity (I), slope gradient (S), land use (U), soil type (ST), distance from drainage/river networks (D), and altitude (E). The results of the study indicate that the potential for flood vulnerability in West Lombok Regency consists of a rather vulnerable class spread across all sub-districts, namely an area of 47.624 Ha (51.80%), not vulnerable to an area of 21.001 Ha (22.84%), and ± 25% of the remaining areas are divided into moderately vulnerable areas of 15.241 Ha (16.58%), vulnerable areas of 7.871 Ha (8.56%), and very vulnerable areas of 195.79 Ha (0.21%). Sustainable land use management is essential to reduce flood vulnerability, especially in areas experiencing rapid development.

Key-words: *Land use; Flood; Vulnerability, Risk; GIS;* Analytical Hierarchy Process (*AHP).*

1. INTRODUCTION

Indonesia is one of the countries in the world that has a fairly high potential for hydrometeorological disasters. Hydrometeorological disasters are disasters that are influenced by weather, climate, and water factors. It is recorded that 86% of disaster events are dominated by hydrometeorological disasters such as floods, droughts, typhoons or tropical cyclones, as well as tidal waves and coastal abrasion (Agonafir et al., 2023). The high frequency of flood disasters requires strategic steps to reduce the impacts caused. One of the steps in reducing the impact and potential for flood disasters is planning and managing land use appropriately and integrating with regional spatial planning (Stedinger et al. 2011; Yuniartanti, 2018; Haikal et al., 2024). However, in reality, there are often inconsistencies between regional spatial plans and actual land use. One of these inconsistencies is the spatial pattern that should function as a green and agricultural area, but the existing land use is used as a settlement (Seyam et al., 2023; Abdullah et al., 2019). Referring to the flood problems that occur in several places, flood control planning is needed by mapping flood-prone areas (Mulliss et al., 1996; Sinha et al., 2008; Györi & Haidu, 2011, Tehrany et al., 2017). Identification and mapping of flood-prone locations is the starting point in conducting disaster risk analysis (Andrade & Szlafsztein, 2015; Haidu & Ivan, 2016a; Lee et al., 2017). Disaster risk analysis is needed as an effort to reduce disaster risk both through physical development and awareness and increasing capacity in dealing with disasters. If spatial information on flood-prone areas through flood-prone maps is available, this information can be used as a basis for analyzing the factors that influence flooding.

[1]*University of Mataram, Departement of Civil Enggineering, 83111, Mataram, Indonesia, Corresponding author* (IWY) yasaiwayan68@unram.ac.id; (HS) h.sulistiyono@unram.ac.id; (MM) muhajirah@unram.ac.id; (DMA) dewandhamas96@staff.unram.ac.id; (UTA) unsilatammiya29@gmail.com*

Likewise, evaluations can be carried out to prepare and improve spatial planning to reduce the potential and impact of flood disasters (Kay et al., 2015; Haidu & Ivan, 2016b; Sari et al., 2025). The vulnerability of an area to flooding and the volume of runoff caused by rainfall exceeding the filter flow rate are both influenced by how the land is used. Land with good vegetation has a high capacity to absorb water because the roots and stems delay the flow of runoff (Revitt & Ellis, 2016; Hidayah et al., 2022). Flood risk is reduced when land is densely vegetated because rainwater can absorb more and runoff takes longer to reach rivers (Seyhan, 1995; Crăciun et al., 2009).

Controlling the use of space is an effort to realize orderly spatial planning. Controlling the use of space is an effort to monitor and prevent inappropriate use of space, which can even result in damage and flooding (Miller & Hutchins, 2017). For this reason, in areas prone to flooding, monitoring efforts need to be carried out by observing the consistency (suitability and harmony) between spatial planning and spatial utilization. Analytical Hierarchy Process (AHP) is a model that can be used in decision-making, and it has a mechanism for sorting several optimal choices based on predetermined criteria. AHP is used to analyze a set of alternatives or objectives to rank them from best to worst using a structured approach (Sinha et al., 2008). The final output is a weight associated with the various alternatives. The weights indicate the preference of the alternatives relative to each other, which can be seen as the perceived gain or loss when changing from one alternative to another (Musungu et al., 2012; Elmoustafa, 2012).

A geographic information system (GIS) is a collection of hardware, software, geographic data, methods, and employees designed efficiently to receive, store, update, manipulate, analyze, and display all types of geographically related information (Malczewski, 2006). The information required can be broken down into two categories: graphical data and attribute data, both of which relate to a specific location. Points, lines, and polygons are standard containers for graphical data. Attribute data, on the other hand, can be qualitative or quantitative and correspond one-to-one to graphical information). As long as the data used contains geographic references, GIS applications can be used for various spatial information purposes. The results of the land use pattern mapping analysis can be used to determine regional spatial plans so that flood-prone areas are not used as residential, office, and industrial areas.

2. STUDY AREA

The research location (**Fig. 1**) was conducted in the administrative area of West Lombok Regency, West Nusa Tenggara Province, Indonesia. Geographically, West Lombok Regency is located at 115° 49.12’ 04” - 116° 20’15.62” East Longitude and 8° 24’ 33.82” - 8° 55’ 19” South Latitude.

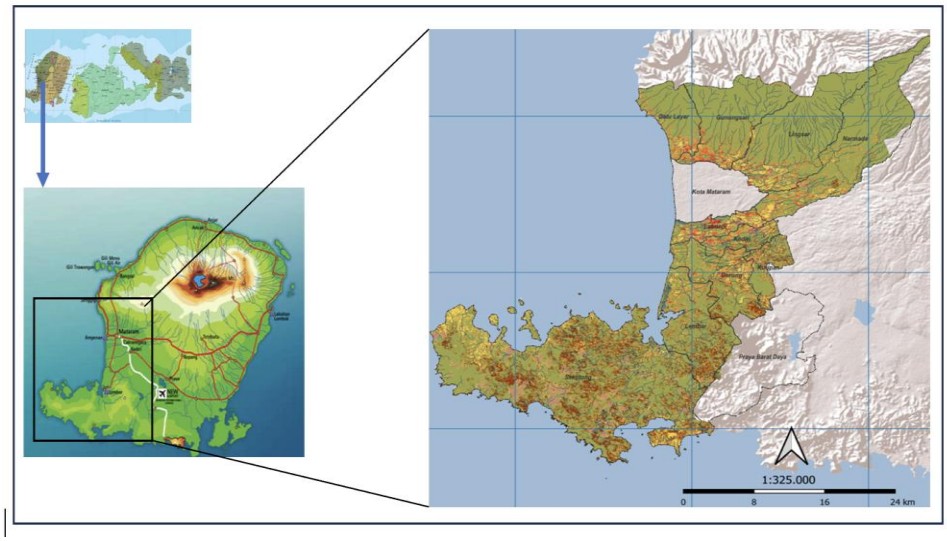

Fig. 1. Research location.

3. DATA AND METHODS

3.1. Data

This study uses primary and secondary data collected from various sources (**Table 1**). The data and parameters are used in the analysis because they are the main components of flooding in an area.

Table 1

Type of data needed in the analysis.

No	Name of data	Data type	Data sources	Use of data in analysis
1.	Administrative boundaries of villages and sub-districts	Secondary	tanahair.indonesia.go.id	As a research area boundary
2.	Watershed Map in West Lombok Regency 1:50,000	Secondary	Nusa Tenggara I River Basin Center	River basin area boundary
3.	Sentinel Image 2A	Secondary	earthexplorer.usgs.gov/	As a material for making land use maps
4.	Alos Palsar	Secondary	https://www.eorc.jaxa.jp/ALOS	As a material for making slope and elevation maps
5.	Rainfall Data 2012-2023 in West Lombok Regency	Secondary	Nusa Tenggara I River Basin Center	As a material for making rainfall maps
6.	Flood Incident Data 2017-2023 in West Lombok Regency	Secondary	Regional Disaster Management Agency, West Lombok Regency	As a consideration in determining flood frequency
7.	Soil Type Map 1: 50,000	Secondary	Nusa Tenggara I River Basin Center	As a risk-forming factor
8.	Spatial planning map of West Lombok Regency 1:50,000	Secondary	Regional Planning Agency, West Lombok Regency	As material for analysis of spatial pattern utilization
9.	Interview with respondents	Primary	Interview	Determining the weight of flood-prone factors

3.2. Analytical Hierarchy Process (AHP)

A decision support model called the Analytical Hierarchy Process (AHP) is used to sort several alternatives into optimal choices based on predetermined criteria (Sinha et al., 2008). Complex multi-criteria problems can be translated into a hierarchy using the Analytic Hierarchy Process (AHP). The purpose of this hierarchy is to solve a complex problem into groups, which are then arranged in a hierarchy to provide an overview of the conditions in are more organized.

The procedures for using the AHP method include:

1. Define the problem and determine the desired solution, then compile a hierarchy of the problems being analyzed;
2. Determine element priorities. The first step in determining element priorities is to make a pairwise comparison, namely by comparing elements in pairs according to the given criteria.
3. Synthetic. In this stage, the following are done:
   a. Adding the values of each column in the matrix;
   b. Dividing each value of the column by the total of the relevant column to obtain the normalization of the matrix;
   c. Adding the values of each row and dividing it by the number of elements to obtain the average value
4. Measuring consistency. In this stage, what is done is:
   a. Multiply each value in the first column by the relative priority of the first element, the value in the second column by the relative priority of the second element, and so on;
   b. Add up each row;

c. The result of the row summation is divided by the relevant relative priority element;
d. Adding the above quotient to the number of existing elements. The result is called λ max
e. Calculating the Consistency Index (CI) with the formula;

$$CI = \frac{\gamma maks - n}{n} \quad (1)$$

f. Calculate the Consistency Ratio (CR) with the formula:

$$CR = \frac{CI}{RI} \quad (2)$$

where:

n = the abundance of elements;
CR = consistency Ratio;
CI = consistency Index;
RI = in-deks Random Consistency (**Table 2**)

g. Check the consistency of the hierarchy. When the CR value is less than 10%, inconsistency of opinion is considered acceptable.

Table 2.

Random konsistensi indeks (RI).

n	1	2	3	4	5	6	7	8	9	10	11	12	13	14	15
RI	0.00	0.00	0.58	0.90	1.12	1.24	1.32	1.41	1.45	1.49	1.51	1.48	1.56	1.57	1.59

The next stage is to score each flood-vulnerability-forming subfactor. The scoring is carried out with the provision of standardization of inverse scale scores, where the influencing factors will have a higher score value compared to the less influential factors, using the equation used by the Center for Soil and Agroclimatic Research:

$$Wj = \frac{(n - rj + 1)}{\sum(n - rj + 1)} \quad (3)$$

where:

Wj = normalized value;
n = number of subfactors (k = 1,2,3, ..., n);
rj = subfactor sequence position

After the weights of each factor and subfactor are known, then the values of each factor and subfactor weight are included in the WLC equation as follows:

$$WLC = \sum_{i=1}^{n} X_{ij} x W_{ij} \quad (4)$$

where:

WLC = weighted Linear Combination;
X_{ij} = degree of suitability of the jth factor/subfactor at the Ith location;
W_{ij} = weight of the jth factor/subfactor in the first location;
n = sum of factors

3.3. Geographic Information System (GIS)

A geographic information system (GIS) is software for collecting, storing, retrieving, and displaying spatial data originating from real-world reality (Burrough, 1986). GIS consists of a collection of users, applications, data, software, and hardware that work together to store, change, delete, and display data in geographic-based information. The data processed in GIS is in the form of geospatial data, namely spatial data and non-spatial data. Data related to geographic conditions, such as rivers, administrative areas, soil types, settlements, vegetation, and so on are forms of spatial data. While data in the form of text or numbers, which are usually called attributes, are forms of non-spatial data.

3.4. Overlay

In the GIS analysis stage, overlay is a crucial stage. The ability to stack one map graphic on top of another map graphic and see the results on a computer screen or graph is called an overlay. In other words, overlay is the process of layering a digital map and its properties onto another digital map, resulting in a composite map that combines attribute data from both maps.

3.5. Research flow chart

Our research was based on a sequence of stages and on the combination of GIS and AHP-inspired working methods, as illustrated in **Fig. 2**.

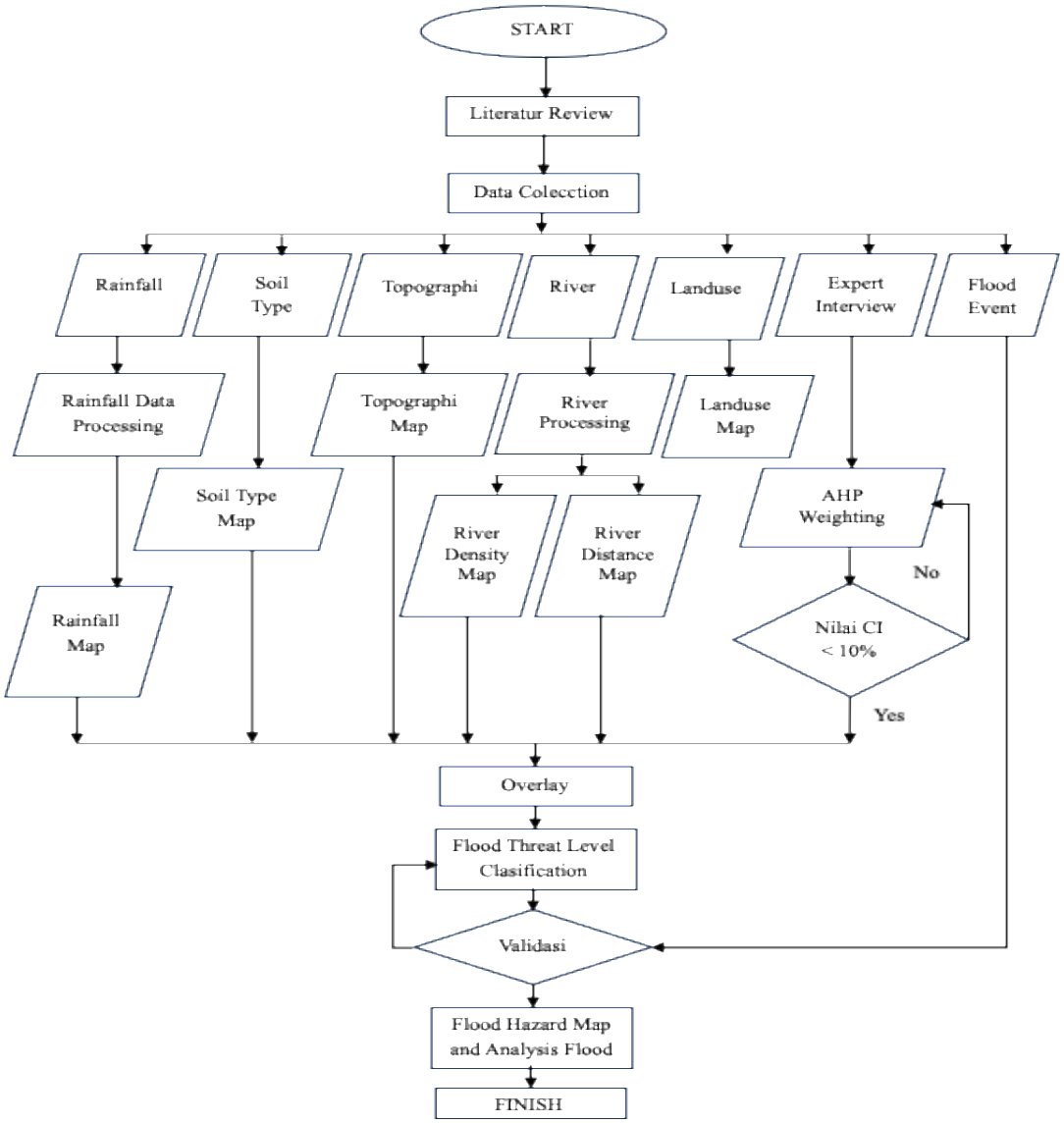

Fig. 2. Research flow chart.

4. RESULTS AND DISCUSSION

4.1. Analysis of Flood Disaster Occurrence

According to flood disaster data obtained from the West Lombok Regency Regional Disaster Management Agency, there were 59 flood incidents between January 2021 and February 2023. Of these, 39 villages across nine sub-districts were affected. The data is presented in **Table 3**.

Table 3.

Flood disaster occurrence per sub-district in West Lombok Regency for the period January 2021 – February 2023.

No.	Subdistrict	Number of Villages Affected	Number of events per year			Number of occurrences
			2021	2022	2023	
1.	Gerung	2	-	-	2	2
2.	Batu Layar	7	3	3	9	15
3.	Gunungsari	8	4	-	4	8
4.	Kediri	3	3	-	-	3
5.	Kuripan	-	-	-	-	0
6.	Labuapi	4	1	2	5	8
7.	Lembar	3	4	1	1	6
8.	Lingsar	3	3	-	-	3
9.	Narmada	2	1	-	1	2
10.	Sekotong	7	6	1	5	12
	Total Number of occurrences	**39**	**25**	**7**	**27**	**59**

Almost all sub-districts in West Lombok Regency experienced flood disasters from January 2021 to February 2023, except for the Kuripan Sub-district. Batu Layar District and Sekotong District occupy the top positions in terms of the number of flood disasters. Several villages in several sub-districts even experienced repeated flooding more than once, such as in Batu Layar Sub-district, Labu Api Sub-district, Lembar Sub-district, and Sekotong Sub-district.

4.2. Vulnerability Level Formation Analysis

This stage is carried out to calculate the level of influence of each factor that forms flood risk through the Analytical Hierarchy Process (AHP) analysis. To simplify and speed up the calculation and analysis process of weighting using Expert Choice 11 software. The assessment of the weighting of the flood vulnerability level in the Analytical Hierarchy Process (AHP) was obtained from primary data through questionnaires and interviews with several sources who are considered experts in determining flood threat parameters. The respondents selected came from several government and private agencies, namely: the Public Works Department, the Environmental Service, the Regional Disaster Management Agency, the Agriculture Service, and housing developers. The results of the Consistency Ratio (CR) from the sources show suitability. So, based on the AHP calculations that have been carried out, the weights per parameter are shown in **Table 4** below.

Table 4.

Scoring subfactors forming flood vulnerability.

No.	Factors and Subfactors	Sequence number	Dignity Values	Scor
1	**Land Slope**			
	0 – 3%	1	7	0.250
	3 – 8 %	2	6	0.214
	8 -15 %	3	5	0.179
	15 – 30 %	4	4	0.143
	30 – 45 %	5	3	0.107
	45 – 65 %	6	2	0.071
	> 65 %	7	1	0.036
2	**Land Use**			
	Water Bodies	1	6	0.286
	Rice Field	2	5	0.238
	Settlement	3	4	0.190
	Open Land	4	3	0.143
	Garden	5	2	0.095
	Forest	6	1	0.048
3	**Rainfall (mm)**			
	> 210	1	6	0.286
	190 - 210	2	5	0.238
	170 - 190	3	4	0.190
	150 - 170	4	3	0.143
	130 - 150	5	2	0.095
	110 - 130	6	1	0.048
4	**Soil Type**			
	Alluvial Brown-Gray	1	6	0.286
	Mediteran Chocolate Complex, Grey Grumusol, Chocolate Regosol and Litosol	2	5	0.238
	Mediterranean Brown and Mediterranean Scarlet Complexes	3	4	0.190
	Reddish-brown Lithosol and Mediterranean Complex	4	3	0.143
	Grey Brown Regosol and Litosol Complex	5	2	0.095
	Mediterranean Chocolate	6	1	0.048
5	**Distance to The River (m)**			
	0 - 50	1	7	0.250
	50 - 100	2	6	0.214
	100 - 150	3	5	0.179
	150 - 200	4	4	0.143
	200 - 300	5	3	0.107
	300 - 500	6	2	0.071
	> 500	7	1	0.036
6	**Elevation**			
	0 – 96	1	7	0.250
	96 – 235	2	6	0.214
	235 – 397	3	5	0.179
	397 – 600	4	4	0.143
	600 – 838	5	3	0.107
	838 – 1.186	6	2	0.071
	> 1.186	7	1	0.036

S*ource: analysis results (2024).*

4.3. Average Area Rainfall

Rainfall data is in the form of secondary data for recording rain events based on several observation stations, including Pelangan Station, Sekotong Station, Serumbung Station, Sesaot Station, Keru Station, Gunungsari Station, and Jurang Malang Station (**Table 5**). Rainfall data from several stations were obtained through the NT1 River Area Agency (attached). In the next stage, the secondary data is transformed into spatial data, where the maximum rainfall serves as a reference in determining the average rainfall based on the isohyet method (**Fig. 3**).

The isohyet method is used for mountainous areas with various elevation differences, this condition is under the description of West Lombok Regency. The average rainfall estimate on this method is based on lines with the same rainfall value. The lines are based on interpolation between rain observation stations.

Table 5.

Average daily rainfall.

Rainfall Station	Elevation	High Rainfall (mm)
Pelangan	37	166
Sekotong	35	113
Serumbung	10	120
Sesaot	302	173
Keru	476	213
Gunung Sari	138	146
Jurang Malang	445	199

Source: analysis results (2024).

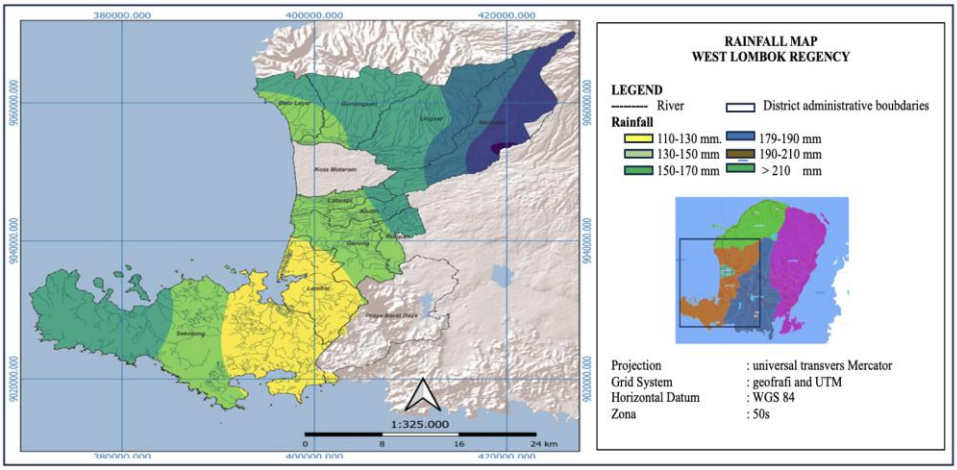

Fig. 3. Map of the distribution of height rainfall in West Lombok Regency.

4.4. Land use map

Land use as a parameter for forming flood vulnerability (**Fig. 4**) was obtained based on the processing of Sentinel-2A remote sensing image data (*data recording/acquisition in July 2023*) which was downloaded in a level-1C product through the USGS website (https://earthexplorer.usgs.gov/), where the data is geometrically and radiometrically corrected, so that the data is by the Top of Atmosphere (TOA) reflectant value. Another fundamental consideration in the selection of remote sensing data is the cloud cover on the image used by <10%; the data used has good multispectral quality (EOSDIS, 2021).

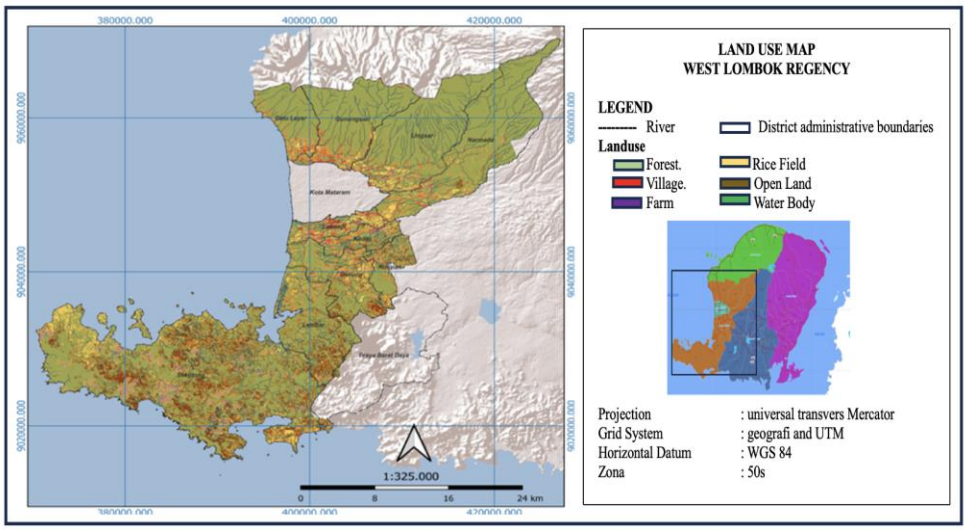

Fig. 4. Landuse map West Lombok Regency.

4.5. Distance to river

Distance data to the river as a parameter for shaping flood vulnerability is spatial data in the form of river vector data in West Lombok Regency (**Fig. 5**). The data is accessed and downloaded through the BIG (*https://tanahair.indonesia.go.id*) website. Processing distance data to rivers as a parameter for forming flood vulnerability, river data is processed using the Buffer feature which is one of the spatial analysis functions in QGIS software.

Through this analysis, river distance parameters are grouped into 7 classes starting from the closest to the farthest distance from the river boundary as follows: 0 – 50 m; 50 – 100 m; 100 – 150 m; 150 – 200 m; 200 – 300 m; 300 – 500 m; and >500 m.

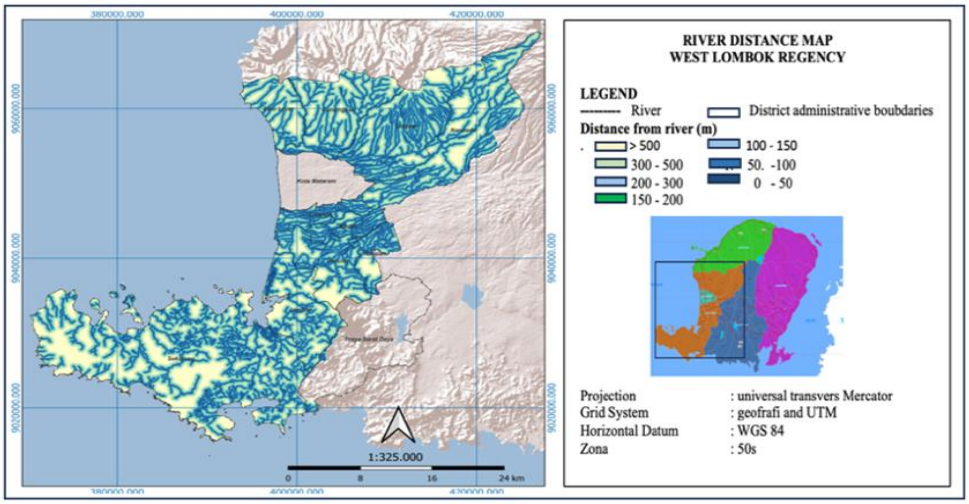

Fig. 5. Distance of the river map.

4.6. Land slope

The slope of the land as a parameter for forming flood vulnerability was obtained based on the processing of DEM (Digital Elevation Model) ALOS Palsar data downloaded through the ASF

website (https://search.asf.alaska.edu/#/). To obtain slope maps, DEM data is processed using the Slope feature (**Fig. 6**), which is one of the spatial analysis functions in QGIS software.

In the next stage, slope reclassification is carried out based on slope classes. Map of the slope of West Lombok Regency, the slope classes are classified into 7 classes as follows; slope class 0 – 3%, slope class 3 – 8%, slope class 8 – 15%, slope class 15 – 30%, slope class 30 – 45%, slope class 45 – 65% and slope class > 65%.

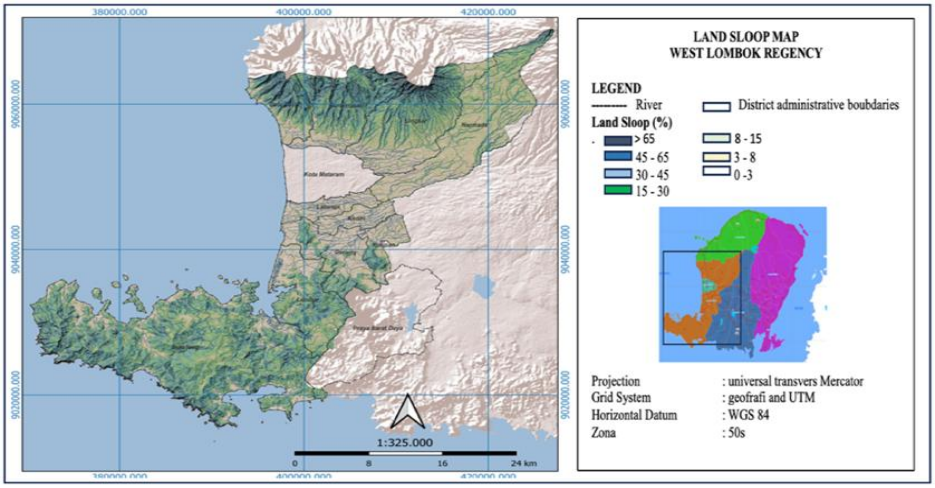

Fig. 6. Land slope map.

4.7. Type of soil

Soil type data as a parameter for forming flood vulnerability is spatial data in the form of vector data sourced from the NT1 River Area Agency. The processing of soil type data as a parameter for forming flood vulnerability includes cutting soil type data according to the scope of the research area, then at the stage of determining the weight and scoring, classification is carried out by considering the characteristics of soil types based on the formation process. An overview of the results of the classification of soil type characteristics. The soil type parameter class is classified into 6 classes covering the following areas:

1. Alluvial brown-grayish, covering a small part of Sekotong and Lembar Districts.
2. The Mediterranean complex of chocolate, gray grumose, brown regosol, and lithosol, covers most of the area of Sekotong District; part of Lembar District; and a small part of Gerung District.
3. The brown Mediterranean and reddish Mediterranean complexes cover a small part of the Kuripan District.
4. The reddish-brown lithosol and Mediterranean complex, cover parts of Gunungsari and Batu Layar Districts.
5. The regosol and lithosol complex, covering the entire area of Labuapi, Kediri, and Kuripan Districts; as well as most of the areas of Gerung District, Lembar District, Narmada District, Lingsar District, Gunungsari District and Batu Layar District.
6. Chocolate Mediteran, covers most of the areas of Narmada District, Lingsar District and Gunungsari District; and a small part of Batu Layar District.

4.8. Elevation area

Elevation as a parameter for forming flood vulnerability was obtained based on DEM (Digital Elevation Model) ALOS Palsar data, which was reclassified into elevation classes (**Fig. 7**). The higher the elevation of an area, the less chance of flooding in that area.

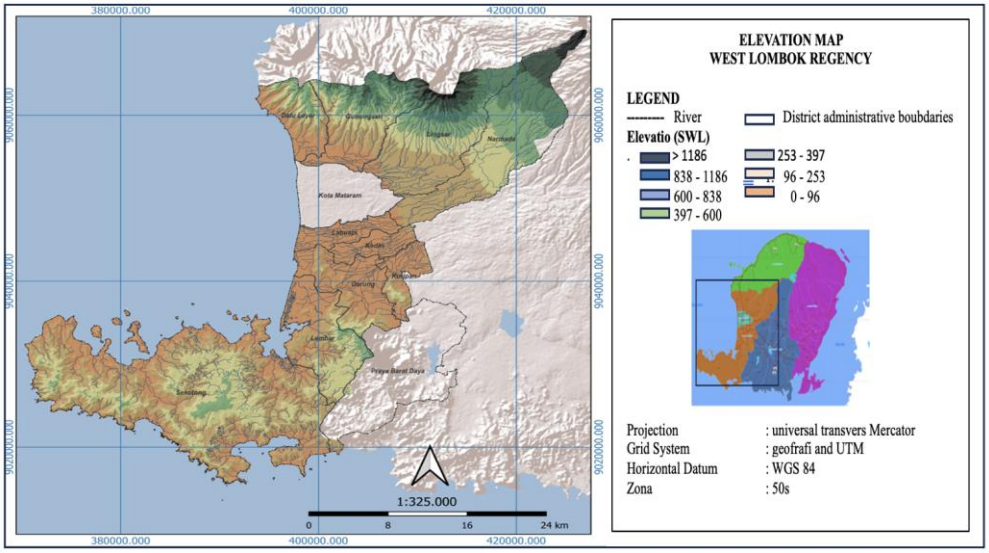

Fig.7. Map of elevation, West Lombok Regency

4.9. Flood vulnerability level

Flood-vulnerability maps with their vulnerability levels are obtained through the integration of flood-vulnerability shaping factors using MCE analysis into the Geographic Information System (**Fig. 8**). As a result of integration into the GIS, the event data was matched (validated) in the field to see the extent of the percentage of match between the flood-vulnerability map and the actual event data. Based on the results of the weighting of flood-vulnerability forming factors, the WLC equation can be written:

$$WLC = 0.0527X1 + 0.1210X2 + 0.1567X3 + 0{,}1660X4 + 0.1843X5 + 0{,}3190X6. \quad (5)$$

where:

WLC	= weighted linear combination
X1	= elevation
X2	= soil Type
X3	= slope Slope
X4	= distance to the River
X5	= rainfall
X6	= land Use

AHP weights were obtained by filling out questionnaires and interviews with sources considered experts in determining flood threat parameters in West Lombok Regency. The sources of this research came from several experts, namely from the Regional Disaster Management Agency, the Public Works and Spatial Planning Service, the Nusa Tenggara I River Basin Center, the Agriculture Service, and the Environmental Service. The consistency index (CI) value is 0.1, meaning that the inconsistency value (CR) is still below or equal to 10%, so that the criteria set by Saaty <10% indicates that the inconsistency that occurs is considered acceptable. Determination of flood vulnerability class is done using the equal interval method, namely dividing the highest vulnerability value minus the lowest vulnerability value by the number of class intervals (**Table 6**). The number of flood vulnerability classes is 5: not vulnerable, rather vulnerable, moderate, vulnerable, and very vulnerable.

Table 6.

Symbols and classification of flood vulnerability classes.

Symbol	Interval	Vulnerability criteria
	0.0129 – 0.0339	Not vulnerable
	0.0339 – 0.0549	Rather vulnerable
	0.0549 – 0.0759	Moderat vulnerable
	0.0759 – 0.0969	Vulnerable
	0.0969 – 0.1180	Very vulnerable

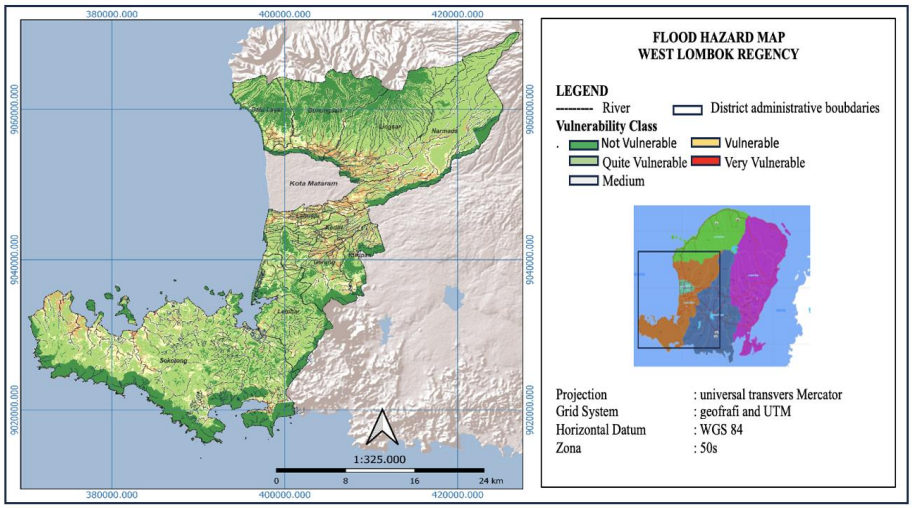

Fig.8. Flood vulnerability classes in West Lombok Regency.

4.10. Distribution of flood areas in West Lombok Regency

Almost all sub-districts in West Lombok Regency have experienced flood disasters in the two years January 2021 – February 2023, except for Kuripan District. Batu Layar District and Sekotong District rank at the top of the number of flood disaster events. Several villages in several sub-districts have even experienced repeated flood events more than once, such as in Batu Layar District, Labu Api District, Lembar District, and Sekotong District. Several sub-districts have become flood areas in the last three years, namely Batu Layar District, Labu Api District, Lembar District, and Sekotong District. Spatially, the distribution of flood events is presented in **Fig. 9**.

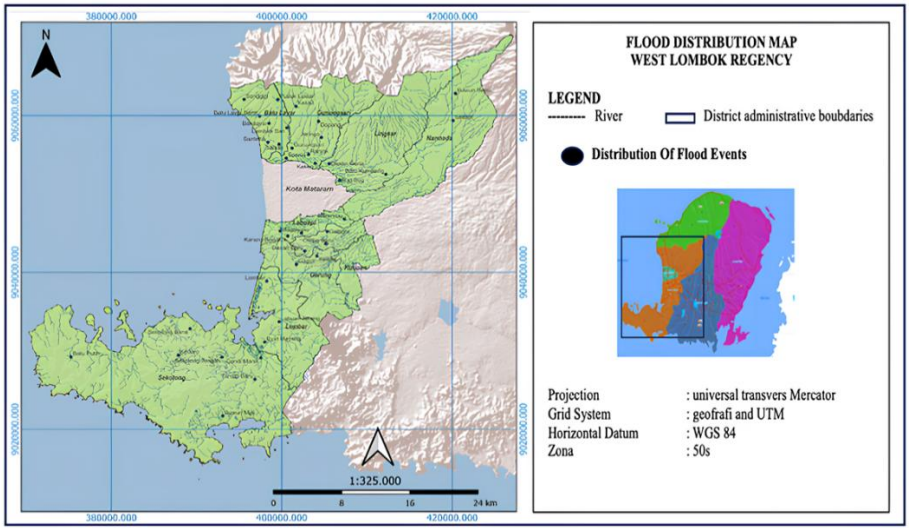

Fig. 9. Map of the distribution of flood Areas in West Lombok Regency.

4.11. Distribution of land use patterns in flooded areas

Based on data from the Sentinel-2/MSI remote sensing satellite acquired in July 2022, there are 6 classes of land use in West Lombok Regency, namely forests, settlements, gardens, rice fields, open land, and water bodies. Land use areas are generally dominated by forest areas with a percentage of area up to 70%, and cultivation activity areas such as rice fields with an area percentage of 12%, and gardens with a percentage of area of 10%.

The forest is an area with an area of 642,711 hectares, which dominates West Lombok Regency and is distributed into several sub-districts, including Sekotong, Narmada, Lingsar, Lembar, Labuapi, Kuripan, Kediri, Gunung Sari, Gerung, and Batu Layar. In more detail, the proportion of area and distribution of land use in West Lombok Regency are presented in **Fig. 10**.

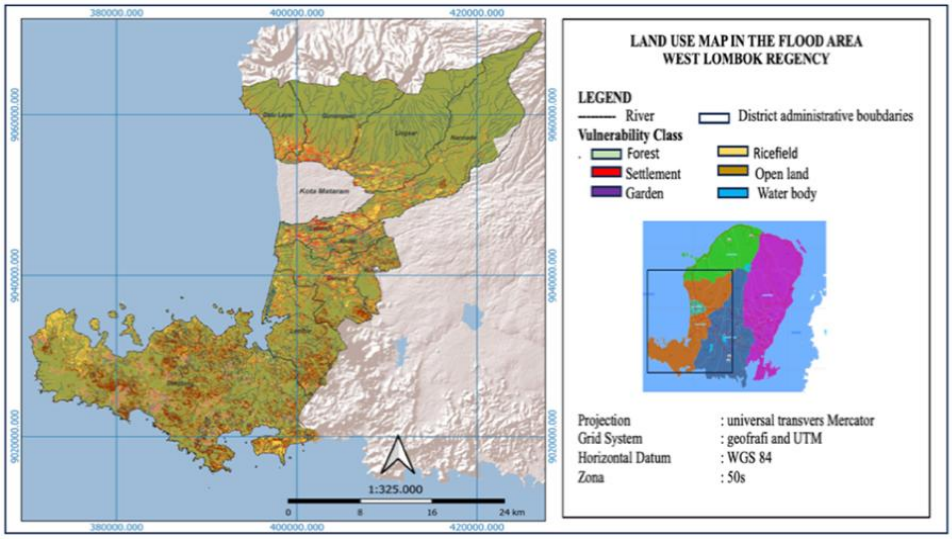

Fig. 10. Map of the spatial distribution of land use in West Lombok Regency.

4.12. Flood Event Validation

Validation of flood hazard maps is carried out by identifying the distribution of sub-districts based on potential hazard classes. The data used are in the form of disaster reports obtained from the West Lombok Regency Regional Disaster Management Agency. The distribution point of the incident is the incident data for each village affected in the period 2021 to 2023, which represents one village affected by the incident, which is the village centre point.

The approach used to determine the level of accuracy of the flood vulnerability map is by looking at the position of the flood event point from the Regional Disaster Management Agency flood disaster data for each vulnerability class on the map. The five flood vulnerability classes need to be grouped again into only 2 classes to adjust the characteristics of the flood incident data, which also consists of 2 (two), namely: there was an incident, and there was no incident.

The two new classes of vulnerability are the class with no potential for flooding (including: not vulnerable and rather vulnerable) and the class with potential for flooding (including: moderate, vulnerable, and very vulnerable). The results of the flood hazard map validation process with flood disaster data (**Table 7**) show that a total of 27 flood points fall into areas with the potential for flooding from the moderate, high, and low vulnerability classes. As many as 32 flood points fall into the non-high and low vulnerability classes.

Table 7.

Validation of hazard map with flood incident data 2017-2023.

Flood Vulnerability Class	Distribution of flood Vulnerability	
	Number of occurrences	Percent (%)
No potential for flooding	***32***	***54.24***
Not vulnerable	20	33.90
Rather Vulnerable	12	20.34
Potential for flooding	***27***	***45.76***
Moderately Vulnerable	10	16.95
Vulnerable	17	28.81
Very vulnerable	0	0.00
Total	**59**	**100**

Table 7 shows that 45.76% of flood disasters occurred in areas that are included in the flood potential class (which includes moderate and vulnerable vulnerability). The remaining 54.24% of flood incident points are included in the non-flood potential class (not vulnerable and rather vulnerable). Thus, this flood vulnerability map shows a level of accuracy that is close to sufficient when associated with the distribution points of flood incidents in West Lombok Regency.

5. DISCUSSION

Based on the scoring results shown in **Table 3,** of the scoring results on the slope factor, the flatter an area (0-3%), the higher the influence on the potential for flood-vulnerability formations, so the score given for flat areas becomes high, on the contrary, with the level of slope classification from flat to steep.

The highest rainfall factor in West Lombok Regency is at >210 mm per year while the lowest is at 110 -130 mm per year. The higher the rainfall in an area, the higher the level of influence on the formation of potential flood vulnerability, so the score given is also high.

The altitude factor in West Lombok Regency shows that the plains area is at 0 – 96 meters above sea level, while for high elevation areas, it is at >1,186 meters above sea level. The lower an area, the higher the potential for flood vulnerability, contrary to the level of altitude classification in West Lombok Regency. The distance to the river in West Lombok Regency, the closest distance is classified as 0 – 50 m from the river boundary line, while the farthest distance is> 500 m. The closer to the river, the higher the potential for flood vulnerability in an area, so the score given is also high, on the contrary, by the classification level of distance to the river in West Lombok Regency.

For land types and land use that are immeasurable factors, the consideration of scoring is carried out based on the characteristics of land use and the type of soil. Land use dominated by vegetation the less influence it has on the potential for flood vulnerability, but if an area is more open/unvegetated, covered with water, and built, the influence on the potential for flood vulnerability is higher. Likewise, the characteristics of soil types are seen from the formation process. Soil formed in floodplain areas will certainly have characteristics that are easily inundated with water, related to the texture of the soil that has absorbed water into the soil. Research on flood disaster risk mapping using the AHP method was conducted in the city of Pekalongan (Wijayanti et.al., 2024), showing that flood classification with high vulnerability occurs in residential locations with low elevations and very extreme changes in land use

Land use and elevation are two important factors that influence the level of vulnerability of an area to flooding. Land use patterns such as the conversion of natural land (forests, swamps, and agricultural land) into built-up areas (settlements, industry, and urban areas) reduce the soil's ability to absorb rainwater. Surfaces covered by layers of pavement, such as concrete and asphalt, increase the volume of surface runoff, thereby increasing the risk of flooding. Meanwhile, areas with low

elevations, especially those close to rivers, floodplains, or coasts, tend to be more prone to flooding because gravity slows the outflow of water. Conversely, areas with higher elevations have a lower risk of flooding, although other factors such as extreme rainfall and poor water management can still increase vulnerability. The interaction between land use change and elevation factors often exacerbates the situation. In lowland areas that previously functioned as natural catchment areas, conversion into built-up areas without considering drainage aspects accelerates the occurrence of flooding even at moderate rainfall intensity. Therefore, land use management that takes elevation characteristics into account is a key strategy in flood risk mitigation. Analysis shows that in West Lombok Regency, there has been an increase in the distribution of flood risk areas and an increase in the frequency of flooding, especially in the Sekotong and Batulayar Districts

6. CONCLUSIONS

Based on the results of research conducted in West Lombok Regency, it can be concluded that:

The area in West Lombok Regency based on the potential level of flood vulnerability is dominated by the rather vulnerable class spread throughout the sub-district, namely 51.80 of the total area, not vulnerable by 22.84%, and ± 25%, the remaining 25% of the remaining areas are divided into the medium by 16.58%, vulnerable by 8.56% and very vulnerable by 0.21%.

The distribution of flood vulnerability based on land use in West Lombok Regency is divided into six classifications of land use, including forests, settlements, gardens, rice fields, open land, and water bodies. As for the classification of flood vulnerability, it is further grouped into two classes, namely the non-vulnerable class (not vulnerable and rather vulnerable) and the vulnerable class (moderate, vulnerable, and very vulnerable). Land use in the form of forests with a total area of 20.8% is included in the flood-vulnerability class, settlements with a total area of 48.3% are included in the flood-vulnerability class, gardens with a total area of 24.5% are included in the flood-vulnerability class, rice fields with a total area of 44% are included in the flood-vulnerability class, open land with a total area of 32.4% is included in the flood-vulnerability class, and the total area of water bodies of 24.8% is included in the flood vulnerability class.

The allocation of space in the spatial pattern plan has followed disaster-based planning, especially flood disasters, where 80% of the protected area is included in areas that do not / have less potential for flooding under its function as an area that protects the area under it. Likewise, 70% of the cultivation areas are located in areas that are free / less vulnerable to flooding.

The results of the analysis can provide a strong basis for the government in designing more effective flood disaster mitigation policies based on data. By mapping locations that have high levels of vulnerability, the government can carry out wiser spatial planning, such as limiting development in red zones and directing development to safer areas. And the results of this mapping can be used as an important reference in formulating regulations and revising development plans that are more resilient to hydrometeorological disaster risks.

The limitation of the study is in the validation of the results, where the data used for validation is only 3 years. This is because the recording of flood incident data carried out by the West Lombok Regency Regional Disaster Management Agency has only started in 2019.

ACKNOWLEDGMENTS

The writing of this article is thanks to the support of various parties, so on this occasion, the author would like to express his gratitude to:

1. Nusa Tenggara I River Area Hall, which has provided rainfall data
2. Meteorological and Geophysical Agency, West Nusa Tenggara Province, with the support of climatological data
3. The Public Works and Spatial Planning Office of West Lombok Regency, which has provided a map of the regional spatial plan

REFERENCES

Abdullah, H.M., Islam, I., Miah, G., Ahmed, Z., (2019), Quantifying the spatiotemporal patterns of forest degradation in a fragmented, rapidly urbanizing landscape: A case study of Gazipur, Bangladesh, Remote Sensing Applications: *Society and Environment*, 13, 457-465, SSN 2352-9385, https://doi.org/10.1016/j.rsase.2019.01.002.

Agonafir, C., Lakhankar, T., Khanbilvardi, R., Krakauer, N., Radell, D., Devineni, N. (2023), A review of recent advances in urban flood research. *Water Security*, 19, SSN 2468-3124, https://doi.org/10.1016/j.wasec.2023.100141.

Andrade, dan Szlafsztein (2015), Community Participation in Flood Mapping in the Amazon Through Interdisciplinary Methods, *Journal of Natural Hazards*, 78, 1491-1500.

Bell, V.A., Kay, A.L., Cole, S.J., Jones, R.G., Moore, R.J., Reynard, N.S. (2012), How might climate change affect river flows across the Thames Basin? An area-wide analysis using the UKCP09 Regional Climate Model ensemble. *J. Hydrol*. 442–443, 89–104. http://dx.doi.org/10.1016/j.jhydrol.2012.04.001

Burrough. (1986). Principles of Geographical Information Systems for Land Resources Assessment. Oxford. *Oxford University Press*.

Crăciun, A. I., Haidu, I., Magyari-Sáska, Zs., and Imbroane, A. I., (2009). Estimation of Runoff Coefficient According to Soil Moisture Using GIS Technique. *Geographia Technica, 4*(2), 1–10.

Elmoustafa MA. (2012), *Weighted Normalized Risk Factor for Flood Risk Assessment*. Ain Shams Engineering Journal. 3(4):327-332, DOI: 10.1016/j.asej.2012.04.001

EOSDIS (2021), Data processing levels: description of data processing levels ranging from 0 to level 4 for NASA EOSDIS data products. https://www.earthdata.nasa.gov/engage/open-data-services-and-software/data-information-policy/data-levels.

Györi M.M. & Haidu, I. (2011). Unit Hydrograph Generation for Ungauged Subwatersheds. Case Study: The Monoroştia River. *Geographia Technica, 6*(2), 23–29.

Haidu, I. & Ivan, K. (2016a). Urban runoff pathways and surface water volumes evolution. Case study : Bordeaux 1984-2014, France. (Évolution du ruissellement et du volume d'eau ruisselé en surface urbaine. Étude de cas : Bordeaux 1984-2014, France). *La Houille Blanche, 5*, 51–56. DOI https://doi.org/10.1051/lhb/2016050.

Haidu, I. & Ivan, K. (2016b). The assessment of the impact induced by the increase of impervious areas on surface runoff. Case study the city of Cluj-Napoca, Romania. *Carpathian Journal of Earth and Environmental Sciences, 11*(2), 331–337.

Haikal R. F., Suprayogi S. (2024). The Application of the SWAT+ Model for Watershed Management Scenarios in Lahar Flow Areas of Merapi Volcano. *Geographia Technica, 19*(2), 223–226. DOI: https://doi.org/10.21163/GT_2024.192.17.

Hidayah, E., Widiarti, W. Y., dan Ammarulsyah, A. R. (2022). Zoning Flash Flood Hazard Level with Geographic Information System in Kaliputih Sub-Watershed, Jember Regency. *Jurnal Teknik Pengairan, 13*(2), 273–282. DOI https://doi.org/10.21776/ub.pengairan.2022.013.02.12.

Kay, A.L., Rudd, A.C., Davies, H.N., Kendon, E.J., Jones, R.G. (2015). Use of very high-resolution climate model data for hydrological modeling, baseline performance, and future flood changes. *Clim. Change*, 133 (2), 193–208. http://dx.doi.org/10.1007/s10584-015-1455-6

Lawal, D.U., Matori, A.N., and Balogun, A.L. (2011), *A Geographic Information System and Multi-Criteria Decision Analysis in Proposing New Recreational Park Sites in Universiti Teknologi Malaysia*. *Modern Applied Science*. 5(3):39-55, DOI: 10.5539/mas.v5n3p39

Lee, S., Kim, J., Jung, H., Lee, J. and Lee, S. (2017). Spatial Prediction of Flood Susceptibility using Random-Forest and Boosted-Tree Models in Seoul Metropolitan City, Korea. *Geomatics, Natural Hazards and Risk, 8*(2), 1185–1203. DOI https://doi.org/10.1080/19475705.2017.1308971.

Miller, J.D., & Hutchins, M. (2017), The impacts of urbanization and climate change on urban flooding and urban water quality: A review of the evidence concerning the United Kingdom, *Journal of Hydrology: Regional Studies,* 12, 345-362, ISSN 2214-5818, https://doi.org/10.1016/j.ejrh.2017.06.006.

Malczewski, J., (2006), GIS-based Multicriteria Decision Analysis: A Survey of the literature, *International Journal of Geographical Information Science*, 20 7, 703-726. DOI: 10.1080/13658810600661508

Musungu, K., Motala, S. & Smith, J., (2012), Using Multi-criteria Evaluation and GIS for Flood Risk Analysis in Informal Settlements of Cape Town, The Case of Graveyard Pond. *South African Journal of Geomatics*, 1,1, 92-108. https://open.uct.ac.za/handle/11427/25937

Mulliss, R.M., Revitt, D.M., Shutes, R.B., (1996). The impacts of urban discharges on the hydrology and water quality of an urban watercourse, *Sci. Total Environ*.189–190, 385–390. http://dx.doi.org/10.1016/0048-9697(96)05235-7.

Revitt, D.M., & Ellis, J.B., (2016), Urban surface water pollution problems arising from misconnections, *Science of The Total Environment*, 551–552, 163-174, ISSN 0048-9697, https://doi.org/10.1016/j.scitotenv.2016.01.198.

Sari, S.P., Suprayogi, S., Budiman, S. (2025), HEC-RAS-based urban flood simulation for enhancing mitigation scenarios in the GAJAHWONG river, Indonesia. *Geographia Technica,* 20(1), 127–142. DOI: 10.21163/GT_2025.201.10

Sinha, R., Ganugula V., V.B., GISp, L.K., Singh, B. R. (2008), Flood Risk Analysis in The Kosi River Basin. North Bihar using Multi-parametric Approach of Analytical Hierarchy Process (AHP*), Journal of Indian Soc. Remote Sens*. 36, 4, 335-349, DOI: 10.1007/s12524-008-0034-y

Stedinger, J.R., Griffis, V.W., (2011). Getting from here to where? Flood frequency analysis and climate. *JAWRA J. Am. Water Resour. Assoc*. 47 (3), 506–513. http://dx.doi.org/10.1111/j.1752-1688.2011.00545.x

Seyam, M.H., Haque, R., Rahman, M., (2023), Identifying the land use land cover(LULC) changes using remote sensing and GIS approach: A case study at Bhaluka in Mymensingh, Bangladesh*, Case Studies in Chemical and Environmental Engineering*, V 7, 100293, ISSN 2666-0164, https://doi.org/10.1016/j.cscee.2022.100293.

Tehrany, S., Shabani, F., Neamah, M., Hong, H., Chen, W. and Xie, X. (2017). GIS-Based Spatial Prediction of Flood-Prone Areas using Standalone Frequency Ratio, Logistic Regression, Weight of Evidence and their Ensemble Techniques. *Geomatics, Natural Hazards and Risk, 8*(2), 1538–1561. DOI https://doi.org/10.1080/19475705.2017.1362038.

Wilby, R.L., Orr, H.G., Hedger, M., Forrow, D., Blackmore, M. (2006). Risks posed by climate change to the delivery of Water Framework Directive objectives in the UK. *Environ. Int.* 32(8), 1043–1055, http://dx.doi.org/10.1016/j.envint.2006.06.017

Wijayanti, R.P., Wijaya, A.P., Rahmawaty, M.A. (2024). Mapping of flood disaster threat in Pekalongan City using Analytical Hierarchy Process (AHP); *(Pemetaan Ancaman Bencana Banjir Di Kota Pekalongan Menggunakan Analytical Hierarchy Process (AHP)). Jurnal Geodesi Undip*, vol. 13, no. 4, pp. 591-600, Jan. 2025. https://doi.org/10.14710/jgundip.2024.44985

Yuniartanti, R. (2018). Structural and non-structural flood mitigation for Rontu watershed in Bima City. *Journal of Watershed Management Research, 2*(2), 137–150. DOI https://doi.org/10.20886/jppdas.2018.2.2.137-150.

GIS AND AHP-BASED FLOOD ZONING AND CONSERVATION STRATEGIES IN THE TARUSAN WATERSHED, INDONESIA

Eri BARLIAN[1*], Iswandi UMAR[2], Indang DEWATA[3], Triyatno TRIYATNO[2], Aprizon PUTRA[4], Eva MUSTIKASARI[4], Sri Endah PURNAMANINGTYAS[4], Erfan Andi HENDRAJAT[5], Serly Mutia SARI[6], Yulius YULIUS[4], Dewi Rahmadani SIREGAR[6]

DOI: 10.21163/GT_2025.202.08

ABSTRACT

This study aims to identify flood hazard zones and formulate flood disaster mitigation strategies through an integrated watershed conservation framework in the Tarusan Watershed, Pesisir Selatan Regency, West Sumatra, Indonesia. This study applied a Geographic Information System (GIS)-based spatial analysis combined with the Analytical Hierarchy Process (AHP) method to map flood hazard zones and prioritize flood mitigation strategies. Flood hazard assessment was carried out using six indicators (rainfall, slope, landform, land use, soil type, and geological formation). Flood hazard zones were classified into three categories (low, medium, and high) based on a composite scoring system ranging from 65 to 325. The results indicated that the high flood hazard zone (22%) was concentrated in the downstream areas, influenced by flat slopes, high rainfall, alluvium deposits, and intensive human activities. Medium hazard zones (58%) were found in the midstream areas, while low hazard zones (20%) were located in upstream regions with steep slopes and dense forest cover. The AHP analysis involved 25 experts from diverse institutions, identifying seven strategic alternatives categorized into three main priorities: regulation, education, and institutional strengthening. The most dominant strategy was increasing community knowledge about forest functions (weight 0.301), followed by strengthening local institutions (0.149), and improving collaboration with government agencies (0.149). Integration between flood hazard zoning and AHP-based strategies shows that upstream areas require forest conservation and environmental education, midstream areas need sustainable livelihood development, while downstream areas demand regulation enforcement and improved land-use control.

Key-words: *Flood Hazard; Watershed Conservation; Analytical Hierarchy Process (AHP); GIS-Based Analysis; Tarusan Watershed.*

1. INTRODUCTION

Flooding is a recurring hydrometeorological event that occurs when precipitation intensity exceeds the capacity of a watershed to manage surface runoff, resulting in the inundation of both urban and rural areas (Cea & Costabile, 2022). As Tang et al. (2021); Merz et al (2021) identified, the key drivers of flood disasters can be grouped into meteorological factors, anthropogenic activities, and geomorphological conditions of the watershed.

---

[1]*Department of Coaching, Universitas Negeri Padang, Padang, Indonesia, (EB) e.barlian@fik.unp.ac.id*
[2]*Department of Geography, Universitas Negeri Padang, Padang, Indonesia, (IU) iswandi_u@fis.unp.ac.id, (TT) triyatno@fis.unp.ac.id*
[3]*Department of Chemistry, Universitas Negeri Padang, Padang, Indonesia, (ID) indangdewata@fmipa.unp.ac.id*
[4]*National Research and Innovation Agency, Cibinong-Bogor, Indonesia, (AP) apri024@brin.go.id, (EM) evam002@brin.go.id, (SEP) srie005@brin.go.id, (YY) yuli058@brin.go.id*
[5]*Research Center for Fisheries, National Research and Innovation Agency (BRIN), Cibinong-Bogor, Indonesia, (EAH) erfa001@brin.go.id*
[6]*Doctoral Program of Environmental Science, Universitas Negeri Padang, Padang-Indonesia, (SMS) serlysari@unp.ac.id, (DRS) dewirahmasir@student.unp.ac.id*
[*]*Corresponding author: e.barlian@fik.unp.ac.id*

Additionally, Umar et al. (2019); Dewata & Umar (2019); Barlian et al (2024) classified flood causative factors into natural causes such as high rainfall, flat topography, sedimentation, and human activities, including extensive deforestation, settlement encroachment on riverbanks, and poor waste management practices.

The accuracy of flood hazard prediction can be significantly improved by utilizing a high-resolution Digital Elevation Model (DEM). Schumann & Andreadis (2016) assert that the application of refined DEM data enhances flood-inundation models by up to 30%, minimizing the extent of population exposure and reducing potential economic losses. They emphasized that "Higher resolution measurements would improve large-scale flood inundation prediction capabilities and significantly reduce the number of people affected as well as the economic losses associated with high magnitude flooding". In the present study, both the Shuttle Radar Topography Mission (SRTM) 1 Arc Second data with approximately 30-meter resolution and the National DEM (DEM-NAS) with an 8-meter spatial resolution were utilized to improve the accuracy of topographic and hydrological modeling. In the present study, both the SRTM 1 Arc Second data with approximately 30-meter resolution and the DEM-NAS with an 8-meter spatial resolution were utilized to improve the accuracy of topographic and hydrological modeling. The integration of these datasets enabled a more precise delineation of watershed boundaries, slope characteristics, and flood-prone zones within the Tarusan Watershed. This multi-scale DEM-NAS approach significantly enhanced the quality of slope classification and runoff direction modeling, thus improving the overall reliability of flood hazard mapping (Abo-Salim, 2023; Javas et al., 2024).

In Indonesia, flood disasters have consistently been the most frequent hazard. According to Data from the Indonesian National Disaster Management Agency (BNPB) from 2009, 2017, and 2018, floods represent 34.7% of all recorded natural disasters from 1815 to 2022, with nearly 45% linked directly to human-induced factors, particularly changes in land use and reduced infiltration. The inclusion of the year 1815 marks the earliest systematically documented flood event in the BNPB historical database, which compiles archival, colonial-era, and geological records as part of Indonesia disaster chronology. This historical baseline is significant because it reflects the beginning of organized documentation during the Dutch East Indies period, making it a useful point of reference for long-term flood trend analysis (Faral et al., 2024). One of the critical flood-prone areas in Indonesia is the Tarusan Watershed, located in Pesisir Selatan Regency, West Sumatra. This watershed experiences frequent flooding, which disrupts vital transportation routes between Padang City, Painan, and Bengkulu Province, with delays in mobility that can extend up to nine hours during severe flood events (Triyatno et al., 2019; Triyatno et al., 2020; Triyatno et al., 2023).

Watershed conservation is recognized as a fundamental component in reducing flood risks and promoting sustainable land and water management. Healthy watersheds regulate hydrological processes, including reducing surface runoff, enhancing infiltration, and maintaining groundwater recharge. Darghouth et al (2008) emphasized that watershed conservation activities are instrumental in maintaining groundwater recharge, reducing erosion, and preventing the degradation of downstream ecosystems, including beaches and coral reefs. In the Indonesian context, watershed conservation and flood risk reduction are strongly supported by a legal framework that includes Law No. 26/2007 on Spatial Planning, Law No. 32/2009 on Environmental Protection and Management, and Government Regulation No. 37/2012 on River Management (Pambudi, 2015; Pambudi & Kusumanto, 2023). These regulations emphasize the importance of protecting watershed areas, ensuring environmental sustainability, and integrating disaster mitigation into spatial development planning. This study aligns with these national policies by combining spatial-based flood hazard analysis with watershed conservation strategies, by Indonesia's regulatory emphasis on integrated, participatory, and ecosystem-based management approaches. In Taiwan, watershed conservation programs have demonstrated significant environmental and economic benefits. Lin et al. (2021) highlighted that government-led investments in watershed restoration resulted in 49% improvement in water quality, 20% increase in water supply stability. This analysis showed that watershed conservation and restoration efforts yield long-term environmental benefits, including sediment reduction, and resilience to natural disasters. In addition, Cheng et al. (2002) described Taiwan

watershed management efforts as a successful integration of soil and water conservation practices aimed at disaster mitigation and sustainable resource development.

Community involvement has been identified as a critical factor for the success of watershed conservation initiatives. Thapa et al. (2022) reported that community participation in soil and water conservation is key to effective disaster mitigation, particularly in upstream watershed areas prone to degradation. Their study underlines the importance of engaging local stakeholders to foster stewardship and ensure the sustainability of conservation programs. In Indonesia, the National Water Rescue Partnership Movement (WRPM), coordinated by the Ministry of Environment and Forestry, exemplifies a national effort integrating community-based watershed conservation through tree planting, soil conservation, and local awareness campaigns (Suwarto et al., 2022).

Another successful initiative is the Desa Tangguh Bencana (Disaster Resilient Village) program, which encourages local communities to participate actively in risk reduction planning and watershed protection at the village level (Sunarto et al., 2025). These programs have demonstrated that empowering local communities leads to more adaptive and sustainable watershed governance. Internationally, the Watershed Management Program in Ethiopia, supported by local institutions and international partners, has mobilized rural communities to construct soil bunds and reforest degraded hillsides, resulting in increased water retention and reduced erosion (Nafli et al., 2024). Similarly, the Payment for Ecosystem Services (PEs) scheme in Costa Rica incentivizes farmers to protect forests and water sources, with community engagement playing a central role in the program transparency and long-term success (Viguera et al., 2024). Furthermore, Debele et al. (2023); Griffiths et al. (2024) argued that Nature-Based Solutions (NBS), including reforestation, wetland restoration, and the protection of riparian buffers, offer cost-effective and sustainable alternatives to conventional engineering approaches for managing hydro-meteorological risks. NBS not only reduces flood risks but also provides multiple co-benefits, such as biodiversity conservation, carbon sequestration, and the enhancement of ecosystem services.

This study aims to identify flood hazard zones and develop flood disaster mitigation strategies as part of an integrated watershed conservation framework in the Tarusan Watershed in Pesisir Selatan Regency, West Sumatra, Indonesia. The novelty of this study lies in integrating flood hazard zoning with the Analytical Hierarchy Process (AHP) based strategy prioritization to develop targeted mitigation actions for each flood risk zone in the Tarusan Watershed. This approach offers a framework by linking spatial flood risk levels with prioritized watershed management strategies.

2. STUDY AREA

This study was conducted in the Tarusan Watershed, situated in Pesisir Selatan Regency, West Sumatra Province, Indonesia. Geographically, the watershed lies between 1°24'00" to 1°47'00" South Latitude and 100°28'00" to 100°42'00" East Longitude. As shown in **Figure 1**, the Tarusan Watershed covers an area of 300.27 km², making it one of the ten largest river basins in the West Sumatra province (Umar & Triyatno, 2024; Umar., 2024).

The Tarusan watershed flows into the Indian Ocean and features diverse topography. Based on SRTM 1 Arc Second data and DEM-NAS analysis, approximately 30% of the area comprises flat terrain, while the remaining regions consist of moderately steep to very steep slopes, particularly in the upstream and midstream areas. The region receives high annual rainfall ± 3,000 mm each year, which significantly impacts the hydrological processes (Hamada et al., 2008); Kaiser et al., 1999).

3. DATA AND METHODS

3.1. Data Sources

This study was conducted over five months, from January to May 2022. Six primary indicators were analyzed to identify flood hazard zones and support conservation planning in the Tarusan Watershed. The data for these indicators, namely rainfall, slope, landform, land use, soil type, and geological formation, were collected from various sources and are detailed in **Table 1**.

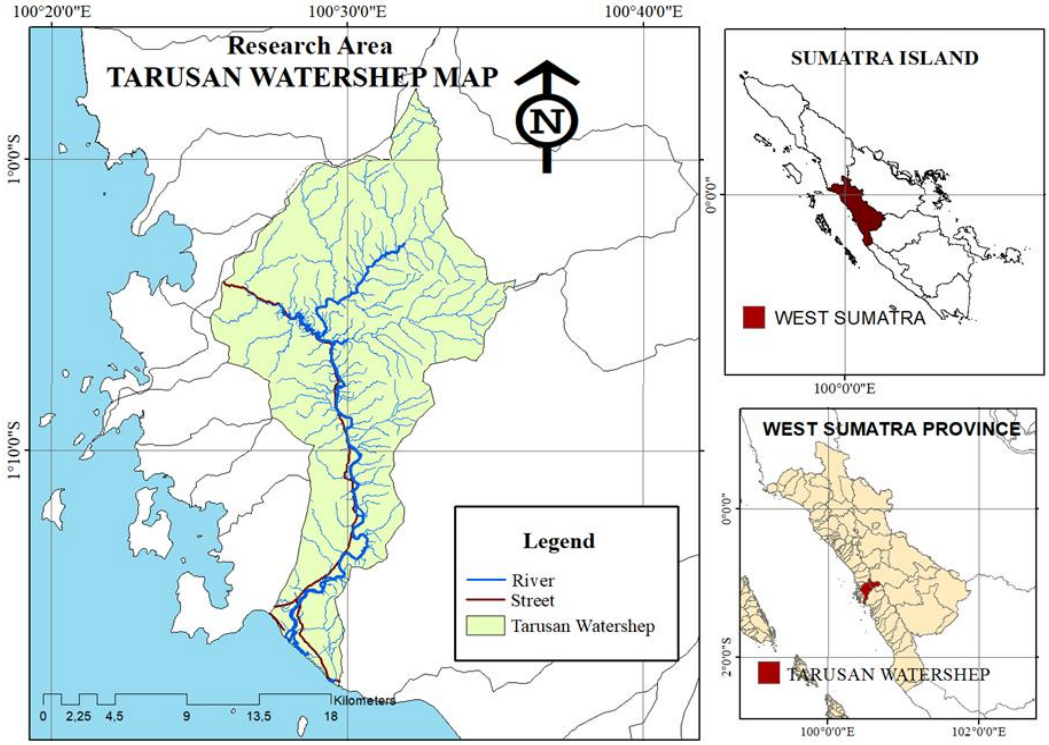

Fig. 1. Location map of Tarusan Watershed in Pesisir Selatan Regency, West Sumatra Province.

Table 1.

Study data and sources.

No	Data	Specification	Source
1	Rainfall	1975–2022	Climatological and Geophysics (BMKG)
2	Land Use	Landsat OLI 8 (2020)	United States Geological Survey (USGS)
4	Slope and slope (High-res)	SRTM 1 Arc Second and DEMNAS (8 m resolution)	USGS and Geospatial Information Agency (BIG)
5	Landform	Geological and DEM Analysis	In-house Interpretation
6	Soil Type	1:250,000 Map (1990)	Research Center of Bogor Soil
7	Geological	1:250,000 Map (2007)	Geological Agency of Bandung

The land use data for the Tarusan Watershed were extracted and analyzed using Landsat Operational Land Imager (OLI) 8 acquired in 2022 from the USGS Earth Explorer. The imagery has a spatial resolution of 30 meters for multispectral bands, which is suitable for medium-scale land cover classification and watershed analysis in large and heterogeneous areas such as the Tarusan Watershed. Several pre-processing steps were undertaken, consisting of:

1) Radiometric correction conducted to correct sensor noise and convert raw Digital Numbers (DN) into surface reflectance values;

2) Geometric correction applied to align the imagery with spatial reference systems, using Universal Transverse Mercator (UTM) Zone 47S, WGS 84, to ensure the spatial accuracy of land use mapping; and

3) Atmospheric correction performed using the Dark Object Subtraction (DOS) method, minimizing the effects of atmospheric scattering and enhancing the clarity of surface features (Bernardo et al., 2017).

A supervised classification technique was implemented using the Maximum Likelihood Classifier (MLC) algorithm. The classification process produced a detailed map of land use categories, consisting of bare land, settlement, farming area, mixed garden, shrub, plantation, and forest (Putra et al., 2023). Although Landsat 8 OLI has a 30-meter spatial resolution, which may not capture very small land patches or narrow land use boundaries, it provides a balanced trade-off between spatial detail and regional coverage. This level of resolution is sufficient for analyzing land use patterns that influence surface runoff, infiltration rates, and flood susceptibility at the watershed scale.

3.2. Data analysis techniques

3.2.1. Flood Hazard Mapping and Scoring Analysis

Each of the six indicators presented in **Table 1** was further classified into sub-indicators based on their characteristics and influence on flood susceptibility. The weighting system was adapted from Umar et al. (2017). The resulting composite scores ranged from 65 (lowest) to 325 (highest). To categorize these scores into distinct hazard classes, Equation 1 was used to calculate the class intervals. The flood hazard zones were subsequently divided into three classes (high, medium, and low). The detailed criteria for each indicator, along with their assigned weights, sub-indicators, values, and corresponding scores, are presented in **Table 2** below.

Table 2.

Indicators for flood hazard assessment.

Indicator (Weight)	Sub-Indicator	Value	Score
Rainfall (mm/year) (15)	> 4500	5	75
	4000 – 4500	4	60
	3500 – 4000	3	45
	3000 – 3500	2	30
	< 3000	1	15
Slope (%) (15)	Flat (0 – 8%)	5	75
	Tilted (9 – 16%)	4	60
	Slightly Steep (17 – 26%)	3	45
	Steep (27 – 40%)	2	30
	Very Steep (> 40%)	1	15
Landform (10)	Marine	5	50
	Fluvial	4	40
	Denudational	1	10
	Structural	1	10
	Volcanic	1	10
Land Use (10)	Bare Land	5	50
	Settlement	4	40
	Farming Area	4	40
	Mixed Garden	3	30
	Shrub	3	30
	Plantation	2	20
	Forest	1	10
Soil Type (10)	Ultisols	5	50
	Entisols	4	40
	Histosols	3	30
	Oxisols	2	20
	Inceptisols	1	10
Geological Formation (5)	Alluvium (Qal)	5	25
	Latih (Tml)	3	15
	Jura Sediment (Jr)	3	15
	Granite (Tgr)	1	5
	Quaternary Volcanic Rocks (Qv)	1	5

The determination of flood-prone zones in the Tarusan Watershed was conducted through a weighted scoring method, utilizing overlay analysis techniques within a GIS. This method integrates multiple spatial data layers corresponding to the six indicators, each of which is subdivided into sub-indicators with specific values and weights. To classify the total scores into distinct flood hazard classes, Equation 1 was applied to determine the class interval as follows.

$$I = \frac{c-d}{k} \quad (1)$$

where: I = Interval; c = Highest total (325); b = Lowest total (65); and k = Number of 3 classes.

By applying Equation 1, the class interval was calculated as follows:

$$I = \frac{325-65}{3} = 86.67 \approx \mathbf{86} \quad (2)$$

Based on the calculated class intervals, the flood hazard zones were classified into three categories, as can be seen in **Table 3** below.

Table 3.

Flood hazard class intervals in the tarusan watershed.

Flood Hazard Class	Score Interval	Category
Low Hazard	65 – 115	Low Risk
Medium Hazard	116 – 237	Medium Risk
High Hazard	238 – 325	High Risk

The resulting flood hazard zones serve as a foundation for watershed conservation strategies and flood disaster mitigation planning. Priority interventions, such as reforestation in high-risk areas and implementation of erosion control measures, are recommended to enhance the resilience of the Tarusan Watershed against flood events (Debele et al., 2023).

3.2.2. Flood Disaster Mitigation Assessment through the AHP Method

The AHP approach was utilized (Saaty, 1983; Marimin & Maghfiroh, 2010). A panel of 25 experts was engaged in this study, representing diverse stakeholders, including the Public Works Department, Regional Disaster Management Agency, local universities, community leaders, Non-Governmental Organizations (NGOs), religious leaders, and the Regional Planning and Development Agency. These experts were selected for their expertise in disaster risk reduction, environmental management, and community development. The experts conducted pairwise comparisons of the identified criteria and sub-criteria for flood mitigation, using a 9-point scale as proposed by Saaty (1983) and refined by Marimin & Maghfiroh (2010). The scale used is presented in **Table 4**, providing a consistent framework for evaluating the relative importance of each criterion, and the hierarchy, shown in **Figure 2**, demonstrates the interconnection between policy, community education, and institutional strengthening.

Table 4.

AHP Assessment Criteria (Saaty's Scale).

Value	Description
1	A is equally important as B
3	A is slightly more important than B
5	A is significantly more important than B
7	A is very strongly more important than B
9	A is absolutely more important than B
2, 4, 6, 8	Intermediate values when compromise is needed between adjacent scales

Sources: Saaty (1983); Marimin & Maghfiroh (2010).

The AHP analysis was conducted using Expert Choice software to process the comparison matrices and calculate the priority weights of each strategy. A critical aspect of AHP is the Consistency Ratio (CR), which measures the consistency of expert judgments. In **Figure 2** shows three core strategic pillars aimed at reducing flood risk and promoting watershed conservation, namely Regulation, Education, and Institutional Strengthening. Each pillar encompasses targeted action programs derived from expert consensus, designed to address the physical and social dimensions of flood disaster mitigation and watershed management. The actions include:

A1: Consistent enforcement of environmental regulations
A2: Establishment of clear and transparent rules for sustainable resource use
A3: Increasing community awareness of the critical role forests play in mitigating floods
A4: Promoting alternative livelihoods for communities dependent on forest resources
A5: Enhancing community skills in the sustainable utilization and value addition of forest products
A6: Strengthening local institutions and customary community groups
A7: Fostering collaborative partnerships between communities and government agencies

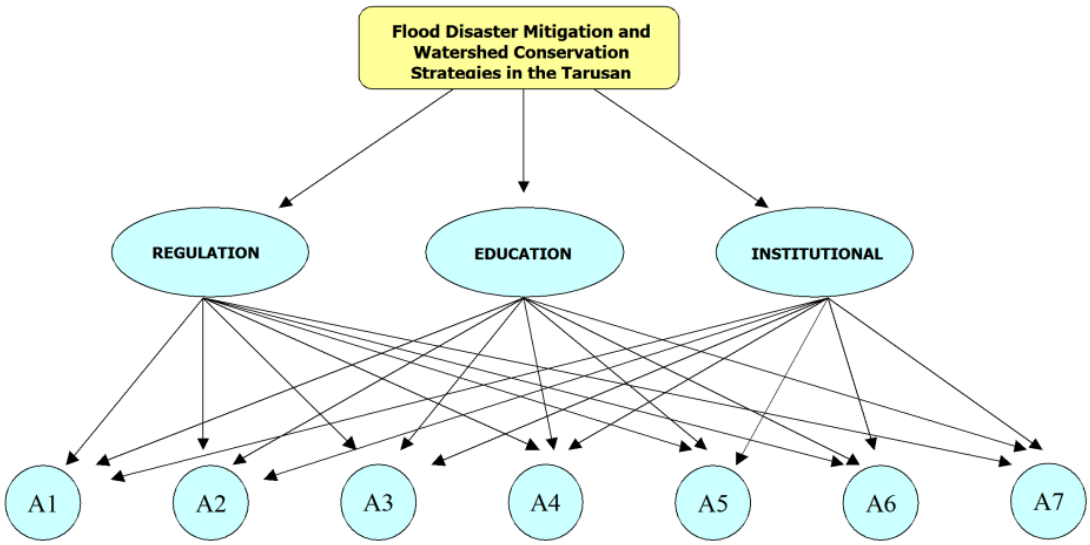

Fig. 2. Hierarchy of flood disaster mitigation and watershed conservation strategies in the Tarusan Watershed.

This strategic framework aligns with the principles of Ecosystem-based Disaster Risk Reduction (Eco-DRR), as recommended by the United Nations Environment Programme (UNEP, 2014), and is supported by findings from Debele et al. (2019). By integrating Nature-Based Solutions (NBS) within a watershed conservation context, the framework not only reduces flood risk but also enhances biodiversity, improves water quality, and sustains local livelihoods.

Furthermore, the AHP-based prioritization process involved 25 experts from various institutions including government agencies, NGOs, academics, and community leaders ensuring that the resulting strategies are context-specific, socially inclusive, and institutionally grounded. The seven action strategies derived from the AHP analysis address key domains such as forest conservation (A3), alternative livelihoods (A4), regulation enforcement (A1), and institutional collaboration (A6, A7), which are all consistent with Eco-DRR principles that emphasize local participation, ecosystem health, and multi-stakeholder governance. Hence, this integrative approach offers not only a technical assessment of flood risk but also a policy-relevant and community-responsive pathway for implementing sustainable watershed management.

4. RESULTS

4.1. Slope and Rainfall

Slope and rainfall characteristics are the main factors that influence the hydrological and flood potential of a watershed area. This study utilized SRTM 1 Arc Second data and long-term rainfall data (1975–2022) to classify the physical characteristics of the Tarusan Watershed. In addition, high-resolution DEMNAS (8-meter) data were incorporated to improve the accuracy of slope gradient analysis, especially in the upstream and midstream regions where topographic complexity is high. The slope classification was used to identify areas with varying degrees of land steepness, while rainfall data provided an overview of the distribution of precipitation intensity throughout the watershed. The results of this spatial analysis are shown in **Figure 3**, which presents the slope classes (**Figure 3a**) and annual rainfall intensity (**Figure 3b**) in the Tarusan Watershed.

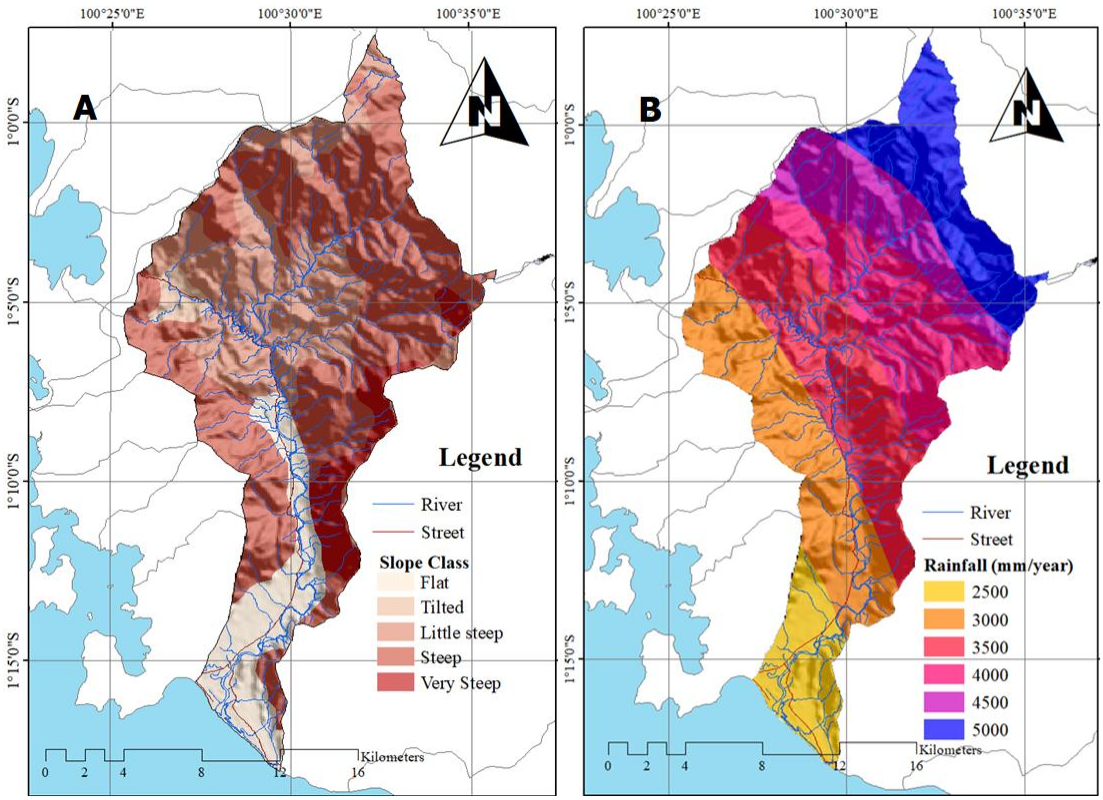

Fig. 3. Map of slope (a) and rainfall (b) in the Tarusan watershed.

The analysis results in **Figure 3** above show that the slope and rainfall characteristics of the Tarusan Watershed are critical factors influencing its hydrological behavior and susceptibility to flooding. The spatial analysis of slope classification (**Figure 3a**) indicates that the Tarusan Watershed is dominated by steep to very steep slopes, particularly in the upstream and midstream regions. Approximately 63% of the total watershed area consists of slopes ranging from 27% to more than 40%, which significantly increases the potential for surface runoff, accelerates soil erosion, and reduces water infiltration capacity, especially in areas undergoing deforestation and land-use changes (Hoch et al., 2019). Meanwhile, the downstream and southern coastal regions of the watershed are characterized by flatter terrain, with slope classes ranging from 0% to 16%. For more details, please see **Table 5** below.

Table 5.

Slope classification and flood hazard score in the Tarusan Watershed.

Slope Class	Area (%)	Score
Flat (0-8%)	5	75
Tilted (9-16%)	10	60
Slightly Steep (17-26%)	22	45
Steep (27-40%)	35	30
Very Steep (>40%)	28	15

Source: Results of data analysis 2023.

In addition to the slope factor, rainfall distribution also plays a significant role in influencing flood risk within the watershed. **Figure 3b** shows that the upstream and central parts of the Tarusan Watershed receive very high annual rainfall, ranging from 4,000 mm to over 5,000 mm. These conditions are primarily caused by orographic precipitation from the Barisan Mountain range. High rainfall intensity increases surface runoff, triggers landslides, and accelerates the flow of water downstream, especially during the peak rainy season. In contrast, the downstream and coastal areas receive lower rainfall intensities, ranging from 2,500 mm to 3,000 mm annually. However, these lower rainfall regions remain vulnerable to flooding due to water accumulation from upstream discharge and limited drainage capacity. For more details, please see **Table 6** below.

Table 6.

Rainfall intensity classification and flood hazard score in the Tarusan Watershed.

Rainfall (mm/year)	Area (%)	Score
<3000	15	15
3000-3500	20	30
3500-4000	25	45
4000-4500	25	60
>4500	15	75

Source: Results of data analysis 2023.

Based on the flood hazard scoring criteria applied in this study, the combination of steep to very steep slopes in the upstream and midstream regions, along with high rainfall intensity exceeding 4,000 mm annually, places these areas within the highest flood hazard category. Conversely, although the downstream and coastal regions experience lower rainfall intensity and gentler slopes, they remain vulnerable to flooding due to sediment deposition and reduced river channel capacity from upstream erosion. Therefore, effective mitigation strategies should prioritize upstream watershed conservation, erosion control, and sustainable land-use practices to reduce surface runoff, enhance infiltration, and minimize sediment transport to downstream areas.

4.2. Soil and Landform

Soil and landform characteristics are essential physical factors that strongly influence the hydrological response and flood vulnerability of a watershed area. The distribution of soil types and landforms in the Tarusan Watershed plays a crucial role in determining surface runoff patterns, erosion potential, sediment transport, and flood risk levels. The results of this spatial analysis are shown in **Figure 4**, which presents the distribution of soil (**Figure 4a**) and landform (**Figure 4b**) in the Tarusan Watershed.

The analysis results in **Figure 4** above indicate that the Tarusan Watershed is dominated by Oxisols and Ultisols soil types (**Figure 4a**). Oxisols cover approximately 45% of the watershed area, while Ultisols cover around 30%. These soil types are highly susceptible to erosion and have low infiltration capacity, which increases surface runoff and sediment transport (Namdar & Pelko, 2009). In contrast, Entisols (15%), Histosols (5%), and Inceptisols (5%) are distributed in specific areas, mainly in the midstream and downstream regions. Among these soil types, Ultisols have the highest flood hazard score (50), followed by Entisols (40), reflecting their critical role in generating sediment and exacerbating flood risks downstream. For more details, please see **Table 7.**

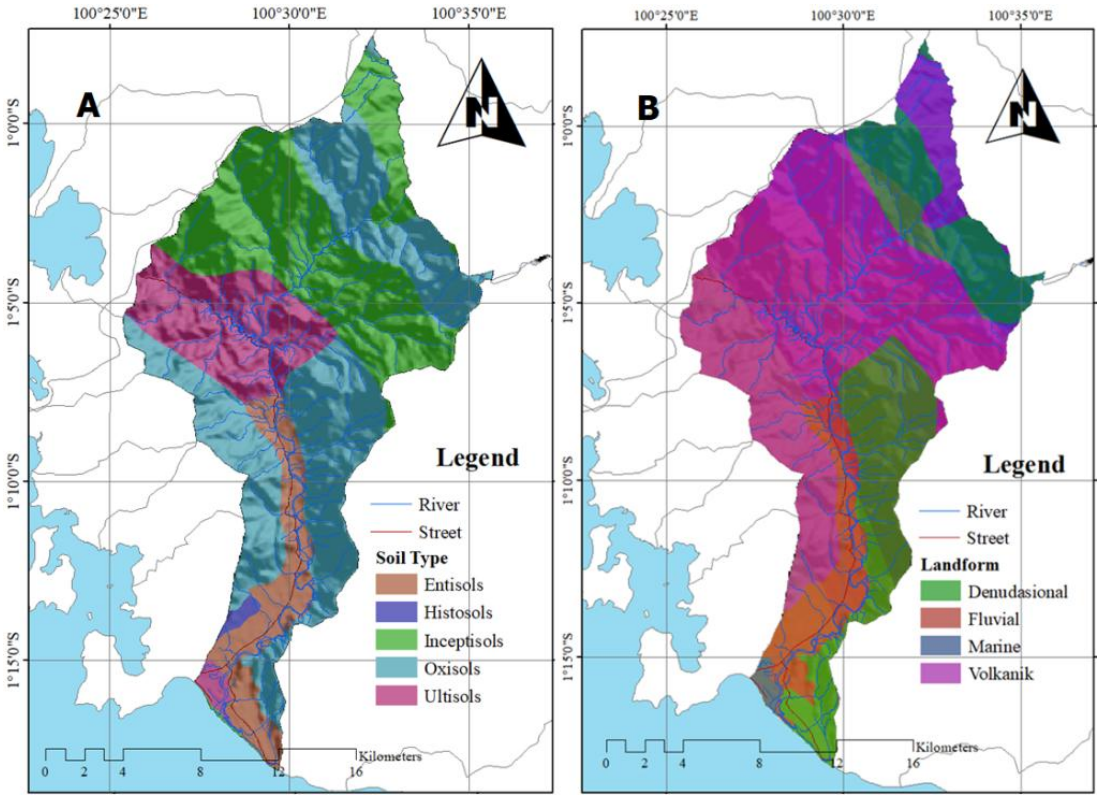

Fig. 4. Map of Soil Types (a) and Landforms (b) in the Tarusan Watershed.

Table 7.

Soil classification and flood hazard score in the Tarusan Watershed.

Soil Type	Area (%)	Score
Ultisols	30	50
Entisols	15	40
Histosols	5	30
Oxisols	45	20
Inceptisols	5	10

Source: Results of data analysis 2023.

Meanwhile, the landform classification (**Figure 4b**) shows that the Tarusan Watershed consists of five primary landform types: Denudational (35%), Structural (25%), Fluvial (20%), Marine (10%), and Volcanic (10%). Fluvial and Marine landforms, primarily located along river systems and the southern coastal area, are particularly vulnerable to flooding due to their low elevation and function as sediment deposition zones (Hoch et al., 2019).

Marine landforms have the highest flood hazard score (50) due to their proximity to estuarine systems and high groundwater influence, while Fluvial landforms have a score of 40. In contrast, Denudational, Structural, and Volcanic landforms in the upstream areas have lower scores but contribute significantly to sediment production and downstream siltation. For more details, please see **Table 8** below.

Table 8.

Landform classification and flood hazard score in the Tarusan Watershed.

Landform Type	Area (%)	Score
Marine	10	50
Fluvial	20	40
Denudational	35	10
Structural	25	10
Volcanic	10	10

Source: Results of data analysis 2023.

The combination of highly erodible soil types (Ultisols and Entisols) and flood-prone landforms (Marine and Fluvial) in the Tarusan Watershed creates critical zones that require priority attention in flood hazard mitigation planning. These fragile physical conditions, when combined with unsustainable land conversion and agricultural expansion, further increase the risk of land degradation, soil erosion, and sediment transport to downstream areas. Conservation strategies should focus on 1) Reforestation of erosion-prone upstream areas; 2) Restoration of riparian buffer zones; 3) Implementation of soil conservation techniques; and 4) Sustainable land-use management practices. Community-based participation and institutional collaboration are also important to support the successful implementation of conservation programs, especially in promoting local awareness and adaptive capacity. These measures are essential to reduce surface runoff, control sedimentation, and enhance the resilience of the Tarusan Watershed to flood disasters, in line with Eco-DRR and NBS approaches (Debele et al., 2019).

4.3. Land Use and Geological Formations

Land use and geological formation represent essential biophysical factors that directly influence flood hazard conditions within the Tarusan Watershed. The integration of these parameters in a GIS-based analysis provides critical insights into the relationship between land cover dynamics, watershed degradation, and flood vulnerability. Land use patterns reflect the intensity of human activities within the watershed, while geological formations determine the physical properties of the landscape, including infiltration capacity, erosion potential, and sediment production.

The overlay analysis of these indicators allows for a more comprehensive assessment of flood-prone areas and the identification of priority zones for conservation and mitigation interventions. In this study, land use data were generated through a supervised classification approach using Landsat 8 OLI (2022) obtained from the USGS Earth Explorer. Pre-processing steps, including radiometric, geometric, and atmospheric corrections, were conducted to improve the accuracy of the satellite imagery. This classification identified seven land use categories (bare land, settlement, farming area, mixed garden, shrub, plantation, and forest). In addition, geological mapping at a 1:250,000 scale was used to determine the distribution of rock formations, lithology, and soil characteristics. Based on the interpretation of Landsat 8 OLI (2022) and geological mapping at a 1:250,000 scale, the spatial distribution of land use types (**Figure 5a**) and geological formations (**Figure 5b**) in the Tarusan Watershed is presented in **Figure 5** below.

An analysis of land use conditions in 2022 shows a heterogeneous landscape within the Tarusan Watershed. The upstream area is still dominated by forest cover, while the midstream and downstream regions have undergone intensive land conversion into agriculture, mixed gardens, settlements, and plantations. In terms of area coverage, forested land has decreased significantly compared to 2019 conditions. Forest areas currently cover only 21.6% of the watershed, while mixed gardens dominate with 32.7%, followed by agricultural land with 25.9%. Settlements and bare land are particularly concentrated in the midstream and downstream regions, contributing significantly to flood vulnerability. This land use change is related to population growth and the expansion of economic activities, especially agricultural development.

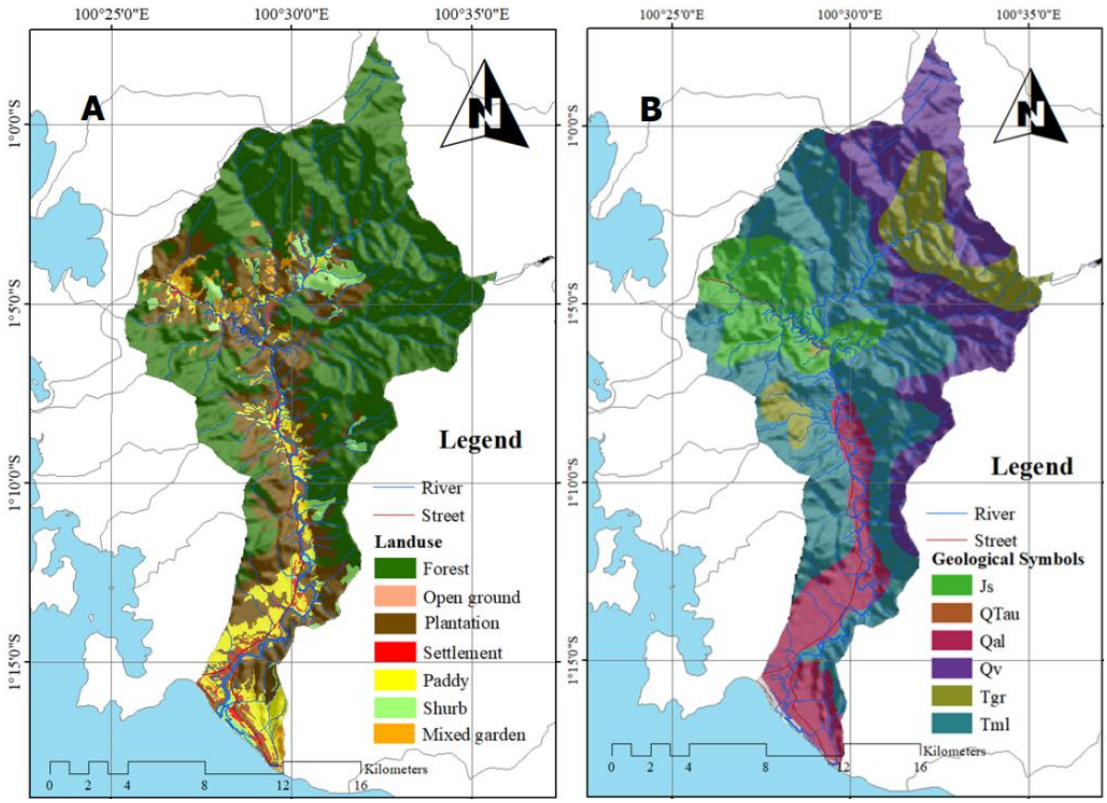

Fig. 5. Map of land use (a) and geological (b) in the Tarusan watershed.

The reduction of forest areas and increase of impermeable surfaces in settlements have reduced the watershed's ability to retain water, triggering more runoff, erosion, and sedimentation. These conditions directly exacerbate flooding in downstream areas. For more details, please see **Table 9** below.

Table 9.

Land use types and flood hazard scores in the Tarusan Watershed.

Land Use Type	Area (%)	Flood Hazard Score
Forest	21.6	10
Mixed Garden	32.7	30
Agriculture/Farming	25.9	40
Settlement	9.8	40
Shrub	6.7	30
Bare Land	2	50
Plantation	1.3	20

Source: Results of data analysis 2023.

The highest flood hazard score is found in bare land (50 points), followed by settlement and agricultural areas (40 points). These land uses contribute to increased surface runoff, decreased infiltration, and accelerated flooding, especially in riverine and downstream areas. On the other hand, forest cover serves as a critical component in flood mitigation due to its ability to absorb water, stabilize slopes, and reduce erosion (Akhter & Hewa, 2016; Chen & Tfwala, 2018; Febriandi et al., 2025).

In particular, the loss of forest and vegetation cover in upstream areas has intensified watershed degradation and heightened flood risk in lower zones. Human activities, such as land clearing, agricultural expansion, and infrastructure development, have significantly altered the natural hydrological cycle, increasing vulnerability to flood hazards. From the geological perspective, **Figure 5b** shows that the Tarusan Watershed consists of six primary geological formations. Alluvium (Qal) deposits are dominantly found in the downstream floodplain areas and are highly vulnerable to flooding due to their loose sedimentary characteristics. Conversely, granite (Tgr) and quaternary volcanic (Qv) formations found in upstream regions exhibit lower flood susceptibility. For more details, please see **Table 10** below.

Table 10.

Geological Formations and Flood Hazard Scores in the Tarusan Watershed.

Geological Formation	Spatial Distribution	Flood Hazard Score
Alluvium (Qal)	Downstream	25
Latih (Tml)	Western & Eastern Margins	15
Jurassic Sediment (Js)	Upstream & Midstream	15
Tau Formation (QTau)	Upstream & Midstream	15
Granite (Tgr)	Upstream	5
Quaternary Volcanic (Qv)	Upstream	5

Source: Results of data analysis 2023.

The integration of land use and geological formations highlights the spatial variability of flood hazard conditions in the Tarusan Watershed. The highest flood vulnerability is concentrated in the downstream regions, where intensive land use changes and the presence of alluvium deposits exacerbate flood risks. To minimize flood impacts, watershed management strategies must focus on 1) Strengthening Forest protection in upstream areaS; 2) Implementing erosion control and soil conservation in midstream zones; 3) Restoring riparian buffer zones; 3) Regulating land use changes, especially in floodplain areas; and 4) Integrating land use planning with geological risk mapping. These efforts are essential to support sustainable watershed management while ensuring the balance between environmental conservation and socio-economic development.

4.4. Flood Hazard Zoning

The delineation of flood-prone zones in the Tarusan Watershed was conducted using a weighted scoring method integrated with GIS-based spatial analysis. This method combines six primary biophysical indicators (rainfall, slope, landform, land use, soil type, and geological formation). Each indicator was classified into sub-indicators, weighted according to their relative importance, and assigned specific scores. The total composite score for each spatial unit (grid) was calculated by multiplying the indicator weight with its corresponding sub-indicator score. This approach allows for a comprehensive and objective assessment of flood risk based on the spatial variability of natural and anthropogenic factors across the watershed. It also helps to prioritize areas for intervention based on their hazard levels. The final score ranges from 65 (lowest hazard) to 325 (highest hazard). To classify flood hazard zones, Eq. 1 was applied to generate class intervals of 86, resulting in three hazard classes (low, medium, and high). The spatial distribution of these flood hazard zones is presented in **Figure 6** below. **Figure 6** shows that flood-prone areas in the Tarusan Watershed are closely correlated with the spatial interaction of biophysical characteristics and land use patterns. The classification results indicate:

1) High Hazard Zone (22% of the watershed, 65.95 km²) concentrated in downstream and lowland areas along the main river corridors. Influenced by flat slopes, high rainfall, alluvium deposits (Qal), and intensive human activities (agriculture and settlements). Similar findings were reported by Barrocu & Eslamian (2022), who found that downstream zones with loose sediment and human pressures are highly vulnerable to flooding;

2) Medium Hazard Zone (58% of the watershed, 174.16 km²) dominant in the midstream region. Characterized by moderate slopes, mixed land uses (gardens and farming), and geological diversity.

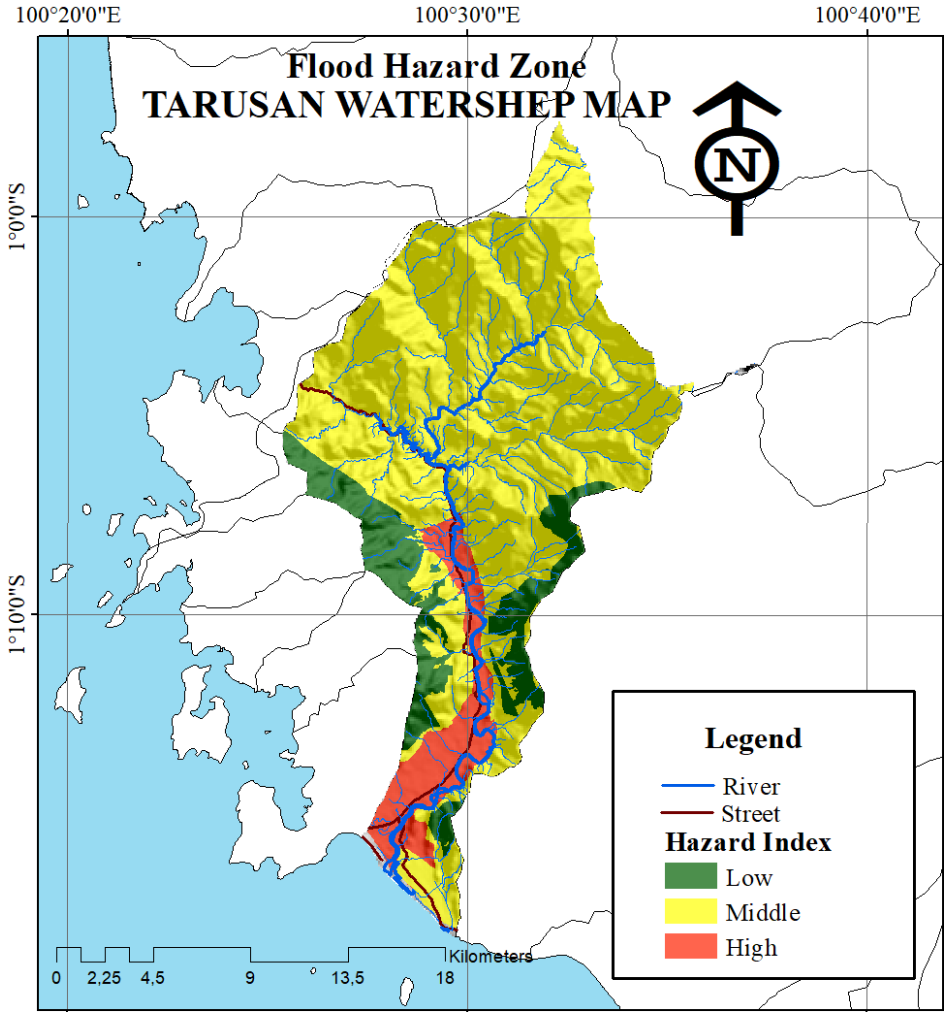

Fig. 6. Map of The Flood Hazard Zone Map in the Tarusan Watershed.

Aligned with findings of Robertella (2010), who emphasized that transitional slopes combined with land conversion activities lead to increased runoff; and 3) Low Hazard Zone (20% of the watershed, 60.16 km²) located in the upstream region with steep slopes, dense forest cover, and resistant geological formations (Granite-Tgr and Volcanic-Qv). This confirms the protective role of forests in reducing runoff and controlling peak discharge, as supported by Sakals et al. (2006). For more details, please see **Table 11.**

The distribution of flood hazard zones in the Tarusan Watershed reflects the interaction of environmental conditions, land cover changes, and geological formations. The results align with previous studies that emphasize the importance of combining structural factors (topography and geology) with non-structural factors (land use and rainfall) for accurate flood hazard assessment. Studies such as Tehrany et al. (2014) in Malaysia; Mohammadifar et al. (2023) in Ghana confirm the effectiveness of integrated geospatial modeling approaches, such as the use of GIS-based multi-criteria evaluation and machine learning, in accurately delineating flood susceptibility zones by combining both structural variables (e.g., slope, elevation, and drainage density) and non-structural factors (e.g., land use, rainfall intensity, and human activity).

Table 11.

Flood Hazard Zone Classification in the Tarusan Watershed.

Flood Hazard Class	Score Interval	Area (km²)	Area (%)	Recommended
Low Hazard	65 – 115	60.16	20	Forest protection, reforestation with native species, check dams, micro-catchments
Medium Hazard	116 – 237	174.16	58	Agroforestry, vegetative buffer strips, contour trenching, sustainable farming practices
High Hazard	238 – 325	65.95	22	Riparian buffer zones, infiltration trenches, retention ponds, settlement zoning regulation

Source: Results of data analysis 2023.

These methods have proven particularly valuable in tropical and developing regions, where rapid land cover change intensifies flood risks. Similarly, Samela et al. (2025) in Italy and Crăciun et al. (2022) in Romania demonstrated that terrain morphology, vegetation cover, and hydrological dynamics significantly influence flood-prone areas. Their findings emphasize the necessity of integrating physical watershed characteristics with anthropogenic drivers to produce realistic and actionable flood hazard maps. Such international evidence reinforces the relevance and applicability of a hybrid structural–non-structural mitigation strategy as proposed for the Tarusan Watershed. Flood hazard mitigation strategies in this watershed should focus on:

1) Reforestation and forest conservation in upstream regions;
2) Slope stabilization and erosion control in midstream areas;
3) Regulation of land use change, especially in downstream floodplain zones; and
4) Integrated watershed management combining structural and non-structural approaches.

Each of these strategies should be supported by specific conservation techniques tailored to the hazard level of the area, such as forest protection and check dams in low-risk zones, agroforestry and contour trenches in moderate-risk areas, and riparian buffers and retention ponds in high-risk floodplains. The approach follows the Indonesian Government's policy on disaster risk reduction (Law No. 24/2007), BNPB's implementation of NBS, and sustainable watershed management practices (Hadi, 2020).

4.5. Integration of AHP-Based Strategies with Flood Hazard Zoning Results in the Tarusan Watershed

The integration between the flood hazard zoning results (**Figure 6**) and the priority strategies produced from the AHP method (**Figure 7** based on **Table 12**) provides a comprehensive framework for designing effective flood disaster mitigation and watershed conservation strategies in the Tarusan Watershed. The flood hazard mapping analysis classified the watershed into three hazard zones (low, medium, and high) based on the weighted scoring of six main indicators (rainfall, slope, landform, land use, soil type, and geological formation).

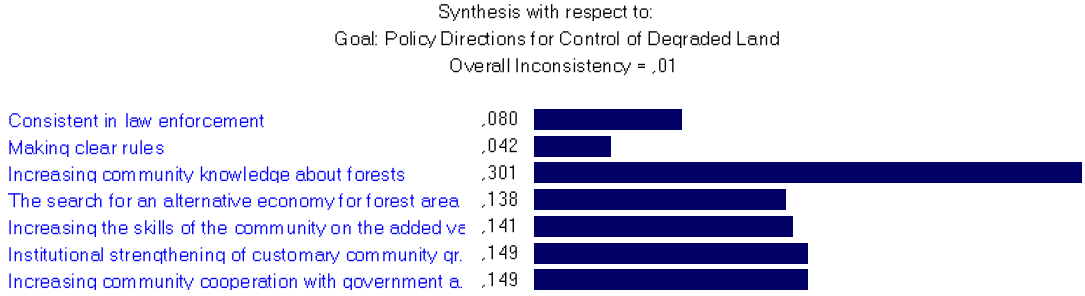

Fig. 7. Priority Weight of Flood Disaster Mitigation Strategies using the AHP in the Tarusan Watershed.

Each zone exhibits different environmental characteristics, requiring different strategic interventions. Meanwhile, the AHP analysis involved 25 experts from various relevant institutions in the Pesisir Selatan Regency. The evaluation identified seven strategic alternatives (A1–A7) under three main strategic pillars (Regulation, Education, and Institutional Strengthening). The highest priority strategy was increasing community knowledge about forests (A3), followed by strengthening customary community institutions (A6), and enhancing community-government collaboration (A7).

Table 12.

Priority Ranking of Flood Disaster Mitigation Strategies in the Tarusan Watershed.

Strategic Action	Code	Priority Weight	Rank
Increasing community knowledge about forests	A3	0.301	1
Strengthening customary community institutions	A6	0.149	2
Increasing community cooperation with government agencies	A7	0.149	2
Enhancing community skills in forest product utilization	A5	0.141	4
Promoting alternative forest-based economies	A4	0.138	5
Consistent enforcement of environmental regulations	A1	0.080	6
Establishment of clear and transparent rules	A2	0.042	7

The integrated analysis shows a strong correlation between the AHP-based strategies and the specific conditions of each flood hazard zone within the Tarusan Watershed. The recommended strategies are summarized in **Table 13** below.

Table 13.

Strategic Relationship between AHP Priority Strategies and Flood Hazard Zones in the Tarusan Watershed.

Flood Hazard Zone	AHP Priority Strategy	Explanation
Upstream (Low Hazard)	A3, A6	Reinforce environmental literacy and participatory forest governance to maintain protective forest functions. Forest conservation is crucial to reduce runoff and prevent land degradation.
Midstream (Medium Hazard)	A4, A5, A7	Promote alternative livelihoods and improve community skills in sustainable forest product utilization. Encourage collaboration between local communities and government to stabilize land use and control erosion.
Downstream (High Hazard)	A1, A2, A7	Strengthen regulation enforcement, formulate clear and transparent land use rules, and foster community-government synergy to manage flood risks effectively in high-risk areas dominated by settlements and agricultural activities

This strategic integration confirms that flood disaster mitigation in the Tarusan Watershed cannot rely solely on structural engineering approaches (such as embankments or dams) but must be strengthened by non-structural measures through community-based efforts, education, and institutional empowerment. In the upstream regions, classified as low hazard zones, the main concern is maintaining forest cover and preventing further degradation through environmental education (A3) and strengthening local institutions (A6). In the midstream areas, categorized as medium-hazard zones, the focus should be on reducing forest exploitation by improving local skills (A5), promoting alternative economies (A4), and enhancing collaboration with the government (A7). Meanwhile, in downstream regions categorized as high hazard zones, regulation and law enforcement (A1 and A2) are essential to control settlement expansion and prevent land use conversion. Community involvement (A7) is also critical in improving adaptive capacity and disaster preparedness.

This finding supports previous study and Indonesian government policies, particularly Law No. 24/2007 concerning "Disaster Management" and Presidential Regulation No. 87/2017 concerning "Social Forestry", which emphasize the importance of Community-based Disaster Risk Reduction (CBDRR) and sustainable watershed management.

5. CONCLUSIONS

This study concludes that the physical and environmental characteristics of the Tarusan Watershed play a crucial role in shaping its hydrological response and vulnerability to flood disasters. A spatial analysis of slope gradients and rainfall intensity shows that the upstream and midstream regions are predominantly characterized by steep to very steep slopes, covering approximately 63% of the total watershed area. These steep slopes significantly increase surface runoff, accelerate erosion, and reduce infiltration capacity, particularly in areas affected by deforestation and land-use change. Moreover, the northern and central zones receive high annual rainfall, ranging from 4,000 mm to over 5,000 mm, which intensifies peak runoff during extreme weather events. Soil and landform analysis further supports the identification of high-risk flood zones. Oxisols and Ultisols dominate the watershed's soil types, accounting for 45% and 30%, respectively. These soils have low infiltration capacity and high erodibility, contributing to rapid water movement and downstream sedimentation.

The presence of fluvial and marine landforms in low-lying areas, especially in the southern coastal region, increases flood susceptibility due to their function as sediment deposition zones and their proximity to estuarine systems. Land use classification reveals significant landscape transformation. Forested areas now cover only 21.6% of the watershed, while mixed gardens (32.7%) and agricultural land (25.9%) have expanded, particularly in the midstream and downstream regions. Settlements and bare land often located near riverbanks contribute heavily to increased flood risk due to impervious surfaces and land degradation.

Flood hazard zoning, derived from a weighted scoring model using six indicators (slope, rainfall, soil, landform, geology, and land use), classifies the watershed into three zones: low (20%), medium (58%), and high (22%) hazard. High-risk zones are concentrated downstream, while low-risk zones lie upstream with steep terrain and dense forest cover.

Integrating these findings with AHP-based strategic priorities shows that different zones require tailored interventions. In upstream areas, priority strategies include increasing environmental knowledge (A3) and strengthening local institutions (A6). Midstream areas benefit from promoting alternative livelihoods (A4), enhancing community skills (A5), and fostering cooperation (A7). Downstream areas require strong regulation (A1), clear land-use rules (A2), and community-government synergy (A7). Where the recommendations from the results of this research are 1) To enhance flood resilience and ensure sustainable watershed management, we recommend; 2) Community-based environmental education and awareness programs in upstream zones; 3) Development of forest-based economies and skill-building programs in midstream areas; 4) Strengthened enforcement of land use regulations and collaborative governance in downstream regions; and 5) Integration of NBS and Eco-DRR into local policy frameworks.

ACKNOWLEDGEMENTS

This article is based on the results of an annual collaborative study project conducted by lecturers at Universitas Negeri Padang (UNP). We extend our sincere gratitude to all parties who participated in the interviews and data collection activities, particularly the government of Pesisir Selatan Regency for their support and cooperation, and support for science and data from the National Research and Innovation Agency (BRIN).

REFERENCES

Abo-Salim, A. A. A. F. M. (2023). *Evaluating and improving the accuracy of global digital elevation models*. (Master's thesis) Benha University, Faculty of Engineering at Shoubra, Geomatics Engineering Department, Cairo, Egypt.

Akhter, M. S., & Hewa, G. A. (2016). The use of PCSWMM for assessing the impacts of land use changes on hydrological responses and performance of WSUD in managing the impacts at Myponga Catchment, South Australia. *Water, 8*(11), 511. https://doi.org/10.3390/w8110511

Barlian, E., Umar, I., Anwar, S., Lanin, D., & Putra, A. (2024). Mitigation of flood hazard areas in Antokan Watershed. *AIP Conference Proceedings*, 3001(1), Article 080042. https://doi.org/10.1063/5.0192510

Barrocu, G., & Eslamian, S. (2022). Geomorphology and flooding. In S. Eslamian & F. Eslamian (Eds.), *Flood Handbook* (1st ed., 32). CRC Press.

Bernardo, N., Watanabe, F., Rodrigues, T., & Alcantara, E. (2017). Atmospheric correction issues for retrieving total suspended matter concentrations in inland waters using OLI/Landsat-8 image. *Advances in Space Research, 59*(9), 2335-2348.

Cea, L., & Costabile, P. (2022). Flood risk in urban areas: Modelling, management and adaptation to climate change. *Hydrology*, 9(3), 50. https://doi.org/10.3390/hydrology9030050

Chen, S.C., Tfwala, S., Wu, T.-Y., Chan, H.-C., & Chou, H.-T. (2018). A hooked-collar for bridge piers protection: Flow fields and scour. *Water, 10*(9), 1251. https://doi.org/10.3390/w10091251

Cheng, J. D., Lin, L. L., & Lu, H. S. (2002). Influences of forests on water flows from headwater watersheds in Taiwan. *Forest Ecology and Management*, 165(1–3), 11–28. https://doi.org/10.1016/S0378-1127(01)00626-0

Choi, K. H. (2021). *Improving the Analytical Hierarchy Process Methodology Through Implementation of Consistency Ratio-Based Weights for Multi-Expert Judgement* (Doctoral praxis, The George Washington University). The George Washington University.

Crăciun, A., Costache, R., Bărbulescu, A., Pal, S. C., Costache, I., & Dumitriu, C. Ș. (2022). Modern techniques for flood susceptibility estimation across the deltaic region (Danube Delta) from the Black Sea's Romanian sector. *Journal of Marine Science and Engineering*, *10*(8), 1149. https://doi.org/10.3390/jmse10081149

Darghouth, S., Ward, C., Gambarelli, G., Styger, E., & Roux, J. (2008). *Watershed management approaches, policies, and operations: Lessons for scaling up* (Water Sector Board Discussion Paper Series No. 11). The World Bank, Washington, DC.

Debele, S. E., Leo, L. S., Kumar, P., Sahani, J., Ommer, J., Bucchignani, E., Vranić, S., Kalas, M., Amirzada, Z., Pavlova, I., Shah, M. A. R., Gonzalez-Ollauri, A., & Di Sabatino, S. (2023). Nature-based solutions can help reduce the impact of natural hazards: A global analysis of NBS case studies. *Science of The Total Environment*, 902, 165824. https://doi.org/10.1016/j.scitotenv.2023.165824

Dewata, I., & Umar, I. (2019). Management of flood hazard areas in Pasaman river basin of West Pasaman Regency, West Sumatra Province. *International Journal of GEOMATE*, 17(64), 230–237. https://doi.org/10.21660/2019.64.64420

Faral, A., Lavigne, F., Sastrawan, W. J., Suryana, I. G. P. E., Schrikker, A., Pageh, M., Made, A. D., Kesiman, M. W. A., Malawani, M. N., & Hadmoko, D. S. (2024). Deadliest natural disaster in Balinese history in November 1815 revealed by Western and Indonesian written sources. *Natural Hazards*, 120, 12001–12041. https://doi.org/10.1007/s11069-024-06719-1

Febriandi., Fatimah, S., Triyatno, T., Hermon, D., Putra, A., Mutmainah, H., Arifin, T., & Akhwady, R. (2025). Predicting of land cover changes until 2030 and assessing sustainability status in the Mandeh region, Indonesia. *Geographia Technica, 20*(1), 263–280. https://doi.org/10.21163/GT_2025.201.18

Griffiths, J., Borne, K. E., Semadeni-Davies, A., & Tanner, C. C. (2024). Selection, planning, and modelling of nature-based solutions for flood mitigation. *Water*, 16(19), 2802. https://doi.org/10.3390/w16192802

Hadi, S. (2020). Disaster management in the implementation of the 2030 Sustainable Development Goals in Indonesia. *The Journal of Indonesia Sustainable Development Planning, 1*(1), 105-111. https://doi.org/10.46456/jisdep.v1i1.49

Hamada, J.-I., Yamanaka, M. D., Mori, S., Tauhid, Y. I., & Sribimawati, T. (2008). Differences of rainfall characteristics between coastal and interior areas of central western Sumatera, Indonesia. *Journal of the Meteorological Society of Japan. Ser. II*, 86(5), 593–611. https://doi.org/10.2151/jmsj.86.593

Hoch, J. M., Eilander, D., Ikeuchi, H., Baart, F., & Winsemius, H. C. (2019). Evaluating the impact of model complexity on flood wave propagation and inundation extent with a hydrologic–hydrodynamic model coupling framework. *Natural Hazards and Earth System Sciences*, 19(8), 1723–1735. https://doi.org/10.5194/nhess-19-1723-2019

Kaiser, B., Pitafi, B., Roumasset, J., & Burnett, K. (2008). The economic value of watershed conservation. *Coastal Watershed Management; Fares, A., El-Kadi, AI, Eds*, 299-329.

Javas, J., Rosebianto, A. S. B., Sihombing, Y. I., Farid, M., Adityawan, M. B., Kuntoro, A. A., Suwarmana, R., & Yosa, I. M. (2024). Open-access digital elevation model (DEM) selection for flood inundation modelling using HEC-RAS in Capital City of Nusantara. *IOP Conference Series: Earth and Environmental Science, 1343*(1), 012036. https://doi.org/10.1088/1755-1315/1343/1/012036

Lin, C., Xiong, J., Ma, R., & Zhu, C. (2021). Identifying the critical watershed regions creating lake nutrient enrichment (SLRs) based on a watershed-lake integrated perspective – A case study of Chaohu Lake Basin, China. *Ecological Indicators*, 121, 107037. https://doi.org/10.1016/j.ecolind.2020.107037

Marimin, M. N., & Maghfiroh, N. (2010). Application of decision making techniques in supply chain management. *Bogor (ID): IPB Pr*.

Merz, B., Blöschl, G., Vorogushyn, S., Dottori, F., Aerts, J. C. J. H., Bates, P., Bertola, M., Kemter, M., Kreibich, H., Lall, U., & Macdonald, E. (2021). Causes, impacts and patterns of disastrous river floods. *Nature Reviews Earth & Environment*, 2, 592–609. https://doi.org/10.1038/s43017-021-00159-2

Mohammadifar, A., Gholami, H., & Golzari, S. (2023). Novel integrated modelling based on multiplicative long short-term memory (mLSTM) deep learning model and ensemble multi-criteria decision making (MCDM) models for mapping flood risk. *Journal of Environmental Management, 345*, 118838. https://doi.org/10.1016/j.jenvman.2023.118838

Nafli, T. A., Teklu, M. A., & Alemu, E. A. (2024). Enhancing watershed management in developing countries: Insights from Ethiopia. *Discover Sustainability, 5*(1), 53. https://doi.org/10.1007/s43621-024-00135-y

Namdar, A., & Pelko, M. K. (2009). Numerical analysis of soil bearing capacity by changing soil characteristics. *Fracture and Structural Integrity, 3*(10), 38-42. https://doi.org/10.3221%2FIGF-ESIS.10.05

Pambudi, A. S. (2015). Watershed management in Indonesia: A regulation, institution, and policy review. *The Indonesian Journal of Development Planning, 3*(2), 185–198.

Pambudi, A. S., & Kusumanto, T. (2023). Water resources governance in Indonesia towards environmental sustainability along with social and economic development. In *Environmental Governance in Indonesia* (pp. 289–311). Cham: Springer International Publishing. https://doi.org/10.1007/978-3-031-37920-5_14

Putra, A., Triyatno., Darwis, R., Dewata, I., Tanto, T. A., Mustapha, M. A., Razi, P., & Zainul, R. (2023). Suitability of Mangrove Ecosystems as a Protected Zone Based on Land-Use Changes. *Physical Oceanography, 30*(6), 866-881.

Robertella, K. (2010). *A heuristic for local land planning: Linking ecological function and policy in context to Charlotte, North Carolina* (Master's thesis, James Madison University). James Madison University

Saaty, T.L. (1983). Decision Making for Leaders. The Analitical Hierarchy Proces for Decision in Complex World. California : Lifetime Learning Publication, Belmont

Sakals, M. E., Innes, J. L., Wilford, D. J., Sidle, R. C., & Grant, G. E. (2006). The role of forests in reducing hydrogeomorphic hazards. *Forest Snow and Landscape Research, 80*(1), 11–22.

Samela, C., Maialetti, M., Doukas, Y. E., Matarazzo, N., D'Emilio, M., Lanfredi, M., & Coluzzi, R. (2025). River basins and rural districts: Toward regional planning for Italian watersheds with a broader European view. In C. Ciaccioli & V. Imbrenda, *Local development and socio-environmental systems*. 1st ed.. 14.

Schumann, G. J.-P., & Andreadis, K. M. (2016). A method to assess localized impact of better floodplain topography on flood risk prediction. *Advances in Meteorology*, 2016, Article 6408319. https://doi.org/10.1155/2016/6408319

Sunarto, H., Nugroho, H. S. W., Suparji, S., Rahayu, T. P., Sulikah, S., Sumasto, H., & Khambali, K. (2025). Strengthening disaster-resilient villages through participatory approaches: Policy recommendations for village governments. *Health Dynamics, 5*(1), 1–6. https://doi.org/10.33846/hd20405

Suwarto, S., Wibowo, A., Lestari, E., & Rahayu, R. (2022). Revitalization of local wisdom in the conservation of the upstream watershed region, on Java Island, Indonesia. *E3S Web of Conferences, 361*, 03019. https://doi.org/10.1051/e3sconf/202236103019

Tehrany, M. S., Pradhan, B., & Neamah Jebur, M. (2014). Flood susceptibility mapping using a novel ensemble weights-of-evidence and support vector machine models in GIS. *Journal of Hydrology*, *512*, 332–343. https://doi.org/10.1016/j.jhydrol.2014.03.008

Thapa, P. S., Chaudhary, S., & Dasgupta, P. (2022). Contribution of integrated watershed management (IWM) to disaster risk reduction and community development: Lessons from Nepal. *International Journal of Disaster Risk Reduction*, 76, 103029. https://doi.org/10.1016/j.ijdrr.2022.103029

Tang, J., Li, Y., Cui, S., Xu, L., Hu, Y., Ding, S., & Nitivatttananon, V. (2021). Analyzing the spatiotemporal dynamics of flood risk and its driving factors in a coastal watershed of southeastern China. *Ecological Indicators*, 121, 107134. https://doi.org/10.1016/j.ecolind.2020.107134

Triyatno., Berd, I., Idris, I., & Putra, A. (2019). Hazard analysis and social vulnerability to predict the loss population is affected by natural disaster of landslides in the Pesisir Selatan District of West Sumatra. *IOP Conference Series: Earth and Environmental Science*, 314(1), 012031. https://doi.org/10.1088/1755-1315/314/1/012031

Triyatno., Berd, I., Idris, I., Herman, D., & Putra, A. (2020). Hazards and morphometry to predict the population loss due to landslide disasters in Koto XI Tarusan - Pesisir Selatan. *International Journal of GEOMATE*, 19(76), 98–103. https://doi.org/10.21660/2020.76.ICGeo12

Triyatno., Berd, I., & Idris. (2023). Spatial model of flood hazard due to land cover change in the Tarusan Watershed, West Sumatra – Indonesia. *International Journal of GEOMATE*, 25(108), 21–29. https://doi.org/10.21660/2023.108.3774

Umar, I., Dewata, I., Barlian, E., Anwar, S., & Suarti, Y. (2019). Priority selection of residential development areas with flood hazard in Limapuluh Kota District, West Sumatra. *International Journal of GEOMATE*, 16(55), 138–144. https://doi.org/10.21660/2019.55.39291

Umar, I., & Triyatno. (2024). Flood hazard mitigation at Tarusan Watershed, South Pesisir District, West Sumatera Province. *Jurnal Pengelolaan Sumberdaya Alam dan Lingkungan*, 14(1), 101–108. http://dx.doi.org/10.29244/jpsl.14.1.101

Viguera, B., Madrigal-Ballestero, R., Pacay, E., & Navarrete Chacón, G. (2024). Alternatives for improving Payment for Ecosystem Services (PES) effectiveness on water resources. *Journal of Soil and Water Conservation, 79*(1), 5A–9A. https://doi.org/10.1080/03650340.2023.2287331

.

ASSESSING THE SUSTAINABILITY OF LAGOON-BASED ENVIRONMENTAL WATERFRONT IN THE COASTAL ZONE OF PARIAMAN CITY, INDONESIA

***Olivia OKTORIE*[1], *Indang DEWATA*[2], *Eri BARLIAN*[3], *Dedi HERMON*[4*], *Aprizon PUTRA*[5]**

DOI: 10.21163/GT_2025.202.09

ABSTRACT

This study aims to assess the environmental characteristics and sustainability potential of lagoon areas along the coastal zone of Pariaman City, Indonesia, for environmental waterfront development. Five natural lagoons, such as Nareh, Manggung, Apar, Talao, and Karan Aur, were selected based on geomorphological analysis and spatial mapping. The study adopts a multi-method approach combining weighted indicator-based environmental assessment and Multidimensional Scaling (MDS) to evaluate sustainability across economic, social, and environmental dimensions. Thirteen environmental indicators were evaluated by six experts using a weighted Likert-scale scoring system. The Intraclass Correlation Coefficient (ICC) analysis confirmed high inter-rater reliability (ICC = 0.82). Results showed that Talao and Karan Aur achieved "Good" environmental quality, while Nareh, Manggung, and Apar were rated "Fair". Key influencing indicators included water quality and riparian buffer vegetation. Spatial zoning analysis further classified development areas into littoral, terrestrial, and urban activity zones based on ecological and planning criteria. Sustainability assessment using MDS identified seven leverage indicators (local revenue, job diversification, accessibility, education, community institutions, environmental conservation, and biodiversity). These indicators were dominant in shaping the coastal development strategy and supported by high model validity (RSQ > 0.74). The study concludes that Environmental Waterfront development in Pariaman City requires integrated strategies that balance ecological integrity, social inclusion, and economic growth. Specific mitigation measures, namely vegetative, structural, and regulatory, are recommended to elevate the environmental quality of all lagoon sites. Findings offer a strategic foundation for sustainable coastal governance and provide a replicable model for similar regions across Indonesia's western coastline.

Key-words: *Coastal zone; Lagoon; Multidimensional Scaling; Pariaman; Waterfront.*

1. INTRODUCTION

Coastal area management has become an increasingly complex and urgent global concern, particularly amid growing pressures of urbanization, climate change, and intensified activities. As transitional zones between land and sea, coastal areas possess high ecological and economic value. However, they remain highly vulnerable to environmental degradation, including coastal erosion, tidal flooding, and unplanned land use (Febriandi et al., 2025). In many cities worldwide, including in Indonesia, the development of waterfront areas has emerged as a key strategy for achieving sustainable coastal management. This approach seeks to holistically integrate ecological, social, and economic functions within waterfront design (Wrenn, 2023; Breen & Rigby, 1993). Cities such as Pontianak, Semarang, and Banda Aceh (Ulee Lheue) have adopted diverse models of waterfront development, ranging from recreational and historical concepts to disaster mitigation-based designs (Rukayah et al., 2018; Uswah & Wang, 2021; Setiawan & Zalfa, 2023).

---

[1]*Doctoral Program of Environmental Science, Universitas Negeri Padang, Indonesia, (OO) ppg026@unp.ac.id*
[2]*Department of Chemistry, Universitas Negeri Padang, Padang, Indonesia, (ID) indangdewata@fmipa.unp.ac.id*
[3]*Department of Coaching, Universitas Negeri Padang, Padang, Indonesia, (EB) e.barlian@fik.unp.ac.id*
[4]*Master Program of Geography Education, Universitas Negeri Padang, Padang, Indonesia, (DH)*
[5]*National Research and Innovation Agency, Cibinong-Bogor, Indonesia, (AP)apri024@brin.go.id*
[*]*Corresponding author: (DH) dedi.hermon@fis.unp.ac.id*

In the Indonesian context, coastal zoning and waterfront development are regulated under Law No. 27/2007 on the Management of Coastal Areas and Small Islands, as amended by Law No. 1/2014. This regulation governs the utilization of coastal and small island marine resources, including provisions for coastal water use permits (Hermon et al., 2018; Prarikeslan et al., 2020; Putra et al, 2023). Furthermore, Ministerial Regulation No. 17/2008 explicitly states that coastal areas are conservation zones where the sustainability of natural resources must be preserved (Suedi et al., 2020; Megawati et al., 2023). On a broader national planning scale, Government Regulation No. 47/1997 concerning the National Spatial Planning Framework identifies 516 strategic cities across Indonesia, 216 of which are classified as waterfront cities located along coasts, rivers, or lakes (Winter, 2019; Kurniati, 2013). This highlights the immense spatial and ecological significance of waterfront zones in Indonesia. However, many of these urban waterfronts have experienced functional decline due to ineffective spatial utilization and unregulated development pressure, leading to the loss of their environmental and socio-economic advantages. Such as Pontianak and Banda Aceh, have begun reconfiguring their waterfronts through thematic planning, many other regions remain vulnerable due to fragmented policy implementation and insufficient conservation integration (Dalila et al., 2021).

The coastal zone of Pariaman City reflects a governance crisis in spatial planning (Oktorie et al., 2019; Hermon et al., 2020). With approximately 12.7 km of coastline and four river basins, Batang Mangguang, Batang Piaman, Batang Jirak, and Batang Mangau, the city is geographically diverse. Three of its four subdistricts, North Pariaman, Pariaman Central, and South Pariaman, are coastal, whereas East Pariaman is inland (Oktorie et al., 2019). The region also features unique coastal morphology, including natural lagoons shaped by sediment deposition and longshore drift. However, it is experiencing severe coastal erosion at a rate of 1.98 m per year and significant shoreline changes between 1988 and 2024 (Hermon et al., 2019). Additionally, frequent tidal flooding in low-lying residential areas has exacerbated ecological stress and disrupted social systems in the region. The absence of conservation and mitigation-oriented spatial planning has hindered the region’s ability to support sustainable community livelihoods. One concept considered relevant and promising is the Environmental Waterfront approach (Girard et al., 2014; Permana et al., 2017). The lack of implementation of this approach in Pariaman City has led to a critical gap in sustainable coastal conservation and development efforts. The absence of scientifically based mapping of potential zones, along with weak integration of spatial data, stakeholder perceptions, and regional planning policies, highlights the necessity of this study.

This study adopts two main analytical frameworks: 1) the Intraclass Correlation Coefficient (ICC), used to assess the consistency of stakeholder perceptions regarding the characteristics of potential Environmental Waterfront zones (Lu, 2018); and 2) Multi-Dimensional Scaling (MDS), applied to identify sustainability-driving factors through multivariate analysis of ecological, spatial, and social indicators (Patawari et al., 2022). The study focuses on three core dimensions: 1) the environmental aspects, such as coastal morphology, erosion, tidal inundation, and sedimentation; 2) ecological aspects, including environmental carrying capacity and local biodiversity; and 3) social aspects, particularly stakeholder perceptions and involvement in coastal development.

The object of the study is the coastal zone of Pariaman City, with particular emphasis on five natural lagoon formations resulting from geomorphological processes, specifically longshore drift creating enclosed water bodies (Barnes, 1980; Bondesan, 2017; Putra et al., 2023). These lagoons, distributed along the coastline, were identified through field surveys and satellite imagery as areas with high potential for environmental waterfront development, either existing or in the planning phase. Furthermore, the findings are expected to inform coastal management policies and support sustainable tourism development in Pariaman City. This study aims to assess the environmental characteristics and sustainability potential of lagoon areas along the coastal zone of Pariaman City, Indonesia, for environmental waterfront development.

The novelty of this study lies in its integrative application of weighted environmental assessment and MDS to evaluate the sustainability of natural lagoons as strategic nodes for waterfront urban development. Unlike previous studies that often focus solely on visual or design-oriented aspects, this research quantitatively incorporates physical, ecological, and participatory indicators, validated

through ICC analysis. It also offers a replicable model for assessing small-scale coastal systems using localized stakeholder inputs and zoning frameworks, contributing a context-specific scientific basis for sustainable coastal urban planning in mid-sized Indonesian cities.

2. STUDY AREA

The study area is located along the coastal zone of Pariaman City, Indonesia, geographically positioned between 0° 34'30" to 0° 43'30" South Latitude and 100° 6'0" to 100° 12'0" East Longitude. This coastal region is bordered by the Indian Ocean to the west and by Padang Pariaman Regency to the east and north. The landscape is predominantly flat to gently sloping, extending parallel to the shoreline, and is highly vulnerable to coastal hazards such as erosion, tidal flooding, and tsunamis. Bathymetric conditions in the surrounding waters range from shallow (1 m) to deep (over 100 m), with depth contours on the bathymetric map indicating a gradient increasing westward and northwestward. Administratively, the study area encompasses the entire territory of Pariaman City, with a 500 m coastal buffer zone established as the main area of analysis. Spatial data used for mapping include *Satellite Pour l'Observation de la Terre* (SPOT)-6 satellite imagery from 2017, the 1985 Rupa Bumi Indonesia (RBI) topographic map, and field survey data collected in 2021. The study area is shown in more detail in **Figure 1** below.

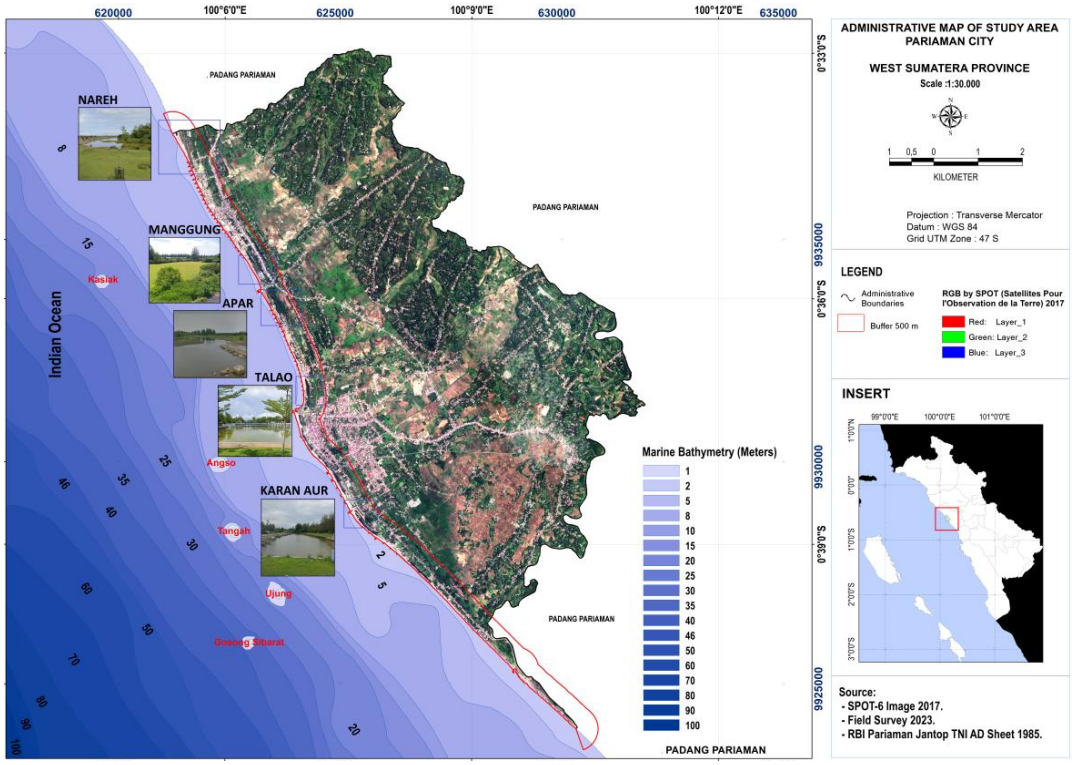

Fig. 1. Location map in the coast of Pariaman City, Indonesia.

This study focuses on five natural lagoons that are geographically distributed along the coastal zone of Pariaman City. These include Nareh Lagoon, located in Padang Birik-Birik and Nareh villages of North Pariaman Subdistrict, covering ±4.8 ha; Manggung Lagoon, situated in Manggung village (North Pariaman), covering ±0.2 ha; Apar Lagoon in Apar village (Central Pariaman), covering ±0.57 ha; Talao Lagoon in Pauh Barat village (South Pariaman), covering ±1.97 ha; and Karan Aur Lagoon, located in Karan Aur village (South Pariaman), covering ±1.24 ha.

These lagoon areas were delineated based on geomorphological features formed by longshore drift and are considered to have high ecological and planning significance for environmental waterfront development. Their spatial extent and strategic positions reflect both natural conservation value and potential for sustainable coastal-based community use.

3. METHODS

3.1. Environmental Quality Assessment Based on Weighted Indicators

This study aimed to evaluate the environmental characteristics of lagoon areas along the coast of Pariaman City, which are considered potential sites for environmental waterfront development. The assessment focused on five primary lagoons, namely Nareh, Manggung, Apar, Talao, and Karan Aur. Each site was evaluated using 13 environmental indicators representing physical, ecological, and spatial aspects through a quantitative approach. The evaluation was conducted by six stakeholders, comprising regional planners, academics, and local government representatives, using a 3-point Likert scale (1 = poor, 2 = fair, 3 = good). Each indicator was assigned a weight determined through expert judgment. The total score for each site was calculated by summing the products of the average rating and the corresponding weight of each indicator. Final scores were then classified into three categories of environmental quality, as shown in **Table 1** below.

Table 1.

Environmental Quality Categories.

Total Score	Category
2.33 – 3.00	Good
1.67 – 2.32	Fair
1.00 – 1.66	Poor

Note: Environmental quality categories are based on the average evaluation scores of lagoon environmental indicators provided by six expert assessors (Primary data, 2025).

3.2. Consistency Testing Using Intraclass Correlation Coefficient (ICC)

To support the classification process of environmental quality categories, the assessment was conducted based on a set of predefined environmental characteristic indicators. These indicators were compiled into an evaluation instrument; each assigned a specific weight based on expert input. The complete list of indicators and their respective weights is presented in **Table 2** below.

Table 2.

Environmental Characteristic Indicators and Assigned Weights according to Leyland & Groenewegen (2024).

No	Indicator	Weight	Data Source
1	Proximity to water body	0.011	Processed data
2	Access to water body	0.007	Processed data
3	Number of water body access points	0.007	Processed data
4	Function of outer buffer zone	0.053	Field observation
5	Building orientation	0.018	Field observation
6	Transport network	0.018	Processed data
7	Building height	0.015	Field observation
8	Structures near buffer zone	0.107	Processed data
9	Riparian buffer vegetation	0.192	Processed data
10	Water quality	0.288	Field observation
11	Aquatic vegetation cover	0.047	Field observation
12	Water odor and color	0.140	Field observation
13	Water body shrinkage	0.097	Environmental Agency

To ensure consistency among assessors, the ICC was calculated using the Two-Way Random Effects, Absolute Agreement model (Model B), as described by Müller & Büttner (1994). This model is appropriate for cases involving multiple raters who are considered a random sample from a larger population, all scoring the same set of items. The ICC formula is expressed as.

$$ICC = \frac{\sigma_s^2}{\sigma_s^2 + \sigma_o^2 + \sigma_e^2}$$

where:
σ_s^2: Variance between subjects (indicators)
σ_o^2: Variance between raters
σ_e^2: Random error

To evaluate the normality of the data, the Shapiro-Wilk test was performed on the residuals. If the data were not normally distributed, the Box-Cox transformation was applied before calculating the ICC. Estimation of the ICC confidence interval was performed using two methods according to Ionan et al. (2014), namely the Generalized Confidence Interval (GCI) for small to medium data, and the Modified Large Sample (MLS) for calculation efficiency in large data. The ICC interpretation can be seen in **Table 3** below.

Table 3.

ICC Value Interpretation.

ICC Value	Reliability Category
ICC > 0.75	High
0.40 ≤ ICC ≤ 0.75	Moderate
ICC < 0.40	Low

3.3. Development Zoning

Interpretation of reliability based on ICC values is the basis for assessing the consistency of assessments between assessors in evaluating environmental characteristics. After the data reliability is declared adequate, the next stage is to determine the area development strategy. One approach used in this study is development zoning based on spatial and functional context, which is divided into two main zones, namely the littoral, terrestrial, and urban activity zones (Clark, 1996; Vallega, 2001), which can be seen in **Table 4** below.

Table 4.

Development Zones according to Clark (1996) and Vallega (2001).

Zone	Description	Examples
Littoral Zone	This zone includes the water bodies (lagoons) as the focal point for environmental activities. Development focuses on water conservation, ecological education, and ecosystem-based tourism.	Coastal lagoons (Talao, Karan Aur), estuaries, river mouths.
Terrestrial Zone	This zone lies within a 100–300 m radius from the coastline, encompassing public green open spaces that function as buffers and ecological corridors. Spatial planning aligns with government regulations on coastal buffer zones.	Beachfront parks (Nareh, Manggung), dune vegetation areas, riparian greenbelts.
Urban Activity Zone	This zone covers the urban hinterland beyond the terrestrial buffer, integrating residential, commercial, and institutional uses while supporting waterfront accessibility, infrastructure, and socio-economic functions.	Market areas, coastal roads, urban settlements (Apar), tourism hubs (Pauh).

3.4. Multi-Dimensional Scaling (MDS)

The analytical method employed in this study is MDS, utilizing the Rapid Appraisal for Sustainability of Environmental Waterfront (Rap-WFS) approach. This technique is adapted from the Rapid Appraisal for Fisheries (RAPFISH) method and has been applied in coastal areas such as the Rapid Appraisal for the Mandeh Region (Rap-MR) studies by Febriandi et al. (2025) and Gusman et al. (2025). The Rap-WFS approach is used to assess the sustainability status of environmental waterfront development in Pariaman City's coastal region in a comprehensive and multidimensional manner. The Rap-WFS analysis consists of six main stages: 1) Identification of sustainability attributes within three main dimensions: economic, social, and environmental; 2) Scoring of each attribute by stakeholders; 3) Application of MDS to map the relative position, influence strength, and relationships among attributes within and across dimensions; 4) Validation of the model using stress and R-squared (RSQ) values; 5) Leverage analysis to determine key attributes influencing sustainability; and 6) Monte Carlo simulation (optional) to test model stability against score variability, although not applied in this study due to sufficient model validity. Scoring was conducted by six key informants representing local government, academics, practitioners, and coastal community members. Data used in MDS were obtained through field observations, structured interviews, and literature review. Analysis was performed using the Statistical Package for the Social Sciences (SPSS) with the Alternating Least Squares Scaling (ALSCAL) module. The sustainability dimensions and corresponding attributes for the Environmental Waterfront development in Pariaman City are presented in **Table 5** below.

Table 5.

Sustainability Dimensions and Attributes for Environmental Waterfront Development.

Dimension	Attributes
Economic	Local Government Revenue (DE_1), Employment Opportunities (DE_2), Household Income (DE_3), Infrastructure Development (DE_4), Job Diversity (DE_5), Accessibility (DE_6), Purchasing Power (DE_7), Job Training (DE_8), Direct Economic Assistance (DE_9), Community Economic Empowerment (DE_10)
Social	Educational Improvement (DS_1), Community Institutions (DS_2), Youth Development (DS_3), Reduction in Illness Ratio (DS_4), Elderly Support Services (DS_5), Community Deliberation Bodies (DS_6), Digital Information Access (DS_7), Mutual Cooperation (DS_8), Social Solidarity (DS_9), Social Norms and Values (DS_10), Environmental Awareness (DS_11), Community Competitiveness (DS_12)
Environmental	Conservation (DL_1), Biodiversity (DL_2), Expansion of Green Open Spaces (DL_3), Soil Quality (DL_4), Drainage Improvement (DL_5), Clean Water Access (DL_6), Provision of Plant Seedlings (DL_7), Coral Reef Protection (DL_8), Groundwater Conservation (DL_9), Watershed Management (DL_10), Waste Management (DL_11)

The MDS configuration results and leverage analysis were used to identify priority sustainability indicators that require attention in the development of environmental waterfront areas in Pariaman City. The outputs displayed in radar charts and two-dimensional plots support the formulation of sustainable development strategies tailored to the local context.

4. RESULTS

4.1. Environmental Characteristic Assessment and Development Strategy for the Environmental Waterfront Area

The assessment was carried out by six expert evaluators using thirteen indicators encompassing spatial, ecological, and physical aspects. The weighting of each indicator was determined through expert judgement. To ensure inter-rater consistency, an ICC reliability test was conducted. The results yielded an ICC value of 0.82, which falls within the high reliability category. This indicates that the assessments among evaluators were statistically reliable and valid. The evaluation process produced an environmental quality classification, as presented in **Table 6** below.

Table 6.
Environmental Characteristic Assessment of Lagoon Areas for Environmental Waterfront Development.

No	Component	Weight	Nareh	Manggung	Apar	Talao	Karan Aur
Environmental Waterfront Development							
1	Proximity to waterbody[1]	0.011	0.03	0.03	0.03	0.03	0.03
2	Access to waterbody[1]	0.007	0.02	0.02	0.02	0.02	0.02
3	Number of waterbody access points[1]	0.007	0.01	0.02	0.01	0.01	0.02
4	Land use beyond buffer[2]	0.053	0.07	0.11	0.11	0.13	0.13
5	Building orientation[2]	0.018	0.03	0.04	0.03	0.04	0.05
6	Transportation network[1]	0.018	0.02	0.02	0.02	0.02	0.02
7	Building height[2]	0.015	0.03	0.05	0.04	0.05	0.04
Riparian Ecosystem Status							
8	Buildings near the riparian area[1]	0.107	0.21	0.11	0.21	0.11	0.11
9	Riparian buffer vegetation[1]	0.192	0.38	0.38	0.38	0.58	0.58
Aquatic Ecosystem Status							
10	Water quality[2]	0.288	0.72	0.82	0.77	0.86	0.72
11	Aquatic plant coverage[2]	0.047	0.14	0.14	0.14	0.14	0.14
12	Odor and color[2]	0.140	0.42	0.33	0.35	0.42	0.42
13	Waterbody shrinkage[3]	0.097	0.19	0.19	0.10	0.19	0.29
Total Score		**1.000**	**2.27**	**2.26**	**2.21**	**2.60**	**2.57**
Category			**Fair**	**Fair**	**Fair**	**B**	**B**

Note: B = Good; CB = Fair
Data sources: [1] field data analysis; [2] site assessment; [3] regional data (Environmental Agency).

The assessment results indicate that Talao Lagoon scored the highest (2.60), placing it in the "Good" category, followed closely by Karan Aur Lagoon with a score of 2.56 (also "Good"). In contrast, the remaining three lagoons Nareh (2.27), Manggung (2.26), and Apar (2.21) were categorized as "Fair". This highlights a clear distinction: the two lagoons already developed as environmental waterfront areas (Talao and Karan Aur) demonstrate superior environmental quality compared to those that have not yet been developed. Apar Lagoon received the lowest score, signaling the need for special attention to its environmental conditions. Among the 13 indicators, two showed the highest influence on the final scores: water quality (0.288) and riparian buffer vegetation (0.192). Talao Lagoon received the highest ratings for both indicators, while Apar Lagoon scored the lowest. These findings underscore the strong interdependence between healthy riparian vegetation and well-maintained water quality. As also noted by Putra et al. (2023), effective conservation of riparian zones plays a critical role in sustaining water quality and supporting biodiversity. The oceanographic setting exhibits bathymetric variation from shallow nearshore areas (-2 m) to deeper zones exceeding 8 m. Tidal patterns are predominantly diurnal, producing two high and low tides each day with an average range of 1–2 m. Coastal currents are influenced not only by tidal motion but also by the freshwater outflow of major rivers such as Batang Piaman and Batang Mangguang. Wind and wave dynamics, driven by the Indian Ocean monsoon system, generate moderate wave heights not exceeding 1.2 m (Candra et al., 2024). These oceanographic forces significantly influence sediment transport, lagoon water renewal, and overall ecological balance, particularly in semi-enclosed systems like Apar and Manggung Lagoons, which are more vulnerable to stagnation and pollution during low tidal exchange.

This mapping used bathymetric data, river networks, administrative boundaries, and key sites, as shown in **Figure 1**. Five areas have been designated as Environmental Waterfront zones. These sites are distributed north to south along Pariaman's coastline and marked by the city's administrative limits, bordering Padang Pariaman Regency to the east. The northern part includes Nareh and Manggung waterfronts near dense residential areas and river mouths. The central area hosts the Apar waterfront, located in the city core. The southern area comprises Talao and Karan Aur, both linked to marine tourism and conservation. These zones are connected by coastal roads and shoreline access, offering strong potential for ecosystem-based, community-driven development. The spatial pattern

also reveals proximity to rivers such as Batang Piaman and Batang Mangau, vital for water and riparian governance. With this understanding, development strategies for Pariaman's waterfront can focus on strengthening connectivity, optimizing lagoon functions, and enhancing community participation. Further detail is shown in **Figure 2** below.

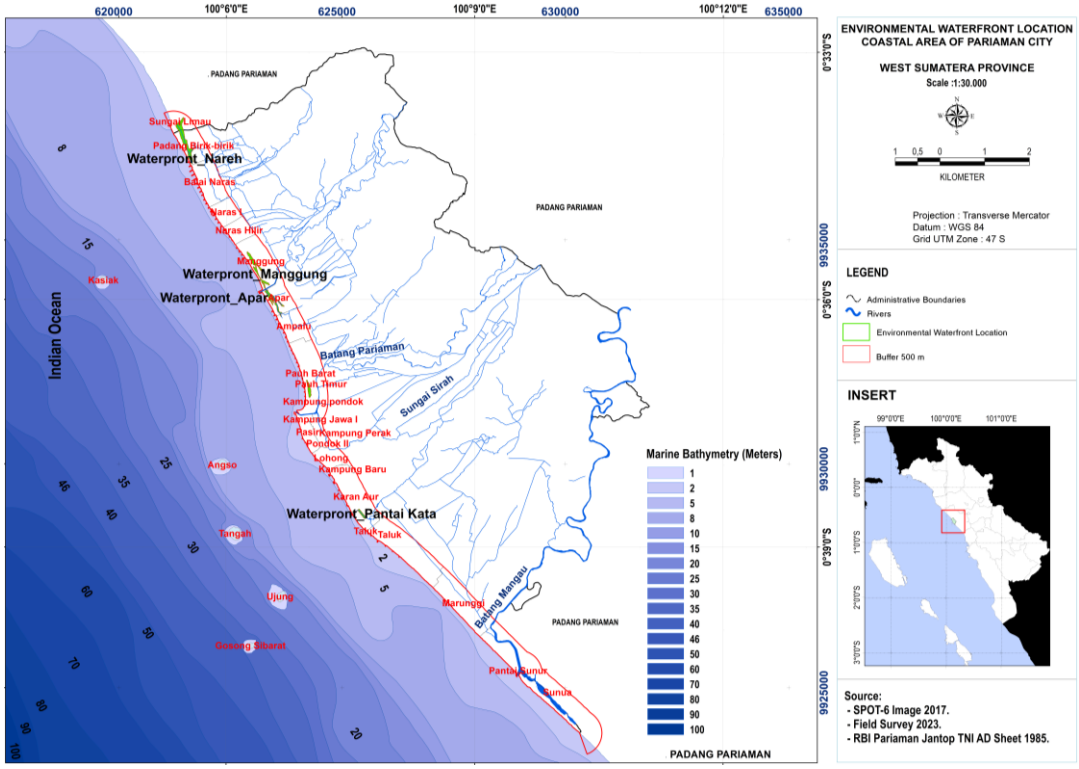

Fig. 2. Location map of Environmental Waterfront Areas in Pariaman City.

The spatial layout of the five waterfront areas demonstrates strong potential for interconnection between water-based zones (lagoons) and adjacent terrestrial zones. These connections could be utilized as green corridors, public open spaces, and ecological linkages. The presence of road infrastructure and the distribution of these areas support an integrated coastal development scenario. Oceanographic factors is essential to spatial planning, as tidal dynamics, river outflows, and wave exposure patterns significantly influence the stability and ecological behavior of both littoral, terrestrial, and urban activity zones. Areas with lower tidal flushing or greater sediment accumulation, such as the northern lagoons of Nareh and Manggung, require zoning strategies that address erosion risks and limited water circulation. Meanwhile, southern lagoons like Talao and Karan Aur, which experience higher tidal exchange and more stable wave conditions, are more conducive to conservation zoning and eco-tourism activities. To guide sustainable coastal development in Pariaman City, all identified environmental waterfront locations were classified into three main spatially and functionally integrated development zones. This classification follows the coastal zoning approach proposed by Clark (1996) and Vallega (2001), as outlined below:

– Littoral Zone: This zone consists of primary water areas, such as lagoons, which serve as focal points for environmentally based activities. Key functions include water quality conservation, aquatic vegetation preservation, and ecosystem-based educational tourism. In locations such as Talao and Karan Aur, the littoral zone has already been optimized as active conservation areas with significant local community involvement. As shown in the spatial map, these lagoons are located near the shoreline and directly connected to river systems like Batang Piaman and Batang Mangau, making them critical for water resource and coastal habitat management.

- Terrestrial Zone: Covering areas within a 100 to 300 m radius inland from the coastline, this zone includes green open spaces, ecological corridors, and coastal buffer strips. It functions as a natural barrier between human activity and the coastal ecosystem. The planning of this zone aligns with national coastal buffer regulations and considers existing infrastructure, residential areas, and connectivity requirements between lagoon zones. Areas like Nareh, Manggung, and Apar show strong potential for terrestrial zone development, particularly due to their proximity to coastal buffers and community access routes.
- Urban Activity Zone: This newly incorporated zone refers to the built-up urban areas beyond the terrestrial buffer that integrate residential, commercial, and socio-economic infrastructure. In the context of Pariaman City, the Urban Activity Zone includes elements such as coastal settlements (e.g., Apar), tourism facilities (e.g., beachfront amenities in Pauh), and transportation corridors that connect inland communities to the coast. This zone plays a pivotal role in supporting waterfront functions through economic activities, accessibility, and institutional presence. Its integration strengthens land-sea interaction and facilitates more inclusive urban coastal planning.

Through a three-zone framework, the development of environmental waterfronts in Pariaman aims not only to provide recreational space but also to emphasize ecological sustainability, spatial control, and community engagement in preserving coastal integrity. The analysis of the five lagoons identified for Environmental Waterfront development reveals varying conditions and characteristics in terms of spatial layout, ecological status, and supporting infrastructure. Not all sites meet the full set of ideal criteria, such as accessibility, land use beyond the riparian zone, riparian buffer vegetation, and water quality aesthetics. These disparities highlight the need for targeted mitigation efforts to elevate the status of those rated as "Fair". A summary of deficiencies and recommended mitigation measures for each site is provided in **Table 7** below.

Table 7.

Mitigation Actions for Components in Lagoon Areas for Environmental Waterfront Development.

No	Component	Lagoon Areas					Mitigation Actions
		[1]	[2]	[3]	[4]	[5]	
1	Proximity to waterbody	√	√	√	√	√	
2	Access to waterbody	√	√	√	√	√	
3	Number of access points to waterbody	-	-	√	√	√	Increasing access to water bodies
4	Land use beyond buffer	√	√	√	√	√	Adding other functions to the area
5	Building orientation	√	√	√	√	√	The building backs onto the area to create a facade that faces the lagoon area
6	Transportation network	√	√	√	√	√	Plan access to the water body so it leads directly there (not cutting through), which affects the orientation of surrounding buildings.
7	Building height	-	-	-	-	√	Set maximum building height to avoid obstructing views into the area under regional regulations.
8	Buildings near riparian buffer	√	√	√	√	√	Confirming border boundaries
9	Riparian buffer vegetation	-	-	√	√	√	Planting trees in riparian areas
10	Water quality	√	√	√	-	-	Controlling domestic waste entering the waters; Making policies and imposing sanctions on perpetrators of pollution, both households and industries; and Monitoring and implementing policies that have been made
11	Aquatic vegetation cover	√	√	√	-	-	
12	Odor and color	√	√		-	-	
13	Waterbody shrinkage	√	√	√	-	√	Dredging for sedimentation material; Planting vegetation in riparian areas; and Equipping inlets with water treatment

Lagoon Area Legend: [1] Nareh; [2] Manggung; [3] Apar; [4] Talao; [5] Karan Aur.

As shown in **Table 7**, the Talao and Karan Aur lagoons have generally met nearly all assessment indicators and require minimal corrective actions. However, continued monitoring is still needed for aquatic vegetation coverage and the control of odor within the water body to maintain current environmental standards. In contrast, the Apar and Manggung lagoons demand special attention, particularly in terms of water quality, riparian buffer vegetation, and the spatial arrangement of buildings near the riparian zone. For instance, in Apar, visible issues such as garbage accumulation and the absence of riparian vegetation highlight the need for reforestation along buffer zones, stricter control of domestic and industrial waste discharge, and a strengthened role of the riparian buffer as an ecological barrier. In the case of Nareh Lagoon, the main constraints are related to building orientation and non-supportive land use beyond the buffer zone. To address this, it is recommended to revise spatial zoning to prevent direct building orientation toward the lagoon and to introduce additional public space functions within the buffer area. Overall, the proposed mitigation strategies can be categorized into three types: vegetative (e.g., reforestation of riparian zones), structural (e.g., improved water access infrastructure), and policy-based (e.g., shoreline zoning regulations and waste discharge control mechanisms). These measures aim to elevate the environmental quality of all lagoon sites to the "Good" category, thereby enabling each to be equally viable for sustainable Environmental Waterfront development, balancing ecological integrity, social function, and economic potential in Pariaman City.

4.2. Assessment of Sustainability Factors and Strategy Identification for Environmental Waterfront Development Using MDS

Economic Dimension

The visualization of the MDS analysis for the economic dimension is presented in **Figure 3**, which displays the relative positioning of ten economic sustainability indicators in a two-dimensional radar graph. The figure illustrates the extent to which each indicator contributes to the sustainability of Environmental Waterfront development in the coastal areas of Pariaman City.

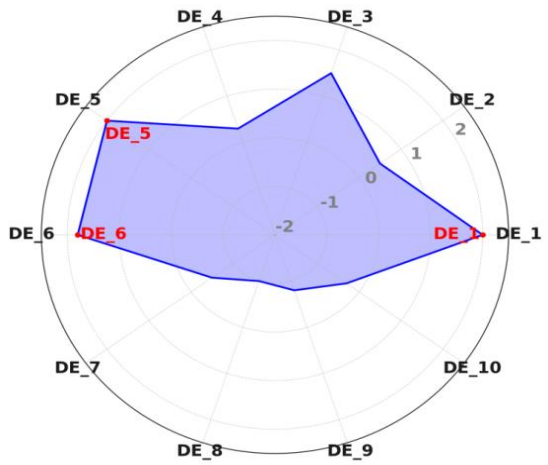

Fig. 3. MDS Modeling Results of Key Economic Sustainability Factors.

Informations:
DE_1 (Local Revenue); DE_2 (Employment Opportunities); DE_3 (Community Income); DE_4 (Facility Development); DE_5 (Job Diversification); DE_6 (Accessibility); DE_7 (Purchasing Power); DE_8 (Workforce Training); DE_9 (Direct Economic Assistance); DE_10 (Community Economic Empowerment).

Based on the radar chart in **Figure 3** above, three indicators DE_1 (Local Revenue), DE_5 (Job Diversification), and DE_6 (Accessibility) stand out with the highest positions relative to others. These indicators, visually highlighted in red, play a dominant role in explaining the economic sustainability of waterfront development in Pariaman. Their elevated scores and prominent locations on the graph indicate their stronger contribution compared to other variables in the model. The validity of the MDS model is supported by a Stress value of 0.68032, which remains within acceptable distortion limits, and an RSQ value of 0.78, indicating that 78% of stakeholder perception variance regarding economic indicators is effectively explained by the MDS configuration. This confirms that the model is sufficiently representative in capturing the complexity of relationships among the economic sustainability indicators. Substantively, DE_1 (Local Revenue) emerges as a critical indicator, underscoring the necessity for coastal development efforts to generate tangible fiscal benefits for the region, whether through optimized tourism, taxation, or service retributions. DE_5 (Job Diversification) reflects the need for inclusive and adaptive employment sectors suited to coastal contexts, such as ecotourism, environmental services, conservation work, and water-based transportation. DE_6 (Accessibility) highlights the importance of developing infrastructure, enhancing inter-area connectivity, and providing public amenities that support the mobility of residents and tourists to and within waterfront zones. These findings suggest that in formulating economic development strategies for the coastal area, the Pariaman City Government should prioritize policies that enhance local revenue, create diverse employment opportunities, and improve integrated access systems. These three pillars serve as the foundation for sustainable Environmental Waterfront development that is not only economically efficient but also inclusive and future-oriented.

Social Dimension

The visualization of the MDS analysis for the social dimension is presented in **Figure 4**, which displays the spatial configuration of twelve social sustainability indicators in a two-dimensional radar chart. This graphic illustrates the relative contribution of each indicator to the social sustainability of the Environmental Waterfront areas in Pariaman City.

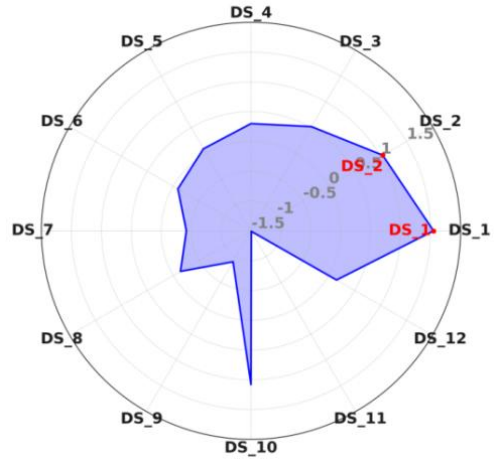

Fig. 4. MDS Modeling Results of Key Social Sustainability Factors.

Informations:
DS_1 (Education Improvement/Human Development Index); DS_2 (Community Institutions); DS_3 (Youth Empowerment Programs); DS_4 (Reduction in Illness Rate); DS_5 (Elderly Care and Support); DS_6 (Consensus-Building Bodies); DS_7 (Digital Information Access); DS_8 (Community Cooperation); DS_9 (Social Solidarity); DS_10 (Values and Morality); DS_11 (Environmental Awareness); DS_12 (Community Competitiveness).

The radar chart in **Figure 4** above DS_1 (Education Improvement/HDI) and DS_2 (Community Institutions) as the two most prominent indicators. Visually marked in red and occupying the highest coordinates in the graph, these indicators play a central role in explaining the social sustainability of coastal Environmental Waterfront development. The MDS model demonstrates strong validity, with a Stress value of 0.78371, which remains within an acceptable threshold for complex social dimensions, and an RSQ value of 0.74, indicating that 74% of stakeholder perception variance is well captured by the model. These values support the strategic significance of DS_1 and DS_2 as key leverage factors. Substantively, DS_1 (Education/HDI) reflects the foundational role of education in advancing social development in coastal communities. Higher levels of education correlate with greater adaptability, broader civic engagement, and stronger capacity for environmental stewardship in waterfront areas. Education also fosters ecological awareness and enhances public understanding of the functions and importance of the coastal environment. Meanwhile, DS_2 (Community Institutions) underscores the importance of active local institutions, such as community organizations, customary councils, and environmental stewardship groups. These institutions serve not only as platforms for mediation and collective decision-making but also as key actors in conservation, spatial consensus-building, and the preservation of local values and norms in the context of coastal development. These findings carry significant strategic implications for the Pariaman City Government, suggesting a need to prioritize education sector strengthening and the establishment or reinforcement of local institutions. These two pillars are critical for building a socially inclusive and sustainable Environmental Waterfront areas.

Environmental Dimension

The visualization of the MDS analysis for the environmental dimension are illustrated in **Figure 5**, which presents a two-dimensional radar chart mapping the relative positions of eleven environmental sustainability indicators. These indicators were used to evaluate their respective contributions to the development of Environmental Waterfront areas in Pariaman City.

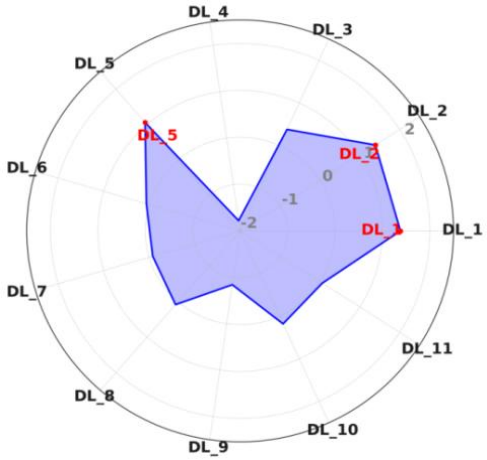

Fig. 5. MDS Modeling Results of Key Environmental Sustainability Factors.

Informations:
DL_1 (Conservation); DL_2 (Biodiversity); DL_3 (Expansion of Green Open Spaces); DL_4 (Soil Quality); DL_5 (Drainage Improvement); DL_6 (Access to Clean Water); DL_7 (Seedling Distribution); DL_8 (Coral Reef Protection); DL_9 (Groundwater Conservation); DL_10 (Watershed Management); DL_11 (Access to Sanitation).

The radar chart in **Figure 5** above three dominant indicators−DL_1 (Conservation), DL_2 (Biodiversity), and DL_5 (Drainage Improvement)−each visually marked in red and positioned within the most influential quadrant. Their prominent spatial locations in the chart indicate shared directional contributions and stronger leverage in promoting environmental sustainability in Pariaman's coastal areas. The MDS model used for this dimension demonstrates sufficient validity, with a Stress value of 0.72161, which remains within acceptable thresholds for interpreting social-environmental systems, and an RSQ value of 0.76, meaning 76% of stakeholder perception variability regarding environmental indicators is well represented by the model. This affirms the spatial configuration's reliability in identifying the most critical sustainability factors. Substantively, DL_1 (Conservation) reflects the importance of preserving coastal ecosystems as ecological buffers for the city. Conservation efforts include the protection of mangrove forests, coastal vegetation, and riparian zones that mitigate disaster risks and maintain ecological balance. DL_2 (Biodiversity) emphasizes safeguarding the richness of local species−both flora and fauna−as an integral part of coastal ecosystems and a valuable resource for sustainable ecotourism development. Meanwhile, DL_5 (Drainage Improvement) points to the necessity of efficient water infrastructure management to prevent tidal flooding and waterlogging, as well as to maintain water quality and public health in coastal settlements. These findings underline that strengthening these three indicators should be a strategic priority in Pariaman's environmental development agenda. This approach not only plays a critical role in mitigating environmental risks but also in supporting the long-term ecological productivity and resilience of the Environmental Waterfront areas.

4.3. Integrated Findings and Strategic Leverage Indicators for Sustainable Environmental Waterfront Development

Based on the results of the MDS analysis across the three main sustainability dimensions, seven key indicators were identified as the most influential in determining the success of Environmental Waterfront development in Pariaman City. These indicators occupy dominant positions in the spatial configuration of the MDS model and hold the highest coordinate values in their respective radar charts, making them leverage indicators for sustainability.

The seven key indicators are DE_1–Local Government Revenue (PAD); DE_5–Job Diversification; DE_6–Accessibility; DS_1–Education Improvement (Human Development Index); DS_2–Community Institutions; DL_1–Conservation; and DL_2–Biodiversity. These indicators serve as the core foundation for designing an adaptive, inclusive, and sustainable coastal development strategy.

The concept of Environmental Waterfront development is not merely a spatial planning framework but represents an integrated approach that addresses environmental degradation while promoting the conservation of coastal resources. From an economic standpoint, sustainability in coastal zones is strongly influenced by the ability of the region to increase local revenue (DE_1) through optimized utilization of spatial potential, particularly in tourism, taxation, and service-based fees. Job diversification (DE_5) underscores the need to expand economic activities in coastal areas, including environmental services, ecotourism, and maritime transportation. Meanwhile, accessibility (DE_6) is vital for enhancing regional connectivity and supporting the mobility of both residents and tourists toward coastal destinations. In the social dimension, sustainability is largely shaped by education (DS_1), which fosters environmental awareness, civic engagement, and community adaptability to environmental changes and emerging economic opportunities. Community institutions (DS_2) play an essential role in spatial governance, social consensus-building, and the preservation of local cultural values relevant to coastal development. From an environmental perspective, the leading indicators, namely conservation (DL_1) and biodiversity (DL_2) highlight the importance of safeguarding coastal ecosystems, including mangrove forests, shoreline vegetation, and marine biodiversity.

These elements serve as ecological buffers and represent a strong foundation for conservation-based ecotourism. These findings provide a solid framework for the Pariaman City Government to develop action plans and strategic policies centered around these seven leverage indicators. The involvement of key stakeholders, including academics, conservation organizations, local communities, and the private sector is essential in co-designing development programs that are collaborative, realistic, and sustainability-oriented.

5. CONCLUSIONS

This study provides a comprehensive assessment of the environmental, spatial, and sustainability characteristics of lagoon areas designated for Environmental Waterfront development in Pariaman City. The environmental assessment revealed that Talao and Karan Aur Lagoons achieved a "Good" classification, supported by strong water quality and riparian vegetation. In contrast, Apar Lagoon, scoring the lowest, requires intervention due to poor buffer conditions and visible waste. Manggung and Nareh Lagoons were also rated "Fair", indicating a need for better land use planning and vegetation restoration. The spatial classification into littoral, terrestrial, and urban activity zones supports an integrated planning approach. Littoral zones in Talao and Karan Aur serve conservation and ecotourism functions, while terrestrial zones in Nareh, Manggung, and Apar offer green infrastructure opportunities. The urban activity zone around the lagoons supports socio-economic functions, access, and governance. This tri-zonal structure enhances spatial clarity and urban ecological integration. To improve environmental quality, three mitigation strategies are proposed: 1) Vegetative (e.g., riparian planting), 2) Structural (e.g., water access improvement), and 3) Policy-based (e.g., zoning enforcement). The MDS analysis identified seven key indicators as critical for sustainable development: DE_1 (Local Revenue), DE_5 (Job Diversification), DE_6 (Accessibility), DS_1 (Education), DS_2 (Community Institutions), DL_1 (Conservation), and DL_2 (Biodiversity). These represent strategic pillars for a resilient waterfront model. Economic sustainability depends on optimizing revenue, job diversity, and access; social sustainability relies on education and local institutions; and environmental sustainability is anchored in conservation and biodiversity. Overall, the integration of weighted indicator analysis, MDS-based evaluation, and tri-zonal planning offers a novel, replicable framework for Indonesia's coastal cities. These findings provide a foundation for an adaptive and inclusive coastal strategy in Pariaman. Its success requires active collaboration among government, communities, conservation groups, and the private sector. With strong synergy, Pariaman's waterfront areas could serve as a national model for sustainable coastal governance, balancing ecological integrity, socio-economic development, and spatial resilience.

ACKNOWLEDGEMENTS

The authors would like to express their deepest gratitude to the Government of Pariaman City for its cooperation and field support throughout the research process. Special thanks are also extended to the Universitas Negeri Padang (UNP) for academic supervision and technical input. Appreciation is further conveyed to the researchers from the Research Center for Conservation of Inland Water Resources, National Research and Innovation Agency (BRIN), for their valuable guidance and mentoring throughout the publication process of this paper.

REFERENCES

Barnes, R. S. K. (1980). *Coastal lagoons: The natural history of a neglected habitat*. Cambridge University Press.

Bondesan, A. (2017). Geomorphological Processes and Landscape Evolution of the Lagoon of Venice. In M. Soldati & M. Marchetti (Eds.), *Landscapes and Landforms of Italy* (pp. 273–282). Springer. https://doi.org/10.1007/978-3-319-26194-2_15

Breen, A., & Rigby, D. (1993). *Waterfronts: Cities reclaim their edge* (1st ed.). McGraw-Hill.

Candra, O., Putra, A., Pryambodo, D. G., Revina, R., & Elfizon. (2024). Variability between wind and sea waves based on environmentally friendly as renewable energy in Pariaman City. *Journal of Sustainability Science and Management*, *19*(10), 39–47. https://doi.org/10.46754/jssm.2024.10.004

Clark, J. R. (1996). *Coastal zone management handbook*. CRC Press.

Dalila, S., Caisarina, I., & Burhan, I. M. (2021). The uses of Peunayong culinary riverwalk for open space: An observation. *IOP Conference Series: Earth and Environmental Science*, *881*(1), 012068. https://doi.org/10.1088/1755-1315/881/1/012068

Febriandi., Fatimah, S., Triyatno, T., Hermon, D., Putra, A., Mutmainah, H., Arifin, T., & Akhwardy, R. (2025). Predicting of land cover changes until 2030 and assessing sustainability status in the Mandeh region, Indonesia. *Geographia Technica*, *20*(1), 263–280. https://doi.org/10.21163/GT_2025.20.1.18

Girard, L. F., Kourtit, K., & Nijkamp, P. (2014). Waterfront areas as hotspots of sustainable and creative development of cities. *Sustainability*, *6*(7), 4580–4586. https://doi.org/10.3390/su6074580

Gusman, M., Efendi, N., Barlian, E., Dewata, I., Syah, N., Iswandi, U., & Putra, A. (2025). Sustainability assessment of post-mining land using multidimensional scaling: Insights from the Indonesian coal mining sector. *Geographia Technica*, *20*(1), 64–78. https://doi.org/10.21163/GT_2025.201.06

Hermon, D., Putra, A., & Oktorie, O. (2018). Suitability evaluation of space utilization based on environmental sustainability at the coastal area of Bungus Bay in Padang City, Indonesia. *International Journal of GEOMATE*, *14*(41), 193–202. https://doi.org/10.21660/2018.41.65443

Hermon, D., Erianjoni., Dewata, I., Putra, A., & Oktorie, O. (2019). Liquefaction vulnerability analysis as a coastal spatial planning concept in Pariaman City – Indonesia. *International Journal of Recent Technology and Engineering*, *8*(2), 4181–4186. https://doi.org/10.35940/ijrte.B3265.078219

Hermon, D., Ikhwan., Putra, A., & Oktorie, O. (2020). Spatial analysis of tsunami vulnerability zones as a basic concept of coastal disaster mitigation in development planning of Pariaman city. *Journal of Advanced Research in Dynamical and Control Systems*, *12*(7 Special Issue), 681–690. https://doi.org/10.5373/JARDCS/V12SP7/20202158

Ionan, A. C., Polley, M.-Y. C., McShane, L. M., & Dobbin, K. K. (2014). Comparison of confidence interval methods for an intra-class correlation coefficient (ICC). *BMC Medical Research Methodology*, *14*(121). https://doi.org/10.1186/1471-2288-14-121

Kurniati, S. (2013). *Bridging spatial & tourism development through effective collaboration (Case study: Sail Morotai 2012, North Maluku – Indonesia)* (Master's thesis, Wageningen University & Research). Wageningen University & Research Centre.

Leyland, A. H., & Groenewegen, P. P. (2024). Intraclass correlation coefficient (ICC). In E. Maggino (Ed.), *Encyclopedia of Quality of Life and Well-Being Research* (2nd ed), 3643–3644. https://doi.org/10.1007/978-3-031-17299-1_1528

Lu, Y. (2018). *How design influences older adults' outdoor space usage and satisfaction: A case study of outdoor environments in Chinese facilities for the elderly* (Doctoral dissertation, Texas A&M University).

Megawati, Tahmirn, T., Hasan, M., & Dinar, M. (2023). Tourism development strategy in improving the community economy at Tanjung Bira Beach, Bonto Bahari District, Bulukumba Regency. *Pinisi Journal of Entrepreneurship Review*, *1*(1), 1–15. https://doi.org/10.62594/pjer.v1i1.36

Müller, R., & Büttner, P. (1994). A critical discussion of intraclass correlation coefficients. *Statistics in Medicine*, *13*(23-24), 2465–2476.

Oktorie, O., Hermon, D., Erianjoni., Syarief, A., & Putra, A. (2019). A calculation and compiling models of land cover quality index 2019 uses the geographic information system in Pariaman City, West Sumatra Province, Indonesia. *International Journal of Recent Technology and Engineering*, *8*(3), 6406–6411. https://doi.org/10.35940/ijrte.C5616.098319

Oktorie, O., Rusdi., Heldi., Barlian, E., Putra, A., & Ramadhan, R. (2019). Disaster mitigation based on environmental of coastal area communities in Pariaman City, Indonesia. *Sumatra Journal of Disaster, Geography and Geography Education*, *3*(2), 202–207. https://doi.org/10.24036/sjdgge.v3i2.288

Patawari, A. M. Y., Anna, Z., Hindayani, P., Dhahiyat, Y., Hasan, Z., & Putri, I. A. P. (2022). Sustainability status of small-scale fisheries resources in Jakarta Bay, Indonesia after reclamation. *Biodiversitas*, *23*(4), 1715–1725. https://doi.org/10.13057/biodiv/d230401

Permana, A. S., Astuti, W., & Erianto. (2017). Waterfront development concepts in Indonesia from the perspective of urban planning and environmental sustainability. *International Journal of Built Environment and Sustainability*, *4*(3). https://doi.org/10.11113/ijbes.v4.n3.207

Prarikeslan, W., Syah, N., Barlian, E., Suasti, Y., & Putra, A. (2020). A potential locations of marine tourism in Pasumpahan Island, Padang city-Indonesia. *International Journal of GEOMATE*, *19*(72), 123–130. https://doi.org/10.21660/2020.72.IGEGOS

Putra, A., Dewata, I., Hermon, D., Barlian, E., Umar, G., Widodo, T., & Damanhuri, H. (2023). Activity recommendations based on an environmental approach in zoning of marine protected areas (MAPS) Pariaman City–Indonesia. *EnvironmentAsia*, *16*(3), 57–67. https://doi.org/10.14456/ea.2023.35

Putra, A., Dewata, I., Hermon, D., Barlian, E., & Umar, G. (2023). Sustainable development-based coastal management policy development: A literature review. *Journal of Sustainability Science and Management*, *18*(1), 237–245. https://doi.org/10.46754/jssm.2023.01.015

Putra, A., Triyatno, Darwis, R., Dewata, I., Tanto, T. A., Mustapha, M. A., Razi, P., & Zainul, R. (2023). Suitability of mangrove ecosystems as a protected zone based on land-use changes. *Physical Oceanography*, *30*(6), 866–881.

Rukayah, R. S., Susilo, E. S., Abdullah, M., & Saputro, S. (2018). Exploring the position of Old Semarang Sea Port: Based on Javanese city pattern. *IOP Conference Series: Earth and Environmental Science*, *116*, 012036. https://doi.org/10.1088/1755-1315/116/1/01203

Setiawan, A., & Zalfa, G. F. (2023). The effect of waterfront city development on the economic welfare of coastal communities (Study in Beting Village, East Pontianak District, Pontianak City). *Jurnal Ilmu Sosial Terapan (JIST)*, *4*(8), 974–982. https://doi.org/10.59141/jist.v4i8.671

Suedi, I., Hajrawati, Humuyani, S. R., Muhayyang, M., & Hartaman, N. (2020). Implementation of good environmental governance in waterfront city development in Majene, Indonesia. *Asian Political Science Review*, *4*(1), 7–15. https://doi.org/10.14456/apsr.2020.2

Uswah, R., & Wang, L. (2021). Waterfront public space planning on Krueng Aceh River in Banda Aceh–Indonesia. *Current Urban Studies*, *9*(2), 218–226. https://doi.org/10.4236/cus.2021.92014

Vallega, A. (2001). Urban waterfront facing integrated coastal management. *Ocean & Coastal Management*, *44*(5–6), 379–410. https://doi.org/10.1016/S0964-5691(01)00056-4

Winter, G. (Ed.). (2009). *Towards sustainable fisheries law: A comparative analysis*. IUCN – International Union for Conservation of Nature, Gland, Switzerland.

Wrenn, D. M. (1983). *Urban waterfront development*. Urban Land Institute.

PREDICTING FOREST FIRE HOTSPOTS IN KALIMANTAN USING BEST SUBSET VARIABLE SELECTION, REGULARIZED REGRESSION MODEL, AND BAYESIAN MODEL AVERAGING

***Sri NURDIATI*[1], *I Wayan MANGKU*[1], *Isnayni Feby HAWARI*[1], *Mohamad Khoirun NAJIB*[1]**

DOI: 10.21163/GT_2025.202.10

ABSTRACT

The forest area in Kalimantan continues to decrease due to forest and land fires. One way to prevent this situation in Kalimantan is by predicting the number of hotspots based on climate indicators. Many modeling approaches, such as statistical and machine learning models, can be used. This study uses the best subset selection to build a regression model with regularization and Bayesian Model Averaging (BMA). Several predictors are used to predict the number of hotspots, including precipitation, precipitation anomalies, dry spells, El Nino Southern Oscillation (ENSO) and Indian Ocean Dipole (IOD) indices, and seasonality. The best model is selected based on the performance of the RMSE and R^2 values. The results of the best subset selection obtained are a model consisting of six terms in polynomial form and interactions of precipitation anomalies, dry spells, and IOD index. It can be concluded that there is a significant role of dry spells as a predictor for hotspots due to their presence in almost every term of the equation. The BMA model outperforms the regularization model, with an RMSE value on the test data of 664 hotspots and an R^2 of 88.58%. Although Ridge, LASSO, and Elastic Net perform similarly to the BMA model during the training phase, their reliance on a single model can restrict their ability to generalize to new data. In contrast, BMA offers a more robust and accurate approach by aggregating predictions from multiple models and accounting for uncertainty. This ensemble method enhances BMA's predictive performance on test datasets, making it a valuable tool for accurate forecasting in complex scenarios.

Key-words: *Bayesian model averaging, best subset, machine learning, regression, regularization.*

1. INTRODUCTION

The island of Borneo has a total forest area of 40.8 million hectares (Hardiyanti & Nurmanina, 2020). However, this area is decreasing yearly due to various problems caused by the environment and humans (Margono et al., 2014). Gaveau et al. (2014) estimated that the forest area in Borneo decreased from 558,060 km^2 (75.7%) in 1973 to 389,566 km^2 (52.8%) in 2010, based on satellite imagery. One of the environmental problems that often occurs in Indonesia, especially on the island of Kalimantan, and causes a reduction in forest land is forest fires (Tacconi, 2016). Some examples of the largest forest fires in Indonesia occurred in 1982, 1997-1998, 2015, and 2019 (Najib et al., 2022b; van der Werf et al., 2017). However, there are still many other cases of forest fires that occur every year until now. Forest fires have many negative impacts on the environment and humans, such as material losses, changes in the composition of forest ecosystems, damage to land and forest vegetation, and disruption of human health, especially in communities around the fire location (Borrego et al., 2025; Jolly et al., 2022; Saharjo & Hasanah, 2023). These negative impacts make forest fires potentially threaten the environment and humans, so further prevention and handling measures are needed (Hu et al., 2018).

[1]*School of Data Science, Mathematics and Informatics, IPB University, Bogor, Indonesia, (SN) nurdiati@apps.ipb.ac.id, (IWM) wayanma@apps.ipb.ac.id, (IFH) ifebyhawari@apps.ipb.ac.id, (MKN) mkhoirun@apps.ipb.ac.id*

[*]*Corresponding author: nurdiati@apps.ipb.ac.id*

Climate is one of the factors causing forest fires (Ertugrul et al., 2021). According to Syaufina and Puspitasari (2015), climate conditions such as precipitation, temperature, humidity, and air stability cause the potential for forest fires directly. As an archipelagic country flanked by the Indian Ocean and the Pacific Ocean, climate conditions in Indonesia are greatly influenced by oceanographic conditions, especially in both oceans (Kurniadi et al., 2021; Iskandar et al., 2022). Two types of natural phenomena are global climate variability and can affect oceanographic conditions, i.e., ENSO (El Nino Southern Oscillation) in the Pacific Ocean and IOD (Indian Ocean Dipole) in the Indian Ocean (Rachman et al., 2024; Hidayat et al., 2025). Both phenomena affect climate conditions in Indonesia, especially in terms of precipitation and drought levels that can cause forest fires (Nurdiati et al., 2021).

Climate conditions form specific patterns over a while (Chi et al., 2023). For example, a region with a tropical climate, such as Indonesia, tends to have high precipitation levels during the rainy season and high drought levels during the dry season. This pattern will repeat itself every year following the season period and is usually called a seasonal pattern. The pattern formed by climate conditions over a certain period makes climate conditions predictable for humans. Currently, experts have developed many methods to predict things that will happen in the future based on past data, such as Artificial Intelligence (AI) and machine learning (Latif et al., 2023; Reichstein et al., 2019).

AI and machine learning are extensively applied in various aspects of human life, including predicting future scenarios (Huntingford et al., 2019; Sarker IH, 2021). Experts across fields continuously refine prediction models to improve accuracy and minimize errors (Basha & Rajput, 2019). From education and healthcare to economics, these technologies assist in decision-making by using past data to model future outcomes (Javeed et al., 2023; Jdey et al., 2023; Pallathadka et al., 2023; Sahu et al., 2023). One example is using machine learning to predict and prevent forest fires by analyzing climate indicators, helping to make proactive decisions for environmental management (Alkhatib et al., 2023).

Many studies on the influence of climate conditions in Indonesia on indications of forest fires have been conducted by researchers. Nugrahani et al. (2024) used information on climate conditions (precipitation, dry spells, ENSO, and IOD) to predict the number of hotspots in Kalimantan as an indicator of forest fires by constructing an artificial neural network, random forest regression, gradient boosting, and Bayesian regression models. Mahendra et al. (2022) classified forest and land fires in Palembang, South Sumatra, using the C4.5 decision tree algorithm based on precipitation, wind speed, and air humidity information. Preeti et al. (2021) compared the decision tree algorithm, support vector machine, and random forest regression to predict forest fires based on information on climate conditions, including temperature, precipitation, wind, and air humidity.

Based on previous studies, many types of prediction models can be used to predict forest fires based on climate indicators, such as the Artificial Neural Network (ANN) model and the Random Forest model. ANN models have been widely used for predicting forest fires due to their ability to model complex, nonlinear relationships between climatic variables and fire occurrences (Jain et al., 2020). Random Forest models, on the other hand, offer robust prediction capabilities with high accuracy and are well-suited for handling large datasets (Kursa, 2014), making them ideal for predicting forest fires based on multiple environmental and climatic factors. The choice of an appropriate prediction model plays a critical role in forest fire prevention and mitigation, depending on the type of research being conducted and the specific fire indicators being used. If conducting research using a classification system such as Mahendra et al. (2022), then the prediction model is also a classification model. However, if researching to determine the effect of the relationship between climate indicators and the potential for forest fires, such as Nugrahani et al. (2024) and Preeti et al. (2021), then the regression model is more appropriate.

Hotspots are widely used as indicators of potential forest fires. Hotspots represent locations with a surface temperature above a certain threshold, identified through satellite imagery interpretation (Saharjo & Nasution, 2021). Generally, hotspots are spread randomly depending on the area's conditions, especially climate conditions. Hotspots are generally distributed across an area in a manner influenced by various environmental factors, particularly climate conditions. For instance,

areas with high precipitation tend to have fewer hotspots, while areas experiencing prolonged drought conditions are more likely to exhibit a higher concentration of hotspots (Giglio et al., 2018). The increasing number of hotspots correlates strongly with the likelihood of forest fires, as they often signal dry and combustible vegetation. Therefore, predicting the number of hotspots in a region based on climate variables, such as temperature or precipitation, could be a crucial step in forest fire prevention.

The number of hotspots based on climate conditions can be predicted by creating a model that can recognize the influence of the relationship between climate conditions and the number of hotspots so that the linear regression model is suitable. Currently, many regression models have been developed to overcome problems that have been experienced in the use of previous regression models. One of the developments of the regression model is the regularized regression model, which can overcome the problem of multicollinearity in data (Fikri et al., 2023; Herawati et al., 2018; Venkatesh et al., 2023). Therefore, this study uses regularized regression models, i.e., a regularization regression model consisting of ridge regression, Least Absolute Shrinkage and Selection Operator (LASSO), and elastic-net as prediction models for the number of hotspots in Kalimantan based on climate indicators.

In addition to the regularization regression model, this study also uses a prediction model that applies the ensemble method, called Bayesian Model Averaging (BMA), based on a polynomial regression model. BMA is a model that bases its predictions on a weighted average of several models rather than just one model (Hinne et al., 2020). Both models were built using a combination of the best predictor variables based on the results of variable selection using the best subset selection method so that the resulting model does not have too high complexity and is easy to implement. Furthermore, the performance of both types of models was compared, and the best model was selected in predicting the number of hotspots in Kalimantan based on specific climate indicators, i.e., precipitation, precipitation anomalies, dry spells, El Nino Southern Oscillation (ENSO) and Indian Ocean Dipole (IOD) indices, and seasonality.

This study aims to develop apredictive model for forecasting the number of hotspots in Kalimantan using a comprehensive statistical approach. The main objectives of this research are as follows. Selecting the Best Combination of Predictors: The first step in this study is to select the best combination of predictors for forecasting the number of hotspots in Kalimantan. This selection process will use the best subset selection method, with the criterion for selection being the lowest Bayesian Information Criterion (BIC) value. This approach ensures that the most relevant and informative predictors are chosen for the predictive model. Constructing Regularization Regression Models: After determining the set of predictors, several regularization regression models will be constructed, including ridge regression, Least Absolute Shrinkage and Selection Operator (LASSO), and elastic-net regression. Additionally, a BMA model based on polynomial regression will also be developed. The use of these regularization methods aims to address multicollinearity and overfitting issues, ensuring that the models produced are stable and accurate. Determining the Best-Performing Model: The final step of the study is to evaluate the performance of each model in predicting the number of hotspots in Kalimantan. The evaluation will be based on two key metrics: Root Mean Square Error (RMSE) and the coefficient of determination (R^2), on both training and test data. The model with the best performance according to these metrics will be selected as the most effective model for accurate prediction. Through this systematic scientific approach, the study aims to produce a reliable predictive model that can be utilized to better understand and mitigate the risks of forest fires in Kalimantan.

This study contributes to the growing body of research on predictive modeling for forest fire management by addressing critical gaps in existing methodologies. While previous studies have utilized machine learning approaches such as Artificial Neural Networks (ANN) and Random Forest (RF) for forest fire prediction, these models often rely on single-model frameworks that may not adequately account for uncertainty or interactions among climate variables. In contrast, this research leverages BMA to integrate multiple model perspectives, enhancing robustness and predictive accuracy.

The novelty of this work lies in its application of BMA in combination with polynomial regression and best subset selection to predict forest fire hotspots. This approach allows for the inclusion of interaction terms and higher-order relationships among climate variables, such as dry spells, precipitation anomalies, and the Indian Ocean Dipole (IOD) index, which are often oversimplified in traditional regression models. Moreover, by incorporating uncertainty into predictions, the BMA model provides more reliable insights for decision-making, a feature critical for managing forest fires in complex environments like Kalimantan.

Additionally, this study emphasizes the role of climate variability indicators in fire hotspot prediction, offering a systematic methodology that bridges the gap between theoretical modeling and practical application. These contributions not only advance the predictive modeling field but also provide actionable insights for environmental management and policy formulation in tropical regions.

2. METHODS

2.1. Multiple Linear Regression

One of the simple and popular machine learning methods is linear regression. In principle, the linear regression method works by measuring the relationship between continuous variables, which, in this case, are assumed to have a linear relationship. The linear regression method that predicts a continuous variable based on more than one predictor variable is called multiple linear regression (Hope, 2020). The model produced by multiple linear regression is represented by

$$y = \beta_0 + \beta_1 x_1 + \beta_2 x_2 + \cdots + \beta_n x_n + \varepsilon \quad (1)$$

where y is a continuous response variable, β_0 is the intercept or intersection, which is defined as the value of the response variable when all predictor variables are zero, β_1 to β_n are the coefficients of the 1st to n-th predictor variables, and ε is the error of the model. Linear regression models involving polynomial variables such as x_i^2 or x_i^3 are called polynomial regression models (Montgomery et al., 2021).

According to Han et al. (2024), regression parameters β_i for $i = 0,1,2, \dots, n$ are estimated by minimizing the sum of the squared errors of the model represented by

$$SSE = \sum_{i=1}^{n} (y_i - \hat{y}_i)^2 \quad (2)$$

where y_i and $\hat{y}_i$ representing the actual and predicted values of the i-th observation point, respectively. Multiple linear regression is increasingly unable to work well using the ordinary least squares (OLS) as the number of predictor variables increases due to the increasing possibility of multicollinearity or linear relationships between predictor variables (Hope, 2020). Thus, a linear regression model with regularization such as ridge regression, Least Absolute Shrinkage and Selection Operator (LASSO), and elastic-net have been developed which has an additional penalty to overcome multicollinearity.

2.2. Best Subset Selection

Best subset selection is a widely used variable selection method for selecting predictor variables in linear models. This method selects a combination of several predictor variables that produce the best model based on specific evaluation metrics such as BIC, adjusted R^2, and Mallows CP. Hastie et al. (2020) stated that if there is a vector Y of size $n \times 1$ containing the response variables, a matrix X of size $n \times k$ containing the predictor variables, and a subset of predictor variables with a size p between 0 and $\min\{n, k\}$, then the best subset selection method will find a combination of k predictor variables that produces the best model. The combination of predictor variables overcomes the problem in the context of squared errors, which are represented by

$$\hat{\beta} = \arg\min_{\beta \in \mathbb{R}^k} \|Y - \beta X\|_2^2 \quad (3)$$

where $\|\beta\|_0 \leq k$ dan $\|\beta\|_0 = \sum_{i=1}^{k} 1\{\beta_i \neq 0\}$.

The best subset selection method has advantages over other variable selection methods, such as forward selection and backward elimination. According to Brooks and Ruengvirayudh (2016), one of

the main advantages of best subset selection is choosing a model with the best combination of predictor variables by considering all models that can be formed based on the number of existing predictor variables. This advantage can overcome the limitations of the forward selection and backward elimination methods to produce a better model. However, if the number of predictor variables is enormous, this method must be considered due to the increasing computation time needed to create all possible models if the number of predictor variables increases (Brooks & Ruengvirayudh, 2016).

2.3. Regularized Regression Methods

Regularization is used to shrink the estimated value of the regression coefficient by providing a penalty when the model does not meet the multicollinearity assumption (Yanke et al., 2022). Regularization has three methods: ridge regression, Least Absolute Shrinkage and Selection Operator (LASSO), and elastic-net.

2.3.1. Ridge Regression

The first regularization method is ridge regression, introduced by Hoerl (1962). Ridge regression overcomes multicollinearity by determining a biased estimator but has a smaller variance value than the variance value in multiple linear regression (Wasilaine et al., 2014). Meanwhile, multicollinearity is a problem that occurs due to two or more correlated predictor variables. According to Saleh et al. (2019), ridge regression provides a penalty to the model to provide limits for the coefficient values of the linear regression model so that they do not have tremendous values without limits.

Ridge regression is represented by

$$\hat{\beta} = \arg\min_{\beta} (Y - X\beta)^T (Y - X\beta) + \lambda \|\beta\|_2^2 \tag{4}$$

where $\beta_{k\times 1}$ contains the regression coefficients to be estimated, $Y_{n\times 1}$ contains the response variables, $X_{n\times k}$ contains the predictor variables, λ is a shrinkage parameter whose value is always positive, and $\|\beta\|_2^2$ is a ridge penalty whose value is equal to $\sum_{j=1}^{k} \beta_j^2$ (Saleh et al., 2019). If λ approaches zero, the value of the regression coefficient will be greater as in OLS regression, but if $\lambda \to \infty$ then the value of the coefficient will be closer to zero.

2.3.2. Least Absolute Shrinkage and Selection Operator (LASSO) Regression

Ridge regression has a disadvantage, i.e., it can only shrink the regression coefficient to near zero, so a regularization method was introduced to overcome this deficiency. Tibshirani (1996) first introduced the Least Absolute Shrinkage and Selection Operator (LASSO) method, which was used to overcome the multicollinearity problem (Andana et al., 2017). According to Saleh et al. (2019), LASSO can overcome the shortcomings of ridge regression by shrinking the regression coefficient to zero. Therefore, LASSO is suitable for high-dimensional data because it can reduce the predictor variables used. If there is high-dimensional data that has as many predictor variables as k and the number of data as n where $k > n$, then LASSO can be represented by

$$\hat{\beta} = \arg\min_{\beta} (Y - X\beta)^T (Y - X\beta) + \lambda \|\beta\|_1 \tag{5}$$

where $\|\beta\|_1$ represents the LASSO penalty, which has the same value as $\sum_{j=1}^{k} |\beta_j|$.

2.3.3. Elastic-Net Regression

Zou and Hastie (2005) introduced a combined method of ridge regression and LASSO, i.e., elastic-net regression. According to Handayani and Wachidah (2022), the advantages of this method are that it can handle multicollinearity problems, can reduce the regression coefficient to precisely zero, can select predictor variables from a group of correlated predictor variables, and can select variables simultaneously. Elastic-net regression can be represented by

$$\hat{\beta} = \arg\min_{\beta} (Y - X\beta)^T (Y - X\beta) + \lambda \left[\alpha \|\beta\|_1 + (\alpha - 1)\|\beta\|_2^2\right] \tag{6}$$

where $[\alpha \|\beta\|_1 + (\alpha - 1)\|\beta\|_2^2]$ is the elastic net penalty with $\alpha \in [0,1]$. If $\alpha = 0$, Eq. 6 becomes the same as the ridge regression equation, while when $\alpha = 1$, Eq. 6 becomes the same as the LASSO regression equation.

2.4. Bayesian Model Averaging (BMA)

BMA is a model that bases its predictions on a weighted average of several models rather than just one model (Alhassan et al., 2024; Huang et al., 2023). BMA applies an ensemble method by combining multiple models based on each model's posterior probability or weight. According to Claeskens and Hjort (2008), if there is a collection of models $M_1, \ldots, M_m$ that predict the value of the response variable y from data D, then BMA bases its prediction results not only using one model but combining all models based on their posterior probabilities. BMA is represented by

$$P(y|D) = \sum_{k=1}^{m} P(M_k|D)P(y|M_k, D) \tag{7}$$

where $P(y|D)$ is the weighted average of the posterior densities of y given the data D, $P(M_k|D)$ is the posterior probability of the model M_k given the data D, and $P(y|M_k, D)$ is the posterior density of y, when the model M_k is the most appropriate model.

$P(M_k|D)$ or the posterior probability of the model M_k is obtained by applying Bayes' theorem and is represented by

$$P(M_k|D) = \frac{P(M_k)\lambda_{n,k}(D)}{\sum_j^m P(M_j)\,\lambda_{n,k}(D)} \tag{8}$$

where $P(M_k)$ is the prior probability of the model M_k, which is typically distributed uniformly $1/m$, while $\lambda_{n,k}(D)$ is the marginal density of the data D represented by

$$\lambda_{n,k}(D) = \int L(D, \theta_k)P(\theta_k|M_k)\, d\theta_k \tag{9}$$

where θ_k is a vector of the parameters of the model M_k, $L(D, \theta_k)$ is the likelihood function of the model M_k, and $P(\theta_k|M_k)$ is the prior density of the model M_k (Claeskens & Hjort, 2008).

Just as the BMA model equation is a weighted average of the posterior densities y, the posterior mean value of the BMA model, denoted by E, is a weighted average of the posterior mean values for each model M_k and is represented by

$$E(y|D) = \sum_{k=1}^{m} P(M_k|D)E(y|M_k, D) \tag{10}$$

where $E(y|M_k, D)$ is the posterior mean value when the model M_k is the most appropriate model.

2.5. Bayesian Information Criterion (BIC)

Various criteria in variable selection have been developed and widely used in various studies. According to Dziak et al. (2020), several criteria in variable selection can be defined as a log-likelihood function with a penalty known as the Information Criterion (ICs). The main objective of ICs is to select a model that minimizes the value of

$$IC = -2l + C_n p \tag{11}$$

where l is the log-likelihood function of the model, C_n is a constant or penalty function whose type depends on the ICs criteria used, n is the number of sample data, and p is the number of parameters in the model (Dziak et al., 2020).

One type of IC widely used and has been widely developed is the Bayesian Information Criterion (BIC). BIC is a criterion widely used in variable selection methods and focuses on models with low complexity. BIC works by giving a high penalty to models with high complexity represented by the number of parameters in the model so that it can reduce the potential for overfitting (Kasali & Adeyemi, 2022). The penalty used in BIC, represented by C_n, is the $\ln(n)$ function (Dziak et al., 2020). The BIC differs from other types of ICs, such as the Akaike Information Criterion (AIC), which focuses on models with high accuracy, so selecting these two criteria is based on research needs.

2.6. Evaluation Metrics

Evaluation metrics are measurement criteria that are often used to determine the level of accuracy and feasibility of a model. One widely used evaluation metric is Root Mean Squared Error (RMSE).

RMSE is a method used to measure a prediction model's accuracy level as a form of model evaluation (Sanjaya & Heksaputra, 2020). RMSE calculates the average squared value of the number of errors in a prediction model. The lower the RMSE value, the more accurate the prediction model produced. The RMSE value is calculated by

$$RMSE = \sqrt{\frac{1}{n}\sum_{i=1}^{n}(\hat{y}_i - y_i)^2} \tag{12}$$

where n represents the number of data, y_i and $\hat{y}_i$ represents the actual and predicted value of the response variable from the i-th observation.

In addition to RMSE, another widely used evaluation metric is the coefficient of determination or R-squared (R^2). R^2 is one of the widely used model evaluation metrics to measure the performance of a prediction model. The R^2 value is used to measure the variance in the response variable that can be explained by the model (Purwanto & Sudargini, 2021). The R^2 value ranges from 0 to 1, with the higher the value, the better the model (Chicco et al., 2021).

3. STUDY AREA AND DATASETS

3.1. The Island of Borneo

Borneo, the third-largest island in the world following Greenland and New Guinea, is a critical region for biodiversity and environmental science (Keong & Onuma, 2021). The island of Borneo covers an area located between 4°S-7°N and 108°E-120°E, covering approximately 743,330 km^2 area (Sa'adi et al., 2020). The island, situated in Southeast Asia, is divided among three countries: Indonesia, Malaysia, and Brunei. The tropical equatorial climate of Borneo is categorized as tropical rainforest (Af), with uniform temperature all year round. Precipitation is substantial, averaging over 3000 mm annually, and is distributed throughout the year, contributing to the island's lush rainforests. Borneo represents a critical region for both scientific inquiry and conservation efforts. Its rich biodiversity, unique geological features, and significant environmental challenges make it a focal point for research to understand and preserve one of the world's most important natural areas (Keong & Onuma, 2021; von Rintelen et al., 2017).

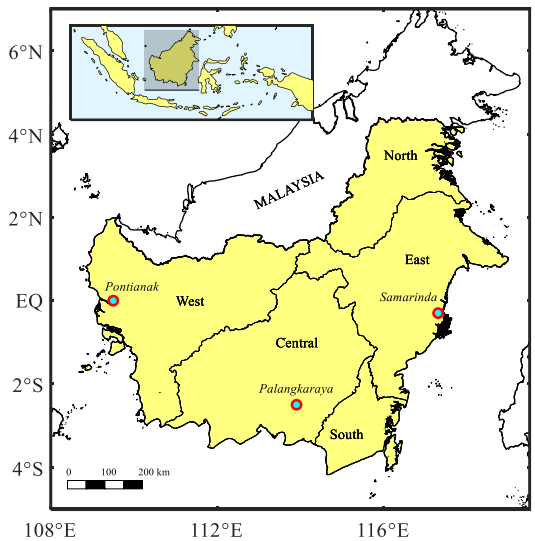

Fig. 1. Map of the island of Borneo.

Kalimantan is the Indonesian portion of the island of Borneo, covering roughly 73% of the island's land area. Kalimantan encompasses five provinces: West, Central, South, East, and North Kalimantan, as shown in **Figure 1**. Each province has distinct geographical features, from the coastal

plains of West Kalimantan to the rugged highlands of East Kalimantan. Kalimantan is highly prone to fires due to natural and human-induced factors. These fires, often called "forest fires" or "slash-and-burn" fires, have significant environmental, social, and health impacts (Harrison et al., 2024). Fires contribute to significant deforestation, loss of biodiversity, and degradation of ecosystems. Peatland fires release large amounts of carbon dioxide and other greenhouse gases, exacerbating climate change (Palamba, 2024). Furthermore, smoke from fires causes severe air pollution, leading to respiratory problems and other health issues for local communities and even affecting neighbouring countries (Sambodo et al., 2024). Moreover, fires can damage crops, disrupt livelihoods, and incur significant costs for firefighting and restoration efforts.

In the lush landscapes of Kalimantan, the natural causes of forest fires are an integral aspect of the region's ecological dynamics. Forest fires in Kalimantan can occur due to several natural factors, each contributing to the intricate fire ecology of this tropical environment. The natural factors contributing to forest fires in Kalimantan are diverse and interconnected. Lightning strikes, land cover, spontaneous combustion, and seasonal weather patterns all play roles in the fire ecology of this region (Barros et al., 2021; Edwards et al., 2020). Understanding these factors is crucial for managing and mitigating the impact of forest fires in Kalimantan. Natural variations in weather patterns, such as El Niño events, can significantly impact fire risks (Brasika et al., 2021; Nurdiati, et al., 2022a). During El Niño years, Kalimantan often experiences prolonged dry periods, reducing soil moisture and increasing the flammability of vegetation. These weather patterns create ideal conditions for fires to ignite and spread, whether from natural or anthropogenic sources.

3.2. Sources and Types of Datasets

This study used hotspot data as an indicator of forest fire in Kalimantan. Hotspots are a crucial indicator for monitoring and predicting forest fires in Kalimantan, as well as in other fire-prone regions (Kadir et al., 2023; Usup & Hayasaka, 2023). In the context of forest fires, a hotspot refers to a location with an unusually high surface temperature, which can be detected using remote sensing technologies. These hotspots indicate areas where combustion or intense heating occurs, often associated with fire activity. In Kalimantan, these hotspots typically emerge during drought, exacerbated by various climatic phenomena.

Total precipitation is one of the factors that influences fire activity (Fanin & Van Der Werf, 2017). During months with below-average precipitation, the forest biomass becomes drier and more susceptible to ignition. In Kalimantan, the relationship between precipitation and fire hotspots is inversely correlated; the likelihood of fire hotspots increases as precipitation decreases. Conversely, higher precipitation levels dampen the forest floor, reducing fire susceptibility. In addition to total precipitation, precipitation anomalies are a climate factor that can significantly impact fire risk (Nurdiati et al., 2022b). Precipitation anomalies refer to deviations from normal precipitation patterns. During years of significant precipitation deficits (often linked to broader climatic trends), Kalimantan experiences an uptick in fire hotspots. For instance, a negative precipitation anomaly can lead to prolonged dry spells, creating ideal conditions for fire ignition and spread. Monitoring these anomalies helps predict potential fire outbreaks, enabling timely intervention.

The number of dry days, called dry spells, is another critical factor in fire dynamics (Kumar & Kumar, 2022; Najib et al., 2024). In Kalimantan, prolonged dry spells can dry out surface litter and deeper soil moisture, making the region more susceptible to fire. Statistical analyses have shown that fire hotspots are more prevalent during periods exceeding a certain threshold of dry spells, emphasizing the cumulative effect of dryness.

The El Niño Southern Oscillation (ENSO) significantly impacts global weather patterns, including Kalimantan. During El Niño years, the region often experiences drier-than-normal conditions, increasing fire hotspots (Najib et al., 2022a). The resulting drought stress on vegetation heightens the risk of fires as lower humidity and higher temperatures prevail. Conversely, during La Niña events, increased precipitation typically reduces fire occurrences. Understanding ENSO patterns aids in predicting fire risk and implementing pre-emptive measures. Elsewhere, the Indian Ocean Dipole (IOD) also plays a vital role in influencing precipitation patterns in Kalimantan. A positive

IOD phase often correlates with drier conditions, further exacerbating the risk of fire hotspots (Nurdiati et al., 2022a). Conversely, a negative IOD phase typically brings increased precipitation, which can mitigate fire risk. The interplay between IOD phases and local climate conditions underscores the complexity of fire dynamics in the region. Moreover, seasonality is another critical factor in understanding fire hotspots in Kalimantan. The dry season, particularly from July to September, often sees the highest incidence of fires (Najib et al., 2022b), coinciding with lower precipitation and higher temperatures. Human activities, such as land clearing for agriculture, often peak during this time, further increasing the risk of ignition.

The interplay of natural factors creates a complex web of influences on fire dynamics. The relationship between fire hotspots in Kalimantan and natural factors like precipitation, climatic indices, and seasonality is intricate and multifaceted. Understanding the interactions between these factors is essential for effective fire management and conserving this vital ecosystem. In this study, we used multiple sources of datasets for each variable ranging from January 2001 until December 2020. The hotspot data comes from the Indonesian Agency for Meteorological, Climatological, and Geophysics, which is processed data from MODIS sensors of the Terra and Aqua satellites curated to exclude false fire hotspots. Meanwhile, local climate data is obtained from CMORPH-CRT, and global climate data is sourced from PSL NOAA. For more details, **Table 1** briefly describes the sources and types of data used.

Table 1.

Description of the sources and types of data used.

Variable	Resolution	Source
Hotspots (Y)	Monthly, 0.25 × 0.25	Retrieved from Indonesian Agency for Meteorological, Climatological and Geophysics
Total Precipitation (X_1)	Monthly, 0.25 × 0.25	Retrieved from monthly data of CMORPH_CRT datasets https://ftp.cpc.ncep.noaa.gov/precip/PORT/SEMDP/CMORPH_CRT/DATA/
Precipitation Anomalies (X_2)	Monthly, 0.25 × 0.25	Retrieved from monthly data of CMORPH_CRT datasets https://ftp.cpc.ncep.noaa.gov/precip/PORT/SEMDP/CMORPH_CRT/DATA/
Dry spells (X_3)	Monthly, 0.25 × 0.25	Retrieved and processed from daily data of CMORPH_CRT datasets https://ftp.cpc.ncep.noaa.gov/precip/PORT/SEMDP/CMORPH_CRT/DATA/
ENSO index (X_4)	Monthly, time series	Retrieved from https://psl.noaa.gov/gcos_wgsp/Timeseries/Nino34/
IOD index (X_5)	Monthly, time series	Retrieved from https://psl.noaa.gov/gcos_wgsp/Timeseries/DMI/
Seasonality (X_6)	Monthly	Month of data

Based on previous studies (Najib et al., 2021), it is well-established that precipitation predictors derived from meteorological data significantly influence the occurrence and distribution of forest fire hotspots in Kalimantan. These predictors capture the dynamic relationship between rainfall patterns and fire activity, helping them to understand and potentially mitigate fire risks. Among these, three predictors stand out due to their strong correlation with hotspot frequency: the two-month average precipitation, the monthly precipitation anomaly, and the three-month number of dry days.

The two-month average precipitation, denoted as X_1, represents the mean rainfall over the observation month and the preceding month. This predictor provides a broader temporal context, smoothing out short-term fluctuations and highlighting the cumulative precipitation available to reduce fire risk. Lower values of X_1 are generally associated with drier conditions that can exacerbate forest fire risks by reducing soil moisture and vegetation dampness.

The monthly precipitation anomaly, referred to as X_2, quantifies the deviation of rainfall during the observation month compared to its long-term historical average, or "normal". This measure serves as a critical indicator of abnormal climatic conditions, such as extended dry spells or unusually wet periods, which can influence fire susceptibility. To ensure clarity in this study, the term "precipitation anomaly" is defined inversely to the typical interpretation: a positive anomaly value signifies a deficit in rainfall relative to the norm, while a negative value indicates an excess of precipitation. This reversed convention is intentional, facilitating a direct association between positive X_2 values and increased fire risks due to insufficient rainfall.

Lastly, the number of dry days over a three-month period, labeled as X_3, captures the cumulative count of days with minimal precipitation, defined as less than 1 mm of rainfall per day. This predictor spans the observation month and the two preceding months, reflecting extended periods of dryness that are crucial for understanding fire dynamics. Prolonged dry periods, as indicated by higher X_3 values, often lead to reduced soil moisture and increased flammability of vegetation, creating favorable conditions for forest fires.

Together, these derived precipitation predictors form a comprehensive framework for analyzing the influence of rainfall variability on forest fire hotspots. By capturing both temporal trends and deviations from the norm, they provide valuable insights into the climatic drivers of fire activity in Kalimantan, enabling more effective risk assessment and management strategies.

4. RESULTS AND DISCUSSION

4.1. Pre-processing of Datasets

In our quest to understand the dynamics of fire hotspots in Kalimantan, we begin by processing satellite data in **Table 1**. This approach allows us to pinpoint specific grid points that are significant to our study of fire incidents. Our research focuses primarily on lowland regions, such as Central and Western Kalimantan, where fire occurrences are more frequent (**Figure 2a** and **2b**). These areas offer critical insights for effective fire management and climate studies. In contrast, regions with high precipitation, such as the Malaysian part of Borneo, experience fewer fire hotspots and are therefore not central to our analysis (**Figure 2c**). The abundant precipitation in these areas complicates the correlation between climate data and fire events, so our research prioritizes the more fire-prone lowland regions.

To focus on regions significantly impacted by fire incidents, we applied a k-means clustering algorithm to identify grid points with the highest correlations to hotspot occurrences. This clustering method grouped spatial data based on similarity in fire activity and climatic conditions, allowing us to isolate areas most vulnerable to fire risks. **Figure 2d** illustrates the clustering results, highlighting the critical grid points selected for further analysis. These areas, primarily in lowland regions of Central and Western Kalimantan, were used to aggregate data for temporal modeling. By employing k-means clustering, we ensured that the analysis targeted regions with consistent patterns of fire occurrence, optimizing the model's ability to capture the relationship between climate indicators and hotspots. This spatial pre-selection process reduced noise in the dataset caused by areas with low fire activity or high precipitation, such as the Malaysian part of Borneo. The selected grid points were aggregated into a time series format, enabling the study to focus on temporal dynamics while retaining spatial relevance through targeted grid selection.

By aggregating the relevant grid points into a time series, we can effectively track fire occurrences over time, identifying patterns and trends that emerge in relation to climatic variations. This focused methodology allows us to disentangle the complex relationships between precipitation and fire activity. Our satellite data processing aims to illuminate the region’s most vulnerable to fire risks while acknowledging the intricate interplay of climatic factors. By concentrating on the low-precipitation areas with high-fire incidents, we hope to provide valuable insights that inform targeted interventions and enhance our understanding of fire dynamics in Kalimantan's unique environment.

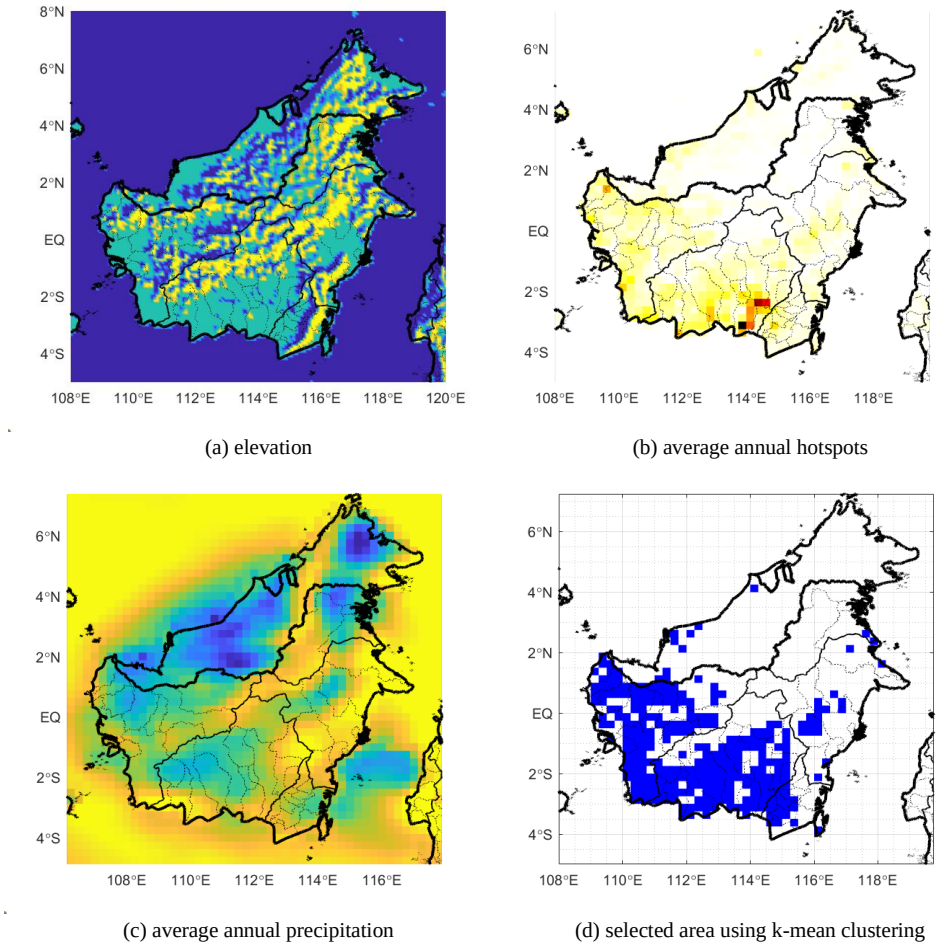

(a) elevation

(b) average annual hotspots

(c) average annual precipitation

(d) selected area using k-mean clustering

Fig. 2. Map of the island of Borneo showing: a) elevation, b) average annual hotspots, c) average annual precipitation, and d) selected area using k-mean clustering.

4.2. Correlation Between Variables

In this section, we conduct a cross-correlation analysis between fire hotspots and climatic factors, as shown in **Figure 3**. Our analysis reveals that the highest correlation with fire hotspots is observed with the variable dry spells, yielding a correlation coefficient of 0.699. This strong positive correlation suggests that prolonged dry conditions significantly increase fire occurrences. Additionally, we find the highest correlation among the climatic factors is between total precipitation and dry spells, with a coefficient of -0.876. This inverse relationship indicates that as total precipitation increases, the frequency or duration of dry spells tends to decrease, which aligns with the understanding that wetter conditions typically mitigate fire risk.

Given these correlations, the implications for predicting fire hotspots using climatic factors are substantial. The strong correlation between dry spells and fire hotspots implies that monitoring and forecasting dry conditions could effectively predict fire risks. In regions with anticipated dry spells, proactive measures can be implemented to mitigate potential fire outbreaks. Furthermore, the inverse relationship between total precipitation and dry spells emphasizes the importance of rainfall patterns in fire prediction models. By integrating total precipitation and dry spells into predictive models, we can improve the accuracy of forecasts regarding fire hotspots. Additionally, understanding the interactions between these climatic factors—such as the influence of the ENSO and IOD indices—can provide further insights into seasonal variations and long-term trends in fire occurrences.

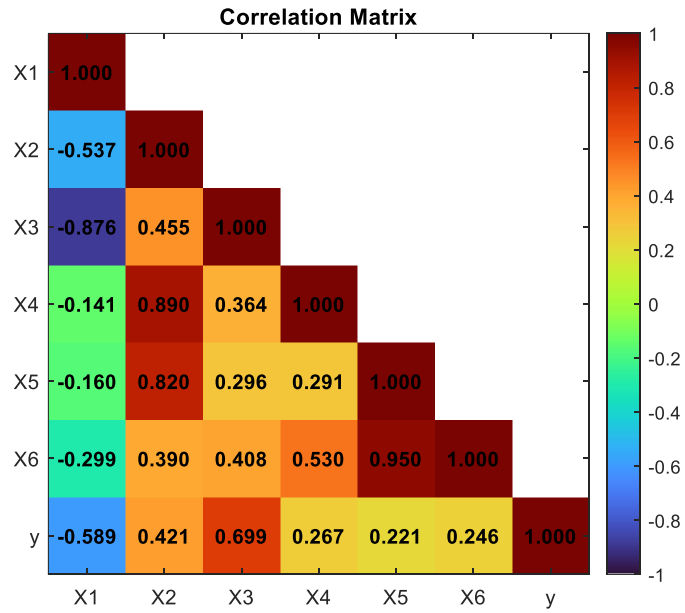

Fig. 3. Heatmap of cross-correlation analysis between fire hotspots and climatic factors.

4.3. Polynomial Features and Variable Selection

The weak linear relationship observed between the response variable and the predictor variable, as shown in **Figure 3**, indicates that the data may not be suitable for input for a linear regression model. This weak correlation can lead to a phenomenon known as underfitting, where the model fails to learn and represent the underlying patterns in the data adequately. Consequently, adopting alternative methods that enhance the model's ability to capture these subtle relationships becomes essential. One such method is the application of polynomial features, as proposed by Maulud and Abdulazeez (2020). This technique transforms the predictor variables by applying specific polynomial degrees, thus generating additional predictor variables. The primary objective of this approach is to increase the complexity of the model, enabling it to learn better and fit the weak linear relationship between the response and predictor variables. The model can address the challenges posed by underfitting by employing polynomial features, improving its predictive performance, and providing a more accurate data representation.

In addition to the challenges of weak linear relationships, linear regression models struggle to capture the interaction effects among variables directly. This is particularly relevant in the context of this study, where the predictor variables consist of multiple climate indicators that typically interact with one another. Adding additional predictor variables in the form of interaction terms becomes necessary to address this limitation. According to Bertsimas and Wiberg (2020), incorporating interaction variables can significantly enhance the model's ability to identify and learn from weak linear relationships among the variables.

Considering this, this research integrates interaction terms as supplementary predictor variables, aiming to effectively capture the interactions between climate indicators in predicting the number of hotspots while simultaneously improving the model's accuracy. The addition of these interaction variables is implemented through the polynomial features method. By applying polynomial transformations up to a maximum degree of three, the analysis generates a total of seventy-seven additional predictor variables, as detailed in **Table 2**. This strategic enhancement broadens the scope of the model's input and allows for a more nuanced understanding of the interplay among climate indicators, leading to more precise and reliable predictions.

Table 2.

Additional predictor variables resulting from the application of polynomial features.

Type of Predictor Variable	Number of Predictors	Members of predictors
variables of degree 2	6	$x_1^2, x_2^2, \dots, x_6^2$
variables of degree 3	6	$x_1^3, x_2^3, \dots, x_6^3$
interaction variables	65	$x_1x_2, x_1^2x_2, \dots, x_1x_5x_6$

The inclusion of additional predictor variables, as illustrated in **Table 2**, brings the total number of predictor variables to eighty-three. This substantial increase in variable count can significantly prolong the computational time required to develop an accurate predictive model. To address this issue, a variable selection technique is employed to reduce the number of predictor variables, streamlining the modelling process. The dataset must first be divided into training and testing subsets before applying the variable selection technique to ensure a valid and reliable model evaluation. The training data, covering the period from January 2001 to December 2018, is utilized for model development, while the testing data, spanning from January 2019 to December 2020, assesses the model's performance.

The selection of these specific time ranges is based on a series of experiments that explored various proportions of data allocation. This approach led to the identification of the optimal division that effectively balances the training and testing datasets. Ensuring that the training and testing periods do not overlap, the model is evaluated on data it never encountered during training. This methodology is essential for validating the robustness of the model's performance, as it allows for a more accurate assessment of how well the model can generalize to unseen data. This strategic division enhances the credibility of the results and contributes to a more reliable predictive framework.

Subsequently, all predictor variables in the training dataset are selected using the best subset selection technique. This approach employs the Bayesian Information Criterion (BIC) as the metric for determining the optimal combination of predictor variables. A lower BIC value indicates a better model fit, which allows us to identify the most effective combination of predictor variables for inclusion in the final model. The maximum number of predictor variables selected through this technique is limited to ten. The results of the variable selection process using best subset selection are visualized in a plot, as shown in **Figure 4**. This visualization clearly represents the selected variables and their respective contributions to the model, facilitating a better understanding of the relationships within the data. By employing this rigorous selection method, the model can achieve a more refined and efficient representation of the underlying patterns, enhancing its predictive capabilities.

Figure 4 illustrates the ten combinations of predictor variables and their corresponding BIC values. Each line in the plot indicates the selected predictor variables for each combination, with the line length reflecting the order in which the variables were chosen. For instance, the combination represented in the second row from the bottom, which yields a BIC value of -293.5739, includes the variables x_3^3 and x_3^2.

The combinations with the highest BIC values appear at the bottom of the plot, while those with the lowest values are positioned at the top. Consequently, the model that results in the lowest BIC value is constructed from a combination of six predictor variables, as highlighted in **Figure 4** and presented in Eq. 13. This model achieves a BIC value of -307.6923, marking it as the best result after conducting various iterations of the best subset selection process with different maximum numbers of predictor variables.

The results from the best subset selection, indicated by Eq. 13, revealed a model comprised of six terms in polynomial form, highlighting the interactions between precipitation anomalies (x_2), dry spells (x_3), and the Indian Ocean Dipole (IOD, x_5) index. This model illustrates the complex relationships among these variables and their combined effect on hotspot occurrences. This finding suggests that these three climate indicators strongly influence the number of hotspots in Kalimantan, underscoring their critical role in environmental monitoring and predictive modelling.

$$\hat{y} = \hat{\beta}_0 + \hat{\beta}_1 x_3^3 + \hat{\beta}_2 x_3^2 + \hat{\beta}_3 x_3 + \hat{\beta}_4 x_2 x_3^2 + \hat{\beta}_5 x_3^2 x_5 + \hat{\beta}_6 x_2^2 x_5 \quad (13)$$

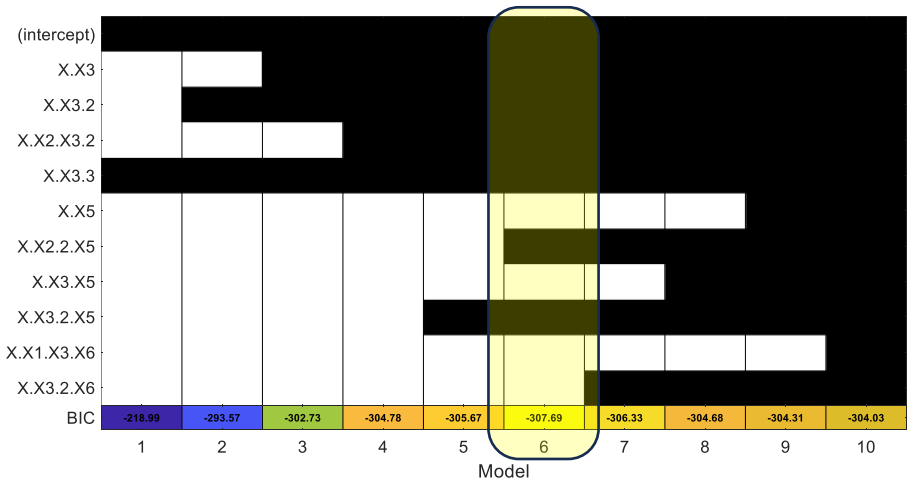

Fig. 4. Results of variable selection using best subset selection.

A key takeaway from the analysis is the prominent role of dry spells as a significant predictor for hotspots. Their presence in nearly every term of the equation underscores their critical influence on environmental conditions that contribute to hotspot formation. Dry spells can exacerbate drought conditions, reducing soil moisture and increasing the likelihood of fire events, leading to higher hotspot counts. The interactions identified in the model further emphasize the importance of considering how these factors interrelate. For instance, the impact of precipitation anomalies may be modulated by the presence of dry spells, indicating that an increase in precipitation does not necessarily mitigate hotspots if dry conditions persist concurrently.

This comprehensive understanding enhances predictive accuracy and provides valuable insights for stakeholders involved in environmental monitoring and management. By recognizing the interplay between these climatic factors, strategies can be developed to address and mitigate the risks associated with hotspot occurrences, particularly in vulnerable regions.

4.4. Training for regularized regression and BMA models

The prepared data was subsequently utilized to develop a regression model based on Equation (13) to predict the number of hotspots in Kalimantan. The first phase of model development involved training the model using a training dataset. This training process encompassed several regression models, specifically regularized regression techniques, including ridge, LASSO, and elastic-net regressions, alongside a BMA approach based on polynomial regression.

4.4.1. Regularized Regression Models

The training of the three regularized regression models begins with determining the hyperparameter values using a 10-fold cross-validation method. This approach is employed to identify the best lambda values for the ridge and LASSO regression models, while alpha and lambda hyperparameters are assessed for the elastic-net regression model. For the ridge and LASSO models, a total of 100 lambda values are randomly sampled from the range 10^{-10} to 10^{10} for application in the cross-validation process. In addition, the alpha value for the elastic-net model is determined by randomly selecting 20 alpha values from 0 to 1. During this procedure, the best lambda is applied in conjunction with each trial of alpha during cross-validation.

The selection of the best hyperparameters is based on the lowest Mean Squared Error (MSE) observed during the validation process. The resulting hyperparameter values for alpha and lambda for each regression model, derived from cross-validation, are summarized in **Table 3**. This systematic approach ensures the models are finely tuned for optimal performance, facilitating more accurate predictions in subsequent analyses.

Table 3.

Optimal hyperparameter values used in each regularized regression model.

Regularized regression model	alpha	Lambda
Ridge	0*	0,01917910
LASSO	1*	0,03053856
Elastic-net	0,6841737	0,17868010

**This hyperparameter value is a fixed value.*

The hyperparameter alpha values for the ridge and LASSO regression models, as indicated in **Table 3**, are fixed at 0 and 1, respectively. This specific allocation signifies the contrasting nature of these two regression techniques, with ridge regression favoring the inclusion of all predictors while LASSO regression actively eliminates some, leading to sparse models. In contrast, the elastic-net regression model employs an alpha value of 0.68, which is notably closer to 1, indicating a predominant reliance on the LASSO mechanism. This suggests that while elastic-net incorporates both ridge and LASSO elements, its behavior is more aligned with LASSO, thus promoting sparsity in the coefficient estimates.

Moreover, the lambda values reflect the degree of regularization imposed on the coefficients of each regression model. The elastic-net model exhibits the highest lambda value of 0.18, as presented in **Table 3**, which is significantly greater than the lambda values of the ridge and LASSO models, both of which remain under 0.05. This elevated lambda in the elastic-net model results in a more substantial penalty on the coefficients, driving them closer to zero compared to those in the ridge and LASSO models. Consequently, this pronounced regularization effect of elastic-net can lead to better performance in scenarios where multicollinearity is present or when there are many predictors, as it combines the strengths of both regularization techniques while managing to reduce overfitting effectively. The interplay of these hyperparameters ultimately illustrates the nuanced approach of elastic-net regression, making it a powerful tool for tackling complex predictive modeling tasks.

After determining the optimal hyperparameter values for alpha and lambda for each model, as presented in **Table 3**, these values were subsequently utilized to train the three regularized regression models for predicting the number of hotspots in Kalimantan. The resulting models included ridge regression, LASSO, and elastic-net, each characterized by distinct intercepts and coefficients detailed in **Table 4**.

Table 4.

Intercept and coefficient values for each predictor variable in the three regularized regression models.

Coeficients*	Regularized regression models		
	Ridge	***LASSO***	***Elastic-net***
$\boldsymbol{\beta_0}$	-3556,39	-4110,76	-1888,26
$\boldsymbol{\beta_1}$	0,122	0,129	0,099
$\boldsymbol{\beta_2}$	-11,50	-12,50	-8,51
$\boldsymbol{\beta_3}$	356,33	398,11	230,76
$\boldsymbol{\beta_4}$	0,043	0,042	0,046
$\boldsymbol{\beta_5}$	-0,384	-0,386	-0,377
$\boldsymbol{\beta_6}$	107,59	106,21	111,31

**Intercept and coefficient values for the best variable combination based on the results of best subset selection in equation (13).*

The results of the regularized regression analysis indicate that the absolute value of the highest coefficient is attributed to the interception. This suggests a strong baseline level of prediction for the model when all predictors are held constant at zero.

Among the predictor coefficients, the highest positive values are observed for β_3 and β_6. Specifically, β_3 representing the coefficient for dry-spells, underscores its significant influence on the prediction of hotspots. This reinforces the finding that dry spells are critical factors contributing to fire risks, as they can create conditions conducive to ignition and spread.

In addition, β_6 which captures the interaction between precipitation anomalies and the IOD index, highlighting the importance of understanding how these two factors work together. This interaction suggests that changes in precipitation patterns, influenced by IOD, can exacerbate or mitigate the effects of dry spells on hotspot occurrences.

4.4.2. Bayesian Model Averaging (BMA) Model

The training of the BMA model, based on polynomial regression, begins by determining the parameters of the BMA model, which consists of the coefficients and weights of the polynomial regression model. Determining the polynomial regression model coefficients is done by generating all possible polynomial regression models based on various combinations of predictor variables and estimating the regression coefficients for each model. Six polynomial regression models are then selected based on the lowest BIC (Bayesian Information Criterion) values, after which each model is assigned, a weight representing the influence of the selected models on the final BMA model. **Table 5** displays the interceptive values, regression coefficients, and weights for each selected polynomial regression model, obtained from the BMA model training process.

Table 5.

Summary of the BMA model components along with their respective weights.

Coefficients	Model 1	Model 2	Model 3	Model 4	Model 5	Model 6
$\boldsymbol{\beta_0}$	-5426,87	-6250,85	-5853,77	-5258,17	-6764,41	-6181,12
$\boldsymbol{\beta_1}$	0,148	0,166	0,157	0,144	0,178	0,165
$\boldsymbol{\beta_2}$	-14,88	-16,88	-15,98	-14,55	-18,20	-16,80
$\boldsymbol{\beta_3}$	497,45	567,61	537,13	485,77	614,88	564,54
$\boldsymbol{\beta_4}$	0,039	0,00	0,042	0,044	0,00	0,00
$\boldsymbol{\beta_5}$	-0,391	-0,411	-0,214	0,00	-0,225	0,00
$\boldsymbol{\beta_6}$	103,05	109,05	0,00	0,00	0,00	0,00
Weight	**0,405**	**0,254**	**0,147**	**0,094**	**0,066**	**0,034**

Table 5 shows that each selected polynomial regression model has a different number of predictor variables. Model 1 is the model that uses all the predictor variables and has the most predictors, while Model 6 is the model with the fewest predictor variables, using only 3. Additionally, it can be observed that the intercept and regression coefficient values for each selected model tend to be small, with some coefficients approaching zero, similar to the regularization regression model. **Table 5** also displays the weights for each selected model, where the total sum of the weights equals 1. Model 1 has the most significant weight, with six predictor variables, indicating that this model best explains the overall data. Therefore, Model 1 will influence the final BMA model the most. Meanwhile, Model 6, with 3 predictor variables, has the most negligible weight, even below 5%.

All the selected polynomial regression models will be combined into a single final BMA model based on the weights shown in **Table 5**. **Table 6** provides detailed insights into the coefficients β of the Bayesian regression model, describing the relationship between each predictor and the response variable. The coefficient column represents the expected effect of each predictor on the response variable. For instance, β_3 has a coefficient of 530, suggesting that a unit increase in the corresponding predictor is associated with an average increase of 530 units in the response variable. These coefficients provide critical insights into the strength and direction of the relationships in the model.

The $p \neq 0$ column indicates the posterior probability that each coefficient is not zero. Predictors β_1, β_2, and β_3 have $p \neq 0$ values of 100%, reflecting strong evidence of their significant impact on the response variable. On the other hand, predictors such as β_4 (64.6%) and β_6 (65.9%) exhibit lower probabilities, suggesting weaker evidence of their relevance. These probabilities highlight the varying levels of certainty about the predictors' importance within the model. Overall, **Table 6** identifies β_1, β_2, and β_3 as the most significant predictors due to their high posterior probabilities, making them reliable contributors to the model. In contrast, β_4, β_5, and β_6 show weaker evidence for inclusion, with lower probabilities, indicating higher uncertainty about their effects.

Table 6.

Summary of the Bayesian Model Averaging (BMA) model.

Coefficient	p!=0 (%)	EV	SD	Upper PI (95%)	Lower PI (95%)
$\boldsymbol{\beta_0}$	100	-5797	2038	-6069	-5525
$\boldsymbol{\beta_1}$	100	0.1558	0.02802	0.1521	0.1595
$\boldsymbol{\beta_2}$	100	-15.8	3.612	-16.3	-15.3
$\boldsymbol{\beta_3}$	100	530	151.2	510	550
$\boldsymbol{\beta_4}$	64.6	0.02613	0.0232	0.02303	0.02922
$\boldsymbol{\beta_5}$	87.2	-0.3088	0.1691	-0.3314	-0.2862
$\boldsymbol{\beta_6}$	65.9	69.41	58.9	61.56	77.26

The inclusion of 95% credible intervals and posterior probabilities enhances the interpretability of the model, offering a comprehensive view of both the strength and reliability of each predictor's impact. Eq. 14 represents the final BMA model obtained. It shows that in the final BMA model, predictor variables are negatively and positively related to the response variable. These negatively and positively related variables are consistent with those in the regularization regression model.

$$\hat{y} = -5797 + 0.16x_3^3 - 15.8x_3^2 + 530.03x_3 + 0.03x_2x_3^2 - 0.32x_3^2x_5 + 69.41x_2^2x_5 \qquad (14)$$

4.5. Testing and Evaluation of Models

Four models have been trained: the ridge regression model, LASSO regression, elastic-net regression, and the final BMA model. The BMA model combines six selected polynomial regression models, with each model weighed according to its performance. These four models were subsequently tested using a separate test dataset. The purpose of testing the models is twofold: first, to evaluate the models' performance when applied to data they have not encountered before, and second, to assess the accuracy of each model in predicting the number of hotspots. This phase is critical in determining how well the models generalize beyond the training data and their reliability in making accurate predictions in real-world scenarios.

The performance of the four models was evaluated using two model evaluation metrics: Root Mean Squared Error (RMSE) and the coefficient of determination (R^2). RMSE indicates how close the model's predictions are to the actual values, whereas a lower RMSE indicates better predictive accuracy. On the other hand, R^2 measures the proportion of variance in the dependent variable that can be explained by the model, with higher values indicating better explanatory power. Performance measurement based on RMSE and R^2 was conducted on the training and test datasets. The best-performing model was selected based on the lowest RMSE and the highest R^2 values. The RMSE and R^2 values for all four models are summarized in **Table 7**.

Table 7.

RMSE and R-squared values on training and testing data for regularized regression and BMA models.

Model	RMSE		R^2 (%)	
	Training	*Testing*	*Training*	*Testing*
Ridge	680,82	764,59	82,56	84,46
LASSO	680,04	752,31	82,6	85,06
Elastic-net	684,77	802,66	82,36	82,58
BMA	681,97	664,33	82,5	88,58

The values presented in **Table 7** indicate no significant differences in RMSE and R^2 values across the models when evaluated on the training data. However, these differences become more apparent when assessing the models on the test data. The final BMA model achieved the lowest RMSE on the test data, although this was not the case for the training data. Notably, the difference between the RMSE values for the BMA model on the training and test datasets was the smallest among all the models, suggesting that the BMA model is less likely to experience overfitting based on RMSE

values. Furthermore, the BMA model also had the highest R^2 value on the test data, reaching 88.58% and its R^2 value on the training data was also relatively high, at 82.5%. These R^2 values demonstrate that the BMA model can explain approximately 88.58% of the variance in the test data and 82.5% of the variance in the training data. Therefore, the BMA model outperforms the other three models and is the best predictor of the number of hotspots in Kalimantan.

BMA demonstrates superior robustness and accuracy in predictive modeling, particularly on test datasets, compared to regularization techniques such as Ridge, LASSO, and Elastic Net. Although these regularization methods effectively prevent overfitting and improve model interpretability by introducing penalties for complexity, they rely on a single model selection approach. This means that their predictive performance is contingent on the specific model chosen, which may not capture the full uncertainty inherent in the data. In contrast, BMA explicitly accounts for model uncertainty by averaging over a set of candidate models, weighted according to their posterior probabilities. This ensemble approach integrates information from multiple models, allowing BMA to leverage diverse perspectives on the data. As a result, it tends to produce more stable predictions, especially in scenarios where the underlying data-generating process is complex or not fully understood.

BMA incorporates prior information and allows for the inclusion of prior beliefs about model parameters, leading to more informed predictions. This characteristic enhances its flexibility and adaptability to various data distributions, improving its performance on unseen data. When regularization methods may inadvertently select suboptimal models, BMA mitigates this risk by pooling information across multiple models, thereby capturing a broader range of possible outcomes. Furthermore, BMA's reliance on a probabilistic framework enables it to provide measures of uncertainty alongside predictions, which is invaluable for decision-making in fields like environmental science and resource management. By quantifying uncertainty, practitioners can make more informed decisions based on the predicted hotspots for forest fires or other critical events.

While Ridge, LASSO, and Elastic Net may perform comparably during training, their single-model focus can limit their generalizability. In contrast, BMA's ensemble approach, which averages predictions across multiple models and incorporates uncertainty, enhances its robustness and predictive accuracy on test datasets.

4.6. Results Validation and Simulation

To ensure the reliability and robustness of the BMA model, a comprehensive validation process was conducted using climate data from 2021 to 2024. This step was critical to assess the model's performance on unseen data, ensuring its predictive accuracy and generalizability under varying climatic conditions. The validation involved applying the trained BMA model to a new dataset, which was processed consistently using the same methodology as the original dataset. Maintaining consistency in data preparation ensured that any observed differences in performance could be attributed solely to the model's capabilities, rather than inconsistencies in data handling.

The validation focused on key climate indicators that significantly influence fire risks. One such indicator was precipitation anomalies (x_2), which measure deviations in rainfall from the long-term average. This variable highlight unusual climatic conditions, such as abnormally dry or wet periods, that can impact fire susceptibility. Another crucial indicator was dry spells (x_3), defined as the number of days with less than 1 mm of rainfall over a specific period. Prolonged dry spells are strongly associated with heightened fire risk due to reduced soil moisture and increased vegetation flammability.

In addition to these local climate variables, the validation also incorporated the Indian Ocean Dipole (IOD) index (x_5), a large-scale climate indicator that measures differences in sea surface temperatures between the western and eastern Indian Ocean. The IOD index has a well-documented influence on regional weather patterns, including rainfall variability across Kalimantan. By including this index, the BMA model was able to account for broader climatic drivers that impact local fire dynamics. Pre-processed data, summarized in **Figure 5**, provides monthly data for three key climate indicators over the period from January 2021 to September 2024: precipitation anomalies (x_2), dry spells (x_3), and the Indian Ocean Dipole index (x_5).

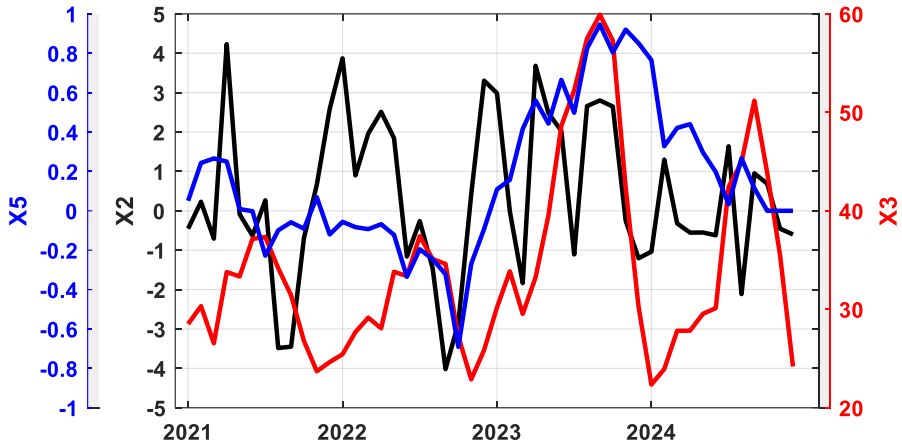

Fig. 5. Pre-processed data for results validation, covering precipitation anomalies (x_2), dry spells (x_3), and the Indian Ocean Dipole index (x_5) from 2021-2024.

Notable dry periods with prolonged dry spells and negative precipitation anomalies occurred in mid-2023 to end-2023, coinciding with positive IOD phases that exacerbate dry conditions. Conversely, wetter conditions with positive precipitation anomalies and fewer dry days were observed during 2022 and parts of 2024. The highest dry spell counts in mid-2023 and increasing dryness toward 2024 highlight periods of elevated fire susceptibility. Using the trained BMA model, validation data from 2021 to 2024 was employed to predict the occurrence of forest fire hotspots in Kalimantan and the results can be seen in **Figure 6**.

Figure 6 displays the predicted number of forest fire hotspots in 2021 to 2024, modeled using BMA. The black line indicates observed historical hotspot data, with a notable spike in late 2019 representing an extreme fire event. This historical pattern was likely used to calibrate its predictive capabilities. Expected values (red line) represents the central predictions of the model for the number of hotspots. It shows a generally low level of fire activity from 2021 to early 2023, with a clear upward trend and peak in mid-to-late 2023. Uncertainty range (yellow shading) represents the 95% confidence interval (CI). This highlights the uncertainty in the model's predictions, widening significantly during periods of high hotspot activity, such as the peaks in 2023 and 2024.

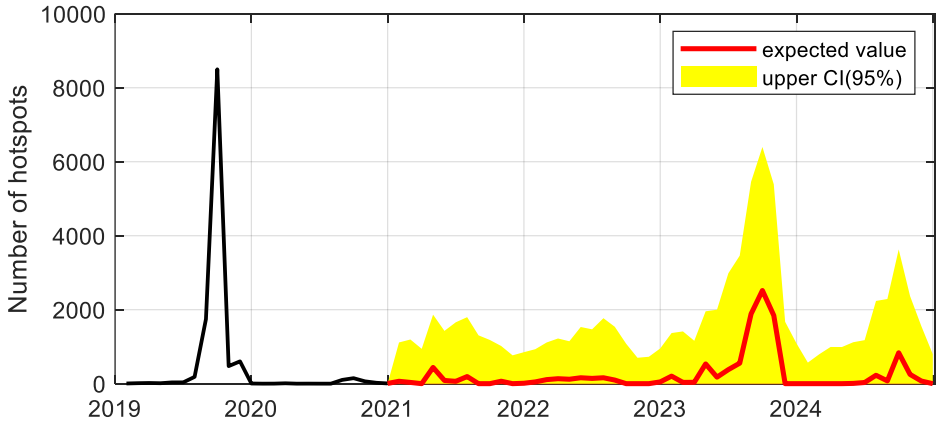

Fig. 6. Predicted number of forest fire hotspots in 2021 to 2024, modeled using BMA.

Predictions suggest a stable and relatively quiet period in terms of hotspots during 2021 and 2022. Starting in mid-2023, the model predicts an increase in fire activity, peaking in late 2023. These peaks

are likely tied to climatic conditions, such as prolonged dry spells or anomalies in rainfall, which are key predictors in the BMA model. During periods of low predicted activity (e.g., 2021-2022), the confidence intervals are narrow, reflecting high model confidence. In contrast, during peak activity (e.g., 2023-2024), the uncertainty widens, indicating the model's acknowledgment of higher variability and unpredictability under extreme conditions.

We compared our results with burned area data from SiPongi KLHK (see https://sipongi.menlhk.go.id/). **Table 8** shows burned area data from SiPongi highlights trends in fire activity across Kalimantan provinces between 2019 and 2023. In 2019, the burned area reached an exceptional total of 684,599 hectares, driven by extensive fires across Kalimantan, especially in Kalimantan Tengah (317,749 hectares). This aligns with the observed spike in hotspots in the historical data used for testing the BMA model. In 2020, the burned area dropped sharply to 26,286 hectares, reflecting a significant reduction in fire activity. This decrease is also reflected in the dramatic reduction in observed hotspots. These trends validate the model's ability to respond to extreme events and to capture transitions between high and low fire activity periods.

Table 8.

Burned area data from SiPongi highlights trends in fire activity across Kalimantan provinces between 2019 and 2023.

Region	2019	2020	2021	2022	2023
Kalimantan Barat	151,919	7,646	20,590	21,836	111,848.4
Kalimantan Selatan	137,848	4,017	8,625	429	190,394.6
Kalimantan Tengah	317,749	7,681	3,653	1,554	165,896.4
Kalimantan Timur	68,524	5,221	3,029	373	39,494.4
Kalimantan Utara	8,559	1,721	1,678	370	796.4
Total (in hectares)	**684,599**	**26,286**	**37,575**	**24,562**	**508,430.2**

During 2021 and 2022, the burned area remained relatively low, at 37,575 hectares and 24,562 hectares, respectively. The BMA model's predictions for this period indicate relatively low numbers of hotspots with narrow confidence intervals, reflecting strong confidence in its forecasts. This alignment with SiPongi data demonstrates that the model effectively captures periods of reduced fire activity, particularly under stable climatic conditions and low fire risk.

In 2023, a sharp increase in burned area is recorded, totaling 508,430 hectares. The most affected provinces were Kalimantan Barat (111,848 hectares), Kalimantan Selatan (190,394 hectares), and Kalimantan Tengah (165,896 hectares). Many recent studies have mentioned this fire incident in their studies (Nurlatifah et al., 2025). Correspondingly, the BMA model predicts a significant rise in hotspots for the same period, with notable peaks in expected values and wider confidence intervals. This reflects the model's awareness of heightened fire risks, and the variability associated with extreme fire seasons. The alignment between the burned area data and hotspot predictions in 2023 validates the model's utility for forecasting high-risk periods.

Furthermore, we simulate the predictions of hotspots using the trained BMA model under neutral and positive Indian Ocean Dipole (IOD) conditions to reveal the relationship between predictor variables x_2 (negative rainfall anomaly) and x_3 (number of dry days) with the predicted number of hotspots. **Figure 7** shows simulation results for various values of x_2 and x_3 under neutral Indian Ocean Dipole (IOD) conditions to predict hotspots in Kalimantan. Meanwhile, **Figure 8** displays simulation results under positive IOD.

Figure 7a illustrates how the number of hotspots increases as x_3 (number of dry days) rises from 25 to 60, under different fixed values of x_2 ranging from -5 to 5. A consistent trend is observed where higher values of x_3 led to a rapid increase in predicted hotspots, particularly when x_3 exceeds 50. This indicates that prolonged periods of dryness have a significant amplifying effect on fire activity. Moreover, for any given x_3, higher values of x_2 (indicating lower rainfall anomalies or drier conditions) result in more hotspots. The steep increase in hotspots with both variables highlights the compounded impact of extended dry periods and reduced rainfall on fire risk.

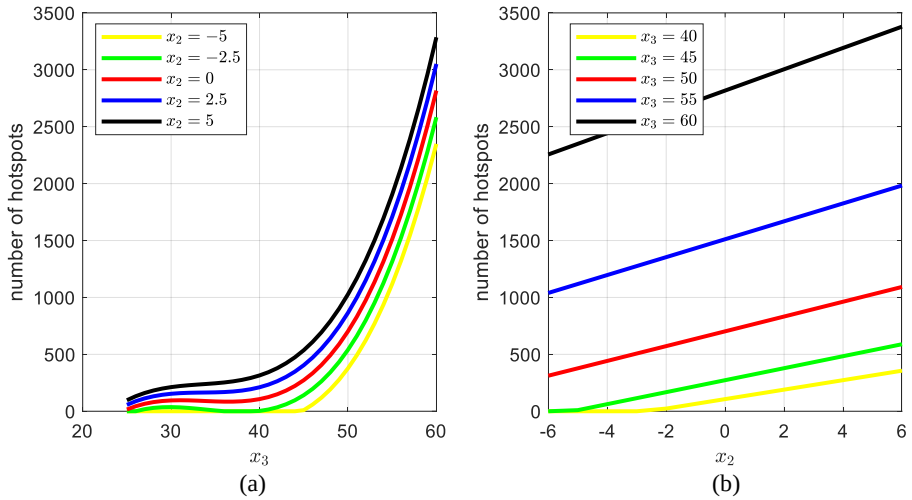

Fig. 7. Simulation results for various values of x_2 and x_3 under neutral Indian Ocean Dipole (IOD) conditions to predict hotspots in Kalimantan: a) influence of x_3 on the number of hotspots under different fixed values of x_2, and b) influence of x_2 on the number of hotspots under different fixed values of x_3.

Otherwise, **Figure 7b** examines the influence of x_2 on the number of hotspots while keeping x_3 constant at values ranging from 40 to 60. For all x_3 scenarios, the number of hotspots increases as x_2 moves from negative (wet conditions) to positive (dry conditions). Notably, the rate of increase in hotspots is steeper for higher x_3 values. For instance, at $x_3 = 60$, even a small shift in x_2 towards drier conditions leads to a marked increase in hotspots, emphasizing the vulnerability of regions with extended dry days to changes in rainfall anomalies.

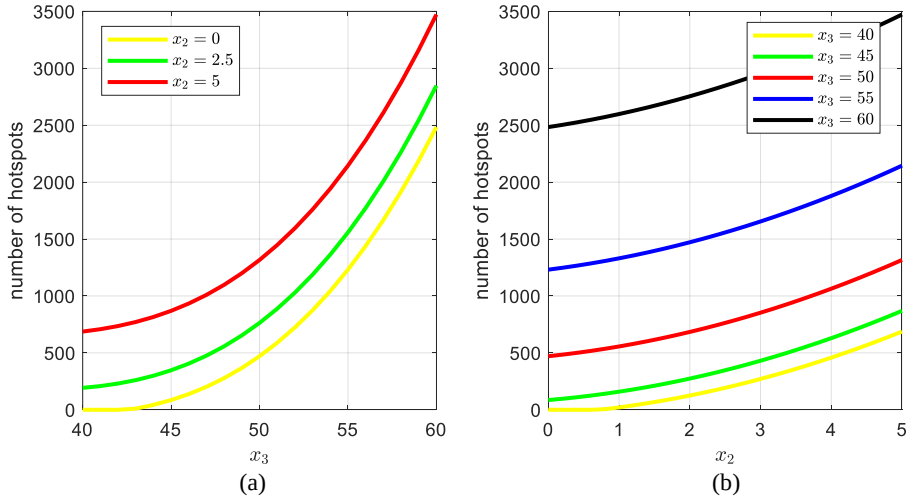

Fig. 8. Simulation results for various values of x_2 and x_3 under positive Indian Ocean Dipole (IOD) conditions to predict hotspots in Kalimantan: a) influence of x_3 on the number of hotspots under different fixed values of x_2, and b) influence of x_2 on the number of hotspots under different fixed values of x_3.

Under positive IOD, the value of x_2 and x_3 generally above their normal conditions. Therefore, the simulated range of x_2 and x_3 will be limited to values above their normal.

Figure 8a shows that as x_3 increases from 40 to 60, the predicted number of hotspots rises steadily for all fixed values of x_2. This indicates that under positive IOD conditions, a longer duration of dry days significantly escalates fire activity. The increase is more pronounced for higher values of x_2 (representing lower rainfall anomalies). For instance, when $x_2 = 5$, the growth in hotspots with increasing x_3 is considerably steeper than for lower x_2 values, highlighting the compounded impact of dry conditions and extended periods without rain. Otherwise, **Figure 8b** examines the impact of x_2 on the number of hotspots for fixed x_3 values ranging from 40 to 60. The number of hotspots increases as x_2 becomes more positive, with the rate of increase being greater for higher x_3 values. For example, at $x_3 = 60$, even small increments in x_2 lead to a substantial rise in predicted hotspots. This result indicates that under positive IOD conditions, the combination of a higher number of dry days and reduced rainfall intensifies fire risk more than each variable individually.

The simulations under both neutral and positive Indian Ocean Dipole (IOD) conditions provide valuable insights into the relationships between the predictor variables x_2 (negative rainfall anomaly) and x_3 (number of dry days) and the predicted number of hotspots. These results highlight distinct patterns influenced by different climatic conditions, which are crucial for understanding and mitigating fire risks in Kalimantan. In **both neutral and positive IOD** conditions, the number of hotspots consistently increases with higher x_3, reflecting the significant role of prolonged dry spells in intensifying fire activity. Under neutral IOD conditions, this relationship is evident but less pronounced compared to positive IOD scenarios. Positive IOD conditions amplify the effect of dry days, with hotspots increasing more steeply as x_3 rises from 40 to 60. This suggests that during positive IOD phases, the combination of regional weather patterns and longer dry periods creates a more conducive environment for fires. Conversely, the simulations show that the number of hotspots increases as x_2 becomes more positive (indicating lower-than-normal rainfall), with the effect being stronger **under positive IOD** conditions. For fixed x_3 values, higher x_2 results in a more rapid escalation of hotspots, particularly when x_3 is already elevated. This compounding effect of reduced rainfall and extended dry periods underscores the critical importance of monitoring rainfall anomalies in predicting fire risk.

The interaction between x_2 and x_3 is particularly noteworthy. During neutral IOD conditions, both variables influence the number of hotspots, but their combined effect is less severe compared to positive IOD conditions. Under positive IOD scenarios, the simultaneous increase in x_2 and x_3 leads to a dramatic rise in predicted hotspots. For instance, when x_3 is at its highest values (e.g., 60), even small increments in x_2 can significantly amplify the number of hotspots. This highlights the synergistic impact of these two variables during positive IOD phases, making such conditions particularly dangerous for fire outbreaks.

These combined results underscore the heightened fire risk during positive IOD conditions due to the stronger influence of both dry spells and rainfall anomalies. While neutral IOD conditions also present fire risks, the amplified effect during positive IOD highlights the importance of tailored fire mitigation strategies based on prevailing climatic conditions. Monitoring both x_2 and x_3 is critical, especially during positive IOD phases, as their interaction can significantly elevate fire activity. Proactive measures, including early warnings and fire prevention efforts, should prioritize areas experiencing prolonged dry spells and below-normal rainfall during these periods.

4.7. Discussion and Limitations of the Study

The findings underscore the practical utility of the BMA model for forest fire management. By accurately predicting hotspots, this model empowers stakeholders to make proactive and data-driven decisions to mitigate forest fire risks. For instance, the integration of climate indicators, particularly dry spells and precipitation anomalies, enables the identification of critical periods when fire risks are heightened due to prolonged dry conditions or abnormal weather patterns. This temporal framework is crucial for optimizing the allocation of resources, such as positioning firefighting teams, enhancing surveillance in high-risk areas, and pre-positioning water storage for firefighting.

Furthermore, the model's predictive capabilities can be integrated into early warning systems, providing timely alerts to local communities and allowing for the implementation of preventive measures such as controlled burns or the temporary suspension of activities like land clearing.

The ability of the BMA model to incorporate uncertainty into its predictions enhances its robustness compared to single-model approaches. By providing probabilistic insights, the BMA model enables stakeholders to assess the likelihood of fire outbreaks under different scenarios. This is particularly important in a complex and dynamic environment like Kalimantan, where variability in climate conditions can lead to unforeseen challenges. By quantifying these uncertainties, decision-makers can implement risk-informed strategies, such as prioritizing areas with a higher probability of fire occurrence while maintaining preparedness for lower-risk zones. This approach minimizes the potential for over-preparedness, which could result in resource wastage, and under-preparedness, which might exacerbate fire impacts. Ultimately, the BMA model equips policymakers and environmental managers with a tool not only for accurate forecasting but also for devising flexible and adaptive fire management strategies that can be dynamically adjusted as conditions evolve.

While the study demonstrates the effectiveness of the BMA model in predicting forest fire hotspots based on temporal climate indicators, it does not incorporate spatial aspects into the prediction framework. This limitation arises because the analysis focuses on temporal patterns, such as dry spells, precipitation anomalies, and climatic indices, without accounting for the geographic variability of these factors across Kalimantan. For example, regions with distinct ecological and topographical characteristics may respond differently to the same climatic conditions, leading to spatial heterogeneity in hotspot occurrences.

The absence of spatial considerations in the model implies that hotspot predictions are generalized across the entire study area, potentially overlooking localized factors such as land cover type, vegetation density, and proximity to human activities. Incorporating spatial data in future studies, such as GIS-based mapping or geostatistical models, could provide a more comprehensive understanding of fire dynamics and improve the model's utility for targeted interventions. For instance, spatially explicit models could help prioritize specific areas for monitoring or intervention, based on both temporal and spatial risk factors.

5. CONCLUSION

The first objective of the study was to identify the best combination of predictors for forecasting forest fire hotspots in Kalimantan based on climate indicators. The selection process aimed at minimizing the Bayesian Information Criterion (BIC) value, ensuring that only the most relevant variables were used. The research successfully used the best subset selection method, incorporating three key variables: precipitation anomalies, dry spells, and the Indian Ocean Dipole (IOD) index, into a mathematical equation consisting of six terms. The results showed that dry spells were a critical factor in predicting the occurrence of fire hotspots, playing a role in almost every significant model term. The use of polynomial interactions among these predictors allowed for a more nuanced understanding of how climate variables interrelate in driving fire risks.

The second goal was to construct and compare multiple regularized regression models, including Ridge, LASSO, and Elastic Net, with a BMA. The regularized regression models aim to address common issues like multicollinearity and overfitting by introducing penalties for complexity. While Ridge, LASSO, and Elastic Net performed adequately, the study found that these single-model approaches had limitations, particularly in their ability to generalize well to new data. In contrast, the BMA model, which averages predictions from multiple models weighted by their posterior probabilities, offered a more comprehensive approach by integrating the benefits of various models and accounting for the inherent uncertainty in the data.

Lastly, the study aimed to determine the best-performing model by evaluating the predictive accuracy of each model using Root Mean Squared Error (RMSE) and the coefficient of determination (R^2). Testing on unseen data revealed that the BMA model outperformed all other models, achieving

the lowest RMSE (664) and the highest R^2 (88.58%) on test data. The BMA model's ensemble approach proved more robust, producing more accurate and reliable predictions, especially in the complex, uncertain scenario of predicting hotspots. This makes BMA a valuable tool for forest fire prediction, particularly in regions like Kalimantan, where climate conditions vary significantly.

The study's results offer promising prospects for implementing more accurate predictive models in forest fire management in Kalimantan, particularly through the superior BMA approach over regularized regression models. Its ability to forecast hotspots with high accuracy provides a strategic advantage for early intervention, resource prioritization, and mitigation planning. For policymakers, the model's predictions can inform proactive measures, such as community evacuation plans, policy adjustments regarding land use during critical periods, and optimizing budget allocation for firefighting efforts. This enables policymakers to predict fire hotspots, paving the way more precisely for effective preventive measures and improved early warning systems.

This study highlights the strength of using BMA for predicting forest fire hotspots based on temporal climate indicators. However, it is important to acknowledge that the model's focus is limited to temporal dynamics, without considering spatial variability in fire occurrence across Kalimantan. This limitation restricts the model's applicability for geographically targeted interventions, which are crucial for efficient resource allocation and localized risk management. Future research should aim to integrate spatial data, such as land use patterns, vegetation types, and geographic features, to enhance the predictive power and applicability of the model. Incorporating these spatial dimensions would enable the development of a more holistic fire risk assessment framework, combining both temporal and spatial predictors to better inform decision-making processes in forest fire management

Future studies could enhance this application by integrating real-time data streams, enabling dynamic updates to risk assessments and further improving the practicality of the model in rapidly changing environmental conditions. The BMA can also be extended to include a wider range of models and not just focus on polynomial models. These models can be tree-based, non-linear, machine learning, probabilistic models like Gaussian process, to neural networks. Moreover, further research should explore incorporating additional climate-related variables and utilizing advanced remote sensing technologies, as well as employing complex machine learning methods like deep learning. Developing adaptive predictive models that account for dynamic climate changes and new variables, such as land use effects, will be crucial for enhancing environmental management policies in Indonesia and other tropical regions.

ACKNOWLEDGEMENTS

We thank the Department of Mathematics, IPB University and the anonymous reviewers for their support throughout this research.

Data availability. Data generated or analysed during this study is provided within this manuscript or available at GitHub site: https://github.com/mkhoirun-najiboi/BMA-hotspots.

Code availability. The codes used during the current study are available at GitHub site: https://github.com/mkhoirun-najiboi/BMA-hotspots.

REFERENCES

Alhassan, E., Rochman, D., Schnabel, G., & Koning, A. J. (2024). Bayesian Model Averaging (BMA) for nuclear data evaluation. *Nuclear Science and Techniques*, 35(11), 1-26. https://doi.org/10.1007/s41365-024-01543-w

Alkhatib, R., Sahwan, W., Alkhatieb, A., & Schütt, B. (2023). A Brief Review of Machine Learning Algorithms in Forest Fires Science. *Applied Sciences (Switzerland)*, 13(14). https://doi.org/10.3390/app13148275

Andana, A. P., Safitri, D., & Rusgiyono, A. (2017). Model regresi menggunakan least absolute shrinkage and selection operator (lasso) pada data banyaknya gizi buruk kabupaten/kota di Jawa Tengah. *Jurnal Gaussian*, 6(1), 21–30.

Barros, A. M. G., Day, M. A., Preisler, H. K., Abatzoglou, J. T., Krawchuk, M. A., Houtman, R., & Ager, A. A. (2021). Contrasting the role of human- And lightning-caused wildfires on future fire regimes on a Central Oregon landscape. *Environmental Research Letters*, 16(6). https://doi.org/10.1088/1748-9326/ac03da

Basha, S. M., & Rajput, D. S. (2019). Survey on Evaluating the Performance of Machine Learning Algorithms: Past Contributions and Future Roadmap. In Deep Learning and Parallel Computing Environment for Bioengineering Systems (pp. 153–164). *Academic Press*. https://doi.org/10.1016/B978-0-12-816718-2.00016-6

Bertsimas, D., & Wiberg, H. (2020). Machine Learning in Oncology: Methods, Applications, and Challenges. *JCO Clinical Cancer Informatics*, 4, 885–894. https://doi.org/10.1200/cci.20.00072

Borrego, C., Miranda, A. I., Carvalho, A. C., & Carvalho, A. (2025). Forest fires and air pollution: A local and a global perspective. *WIT Transactions on Ecology and the Environment*, 37. https://doi.org/10.2495/AIR990711

Brasika, I. B. M., Antara, I. M. O. G., & Karang, I. W. G. A. (2021). Investigating El Nino Southern Oscillation as the main driver of forest fire in Kalimantan. *Malaysian Journal of Society and Space*, 17(4). https://doi.org/10.17576/geo-2021-1704-21

Brooks, G. P., & Ruengvirayudh, P. (2016). Best subset selection criteria for multiple linear regression. *General Linear Model Journal*, 42(2), 14–25.

Chi, H., Wu, Y., Zheng, H., Zhang, B., Sun, Z., Yan, J., ... & Guo, L. (2023). Spatial patterns of climate change and associated climate hazards in Northwest China. *Scientific Reports*, 13(1), 10418. https://doi.org/10.1038/s41598-023-37349-w

Chicco, D., Warrens, M. J., & Jurman, G. (2021). The coefficient of determination R-squared is more informative than SMAPE, MAE, MAPE, MSE and RMSE in regression analysis evaluation. *PeerJ Computer Science*, 7, 1–24. https://doi.org/10.7717/PEERJ-CS.623

Claeskens, G., & Hjort, N. L. (2008). Frequentist and Bayesian model averaging. In *Model Selection and Model Averaging* (pp. 192–226). Cambridge University Press. https://doi.org/10.1017/CBO9780511790485.008

Dziak, J. J., Coffmann, D. L., Lanza, S. T., Li, R., & Jermiin, L. S. (2020). Sensitivity and specificity of information criteria. *Briefings in Bioinformatics*, 21(2), 553–565. https://doi.org/10.1093/bib/bbz016

Edwards, R. B., Naylor, R. L., Higgins, M. M., & Falcon, W. P. (2020). Causes of Indonesia's forest fires. *World Development*, 127. https://doi.org/10.1016/j.worlddev.2019.104717

Ertugrul, M., Varol, T., Ozel, H. B., Cetin, M., & Sevik, H. (2021). Influence of climatic factor of changes in forest fire danger and fire season length in Turkey. *Environmental monitoring and assessment*, 193, 1-17. https://doi.org/10.1007/s10661-020-08800-6

Fanin, T., & Van Der Werf, G. R. (2017). Precipitation-fire linkages in Indonesia (1997-2015). *Biogeosciences*, 14(18), 3995–4008. https://doi.org/10.5194/bg-14-3995-2017

Fikri, A. F., Agwil, W., & Agustina, D. (2023). Performa Teknik Regularisasi Dalam Penanganan Masalah Multikolinieritas. *Diophantine Journal of Mathematics and Its Applications*, 2(1), 45–51. https://doi.org/10.33369/diophantine.v2i01.28480

Gaveau, D. L. A., Sloan, S., Molidena, E., Yaen, H., Sheil, D., Abram, N. K., Ancrenaz, M., Nasi, R., Quinones, M., & Wielaard, N. (2014). Four decades of forest persistence, clearance and logging on Borneo. *PLoS ONE*, 9(7), 1–11. https://doi.org/10.1371/journal.pone.0101654

Giglio, L., Boschetti, L., Roy, D. P., Humber, M. L., & Justice, C. O. (2018). The Collection 6 MODIS burned area mapping algorithm and product. *Remote Sensing of Environment*, 217, 72–85. https://doi.org/10.1016/j.rse.2018.08.005

Han, J., Pei, J., & Tong, H. (2024). *Data Mining: Concepts and Techniques*, 4th ed. (Fourth Edi). Morgan Kaufmann. https://doi.org/10.1016/C2013-0-18660-6

Handayani, A., & Wachidah, L. (2022). Metode Regresi Elastic-Net untuk Mengatasi Masalah Multikolinearitas pada Kasus Tingkat Pengangguran Terbuka di Provinsi Jawa Barat. *Bandung Conference Series: Statistics*, 2(2), 459–465. https://doi.org/10.29313/bcss.v2i2.4722

Hardiyanti, O., & Nurmanina, A. (2020). Analysis of The Utilization of the Social Center for Orangutan Protection (COP) In Kalimantan in Orangutan Saving Efforts. *Progress In Social Development*, 1(1), 9–17. https://doi.org/10.30872/psd.v1i1.14

Harrison, M. E., Deere, N. J., Imron, M. A., Nasir, D., Adul, Asti, H. A., Soler, J. A., Boyd, N. C., Cheyne, S. M., Collins, S. A., D'Arcy, L. J., Erb, W. M., Green, H., Healy, W., Hendri, Holly, B., Houlihan, P. R., Husson, S. J., Iwan, … Struebig, M. J. (2024). Impacts of fire and prospects for recovery in a tropical peat forest ecosystem. *Proceedings of the National Academy of Sciences of the United States of America*, 121(17). https://doi.org/10.1073/pnas.2307216121

Hastie, T., Tibshirani, R., & Tibshirani, R. (2020). Best Subset, Forward Stepwise or Lasso? Analysis and Recommendations Based on Extensive Comparisons. *Statistical Science*, 35(4), 579–592. https://doi.org/10.1214/19-STS733

Herawati, N., Nisa, K., & Setiawan, E. (2018). Regularized Multiple Regression Methods to Deal with Severe Multicollinearity. *International Journal of Statistics and Applications*, 8(4), 167–172.

Hidayat, M. N., Wafdan, R., Iskandar, T., Dewi, C. D., Nurhayati, N., Ramli, M., ... & Rizal, S. (2025). The influence of El Niño-Southern Oscillation and the Indian Ocean Dipole on chlorophyll-a in the Aceh waters during 1999–2023. *Int. Journal of Remote Sensing*, 1-21. https://doi.org/10.1080/01431161.2025.2460244

Hinne, M., Gronau, Q. F., van den Bergh, D., & Wagenmakers, E. J. (2020). A Conceptual Introduction to Bayesian Model Averaging. *Advances in Methods and Practices in Psychological Science*, 3(2), 200–215. https://doi.org/10.1177/2515245919898657

Hoerl, A. E. (1962). Application of ridge analysis to regression problems. *Chemical Engineering Progress*, 58, 54–59.

Hope, T. M. H. (2020). Chapter 4 - Linear regression. In A. Mechelli & S. Vieira (Eds.), *Machine Learning* (pp. 67–81). Academic Press. https://doi.org/https://doi.org/10.1016/B978-0-12-815739-8.00004-3

Hu, Y., Fernandez-Anez, N., Smith, T. E. L., & Rein, G. (2018). Review of emissions from smouldering peat fires and their contribution to regional haze episodes. *International Journal of Wildland Fire*, 27(5), 293–312. https://doi.org/10.1071/WF17084

Huang, T., & Merwade, V. (2023). Uncertainty analysis and quantification in flood insurance rate maps using Bayesian model averaging and hierarchical BMA. Journal of Hydrologic Engineering, 28(2), 04022038. https://doi.org/10.1061/JHYEFF.HEENG-5851

Huntingford, C., Jeffers, E. S., Bonsall, M. B., Christensen, H. M., Lees, T., & Yang, H. (2019). Machine learning and artificial intelligence to aid climate change research and preparedness. *Environmental Research Letters*, 14(12). https://doi.org/10.1088/1748-9326/ab4e55

Iskandar, I., Lestari, D. O., Saputra, A. D., Setiawan, R. Y., Wirasatriya, A., Susanto, R. D., ... & Kunarso. (2022). Extreme positive Indian Ocean Dipole in 2019 and its impact on Indonesia. *Sustainability*, 14(22), 15155. https://doi.org/10.3390/su142215155

Jain, P., Coogan, S. C. P., Subramanian, S. G., Crowley, M., Taylor, S., & Flannigan, M. D. (2020). A review of machine learning applications in wildfire science and management. *Environmental Reviews*, 28(4), 478–505. https://doi.org/10.1139/er-2020-0019

Javeed, A., Dallora, A. L., Berglund, J. S., Ali, A., Ali, L., & Anderberg, P. (2023). Machine Learning for Dementia Prediction: A Systematic Review and Future Research Directions. *Journal of Medical Systems*, 47(1). https://doi.org/10.1007/s10916-023-01906-7

Jdey, I., Hcini, G., & Ltifi, H. (2023). Deep Learning and Machine Learning for Malaria Detection: Overview, Challenges and Future Directions. *International Journal of Information Technology and Decision Making*. https://doi.org/10.1142/S0219622023300045

Jolly, C. J., Dickman, C. R., Doherty, T. S., van Eeden, L. M., Geary, W. L., Legge, S. M., ... & Nimmo, D. G. (2022). Animal mortality during fire. *Global Change Biology*, 28(6), 2053-2065. https://doi.org/10.1111/gcb.16044

Kadir, E. A., Kung, H. T., AlMansour, A. A., Irie, H., Rosa, S. L., & Fauzi, S. S. M. (2023). Wildfire Hotspots Forecasting and Mapping for Environmental Monitoring Based on the Long Short-Term Memory Networks Deep Learning Algorithm. *Environments - MDPI*, 10(7). https://doi.org/10.3390/environments10070124

Kasali, J., & Adeyemi, A. A. (2022). Model-Data Fit using Akaike Information Criterion (AIC), Bayesian Information Criterion (BIC), and The Sample-Size-Adjusted BIC. *Square : Journal of Mathematics and Mathematics Education*, 4(1), 43–51. https://doi.org/10.21580/square.2022.4.1.11297

Keong, C. Y., & Onuma, A. (2021). Transboundary ecological conservation, environmental value and environmental sustainability: Lessons from the heart of borneo. *Sustainability (Switzerland)*, 13(17). https://doi.org/10.3390/su13179727

Kumar, S., & Kumar, A. (2022). Hotspot and trend analysis of forest fires and its relation to climatic factors in the western Himalayas. *Natural Hazards*, 114(3), 3529–3544. https://doi.org/10.1007/s11069-022-05530-5

Kurniadi, A., Weller, E., Min, S. K., & Seong, M. G. (2021). Independent ENSO and IOD impacts on rainfall extremes over Indonesia. *International Journal of Climatology*, 41(6), 3640-3656. https://doi.org/10.1002/joc.7040

Kursa, M. B. (2014). Robustness of Random Forest-based gene selection methods. BMC Bioinformatics, 15(1). https://doi.org/10.1186/1471-2105-15-8

Latif, S. D., Alyaa Binti Hazrin, N., Hoon Koo, C., Lin Ng, J., Chaplot, B., Feng Huang, Y., El-Shafie, A., & Najah Ahmed, A. (2023). Assessing rainfall prediction models: Exploring the advantages of machine learning and remote sensing approaches. *Alexandria Engineering Journal*, 82, 16–25. https://doi.org/10.1016/j.aej.2023.09.060

Mahendra, A. P., Pradipta, D., Saputro, Moh. R. B., & Kusrini, K. (2022). Application of the Decision Tree Method to Forest Fire Detection (Case Study: in Palembang, South Sumatra). *JTECS : Jurnal Sistem Telekomunikasi Elektronika Sistem Kontrol Power Sistem Dan Komputer*, 2(1), 75. https://doi.org/10.32503/jtecs.v2i1.2196

Margono, B. A., Potapov, P. V, Turubanova, S., Stolle, F., & Hansen, M. C. (2014). Primary forest cover loss in indonesia over 2000-2012. *Nature Climate Change*, 4(8), 730–735. https://doi.org/10.1038/nclimate2277

Maulud, D., & Abdulazeez, A. M. (2020). A Review on Linear Regression Comprehensive in Machine Learning. *Journal of Applied Science and Technology Trends*, 1(2), 140–147. https://doi.org/10.38094/jastt1457

Montgomery, D. C., Peck, E. A., & Vining, G. G. (2021). 7. Polynomial Regression Models. In *Introduction to Linear Regression Analysis*, 6th Edition (pp. 230–267). John Wiley & Sons.

Najib, M. K., Nurdiati, S., & Sopaheluwakan, A. (2021). Quantifying the joint distribution of drought indicators in Borneo fire-prone area. *IOP Conference Series: Earth and Environmental Science*, 880(1), 012002. https://doi.org/10.1088/1755-1315/880/1/012002

Najib, M. K., Nurdiati, S., & Sopaheluwakan, A. (2022a). Copula-based joint distribution analysis of the ENSO effect on the drought indicators over Borneo fire-prone areas. *Modeling Earth Systems and Environment*, 8(2), 2817–2826. https://doi.org/10.1007/s40808-021-01267-5

Najib, M. K., Nurdiati, S., & Sopaheluwakan, A. (2022b). Multivariate fire risk models using copula regression in Kalimantan, Indonesia. *Natural Hazards*, 113(2), 1263–1283. https://doi.org/10.1007/s11069-022-05346-3

Najib, M. K., Nurdiati, S., & Sopaheluwakan, A. (2024). Prediction of hotspots pattern in Kalimantan using copula-based quantile regression and probabilistic model: a study of precipitation and dry spells across varied ENSO conditions. *Vietnam Journal of Earth Sciences*, 46(1), 12–33. https://doi.org/10.15625/2615-9783/19302

Nugrahani, E. H., Nurdiati, S., Bukhari, F., Najib, M. K., Sebastian, D. M., & Fallahi, P. A. N. (2024). Sensitivity and feature importance of climate factors for predicting fire hotspots using machine learning methods. *IAES International Journal of Artificial Intelligence*, 13(2), 2210–2223. https://doi.org/10.11591/ijai.v13.i2.pp2212-2225

Nurdiati, S., Bukhari, F., Julianto, M. T., Najib, M. K., & Nazria, N. (2021). Heterogeneous Correlation Map Between Estimated ENSO And IOD From ERA5 And Hotspot In Indonesia. *Jambura Geoscience Review*, 3(2), 65–72. https://doi.org/10.34312/jgeosrev.v3i2.10443

Nurdiati, S., Bukhari, F., Julianto, M. T., Sopaheluwakan, A., Aprilia, M., Fajar, I., Septiawan, P., & Najib, M. K. (2022a). The impact of El Niño southern oscillation and Indian Ocean Dipole on the burned area in Indonesia. *Terrestrial, Atmospheric and Oceanic Sciences*, 33(15). https://doi.org/10.1007/S44195-022-00016-0

Nurdiati, S., Sopaheluwakan, A., Septiawan, P., & Ardhana, M. R. (2022b). Joint Spatio-Temporal Analysis of Various Wildfire and Drought Indicators in Indonesia. *Atmosphere*, 13(10). https://doi.org/10.3390/atmos13101591

Nurlatifah, A., Kombara, P. Y., Pratama, A., Faristyawan, R., Rakhman, A. A., & Noviastuti, N. (2025). Utilisation of WRF-HYSPLIT modelling approach and GEMS to identify PM2.5 sources in Central Kalimantan – study case: 2023 forest fire. *Journal of Southern Hemisphere Earth Systems Science*, 75(1). https://doi.org/10.1071/ES24006

Palamba, P. (2024). Understanding the environmental impacts of peatland fires: optical density, gas emissions and airflow effects. *International Journal of Environmental Engineering*, 12(4), 330–343. https://doi.org/10.1504/ijee.2024.10063659

Pallathadka, H., Wenda, A., Ramirez-Asís, E., Asís-López, M., Flores-Albornoz, J., & Phasinam, K. (2023). Classification and prediction of student performance data using various machine learning algorithms. *Materials Today: Proceedings*, 80, 3782–3785. https://doi.org/10.1016/j.matpr.2021.07.382

Preeti, T., Kanakaraddi, S., Beelagi, A., Malagi, S., & Sudi, A. (2021). Forest Fire Prediction Using Machine Learning Techniques. *2021 International Conference on Intelligent Technologies, CONIT 2021*. https://doi.org/10.1109/CONIT51480.2021.9498448

Purwanto, A., & Sudargini, Y. (2021). Partial Least Squares Structural Squation Modeling (PLS-SEM) Analysis for Social and Management Research : A Literature Review. *Journal of Industrial Engineering & Management Research*, 2(4), 114–123.

Rachman, H. A., Setiawati, M. D., Hidayah, Z., Syah, A. F., Nandika, M. R., Lumban-Gaol, J., ... & Syamsudin, F. (2024). Dynamic of upwelling variability in southern Indonesia region revealed from satellite data: Role of ENSO and IOD. Journal of Sea Research, 202, 102543. https://doi.org/10.1016/j.seares.2024.102543

Reichstein, M., Camps-Valls, G., Stevens, B., Jung, M., Denzler, J., Carvalhais, N., & Prabhat. (2019). Deep learning and process understanding for data-driven Earth system science. *Nature*, 566(7743), 195–204. https://doi.org/10.1038/s41586-019-0912-1

Sa'adi, Z., Shiru, M. S., Shahid, S., & Ismail, T. (2020). Selection of general circulation models for the projections of spatio-temporal changes in temperature of Borneo Island based on CMIP5. *Theoretical and Applied Climatology*, 139(1–2), 351–371. https://doi.org/10.1007/s00704-019-02948-z

Saharjo, B. H., & Hasanah, U. (2023). Analisis Faktor Penyebab Terjadinya Kebakaran Hutan Dan Lahan Di Kabupaten Pulang Pisau, Kalimantan Tengah. *Journal of Tropical Silviculture*, 14(1), 25–29. https://doi.org/10.29244/j-siltrop.14.01.25-29

Saharjo, B. H., & Nasution, M. R. A. (2021). Hotspot Distribution Pattern as an Indicator of Forest and Land Fires in West Aceh District. *Journal of Tropical Silviculture*, 12(2), 60–66. https://doi.org/10.29244/j-siltrop.12.2.60-66

Sahu, S. K., Mokhade, A., & Bokde, N. D. (2023). An Overview of Machine Learning, Deep Learning, and Reinforcement Learning-Based Techniques in Quantitative Finance: Recent Progress and Challenges. *Applied Sciences (Switzerland)*, 13(3). https://doi.org/10.3390/app13031956

Saleh, A. K. Md. E., Arashi, M., & Kibria, B. M. G. (2019). *Theory of Ridge Regression Estimation with Application*. John Wiley & Sons, Inc. https://doi.org/10.1002/9781118644478

Sambodo, N. P., Pradhan, M., Sparrow, R., & van Doorslaer, E. (2024). When the smoke gets in your lungs: short-term effects of Indonesia's 2015 forest fires on health care use. *Environmental Health: A Global Access Science Source*, 23(1). https://doi.org/10.1186/s12940-024-01079-x

Sanjaya, F. I., & Heksaputra, D. (2020). Prediksi Rerata Harga Beras Tingkat Grosir Indonesia dengan Long Short Term Memory. *JATISI (Jurnal Teknik Informatika Dan Sistem Informasi)*, 7(2), 163–174. https://doi.org/10.35957/jatisi.v7i2.388

Sarker IH. (2021). Machine learning: Algorithms, real-world applications and research directions. *SN Computer Science*, 2(3), 1–21. https://doi.org/10.1007/s42979-021-00592-x

Syaufina, L., & Puspitasari, N. (2015). Correlation of Weather Factors and Forest Fire Occurence in KPH Bogor, Perum Perhutani Unit III West Java and Banten. *Journal of Tropical Silviculture*, 06(1), 43–48.

Tacconi, L. (2016). Preventing fires and haze in Southeast Asia. *Nature Climate Change*, 6(7), 640–643. https://doi.org/10.1038/nclimate3008

Tishbirani, R. (1996). Regression shrinkage and selection via the Lasso. *Journal of the Royal Statistical Society*. Series B (Methodological), 58(1), 267–288.

Usup, A., & Hayasaka, H. (2023). Peatland Fire Weather Conditions in Central Kalimantan, Indonesia. *Fire*, 6(5). https://doi.org/10.3390/fire6050182

van der Werf, G. R., Randerson, J. T., Giglio, L., van Leeuwen, T. T., Chen, Y., Rogers, B. M., Mu, M., van Marle, M. J. E., Morton, D. C., Collatz, G. J., Yokelson, R. J., & Kasibhatla, P. S. (2017). Global fire

emissions estimates during 1997-2016. *Earth System Science Data*, 9(2), 697–720. https://doi.org/10.5194/essd-9-697-2017

Venkatesh, K. A., Mishra, D., & Manimozhi, T. (2023). Model selection and regularization. In T. Goswami & G. R. Sinha (Eds.), *Statistical Modeling in Machine Learning* (pp. 159–178). Academic Press. https://doi.org/https://doi.org/10.1016/B978-0-323-91776-6.24001-3

von Rintelen, K., Arida, E., & Häuser, C. (2017). A review of biodiversity-related issues and challenges in megadiverse Indonesia and other Southeast Asian countries. *Research Ideas and Outcomes*, 3. https://doi.org/10.3897/rio.3.e20860

Wasilaine, T. L., Talakua, M. W., & Lesnussa, Y. A. (2014). Model Regresi Ridge Untuk Mengatasi Model Regresi Linier Berganda Yang Mengandung Multikolinieritas. *BAREKENG: Jurnal Ilmu Matematika Dan Terapan*, 8(1), 31–37. https://doi.org/10.30598/barekengvol8iss1pp31-37

Yanke, A., Zendrato, N. E., & Soleh, A. M. (2022). Handling Multicollinearity Problems in Indonesia's Economic Growth Regression Modeling Based on Endogenous Economic Growth Theory. *Indonesian Journal of Statistics and Its Applications*, 6(2), 228–244. https://doi.org/10.29244/ijsa.v6i2p214-230

Zou, H., & Hastie, T. (2005). Regularization and variable selection via the elastic net. Journal of the Royal Statistical Society. *Series B: Statistical Methodology*, 67(2), 301–320. https://doi.org/10.1111/j.1467-9868.2005.00503.x

FORECASTING REGIONAL TOURISM FLOWS IN ALBANIA USING ARIMA AND SPATIAL ANALYSIS: A DATA-DRIVEN APPROACH BASED ON NATIONAL ACCOMMODATION STATISTICS

Medjon HYSENAJ [1*] ***and Ditmira TAHIRI*** [2]

DOI : 10.21163/GT_2025.202.11

ABSTRACT

Geographic Information Systems (GIS) have become essential tools for tourism planning and management, enabling spatial analysis and advanced data visualization. This study adopts a data-driven approach to forecast and interpret regional tourism flows in Albania by integrating GIS techniques with statistical time series modelling. The spatial component involves mapping tourism activity across three macro-regions North, Centre, and South while distinguishing between coastal and non-coastal zones using official data from the Albanian Institute of Statistics (INSTAT). To complement the spatial analysis, the study introduces a temporal dimension using a matrix-style visualization that highlights seasonal tourism trends throughout 2024, and applies the ARIMA (AutoRegressive Integrated Moving Average) model to generate regional forecasts for 2025. This combination of spatial and temporal methods enables a more comprehensive understanding of tourism dynamics, revealing both geographic concentration and predictive seasonal patterns. The findings underscore the dominance of the Central Region, the growing potential of the North, and the strong seasonal pressure on coastal areas during peak months. By integrating GIS, heatmaps, and ARIMA forecasts, the study provides a strategic framework for sustainable tourism development and more informed regional policy interventions.

Key-words: *GIS, ARIMA, tourism forecasting, spatial analysis, heatmap, seasonality modelling.*

1. INTRODUCTION

In recent years, spatial and temporal analysis tools have become increasingly important for understanding regional disparities in tourism flows. Tourism, as a dynamic and seasonal sector, requires both geographical and predictive modelling approaches to inform strategic development, infrastructure planning, and sustainable growth. Geographic Information Systems (GIS) enable policymakers and researchers to visualize, quantify, and interpret visitor behaviours based on spatial zones, density, and accessibility (Longley et al., 2010).

Albania has experienced steady growth in tourism, both from domestic and international markets, contributing substantially to national economic performance (Merko, Ndreu, & Merko, 2025). This trajectory has been reinforced by academic studies that highlight Albania's long-term tourism potential and the need for strategic sectoral development (Burlea-Schiopoiu & Ozuni, 2021).

Tourism has been identified by international institutions as a pillar of Albania's economic diversification and regional development strategy (World Bank, 2025). This trend has been identified as a key economic pillar in recent national assessments, with tourism contributing significantly to employment and regional development (International Monetary Fund, 2025). The country's diverse geography ranging from alpine northern areas to Adriatic and Ionian coastlines results in regionally uneven visitor patterns. Understanding the spatial and seasonal distribution of visitors, especially distinguishing between coastal and non-coastal areas, is crucial for balanced tourism planning and infrastructure investment. This growth has also been recognized at the international level, where Albania is increasingly positioned as a strategic destination for tourism investment and development (World Tourism Organization, 2024). This aligns with previous research highlighting the need for integrated and sustainable tourism development strategies in Albania (Ciro & Toska, 2018), particularly those that consider territorial disparities and environmental capacity limits

---

[1*] *Dept. of Geography, Universiteti i Shkodrës "Luigj Gurakuqi", Albania. Corresponding author* medjon.hysenaj@unishk.edu.al

[2] *Dept. of Informatics, Universiteti i Shkodrës "Luigj Gurakuqi", Albania.* ditmira.tahiri@unishk.edu.al

While previous studies have employed GIS to identify spatial trends and regional concentrations (Hysenaj, 2015), this study introduces an integrated approach that combines spatial visualization with time series modelling. By incorporating the ARIMA (AutoRegressive Integrated Moving Average) model, the research forecasts regional tourism flows based on monthly visitor data from 2021 to 2024.

This predictive component allows for a forward-looking understanding of visitor patterns, particularly useful in assessing regional seasonality and planning off-peak strategies.

In parallel, a seasonal intensity chart is employed to capture intra-annual fluctuations in tourism activity across the North, Center, and South regions. By presenting monthly visitor distributions in a matrix format, the heatmap highlights the seasonality and intensity of tourism loads across regions, offering a compact and intuitive interpretation of temporal trends (Zhou & Liu, 2022).

The combined use of GIS, heatmap visual analytics, and ARIMA modelling represents a methodological advancement in tourism studies. It bridges the gap between spatial observation and temporal forecasting, enabling evidence-based policy decisions for resource allocation, infrastructure scaling, and marketing diversification. This integrated approach responds to the growing need for predictive spatial intelligence in tourism governance, especially in countries like Albania where regional imbalances and seasonal pressures are significant.

2. LITERATURE REVIEW

Prior studies have emphasized the pivotal role of spatial databases (SDBMS) and GIS technologies in supporting complex territorial decisions. Longley et al. (2010) established GIS as an essential tool for mapping spatial patterns in tourism, enabling planners to visualize accessibility, service dispersion, and environmental constraints. In Albania's context, Hysenaj (2015) demonstrated the use of geo-indexing and digital mapping to support urban and tourism development strategies, highlighting GIS's role in optimizing infrastructure and marketing initiatives.

More recent developments have extended GIS beyond static visualization to include real-time data integration and predictive modelling. Among these innovations, the emergence of digital twins virtual replicas used to simulate tourism dynamics has gained traction for its potential to enhance planning, personalization, and sustainability (Sampaio de Almeida, Brito e Abreu, & Boavida-Portugal, 2025).

Zhou and Liu (2022) conducted a bibliometric analysis showing a rise in research that combines GIS with advanced analytics such as machine learning, AI, and real-time sensor data to better predict tourism flows and environmental impact. This trend is further supported by Duarte et al. (2020), who provide a comprehensive overview of AI systems currently being applied to tourism optimization, forecasting, and user personalization. This integration enhances tourism resilience, particularly in regions facing seasonal overcrowding or ecological vulnerability.

A growing body of literature also points to the role of visual analytics, including intensity mapping techniques such as heatmaps, in tourism research. Heatmaps offer a clear and compact visual summary of seasonal variation and regional intensity in tourism flows (Kulyk & Sossa, 2018). When applied to monthly tourism data, they allow for intuitive comparisons between regions and reveal temporal spikes that can inform targeted marketing and service provision.

This approach is echoed in prior research published in Geographia Technica, where GIS tools and heatmap-style spatial analyses have been effectively applied to tourism planning and flow analysis (Nistor & Nicula, 2021; Ruda, 2016). For instance, Nistor and Nicula (2021) used GIS techniques to model tourism behaviour across spatial contexts, while Ruda (2016) demonstrated how spatial associations can reveal hidden tourism potential.

For instance, Šoltésová et al. (2025) applied GIS tools to guide sustainable tourism development in the Gelnica region, demonstrating how spatial technologies can support planning decisions at the local and regional level. In parallel, advanced data mining techniques such as market basket analysis are increasingly being applied to tourism data to uncover visitor behaviour patterns and inform decision-making strategies (Vavpotič, Knavs, & Knežević Cvelbar, 2021). These studies affirm the importance of combining spatial visualization with data interpretation to support evidence-based tourism policy.

The use of time series forecasting models, particularly ARIMA, is also gaining momentum in tourism analytics. ARIMA models have proven effective in forecasting short-term tourism demand by analyzing historical patterns (Song & Li, 2008). They are especially valuable in post-pandemic recovery planning and peak-load infrastructure management. Fathi et al. (2019) further expanded the use of ARIMA-based models in hydrological and climatic contexts, showing their versatility and robustness across spatial-temporal domains. This study builds on these foundations by combining GIS-based spatial classification, heatmap visualization, and ARIMA time series forecasting. This integrated approach enhances the ability to identify both current disparities and future tourism dynamics across Albania's macro-regions. It provides an evidence-based framework for proactive tourism planning that balances seasonal fluctuations with regional equity.

Foundational literature on time series analysis emphasizes the importance of ARIMA models in both theoretical and applied research. The classic work by Box and Jenkins (1970) laid the groundwork for ARIMA-based forecasting methods, which remain widely used across disciplines. Brockwell and Davis (2016) further advanced the field by integrating statistical theory with practical software applications. Haidu et al. (1987) applied Fourier-ARIMA modelling in hydrology, highlighting the model's flexibility in environmental forecasting. Additionally, Haidu (1997) provides a comprehensive treatment of time series methods applied in hydrology, contributing significantly to the methodological literature in the region.

3. DATA AND METHODS

3.1. Data Source

This study utilized official tourism statistics published by the Albanian Institute of Statistics (INSTAT), specifically the monthly dataset on accommodation establishments. The core dataset covers monthly arrivals of resident and non-resident tourists from January 2021 to March 2025. For spatial analysis, data from March 2025 were emphasized due to their availability and relevance for off-season tourism trends. For forecasting, monthly time series data from 2021-2024 were used as the training set. Administrative boundaries were retrieved from the GADM database (version 4.0), and macro-regions were defined following the national classification into North, Centre, and South. Each macro-region comprises several counties under the NUTS 3 classification.

3.2. GIS Data Processing

All spatial processing was conducted using QGIS 3.28, an open-source geographic information system. The geospatial methodology included the following steps:

a) Dissolution of Administrative Units: Albania's 12 counties were grouped and dissolved into three macro-regions (North, Centre, South).
b) Coastal Zone Identification: Municipalities within a 10 km buffer from the coastline were selected and classified as coastal areas, using spatial queries and buffer tools.
c) Overlay and Aggregation: Visitor data from INSTAT were manually joined to spatial layers using unique municipality identifiers. Regional totals and coastal/non-coastal classifications were computed.
d) Choropleth Map Generation: A graduated color ramp was applied to show the percentage share of visitor arrivals by region, using a green scale from light (low) to dark (high).

3.3. Heatmap Generation

To visualize seasonal fluctuations in tourism across Albania's macro-regions, a monthly matrix-style heatmap was generated (**Fig. 1**) using Python 3.11, with the help of the Pandas, Seaborn, and Matplotlib libraries (Waskom, 2021). The dataset included total monthly arrivals (resident + non-resident) from January to December 2024 for each macro-region. The heatmap used the YlOrRd color palette to represent intensity of tourist volumes. Annotated numerical values were embedded in each cell to improve readability. This approach allowed compact visualization of regional seasonality and intra-annual trends.

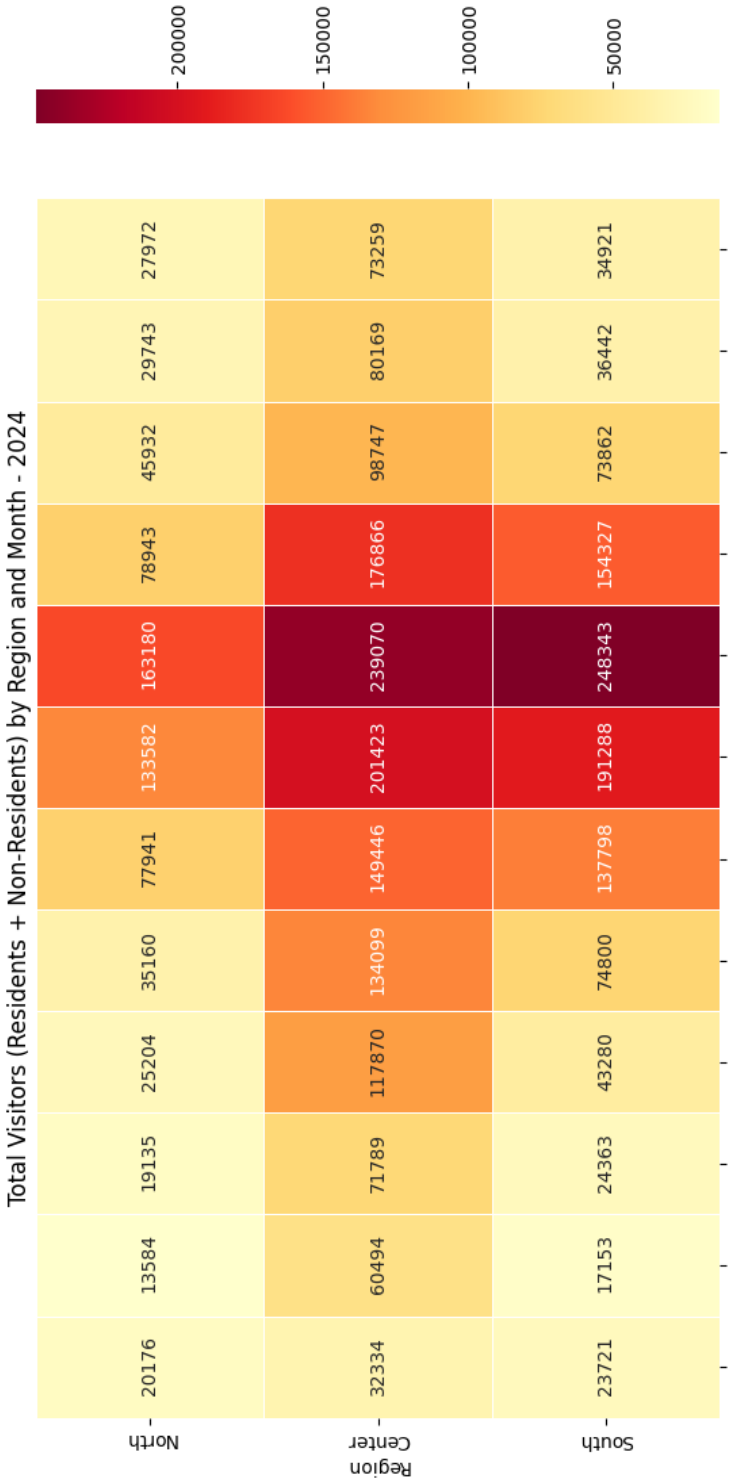

Fig 1. Regional Heat Map of Tourism Activity in 2024

The resulting heatmap revealed distinct seasonal patterns. Both the Center and South regions experienced a dramatic increase in visitor numbers during the summer months, peaking in July and August. In contrast, the North region showed a more modest but still notable seasonal trend. The visual clearly illustrated the cyclical nature of tourism, characterized by high concentration during the summer season and a decline in winter. This chart provided a compact yet comprehensive view of Albania's tourism distribution, supporting further analysis and offering a visually intuitive tool for stakeholders involved in regional planning and tourism development.

3.4. Time Series Forecasting Using ARIMA

To predict visitor flows for 2025, ARIMA (AutoRegressive Integrated Moving Average) models were developed for each macro-region: North **(Fig. 2)**, Center **(Fig. 3)**, South **(Fig. 4)**. The ARIMA model is formally denoted as ARIMA(p, d, q), where:

p is the number of autoregressive terms (AR),
d is the number of nonseasonal differences needed for stationarity,
q is the number of lagged forecast errors in the moving average model (MA).

Mathematically, the general ARIMA model can be written as:

$$\phi(B)(1 - B)^d y_t = \theta(B)\epsilon_t$$

where $\phi(B)$ and $\theta(B)$ are polynomials in the backshift operator B, and ϵ_t represents white noise.

Since the monthly data exhibit seasonality, we used the Seasonal ARIMA form, SARIMA(p, d, q)(P, D, Q, s), where the uppercase parameters refer to the seasonal components and s=12 represents the 12-month cycle. Model parameters were selected using the *auto_arima()* function from Python's *pmdarima* library. Forecasting was performed using the *SARIMAX* class in *statsmodels*, following a standard pipeline of differencing tests (ADF), model fitting, and forward prediction. The models were implemented in Python using the Statsmodels package (Seabold & Perktold, 2010).

The following steps were taken:

- Monthly visitor totals from January 2021 to December 2024 were used as the training data.
- Time series were tested for stationarity using the Augmented Dickey-Fuller test.
- Optimal SARIMA parameters (p, d, q)(P, D, Q, s) were selected using the Akaike Information Criterion (AIC) and autocorrelation diagnostics (ACF and PACF).
- Separate SARIMA models were fitted for each region, and forecasts for 2025 were generated.
- The forecasted values were visualized using line charts for each region and overlaid with 95% confidence intervals.

This forecasting method enabled short-term prediction of regional tourism trends and provided actionable insights for policy and planning.

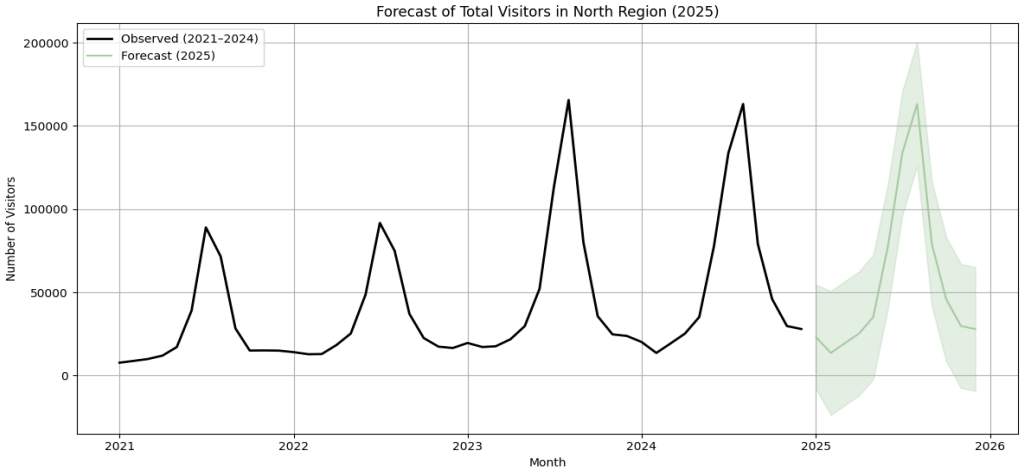

Fig 2. ARIMA-Based Time Series Forecast for Northern Region (2025). The shaded area around the forecast curve represents the 95% confidence interval.

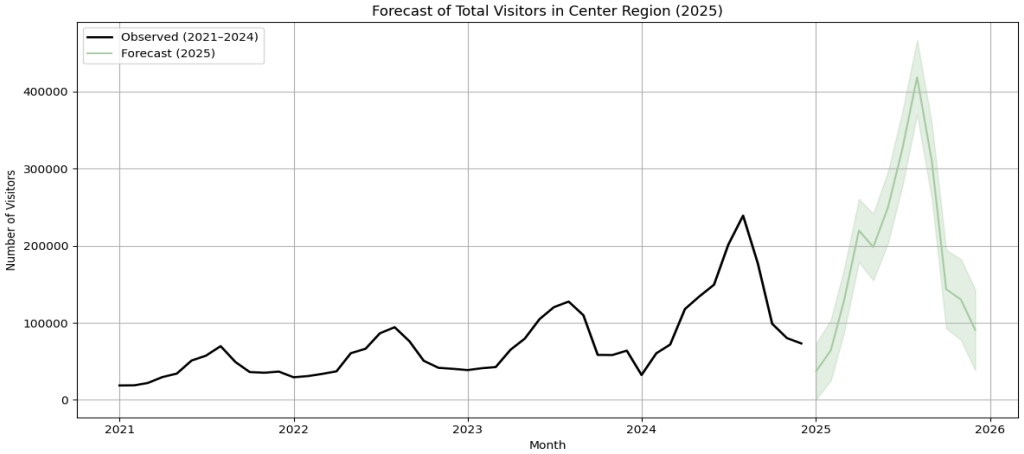

Fig 3. ARIMA-Based Time Series Forecast for Center Region (2025). The shaded area around the forecast curve represents the 95% confidence interval.

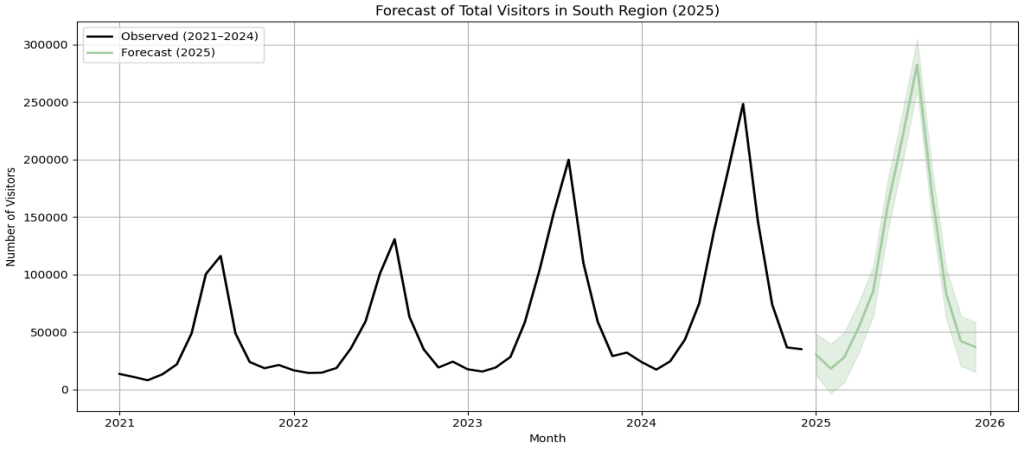

Fig 4. ARIMA-Based Time Series Forecast for South Region (2025). The shaded area around the forecast curve represents the 95% confidence interval.

3.5. Descriptive Statistics and Comparative Analysis

To complement the spatial and temporal modeling, descriptive statistics were computed to evaluate the share of tourism flows across macro-regions and between coastal and non-coastal zones. INSTAT visitor data were manually cross-referenced with GIS-classified municipalities. Total counts and percentages were calculated to reflect the relative contributions of each zone to national tourism activity. To highlight seasonal disparities, visitor data from March 2025 were compared with the peak tourism month of August 2024 **(Tab. 1, Tab. 2** and **Tab. 3).** These comparisons were visualized using tables and thematic maps created in QGIS. For example, while coastal areas accounted for 35.4% of visitors in March, this figure rose to 75.6% in August. This approach enabled a clearer understanding of off-peak vs. peak dynamics and informed spatial equity assessments. All analytical scripts and visualizations were developed using Python (v3.11) and QGIS (v3.28), ensuring reproducibility and alignment with open-source scientific standards.

Table 1.

Regional Distribution of Visitors in Albania

Region	Total Visitors	Percentage (%)
North	25,113	17.8%
Center	86,050	61.3%
South	29,315	20.9%

Table 2.

Regional Visitor Growth Comparison (2024–2025, Period: March)

Region	2024	2025	Growth
North	19,135	25,113	31.24%
Center	71,789	86,050	19.87%
South	24,363	29,315	20.33%

Table 3.

Visitor Distribution by Area Type

Area Type	Total Visitors (August 2024)	Total Visitors (March 2025)
Coastal	491,903	49,701
Non-Coastal	158,690	90,777
Total (Albania)	650,593	140,478

4. RESULTS AND DISCUSSIONS

The analysis of Albania's tourism dynamics integrates spatial classification, heatmap visualization, and ARIMA-based forecasting to provide a holistic picture of regional visitor flows.

4.1. Spatial Patterns

The core spatial analysis focused on visitor data for March 2025, using INSTAT data combined with GIS-based classification of administrative units. Three macro-regions North, Center, and South were analyzed, along with a binary distinction between coastal and non-coastal areas based on proximity to the coastline.

The spatial mapping revealed that the Center Region attracted the majority of visitors (61.3%), followed by the South (20.9%) and North (17.8%). Notably, coastal zones accounted for 35.4% of visits during March, rising to 75.6% during the peak month of August 2024. This confirms the seasonal pressure on coastal infrastructure, a phenomenon that demands spatial planning approaches tailored to resilience and sustainability in coastal communities (Abdullah et al., 2025), while also underlining the increasing relevance of inland destinations during the off-season.

A choropleth map and spatial overlay of visitor concentration effectively illustrated these disparities, validating GIS as a tool for strategic zone-based planning and resource distribution **(Fig. 5, Fig. 6** and **Fig. 7).**

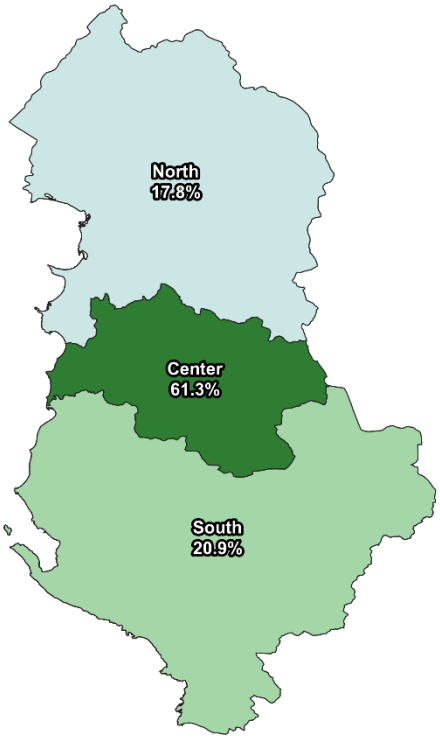

Fig. 5. Spatial Distribution of Tourist Visits by Region (March 2025)

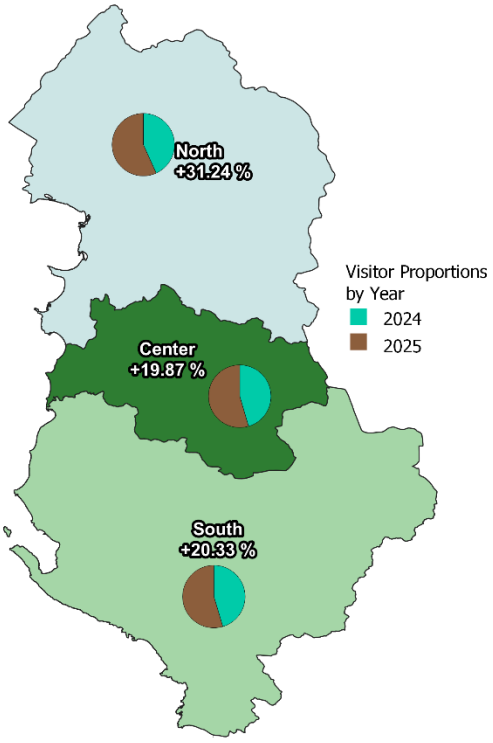

Fig 6. Year-over-year growth comparison

Fig 7. Coastal vs. non-coastal visitor distribution

4.2. Seasonal Trends: Visual Analysis of Monthly Visitor Fluctuations

To complement the March snapshot, a monthly intensity chart of monthly visitor flows across 2024 was generated using Python's Seaborn and Matplotlib libraries. The matrix-format heatmap displayed months along the horizontal axis and macro-regions along the vertical axis, with color intensity representing the number of visitors.

The visualization revealed:

- A sharp peak in the Center and South regions during July and August, reflecting classic summer tourism behavior.
- A more moderate but steady trend in the North region, with increased activity in spring and early autumn, aligning with nature-based and cultural tourism preferences.

This visualization not only clarified seasonal intensity and distribution, but also revealed opportunities for developing counter-seasonal tourism offers, especially in less saturated inland areas.

4.3. Forecasting Tourism Flows: ARIMA Results

ARIMA models were built separately for the North, Center, and South regions using monthly tourism data from 2021 to 2024. The models forecasted visitor numbers for 2025, offering a predictive layer to complement the spatial and historical insights.

Key findings:

- The Center region is expected to maintain its dominance, with steady growth continuing into the early summer of 2025.
- The South region shows significant seasonal fluctuation, with forecasts indicating a sharp rise beginning in May.
- The North region, while having the lowest absolute visitor numbers, shows the highest relative growth rate, especially in spring, suggesting a rising interest in alpine and eco-tourism. As demonstrated in similar GIS-based studies in national parks (Amangeldi et al., 2025), the integration of innovative mapping technologies can significantly enhance visitor experience and support sustainable destination development in protected natural areas.

The ARIMA forecasts provide vital input for pre-season planning and regional investment prioritization. Forecast curves also help stakeholders anticipate pressure on transport, accommodation, and cultural services across regions.

5. DISCUSSION

The integrated use of GIS, seasonal intensity charts, and ARIMA forecasting validates a multi-dimensional approach to tourism analysis. While GIS helps localize and quantify regional disparities, heatmaps offer clarity on seasonal intensity, and ARIMA models provide foresight into emerging trends.

The observed growth in the North region both in actual March data (31.24% YoY growth) and in forecasted values signals a shift in tourist preferences toward natural and cultural destinations outside traditional coastal zones. Destinations like Shkodër, Valbona, and Theth are emerging as strategic nodes for adventure and eco-tourism. This growth highlights the urgency of targeted investment in infrastructure and digital services in Northern Albania.

Meanwhile, the seasonal concentration in the South and Center, especially in summer, underscores the ongoing challenge of managing tourism saturation. The steep forecasted rise in visitors during May-July in these regions necessitates proactive service scaling, especially in coastal municipalities.

The use of heatmaps enabled intuitive communication of seasonality, particularly to non-technical stakeholders, while the ARIMA models offered data-backed projections that can inform policy decisions well in advance of tourism peaks. These tools are aligned with national priorities outlined in Albania's 2025–2030 country strategy, which emphasizes sustainable infrastructure, regional development, and digital modernization as key drivers of economic resilience (European Bank for Reconstruction and Development, 2025).

Looking ahead, integrating real-time mobility data (e.g., anonymized GPS tracking) and climate-adjusted predictive models could further enhance tourism governance. Albania can also draw lessons from neighboring countries like Croatia and Slovenia, which have successfully applied GIS and forecasting techniques to balance coastal and inland tourism, and mitigate environmental pressures. A national-level SWOT analysis by Leskaj and Lazimi (2024) similarly underscores the urgent need to diversify tourism offerings beyond the coastal concentration, highlighting internal disparities and capacity limitations that GIS-based planning can help address.

6. CONCLUSIONS

This study demonstrates the value of integrating spatial analysis, visual analytics, and predictive modeling to understand and manage tourism flows in Albania. By combining GIS-based spatial classification with heatmap visualization and ARIMA time series forecasting, the research provides a robust, multi-dimensional perspective on both the current distribution and future dynamics of regional tourism.

The spatial analysis confirmed the dominance of the Central Region, the emerging role of the North, and the continued seasonal dependence on coastal areas. The seasonal intensity visualization offered a clear, month-by-month view of seasonal trends, helping to pinpoint periods of over-concentration and underutilization across regions. Meanwhile, ARIMA-based forecasts provided forward-looking insights that are essential for pre-season planning, infrastructure investment, and strategic marketing.

This integrative approach not only enhances academic understanding but also supports evidence-based decision-making for tourism policymakers, local governments, and industry stakeholders. The findings underscore the need for regionally differentiated strategies, prioritizing capacity management in peak zones while stimulating growth in underutilized inland destinations.

Looking forward, future work should incorporate real-time mobility data, climate variables, and tourist sentiment analysis to build more adaptive and responsive tourism forecasting models. Furthermore, the development of an open-access, centralized GIS and forecasting platform could empower Albanian institutions to manage tourism in a smarter, more sustainable, and more inclusive manner.

REFERENCES

Abdullah, S. N. F., Kamarudin, M. K. A., Mat Som, A. P., Sanopaka, E., & Ferizone. (2025). GIS-based spatial modelling to enhance tourism resilience and conservation for sustainable leadership in coastal communities. Planning Malaysia, 23(1), Article 1659. https://doi.org/10.21837/pm.v23iS3.1659 .

Amangeldi, A., Seidullina, D., Mukatov, A., Mukatova, R., Bilisbekov, T., & Sagtbayev, Y. (2025). Innovative technologies to improve tourism experience in national parks: Development of GIS maps and their value. GeoJournal of Tourism and Geosites, 58(1), 210–224. https://doi.org/10.30892/gtg.58118-1403 .

Box, G. E. P., & Jenkins, G. M. (1970). Time Series Analysis: Forecasting and Control. Holden-Day, San Francisco.

Brockwell, P. J., & Davis, R. A. (2016). Introduction to Time Series and Forecasting (3rd ed.). Springer.

Burlea-Schiopoiu, A., & Ozuni, F. (2021). The potential of Albanian tourism sector. Sustainability, 13(7), 3928. https://doi.org/10.3390/su13073928 .

Ciro, A., & Toska, M. (2018). Sustainable tourism development in Albania / Zhvillimi i turizmit të qëndrueshëm në Shqipëri. Annual Review of Territorial Governance in Albania, 1, 84–91. https://doi.org/10.32034/CP-TG-CA2018-08 .

Duarte, L., Torres, J., Ribeiro, V., & Moreira, I. (2020). Artificial intelligence systems applied to tourism: A survey. arXiv. https://arxiv.org/abs/2010.14654 .

European Bank for Reconstruction and Development. (2025). Albania country strategy 2025–2030. https://www.ebrd.com/publications/country-strategy-albania .

Fathi, M. M., Awadallah, A. G., Abdelbaki, A. M., & Haggag, M. (2019). A new Budyko framework extension using time series SARIMAX model. Journal of Hydrology, 570, 827–838. 8. https://doi.org/10.1016/j.jhydrol.2019.01.037

GADM (2024). Database of Global Administrative Areas. Retrieved from https://gadm.org .

Haidu, I., Serban, P., & Simota, M. (1987). Fourier-ARIMA Modelling of the Multiannual Flow Variation. In vol. The Influence of the Climatic Change and Climatic Variability on Hydrologic Regime and Water Resources, IAHS Publ.- Red Books No. 168, pp. 281-286. https://www.researchgate.net/publication/237075838_Fourier-ARIMA_modeling_of_the_multiannual_flow_variation .

Haidu, I. (1997). Analiza seriilor de timp. Aplicații în hidrologie (Time series analysis. Applications in hydrology). Editura H*G*A*, București. ISBN: 973-98077-3-9. https://www.researchgate.net/publication/297032182_Analiza_seriilor_de_timp_Aplicatii_in_hidrologie

Hysenaj, M., & Hoxha, E. (2015). Modelimi hapësinor potencial i së ardhmes, , BSHN (UT) 20/2015.

Hysenaj, M., & Hoxha, E. (2015). Analiza gjeo-hapësinore oportunitet për zhvillimin e një plani strategjik, BSHN (UT) 20/2015.

Institute of Statistics (INSTAT). (2025). Tourism statistics: Accommodation establishments, March 2025. https://www.instat.gov.al/en/themes/industry-trade-and-services/tourism-statistics/ .

International Monetary Fund. (2025). Albania: Selected issues. https://www.imf.org/en/Publications/CR/Issues/2025/04/01/Albania-Selected-Issues-530600 .

Kulyk, V., & Sossa, R. (2018). Determining the tourist attractive regions by GIS analysis using heatmaps. Geodesy and Cartography, 44(2), 52–57. https://doi.org/10.3846/gac.2018.8322 .

Leskaj, E., & Lazimi, L. (2024). Albania's tourism landscape: A SWOT analysis for sustainable development. In International Scientific Conference EMAN 2024 – Conference Proceedings. https://doi.org/10.31410/EMAN.2024.459 .

Longley, P. A., Goodchild, M. F., Maguire, D. J., & Rhind, D. W. (2010). Geographic Information Systems and Science (3rd ed.). Wiley.

Merko, F., Ndreu, G., & Merko, F. (2025). The progress and economic effects of tourism on the Albanian economy (Version 2). Zenodo. https://doi.org/10.5281/zenodo.15010809.

Nistor, M.-M., & Nicula, A.-S. (2021). Application of GIS Technology for Tourism Flow Modelling in the United Kingdom. Geographia Technica, 16(1), 1–12. DOI: 10.21163/GT_2021.161.01. https://technicalgeography.org/pdf/1_2021/01_nistor.pdf

Ruda, A. (2016). Exploring Tourism Possibilities Using GIS-Based Spatial Association Methods. Geographia Technica, 11(2), 87–101. DOI: 10.21163/GT_2016.112.09. https://technicalgeography.org/pdf/2_2016/09_ruda.pdf

Sampaio de Almeida, D., Brito e Abreu, F., & Boavida-Portugal, I. (2025). Digital twins in tourism: A systematic literature review. arXiv. https://arxiv.org/abs/2502.00002 .

Seabold, S., & Perktold, J. (2010). Statsmodels: Econometric and statistical modeling with Python. Proceedings of the 9th Python in Science Conference.

Šoltésová, M., Iannaccone, B., Štrba, Ľ., & Sidor, C. (2025). Application of GIS technologies in tourism planning and sustainable development: A case study of Gelnica. ISPRS International Journal of Geo-Information, 14(3), 120. https://doi.org/10.3390/ijgi14030120 .

Song, H., & Li, G. (2008). Tourism demand modelling and forecasting—A review of recent research. Tourism Management, 29(2), 203–220.

Vavpotič, D., Knavs, K., & Knežević Cvelbar, L. (2021). Using a market basket analysis in tourism studies. arXiv. https://arxiv.org/abs/2110.10679 .

Waskom, M. L. (2021). Seaborn: Statistical data visualization. Journal of Open-Source Software, 6(60), 3021. https://doi.org/10.21105/joss.03021 .

World Bank. (2025). Albania overview. https://www.worldbank.org/en/country/-albania/overview .

World Tourism Organization. (2024). Tourism doing business – Investing in Albania. UN Tourism. https://doi.org/10.18111/9789284425426 .

Zhou, L., & Liu, X. (2022). Bibliometric analysis of GIS-based tourism research. SAGE Open, 12(4), 1–15. https://doi.org/10.1177/21582440251335733 .

PREDICTING EARTHQUAKE POTENTIAL THROUGH MORPHODEFORMATION MODELING USING SENTINEL-1A IMAGERY IN THE SINGKARAK SEGMENT, INDONESIA

Triyatno TRIYATNO [1*], Dipo CAESARIO [1], Febriandi FEBRIANDI [1], Beni AULIA [1], Azhari SYARIEF [1]

DOI: 10.21163/GT_2025.202.12

ABSTRACT

This study aims to analyze geological and geomorphological conditions, develop a morphodeformation model, and predict potential magnitude, epicenter depth, and Peak Ground Acceleration (PGA) values in the Singkarak Segment, West Sumatra, Indonesia. The Singkarak Segment, intersected by the active Sumatran Great Fault and influenced by nearby Mount Marapi, exhibits high seismic risk due to its complex tectonic and volcanic settings. The research employed multi-phase spatial analysis using secondary data sources, including Sentinel-1A satellite imagery, Digital Elevation Model Nasional (DEMNAS), geological and geomorphological maps from the Indonesian Geospatial Information Agency, and seismic records from the United States Geological Survey (USGS). Morphodeformation was analyzed using Sentinel Application Platform (SNAP) for radar data processing. ArcGIS, including kriging interpolation and raster calculator, was used to model spatial variations in earthquake magnitude, epicenter depth, and PGA. Results showed denudational and fluvial landforms are most susceptible to seismic activity, with magnitudes ranging from 3.00 to 6.39 Mw and PGA values up to 368.83 gal. The highest magnitude events (≥6.0 Mw) and strongest ground accelerations were concentrated in central and southern zones. Morphodeformation analysis indicated vertical displacements of −0.52 to +0.20 mm (2019–2023) and increased activity in 2023–2024, with values ranging from −0.85 to +0.45 mm. Shallow epicenter depths (18.37–36.64 km) dominated the area, particularly within denudational and fluvial terrains. In conclusion, integrating geological, geomorphological, and deformation modeling confirms that the Singkarak Segment is an active and vulnerable seismic zone. The findings underscore the importance of incorporating morphodeformation and spatial modeling in earthquake risk mitigation, land-use planning, and infrastructure resilience in tectonically dynamic areas.

***Key-words**: Morphodeformation; Earthquake Hazard; PGA; Kriging; Singkarak Segment.*

1. INTRODUCTION

Earthquakes represent one of the most devastating natural disasters, frequently resulting in substantial losses for communities, including both property damage and loss of human life (Razi et al., 2023; Samsonov et al., 2024). These catastrophic events predominantly occur along active fault lines, particularly in areas underlain by geologically weak or fractured rock formations that are less capable of withstanding seismic stress (Appel & Pebesma, 2020; Huang et al., 2022; Jarder et al., 2024). Due to earthquakes' unpredictable and sudden onset, populations are often caught unprepared, amplifying the impact and limiting emergency response effectiveness (Arlym et al., 2019; Hermon et al., 2020; Yang et al., 2022). Earthquakes cause direct destruction and long-term socio-economic disruption by displacing communities, damaging infrastructure, and interrupting essential services such as water supply, electricity, and transportation. One of the areas with significant potential for earthquake-related disasters is the area surrounding Lake Singkarak. Located in West Sumatra Province, Indonesia, Lake Singkarak is classified as a tectonic lake (Novianti et al., 2023), meaning its formation is closely tied to tectonic processes. A major geological structure, the Sumatran Fault, commonly called the Semangko Fault, runs through this area. This extensive fault system stretches from Semangko Bay in Lampung Province to the Alas Valley in Aceh Province, spanning the entire western spine of Sumatra (Guntoro et al., 2024).

---

[1]*Department of Geography, Universitas Negeri Padang, Padang, Indonesia, (TT) triyatno@fis.unp.ac.id, (DC) caesariodipo@fis.unp.ac.id, (FF) andi_geografi@fis.unp.ac.id, (BA) beniaulia@fis.unp.ac.id, (AS) azharief@fis.unp.ac.id. *Corresponding author email: triyatno@fis.unp.ac.id*

The section that passes through Lake Singkarak is known as the Singkarak Segment (Amir et al., 2021). The Singkarak Segment is recognized as one of the most active fault segments on Sumatra. Notably, it lies near Mount Marapi, one of Indonesia's active stratovolcanoes (Rozaki et al., 2024; Hermon et al., 2019). Sumatra has experienced devastating earthquake events, including the 2004 Indian Ocean earthquake and tsunami, which claimed over 230,000 lives, and the 2009 Padang earthquake, which caused widespread damage and over 1,100 fatalities (Chang Seng, 2010; Ranke, 2016). These disasters underscore the urgent need for advanced geospatial modeling and seismic risk assessment, particularly in tectonically active segments like Singkarak. The Semangko Fault produces structural landforms such as fault scarps and lineaments, and volcanic processes from Mount Marapi contribute to volcanic landforms, including cones and pyroclastic deposits. Landform types indicate dynamic geological processes and underscore dual exposure to seismic and volcanic hazards. As such, the area around Lake Singkarak requires continuous geological monitoring and disaster risk management strategies to mitigate potential impacts, including secondary hazards like landslides or lahars. Previous studies have explored natural disasters such as earthquakes (Feng et al., 2024), as well as surface deformation of the earth's crust (Gama et al., 2017; Ghaderpour et al., 2024). However, limited attention has been given to integrated studies of morphodeformation as a method to predict potential earthquake magnitude, epicenter depth, and Peak Ground Acceleration (PGA) values in high-risk areas like the Singkarak Segment, where seismic activity intersects with complex geological and geomorphological characteristics. This study combines several techniques, including kriging interpolation, algebraic map analysis using raster calculator tools in ArcGIS, and satellite-based deformation modeling with Sentinel Application Platform (SNAP) software. This study aims to analyze geological and geomorphological conditions, develop a morphodeformation model, and predict potential magnitude, epicenter depth, and PGA values in the Singkarak Segment area. The novelty of this study lies in its ability to quantify and map the relationship between vertical morphodeformation (uplift and subsidence) and seismic parameters (magnitude, depth, PGA) within a tectono-volcanic zone

2. STUDY AREA

This study was conducted in the Singkarak Segment area, which is geographically located at coordinates 0°36′44.17″S and 100°32′21.14″E, covering the administrative areas of Tanah Datar Regency and Solok Regency, West Sumatra Province, Indonesia, with a surface height of 363.5 m above sea level. For more details, see **Fig 1**.

Fig. 1. Location map in the Singkarak Segment, West Sumatra, Indonesia

The map in **Fig** 1 above shows the of the Singkarak Segment in the regional context of Sumatra Island and shows its strategic position on the Semangko Fault line. The Sumatra region with provincial boundaries and active fault lines extending from Semangko Bay in Lampung to Alas Valley in Aceh. The study area is marked with a red box, showing the focus area in the regional tectonic context. This map serves as an important basis in demonstrating the spatial relationship between the study site and the main tectonic system of Sumatra, while also emphasizing the need for integrated deformation mapping and morphodeformation studies in this earthquake-prone area.

3. DATA AND METHODS

3.1. Data Sources

The data utilized in this study were gathered from multiple sources to facilitate spatial and deformation modeling. **Table 1** presents the datasets employed, which include satellite imagery, digital elevation models, seismic data, and thematic maps concerning geology and geomorphology. Each dataset is provided with its corresponding source and a concise explanation of its relevance to the study.

Table 1.

Study data and sources.

No	Data	Source	Information
1	Sentinel-1A Imagery	United States Geological Survey (USGS)	Deformation modeling
2	Earthquake Data		Spatial modeling of magnitude, epicenter depth, and PGA
3	Digital Elevation Model Nasional (DEMNAS)	Indonesian Geospatial Information Agency	Hillshade modeling
4	Geomorphological Map		Spatial distribution of landforms
5	Geological Map	Indonesian Ministry of Energy and Mineral Resources	Spatial distribution of lithological units

3.2. Study Process

The study on morphological deformation in the Singkarak segment was carried out through several structured phases. The first stage involved acquiring secondary data from authorized institutions, such as Sentinel satellite imagery obtained via the USGS, Digital Elevation Model Nasional (DEMNAS) elevation data, geological and geomorphological maps from the Indonesian Geospatial Information Agency, and earthquake records also retrieved from the USGS. The next phase focused on spatially interpolating earthquake epicenter data using the ordinary kriging method within ArcGIS software, selected for its robustness in estimating spatial autocorrelation in geophysical datasets**.** Simultaneously, Sentinel-1A radar imagery was analyzed using SNAP software to assess deformation levels within the Singkarak segment. Subsequent analytical steps involved algebraic overlay analysis using the Raster Calculator in ArcGIS, integrating interpolated seismic parameters with deformation data to construct a composite morphodeformation model. To develop a comprehensive morphological deformation model for the Singkarak segment, the integrated datasets, including deformation distribution, earthquake magnitudes, epicenter depths, PGA values, and geological-geomorphological layers, were processed using algebraic raster modeling techniques. This geospatial approach, based on kriging interpolation, facilitated the prediction of seismic characteristics such as earthquake magnitudes, epicenter locations, and PGA values across different geomorphological units in the study area. For a detailed illustration, please refer to **Fig 2**.

To assess the geospatial distribution of geological and geomorphological features within the Singkarak segment, geological maps issued by the Geological Agency under the Indonesian Ministry of Energy and Mineral Resources, along with geomorphological maps from the Indonesian Geospatial Information Agency, were employed as primary reference data. The geological features considered in this analysis include lithological units such as volcanic rocks (e.g., andesite, lava, tuff), sedimentary formations (e.g., limestone, alluvium), and intrusive bodies (e.g., granite, diorite).

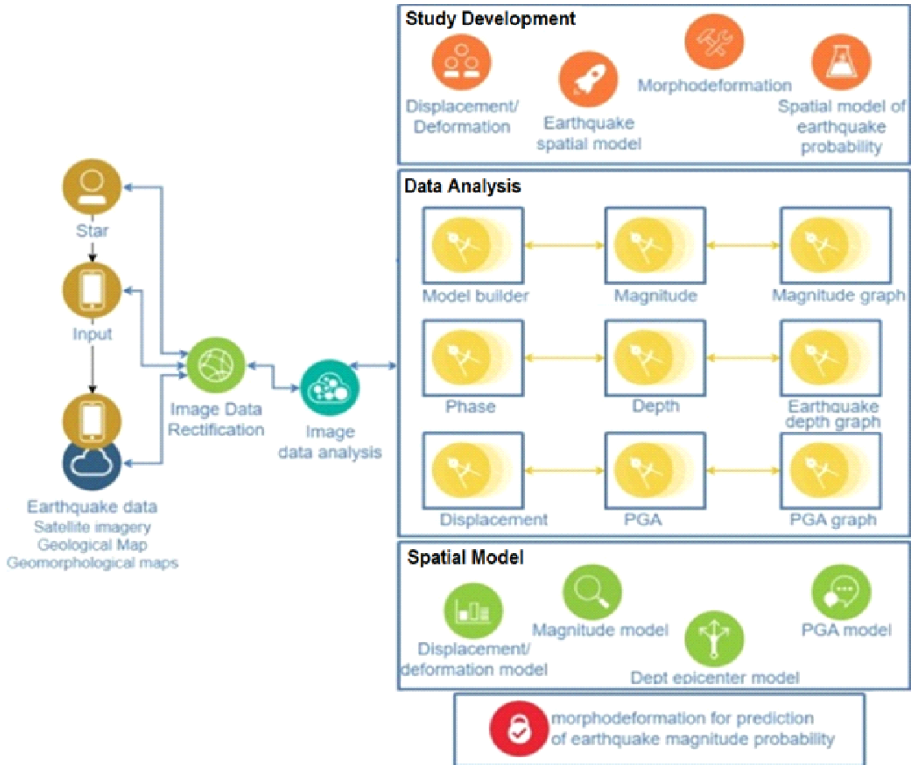

Fig. 2. Morphodeformation-Based Earthquake Spatial Modeling Workflow.

Meanwhile, the geomorphological features encompass denudational, fluvial, karst, volcanic, and structural landforms. The delineation of the study area covers the Singkarak Segment, geographically bounded by coordinates 0°36′44.17″S and 100°32′21.14″E, and administratively includes Tanah Datar and Solok Regencies in West Sumatra Province, Indonesia.

These datasets were integrated into the image analysis workflow (refer to the Image Data Analysis and Study Development sections in **Fig 2**). To generate these spatial models, the kriging interpolation technique was applied to the earthquake dataset, as illustrated in the Data Analysis section of the diagram. This analytical step supported the development of earthquake magnitude models, epicenter depth models, and the PGA model, which collectively contributed to the construction of a comprehensive spatial morphodeformation model. The spatial interpolation process was carried out following the methodology outlined by Njifon & Schuhmacher (2024), Atkinson et al. (2022); Guo et al. (2022), using the following equation:

$$Z = (x_p) = \sum_{i=1}^{n} \quad \lambda_{i\,.}\, Z\,(x_i)\; with \;\; \sum_{i=1}^{n} \quad \lambda_{i\,.} = 1 \qquad (1)$$

where $\lambda_{i\,.}$ represents the kriging weight, and $Z\,(x_i)$ is the observed value at a known location, while $Z(x_p)$ denotes the estimated value at an unknown location x_p.

Inverse Distance Weighting (IDW) is a deterministic interpolation method used to estimate the value of a variable at unsampled points based on the weighted average of nearby known values. To calculate the weight coefficients in kriging interpolation, the procedure follows the approach described by Triyatno et al. (2020); Payares-Garcia et al. (2023); Suesse et al. (2023), using the following equation.

$$\lambda_{i\,.} = \frac{D_i^{-a}}{\sum_{i=1}^{n} D_i^{-a}} \quad (2)$$

where: $\lambda_{i\,.}$ denotes the weight assigned to point i, D_i represents the distance from point i to the location of the unknown value, and the weight is raised to the tenth power to emphasize the influence of proximity in the interpolation process (Cimellaro et al., 2024).

To quantify the extent of ground deformation in the Singkarak segment, the following formulations were applied based on the approaches outlined by Razi et al. (2023).

$$\Delta\varphi_{m.s}^{disp}(T) = \frac{4\pi}{\lambda}\beta_t \Delta v(T) \quad (3)$$

where: $\Delta\varphi(T)$ refers to the target velocity at time T, $\Delta\varphi_{m.s}^{disp}(T)$ denotes the atmospheric phase component, which can be estimated through residual modeling techniques, and $\Delta\varphi_{m.s}^{disp}(T)$ represents the phase noise contribution, derived from Synthetic Aperture Radar (SAR) data conversion and and subsequently excluded from the residual phase model (Babaee et al., 2024).

4. RESULTS

4.1. Morphodeformation using Geomorphological, Geological, and Seismicity Data

To understand the morphotectonic dynamics of the Singkarak segment, this study utilized geomorphological maps, geological maps, and the spatial distribution of earthquake epicenters. These spatial data were analyzed as part of the morphological deformation assessment to determine how landform types and lithological structures influence seismic activity in the area. **Fig 3** shows the geomorphological and geological characteristics of the Singkarak segment, along with the distribution of recorded earthquake points.

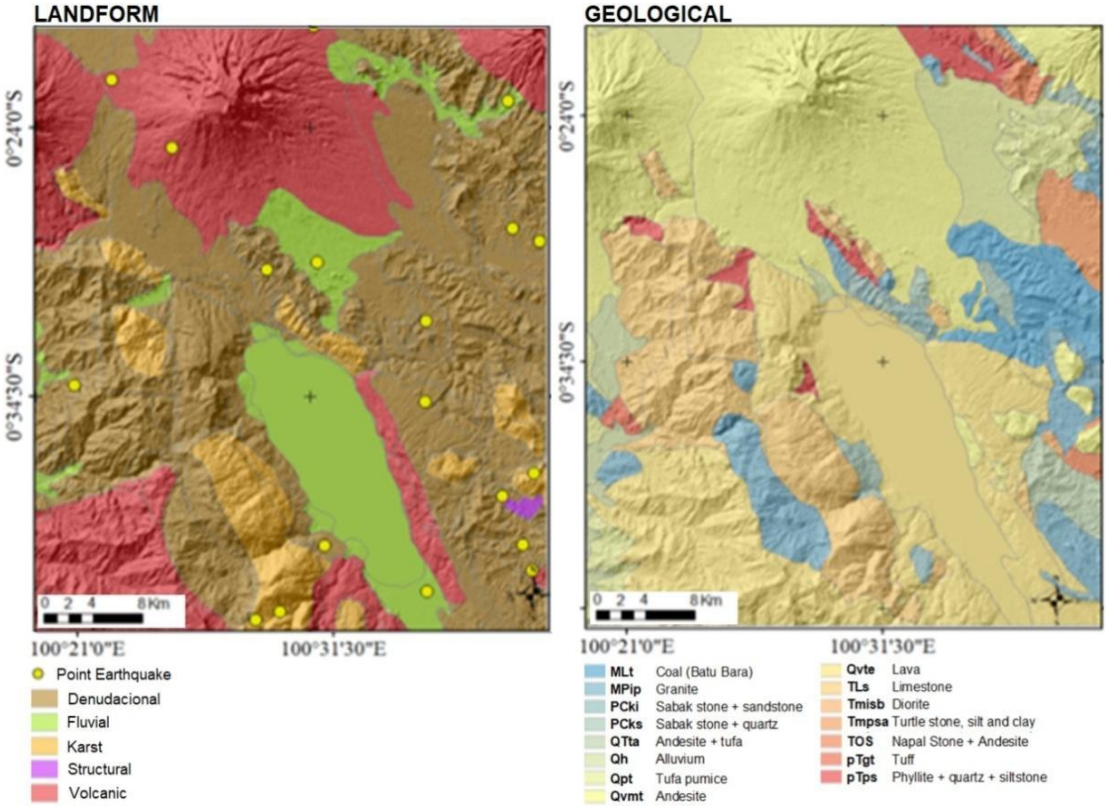

Fig. 3. Geomorphological (left) and Geological (left) Maps of the Singkarak Segment, showing earthquake distribution, surface lithology, and landform units.

The geomorphological map (left) shows that the Singkarak segment comprises various landform units, including denudational, fluvial, karst, volcanic, and structural landforms. Denudational landforms dominate the western and northern areas, while fluvial landforms are concentrated along the low-lying central basin surrounding Lake Singkarak. Volcanic landforms are prominent in the northwestern and southeastern zones. The distribution of earthquake points (shown as yellow dots) appears clustered along the boundary zones between different landforms, particularly where fluvial areas meet denudational and volcanic zones, indicating active deformation fronts. Meanwhile, the geological map (left) reveals a complex assemblage of rock types in the study area. The dominant lithological units include volcanic rocks such as andesite (Qvmt, QTta), lava (Qvte), and tuff (pTgt), as well as sedimentary deposits like limestone (TLs), alluvium (Qh), and phyllite (pTps). Intrusive rocks such as granite (MPip) and diorite (Tmisb) are also identified. Zones composed of andesite and tuff are more susceptible to ground uplift and correlate with areas showing higher earthquake frequencies, while sediment-dominated units such as alluvium tend to associate with subsidence. The spatial distribution and magnitude model were developed using ArcGIS to create predictive spatial representations of earthquake behavior within the study area. The interpolation results in **Fig 4** show an overview of both the magnitude intensity and the distribution of epicenters across the Singkarak Segment.

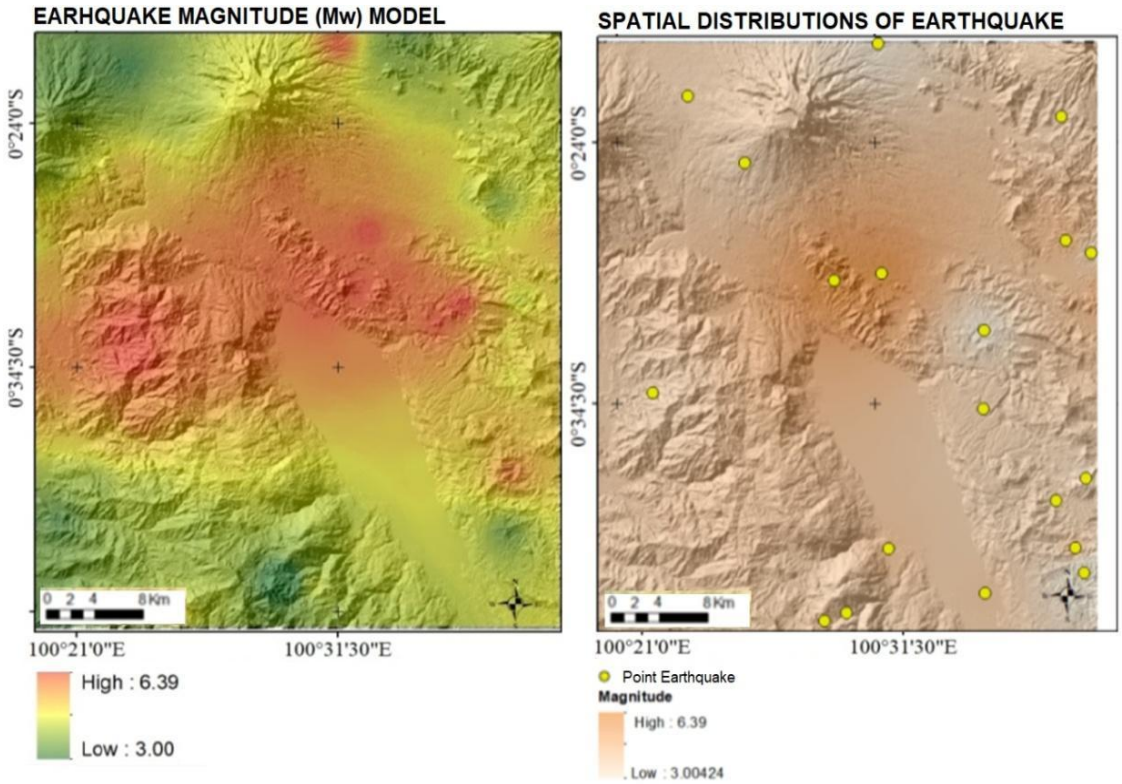

Fig. 4. Earthquake Magnitude Model (left) and Spatial Distribution of Earthquake Epicenters (right) in the Singkarak Segment.

Fig 4 above displays two key outputs of the spatial earthquake analysis. The left map shows the Earthquake Magnitude (Mw) Model, while the right map depicts the Spatial Distribution of Earthquake Epicenters. Based on the magnitude model, the intensity of earthquakes ranges from 3.00 Mw to 6.39 Mw, with higher magnitudes (≥ 6.0 Mw) predominantly concentrated in the central part of the study area. These zones correspond with areas characterized by complex geological and geomorphological transitions, particularly where denudational and volcanic landforms intersect. The

right map further supports these findings, showing that the epicenters of earthquakes are scattered across the segment but tend to cluster in the central and southeastern areas. The presence of multiple epicenters in this area indicates zones of high tectonic stress, likely associated with active fault segments such as the Semangko Fault that bisects the study area. Meanwhile, lower-magnitude events (3.0–4.5 Mw) are more widely dispersed, particularly in the northern and southern zones, which are dominated by softer lithologies such as alluvium and tufa pumice. To further support the morphological deformation analysis in the Singkarak Segment, this study includes a geological and morphological cross-section along the A–B transect line. This cross-section was developed by integrating surface geological data with subsurface interpretations derived from tectonic structures, fault orientations, and lithological layers. The tectonic block on the eastern side of the fault appears uplifted and intruded by larger magmatic bodies, while the western block, though elevated, is more eroded and composed of more sedimentary deposits. **Fig 5** shows the contour map, 3D terrain model, and longitudinal profile of the study area, providing a detailed geomorphological characterization that complements the geological and seismic analysis.

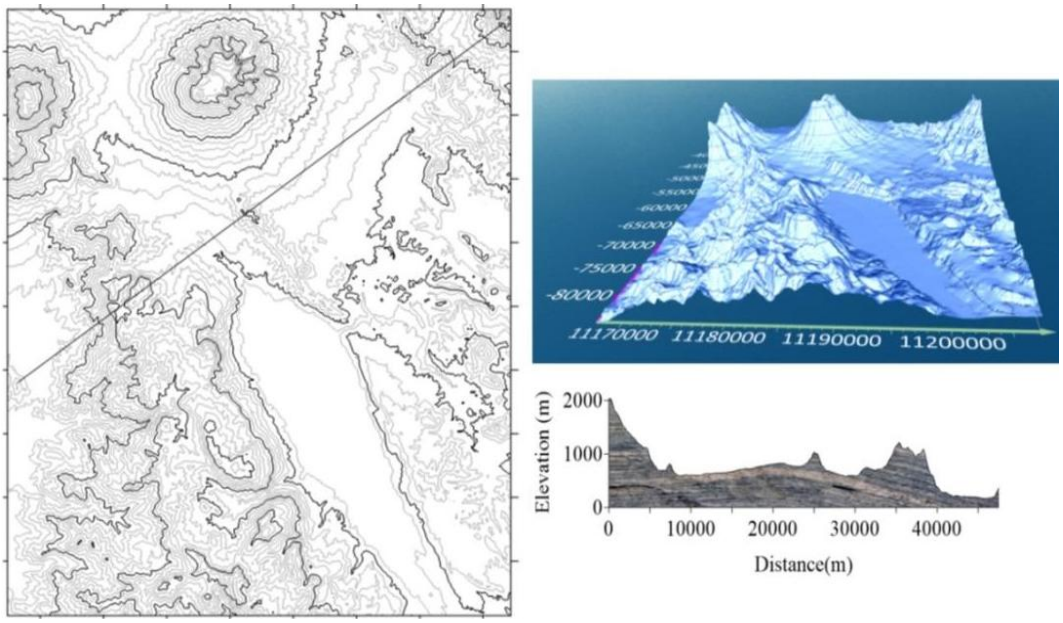

Fig. 5. Contour Line Map (left), 3D Terrain Model (top right), and Longitudinal Elevation Profile (bottom right) of the Singkarak Segment, illustrating morphological variation and elevation gradients across

Fig 5 above shows the morphological structure of the Singkarak Segment through three complementary visualizations: a contour map (left), a 3D surface model (top right), and a longitudinal topographic cross-section (bottom right). The contour lines show dense clustering in some zones, indicating steep terrain, while wider spacing reveals gentler slopes. The 3D model highlights elevation contrasts across the segment, emphasizing mountainous areas, valleys, and basins surrounding Lake Singkarak. The elevation profile shows that the area consists of asymmetrical blocks ranging from near 0 m to above 2,000 m, forming a pronounced morphological tilt from east to west and vice versa. This aligns with the geological structure governed by the Semangko Fault, which segments the area into uplifted and subsided blocks. The slope angle, ranging from 23° to 45°, reflects the tectonically active nature of the region, where faulting and magmatic processes shape the surface. Overall, this cross-section confirms the complex tectono-morphological dynamics of the Singkarak segment, reinforcing deformation and seismic model outputs from kriging and Sentinel-1A radar analysis. **Tables 2** and **3**, and **Fig 6** show the formation distribution for 2019–2023 and 2023–2024. This analysis identifies uplift or subsidence zones critical to understanding regional tectonic behavior.

Table 2.

Morphodeformation Frequency Distribution in 2019–2023.

Interval Morphodeformation (cm)	Denudasional	Fluvial	Karst	Volcanic
−0.398 – −0.264	4	1	4	2
−0.265 – −0.131	12	3	2	2
−0.132 – 0.002	13	6	3	15
0.003 – 0.137	15	3	2	13

Source: Data Analytics 2024.

Table 3.

Morphodeformation Frequency Distribution in 2023–2024.

Interval Morphodeformation (cm)	Denudasional	Fluvial	Karst	Volcanic
−0.748 – −0.503	1	2	0	3
−0.504 – −0.259	22	4	1	8
−0.260 – −0.015	13	5	4	12
−0.016 – 0.229	8	4	6	9

Source: Data Analytics 2024.

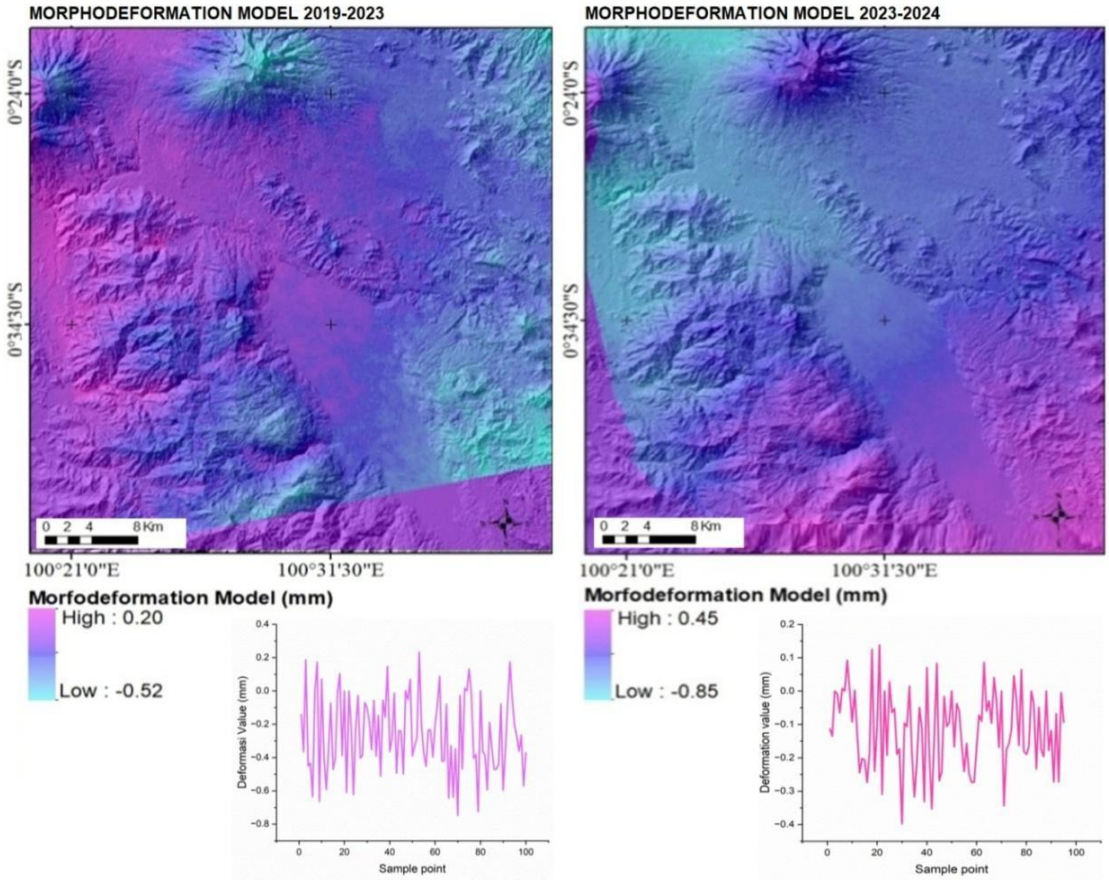

Fig. 6. Comparison of Morphodeformation Models in the Singkarak Segment for 2019–2023 (left) and 2023–2024 (right), showing uplift and subsidence patterns in mm based on Sentinel-1A analysis.

Fig 6 above shows the Morphodeformation Model for two timeframes. During the 2019–2023 period, deformation values ranged from 0.52 mm (subsidence) to +0.20 mm (uplift). In contrast, during the 2023–2024 period, the deformation intensified, with subsidence reaching −0.85 mm and uplift rising to +0.45 mm. The corresponding statistical frequencies for each deformation interval and

geomorphological unit are shown in **Tables 2 and 3**. It is observed that during 2019–2023, deformation was relatively balanced, with uplift more prominent in volcanic and denudational landforms. In 2023–2024, deformation frequency rose sharply, especially in denudational units, which showed greater subsidence (−0.504 to −0.259 cm). This trend indicates an intensifying tectonic regime in the Singkarak Segment, particularly in boundary zones where uplift and subsidence overlap.

4.2. Spatial Modeling of Earthquake Magnitude, Epicenter Depth, and PGA

This study utilized kriging interpolation and spatial randomization techniques applied to earthquake magnitude, epicenter depth, and PGA data to estimate the spatial potential of earthquake occurrence in the Singkarak Segment. The spatial model produced allows for the simulation of high-risk zones across the segment, reflecting areas with similar seismic characteristics based on observed geophysical parameters. **Fig 7** shows the spatial distribution of Mw, helping to identify areas with higher earthquake susceptibility.

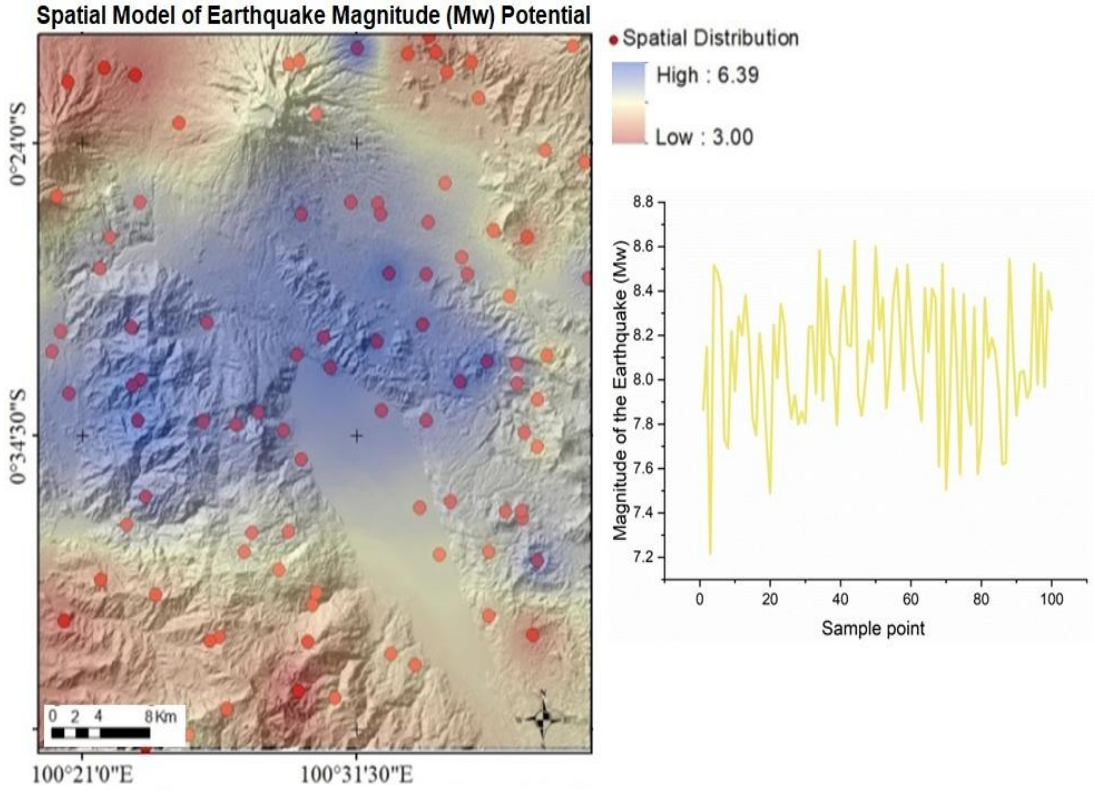

Fig. 7. Spatial distribution of estimated Mw in the Singkarak Segment using kriging interpolation (left) and magnitude variation across sample points (right).

Fig 7 shows a spatial model of Mw across the Singkarak Segment. The color gradient represents estimated magnitudes from 3.00 Mw (blue) to 6.39 Mw (red), while red and blue dots indicate distribution points used in interpolation. Higher-magnitude zones (≥6.0 Mw) are concentrated in the central and southern parts, aligning with fluvial and denudational landforms where structural deformation is more active. In contrast, lower-magnitude zones (≈3.0 Mw) appear in the northern, eastern, and far southern areas, dominated by volcanic, denudational, or karstic landforms. The line graph shows magnitude variation across sample points, indicating fluctuating yet generally high values and non-uniform seismic potential. Geomorphological transitions, such as between fluvial and volcanic terrain, often act as seismic accumulation or release zones. For more details, see **Table 4** below.

Table 4.

Frequency Distribution of Earthquake Magnitudes (Mw).

Magnitude Interval (Mw)	Denudasional	Fluvial	Karst	Volcanic
7.216 – 7.568	1	0	2	1
7.569 – 7.921	5	2	3	12
7.921 – 8.273	19	5	6	14
8.274 – 8.625	19	6	0	5

Source: Data Analytics 2024.

Table 4 shows that the highest frequency of large-Mw (7.921–8.625 Mw) earthquakes occurred in denudational landforms, with 19 events recorded in each upper interval. Volcanic landforms also showed notable seismicity, especially in the 7.569–8.273 Mw range, with 12 and 14 events. Karst and fluvial units experienced fewer but still significant events, indicating that all geomorphological settings in the Singkarak Segment are affected by earthquake activity at different intensities. Epicenter depth is critical for surface damage, ranging from 18.37 to 91.41 km, indicating shallow to intermediate-depth events. **Fig 8** shows the spatial distribution and depth variation of epicenters derived from seismic modeling and interpolation.

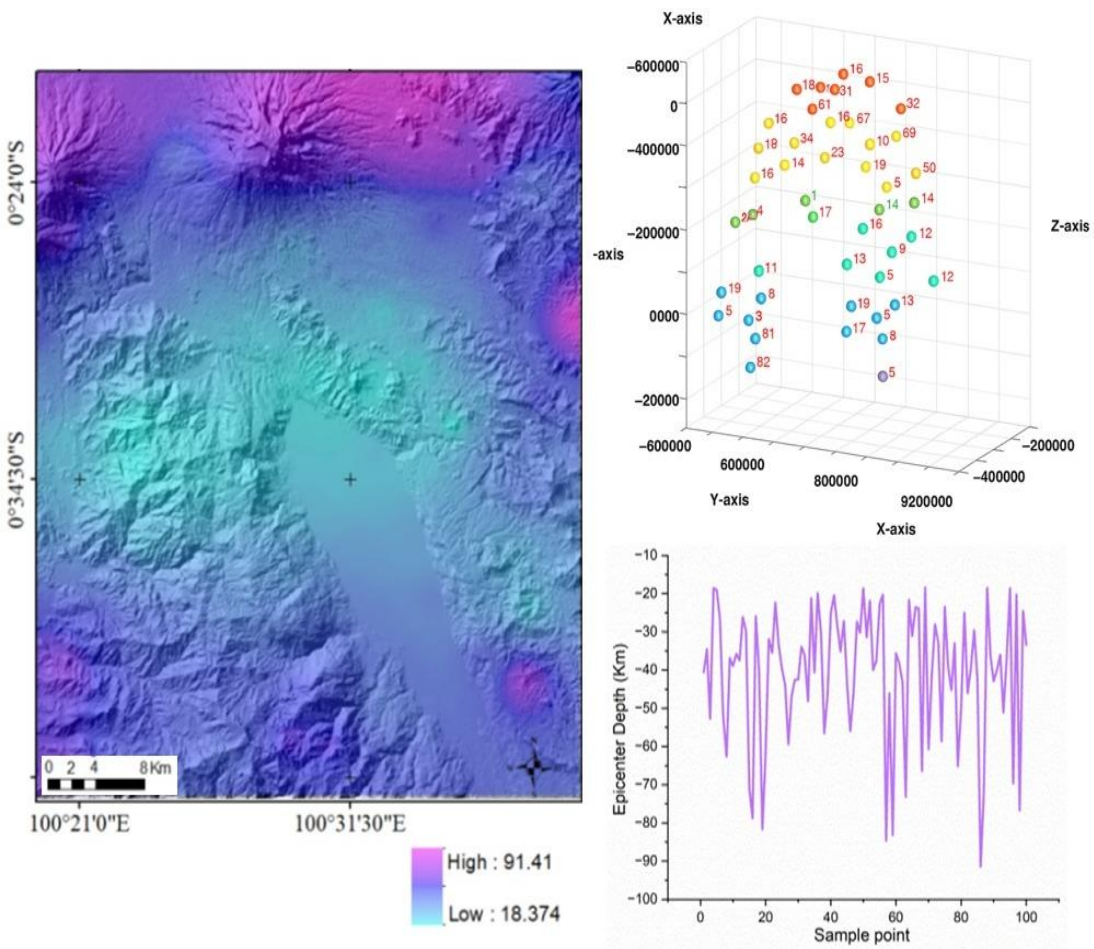

Fig. 8. Spatial model of earthquake epicenter depth in the Singkarak Segment (left), 3D scatter plot of epicenter distribution (top right), and depth variation across sample points (bottom right).

The map (left) shows the spatial model of epicenter depth, where shallower earthquakes (18.37–36.64 km) dominate the central part of the Singkarak Segment, marked by cyan to blue zones. In contrast, deeper events are concentrated toward the northern and southeastern flanks, indicated by pink to purple shades. The 3D scatter plot (top right) displays the vertical and horizontal distribution of earthquake epicenters across the segment, confirming seismic stratification at different depths. The line graph (bottom right) illustrates variations in epicenter depth across 100 sample points, showing that most events fall within −20 to −40 km, supporting the conclusion that shallow earthquakes are most prevalent. For more details, see **Table 5** below.

Table 5.

Frequency Distribution of Earthquake Epicenter Depths.

Dept Interval (km)	Denudasional	Fluvial	Karst	Volcanic
-18.36 – -36.64	28	9	6	7
-36.64 – -54.91	5	0	5	13
-54.91 – -73.19	2	3	0	9
-73.19 – -91.47	9	1	0	3

Source: Data Analytics 2024.

Table 5 shows that denudational and fluvial geomorphological units most commonly host shallow epicenters, with 28 and 9 occurrences, respectively, in the depth range of −18.36 to −36.64 km. Volcanic terrains show greater activity at intermediate depths (−36.64 to −73.19 km), indicating tectono-magmatic influences. Most seismic activity in the Singkarak Segment originates at shallow depths, especially in zones affected by faulting and uplift, making them critical for hazard mitigation and spatial planning. Seismic shaking intensity is strongly influenced by geological structure and surface morphology. **Fig 9** shows the PGA spatial model, with a 3D view and graph of PGA variation across sampling points.

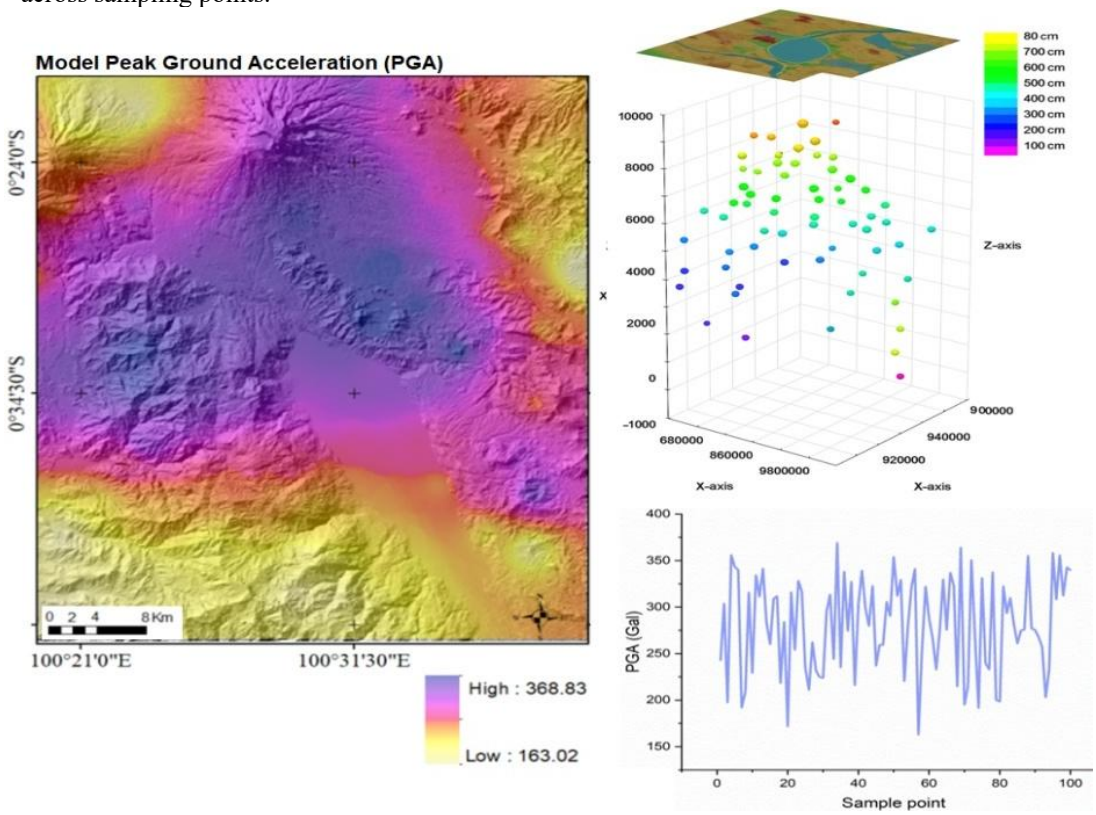

Fig. 9. Spatial model of PGA in the Singkarak Segment (left), 3D distribution of PGA intensity (top right), and PGA variation across sample points (bottom right).

The PGA map (left) shows the spatial distribution of maximum ground acceleration in the Singkarak Segment. The PGA values range from 163.02 gal (low) to 368.83 gal (high). The highest acceleration values are concentrated in the central zone, corresponding to tectonically active areas with fluvial and denudational geomorphological units. These zones also overlap with areas previously identified as having shallow epicenters and significant uplift/subsidence, making them highly vulnerable to strong ground motion. Higher PGA values (yellow to red) are more densely clustered in elevated or fault-affected areas, consistent with the surface model. The line graph (bottom right) confirms PGA fluctuation across 100 sample points, with many points recording values between 250–370 gal, indicating widespread moderate to high seismic acceleration across the segment. Areas with high PGA values are priority zones for earthquake risk reduction strategies, including building reinforcement, land-use planning, and community preparedness. To support the spatial model results of PGA distribution, the following **Table 6** shows a more detailed breakdown of PGA frequency distribution across different geomorphological units in the Singkarak Segment.

Table 6.

Frequency Distribution of PGA.

PGA Interval	Denudasional	Fluvial	Karst	Volcanic
162.98 – 214.47	2	0	1	5
215.00 – 266.49	2	2	3	14
267.00 – 318.49	10	6	4	8
319.00 – 370.49	30	5	3	5

Source: Data Analytics 2024.

Table 6 shows that the highest concentration of PGA values (319.00–370.49 gal) occurs predominantly in denudational landforms, with 30 recorded events, highlighting this unit as the most affected by strong ground motion. These areas are typically characterized by steep slopes and active tectonic deformation, making them highly responsive to seismic wave amplification. Volcanic landforms also exhibit elevated PGA values across all intervals, particularly in the 215.00–266.49 gal range, where 14 occurrences were recorded. This suggests a strong influence of past magmatic activity and fractured rock structures in facilitating seismic energy transmission. Fluvial units, commonly found in low-lying valleys and sedimentary basins, show a moderate distribution of PGA, with 5 occurrences in the highest range, possibly due to sediment amplification effects that intensify ground shaking. Although karst landforms recorded fewer high-PGA events, they still appear in moderate ranges, indicating localized vulnerability depending on structural fractures and subsurface voids. The final overlay results show the distribution of morphodeformation zones, which represent areas where vertical ground deformation (uplift and subsidence) intersects with high seismic vulnerability. These integrated zones combine deformation modeling with seismic hazard indicators, providing essential spatial insight for regional disaster mitigation strategies, land-use planning, and infrastructure resilience development.

4.3. Discussions

Geologically, the area is dominated by sedimentary and volcanic rocks, which are structurally unstable and tectonically complex, increasing the risk of high-magnitude seismic events (Parmar, 2019; Yang et al., 2022). This risk is further exacerbated by the presence of the active Sumatran Great Fault, known locally as the Semangko Fault, and volcanic activity from Mount Marapi, which demonstrated clear tectono-volcanic interaction during its eruption on December 3, 2023 (Istijono et al., 2025). Geomorphologically, the Singkarak Segment consists of fluvial, denudational, and volcanic landforms, each exhibiting different levels of vulnerability (Parmar, 2019; Verma et al., 2020; Zocchi et al., 2025). Earthquake epicenters are concentrated in denudational and volcanic landforms, which also show higher values of earthquake magnitude and PGA (Barbi et al., 2023; Fend & Redenbach, 2024). From 2019 to 2023, deformation ranged between +0.20 mm (uplift) and −0.52 mm (subsidence). During 2023–2024, deformation intensified with uplift reaching +0.45 mm and subsidence deepening to −0.85 mm, particularly along morphological boundaries. The earthquake magnitude ranges from 3.00 to 6.39 Mw, with higher magnitudes (≥6.0 Mw) clustering in the central

and southern parts of the segment, especially in denudational and fluvial areas (Chen & Sharma, 2024; Guo et al., 2022; Heuvelink & Webster, 2022). These magnitudes, though moderate, are capable of causing moderate structural damage, especially in densely populated or poorly built areas (Gama et al., 2017). Most events occur in the shallow range of −18.36 to −36.64 km, concentrated in denudational and fluvial landforms, which intensifies surface shaking. The highest PGA values (up to 368.83 gal) are also found in these units, particularly in the central zone, confirming it as a seismically critical area (Feng et al., 2024). The vulnerability map indicates that high-vulnerability zones are predominantly located in densely populated lowland areas, particularly those with proximity to fault lines and insufficient infrastructure resilience. These regions often feature soft sedimentary soils, limited evacuation routes, and high building density, all of which exacerbate the potential impact of seismic events. Population concentration amplifies exposure and hampers rapid emergency response, making these zones critically susceptible to ground shaking and secondary hazards such as liquefaction or landslides. In conclusion, the integration of geological, geomorphological, and morphodeformation data reveals that the Singkarak Segment is an active deformation zone with considerable earthquake risk. The combination of shallow epicenters, intense PGA, and active tectonics demands priority in hazard mitigation, urban planning, and earthquake preparedness strategies.

5. CONCLUSIONS

This study assessed the geospatial distribution of geological and geomorphological features within the Singkarak Segment, using integrated remote sensing, GIS-based interpolation, and deformation modeling. The key findings indicate that the Singkarak Segment is a morphotectonically active zone characterized by complex lithological compositions and diverse landform units, including denudational, fluvial, volcanic, and karstic terrains. Earthquake epicenters, magnitudes, and PGA values were found to cluster within denudational and fluvial units, where active faulting and deformation are concentrated. Moreover, vertical surface displacement ranging from uplift to subsidence intensified from 2019–2023 to 2023–2024, signaling increasing tectonic stress within the region. The practical implications of these findings are significant for disaster risk reduction and spatial planning in West Sumatra. Identifying zones with high PGA and shallow epicenters enables authorities to prioritize infrastructure retrofitting and land-use regulation in high-risk areas. The morphodeformation modeling approach also provides an early-warning framework that can be updated regularly using new satellite imagery and seismic data. This supports proactive decision-making in earthquake-prone zones like the Singkarak Segment. However, several limitations were encountered in this study. The accuracy of deformation estimates depends on the temporal resolution and atmospheric correction of Sentinel-1A data. Additionally, the kriging interpolation technique, while effective, is influenced by the spatial distribution and density of available seismic records, which may not capture all microseismic activity. Geological and geomorphological maps, though official, may require more frequent updates to reflect landscape changes. Future research should explore machine learning models to complement geostatistical approaches, incorporate near-real-time InSAR datasets, and assess post-seismic ground responses. Furthermore, expanding the study area to include adjacent fault segments may yield broader insights into regional tectonic interactions. Overall, this study contributes a replicable method for integrated seismic hazard mapping in tectonically complex regions.

ACKNOWLEDGEMENTS

The authors would like to express their deepest gratitude to the Universitas Negeri Padang (UNP) for providing study support and access to relevant data and analytical tools. We thank the local governments of Tanah Datar and Solok Regencies for facilitating field visits and providing logistical support during data validation in the Singkarak Segment. This study would not have been possible without the combined efforts and collaboration of institutions and individuals committed to improving earthquake risk reduction and geospatial hazard analysis in Indonesia.

REFERENCES

Amir, H., Bijaksana, S., Dahrin, D., Nugraha, A. D., Arisabaya, I., Pratama, A., & Suryanata, P. B. (2021). Subsurface structure of Sumani segment in the Great Sumatran Fault inferred from magnetic and gravity modeling. Tectonophysics, 821, 229149. https://doi.org/10.1016/j.tecto.2021.229149

Arlym, L., Hermon, D., Lanin, D., Oktorie, O., & Putra, A. (2019). A policy model of preparedness the general hospital in reducing victims of earthquake and tsunami disasters in Siberut Mentawai Island, Indonesia. *International Journal of Recent Technology and Engineering*, 8(3), 89–93. https://doi.org/10.35940/ijrte.C3890.098319

Appel, M., & Pebesma, E. (2020). Spatiotemporal multi-resolution approximations for analyzing global environmental data. Spatial Statistics, 38, 100465. https://doi.org/10.1016/j.spasta.2020.100465

Atkinson, P. M., Stein, A., & Jeganathan, C. (2022). Spatial sampling, data models, spatial scale and ontologies: Interpreting spatial statistics and machine learning applied to satellite optical remote sensing. Spatial Statistics, 50, 100646. https://doi.org/10.1016/j.spasta.2022.100646

Babaee, S., Khalili, M. A., Chirico, R., Sorrentino, A., & Di Martire, D. (2024). Spatiotemporal characterization of the subsidence and change detection in Tehran plain (Iran) using InSAR observations and Landsat 8 satellite imagery. Remote Sensing Applications: Society and Environment, 36, 101290. https://doi.org/10.1016/j.rsase.2024.101290

Barbi, C., Menafoglio, A., & Secchi, P. (2023). An object-oriented approach to the analysis of spatial complex data over stream-network domains. Spatial Statistics, 58, 100784. https://doi.org/10.1016/j.spasta.2023.100784

Chang Seng, D. (2010). Disaster risk preparedness: The role of risk governance, multi-institutional arrangements and polycentric frameworks for a resilient tsunami early warning system in Indonesia (Doctoral dissertation, Rheinische Friedrich-Wilhelms-Universität Bonn).

Chen, Z., & Sharma, P. (2024). Nonparametric statistical analysis of system resilience migration and application for electric distribution structures. Resilient Cities and Structures, 3(3), 92–105. https://doi.org/10.1016/j.rcns.2024.07.005

Cimellaro, G. P., Cardoni, A., & Reinhorn, A. (2024). Modelling infrastructure interdependencies and cascading effects using temporal networks. Resilient Cities and Structures, 3(3), 28–42. https://doi.org/10.1016/j.rcns.2024.05.002

Fend, C., & Redenbach, C. (2024). Nonparametric isotropy test for spatial point processes using random rotations. Spatial Statistics, 64, 100858. https://doi.org/10.1016/j.spasta.2024.100858

Feng, K., Wang, C., & Li, Q. (2024). Evaluating the role of transportation system in community seismic resilience. Resilient Cities and Structures, 3(3), 65–78. https://doi.org/10.1016/j.rcns.2024.05.003

Gama, F. F., Cantone, A., Mura, J. C., Pasquali, P., Paradella, W. R., Dos Santos, A. R., & Silva, G. G. (2017). Monitoring subsidence of open pit iron mines at Carajás Province based on SBAS interferometric technique using TerraSAR-X data. Remote Sensing Applications: Society and Environment, 8, 199–211. https://doi.org/10.1016/j.rsase.2017.09.001

Ghaderpour, E., Mazzanti, P., Bozzano, F., & Scarascia Mugnozza, G. (2024). Ground deformation monitoring via PS-InSAR time series: An industrial zone in Sacco River Valley, central Italy. Remote Sensing Applications: Society and Environment, 34, 101191. https://doi.org/10.1016/j.rsase.2024.101191

Guntoro, A., Triany, N., Adhitama, R., Anugrahadi, A., & Parlindungan, B. (2024). Analysis of tectonic structure and its implications on petroleum systems in the Southeastern arc, Bengkulu Basin, Indonesia. AIP Conference Proceedings, 3019(1), 050004. https://doi.org/10.1063/5.0225803

Guo, X., Kurtek, S., & Bharath, K. (2022). Variograms for kriging and clustering of spatial functional data with phase variation. Spatial Statistics, 51, 100687. https://doi.org/10.1016/j.spasta.2022.100687

Hermon, D., Erianjoni, Dewata, I., Putra, A., & Oktorie, O. (2019). Liquefaction vulnerability analysis as a coastal spatial planning concept in Pariaman City – Indonesia. *International Journal of Recent Technology and Engineering*, 8(2), 4181–4186. https://doi.org/10.35940/ijrte.B3265.078219

Hermon, D., Ganefri., Putra, A., & Oktorie, O. (2019). Characteristics of melanic epipedon based on biosequence in the physiography of Marapi - Singgalang, West Sumatra. *IOP Conference Series: Earth and Environmental Science*, 314(1), 012010. https://doi.org/10.1088/1755-1315/314/1/012010

Hermon, D., Ikhwan., Putra, A., & Oktorie, O. (2020). Spatial analysis of tsunami vulnerability zones as a basic concept of coastal disaster mitigation in development planning of Pariaman City. *Journal of Advanced Research in Dynamical and Control Systems*, 12(7), 681–690. https://doi.org/10.5373/JARDCS/V12SP7/20202158

Heuvelink, G. B. M., & Webster, R. (2022). Spatial statistics and soil mapping: A blossoming partnership under pressure. Spatial Statistics, 50, 100639. https://doi.org/10.1016/j.spasta.2022.100639

Huang, Z., Pitilakis, K., Zhang, D., Tsinidis, G., & Argyroudis, S. (2022). On the effects of salient parameters for an efficient probabilistic seismic loss assessment of tunnels in alluvial soils. Resilient Cities and Structures, 1(3), 24–39. https://doi.org/10.1016/j.rcns.2022.10.006

Istijono, B., Fauzi, M. A. G., Hadiyansyah, D., Andriani, N. S. S., Prastiyo, A., & de Luna Era, M. (2025). Lessons learnt from community preparedness for Mount Merapi and Mount Marapi eruption disasters. E3S Web of Conferences, 604, 13004. https://doi.org/10.1051/e3sconf/202560413004

Jarder, S. L. N., Maruyama, O., & Garciano, L. E. O. (2024). A probabilistic estimation model for seismic physical portfolio loss of a water supply pipeline system. Resilient Cities and Structures, 3(1), 44–54. https://doi.org/10.1016/j.rcns.2024.01.001

Njifon, M.A, & Schuhmacher, D. (2024). Graph convolutional networks for spatial interpolation of correlated data. Spatial Statistics, 60, 100822. https://doi.org/10.1016/j.spasta.2024.100822

Novianti, R., Yuniarti, I., Ajie, G. S., Setiawan, F., Yuerlita, Y., Handoko, U., Triharyuni, S., & Afandi, A. Y. (2023). Towards sustainable management of Lake Singkarak, Indonesia: System analysis and research priorities. IOP Conference Series: Earth and Environmental Science, 1266(1), 012022. https://doi.org/10.1088/1755-1315/1266/1/012022

Parmar, S. (2019). Morphometry analysis using SAGA GIS: A case study of Watershed – 63 of Narmada River, Gujarat, India. International Journal of Engineering Research and Application, 9(2, Series II), 39–51. https://doi.org/10.9790/9622-090203951

Payares-Garcia, D., Osei, F., Mateu, J., & Stein, A. (2023). A Poisson cokriging method for bivariate count data. Spatial Statistics, 57, 100769. https://doi.org/10.1016/j.spasta.2023.100769

Ranke, U. (2016). Natural disaster risk management: Geosciences and social responsibility. Springer.

Razi, P., Sumantyo, J. T. S., Chua, M. Y., Ganefri, Perissin, D., & Tadono, T. (2023). Monitoring of tectonic deformation in the seismic gap of the Mentawai Islands using ALOS-1 and ALOS-2. Remote Sensing Applications: Society and Environment, 30, 100973. https://doi.org/10.1016/j.rsase.2023.100973

Rozaki, Z., Aini, N. N., Kamarudin, M. F., & Triyono, T. (2024). Developing farmers' community resilience in the volcanic area of Mount Merapi, Indonesia. Diyala Agricultural Sciences Journal, 16(1), 41–51.

Samsonov, S. V., Feng, W., Blais-Stevens, A., & Eaton, D. W. (2024). Ground deformation due to natural resource extraction in the Western Canada Sedimentary Basin. Remote Sensing Applications: Society and Environment, 34, 101159. https://doi.org/10.1016/j.rsase.2024.101159

Suesse, T., Brenning, A., & Grupp, V. (2023). Spatial linear discriminant analysis approaches for remote-sensing classification. Spatial Statistics, 57, 100775. https://doi.org/10.1016/j.spasta.2023.100775

Triyatno., Berti, I., Idris., Hermon, D., & Putra, A. (2020). Hazards and morphometry to predict the population loss due of landslide disasters in Koto XI Tarusan - Pesisir Selatan. *International Journal of GEOMATE*, 19(76), 98–103. https://doi.org/10.21660/2020.76.ICGeo12

Verma, S., Khalkho, D., & Gupta, L. K. (2020). Morphometric Analysis of a Drainage Basin using Remote Sensing and Geographical Information System (GIS). International Journal of Current Microbiology and Applied Sciences, 9(4), 1950–1959. https://doi.org/10.20546/ijcmas.2020.904.232

Yang, T. Y., Lepine-Lacroix, S., Guerrero, J. A. R., McFadden, J. B. W., & Al-Janabi, M. A. Q. (2022). Seismic performance evaluation of innovative balloon type CLT rocking shear walls. Resilient Cities and Structures, 1(1), 44–52. https://doi.org/10.1016/j.rcns.2022.03.004

Zocchi, M., Masciulli, C., Mastrantoni, G., Troiani, F., Mazzanti, P., & Scarascia Mugnozza, G. (2025). Automatic landslide prioritization at regional scale through PS-InSAR cluster analysis and socio-economic impacts. Remote Sensing Applications: Society and Environment, 37, 101414. https://doi.org/10.1016/j.rsase.2024.101414

A COMPARATIVE EVALUATION OF GEOREFERENCING TECHNIQUES IN UAV PHOTOGRAMMETRY: A CASE STUDY FROM THE CZECH REPUBLIC

Velile MOYO [1*], ***Michal KAČMAŘÍK*** [1]

DOI : 10.21163/GT_2025.202.13

ABSTRACT

The study evaluates the positional accuracy of geospatial products generated using direct (GNSS RTK-based) and indirect (Ground Control Points-based) georeferencing methods in UAV photogrammetry. Using the DJI Mavic 3 Enterprise quadcopter, surveys were conducted at two contrasting sites in the Czech Republic: a flat agricultural area and rugged terrain in the area affected by a landslide. Acquired RGB image sets were processed using consistent photogrammetric workflows. Resulting digital elevation models (DEMs) and orthophoto mosaics were analyzed against independently measured control points. Vertical and horizontal accuracies were assessed through RMSE and haversine-based distance calculations. Findings indicate that while both georeferencing methods produced centimeter-level accuracy, indirect georeferencing using GCPs yielded better quality in height. For horizontal accuracy, the results slightly varied between the two areas. In the flat area, direct georeferencing produced slightly better accuracy than indirect georeferencing whereas in the hilly area, the GCP-based approach was slightly superior. The study concludes that while GCPs can still provide some benefits in the quality of georeferencing, RTK-enabled UAVs offer a practical alternative for rapid, efficient deployment in suitable contexts.

Key-words: *UAV photogrammetry; Georeferencing; RTK; Digital Elevation Model; Orthomosaic*

1. INTRODUCTION

Unmanned Aerial Vehicles (UAVs) have quickly become a mature technology for capturing high quality spatial data with reasonable cost as shown e.g. by Colomina & Molina (2014), Gomez and Purdie (2016), Cromwell et al. (2021) or Mohsan et al. (2022). A set of properly acquired RGB images with sufficient overlaps in combination with their photogrammetric processing (Colomina et al., 2008) enable the production of detailed outputs such as digital elevation models (DEMs), 3D models or orthophoto mosaics. For practical use of these outputs, it is usually necessary to ensure their georeferencing to a selected spatial coordinate system. The standard solution is based on using a set of ground control points (GCPs) that are signaled in the area of interest at the time of image acquisition, and their position is accurately determined by some independent measurement technique. This approach is usually referred to as in-direct georeferencing. Since GCPs do not usually occur naturally in the selected area, they need to be manually positioned and collected again after the flight. This work, of course, adds significantly to the total time spent on data collection. If the imaging sensor or carrier used is equipped with its own localization unit, it is possible to use the information about the position of the device at the moment of image creation directly for georeferencing. This method is known as direct georeferencing. Localization units almost always rely on Global Navigation Satellite System (GNSS) technology, sometimes in combination with measurements from an Inertial Measurement Unit (IMU).

[1] *Department of Geoinformatics, Faculty of Mining and Geology, VŠB-Technical University of Ostrava, Czech Republic; velile.moyo.st@vsb.cz* [*], *michal.kacmarik@vsb.cz.*

Recently, the integration of Real-Time Kinematic (RTK) GNSS positioning technology into UAVs has begun. RTK is an advanced and widely used positioning technique based on differential measurements, typically achieving positioning accuracy within a few centimeters (Teunissen & Montenbruck, 2017). This represents a significant improvement in accuracy compared to common GNSS receivers that utilize the basic Standard Point Positioning (SPP) technique. Initially, only high-end devices were equipped with RTK GNSS receivers. The situation changed in year 2018 with announcement of the DJI Phantom 4 RTK quadcopter with a price below 6000 EUR (https://www.dji.com/newsroom/news/dji-launches-the-phantom-4-rtk-globally). Today, the market offers several comparable solutions at a similar cost.

Implementation of GNSS RTK technique in easily accessible UAVs has significantly advanced remote sensing applications, particularly in enhancing the accuracy of direct georeferencing. The comparative analysis of using RTK systems with traditional Ground Control Points (GCPs) has generated considerable interest in the remote sensing and photogrammetry communities, leading to new insights relevant to the accuracy of geospatial products. Recent studies such as Nakata et al. (2023) and Tomaštík et al. (2019) indicated that RTK-equipped UAVs can produce reliable geospatial datasets with reduced reliance on GCPs. Czyża et al. (2023) demonstrated advancements in UAV pose estimation accuracy due to RTK, suggesting that high-precision outputs can be achieved even without traditional GCPs. Both Nam-Bui et al. (2020) and Rauhala et al. (2023) discussed the use of RTK positioning over traditional GCPs for UAV-based topographic mapping. Nam-Bui et al. (2020) emphasized the importance of RTK in improving the accuracy of DEMs in complex open-pit mine environments, reducing reliance on GCP placement. Similarly, Rauhala et al. (2023) compared multiple UAV platforms and highlighted the advantages of RTK-enabled UAVs, such as the DJI Phantom 4 RTK, which significantly reduced georeferencing errors compared to traditional GCP-based methods.

The limitations associated with GCP-dependent methodologies have been analyzed in several studies. Štroner et al. (2021), highlighting the time and resource investments required for effective georeferencing. Stott et al. (2020) emphasized that while GCPs improve geometric accuracy, they complicate the operational logistics of UAV surveying, which can potentially compromise rapid response times in critical applications such as disaster management. However, several studies such as Atik & Arkali (2025) indicated that removing all GCPs can lead to significant errors, especially in regions with complex landforms and potential instability. Przybilla et al. (2020) noted that in certain contexts, particularly in variable or obstructed environments, maintaining a few GCPs can prevent accuracy deficits. Hence it is crucial to understand the variabilities in positional accuracy.

The performance of RTK in various environments presents unique challenges that necessitate careful examination. Nakata et al. (2023) explored microtopography changes due to soil erosion in agricultural landscapes using the UAV-RTK-PPK (Post-Processing Kinematic) method. Building on previous studies such as Przybilla et al. (2020), which primarily focused on flat or moderate terrain under favorable conditions, Elias et al. (2024) extended the application of RTK-based UAV photogrammetry to complex landscapes. Their findings demonstrate that high-accuracy 3D point clouds, with errors limited to a few centimeters, can be achieved even in challenging terrains by leveraging advanced image processing techniques, direct georeferencing, and optimized flight configurations, such as cross-grid and oblique imaging strategies.

Other factors contribute to the quality of data derived from UAVs which go alongside georeferencing techniques for example, the inclusion of oblique photographs. Martínez-Carricondo et al. (2023) conducted thorough accuracy assessments of RTK/PPK UAV-photogrammetry projects, highlighting that differential corrections from multiple GNSS fixed base stations significantly impact data quality. Their research aimed to enhance the accuracy of UAV photogrammetric projects by leveraging GNSS RTK receivers for direct georeferencing, eliminating the need for GCPs or oblique photographs. Szypuła (2024)'s findings indicated that the quality of elevation models derived from UAV measurements fluctuates based on the UAV equipment used and the terrain conditions. Szypuła (2024) discussed the improvement of accuracy for UAV-based DEMs without GCPs but implies that achieving optimal results often still relies on GCP methodologies in complex environments. This

perspective indicates that while RTK systems provide a valuable alternative, there remains a knowledge gap in understanding the accuracy thresholds across different applications and landscape complexities. The comparative accuracy using both methods across different terrains remains inadequately addressed.

This study systematically compares the accuracy of geospatial products generated using RTK (direct georeferencing) and non-RTK (in-direct georeferencing) datasets from the widespread quadcopter DJI Mavic 3 Enterprise in two contrasting areas in the Czech Republic. By evaluating both vertical and horizontal accuracies and by considering factors such as the influence of direct georeferencing versus traditional GCP deployment, this study aims to reconcile conflicting findings in previous studies and offer practical recommendations for UAV-based mapping. The findings can significantly contribute to this dialogue, addressing gaps related to the comparative performance of RTK/PPK based and GCPs based workflows in diverse landscapes.

2. METHODS AND MATERIALS

2.1. Study area

This study was conducted in two distinct areas of interest within the Czech Republic, each characterized by unique topographical and environmental features. The contrasting landscapes - one flat and agricultural, the other mountainous and landslide-prone, provide an ideal setting to assess and compare the accuracy of UAV products derived under direct and in-direct georeferencing setup.

Area 1 is situated in a flat, predominantly agricultural landscape near the city of Ostrava, Czech Republic (**Fig. 1**). The selected area covers about 4 ha where the range of altitudes is in the order of a few meters. At the time of data collection, the field was covered with low growing crops, with part of the area occupied by bare soil. The closest GNSS reference station is located at a short distance of 1.5 km. The relatively uniform terrain and close GNSS infrastructure offers a controlled environment for assessing UAV performance under optimal mapping conditions.

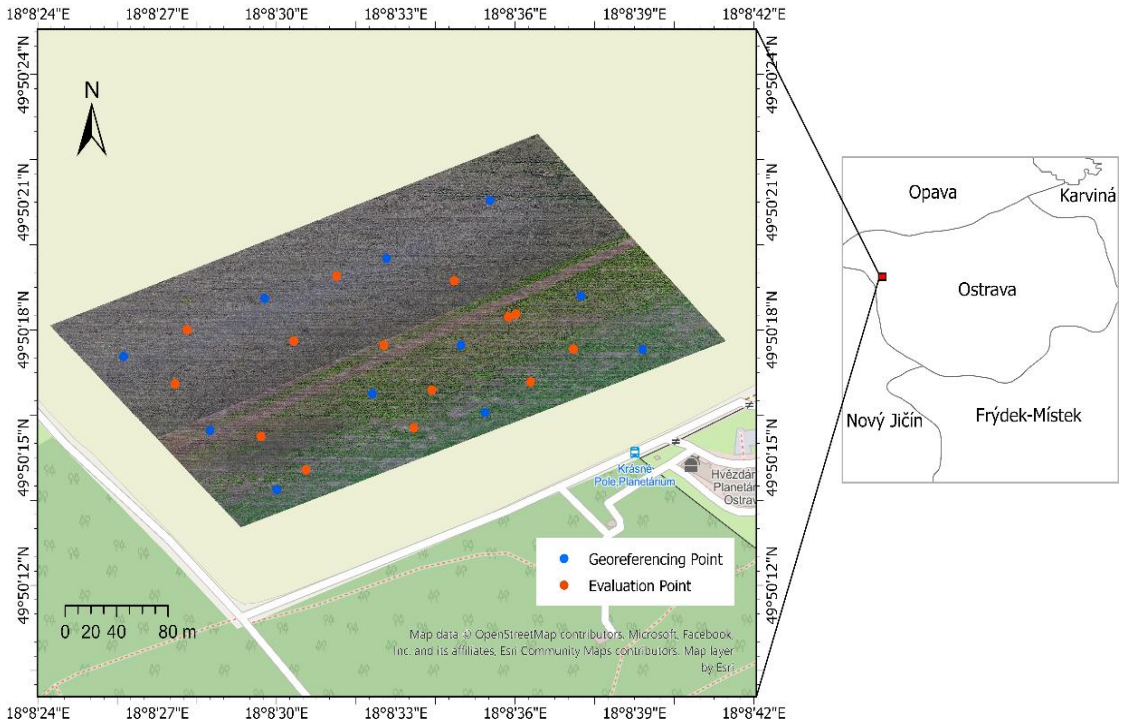

Fig. 1. Ostrava Area of Interest. Source of background map: Open Street Map.

In contrast, Girova (Area 2) is located in the Moravian-Silesian Region near the town Jablunkov in the Silesian Beskydy mountain range (**Fig. 2**). The selected area lies in the site of a large landslide which happened in May 2010. With its length of about 1.1 km and maximum width of 280 m, it has been one of the largest landslides in the Czech Republic in the last decades (Baroň et al., 2011). On the selected site of approximately 4 ha there is a very diverse terrain with a difference in elevation of about 40 m, parts of which are covered with bare land and others with different vegetation (mature forest, low forest, scrub). The complex topography and the whole environment make it an ideal testbed for evaluating the performance of UAV-derived DEMs and orthophoto mosaics under challenging conditions. The site is located close to the border with Slovakia and Poland, the nearest GNSS reference station is at a distance of 25 km.

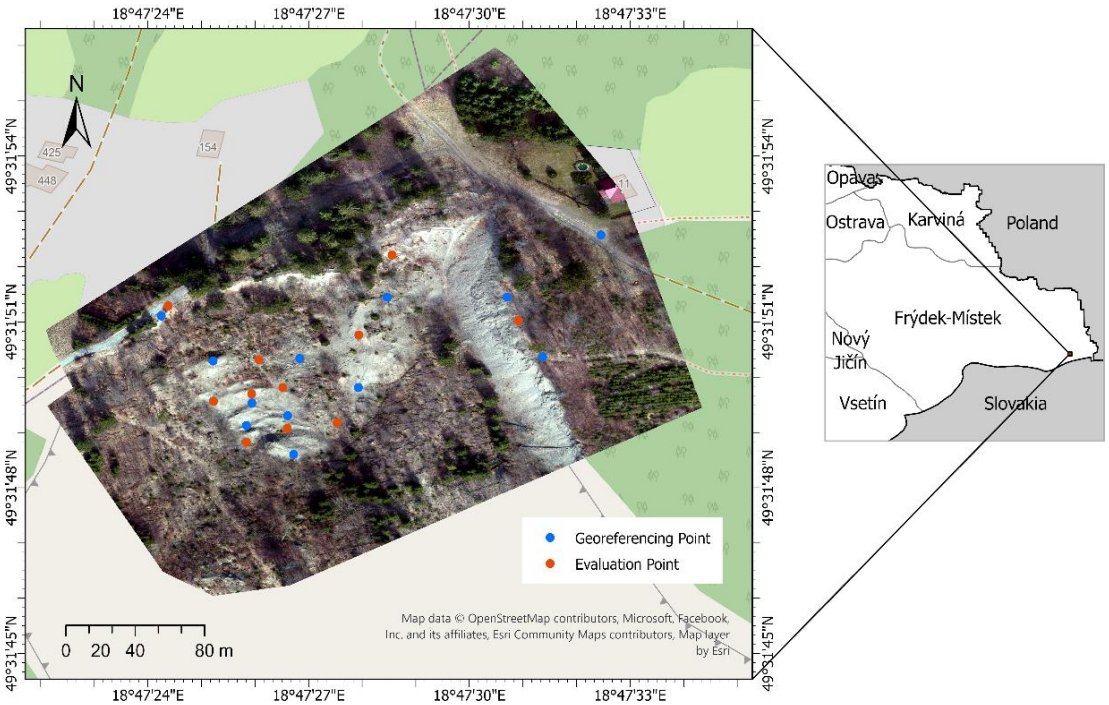

Fig. 2. Girova Area of Interest. Source of background map: Open Street Map.

Together, these two study areas allow for a robust comparison of UAV survey performance across different environmental settings, offering insights into the influence of terrain complexity and proximity of GNSS infrastructure for RTK positioning on the realized georeferencing approaches.

2.2. Data acquisition

Data collection was carried out using a DJI Mavic 3 Enterprise quadcopter equipped with an RGB sensor. This model is currently one of the most widely used drones for photogrammetric data acquisition. The main RGB camera of the DJI Mavic 3 Enterprise features a CMOS sensor with an effective resolution of 20 megapixels. The 4/3" sensor dimensions are approximately 17.3 × 13.0 mm, paired with a fixed lens that provides a 35-mm equivalent focal length of 24 mm. The camera also offers an adjustable aperture range from f/2.8 to f/11 (https://enterprise.dji.com/mavic-3-enterprise/specs). The UAV is equipped with a conventional GNSS receiver, relying on a basic SPP positioning technique. However, additional GNSS RTK module can be mounted on the UAV which offers accurate RTK positioning. Its performance was tested in this work. Data collection was realized on November 1, 2023 at the Ostrava site and on March 15, 2024 at the Girova Area of interest (AOI). Basic information about the image acquisition is provided in **Table 1**.

All flights were realized in automatic mode via the DJI Pilot app. At both sites, a flight with active GNSS RTK positioning was first performed, immediately followed by a second flight according to an identical flight mission, but with only a standard GNSS receiver. In area Ostrava, only nadiral images were acquired. In the mountainous area Girova, nadiral images were complemented with a set of side-looking (oblique) images from a manual flight to improve quality of model reconstruction. Weather conditions were good, with minimal wind and stable lighting.

To enable accurate indirect georeferencing of products derived from image sets captured using only a standard GNSS receiver, and to allow for an independent comparison of both approaches (direct and indirect georeferencing), a set of ground control points (GCPs) was temporarily signalized in both areas of interest (AOIs). A total of 20 GCPs were established in the Girova area, and 25 GCPs in the Ostrava area. Their positions were measured using a geodetic-grade Trimble R10 GNSS receiver operating in RTK mode.

At the Ostrava site, the RTK solution was obtained by connecting to the nearest GNSS reference station, located just 1.6 km from the AOI. In Girova, the network RTK service provided by the commercial GNSS reference station network TopNET was used. As the closest physical reference station is approximately 25 km away, the network-based solution was employed to ensure higher positioning accuracy. The same RTK correction sources were used by the DJI Mavic 3 Enterprise UAV during image acquisition at both sites.

In Ostrava, GCPs were evenly distributed across the entire area, including all corners and the central region. In Girova, a uniform distribution of GCPs was not possible due to challenging topography and vegetation, which in some locations prevented fixed RTK positioning. Therefore, the GCPs were positioned to maximize area coverage and include all elevation levels under the given constraints. As described below, part of the GCPs was used for georeferencing during processing, while the remaining points were used to evaluate the positional accuracy of the derived products.

Table 1.

Flight and imaging parameters by area.

Parameter	Ostrava	Girova
Average height of flight	60 m	70 m
Average ground sample distance (GSD)	1.6 cm	1.9 cm
Front, side image overlap	80%, 80%	85%, 85%
Number of images	328 (RTK mode), 324 (standard mode)	211 (RTK mode), 210 (standard mode)

2.3. Image processing

Image processing was carried out using Agisoft Metashape Professional software v.2.1.3 (https://www.agisoft.com/). Identical workflow and parameters settings was applied to process all four sets of images. The only difference was in georeferencing the products which was based either on a set of GCPs (non-RTK datasets) or directly on position of images estimated by drone's own RTK receiver (RTK datasets).

In the initial stage of the workflow, images in the raw DGN file format were imported into the software and aligned using accuracy settings on High with a key points limit of 40,000 and a tie points limit of 10,000. This configuration ensured robust feature matching across overlapping images, yielding a reliable sparse point cloud as the foundation for subsequent analyses.

For the non-RTK datasets, a georeferencing procedure incorporating GCPs was implemented. For AOI Ostrava, 11 GCPs were utilized in the processing stage, with 14 GCPs designated for accuracy validation. Similarly, For AOI Girova, a total of 9 GCPs were used for georeferencing, while an additional 11 GCPs were reserved for independent accuracy assessment. The selection of GCPs used for georeferencing was evenly distributed across both study areas to ensure comprehensive spatial coverage. GCPs were imported into the project, and corresponding markers were manually placed across all the relevant images. Georeferencing including camera optimization was performed

using the GCPs data. In contrast, the RTK datasets benefitted from the pre-embedded high-precision camera location data, allowing the workflow to focus solely on optimizing the camera alignment based on these coordinates without the time-consuming manual work with GCPs. In both RTK and non-RTK modes, the calibration parameters—including the focal length (f), affinity and non-orthogonality coefficients (b1 and b2), principal point coordinates (cx and cy), radial distortion coefficients (k1 through k4), and tangential distortion coefficients (p1 and p2)—were optimized.

After georeferencing, depth maps were generated using quality settings on High combined with aggressive filtering. These depth maps served as the basis for constructing a dense point cloud, which in turn was used to generate a raster Digital Elevation Model (DEM). The DEM then provided the reference surface for the orthophoto mosaic creation process; notably, hole filling was disabled during orthophoto mosaic generation to preserve the integrity of the raw data. Throughout all processing steps, the WGS-84 coordinate system was employed to ensure consistency across all derived products. Additionally, all other processing settings, including image alignment, point cloud generation, digital elevation model (DEM) creation, and orthophoto mosaic production, were kept identical for both study areas. This standardized approach was essential to maintaining consistency across datasets and ensuring a fair comparison between RTK and non-RTK results.

The final outputs, including the DEM and orthophoto mosaic, were generated for both the Ostrava and Girova areas of interest using RTK and non-RTK workflows. For the Ostrava area, the DEM has a spatial resolution of 3.16 cm/pixel, while the orthophoto mosaic has a resolution of 1.58 cm/pixel. For the Girova area, the DEM resolution is 3.76 cm/pixel, and the orthophoto mosaic resolution is 1.88 cm/pixel. These datasets were then exported for further comparative analysis.

2.4. Accuracy Assessment

A set of GCPs that were not incorporated into the image processing stage was employed as independent validation markers. Elevation values corresponding to the horizontal position of these GCPs were extracted from the generated DEMs. Differences between the elevation of GCPs and the corresponding extracted DEM values were computed, thus quantifying the vertical discrepancies between the field measurements and the modelled data. Specifically, for each point i, the error is defined as:

$$e_i = Z_i^{DEM} - Z_i^{GCP} \tag{1}$$

where Z_i^{DEM} is the elevation extracted from the DEM and Z_i^{GCP} is the GCP elevation.

These differences were subsequently analyzed using a range of statistical measures, including the mean error to gauge overall bias, standard deviation or the root mean square error (RMSE) as shown below.

$$\text{Mean of Errors (ME)} = \frac{1}{n}\sum_{i=1}^{n} e_i \tag{2}$$

$$Standard\ Deviation\ of\ Errors\ \ (SDEV) = \sqrt{\frac{1}{n-1}\sum_{i=1}^{n}(e_i - ME)^2} \tag{3}$$

$$Root\ Mean\ Square\ Error\ (RMSE) = \sqrt{\frac{1}{n}\sum_{i=1}^{n} e_i^2} \tag{4}$$

The evaluation of the horizontal accuracy was realized on the orthophoto mosaics. Differences in the X (longitude) and Y (latitude) coordinates between the centers of GCP targets on the orthophoto mosaics and their position obtained by field measurement were computed. To integrate the individual coordinate differences into a single measure of positional accuracy, the Haversine formula was applied to compute the horizontal distance. The haversine formula, which calculates the great-circle distance based on latitude and longitude is expressed as:

$$a = sin^2\left(\frac{\Delta\varphi}{2}\right) + \cos(\varphi_1)cos(\varphi_2)sin^2\left(\frac{\Delta\lambda}{2}\right) \quad (5)$$

$$c = 2.atan2\left(\sqrt{a}, \sqrt{(1-a)}\right) \quad (6)$$

$$d = R.c \quad (7)$$

where φ_1 and φ_2 are the latitudes

$\Delta\varphi$ and $\Delta\lambda$ are the differences in latitude and longitude (in radians)

R is the Earth's radius (approximately 6,371 km), (Sinnott, 1984).

The resulting latitude and longitude errors, as well as the derived horizontal distance, were again analyzed statistically.

3. RESULTS

Table 2 summarizes the elevation accuracy statistics for the DEMs derived from both RTK and non-RTK datasets in the two areas of interest. All statistical parameters fall within expected ranges, not exceeding a few centimeters. However, the results indicate that the mean error was significantly higher for datasets produced using direct georeferencing compared to those produced using indirect georeferencing in both Ostrava and the Girova AOI. In terms of standard deviation, both approaches yielded similar results, with a difference of only about 0.5 cm. The standard deviation values were notably higher in the Girova AOI, which can be attributed to the complex topography and the relatively large distance to the nearest GNSS reference station.

Table 2.

DTM accuracy statistics (vertical error) statistics in cm.

	Ostrava AOI		**Girova AOI**	
	RTK	Non-RTK	RTK	Non-RTK
ME	-6.47	-1.15	2.28	0.30
SDEV	0.88	1.46	3.80	3.33
RMSE	6.52	1.82	4.28	3.19

More detailed results at the level of individual control points are presented in **Fig. 3** for Ostrava and in **Fig. 4** for Girova, along with the corresponding DEMs illustrating the topography of each area of interest. The results from Ostrava reveal a clear systematic error in the DEM heights derived from the RTK-based dataset, as all control points exhibit a similar negative vertical offset. This may be attributed to an error in determining the focal length of the camera during photogrammetric processing under direct georeferencing, as documented by Štroner et al. (2021).

In contrast, this issue did not appear in the Girova AOI, likely due to the inclusion of both nadir and oblique images in the dataset. The effectiveness of combining image perspectives to improve model accuracy has also been confirmed by Štroner et al. (2021). Aside from the observed systematic bias in Ostrava, there is no distinct spatial pattern in the error distribution across individual control points. In the Ostrava AOI, none of the points showed anomalous behavior relative to the rest.

In the Girova AOI, the maximum error was observed at control point no. 11, located in the eastern part of the area at the top of the landslide. The error at this point reached 12.18 cm in the RTK-based dataset and 6.76 cm in the non-RTK dataset. In the latter case, two GCPs used for georeferencing were located within approximately 30 meters of this control point, which likely contributed to improved DEM accuracy in this part of the AOI. Nevertheless, the elevated error at point no. 11 may also have been influenced by inaccuracies in the vertical positioning of the point itself.

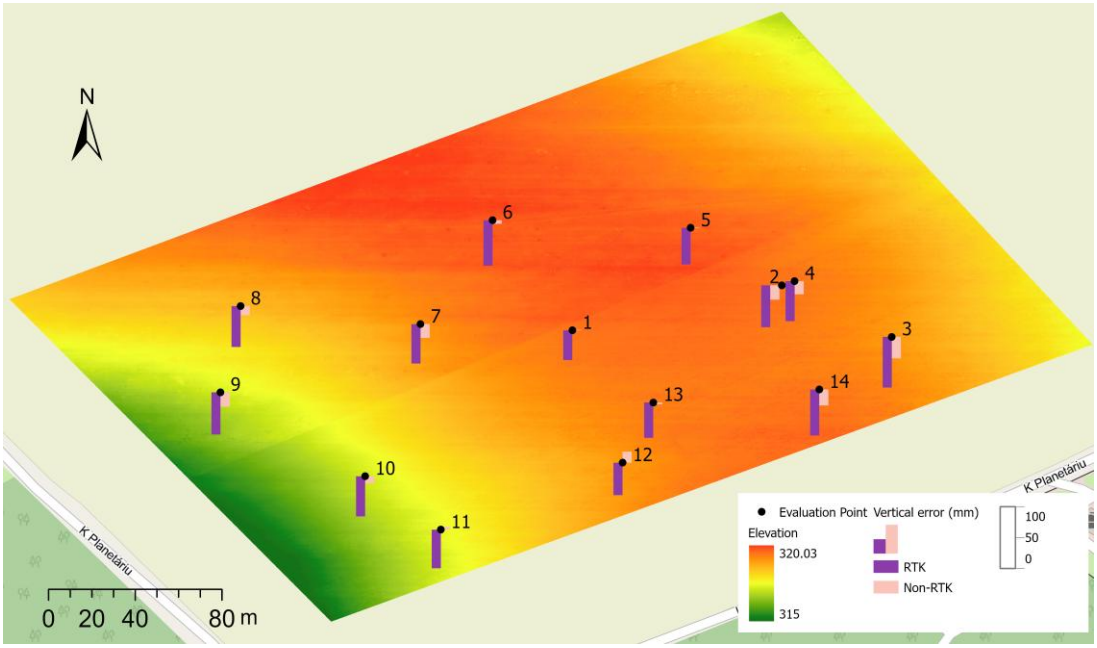

Fig. 3. Vertical error of individual control points in the Ostrava AOI from RTK and Non-RTK datasets shown on top of the DEM. Source of background map: Open Street Map.

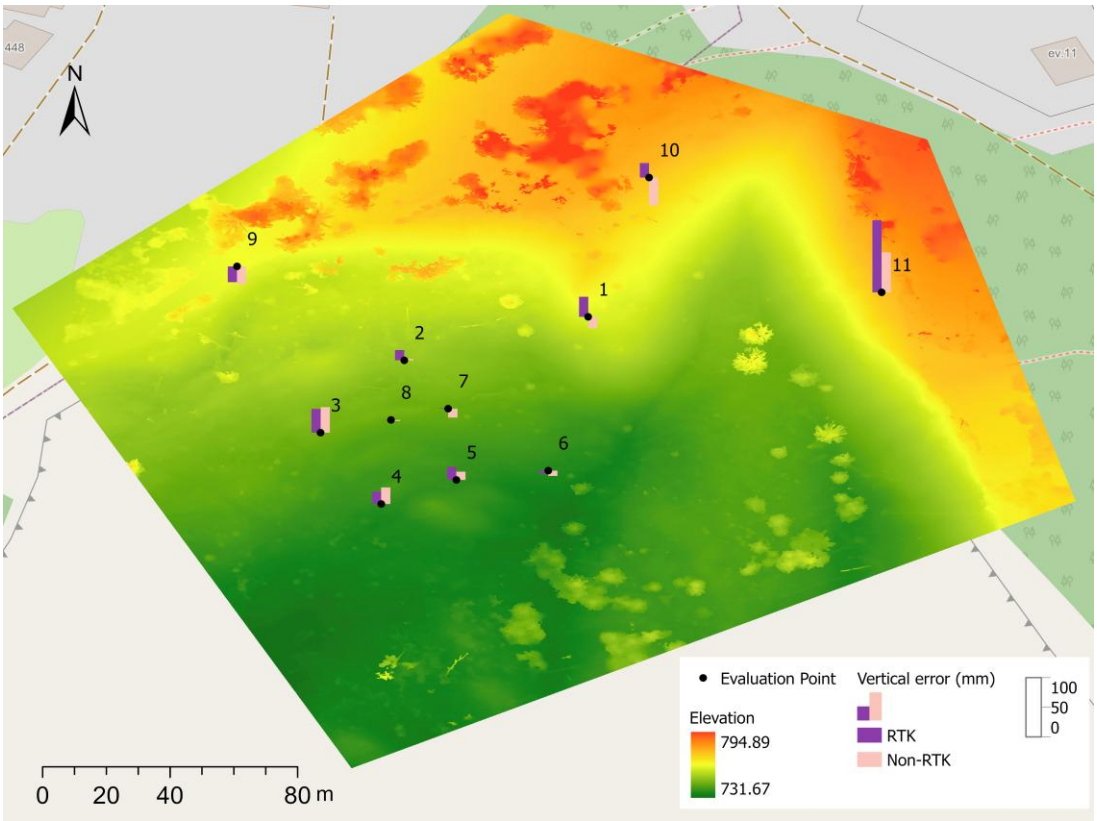

Fig. 4. Vertical error of individual control points in the Girova AOI from RTK and Non-RTK datasets shown on top of the DEM. Source of background map: Open Street Map.

Table 3 presents the statistics for the latitude and longitude differences between position of GCPs measured in the field and derived from orthophoto mosaics, as well as the statistics for their distances. The horizontal accuracy assessment of the orthophoto mosaics for the Ostrava AOI reveals small differences between the RTK and non-RTK datasets. For the RTK data, the mean errors were –1.31 cm in longitude and –0.66 cm in latitude, resulting in a mean horizontal distance error of 3.75 cm. The standard deviation was 1.50 cm for the distance error, while the RMSE 4.02 cm, respectively. In comparison, the non-RTK dataset exhibited slightly larger values with mean horizontal distance error of 4.74 cm, standard deviation of 2.60 cm and the RMSE of 5.36 cm, respectively. Nevertheless, both approaches led to similar results with expectable statistics reaching a few centimeters level. The horizontal accuracy assessment for the orthophoto mosaics in the Girova AOI are also summarized in **Table 3**. For the RTK (non-RTK) dataset, the mean horizontal distance error was 3.75 cm (3.34 cm), standard deviation computed from distances of 1.83 cm (1.48 cm) and RMSE computed from distances of 4.13 cm (3.63 cm). The results of the two approaches are again comparable, with slightly lower values of statistical parameters this time achieved by the georeferencing based on GCPs.

Table 3.

Horizontal error statistics in cm.

	Ostrava AOI						**Girova AOI**					
	RTK			**Non-RTK**			**RTK**			**Non-RTK**		
	Long error	Lat error	Dist	Long error	Lat error	Dist	Long error	Lat error	Dist	Long error	Lat error	Dist
ME	-1.31	-0.66	3.75	-2.56	2.83	4.74	1.97	-0.9	3.75	-1.27	-0.31	3.34
SDEV	3.18	3.29	1.5	2.69	3.88	2.6	2.22	3.3	1.83	2.19	3.05	1.48
RMSE	3.33	3.24	4.02	3.65	4.69	5.36	2.89	3.27	4.13	2.44	2.93	3.63

Latitude and longitude errors at individual control points are presented in **Fig. 5** for the Ostrava AOI and in **Fig. 6** for the Girova AOI, respectively.

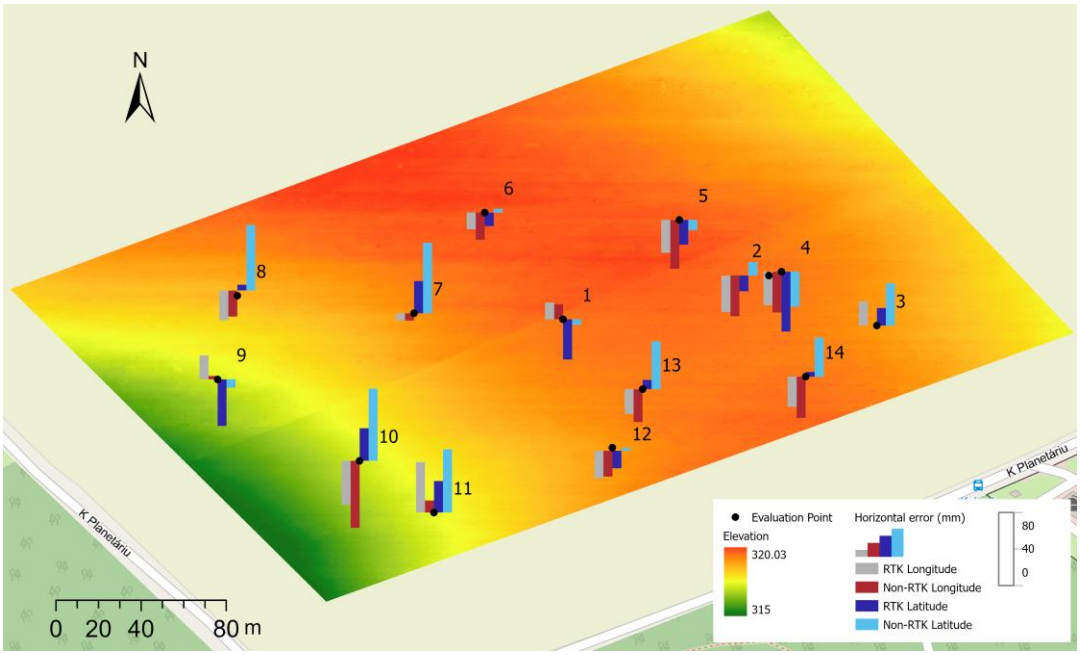

Fig. 5. Horizontal (latitude, longitude) errors of individual control points in the Ostrava AOI from RTK and Non-RTK datasets shown on top of the DEM. Source of background map: Open Street Map.

In Ostrava, there is no clear systematic pattern observable across the entire area, nor does any single control point exhibit significantly different behavior compared to the others. However, some local groupings with similar error characteristics can be identified.

Specifically, control points no. 7, 8, 10, and 11, located in the western part of the Ostrava AOI, showed similarly elevated latitude errors in the non-RTK dataset. Conversely, in the eastern part of the AOI, points no. 2, 4, 5, and 14 exhibited similar longitude errors in both RTK and non-RTK datasets. These observations suggest that the spatial distribution of horizontal errors in the Ostrava AOI is not entirely random and may reflect localized effects, possibly related to image geometry or processing parameters.

In contrast, horizontal error values in the Girova AOI appear to be randomly distributed. No systematic spatial patterns are visible across the entire area or within any sub-regions, regardless of whether direct or indirect georeferencing was applied. Interestingly, control point no. 11, which exhibited the highest vertical error, was among the points with the lowest horizontal errors in Girova, with latitude and longitude errors around 2 cm.

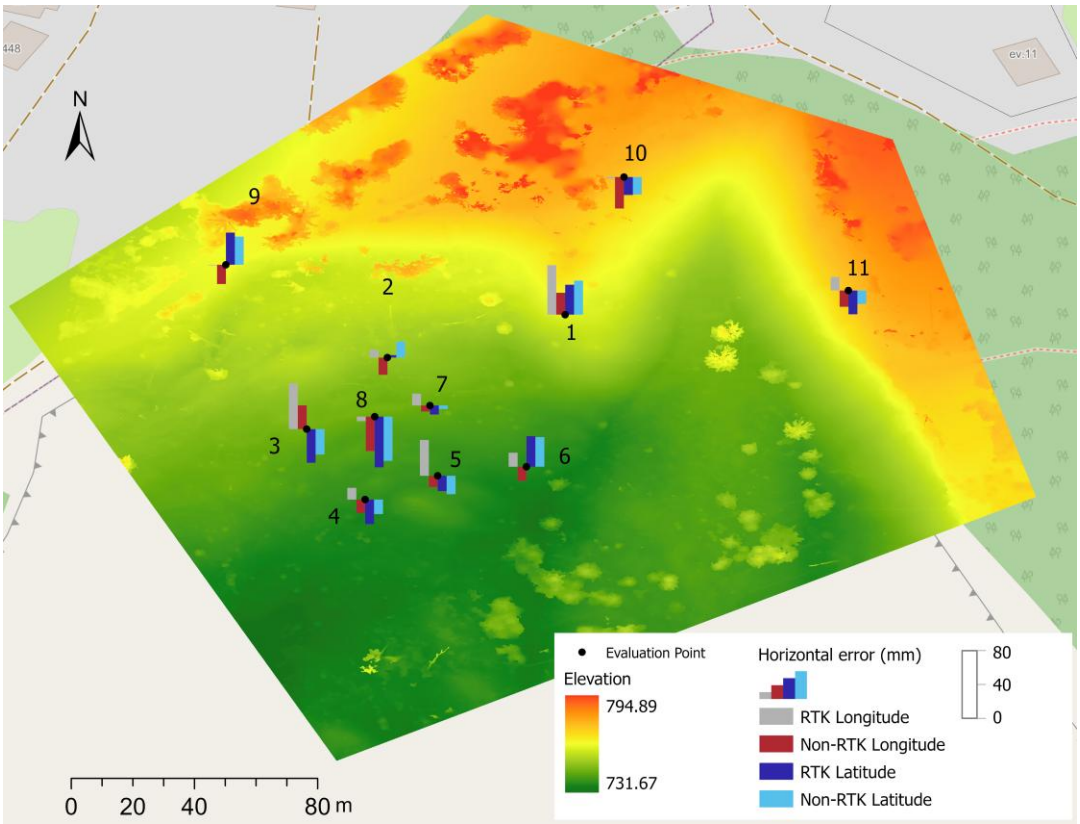

Fig. 6. Horizontal (latitude, longitude) errors of individual control points in the Girova AOI from RTK and Non-RTK datasets shown on top of the DEM. Source of background map: Open Street Map.

4. DISCUSSION AND CONCLUSION

This study provides a comparative assessment of direct and indirect georeferencing methods in UAV-based mapping across two contrasting landscapes. UAV surveys were conducted using a DJI Mavic 3 Enterprise quadcopter equipped with an RTK module at two sites in the Czech Republic: a flat agricultural area near Ostrava and a mountainous region with complex topography in the Girova area of the Silesian Beskydy Mountains. From these surveys, DEMs and orthophoto mosaics were

generated through photogrammetric processing and subsequently analyzed to evaluate the accuracy of each georeferencing approach under varying terrain conditions. The comparison was based on horizontal and vertical error measurements relative to control reference points.

In general, both georeferencing techniques provided the expected level of accuracy for DEMs and orthophoto mosaics, typically within a few centimeters. However, some differences between the methods were observed. The results indicate that indirect georeferencing using ground control points (GCPs) yielded slightly better vertical accuracy compared to direct georeferencing with RTK. DEMs generated from non-RTK workflows exhibited lower RMSE values and no apparent systematic errors across both areas of interest, suggesting that RTK-based direct georeferencing did not significantly improve vertical accuracy under the given conditions. These findings are consistent with those of Martínez-Carricondo et al. (2023), who reported improved accuracy using GCPs, and with Przybilla et al. (2020) and Štroner et al. (2021), who showed that the absence of GCPs can lead to substantial systematic height deviations—up to 30 times the ground sampling distance (GSD). However, this observation contrasts with the results of Tomaštík et al. (2019), who demonstrated that UAV-RTK systems can achieve vertical accuracies comparable to workflows using nine GCPs, and significantly better than those using only four GCPs. It is worth noting that their study was conducted over a large and complex area of 270 hectares, where the number of GCPs may have been insufficient for optimal georeferencing. Additionally, differences in UAV platforms may have contributed to the varying results. The studies reporting better performance with GCPs all used the DJI Phantom 4 RTK quadcopter, whereas Tomaštík et al. (2019) employed the more advanced fixed-wing SenseFly eBee Plus, which may offer enhanced flight stability and positioning capabilities.

For horizontal accuracy, the results varied between the two areas of interest. In Ostrava, direct georeferencing (RTK) yielded slightly better accuracy than the GCP-based approach, while in Girova, the opposite was observed. These findings are consistent with the conclusions of Szypuła (2024) and Elias et al. (2024), who emphasized that the use of GCPs enhances positional accuracy, particularly in complex terrain. Nevertheless, the differences in horizontal accuracy between the two georeferencing methods in this study were minimal, with discrepancies in the reported statistical parameters generally below or around 1 cm.

The quality of GNSS differential positioning, including RTK and PPK techniques, is influenced by the length of the baseline—defined as the distance between the reference station providing corrections and the rover receiver used to determine the coordinates of measured objects. As baseline length increases, positioning accuracy generally decreases. To maintain high accuracy over longer baselines, network RTK solutions are typically employed, which combine observations from multiple reference stations or from an entire reference station network. As described in Section 2.2, a direct connection to a nearby GNSS reference station was used in the Ostrava AOI, while a network RTK solution was applied in the Girova AOI for both UAV image acquisition and ground control point positioning. The DJI Mavic 3 Enterprise quadcopter automatically records a file containing the formal RTK positioning errors (i.e., standard deviations of the estimated positioning errors) for each captured image. In the Ostrava AOI, the mean formal RTK positioning errors recorded by the UAV were 1.1 cm in latitude, 0.8 cm in longitude, and 1.8 cm in height. In contrast, the corresponding values in the Girova AOI were 1.8 cm in latitude, 1.2 cm in longitude, and 3.1 cm in height. The lower error values in Ostrava can be attributed to the much shorter baseline, as opposed to the Girova site, where the nearest physical reference station in the network solution was approximately 25 km away. Nevertheless, these differences in formal positioning errors did not appear to significantly affect the georeferencing quality of the resulting orthophoto mosaics and digital elevation models (DEMs).

This study reinforces previous research findings that GCPs remain essential for achieving optimal georeferencing accuracy, particularly in the vertical (height) component. However, in scenarios where rapid deployment and operational efficiency are prioritized, RTK enabled UAVs offer a viable alternative. The effectiveness of RTK positioning relies on phase measurements with fixed integer ambiguities, making it suitable primarily for environments with unobstructed sky visibility. Temporary or permanent obstructions between the GNSS receiver and satellites such as vegetation, buildings, or steep terrain can significantly degrade positioning accuracy. These limitations are

generally not relevant during UAV based image acquisition, as the UAV typically operates above such obstacles. In this context, our review of scientific literature did not identify any reported stability issues of UAV mounted RTK systems related to these obstructions. Conversely, such obstacles can present challenges for the precise positioning of GCPs or may restrict their deployment within the area of interest. Another potential limitation of RTK is its reliance on a stable internet connection for receiving real time correction data. Limited mobile network coverage can impair both UAV data acquisition and ground based GCP measurements. In areas lacking sufficient connectivity, alternative techniques such as PPK positioning must be employed.

Future research should explore hybrid approaches that integrate RTK with a minimal set of GCPs to balance efficiency and accuracy. This approach was suggested, for example, by Benassi et al. (2017) and has proven effective in various applications, as demonstrated by Przybilla et al. (2020) and Elias et al. (2024). In addition, future studies should consider expanding into more diverse and operationally challenging terrains, such as urban canyons or forested ridges, to better assess RTK performance under conditions where signal degradation, multipath errors, and occlusions are more prevalent. Such environments would offer further insight into the robustness and practical limitations of RTK-based workflows.

ACKNOWLEDGEMENT

This work was partially supported by Grant of SGS No. SP2025/040, Faculty of Mining and Geology, VSB - Technical University Ostrava.

REFERENCES

Atik, M. E., & Arkali, M. (2025). Comparative Assessment of the Effect of Positioning Techniques and Ground Control Point Distribution Models on the Accuracy of UAV-Based Photogrammetric Production. Drones, 9(1). https://doi.org/10.3390/drones9010015.

Baroň, I., Řehánek, T., Vošmik, J., Musel, V., & Kondrová, L. (2011). Report on a recent deep-seated landslide at Gírová Mt., Czech Republic, triggered by a heavy rainfall: The Gírová Mt., Outer West Carpathians; Czech Republic. Landslides, 8(3), 355–361. https://doi.org/10.1007/s10346-011-0255-y.

Benassi, F., Dall'Asta, E., Diotri, F., Forlani, G., di Cella, U.M., Roncella, R., Santise, M. (2017). Testing accuracy and repeatability of UAV blocks oriented with gnss-supported aerial triangulation. Remote Sensing, 9, 172. https://doi.org/10.3390/rs9020172.

Colomina, I., Blázquez, M., Molina, P., Parés, M. E., & Wis, M. (2008). Towards a new paradigm for high-resolution low-cost photogrammetry and remote sensing. Int. Archives of Photogrammetry, Remote Sensing and Spatial Information Sciences, Beijing, China, 37(B1), 1201–1206.

Colomina, I., & Molina, P. (2014). Unmanned aerial systems for photogrammetry and remote sensing: A review. In ISPRS Journal of Photogrammetry and Remote Sensing (Vol. 92, pp. 79–97). Elsevier B.V. https://doi.org/10.1016/j.isprsjprs.2014.02.013.

Cromwell, C., Giampaolo, J., Hupy, J., Miller, Z., & Chandrasekaran, A. (2021). A systematic review of best practices for uas data collection in forestry-related applications. In Forests (Vol. 12, Issue 7). MDPI AG. https://doi.org/10.3390/f12070957.

Czyża, S., Szuniewicz, K., Kowalczyk, K., Dumalski, A., Ogrodniczak, M., & Zieleniewicz, Ł. (2023). Assessment of Accuracy in Unmanned Aerial Vehicle (UAV) Pose Estimation with the REAL-Time Kinematic (RTK) Method on the Example of DJI Matrice 300 RTK. Sensors, 23(4). https://doi.org/10.3390/s23042092.

Elias, M., Isfort, S., Eltner, A., & Maas, H. G. (2024). UAS Photogrammetry for Precise Digital Elevation Models of Complex Topography: A Strategy Guide. ISPRS Annals of the Photogrammetry, Remote Sensing and Spatial Information Sciences, 10(2), 57–64. https://doi.org/10.5194/isprs-annals-X-2-2024-57-2024.

Gomez, C., & Purdie, H. (2016). UAV- based Photogrammetry and Geocomputing for Hazards and Disaster Risk Monitoring – A Review. In Geoenvironmental Disasters (Vol. 3, Issue 1). Springer. https://doi.org/10.1186/s40677-016-0060-y.

Martínez-Carricondo, P., Agüera-Vega, F., & Carvajal-Ramírez, F. (2023). Accuracy assessment of RTK/PPK UAV-photogrammetry projects using differential corrections from multiple GNSS fixed base stations. Geocarto International, 38(1). https://doi.org/10.1080/10106049.2023.2197507.

Mohsan, S. A. H., Khan, M. A., Noor, F., Ullah, I., & Alsharif, M. H. (2022). Towards the Unmanned Aerial Vehicles (UAVs): A Comprehensive Review. In Drones (Vol. 6, Issue 6). Multidisciplinary Digital Publishing Institute (MDPI). https://doi.org/10.3390/drones6060147.

Nakata, Y., Iwasaki, K., Shimoda, S., & Torita, H. (2023). Understanding microtopography changes in agricultural landscapes through precision assessments of digital surface models by the UAV-RTK-PPK method without ground control points. Smart Agricultural Technology, 5. https://doi.org/10.1016/j.atech.2023.100269.

Nam-Bui, X., Quoc Long, N., Thi Thu Ha, L., Ngoc Quy, B., Goyal, R., Trong Hung, V., van Chung, P., Xuan Cuong, C., van Canh, L., & Hong Viet, L. (2020). Flight Height of UAV and Its Influence on the Precise Digital Elevation Model of Complex Terrain. Inzynieria Mineralna, 2020(1), 179–186. https://doi.org/10.29227/IM-2020-01-27.

Przybilla, H. J., Bäumker, M., Luhmann, T., Hastedt, H., & Eilers, M. (2020). Interaction between direct georeferencing, control point configuration and camera self-calibration for RTK-based UAV photogrammetry. International Archives of the Photogrammetry, Remote Sensing and Spatial Information Sciences - ISPRS Archives, 43(B1), 485–492. https://doi.org/10.5194/isprs-archives-XLIII-B1-2020-485-2020.

Rauhala, A., Meriö, L. J., Kuzmin, A., Korpelainen, P., Ala-Aho, P., Kumpula, T., Kløve, B., & Marttila, H. (2023). Measuring the spatiotemporal variability in snow depth in subarctic environments using UASs - Part 1: Measurements, processing, and accuracy assessment. Cryosphere, 17(10), 4343–4362. https://doi.org/10.5194/tc-17-4343-2023.

Sinnott, R. W. (1984). Virtues of the haversine. Sky and Telescope, 68(2), 159.

Stott, E., Williams, R. D., & Hoey, T. B. (2020). Ground control point distribution for accurate kilometre-scale topographic mapping using an rtk-gnss unmanned aerial vehicle and sfm photogrammetry. Drones, 4(3), 1–21. https://doi.org/10.3390/drones4030055.

Štroner, M., Urban, R., Seidl, J., Reindl, T., & Brouček, J. (2021). Photogrammetry using UAV-mounted GNSS RTK: Georeferencing strategies without GCPs. Remote Sensing, 13(7). https://doi.org/10.3390/rs13071336

Szypuła, B. (2024). Accuracy of UAV-based DEMs without ground control points. GeoInformatica, 28(1), 1–28. https://doi.org/10.1007/s10707-023-00498-1.

Teunissen, P.J.G., Montenbruck, O. (eds.) (2017). Springer Handbook of Global Navigation Satellite Systems. Springer International Publishing. ISBN 978-3-319-42926-7. doi:10.1007/978-3-319-42928-1.

Tomaštík, J., Mokroš, M., Surový, P., Grznárová, A., & Merganič, J. (2019). UAV RTK/PPK method-An optimal solution for mapping inaccessible forested areas? Remote Sensing, 11(6). https://doi.org/10.3390/RS11060721.

AN ANALYSIS OF ECONOMIC CROP PLANTING CALENDAR USING DATA FROM THE MODERATE RESOLUTION IMAGING SPECTRORADIOMETER ON THE TERRA SATELLITE

***Jumpol ITSARAWISUT*[1,2], *Tanutdech ROTJANAKUSOL*[1,2], *Chaiphat PLYBOUR*[1,2], *Mehsa SINGHARATH*[3], *Teerawong LAOSUWAN*[1,2*]**

DOI: 10.21163/GT_2025.202.14

ABSTRACT

Agriculture is a highly significant activity for humanity, serving as a primary food source and a cornerstone of many countries' economies. This research focuses on studying crop planting calendars using data from the Moderate Resolution Imaging Spectroradiometer on the Terra satellite. The study analyzes the Normalized Difference Vegetation Index (NDVI) from May 2022 to December 2023 across various districts in Nong Bua Lam Phu Province. It specifically examines four types of economic crops: rice, fruit trees, perennial trees, and field crops. The study involves random sampling of the largest area within each district and compares these findings to crop planting calendars in the Si Bun Rueang and Suwannakuha districts, with a focus on rice field areas within these two districts. Results indicate distinct differences in NDVI values across times and locations, attributed to varying crop planting cycles in each district. Satellite data clearly illustrate plant growth and changes in NDVI values. This research provides a framework for relevant agencies to manage agricultural water resources more efficiently.

Keywords: *Crop Planting Calendar, Economic Crops, Remote Sensing, Terra MODIS, NDVI*

1. INTRODUCTION

Agriculture is one of humanity's most critical activities, serving not only as a primary food source sustaining people worldwide but also as a cornerstone of many countries' economies. Effective and sustainable agricultural development is essential to addressing various challenges such as climate change and population growth (Pawlak & Kołodziejczak, 2020). Agriculture contributes not only to food production but also to broader economic and social development (Sibhatu & Qaim, 2017). Countries with robust agricultural systems often experience higher rates of economic growth (Devaux et al., 2020). In addition, agriculture plays a significant role in job creation, particularly in developing countries (Wageningen University, 2015).

A notable study by Viana et al. (2022) emphasized the importance of agriculture for global food security, explaining that it provides stability for billions of people and helps reduce poverty in many regions. In Africa, the World Bank (2022) highlighted agriculture's crucial role in combating hunger and enhancing food security, stressing the need to adopt new technologies to increase productivity and help farmers adapt to climate change. In Asia, IFAD (2019) conducted research on agriculture's role in economic development in developing countries, finding that it contributes to raising rural household incomes and promoting access to better nutrition. These studies illustrate agriculture's vital role in both global and regional development, underscoring the need to support and advance agriculture to create a sustainable and secure future for all.

[1]*Department of Physics, Faculty of Science, Mahasarakham University, Maha Sarakham, Thailand., (JI) drjumpol.i@gmail.com, (TR) tanutdech.r@msu.ac.th, (CP) chaiphat.p@msu.ac.th, (TL)teerawong@msu.ac.th*
[2]*Space Technology and Geo-Informatics Research Unit, Faculty of Science, Mahasarakham University, Maha Sarakham, Thailand*
[3]*Nampapa Nakhoneluang, Vientiane Capital Water Supply State Enterprise, Kaisone Road, Xaysettha District, Vientiane City, Lao P.D.R., (MS) mesha_coltd@yahoo.com*
**Corresponding author: teerawong@msu.ac.th*

Thailand covers a total area of approximately 513,000 km², with around 22.08 million hectares (43% of the country's area) dedicated to agriculture (Sciyouthvolunteer, n.d.). In 2022, Thailand's gross domestic product (GDP) was valued at 17,370,240 million baht. The agricultural sector contributed 1,531,120-million-baht, accounting for 8.81% of the total GDP. Meanwhile, 149.75 million rai of land was used for agricultural purposes, with 34.88 million rai being irrigated land, 23.29% of the total agricultural area. Agricultural land constituted a significant 46.69% of the country's total area. There were 11.63 million agricultural workers, representing 29.31% of the total labor force (Ministry of Commerce, 2024).

Several Thai economic crops have gained global recognition for their quality, particularly rice. In 2023, Thailand exported 3.47 million tons of rice, making it the world's fifth-largest rice exporter (Bangkokbiznews, 2023). Another key economic crop is sugarcane, with Thailand ranked as the world's second-largest sugar exporter. Annual sugar exports exceed 6 million tons, generating $2.961 billion from 47 sugar mills that require over 100 million tons of sugarcane annually (ThaiPBS, 2023). Cassava is also an essential economic crop, with a significant market in China, where it is processed into products such as animal feed, food flavorings, and ethanol (DITP, 2020).

Currently, Thai farmers face challenges in agricultural water use, making water a critical factor in agricultural activities. Understanding the crop growth cycle throughout the year is beneficial for efficient agricultural water management (Jitae, 2019). Remote sensing technology has become a vital tool for studying and monitoring environmental changes, vegetation, and agricultural yields (Laosuwan et al., 2011; Uttaruk & Laosuwan, 2018; Sangpradid et al., 2021; Itsarawisut et al., 2024; Laosuwan et al., 2024). These data are collected from Earth's surface through interactions between electromagnetic radiation and terrestrial materials (Auntarin et al., 2021; Laosuwan et al., 2022; Uttaruk et al., 2022). Remote sensing data form part of high-quality digital geospatial technology that can be analyzed over time (Itsarawisut & Laosuwan, 2022; Ounrit et al., 2022; Turton et al., 2022; Laosuwan et al., 2023; Plybour & Laosuwan, 2023a). Recently, remote sensing technology has advanced significantly, particularly with data obtained from satellites and unmanned aerial vehicles or drones, offering improvements in spatial resolution (Phoophiwfa et al., 2023; Plybour & Laosuwan, 2023b; Zhang & Zhu, 2023). Moreover, data can now be collected across multiple spectral bands, allowing researchers to select specific wavelengths suited for efficient study in various fields (Cottrell et al., 2024). Studies show that remote sensing technology is an effective tool for managing and improving economic crop yields. It enables accurate monitoring of environmental conditions and crop growth (Hatfield et al., 2011; Najafi et al., 2018; Yadav & Geli, 2021; Laosuwan et al., 2024). Remote sensing offers several benefits for managing economic crops: it reduces production risks by continuously monitoring weather and soil conditions, and it optimizes the use of resources such as water and fertilizers by assessing the actual needs of crops at each growth stage. Given these important factors, this study aims to analyze crop planting calendars using data from the Moderate Resolution Imaging Spectroradiometer (MODIS) on the Terra satellite.

2. MATERIALS AND METHODS

2.1. Study Area

Nong Bua Lam Phu Province (**Fig. 1**) is located in the northeastern region of Thailand, between latitudes 16°45′ to 17°40′N and longitudes 101°57′ to 102°30′E, with an elevation of approximately 200 meters above sea level. The terrain primarily consists of highlands and plains. The climate is divided into three seasons, similar to other provinces in the northeastern region: summer, rainy season, and winter. It is influenced by the annual monsoon and classified as a tropical savanna climate, meaning rainfall occurs mainly during the rainy season, alternating with dry periods in winter and summer. (1) Summer occurs from March to April, with average maximum temperatures ranging from 34°C to 36°C. (2) Rainy Season lasts from May to October, with the heaviest rainfall in August and September due to tropical depressions. (3) Winter spans from November to February, with the coldest months being December and January, when average temperatures range from 15°C to 16°C. The average annual rainfall in Nong Bua Lam Phu Province ranges from 978.3 mm to 1,348.9 mm (Royal Irrigation Department, n.d.).

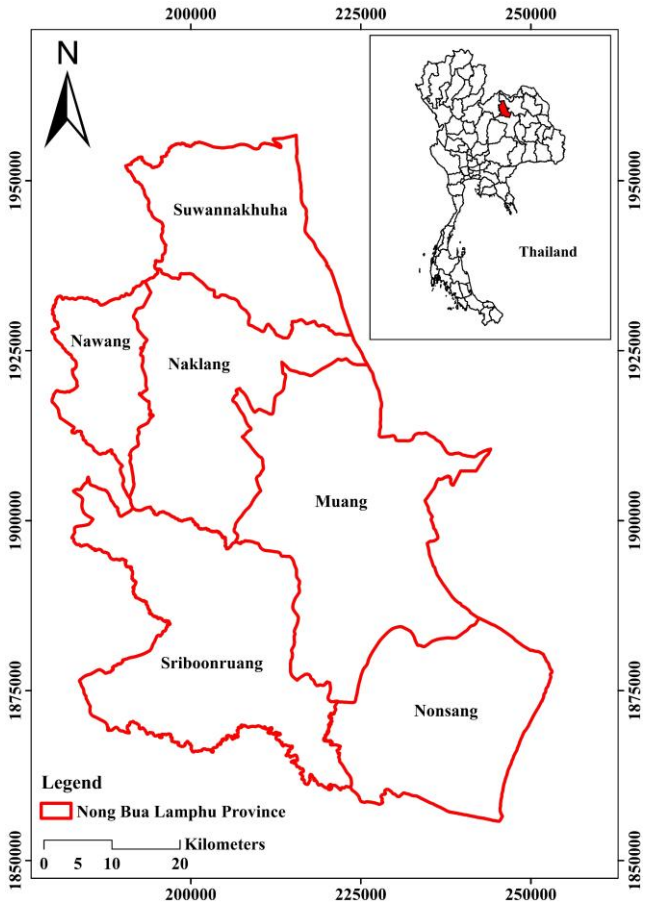

Fig. 1. Study Area.

2.2. Data Collection

The MOD13Q1 dataset provides vegetation index data from the MODIS on NASA's Terra satellite. It includes 16-day composites of vegetation indices at a spatial resolution of 250 meters. The dataset contains the Normalized Difference Vegetation Index (NDVI) and the Enhanced Vegetation Index, along with quality assessment layers and reflectance bands (Earth Engine Data Catalog, n.d.). . This study focuses on the NDVI product from the MOD13Q1 dataset, derived from the MODIS sensor on the Terra satellite, which records reflectance data. NDVI is widely valued for its spatial and temporal resolution, offering 250-meter spatial resolution with data available every 16 days. For this research, NDVI data from May 2022 to December 2023 covering the study area were selected.

2.3. Land Use Data

Land use data for Nong Bua Lam Phu Province were obtained from the Land Development Department in the form of shapefiles, which include layers detailing land use, land utilization, and administrative boundaries (district, sub-district, and provincial levels). The 2021 dataset, the most recent available for the province, was used in this study.

2.4. Crop Planting Calendar Data

Data on the economic crop planting calendar were collected from the Provincial Agricultural Office of Nong Bua Lam Phu.

2.5. Methodology

This study focuses on analyzing NDVI values. Normally, NDVI is calculated using Equation 1 (Tucker, 1979). For this research, the MOD13Q1 dataset – a Terra/MODIS satellite product that provides NDVI values – was used. The data were adjusted to accurate values using Equation 2 (Geographic Information Systems, n.d.). After calculating NDVI values, the coordinate system was converted to WGS 1984 UTM Zone 47N to ensure accurate geospatial mapping. The next step involved randomly selecting the largest cultivation areas of four major economic crops: rice fields, fruit trees, perennial plants, and field crops. This selection focused on identifying large, representative plots to facilitate data analysis and effectively monitor changes in cultivated areas. The process of randomly selecting cultivation areas was conducted in each district of Nong Bua Lam Phu Province. Graphs were then created to present the NDVI values obtained from this analysis.

$$NDVI = (NIR - RED) / (NIR + RED) \quad (1)$$

The well-known NDVI is a simple yet effective index for assessing green vegetation. It evaluates the reflectance of green leaves in the near-infrared spectrum relative to the absorption of chlorophyll in the red spectrum. NDVI values range from −1 to 1. Negative NDVI values (approaching −1) indicate the presence of water bodies. Values near zero (−0.1 to 0.1) generally represent barren areas such as rock, sand, or snow. Low positive values suggest the presence of shrubs and grasslands (approximately 0.2 to 0.4), whereas high values denote temperate and tropical rainforests (values approaching 1).

$$NDVI = [(QC == 0) * (NDVI > 2000) * NDVI] * 0.0001 \quad (2)$$

The formula provided, ndvi = [(qc==0)*(ndvi>2000)*ndvi]*0.0001, is used to modify MOD13Q1 NDVI data. It incorporates a quality control (QC) filter along with a thresholding procedure before scaling the NDVI values. Let us analyze it step by step:

1. QC Filter:

qc==0: This component evaluates the QC band of the MOD13Q1 dataset. It identifies pixels where the QC value equals 0, indicating potentially high-quality data.

2. Thresholding:

ndvi>2000: This phase filters the NDVI values, retaining only those exceeding 2000. This is because the raw NDVI values in the MOD13Q1 product are scaled by a factor of 10,000. Thus, a value of 2000 corresponds to an actual NDVI of 0.2. The threshold effectively isolates vegetation by removing non-vegetative pixels.

3. Scaling:

* 0.0001: Finally, the selected NDVI values are multiplied by 0.0001. This operation converts them to the conventional NDVI range of −1 to 1. Typically, MODIS NDVI data, before scaling, ranges from −2000 to 10,000.

3. RESULTS AND DISCUSSION

3.1. NDVI Analysis

The analysis of NDVI data, collected every 16 days, was limited to high-quality values, resulting in a dataset of 36 entries. This allowed for an effective assessment of vegetation density and richness. In Nong Bua Lam Phu Province, the NDVI analysis revealed a minimum value of 0.3, indicating low-density vegetation typically found in agricultural areas, and a maximum value of 0.8, representing high-density vegetation commonly seen in forested regions. Furthermore, the NDVI values for economic crops in each district of Nong Bua Lam Phu Province (**Fig. 2**) provide insights into vegetation health and growth at different times. The analysis, covering October 2022 to March 2023, is detailed by crop type as follows:

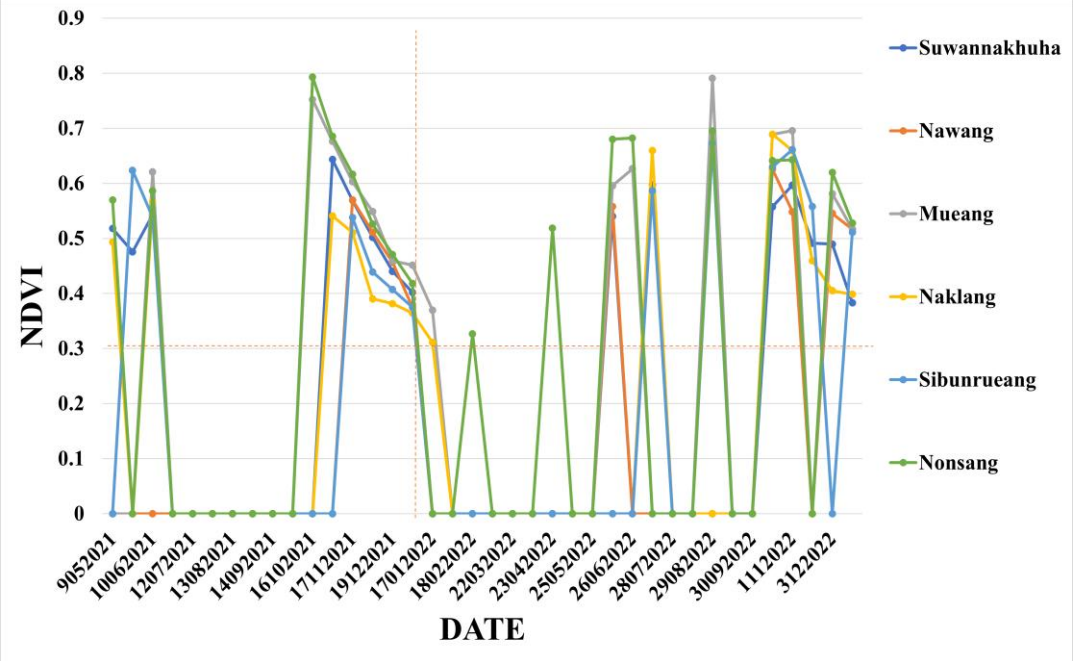

Fig. 2. NDVI Analysis from 2022–2023.

- Rice fields: Nong Singh District recorded the highest NDVI from August 13 to September 14, 2023. In general, rice NDVI values in each district were high from November 2022 to February 2023.

- Field crops: Nong Singh District recorded the highest NDVI from September 30, 2022, to January 17, 2023. Typically, field crop NDVI values were high across districts from September 2022 to November 2023.

- Perennial trees: Si Bun Rueang District had the highest NDVI from November 1, 2022, to January 17, 2023. Overall, perennial tree NDVI values in each district were elevated from November 2022 to January 2023.

- Fruit trees: Nong Singh District showed the highest NDVI from September 30, 2022, to January 17, 2023. Generally, fruit tree NDVI values across districts were high from November 2022 to January 2023. This analysis demonstrates that NDVI data can be effectively utilized for crop planning and maintenance, contributing to improved yields and promoting agricultural sustainability in the region.

3.2. Economic Crop Sampling Results

Studying areas cultivated with economic crops is essential for monitoring changes in crop coverage, which has implications for both economic and environmental outcomes. For the four sampled economic crops – rice, field crops, perennial trees, and fruit trees – **Fig. 3** illustrates their spatial distribution. This study focused on six districts: Suwannakuha, Na Wang, Mueang Nong Bua Lam Phu, Na Klang, Nong Singh, and Si Bun Rueang. The largest cultivation areas in each district were selected for NDVI analysis based on land use data from the Land Development Department. NDVI analysis enables the monitoring of crop health and growth by assessing changes in selected cultivated areas to better understand environmental factors affecting economic crops. According to the sampling results (**Table 1**), Si Bun Rueang District had the largest rice field area at 0.0999 km². Na Klang had the largest area for field crops at 0.0998 km². Na Klang and Nong Singh shared the largest areas for perennial trees at 0.0999 km², while Mueang District had the largest area for fruit trees at 0.0934 km².

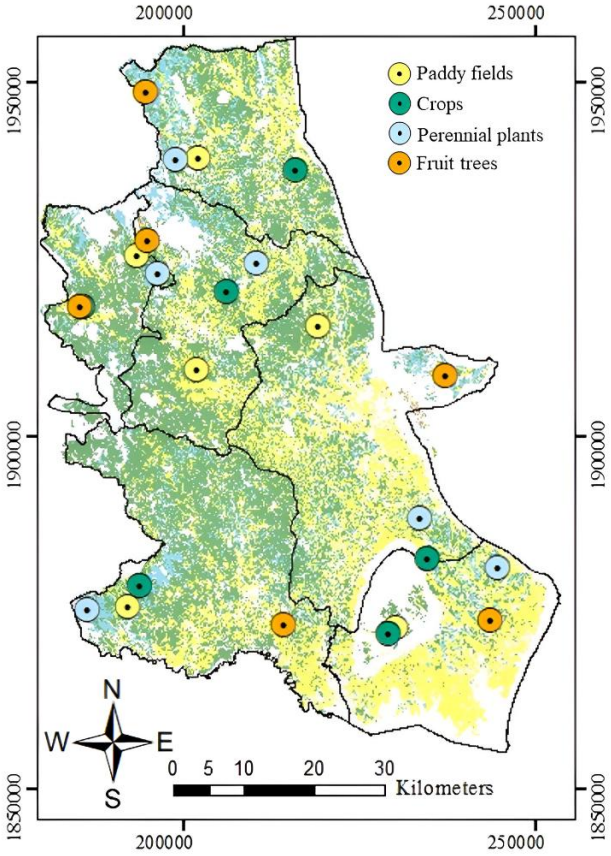

Fig. 3. Economic Crop Sampling.

Table 1.

Largest Area of Economic Crops in Each District.

		Area (km^2)			
Rank	**District**	**Rice Fields**	**Crops**	**Perennial Plants**	**Fruit Trees**
1	Suwannakuha	0.0998	0.0996	0.0997	0.0903
2	Nawang	0.0990	0.0995	0.0972	0.0879
3	Mueang	0.0993	0.0990	0.0996	0.0934
4	Naklang	0.0992	0.0998	0.0999	0.0894
5	Non Sing	0.0997	0.0983	0.0999	0.0706
6	Si Bun Rueang	0.0999	0.0996	0.0985	0.0930

3.3. NDVI Analysis Results Compared to Economic Crop Planting Calendar

To illustrate the comparison between NDVI analysis results and the economic crop planting calendar, this study presents an example from the Suwannakuha District. NDVI values for the district were compared with the economic crop planting calendar from May 2023 to December 2023, as shown in **Fig. 4**. Based on **Fig. 4**, the NDVI values can be analyzed in relation to the crop calendar as follows:

NDVI analysis showed that values for rice fields were recorded from October 16, 2022, to January 17, 2023. When compared with the crop planting calendar (**Fig. 5**), this period corresponds to the planting of dry-season rice from October 2022 to February 2023, with harvesting occurring from March to April 2023. Wet-season rice was planted earlier, from April to September 2022, and harvested from October to December 2022.

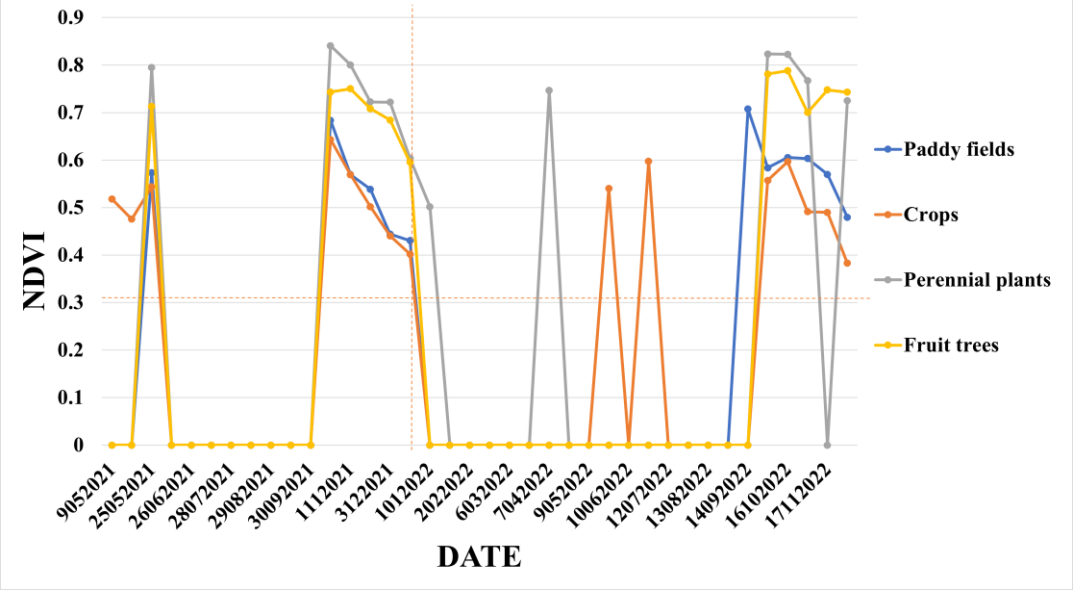

Fig. 4. Economic Crop Sampling NDVI Analysis Results.

No.	Plant Name	Calendar Year												Next Calendar Year											
		Jan	Feb	Mar	Apr	May	Jun	Jul	Aug	Sep	Oct	Nov	Dec	Jan	Feb	Mar	Apr	May	Jun	Jul	Aug	Sep	Oct	Nov	Dec
1	Wet season rice				Sowing/transplanting			Growing			Harvesting														
2	Dry season rice										Sowing			Growing		Harvesting									
3	Animal feed corn					*Plant		Growing		Harvesting		**Plant		Growing		Harvesting									
4	Sweet corn										**Plant			Growing		Harvesting									
5	Fresh cob corn										**Plant			Growing		Harvesting									
6	Cassava			**Plant		Growing							Harvesting												
											Plant		Growing								Harvesting				
7	Sugarcane	Harvesting									Plant			Growing										Harvesting	
8	Longan		Flower		Growing			Harvesting																	
9	Mango										Flower			Growing			Harvesting								
10	Oil palm	Growing /Harvesting				Plant		Growing /Harvesting											Plant		Growing /Harvesting				
11	Rubber	Cut	Shed leaves			Plant					Cut				Shed leaves			Plant			Cut				
12	Eucalyptus	Growing /Harvesting				Plant			Growing /Harvesting										Plant		Growing /Harvesting				

Fig. 5. Crop Planting Calendar.

- Field crops: NDVI values were recorded from October 16, 2022, to January 17, 2023, aligning with the corn planting season from October 2022 to February 2023, with harvesting from March to April 2023.

- Perennial trees: NDVI values were recorded from October 16, 2022, to February 2, 2023, corresponding to the rubber tapping season from October 2022 to January 2023, followed by leaf shedding from February to April 2023.
- Fruit trees: NDVI values were recorded from October 16, 2022, to January 17, 2023, aligning with the flowering and growth period of mango trees from October 2022 to February 2023.

4. CONCLUSION

The NDVI data analysis and study of economic crops in Nong Bua Lam Phu Province demonstrate the capability to monitor and track vegetation growth in the area. The NDVI analysis using 16-day interval data enables a detailed and accurate assessment of vegetation density and richness, with the lowest NDVI value of 0.3 found in agricultural areas and the highest value of 0.8 in forested areas. Additionally, the NDVI analysis for economic crops in each district from October 2022 to March 2023 provides further insights into crop growth.

The sampling of four types of economic crop cultivation areas across six districts – Suwannakuha, Na Wang, Mueang Nong Bua Lam Phu, Na Klang, Nong Singh, and Si Bun Rueang – shows that Si Bun Rueang District had the largest rice field area at 0.0999 km², while Na Klang had the largest field crop and perennial tree areas at 0.0998 km² and 0.0999 km², respectively. Mueang District had the largest fruit tree area at 0.0934 km². The comparison of NDVI values with the planting calendar in Suwannakuha District reveals consistency with the planting and harvesting periods for economic crops, such as dry-season rice planted from October to February and harvested from March to April.

This research highlights the role of NDVI data in effective crop planning, supporting yield enhancement and agricultural sustainability in the area. Additionally, this data can be used to efficiently assess environmental changes that impact economic crop cultivation.

When comparing the results of this study with similar research, the findings are consistent. For example, the study 'Beyond Fixed Dates and Coarse Resolution: Developing a Dynamic Dry Season Crop Calendar for Paddy in Indonesia from 2001 to 2021' (Irawan & Komori, 2024) examined the development of a dry-season paddy crop calendar using NDVI data to improve calendar accuracy. This research demonstrated significant potential for enhancing agricultural management in Indonesia by using NDVI to determine optimal planting and harvesting times.

The authors emphasized the importance of technology in supporting sustainable and efficient agriculture. Similarly, the study 'Mapping Crop Calendar Events and Phenology-Related Metrics at the Parcel Level by object-based image analysis (OBIA) of MODIS-NDVI Time-Series: A Case Study in Central California' (De Castro et al., 2018) explored the use of NDVI in satellite image analysis to map crop calendar events and phenology-related metrics at the parcel level.

Using OBIA with MODIS-NDVI time-series data, the study found that NDVI assists in assessing crop status at different times of the year and in analyzing long-term vegetation change trends. In another study, 'Crop Mapping Using PROBA-V Time Series Data at the Yucheng and Hongxing Farm in China' (Zhang et al., 2016), researchers investigated crop mapping using PROBA-V satellite time series data. The study found that NDVI plays a crucial role in crop mapping and supports efficient and sustainable agricultural practices.

ACKNOWLEDGMENTS

This research project was financially supported by Mahasarakham University.

REFERENCES

Auntarin, C., Chunpang, P., Chokkuea, W., & Laosuwan, T. (2021). Using a Split-window Algorithm for the Retrieval of the Land Surface Temperature via Landsat-8 OLI/TIRS. Geographia Technica, 6 (Special Issue), 30-42. https://doi.org/10.21163/GT_2021.163.03

Bangkokbiznews. (2023). Where is 'Thai rice exports' in the world market in an era where 'India and Vietnam' are still strong? Available online: https://www.bangkokbiznews.com/business/1080192 (accessed on 02 August 2024).

Cottrell, B., Kalacska, M., Arroyo-Mora, J.-P., Lucanus, O., Inamdar, D., Løke, T., & Soffer, R.J. (2024). Limitations of a Multispectral UAV Sensor for Satellite Validation and Mapping Complex Vegetation. Remote Sensing, 16(13), 2463. https://doi.org/10.3390/rs16132463

De Castro, A. I., Six, J., Plant, R. E., & Peña, J. M. (2018). Mapping Crop Calendar Events and Phenology-Related Metrics at the Parcel Level by Object-Based Image Analysis (OBIA) of MODIS-NDVI Time-Series: A Case Study in Central California. Remote Sensing, 10(11), 1745.

Devaux, A. et al. (2020). Global Food Security, Contributions from Sustainable Potato Agri-Food Systems. In: Campos, H., Ortiz, O. (eds) The Potato Crop. Springer, Cham. https://doi.org/10.1007/978-3-030-28683-5_1

DITP. (2020). Cassava trends in the Chinese market. Available online: https://www.ditp.go.th/contents_attach/669761/669761.pdf (accessed on 05 August 2024).

Earth Engine Data Catalog. (n.d.). MOD13Q1.061 Terra Vegetation Indices 16-Day Global 250m. Available online: https://developers.google.com/earth-engine/datasets/catalog/MODIS_061_MOD13Q1 (accessed on 12 Feb 2025).

Geographic Information Systems. (n.d.). Reprojected MODIS NDVI has range from -32768 to 32767, expected -1 to 1. Available online: https://gis.stackexchange.com/questions/84058/reprojected-modis-ndvi-has-range-from-32768-to-32767-expected-1-to-1 (accessed on 20 Jan 2025).

Hatfield, J. L., Boote, K. J., Kimball, B. A., Ziska, L. H., Izaurralde, R. C., Ort, D., Thomson, A. M., & Wolfe, D. (2011). Climate impacts on agriculture: Implications for crop production. Agronomy Journal, 103(2), 351–370.

IFAD. (2019). AN OUTLOOK ON ASIA'S AGRICULTURAL AND RURAL TRANSFORMATION. Available online: https://www.ifad.org/documents/38714170/41201480/apr_outlook.pdf (accessed on 20 July 2024).

Irawan, A. N. R., & Komori, D. (2024). Beyond Fixed Dates and Coarse Resolution: Developing a Dynamic Dry Season Crop Calendar for Paddy in Indonesia from 2001 to 2021. Agronomy, 14(3), 564.

Itsarawisut, J., & Laosuwan, T. (2022). Estimation of Particulate Matter Less Than 10 Microns Volume through Various Formats of Spatial Interpolation Methods. Geographia Technica, 17(2), 26-34. https://doi.org/10.21163/GT_2022.172.03

Itsarawisut, J., Puckdeevongs, A., & Laosuwan, T. (2024). Environmental Monitoring on the Surface of the Andaman Sea over the Southwestern Coast of Thailand: A Case Study of Spatial and Temporal Variability of Chlorophyll-A. Geographia Technica, 19(2), 57-69. https://doi.org/10.21163/GT_2024.192.05

Jitae, S. (2019). Participation of farmers, activities in water resource management in Li watershed, Lamphun province. King Mongkut's Agricultural Journal, 37(3), 519-526.

Laosuwan, T., Chunpang, P., & Sukkasena, S. (2011). Development of Robotic Aerial Remote Sensing System for Field Educational Purposes. International Journal of Geoinformatics, 17(4), 21-27.

Laosuwan, T., Uttaruk, Y., & Rotjanakusol, T. (2022). Analysis of Content and Distribution of Chlorophyll-a on the Sea Surface through Data from Aqua/MODIS Satellite. Polish Journal of Environmental Studies, 31(5), 4711-4719. https://doi.org/10.15244/pjoes/150731

Laosuwan, T., Uttaruk, Y., & Rotjanakusol, T. (2023). Atmospheric Environment Monitoring in Thailand via Satellite Remote Sensing: A Case Study of Carbon Dioxide. Polish Journal of Environmental Studies, 32(4), 3645-3651. https://doi.org/10.15244/pjoes/166170

Laosuwan, T., Uttaruk, Y., Jeefoo, P., & Itsarawisut, J. (2024). Comparison of Drought Indices for Evaluating Agricultural Drought Risk in Highland Regions. Geographia Technica, 19(2), 152-163. https://doi.org/10.21163/GT_2024.192.12

Ministry of Commerce. (2024). Household economic situation in the agricultural sector to improve and increase income for farmers. Available online: https://www.moc.go.th/th/gallery/article/detail/id/5/iid/353 (accessed on 30 July 2024).

Najafi, E., Devineni, N., Khanbilvardi, R. M., & Kogan, F. (2018). Understanding the changes in global crop yields through changes in climate and technology. Earth's Future, 6(3), 410–427.

Ounrit, I., Sinnung, S., Meena, P., & Laosuwan, T. (2022). Flash Flood Mapping based on Data from Landsat-8 Satellite and Water Indices. International Journal on Technical and Physical Problems of Engineering, 12(1), 1-6.

Pawlak, K., & Kołodziejczak, M. (2020). The role of agriculture in ensuring food security in developing countries: Considerations in the context of the problem of sustainable food production. Sustainability, 12(13), 5488. https://doi.org/10.3390/su12135488

Phoophiwfa, T., Laosuwan, T., Volodin, A., Papukdee, N., Suraphee, S., & Busababodhin, P. (2023). Adaptive Parameter Estimation of the Generalized Extreme Value Distribution Using Artificial Neural Network Approach. Atmosphere, 14(8), 1197. https://doi.org/10.3390/atmos14081197

Plybour, C., & Laosuwan, T. (2023a). Estimation of Chlorophyll-a Contents on the Sea Surface by Remote Sensing Technology. ARPN Journal of Engineering and Applied Sciences, 18(8), 900–905.

Plybour, C., & Laosuwan, T. (2023b). The Application of Remote Sensing Technology to Investigation of Areas Burned by Forest Fires. ARPN Journal of Engineering and Applied Sciences, 18(9), 1039–1045.

Royal Irrigation Department. (n.d.). Topography. Available online: http://irrigation.rid.go.th/rid5/web-bua/_private/globe1.htm (accessed on 30 Jan 2025).

Sangpradid, S., Uttaruk, Y.,Rotjanakusol, T., & Laosuwan T. (2021): Forecasting time series change of the average enhanced vegetation index to monitoring drought condition by using Terra/Modis data. Agriculture and Forestry, 67 (4), 115-129. https://doi.org/10.17707/AgricultForest.67.4.10

Sibhatu, K. T., & Qaim, M. (2017). Rural food security, subsistence agriculture, and seasonality. PLoS ONE, 12(10), e0186406. https://doi.org/10.1371/journal.pone.0186406

Sciyouthvolunteer. (n.d.). The future of agriculture in Thailand 4.0. Available online: https://sciyouthvolunteer.rmutt.ac.th/?page_id=358 (accessed on 25 July 2024).

Thaipbs. (2023). Trade routes of "Sugar Market" from Thai prices to foreign countries. Available online: https://www.thaipbs.or.th/news/content/333472 (accessed on 03 August 2024).

Tucker, C. J. (1979). Red and photographic infrared linear combinations for monitoring vegetation. Remote Sensing of Environment, 8, 127–150.

Turton, A. E., Augustin, N. H., & Mitchard, E. T. A. (2022). Improving Estimates and Change Detection of Forest Above-Ground Biomass Using Statistical Methods. Remote Sensing, 14(19), 4911. https://doi.org/10.3390/rs14194911

Uttaruk, Y., & Laosuwan, T. (2018). Community Forest for Global Warming Mitigation: the Technique for Estimation of Biomass and Above Ground Carbon Storage using Remote Sensing Method. Agriculture and Forestry, 64 (3), 47-57. DOI: 10.17707/AgricultForest.64.3.04

Uttaruk, Y., Rotjanakusol, T., Laosuwan, T. (2022). Burned Area Evaluation Method for Wildfires in Wildlife Sanctuaries Based on Data from Sentinel-2 Satellite. Polish Journal of Environmental Studies, 31(6), 5875-5885. https://doi.org/10.15244/pjoes/152835

Viana, C. M., Freire, D., Abrantes, P., Rocha, J., & Pereira, P. (2022). Agricultural land systems importance for supporting food security and sustainable development goals: A systematic review. Science of The Total Environment, 806 (Part 3), 150718. https://doi.org/10.1016/j.scitotenv.2021.150718

Wageningen University. (2015). The development of the share of agriculture in GDP and employment. Available online: https://edepot.wur.nl/342795 (accessed on 02 July 2024).

WORLD BANK. (2022). Adapting Africa's food system to climate change is an imperative; it's time for action. Available online: https://blogs.worldbank.org/en/africacan/adapting-africas-food-system-climate-change-imperative-its-time-action (accessed on 08 July 2024).

Yadav, K., & Geli, H. M. E. (2021). Prediction of crop yield for New Mexico based on climate and remote sensing data for the 1920–2019 period. Land, 10(12), 1389. https://doi.org/10.3390/land10121389

Zhang, Z., & Zhu, L. (2023). A Review on Unmanned Aerial Vehicle Remote Sensing: Platforms, Sensors, Data Processing Methods, and Applications. Drones, 7(6), 398. https://doi.org/10.3390/drones7060398

Zhang, X., Zhang, M., Zheng, Y., & Wu, B. (2016). Crop Mapping Using PROBA-V Time Series Data at the Yucheng and Hongxing Farm in China. Remote Sensing, 8(11), 915.

GEOGRAPHICALLY WEIGHTED REGRESSION (GWR) MODEL FOR ANALYZING FACTORS OF LAND SUBSIDENCE IN JAKARTA PROVINCE

Cahyadi SETIAWAN[1]*, *Fauzi Ramadhoan A'RACHMAN*[2], *Ode Sofyan HARDI*[2], *Ika Muti RAHMAH*[1], *Muhammad DEFFRY*[1], *Zidan FURQON*[2], *Nabilah Firdha KHAIRUNNISA*[1], *and Muhammad Wahyu WARDANA*[2]

DOI: 10.21163/GT_2025.202.15

ABSTRACT

Land subsidence was a serious issue affecting infrastructure, water resources and human safety on various countries in the world, including Indonesia. Jakarta as one of the Capital cities in Indonesia is also experiencing land subsidence at varying rates which has many impacts. This study aims to analyze the influence of built-up areas, population density, groundwater, elevation, and distance from the coastline against land subsidence in Jakarta. Data was obtained using the InSAR method, Landsat 8 imagery, Statistic Central Bureau, Indonesian Geospatial Bureau, and Water Resources Agency. The analysis was conducted using Geographically Weighted Regression (GWR). The results indicate that land subsidence in Jakarta is influenced by several parameters, including groundwater levels, population density, built-up areas, elevation, and distance from the coast. The overall R^2 value of the Geographically Weighted Regression (GWR) model was 0.566, suggesting a moderate explanatory power. Among the variables, groundwater exhibited the strongest correlation with land subsidence ($R^2 = 0.829$), whereas elevation ($R^2 = 0.255$) and distance from the coast ($R^2 = 0.249$) showed the weakest correlations. These findings suggest that anthropogenic factors, particularly related to human activities, have a more significant impact on land subsidence than natural topographic features. High GWR values were primarily concentrated in several districts, including Penjaringan, Pademangan, Cilincing, Tanjung Priok, and Kalideres.

Key-words: *Geographically Weighted Regression, Jakarta, Land Subsidence, InSAR Method, Landsat 8 Imagery*

1. INTRODUCTION

Land subsidence has emerged as a critical issue that spans multiple disciplines due to its widespread and multifaceted impacts across various regions of the world. It poses significant threats to infrastructure, including road networks, power grids, water supply systems, substations, farmland, sewage systems, railways, aquifer layers, and even human safety (Choubin et al., 2023; Sadeghi et al., 2023). Land subsidence refers to the gradual or rapid downward movement of the Earth's surface, which can occur over hours or extend across decades, and may affect areas ranging in size from a few square meters to several square kilometers (Botey i Bassols et al., 2023; Bremard, 2022; Declercq et al., 2021).

Land subsidence stems from combination of natural processes and human activities (Gao et al., 2019; Wang et al., 2023). Contributing factors include low annual rainfall, climatic and topographic conditions, soil characteristics, geological structures, underground mining activities, and large-scale infrastructure development (Bagheri-Gavkosh et al., 2021; Sadeghi et al., 2023). Moreover, rapid urbanization and population growth have led to increased groundwater extraction, which significantly contributes to land subsidence (Gao et al., 2019; Tirmizi & Khan, 2023; Younas et al., 2023).

[1] *Geography Study Program, Faculty of Social Sciences and Law, Universitas Negeri Jakarta, Indonesia, (CS) Cahyadi-Setiawan@unj.ac.id, (IMR) ikamrahmah@gmail.com, (MD) mdefri35@gmail.com, (NFK) nfirdha22@gmail.com*

[2] *Geography Education Study Program, Faculty of Social Sciences and Law, Universitas Negeri Jakarta, Indonesia, (FRA) fauzi.ramadhoan@unj.ac.id, (OSH) Ode-sofyan-hardi@unj.ac.id, (ZF) zidanf73@gmail.com, (MWW) wahyuwardana1682@gmail.com*

Excessive groundwater withdrawal, especially when combined with extensive infrastructure expansion, exacerbates the rate and severity of land subsidence (Z. Du et al., 2018; Gao et al., 2019; Tran et al., 2022).

Several studies have identified numerous countries around the world that are experiencing land subsidence, including Belgium, Mexico, the United States, Taiwan, Thailand, China, Japan, Egypt, Iran, Pakistan, and many others (Declercq et al., 2021; Kamh et al., 2016; Khan et al., 2023; Sadeghi et al., 2023; Tirmizi & Khan, 2023). In Belgium, subsidence rates of approximately 2.1 mm/year have been recorded across various districts along the Scheldt River (Declercq et al., 2021). In Mexico, several states such as Mexico, Jalisco, and Chihuahua have been affected (Figueroa-Miranda et al., 2018). Specifically, in the Toluca Valley and Mexico City, land subsidence is notably prevalent in industrial areas, with rates reaching up to 10 cm/year (Calderhead et al., 2011). In the United States, land subsidence has been reported from Louisiana to the Mexican border, affecting at least 56 counties. Between 1970 and 2010, the average subsidence rate in Montgomery, Harris, Karnes, and Fort Bend counties was approximately 1.4 mm/year (Younas et al., 2023). Houston is one of the most affected areas, with downtown subsidence rates reaching 7 cm/year between 1996 and 2003, and recent rates of 2 cm/year in the western areas (Khan et al., 2022; Tirmizi & Khan, 2023), Additionally, in Katy, Texas, subsidence has been recorded at a rate of 1.4 mm/year from 2017 to 2023 (Tirmizi &; Khan, 2023).

In Asia, numerous areas in China are experiencing land subsidence. The Hangzhou‐Jiaxing‐Huzhou Plain has recorded subsidence depths of up to 1.1 meters and 0.5 meters (Wang et al., 2023; Zhu et al., 2015). The Yellow River Delta has experienced a subsidence with 250 mm/year, while the Northern Region (Beijing Plain) has a subsidence rate 52 mm/year (Higgins et al., 2013; Pang et al., 2022; Zhu et al., 2015). In Thailand, Bangkok experiences subsidence of approximately 120 mm/year (Aobpaet et al., 2013; Bremard, 2022). Vietnam's Mekong Delta records an average subsidence rate of 6–7 mm/year in forest and swamp areas, while rates reach 18–20 mm/year in mixed agricultural and urban zones (Minderhoud et al., 2018). In Iran, several cities including Yazd, Qom, Kerman, Isfahan, and Mashhad experience subsidence rates of 15–20 cm/year (Sadeghi et al., 2023).

Indonesia has experienced setbacks including Jakarta, Semarang, Bekasi, Tangerang, Surabaya and Bandung (Asmadin et al., 2021; Bagheri-Gavkosh et al., 2021; Bott et al., 2021; Z. Du et al., 2018; Illigner et al., 2021; Minderhoud et al., 2019; H. Sari et al., 2023; Situmorang et al., 2021). A similar phenomenon has occurred in Jambi, where the city experiences a high subsidence rate, averaging 11.28 cm per year (Akbar & Setiawan, 2022). Other coastal cities in Indonesia, such as Padang, have also been affected, with land subsidence ranging from 0 to 40 mm across residential areas (Syafriani et al., 2022). Meanwhile, Semarang records one of the highest land subsidence rates, reaching 1.795 cm per year (Syafriani et al., 2022).

Jakarta is a major metropolitan area where several locations have experienced land subsidence at varying rates (Bott et al., 2021; Rahman et al., 2018; Yudhistira et al., 2020). It is among the fastest-subsiding cities globally, with subsidence rates reaching up to 28 cm per year (Abidin et al., 2011; Agustan et al., 2021; Bott et al., 2021; Z. Du et al., 2018; Minderhoud et al., 2019; H. Sari et al., 2023). Land subsidence that occurs in these areas is caused by many changes in land use from open field to built-up area as a result of increasing demand land availability for development, such as residential areas, toll roads, and infrastructure for industrial and economic activities (Bott et al., 2021; Dewi et al., 2020; Kurnianti et al., 2015; Rachma et al., 2022; Rahman et al., 2018; Rashid et al., 2022; D. P. Sari et al., 2021). The increasing density of the built-up area can also occur on the large growth of the population in Jakarta Metropolitan Area, the excessive use of land use has been a ground water exploitation that may cause some land subsidence in Jakarta.

Land subsidence has become a serious problem in the Jakarta Metropolitan Area in recent decade, especially in the Jakarta (Bott et al., 2021; Illigner et al., 2021; Rahman et al., 2018). The Damage to building infrastructure, increased risk of building collapse, flooding, and some areas have been below sea level (Bott et al., 2021; Cao et al., 2021; Hasibuan et al., 2023; Kamh et al., 2016; Koto & Negara, 2018). This event was caused by several factors, including excessive exploitation of groundwater, compaction of clay deposits underneath, and excessive load addition due to rapid urbanization in the Jakarta Metropolitan Area (Hasibuan et al., 2023; Rahman et al., 2018; Tambunan, 2017).

Rapid population growth and massive infrastructure development have led the area to higher groundwater demand resulting in overexploitation and land subsidence (Sajjad et al., 2023). The government has worked to address this problem, including by limiting groundwater exploitation, adopting soil reinforcement technologies, and building water retention infrastructure. However, these efforts have not yet provided a comprehensive solution to the problem. Therefore, there is a pressing need for more innovative and integrated approaches to effectively address land subsidence in the Jakarta Metropolitan Area. While various studies have explored the causes of land subsidence in Jakarta, most have not yet utilized spatial statistical approaches such as Geographically Weighted Regression (GWR) to examine how each contributing factor varies across different locations. In this context, this study seeks to fill that gap by using the GWR method to analyze the spatial relationships between land subsidence and several influencing variables, including built-up areas, population density, groundwater, elevation, and distance from the coastline.

2. STUDY AREA

This research focuses on Jakarta Province. Geographically, Jakarta is located between 6°12′ South Latitude and 106°48′ East Longitude. Jakarta City is located in a lowland area with an average elevation of approximately +7 meters above sea level. Geographically, it is bordered by the Java Sea to the north, West Java Province to the south and east, and Banten Province to the west (**Fig. 1**).

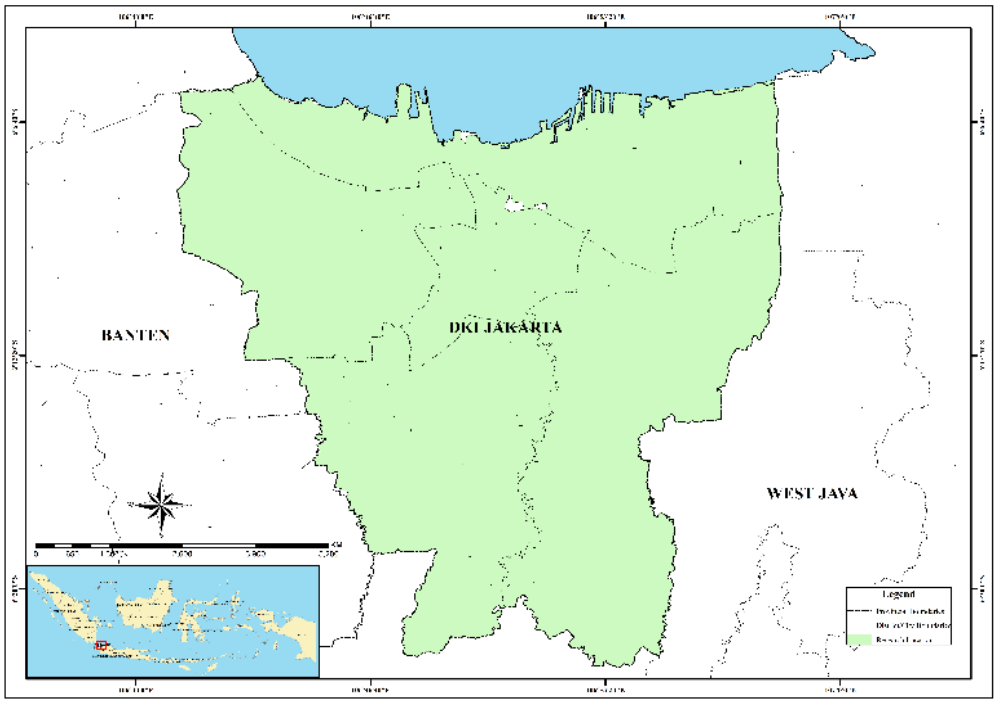

Fig. 1. Location of Jakarta.
(Source: InaGeospatial)

The administrative and geographical layout of Jakarta, including its boundaries with neighboring provinces and coastal positioning along the northern part of Java Island (**Fig.1**). Based on information from the official portal of the Jakarta Provincial Government, the Special Capital Region of Jakarta (DKI Jakarta) is administratively divided into five municipalities: Central Jakarta, North Jakarta, West Jakarta, East Jakarta, and South Jakarta. In addition to these, there is one administrative regency, namely the Thousand Islands (Kepulauan Seribu). The total area of the province covers approximately 662.33 square kilometers.

3. DATA AND METHODS

3.1. Land Subsidence Data

The data used is InSAR data obtained using the Small Baseline Area Subset (SBAS) method in generating land subsidence data. This InSAR SBAS method was proposed by Berardino in 2002 in producing spatial-temporal movements of several interferometric pairs with short spatial and temporal baselines (Berardino et al., 2002; Chang et al., 2022). InSAR (Interferometric Synthetic Aperture Radar) is a remote sensing method that works by combining pixel values from two radar datasets. This study uses Sentinel-1 imagery with the InSAR method. The Sentinel-1 data used in this study were obtained from the Copernicus Open Access Hub. Sentinel-1 is a satellite pair consisting of Sentinel-1A and Sentinel-1B, launched by ESA with the main goal of monitoring land and ocean surfaces. Sentinel-1 uses a C-SAR sensor, which offers medium to high-resolution imaging in all weather conditions (Sunu et al., 2019). This method is used to monitor land surface movements that occur by maintaining interferometric coherence in eliminating the effects of temporal decorrelation and atmospheric disturbances (Chang et al., 2022). The data used is LOS (Line of Sight) data from two recording directions which we can call ascending and descending data. The ascending data ranges from August 26, 2016 to August 31, 2022, while the descending data spans from February 17, 2015 to December 13, 2022. The data were then decomposed to generate vertical displacement data using the following formula (Fuhrmann & Garthwaite, 2019) (Eq. (1)). Data usage begins in 2015, as this year marks the overlapping period between the ascending and descending tracks.

$$\begin{pmatrix} V^{asc} \\ V^{desc} \end{pmatrix} = \begin{pmatrix} cos\theta^{asc} - cos\alpha^{asc}\, sin\theta^{asc} \\ cos\theta^{desc} - cos\alpha^{desc}\, sin\theta^{desc} \end{pmatrix} \begin{pmatrix} V^{UD} \\ V^{EW} \end{pmatrix} \quad (1)$$

where:

V^{asc}	-LOS displacement from ascending satellite pass (in mm/year)
V^{desc}	-LOS displacement from descending satellite pass (in mm/year)
V^{UD}	-Vertical displacement component (Up-Down), representing land subsidence (in mm/year)
V^{EW}	-Horizontal displacement component in the East-West direction (in mm/year)
$\theta^{asc}, \theta^{desc}$	-Incidence angles of the radar signal for ascending and descending paths (in degrees)
$\alpha^{asc}, \alpha^{desc}$	-Azimuth angles (or satellite heading angles) for ascending and descending tracks (in degrees)
cos, sin	-Trigonometric functions used to project LOS displacements onto vertical and horizontal planes

With the formula, it is able to provide a vertical value by using a data slice between ascending and descending data which will be used as a land subsidence variable. The decomposition data contains the recording results from August 26, 2016 to December 13, 2022 in the Jakarta area.

3.2. Built-Up Area Data

Landsat imagery, including data from Landsat 8, provides multispectral remote sensing information with a medium spatial resolution of 30 × 30 meters. This spatial resolution is sufficient for detecting changes in land cover, including the identification of Built-Up Areas. In this study, Landsat 8 OLI imagery is used to obtain Built-Up Area data in Jakarta for the period 2015–2022. Landsat 8 OLI was selected due to its higher accuracy in mapping Built-Up Areas (Bhatti & Tripathi, 2014). The method used to process Landsat 8 OLI imagery is supervised classification, which transforms multispectral image data into specific land cover classes based on spatial characteristics and training samples (Prahasta, 2008a). This method is widely used and considered suitable for land cover mapping, including the delineation of Built-Up Areas in urban environments like Jakarta (Septiani et al., 2019). To extract Built-Up Area data from Landsat 8 OLI imagery, several spectral bands were utilized, including Band 4 (Red), Band 5 (Near Infrared/NIR), and Band 6 (Shortwave Infrared 1/SWIR1). These bands were chosen because built-up surfaces generally reflect more strongly in the SWIR band and less in the Red and NIR bands, allowing for clearer differentiation from vegetation and bare soil. The combination of these bands, processed through supervised classification, enhances the accuracy of identifying land cover types, especially built-up areas (Bhatti & Tripathi, 2014; Prahasta, 2008).

Furthermore, supervised classification allows for temporal analysis of Landsat imagery, enabling the detection of spatial trends and the growth of urban areas over time (Mailendra & Buchori, 2019). In addition, this method also has the advantage of having better accuracy than the unsupervised method. Below is the overall accuracy formula used to measure accuracy in the built-up area (Eq.(2)).

$$Overall\ Accuracy = \frac{\Sigma Xii}{N}\ x\ 100\% \quad (2)$$

where:

ΣXii	-Total number of correctly classified pixels (sum of diagonal values in the confusion matrix)
N	-Total number of sample pixels tested
$x\ 100\%$	-Converts the result to a percentage

3.3. Population Density Data

Population density data at the sub-district level in Jakarta was obtained from secondary sources, specifically from Statistics Indonesia (Badan Pusat Statistik, BPS) in 2022. BPS serves as the central government agency responsible for conducting statistical surveys, compiling data, and providing official statistics to support national development planning and policy-making in Indonesia. The data processing began by collecting population figures for each sub-district in Jakarta. These figures were then imported into ArcGIS software and joined with the administrative boundary data of Jakarta's sub-districts. To visualize population distribution, a choropleth technique was applied using a color gradient, where darker shades represent areas with higher population density. This method enables a clear spatial interpretation of population concentration patterns across Jakarta.

3.4. Groundwater Data

The groundwater map utilizes secondary data from the Water Resources Agency of Jakarta Province. The agency's official website provides various publicly accessible datasets, including groundwater data, which in this study specifically refers to the number of wells in Jakarta in 2022. The process of creating the groundwater map begins with collecting and processing the 2022 well data by sub-district. This data is then input into ArcGIS software and combined with the administrative boundary data of Jakarta's sub-districts to display the number of wells per sub-district, symbolized using a color gradient based on the level of usage intensity.

3.5. Elevation Data

The elevation data used in this study is based on secondary data derived from the Digital Elevation Model (DEM) SRTM, sourced from the Geospatial Information Agency. The DEM from the Shuttle Radar Topography Mission (SRTM) has a spatial resolution of 30 × 30 meters, meaning each pixel represents a 30-meter square on the ground. This resolution is considered adequate for regional-scale topographic analysis, such as identifying elevation and slope patterns in urban areas like Jakarta. To analyze elevation, the data was processed using the Slope Tool in ArcGIS, which calculates the steepness or degree of slope from each cell in the elevation raster. The resulting slope values were then classified based on the minimum and maximum elevation found in Jakarta, allowing for the interpretation of terrain variation across the study area. The 30-meter SRTM data is commonly used in geospatial studies due to its balance between detail and manageable data volume (Prahasta, 2008)

3.6. Distance from the Coast for Land Subsidence Data

The land to coast distance map utilizes secondary spatial data from the Jakarta Satu website, including administrative boundaries for each sub-district in Jakarta and toponymic data for these sub-districts. The method for creating this coastal distance map employs an overlay technique, where the administrative boundary data is overlaid with the sub-district toponymic data. Then, a line is drawn from the centroid point of each sub-district to the coastline to obtain the distance from the land to the coast.

3.7. Data processing method with GWR (Geographically Weighted Regression)

Geographically weighted regression (GWR) is a modelling technique designed to deal with spatial non-stationarity, e.g., the mean values vary by locations. It has been widely used as a visualization tool to explore the patterns of spatial data (Leong & Yue, 2017). The GWR model has advantages over standard regression models, namely that it can offer a local model at each location and can display variables that influence the response variable in relation to spatial characteristics (Dur et al., 2023). The general formulation of the GWR model which reflects the localized nature of this method (Eq.(3)).

$$\hat{y}^0 = \beta_0 (u_0, v_0) + \sum_{k=1}^{p} \beta_k (u_0, v_0) \chi_{0k} \quad (3)$$

where:

$\hat{y}^0$	-Predicted value of the dependent variable at location
$\beta_0 (u_0, v_0)$	-Intercept term estimated at location
$\beta_k (u_0, v_0)$	-Coefficient of the k independent variable at location
χ_{0k}	-Value of the k independent variable at location
p	-Number of independent variables
(u_0, v_0)	-Spatial coordinates of the observation point

This study uses the Geographically Weighted Regression method, which analyzes spatial data by extending global regression to local models that create parameter estimates at each Geographic location (Bivand & Yu, 2015). This technique uses weighting functions, such as Gaussian Kernel and bi-square, to include spatial effects. In this research, the bi-square weighting function is applied, as it offers localized weighting that is effective in capturing spatial heterogeneity. This method is suitable for application in various fields, including land subsidence assessment (Blachowski & Gutkowski, 2016). This study will analyze the influence of Built-Up Area factors, Population Density, Groundwater, Elevation, and Distance from the Coast to Land Subsidence in several districts in Jakarta.

4. RESULTS AND DISCUSSIONS

4.1. Land Subsidance Rate

The map illustrates the land subsidence rate in Jakarta from 2016 to 2022, measured in millimeters per year (mm/year). This map was produced using InSAR (Interferometric Synthetic Aperture Radar) technology, utilizing data from the Sentinel-1 satellite. The colors on the map represent different levels of land subsidence, where blue indicates lower subsidence rates, while yellow, orange, and red indicate higher rates (**Fig. 2**).

Fig. 2 illustrates the spatial distribution of land subsidence rates in Jakarta between 2016 and 2022, measured in millimeters per year (mm/year). The map was generated using InSAR (Interferometric Synthetic Aperture Radar) data from the Sentinel-1 satellite. The color gradient represents varying levels of land subsidence: areas in dark blue indicate low subsidence rates (between 0 and 5 mm/year), while areas shaded in lighter blue, cyan, yellow, orange, and red represent increasingly higher rates of subsidence.

Red areas experience the most severe subsidence, exceeding 50 mm/year. Based on the Land Subsidence Rate (2016–2022) map, the highest land subsidence rates (marked in red) are primarily concentrated in the northern part of Jakarta, particularly in Penjaringan and the surrounding coastal area. Moderate to high subsidence rates (30–50 mm/year, marked in orange) are also observed in parts of Kalideres, Kembangan, and Cengkareng in West Jakarta. Subsidence in the range of 19–30 mm/year (marked in yellow) occurs in the same general vicinity, gradually decreasing in intensity toward the central and southern regions. The majority of South Jakarta and parts of East Jakarta experience lower subsidence rates between 0 and 11 mm/year (shaded in dark to light blue), with some areas even showing slight uplift (white areas).

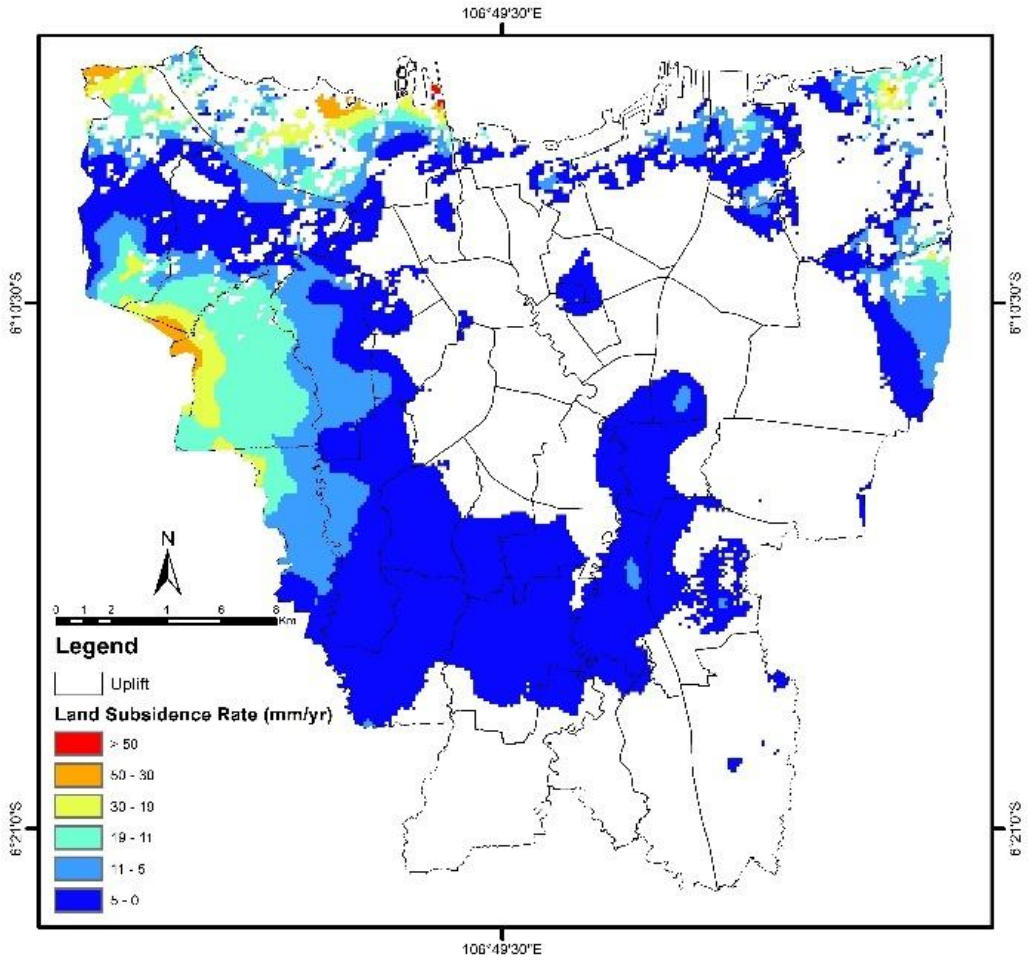

Fig. 2. Land Subsidance Rate (2016-2022).

4.2. Classification of Land Subsidence Parameters

The spatial distribution of five key variables, built-up area, population density, groundwater, elevation, and distance from the coastline shows considerable variation across different sub-districts in Jakarta (**Fig. 3**). Each of these factors varies from one region to another. By looking at these maps, we can get a better understanding of how these five factors are spread across Jakarta. These factors will be analyzed to see how they contribute to land subsidence in the Jakarta Metropolitan Area. The goal of this study is to understand the relationship between urban development (built-up land) and land subsidence, which can help in making better decisions for future urban planning.

Based on the land subsidence parameters map in the **Fig. 3**, the first parameter (**Fig. 3a**) illustrates built-up area in Jakarta. The land subsidence parameter map was used to generate the land subsidence rate map for Jakarta Province from 2016 to 2022. The green color represents settlement areas with the least coverage. The red-colored areas represent built-up land across Jakarta Province, covering most of the city. The second parameter (**Fig. 3b**) shows population density in Jakarta, using a color gradient to indicate the range of population per square kilometer. The lightest color (pink) represents a population density ranging from 8,490,000 to 12,970,000 people per km², indicating areas with low population density. In contrast, the dark red color represents a population density between 39,040,001 and 49,970,000 people per km², indicating areas with very high population density. The third parameter, shown in **Fig. 3c**, represents groundwater in Jakarta using a color gradient to indicate different consumption levels. The lightest color (light blue) represents the lowest groundwater consumption,

ranging from 0 to 5,043 liters. In contrast, the dark blue color represents higher groundwater consumption, ranging from 412,790 to 1,456,582 liters. The fourth parameter, shown in **Fig. 3d**, presents a map of the distance from the coast. The blue lines indicate the distance to the coastline, illustrating the spatial distribution of areas based on their proximity to the shore. These lines provide a visual representation of how close different regions are to the coast, while building symbols mark the locations of each district in Jakarta Province. The fifth parameter, shown in **Fig. 3e**, is a map representing elevation in Jakarta Province using color variations to indicate different heights above sea level. Dark green to light green represents the highest elevations, ranging from 92 to 60 meters, primarily located in the southern and eastern parts of Jakarta. The yellow areas indicate an elevation of 50 meters, also found in the south and east. Meanwhile, orange to red shades represent lower elevations, ranging from 40 to 1 meter, which are concentrated in northern Jakarta.

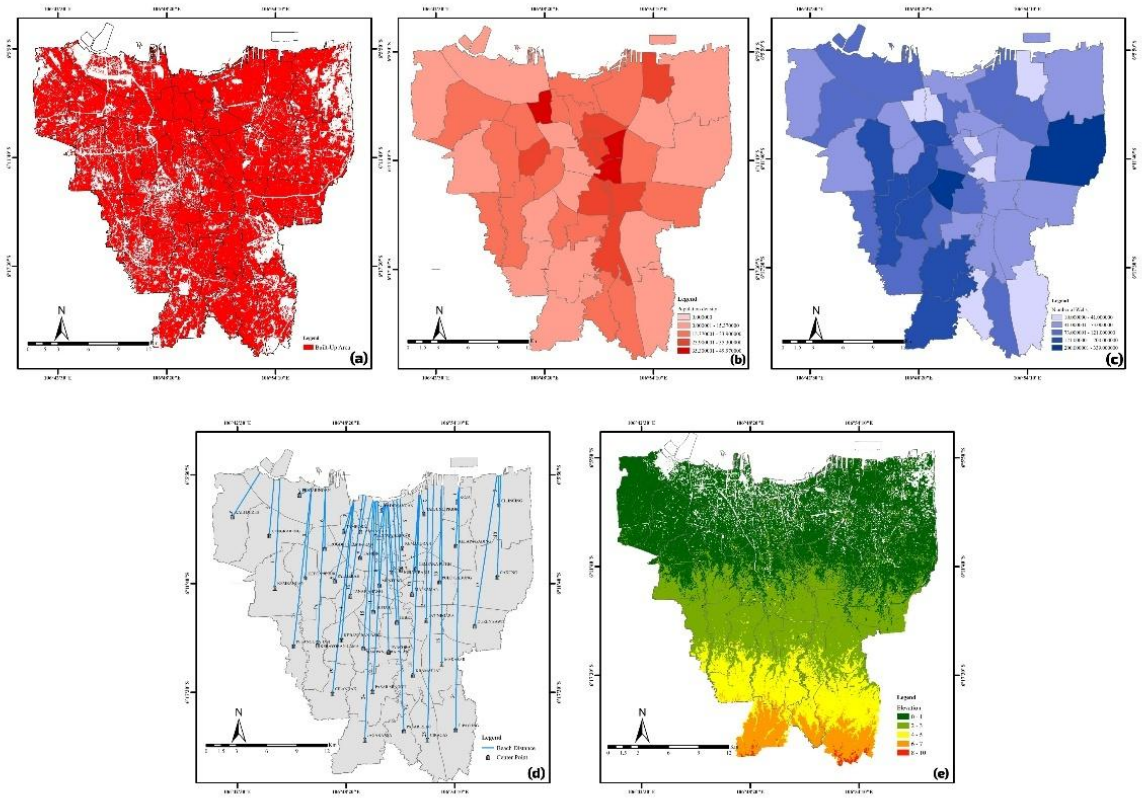

Fig. 3. Land Subsidence Parameters for (a) built-up area, (b) population density, (c) groundwater, (d) distance from the coast, (e) elevation.

4.3. GWR Model of the Distance from the Coast for Land Subsidence

The land to coast variable is a factor that cannot be separated, as Jakarta Province is defined by the coastal city of Jakarta, which has a large population in Indonesia. Development in Jakarta is continuously driven by massive infrastructure projects, which contribute to changes in the distance toward the coastline due to sediment compaction. This process contributes to land subsidence and increases the effects of tidal flooding in Jakarta (Erban et al., 2014). Even though land subsidence in Jakarta will continue, it can affect areas that are more vulnerable to sea level rise (Du et al., 2020; Abidin et al., 2011) Therefore, it is not impossible that in the coming decades, coastal areas with higher population densities will be more affected by tidal flooding in the long term, which will impact settlements and infrastructure in those areas.

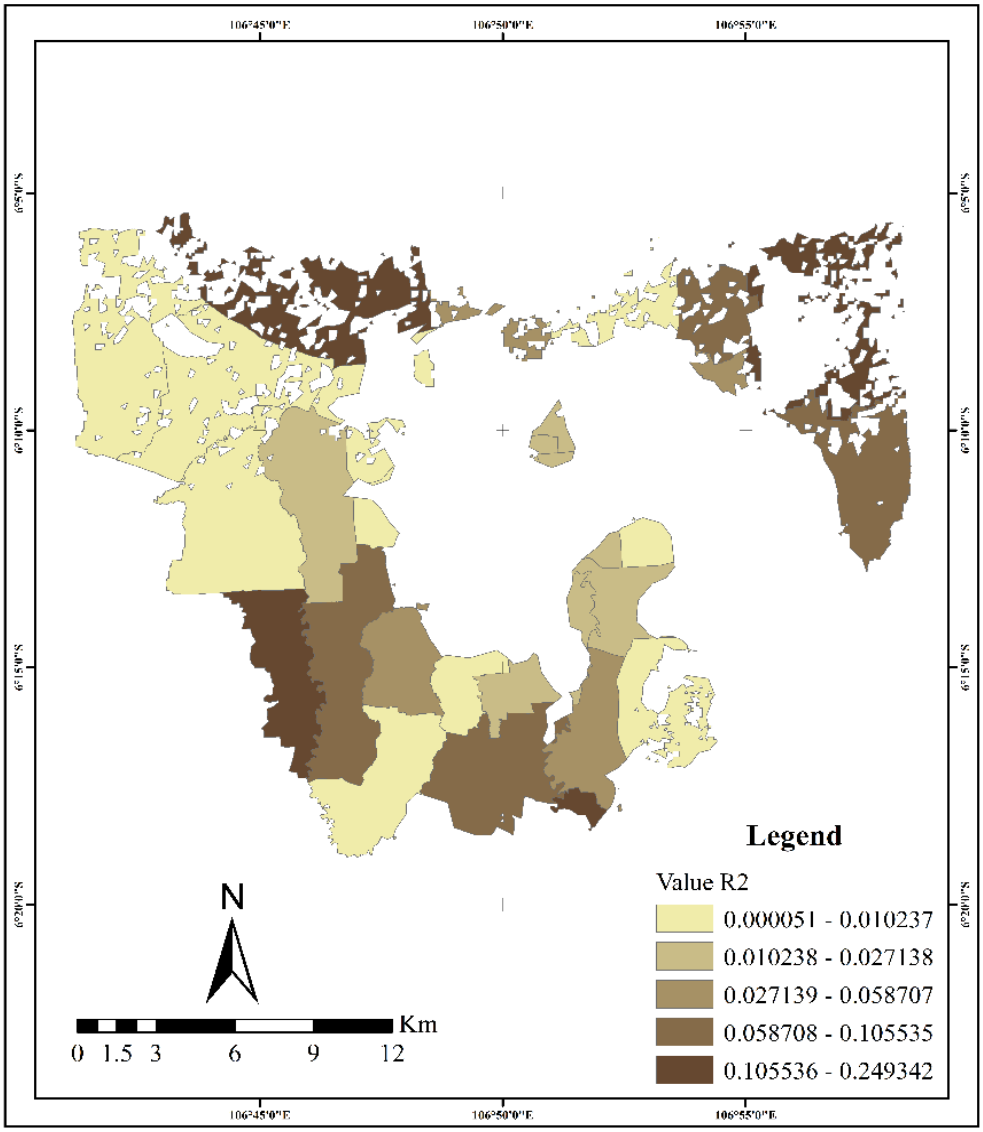

Fig. 4. $R^2$of the Distance from the Coast Variable.

To measure the distance from the coastline, this study utilized the centroid point of each administrative boundary polygon of sub-districts in Jakarta, ensuring a more spatially representative calculation. The map in **Fig. 4** presents the GWR results for the coastline distance variable. The local R^2 values for this variable range from as low as 0.00 to as high as 0.24, with notable concentrations in North and South Jakarta. The highest spatial correlation was observed in the districts of Penjaringan and Pesanggrahan. From the map, we can see differences in color across the areas of Jakarta. The color variations represent the different R^2 values from the GWR, indicating that there is a correlation between one location and another, with different R^2 values for each district. A few areas in Jakarta province have already experienced tidal flooding during high tide, which typically occurs in areas with biggest land subsidence (Abidin et al., 2015). Because of this, sea level rise will worsen land subsidence, with the potential continuation of rising sea levels along Jakarta's coastal areas, which are increasing at a rate of about 4–5 mm per year (Nurmaulia et al., 2010).

Jakarta's coastline generally has low wave energy, but sedimentation still occurs, especially in delta areas. Evidence of land growth over thousands of years can be seen in shoreline changes. The Cisadane and Citarum rivers have shifted their flow over time, but both have played a key role in shaping the land around Jakarta, especially in building coastal landforms. Marunda is one of the most affected areas, with the coastline retreating up to 750 meters over the past 40 years. Without adequate protection, around 225 hectares of land have been submerged by seawater, forcing thousands of residents to relocate. Tanjung Pasir, located in the northwest of Jakarta Bay, has also experienced severe coastal erosion. Once part of the old Cisadane River delta, this area is exposed to southwest monsoon winds, worsening erosion between 1948 and 1982, causing the coastline to recede by 250 meters and resulting in the loss of approximately 150 hectares of land. (Verstappen, 2000).

Based on the research of Zoysa et al., (2021) the rate of land subsidence along the Jakarta coastline varies significantly. When averaged over a 10-year period, the Penjaringan area shows a subsidence rate of up to 85 mm/year. This is similar to the changes in the distance from the coast observed in Muara Gembong, Bekasi, and Legon Kulon, Subang, where the distance from the coast has increased at rates of 200 and 150 meters per year, over the past two decades (2000-2020). This phenomenon is attributed to coastal inundation, coupled with hydrological changes and the expansion of built-up areas. (Solihuddin et al., 2021).

4.4. GWR Model of the Elevation

The elevation topography of a region is a key parameter that influences many processes in coastal changes (Gesch, 2009). As a result of low elevation areas or subsidence occurring in several regions in Jakarta, the city and low-lying coastal areas are now vulnerable to flooding triggered by seawater and sea level rise, with projections indicating increasing vulnerability by 2100 (Lakshmi, 2024). High-risk areas are characterized by low coastal relief, easily erodible substrates, evidence of past and present subsidence, widespread shoreline retreat, and high wave energy (Gornitz & Kanciruk, 1989).

The GWR analysis results of the elevation variable in relation to land subsidence in Jakarta are illustrated in **Fig. 5.** The R^2 values range from 0.00 to 0.25, indicating varying degrees of spatial correlation across sub-districts, The strongest spatial relationships with R^2 values approaching 0.25 are concentrated in North Jakarta and West Jakarta, particularly in Koja, Cilincing, Kalideres, Kembangan, and Pesanggrahan, with Koja and Cilincing standing out as the sub-districts with the highest values. In contrast, the lowest R^2 values close to 0.00 are generally found in the central and southern parts of Jakarta, suggesting a minimal influence of elevation on land subsidence in those areas. Jakarta's geomorphology plays a crucial role in these patterns. The city is traversed by 13 rivers that discharge into Jakarta Bay, with the Cisadane River in the west and the Citarum River in the east being the most significant in shaping sediment distribution. Historical shifts in the Citarum River's course and the accumulation of sediment in estuarine areas such as Gembong have significantly influenced the elevation profile along the coast (Verstappen, 2000). This shows high geomorphological activity in the area, where changing river patterns and river mouth shifts can affect the shape and elevation of the coastal areas (Holzer & Galloway, 2005).

In eastern Jakarta, the land is wider (60 km) due to the influence of the Citarum Delta. In contrast, Jakarta itself has a narrower coastal plain (only 7 km) because there are fewer large rivers carrying sediment to the shore. Meanwhile, the western part is lower, swampy, and has been affected by urban waste and housing projects over the past few decades. Areas with low elevation, especially near or below sea level, are more prone to flooding and tidal inundation. Coastal areas with low elevation are at high risk of sea-level rise. Low-lying coastal areas are at high risk of sea level rise due to the combination of low elevation. As a result, these materials will compact over time, especially with human activities and development occurring in the coastal areas. The dominant processes that determine the fate of the coastline are inundation (elevation loss due to sea level rise) and accretion/sedimentation (Chu, et.al. 2011). The sea level rise causes flooding in coastal areas, as seen in the coastal region of Semarang, which has already experienced coastal hazards due to tidal flooding and land subsidence (Marfai & King, 2008).

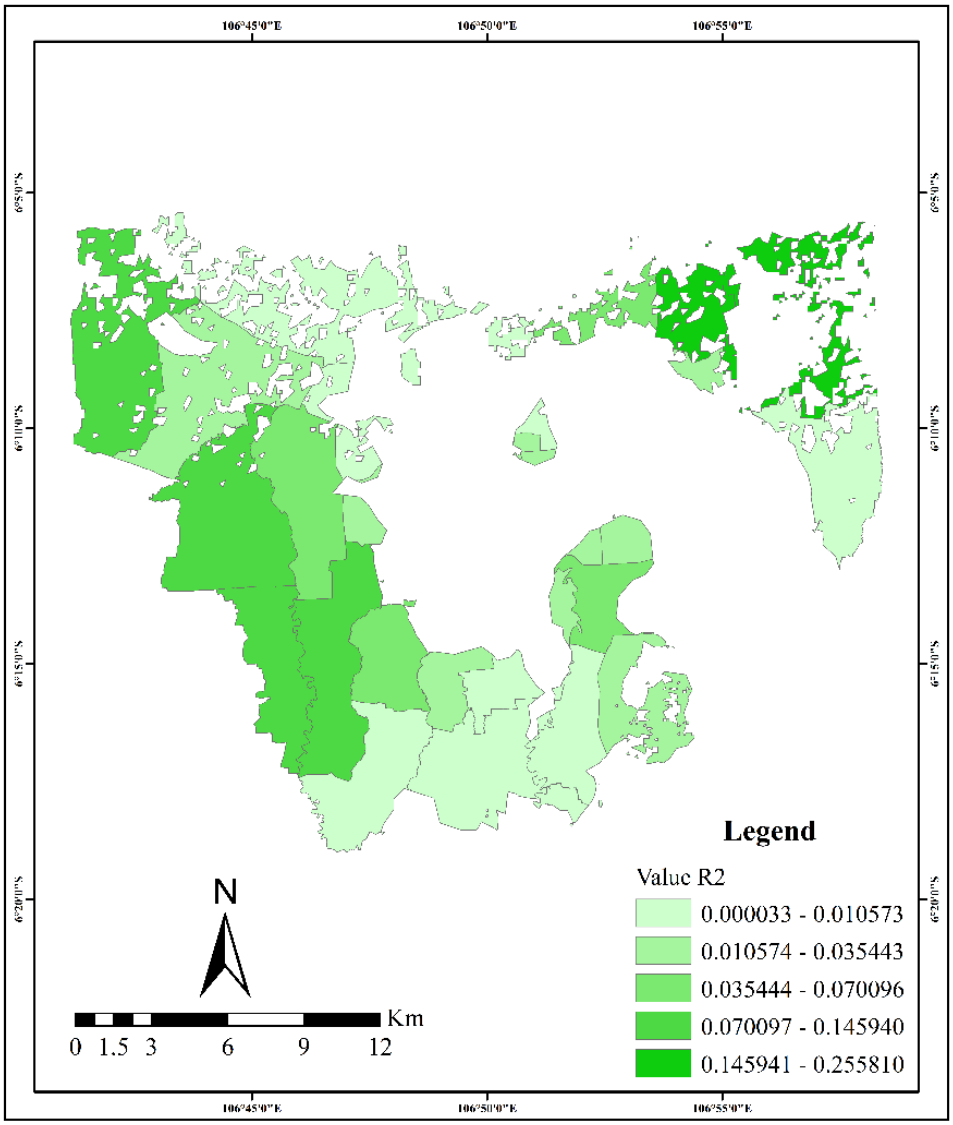

Fig. 5. $R^2$of Elevation Variable.

Coastal areas that have already experienced subsidence will continue to sink and worsen. As a result, seawater infiltrating the aquifer causes groundwater contamination (Gornitz, 1991). Based on the research of Nicholls et al., (2021) it is stated that the global average for relative sea level rise is 2.6 mm per year over the past two decades. However, because coastal populations tend to live in areas that are experiencing subsidence, they experience relative sea level rise at a rate up to four times faster, ranging from 7.8 to 9.9 mm per year.

Coastal wetlands are at risk from accelerated sea level rise because their ability to build up vertically is limited. This can lead to flooding, which causes sand to settle in tidal deltas and erosion of the coastline (Kanciruk, 1989). In the United States, approximately 26,000 km^2 of land has permanently subsided. Land subsidence causes permanent inundation, worsens flooding, changes topographic gradients, damages the land surface, and reduces the capacity of aquifers to store water (Galloway et al., 2008).

4.5. GWR Model of the Groundwater

Groundwater extraction, indicated by the number of wells in use, has increased due to the declining availability of surface water. This has led to a drop in groundwater levels and has accelerated the rate of land subsidence (Zhou et al., 2020; Faunt et al., 2016). Wells are widely used not only to meet household water needs but also to support industrial and factory operations in Jakarta. Approximately 64% of Jakarta's water consumption is still fulfilled through groundwater extraction from wells (Ali, 2011). The expansion of industrial activities and residential areas has contributed to a rise in groundwater use, resulting in land subsidence in many regions (Guzy & Malinowska, 2020; Chiao et al., 2014). This study finds a similar pattern in organic settlements, where many households rely on groundwater wells for more than 80% of their daily water use. Households frequently affected by flooding also tend to have higher water demand during the rainy season, particularly for cleaning purposes after flood events (Setiawan et al., 2017). The GWR map for the variable representing the number of wells used in Jakarta shows varying levels of spatial correlation with land subsidence across different regions, as illustrated in **Fig. 6**. The R^2 values for this variable range from 0.00 to 0.82, indicating that groundwater has a significant spatial influence in certain areas.

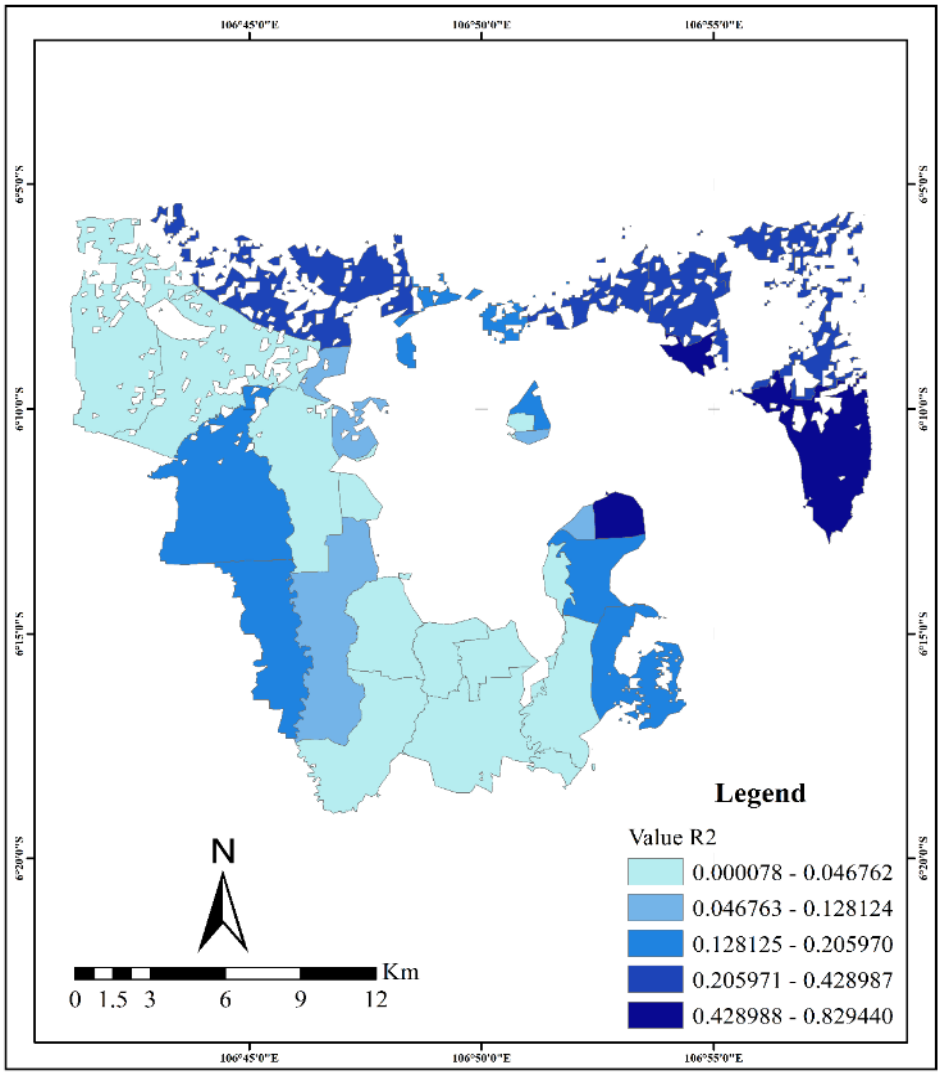

Fig. 6. $R^2$of Groundwater Variables.

The highest GWR values are observed in North Jakarta, particularly in the sub-districts of Penjaringan, Pademangan, and Cilincing, lower GWR values close to 0.00 are generally found in South Jakarta, East Jakarta, and parts of West Jakarta, suggesting weaker spatial relationships in these areas. Jakarta has experienced rapid development in land use change, from areas covered with vegetation to built-up areas. The increasing development of residential, industrial, and office areas, along with supporting infrastructure, has driven large-scale land conversion. Rising population density has contributed to the growing number of wells in use, and this trend continued in the following years (Setiawan et al., 2017). In this study, the groundwater variable is represented by the number of registered wells in Jakarta in 2022. The underlying assumption is that a higher number of wells reflects greater demand for groundwater due to densely populated residential areas. As built-up areas expand, the land's capacity for natural groundwater recharge declines, further accelerating the rate of land subsidence in affected regions.

Land subsidence shows a positive correlation with groundwater, particularly in urban city (Sajjad et al., 2023). This can lead to a decrease in the capacity of deep groundwater supply and groundwater storage resources (Liu et al., 2022; Ghazifard et al., 2016). Groundwater in North Jakarta, in addition to residential needs, has also significantly increased due to the tourism sector. This is similar from the reasearch by Teatini et al. (2006) in their study in Italy, which revealed that the southern region of the Po River Delta experienced dramatic land subsidence. This subsidence was largely caused by large-scale groundwater exploitation linked to economic development and the local tourism sector since the early 1950s could lead to sustained land subsidence. The land subsidence observed today is likely the result of past groundwater exploitation, further exacerbated by delayed compaction processes in clay aquitard layers between the depleted aquifers (Hutabarat, 2017; Abidin et al., 2004). In addition to sea water inundation many are unaware that low-lying coastal areas are also susceptible to groundwater inundation, which causes coastal flooding due to the rise in groundwater levels with sea level rise.

Apart from sea water inundation, many are unaware that low-lying coastal areas are also vulnerable to groundwater inundation, which occurs due to the rise in groundwater levels along with the increase in sea level. This also contributes to land subsidence, making the area increasingly saturated and leading to waterlogging. A sea level rise of 0.6 meters could cause significant flooding, and a 1-meter rise could inundate 10% of the densely populated coastal zone, with a width of 1 km. A study by Marfai & King (2008) in Hawaii found that the submerged area, including groundwater inundation, is more than twice the area submerged by seawater alone. Based on research in Shanghai city, groundwater exploitation and rapid urbanization are the main causes of most land subsidence. Although urbanization accelerates economic growth, human activities such as large-scale construction of skyscrapers, metro lines, and highways also contribute to this issue (Dong et al., 2014).

4.6. GWR Model of the Population Density

Land subsidence does not happen accidentally without reason. It results from a combination of natural and human activities (Gao et al., 2019; Wang et al., 2023). Jakarta Province, with its high population density, leads to increased human activities that impact water consumption (Setiawan et al., 2017). Meanwhile, limited groundwater resources are being over-exploited to meet these needs. This excessive exploitation leads to land subsidence, which affects soil stability and infrastructure, posing a risk of damage to buildings and drainage systems in the city. This happens in Jakarta's coastal areas, where the high population density increases the building load each year (Delinom et al., 2009) contributing to land subsidence (Hutabarat, 2017). The GWR analysis of the population density variable uncovers spatial variations in its influence on land subsidence across Jakarta, as represented in **Fig. 7.** The R^2 values for this variable range from 0.00 to 0.63, with higher values observed predominantly in North Jakarta, and in the northern areas of East and West Jakarta. Coastal areas with high population density, including population growth, unprecedented urbanization, and climate change, require significant amounts of groundwater, leading to excessive exploitation and resulting in land subsidence (Jia et al., 2019; Abidin et al., 2004). Excessive groundwater extraction, combined with large-scale infrastructure development, will have a major impact on land subsidence (Z. Du et al., 2018; Gao et al., 2019; Tran et al., 2022).

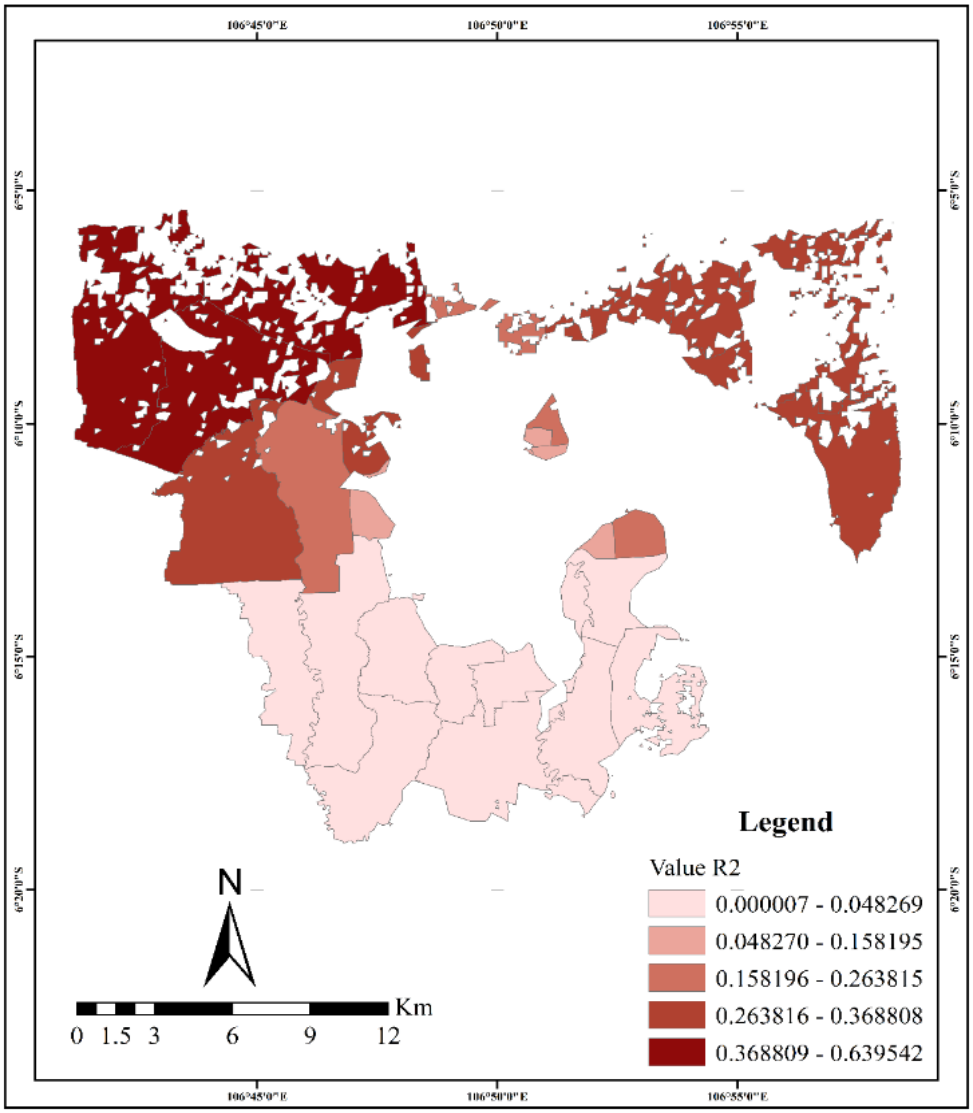

Fig. 7. R^2 of Population Density Variables.

Population growth in Jakarta has driven an increase in population density, accompanied by a rise in economic activities. This density has contributed to the expansion of various sectors, including entertainment, education, and the economy, even extending to reclaimed coastal areas designed to accommodate more infrastructure and residential developments. Even though Jakarta's economy is growing, there are also negative effects. One big problem is land subsidence, which means the ground is sinking. This can damage buildings and make floods worse, especially in coastal areas. The demand for water keeps increasing, but most of the water supply still comes from groundwater. Taking too much groundwater makes the land sink even more, especially in North Jakarta (Y. Du et al., 2020). Tanjung Priok and its surrounding areas have undergone significant changes due to erosion, seawater intrusion, and human activities. To the west of the port, the area mainly consists of wetlands, while to the east in Marunda, seawater intrusion has worsened due to river mouth changes and land subsidence (Verstappen, 2000). The same thing happened in Riyadh, Saudi Arabia. Because the city's population grew quickly, the land started sinking a lot up to 21 mm per year (Aljammaz et al., 2021).

4.7. GWR Model of the Built-Up Area

Land subsidence is closely linked to the expansion of built-up areas, which continues to grow due to population growth, economic activities, and industrialization. This issue is particularly evident in residential, industrial, and agricultural land use. Land subsidence happens mostly because of big changes in how land is used. At first, open land is used for farming or green spaces. But as more land is needed, these areas are turned into houses, roads, and factories. This change makes the ground heavier and more compact, causing it to sink over time. This happens because buildings and roads put extra weight and pressure on the ground (Faunt et al., 2016). As cities grow quickly, the land sinks even faster (Abidin et al., 2011). Areas with lots of houses and factories tend to sink more than other places (Zhou et al., 2020). To support spatial analysis related to land subsidence, built-up area data was extracted using Landsat 8 OLI imagery and processed with a supervised classification method. This approach produced a high overall accuracy of 95.45%, indicating that the classification results are highly reliable and closely match actual land cover conditions.

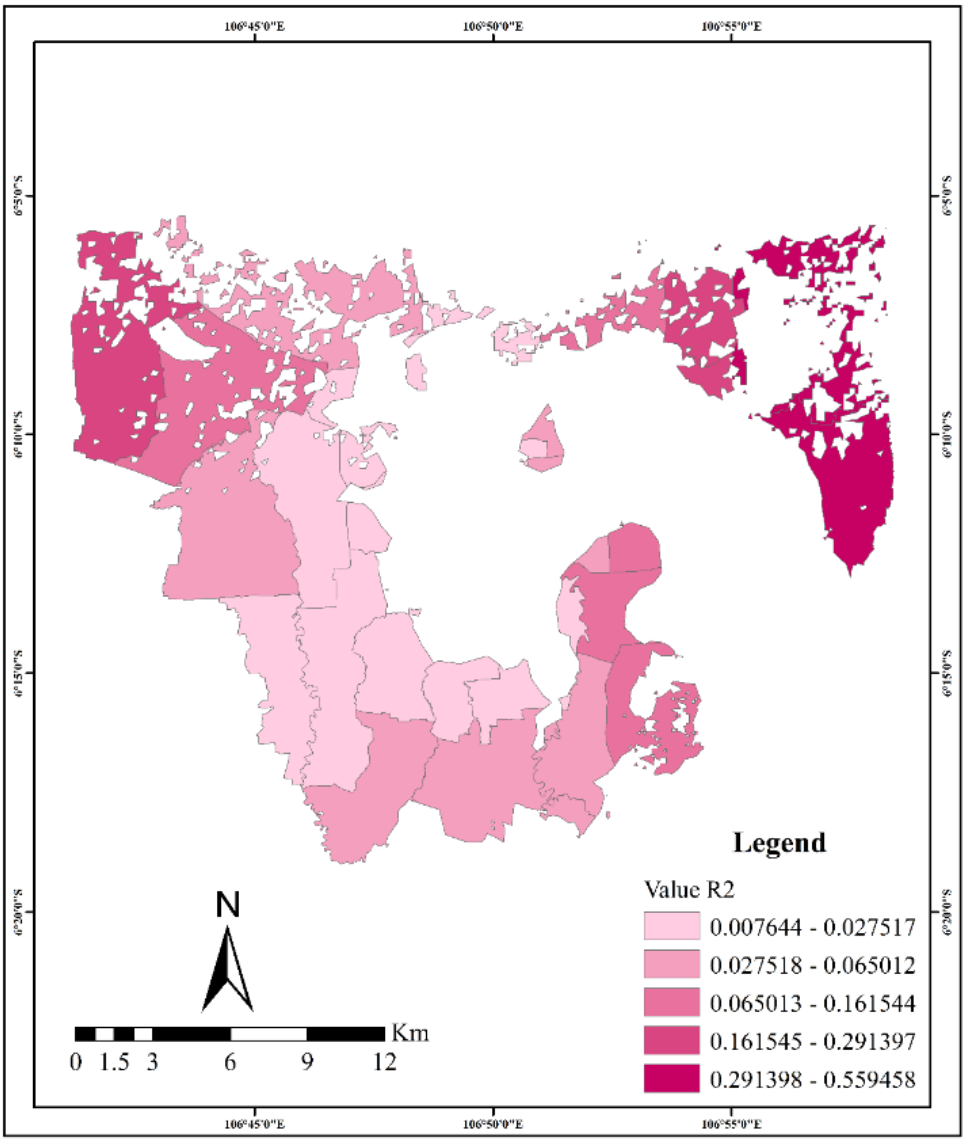

Fig. 8. $R^2$of Built Up Area Variables

The GWR analysis results for the built-up land variable show R^2 values ranging from 0.00 to 0.55, with relatively even distribution across various areas, particularly in North Jakarta, East Jakarta, and West Jakarta (**Fig. 8**). The highest GWR values are observed in Cilincing, Cakung, and Kalideres Districts, indicating a strong spatial relationship between built-up land and land subsidence in these regions. Urban development in these districts appears to play a significant role, likely due to increased surface pressure and reduced natural groundwater recharge. If this trend continues, many densely populated coastal zones could sink below sea level in the coming decades, increasing the risk of coastal flooding, endangering infrastructure, and posing serious challenges for sustainable development in Jakarta's coastal areas (Chaussard et al., 2013).

There is a strong relationship between built-up land use and land subsidence (Minderhoud et al., 2018). Land subsidence can significantly impact soil stability and its ability to support buildings. If subsidence continues, the risk of structural damage to infrastructure, buildings, and public facilities will increase, especially in densely populated areas with extensive urban development (Delinom et al., 2009). In North Jakarta, land subsidence can be observed through various physical indicators, such as cracks in permanent buildings and roads, changes in river and drainage flow patterns, and the expansion of flood-prone areas. These signs indicate significant subsidence in the region, affecting both coastal and inland areas (Abidin et al., 2015).

Similar to what has happened in Pakistan, land subsidence is classified based on land cover types, showing a strong correlation between variables. Urban areas and plantation vegetation, which require large amounts of groundwater extraction, also experience significant land subsidence (Ahmad et al., 2019). A similar situation is occurring in Iran, where the demand for groundwater resources continues to rise uncontrollably, particularly for domestic, agricultural, and industrial needs. As a result, the depletion of groundwater supplies has led to severe consequences. Per capita water resources in Iran have already decreased by more than 65% over the past four decades and are expected to decline by another 16% by 2025 (Motagh et al., 2008).

4.8. GWR Model for the Impact of Land Subsidence with All Parameters

Based on data processing using the Geographically Weighted Regression (GWR) model, the R-squared values were obtained and categorized into different ranges. This map serves as a model to illustrate the relationship between land subsidence and the selected variables or parameters. These variables include Built-Up Area, Population Density, Groundwater, Elevation, and Distance from the Coast, analyzed across several districts in Jakarta. The resulting R-squared values represent the strength of the relationship between land subsidence and these variables, which varies across different areas within the province of Jakarta.

The highest GWR values ranged from 0.00 to 0.56, indicating a strong spatial relationship between these variables and the rate of land subsidence (**Fig. 9**). Almost all areas in Jakarta exhibit high GWR influence values, with the highest observed ranging from 0.42 to 0.56, primarily in North Jakarta. Meanwhile, the lowest GWR values range from 0.17 to 0.22, showing spatial relationships between different regions. These interactions reflect a mutual influence between land subsidence and variables such as distance from the coast, elevation, groundwater, population density, and built-up area. The other research also shows similarities in that the variables of population density (Gao et al., 2019; Tirmizi & Khan, 2023; Younas et al., 2023), groundwater, and built-up area affect the rate of land subsidence (Faunt et al., 2016).

To verify the land subsidence data, GPS data from CORS (Continuously Operating Reference Station) stations were used as a reference dataset. This verification is crucial to clarify and ensure the quality and accuracy of the land subsidence measurements obtained from the SBAS-InSAR method. **Table 1** presents the verification results of land movement at several locations in Jakarta during the period 2017–2021, using data from the Sentinel-1 satellite and the GNSS CORS system managed by the Geospatial Information Agency (BIG) (Harintaka et al., 2024).

To verify the accuracy of the land subsidence data used in the GWR analysis, additional validation was conducted using GPS data measuring vertical displacement. Two monitoring points, UD and CORS CJKT, both located in the northern area of Jakarta, showed positive vertical displacement values.

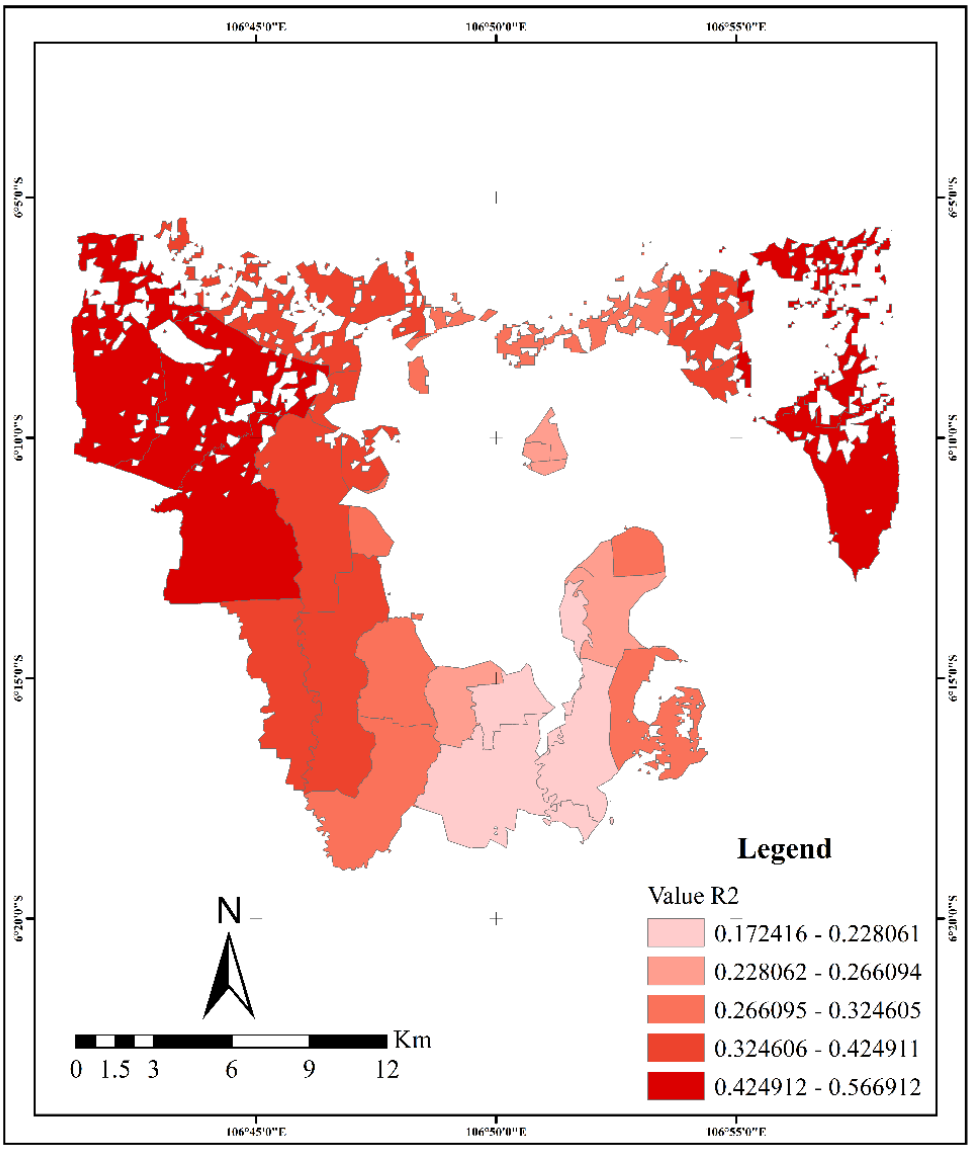

Fig. 9. $R^2$of GWR Land Subsidence Variables

Table 1.
Verification of Land Subsidence Measurements from SBAS-InSAR with GNSS CORS Stations

Data	Long	Lat	Value (mm/year)
UD	106.8786°	-6.1101°	1.590
CORS CJKT	106.8845°	-6.1101°	1.154

(Source: Harintaka et al., 2024)

The UD point recorded a ground surface uplift of approximately 1.590 mm/year, while CORS CJKT recorded an uplift of about 1.154 mm/year. These positive vertical values, often referred to as up and down displacement, indicate that the ground surface at these locations moved upward. This condition can be caused by several factors such as reduced groundwater extraction resulting in natural soil rebound and land stabilization efforts.

The North Jakarta has the highest GWR values, particularly in districts such as Penjaringan, Pademangan, Cilincing, and Tanjung Priok. This indicates that these areas experience higher rates of land subsidence compared to other parts of Jakarta, based on variables such as distance from the coast, elevation, groundwater, population density, and built-up land. These factors collectively show that North Jakarta consistently has higher GWR values than other areas in the city (Du et al., 2020; Abidin et al., 2011). West Jakarta and the northern part of East Jakarta also show relatively high GWR values, although not as high as North Jakarta. Districts such as Kalideres, Cengkareng, and Duren Sawit are significantly affected by high population density and rapid built-up land expansion, which increase surface load and accelerate land subsidence. In contrast, Central Jakarta and most of South Jakarta have lower GWR values compared to North and West Jakarta.

Based on the GWR results shown that the Kalideres District in West Jakarta has the highest influence, with a GWR value of 0.56, indicating a strong relationship between built-up land, elevation, population density, groundwater, and distance from the coast. Pasar Rebo District in East Jakarta has the lowest influence, with a GWR value of 0.17, showing a weaker relationship with the same variables. Other areas display varying degrees of influence, as seen in the map, which categorizes the R^2 values into five groups, illustrating their interconnected effects. The GWR model for overall land subsidence in Jakarta Province is based on the variables built-up land, elevation, population density, groundwater, and distance from the coast. The GWR model for overall land subsidence in Jakarta Province, based on the variables of built-up land, elevation, population density, groundwater, and distance from the coast (Eq. (4)).

$$\hat{y} = 5.05 + 0.23BuiltUpArea + (-0.027)Elevation + (-0.182)Population + (-0.004)Groundwater + (-0.214)CoastDistance \quad (4)$$

This formulation is the result of GWR calculations using data sourced from Jakarta. Therefore, it is most suitable for application in Jakarta. However, the model may also be applied to other regions that have similar geographical, environmental, and socio-economic characteristics. The applicability of the model in other areas depends on how closely their spatial conditions resemble those of Jakarta. Jakarta, known as the most densely populated city in Indonesia, continues to grow rapidly, leading to increased human activities, especially in expanding built-up areas. The rising population has also caused excessive groundwater (Setiawan et al., 2017). Over-extraction of groundwater contributes to land subsidence, as sand deposits on the bay floor are gradually eroded by strong currents due to the abrasion of previously stable sand ridges and surrounding areas.This abrasion can lead to sedimentation, especially in Jakarta's delta areas, which is visible through changes in the coastline. Since Jakarta Bay is the mouth of 13 rivers, erosion has caused the coastline to retreat by up to 250 meters (Verstappen, 2000). This process is part of natural activity, which contributes to land subsidence in Jakarta. As a result, fine materials in delta areas compact over time, especially with human activities and coastal development.

Land subsidence in Jakarta is significantly influenced by various spatial variables, including groundwater, elevation, distance from the coast, population density, and built-up areas. Among these variables, groundwater showed the highest R^2 value at 0.829, indicating the strongest relationship with land subsidence in the region. This suggests that excessive groundwater extraction is the primary factor accelerating subsidence, especially in urban areas with high water demand. Population density emerged as the second most influential variable, with an R^2 value of 0.639. This finding aligns with previous research conducted in Wuhan, China, which employed the Geographically Weighted Regression (GWR) method to examine the impact of urbanization on land subsidence. The study analyzed the impact of urbanization variables on land subsidence and found that all urbanization indicators were significantly correlated with land subsidence across the study area (Wang et al., 2022). This supports the conclusion that human activitiesparticularly in densely populated zones are the main drivers of land subsidence in Jakarta Province.

Built-up areas also showed a strong correlation, with an R^2 value of 0.559. Meanwhile, elevation and distance from the coast exhibited lower R^2 values of 0.255 and 0.249 respectively. Nevertheless, these values still indicate a relationship, especially in coastal zones that are naturally more vulnerable

to subsidence due to geological and hydrological conditions. The overall GWR model produced an R^2 value of 0.566, demonstrating a fairly strong spatial relationship between the combination of variables and land subsidence in Jakarta. The Geographically Weighted Regression (GWR) model produced an R^2 value of 0.566, indicating a moderately strong spatial correlation between the selected variables (such as distance from the coast, elevation, population density, groundwater, and built-up area) and land subsidence in Jakarta.This R^2 value means that approximately 56.6% of the variation in land subsidence across the study area can be explained by the combination of these variables included in the model.

5. CONCLUSIONS

Based on this study, Jakarta as a whole experiences significant land subsidence. Among the analyzed areas, North Jakarta has the highest subsidence rates, indicating a more severe impact in coastal regions. Groundwater shows the strongest correlation with land subsidence, suggesting that densely populated areas are more prone to ground sinking. In contrast, the distance from the coast and elevation has the least impact, implying that human activities play a more dominant role than natural topographic factors. The overall analysis highlights a strong relationship between land subsidence and factors such as groundwater, population density, built-up area, elevation, and the distance from the coast, emphasizing the urgent need for sustainable land and water resource management.

6. ACKNOWLEDGEMENT

We would like to extend heartfelt thanks to the research team for their dedicated efforts in completing this paper. Additionally, this research was made possible through the financial support from the DIPA BLU, Universitas Negeri Jakarta, under the grant number 368/UN39/HK.02/2023. The researchers also appreciate the blind reviewers for their insightful feedback, which greatly contributed to the enhancement of this paper.

REFERENCES

Abidin, H. Z., Andreas, H., Gumilar, I., Fukuda, Y., Pohan, Y. E., & Deguchi, T. (2011). Land subsidence of Jakarta (Indonesia) and its relation with urban development. *Natural Hazards*, *59*(3), 1753–1771. https://doi.org/10.1007/s11069-011-9866-9

Abidin, H. Z., Andreas, H., Gumilar, I., & Wibowo, I. R. R. (2015). On correlation between urban development, land subsidence and flooding phenomena in Jakarta. *IAHS-AISH Proceedings and Reports*, *370*, 15–20. https://doi.org/10.5194/piahs-370-15-2015

Agustan, A., Kriswati, E., Ito, T., Abdullah, F. M., Anantasena, Y., & Nugroho, D. (2021). Land Subsidence Rate of Jakarta Metropolitan Area Observed By Stacking Sentinel-1 Data. *IEEE Asia-Pacific Conference on Geoscience, Electronics and Remote Sensing Technology (AGERS) Land*, *September*, 1–5. https://doi.org/10.1109/AGERS53903.2021.9617239

Ahmad, W., Choi, M., Kim, S., & Kim, D. (2019). Detection of land subsidence and its relationship with land cover types using ESA Sentinel satellite data: a case study of Quetta Valley, Pakistan. *International Journal of Remote Sensing*, *40*(24), 9572–9603. https://doi.org/10.1080/01431161.2019.1633704

Akbar, G. D. P. N., & Setiawan, B. (2022). Analisis Penurunan Muka Tanah Kota Jambi Dengan Metode Differential Interferometry Synthetics Aperture Radar Tahun 2016 – 2021. *Jurnal Geosains Dan Remote Sensing*, *3*(1), 20–29. https://doi.org/10.23960/jgrs.2022.v3i1.71

Ali, F. (2011). *Personal communication. Technical board member of Jakarta Water Supply Regulatory Body*.

Aljammaz, A., Sultan, M., Izadi, M., Abotalib, A. Z., Elhebiry, M. S., Emil, M. K., Abdelmohsen, K., Saleh, M., & Becker, R. (2021). Land subsidence induced by rapid urbanization in arid environments: A remote sensing-based investigation. *Remote Sensing*, *13*(6), 1–24. https://doi.org/10.3390/rs13061109

Aobpaet, A., Cuenca, M. C., Hooper, A., & Trisirisatayawong, I. (2013). InSAR time-series analysis of land subsidence in Bangkok, Thailand. *International Journal of Remote Sensing*, *34*(8), 2969–2982. https://doi.org/10.1080/01431161.2012.756596

Asmadin, Siregar, V. P., Sofian, I., Jaya, I., & Wijanarto, A. B. (2021). *The Change in Elevation , Land Subsidence and Local Sea Level Rise Using Coastal Response Model in Jakarta The Change in Elevation , Land Subsidence and Local Sea Level Rise Using Coastal Response Model in Jakarta*. https://doi.org/10.1088/1755-1315/750/1/012010

Bagheri-Gavkosh, M., Hosseini, S. M., Ataie-Ashtiani, B., Sohani, Y., Ebrahimian, H., Morovat, F., & Ashrafi, S. (2021). Land subsidence: A global challenge. *Science of the Total Environment*, *778*. https://doi.org/10.1016/j.scitotenv.2021.146193

Berardino, P., Fornaro, G., Lanari, R., & Sansosti, E. (2002). A new algorithm for surface deformation monitoring based on small baseline differential SAR interferograms. *IEEE Transactions on Geoscience and Remote Sensing*, *40*(11), 2375–2383. https://doi.org/10.1109/TGRS.2002.803792

Bhatti, S. S., & Tripathi, N. K. (2014). Built-up area extraction using Landsat 8 OLI imagery. *GIScience and Remote Sensing*, *51*(4), 445–467. https://doi.org/10.1080/15481603.2014.939539

Bivand, R., & Yu, D. S. (2015). *Geographically Weighted Regression.*

Blachowski, B., & Gutkowski, W. (2016). Effect of damaged circular flange-bolted connections on behaviour of tall towers, modelled by multilevel substructuring. *Engineering Structures*, *111*, 93–103. https://doi.org/10.1016/j.engstruct.2015.12.018

Botey i Bassols, J., Declercq, P.-Y., Vàzquez-Suñé, E., & Gerard, P. (2023). PS-InSAR data, key to understanding and quantifying the hydromechanical processes underlying the compaction of aquifer systems. Case of West- and East-Flanders, Belgium. *Journal of Hydrology*, *624*, 129980. https://doi.org/https://doi.org/10.1016/j.jhydrol.2023.129980

Bott, L. M., Schöne, T., Illigner, J., Haghshenas Haghighi, M., Gisevius, K., & Braun, B. (2021). Land subsidence in Jakarta and Semarang Bay – The relationship between physical processes, risk perception, and household adaptation. *Ocean and Coastal Management*, *211*. https://doi.org/10.1016/j.ocecoaman.2021.105775

Bremard, T. (2022). Monitoring Land Subsidence: The Challenges of Producing Knowledge and Groundwater Management Indicators in the Bangkok Metropolitan Region, Thailand. *Sustainability (Switzerland)*, *14*(17). https://doi.org/10.3390/su141710593

Calderhead, A. I., Therrien, R., Rivera, A., Martel, R., & Garfias, J. (2011). Simulating pumping-induced regional land subsidence with the use of InSAR and field data in the Toluca Valley, Mexico. *Advances in Water Resources*, *34*(1), 83–97. https://doi.org/https://doi.org/10.1016/j.advwatres.2010.09.017

Cao, A., Esteban, M., Paolo, V., Valenzuela, B., Onuki, M., Takagi, H., Thao, N. D., & Tsuchiya, N. (2021). ScienceDirect Future of Asian Deltaic Megacities under sea level rise and land subsidence : current adaptation pathways for Tokyo , Jakarta , Manila , and Ho Chi Minh City. *Current Opinion in Environmental Sustainability*, *50*(June 2020), 87–97. https://doi.org/10.1016/j.cosust.2021.02.010

Chang, F., Dong, S., Yin, H., & Wu, Z. (2022). Using the SBAS InSAR technique to monitor surface deformation in the Kuqa fold-thrust belt, Tarim Basin, NW China. In *Journal of Asian Earth Sciences* (Vol. 231, Issue 163). https://doi.org/10.1016/j.jseaes.2022.105212

Chaussard, E., Amelung, F., Abidin, H., & Hong, S. H. (2013). Sinking cities in Indonesia: ALOS PALSAR detects rapid subsidence due to groundwater and gas extraction. *Remote Sensing of Environment*, *128*, 150–161. https://doi.org/10.1016/j.rse.2012.10.015

Choubin, B., Shirani, K., Hosseini, F. S., Taheri, J., & Rahmati, O. (2023). Scrutinization of land subsidence rate using a supportive predictive model: Incorporating radar interferometry and ensemble soft-computing. *Journal of Environmental Management*, *345*, 118685. https://doi.org/https://doi.org/10.1016/j.jenvman.2023.118685

Chu-Agor, M. L., Muñoz-Carpena, R., Kiker, G., Emanuelsson, A., & Linkov, I. (2011). Exploring vulnerability of coastal habitats to sea level rise through global sensitivity and uncertainty analyses. *Environmental Modelling & Software*, *26*(5), 593–604.

Declercq, P. Y., Gérard, P., Pirard, E., Walstra, J., & Devleeschouwer, X. (2021). Long-term subsidence monitoring of the alluvial plain of the scheldt river in antwerp (Belgium) using radar interferometry. *Remote Sensing*, *13*(6). https://doi.org/10.3390/rs13061160

Delinom, R. M., Assegaf, A., Abidin, H. Z., Taniguchi, M., Suherman, D., Lubis, R. F., & Yulianto, E. (2009). The contribution of human activities to subsurface environment degradation in Greater Jakarta Area, Indonesia. *Science of the Total Environment*, *407*(9), 3129–3141. https://doi.org/10.1016/j.scitotenv.2008.10.003

Dewi, R. P., Khofianida, A., Agista, D. E., Arrasyid, F. P., Kurniawati, Damayanti, S. I., & Putri, R. F. (2020). Landuse change in Jakarta Province: Trend, types, and socio-demographic factors. *IOP Conference Series: Earth and Environmental Science*, *451*(1). https://doi.org/10.1088/1755-1315/451/1/012055

Dong, S., Samsonov, S., Yin, H., Ye, S., & Cao, Y. (2014). Time-series analysis of subsidence associated with rapid urbanization in Shanghai, China measured with SBAS InSAR method. *Environmental Earth Sciences*, *72*(3), 677–691. https://doi.org/10.1007/s12665-013-2990-y

Du, Y., Feng, G., Liu, L., Fu, H., Peng, X., & Wen, D. (2020). Understanding land subsidence along the coastal areas of Guangdong, China, by analyzing multi-track MTInSAR data. *Remote Sensing*, *12*(2), 1–20. https://doi.org/10.3390/rs12020299

Du, Z., Ge, L., Ng, A. H. M., Zhu, Q., Yang, X., & Li, L. (2018). Correlating the subsidence pattern and land use in Bandung, Indonesia with both Sentinel-1/2 and ALOS-2 satellite images. *International Journal of Applied Earth Observation and Geoinformation*, *67*(November 2017), 54–68. https://doi.org/10.1016/j.jag.2018.01.001

Erban, L. E., Gorelick, S. M., & Zebker, H. A. (2014). Groundwater extraction, land subsidence, and sea-level rise in the Mekong Delta, Vietnam. *Environmental Research Letters*, *9*(8). https://doi.org/10.1088/1748-9326/9/8/084010

Faunt, C. C., Sneed, M., Traum, J., & Brandt, J. T. (2016). Water availability and land subsidence in the Central Valley, California, USA. *Hydrogeology Journal*, *24*(3), 675–684. https://doi.org/10.1007/s10040-015-1339-x

Figueroa-Miranda, S., Tuxpan-Vargas, J., Ramos-Leal, J. A., Hernández-Madrigal, V. M., & Villaseñor-Reyes, C. I. (2018). Land subsidence by groundwater over-exploitation from aquifers in tectonic valleys of Central Mexico: A review. *Engineering Geology*, *246*, 91–106. https://doi.org/10.1016/j.enggeo.2018.09.023

Fuhrmann, T., & Garthwaite, M. C. (2019). Resolving three-dimensional surface motion with InSAR: Constraints from multi-geometry data fusion. *Remote Sensing*, *11*(3). https://doi.org/10.3390/rs11030241

Galloway, D. L., Bawden, G. W., Leake, S. A., & Honegger, D. G. (2008). Land Subsidence Hazards. *Land Subsidence Hazards*, *Open-File Report 2008–1164*, 74 p. http://pubs.usgs.gov/of/2008/1164/

Gao, M., Gong, H., Li, X., Chen, B., Zhou, C., Shi, M., Guo, L., Chen, Z., Ni, Z., & Duan, G. (2019). Land subsidence and ground fissures in Beijing Capital International Airport (BCIA): Evidence from Quasi-PS InSAR analysis. *Remote Sensing*, *11*(12). https://doi.org/10.3390/rs11121466

Gesch, D. B. (2009). Analysis of lidar elevation data for improved identification and delineation of lands vulnerable to sea-level rise. *Journal of Coastal Research*, *2009*(SPECIAL ISSUE 53), 49–58. https://doi.org/10.2112/SI53-006.1

Gornitz, V. (1991). Global coastal hazards from future sea level rise. *Palaeogeography, Palaeoclimatology, Palaeoecology*, *89*(4), 379–398. https://doi.org/10.1016/0031-0182(91)90173-O

Guzy, A., & Malinowska, A. A. (2020). State of the art and recent advancements in the modelling of land subsidence induced by groundwater withdrawal. *Water (Switzerland)*, *12*(7). https://doi.org/10.3390/w12072051

Harintaka, H., Suhadha, A. G., Syetiawan, A., Ardha, M., & Rarasati, A. (2024). Current land subsidence in Jakarta: a multi-track SBAS InSAR analysis during 2017–2022 using C-band SAR data. *Geocarto International*, *39*(1). https://doi.org/10.1080/10106049.2024.2364726

Hasibuan, H. S., Tambunan, R. P., Rukmana, D., Permana, C. T., Elizandri, B. N., Putra, G. A. Y., Wahidah, A. N., & Ristya, Y. (2023). Policymaking and the spatial characteristics of land subsidence in North Jakarta. *City and Environment Interactions*, *18*(January), 100103. https://doi.org/10.1016/j.cacint.2023.100103

Higgins, S., Overeem, I., Tanaka, A., & Syvitski, J. P. M. (2013). Land subsidence at aquaculture facilities in the Yellow River delta, China. *Geophysical Research Letters*, *40*(15), 3898–3902. https://doi.org/10.1002/grl.50758

Holzer, T. L., & Galloway, D. L. (2005). *Impacts of land subsidence caused by withdrawal of underground fluids in the United States*.

Hutabarat, L. E. (2017). Study of Land Subsidence Due to Excessive Groundwater Extraction in DKI Jakarta. In *Kumpulan Karya Ilmiah Dosen Universitas Kristen Indonesia Delapan Windu* (pp. 360–374).

Illigner, J., Haghshenas, M., Gisevius, K., & Braun, B. (2021). *Land subsidence in Jakarta and Semarang Bay – The relationship between physical processes , risk perception , and household adaptation*. *211*. https://doi.org/10.1016/j.ocecoaman.2021.105775

Jia, X., O'Connor, D., Hou, D., Jin, Y., Li, G., Zheng, C., Ok, Y. S., Tsang, D. C. W., & Luo, J. (2019). Groundwater depletion and contamination: Spatial distribution of groundwater resources sustainability in China. *Science of the Total Environment*, *672*, 551–562. https://doi.org/10.1016/j.scitotenv.2019.03.457

Kamh, Y. Z., Khalifa, M. A., & El-Bahrawy, A. N. (2016). Comparative Study of Community Resilience in Mega Coastal Cities Threatened by Sea Level Rise: The Case of Alexandria and Jakarta. *Procedia - Social and Behavioral Sciences*, *216*(October 2015), 503–517. https://doi.org/10.1016/j.sbspro.2015.12.007

Kanciruk, V. G. P. (1989). *ASSESSMENT OF GLOBAL COASTAL HAZARDS FROM SEA LEVEL RISE*. *April*, 18–21.

Khan, S. D., Faiz, M. I., Gadea, O. C. A., & Ahmad, L. (2023). Study of land subsidence by radar interferometry and hot spot analysis techniques in the Peshawar Basin , Pakistan. *The Egyptian Journal of Remote Sensing and Space Sciences*, *26*(1), 173–184. https://doi.org/10.1016/j.ejrs.2023.02.001

Khan, S. D., Gadea, O. C. A., Tello Alvarado, A., & Tirmizi, O. A. (2022). Surface Deformation Analysis of the Houston Area Using Time Series Interferometry and Emerging Hot Spot Analysis. *Remote Sensing*, *14*(15). https://doi.org/10.3390/rs14153831

Koto, J., & Negara, R. B. (2018). *Review on Flood Prevention Remedies Conducted by Government of DKI Jakarta*. *9*(1), 7–16.

Kurnianti, D. N., Rustiadi, E., & Baskoro, D. P. T. (2015). Land Use Projection for Spatial Plan Consistency in Jabodetabek. *Indonesian Journal of Geography*, *47*(2), 124–131.

Lakshmi, V. (2024). Enhancing human resilience against climate change: Assessment of hydroclimatic extremes and sea level rise impacts on the Eastern Shore of Virginia, United States. *Science of The Total Environment, 947*, *17428*.

Leong, Y. Y., & Yue, J. C. (2017). A modification to geographically weighted regression. *International Journal of Health Geographics*, *16*(1), 1–18. https://doi.org/10.1186/s12942-017-0085-9

Liu, R., Zhao, Y., Cao, G., Wang, Q., Ma, M., Li, E., & Deng, H. (2022). Threat of land subsidence to the groundwater supply capacity of a multi-layer aquifer system. *Journal of Hydrology: Regional Studies*, *44*(October), 101240. https://doi.org/10.1016/j.ejrh.2022.101240

Mailendra, M., & Buchori, I. (2019). Kerusakan Lahan Akibat Kegiatan Penambangan Emas Tanpa Izin Disekitar Sungai Singingi Kabupaten Kuantan Singingi. *Jurnal Pembangunan Wilayah & Kota*, *15*(3), 174–188. https://doi.org/10.14710/pwk.v15i3.21304

Marfai, M. A., & King, L. (2008). Potential vulnerability implications of coastal inundation due to sea level rise for the coastal zone of Semarang city, Indonesia. *Environmental Geology*, *54*(6), 1235–1245. https://doi.org/10.1007/s00254-007-0906-4

Minderhoud, P. S. J., Coumou, L., Erban, L. E., Middelkoop, H., Stouthamer, E., & Addink, E. A. (2018). The relation between land use and subsidence in the Vietnamese Mekong delta. *Science of the Total Environment*, *634*, 715–726. https://doi.org/10.1016/j.scitotenv.2018.03.372

Minderhoud, P. S. J., Erkens, G., Sidiq, T. P., & Gumilar, I. (2019). *Land subsidence rate analysis of Jakarta Metropolitan Region based on D-InSAR processing of Sentinel data C-Band frequency Land subsidence rate analysis of Jakarta Metropolitan Region based on D-InSAR processing of Sentinel data C-Band frequency*. https://doi.org/10.1088/1742-6596/1185/1/012004

Motagh, M., Walter, T. R., Sharifi, M. A., Fielding, E., Schenk, A., Anderssohn, J., & Zschau, J. (2008). Land subsidence in Iran caused by widespread water reservoir overexploitation. *Geophysical Research Letters*, *35*(16), 1–5. https://doi.org/10.1029/2008GL033814

Nicholls, R. J., Lincke, D., Hinkel, J., Brown, S., Vafeidis, A. T., Meyssignac, B., Hanson, S. E., Merkens, J. L., & Fang, J. (2021). A global analysis of subsidence, relative sea-level change and coastal flood exposure. In *Nature Climate Change* (Vol. 11, Issue 4). https://doi.org/10.1038/s41558-021-00993-z

Nurmaulia, S. L., Fenoglio-marc, L., & Becker, M. (2010). Long-Term Sea Level Change From Satellite Altimetry and Tide Gauges in the Indonesian Region. *ESA Living Planet Symposium*, *2*(July), 2–8.

Pang, M., Du, E., Shoemaker, C. A., & Zheng, C. (2022). Efficient, parallelized global optimization of groundwater pumping in a regional aquifer with land subsidence constraints. *Journal of Environmental Management*, *310*, 114753. https://doi.org/https://doi.org/10.1016/j.jenvman.2022.114753

Prahasta. (2008a). *REMOTE SENSING : Praktis Pengindraan Jauh & Pengolahan Citra Dijital dengan Perangkat Lunak ER Maper*. Informatika Bandung.

Prahasta, E. (2008b). *Remote sensing: praktis penginderaan jauh dan pengolahan citra dijital dengan perangkat lunak er mapper* (Informatik).

Rachma, T. R. N., Silalahi, F. E. S., & Oktaviani, N. (2022). Monitoring 20 Years of Land Cover Change Dynamics in the Satellite Cities of Jakarta, Indonesia. *IOP Conference Series: Earth and Environmental Science*, *1111*(1). https://doi.org/10.1088/1755-1315/1111/1/012034

Rahman, S., Sumotarto, U., & Pramudito, H. (2018). Influence the condition land subsidence and groundwater impact of Jakarta coastal area. *IOP Conference Series: Earth and Environmental Science*, *106*(1). https://doi.org/10.1088/1755-1315/106/1/012006

Rashid, N., Alam, J. A. M. M., Chowdhury, M. A., & Islam, S. L. U. (2022). Impact of landuse change and urbanization on urban heat island effect in Narayanganj city, Bangladesh: A remote sensing-based estimation. *Environmental Challenges*, *8*(October 2021), 100571. https://doi.org/10.1016/j.envc.2022.100571

Sadeghi, H., Golaghaei Darzi, A., Voosoghi, B., Akbari Garakani, A., Ghorbani, Z., & Fazel Mojtahedi, S. F. (2023). Assessing the vulnerability of Iran to subsidence hazard using a hierarchical FUCOM-GIS framework. *Remote Sensing Applications: Society and Environment*, *31*, 100989. https://doi.org/https://doi.org/10.1016/j.rsase.2023.100989

Sajjad, M. M., Wang, J., Afzal, Z., Hussain, S., Siddique, A., Khan, R., Ali, M., & Iqbal, J. (2023). Assessing the Impacts of Groundwater Depletion and Aquifer Degradation on Land Subsidence in Lahore, Pakistan: A PS-InSAR Approach for Sustainable Urban Development. *Remote Sensing*, *15*(22). https://doi.org/10.3390/rs15225418

Sari, D. P., Wartaman, A. S., & Luru, M. N. (2021). The characteristic of urban sprawl in Bekasi City, Indonesia. *IOP Conference Series: Earth and Environmental Science*, *737*(1). https://doi.org/10.1088/1755-1315/737/1/012029

Sari, H., Parluhutan, R., Rukmana, D., Permana, C. T., Nur, B., Aswin, G., Putra, Y., Nurul, A., & Ristya, Y. (2023). Policymaking and the spatial characteristics of land subsidence in North Jakarta. *City and Environment Interactions*, *18*(March), 100103. https://doi.org/10.1016/j.cacint.2023.100103

Septiani, R., Citra, I. P. A., & Nugraha, A. S. A. (2019). Perbandingan Metode Supervised Classification dan Unsupervised Classification terhadap Penutup Lahan di Kabupaten Buleleng. *Jurnal Geografi : Media Informasi Pengembangan Dan Profesi Kegeografian*, *16*(2), 90–96. https://doi.org/10.15294/jg.v16i2.19777

Setiawan, C., Suratman, S., & Marfai, M. A. (2017). The Relationship between Total Income and Groundwater Utilization on Fluviomarine Landform Area in Jakarta. *Forum Geografi*, *31*(1), 69–82. https://doi.org/10.23917/forgeo.v31i1.2851

Situmorang, D., Arhatin, R. E., & Lumban-Gaol, J. (2021). Land subsidence detection in Jakarta Province using Sentinel-1A Satellite Imagery Land subsidence detection in Jakarta Province using Sentinel- 1A Satellite Imagery. *IOP Conf. Series: Earth and Environmental Science*. https://doi.org/10.1088/1755-1315/944/1/012036

Solihuddin, T., Husrin, S., Mustikasari, E., Heriati, A., Kepel, T. L., Salim, H. L., Risandi, J., & Dwiyanti, D. (2021). Coastal Inundation and Land Subsidence in North Coast of West Java: A New Hazard? *IOP Conference Series: Earth and Environmental Science*, *925*(1). https://doi.org/10.1088/1755-1315/925/1/012015

Syafriani, D., Fikri, S., & Guvil, Q. (2022). Monitoring of Land Surface Change in Padang City Using Dinsar Sentinel-1a Method. *Journal of Applied Geospatial Information*, *6*(2), 615–619. https://doi.org/10.30871/jagi.v6i2.4134

Tambunan, M. P. (2017). The pattern of spatial flood disaster region in DKI Jakarta. *IOP Conference Series: Earth and Environmental Science*, *56*(1). https://doi.org/10.1088/1755-1315/56/1/012014

Teatini, P., Ferronato, M., Gambolati, G., & Gonella, M. (2006). Groundwater pumping and land subsidence in the Emilia-Romagna coastland, Italy: Modeling the past occurrence and the future trend. *Water Resources Research*, *42*(1), 1–19. https://doi.org/10.1029/2005WR004242

Tirmizi, O., & Khan, S. D. (2023). Factors of Subsidence in Katy, Texas, USA. *Remote Sensing*, *15*(18), 4424. https://doi.org/10.3390/rs15184424

Tran, D.-H., Wang, S.-J., & Nguyen, Q. C. (2022). Uncertainty of heterogeneous hydrogeological models in groundwater flow and land subsidence simulations – A case study in Huwei Town, Taiwan. *Engineering Geology*, *298*, 106543. https://doi.org/https://doi.org/10.1016/j.enggeo.2022.106543

Verstappen, H. T. (2000). *Outline of the Geomorphology of Indonesia: A Case Study on Tropical Geomorphology of a Techtogene Region* (79th ed.). ITC Publication.

Wang, Z., Guo, L., Gong, H., Li, X., Zhu, L., Sun, Y., Chen, B., & Zhu, X. (2023). Land subsidence simulation based on Extremely Randomized Trees combined with Monte Carlo algorithm. *Computers and Geosciences*, *178*(July), 105415. https://doi.org/10.1016/j.cageo.2023.105415

Wang, Z., Liu, Y., Zhang, Y., Liu, Y., Wang, B., & Zhang, G. (2022). Spatially Varying Relationships between Land Subsidence and Urbanization: A Case Study in Wuhan, China. *Remote Sensing*, *14*(2). https://doi.org/10.3390/rs14020291

Younas, M., Khan, S. D., Tirmizi, O., & Hamed, Y. (2023). Geospatial analytics of driving mechanism of land subsidence in Gulf Coast of Texas, United States. *Science of The Total Environment*, *902*, 166102. https://doi.org/https://doi.org/10.1016/j.scitotenv.2023.166102

Yudhistira, M. H., Sastiono, P., & Meliyawati, M. (2020). Exploiting unanticipated change in block rate pricing for water demand elasticities estimation: Evidence from Indonesian suburban area. *Water Resources and Economics*, *32*, 100161. https://doi.org/https://doi.org/10.1016/j.wre.2020.100161

Zhou, C., Gong, H., Chen, B., Gao, M., Cao, Q., Cao, J., Duan, L., Zuo, J., & Shi, M. (2020). Land subsidence response to dierent land use types and water resource utilization in Beijing-Tianjin-Hebei, China. *Remote Sensing*, *12*(3). https://doi.org/10.3390/rs12030457

Zhu, L., Gong, H., Li, X., Wang, R., Chen, B., Dai, Z., & Teatini, P. (2015). Land subsidence due to groundwater withdrawal in the northern Beijing plain, China. *Engineering Geology*, *193*(June 2020), 243–255. https://doi.org/10.1016/j.enggeo.2015.04.020

Zoysa, R. S. De, Schöne, T., Herbeck, J., Illigner, J., Haghighi, M., Simarmata, H., Porio, E., Rovere, A., & Hornidge, A. K. (2021). The “wickedness” of governing land subsidence: Policy perspectives from urban southeast Asia. *PLoS ONE*, *16*(6 June), 1–25. https://doi.org/10.1371/journal.pone.0250208

SPATIO-TEMPORAL MODELING FOR THE ANALYSIS OF HYDROLOGICAL DROUGHT AND ITS IMPACT ON RICE PRODUCTION IN THE UPPER BENGAWAN SOLO BASIN, CENTRAL JAVA, INDONESIA

Santhyami SANTHYAMI [1,2] *, ***Jumadi JUMADI*** [2,3], ***Kuswaji Dwi PRIYONO*** [2,3], ***Triastuti RAHAYU*** [1,2], ***Dewi Novita SARI*** [2,3], ***Murnira OTHMAN*** [4], ***Rudiyanto RUDI*** [2,3]

DOI: 10.21163/GT_2025.202.16

ABSTRACT

Hydrological drought is a climate-induced disaster that directly impacts the agricultural sector, particularly rice production. This study aims to model drought in a spatial-temporal context and analyse its impact on rice production in the Upper Bengawan Solo River Basin, Central Java, Indonesia, over the period 2017–2024. The analysis was conducted using Geographic Information Systems (GIS) based on Sentinel-2A satellite imagery, annual rainfall data, and rice production records. Drought severity was quantified using the Normalised Difference Drought Index (NDDI). The results of the drought modelling were validated through correlation and regression analyses with rainfall data and the extent of drought-affected areas. Meanwhile, the impact of drought on rice production was assessed using non-parametric analysis via the LOWESS method. The findings indicate that the spatial-temporal approach is effective in identifying drought distribution and trends. Spatially, severe drought occurred in Wonogiri Regency, covering up to 1,203,014.20 hectares, while temporally, the peak occurred in 2018 with a drought area of 571,438.60 hectares. Validation tests revealed a strong positive correlation between NDDI values and drought extent ($r = 0.84$), and a negative correlation between NDDI and rainfall ($r = -0.74$), indicating that higher NDDI values correspond with wider drought-affected areas and lower rainfall. Linear regression analysis confirmed NDDI as a significant indicator for drought monitoring, with a coefficient of determination $R^2 = 0.706$, suggesting that 70.6% of the variance in drought area can be explained by NDDI, and a statistically significant p-value ($p = 0.009$, $p < 0.05$). Moreover, LOWESS analysis showed a non-linear (U-shaped) relationship between NDDI and rice production, with the highest yields at low NDDI values (2.42–2.44 million tons), declining at medium NDDI levels (~2.20 million tons), and rising again at high NDDI values (2.35 million tons). This pattern suggests that the impact of drought on rice production is not linear and is likely influenced by additional factors such as irrigation infrastructure and crop management practices. Overall, this study affirms that satellite-based spatial-temporal modelling is an effective approach for analysing hydrological drought and understanding its implications for agricultural productivity.

Key-words: *Spatio-temporal modelling; Hydrological drought; Sentinel-2A satellite imagery; Rice production.*

1. INTRODUCTION

Ongoing global climate change is contributing to rising temperatures and increasing instability in atmospheric conditions worldwide, resulting in more frequent extreme weather events (Hadibasyir et al., 2023; Mustikaningrum et al., 2023).

---

[1] *Department of Biology Education, Faculty of Teacher Training and Education, Universitas Muhammadiyah Surakarta, 57162 Surakarta, Jawa Tengah, Indonesia. (SS) san915@ums.ac.id, (TR) triastuti.rahayu@ums.ac.id*

[2] *Center for Research Innovation in Mitigation and Adaptation of Tropical Climate Change, Universitas Muhammadiyah Surakarta, 57162 Surakarta, Jawa Tengah,Indonesia. (JJ) jumadi@ums.ac.id, (KDP) kdp130@ums.ac.id, (DNS) dns104@ums.ac.id, (RR) rud148@ums.ac.id*

[3] *Department of Geography, Faculty of Geography, Universitas Muhammadiyah Surakarta, Indonesia.*

[4] *Institute for Environment and Development (LESTARI), Universiti Kebangsaan Malaysia, 43600 Bangi, Selangor, Malaysia. (MO) murnira@ukm.edu.my*

** Corresponding author:) san915@ums.ac.id*

According to the Meteorology, Climatology, and Geophysics Agency (BMKG), Indonesia is generally experiencing higher-than-average air temperatures. In fact, the average air temperature in September 2024 was the highest ever recorded for that month since 1981 (BMKG, 2025). These climate dynamics are causing fluctuations in regional water availability and have the potential to elevate the risk of drought, ultimately exerting negative impacts on the agricultural sector, particularly rice production (Anna et al., 2024; Arifin et al., 2023; Kumar et al., 2022; Sigit & Anna, 2023).

Drought is a hydrometeorological disaster that frequently affects various regions across Indonesia. Over the five-year period from 2020 to 2024, a total of 1,088 drought-related disasters were recorded, resulting in 23 fatalities, 104 injuries, 6,349,633 people affected, 810 displaced persons, and 11,895 damaged houses. In the Upper Bengawan Solo River Basin, which encompasses the cities and regencies of Surakarta, Boyolali, Klaten, Wonogiri, Sukoharjo, Sragen, and Karanganyar, 36 drought incidents were reported, causing 3 deaths, 4 injuries, 108,742 people affected, 5 displaced persons, and 321 damaged houses (National Disaster Management Agency, 2025).

The severity of the drought's impact has led residents in the study area to become more alert to such disasters, particularly as the region is dominated by food crop agriculture, with approximately 60% of the population engaged in the agricultural sector (Central Java Provincial Statistics Agency, 2024). Prolonged droughts can reduce water availability for irrigation and domestic use (Bibi & Rahman, 2023; Christian et al., 2023; Hussain et al., 2023; Zhang et al., 2023), and diminish rice production, ultimately threatening local food security (Laksono & Nurgiyatna, 2020; Safura & Sekaranom, 2024).

With technological advancements, the detection of hydrological drought can now be conducted rapidly using satellite imagery data through several approaches, including the Normalised Difference Vegetation Index (NDVI), Vegetation Health Index (VHI), Normalised Difference Water Index (NDWI), Land Surface Temperature (LST), and Normalised Difference Drought Index (NDDI). Each approach has its own strengths and limitations. A detailed summary of the advantages and disadvantages of each method is presented in **Table 1**.

Table 1.
Advantages and Limitations of Satellite Image-Based Drought Detection Index Methods.

Method	Drought Detection Process	Advantages	Limitations	Reference
Normalised Difference Vegetation Index NDVI)	Drought detection based on plant greenness	Most widely used for vegetation monitoring	Relies on a single parameter	(Mirzaee & Mirzakhani Nafchi, 2023)
Vegetation Health Index (VHI)	Drought detection based on vegetation health	More accurate than NDVI as it incorporates temperature factors	Requires additional indices	(Zeng et al., 2022)
Normalised Difference Water Index (NDWI)	Drought detection based on moisture and water content	More accurate than NDVI as it incorporates water-related factors	Susceptible to atmospheric interference and open land conditions	(Marfuah & Useng, 2023)
Land Surface Temperature (LST)	Detects drought based on land surface temperature	Capable of detecting drought thermally	Requires calibration due to strong influence of land cover and atmosphere	(Shashikant et al., 2021)
Normalised Difference Drought Index NDDI)	Drought detection combining vegetation, soil moisture, and water	More accurate than other methods as it combines NDVI and NDWI	Requires more complex multispectral data	(Artikanur et al., 2022; Mujiyo et al., 2023)

Meanwhile, drought trends and distribution can be effectively identified through spatio-temporal modelling using Geographic Information Systems (GIS) (Boori et al., 2022; Mohammed et al., 2023). Satellite imagery employed for hydrological drought analysis varies and includes Landsat, MODIS, and SENTINEL. Sentinel-2A satellite imagery is among the most widely used types due to its high spatial resolution and its capability to monitor vegetation and soil moisture regularly (Alonzo et al., 2023; Staszel et al., 2024; Varghese et al., 2021).

Several previous studies have analysed drought using satellite imagery through various vegetation index approaches. Almouctar et al. (2024) analysed drought using the NDVI index and soil surface temperature. Bashit et al. (2022) combined NDVI, NDWI, and LST in their research. Meanwhile, Wolteji et al. (2022) applied a satellite image-based approach incorporating several indices, namely the Normalised Difference Vegetation Index (NDVI), Vegetation Health Index (VHI), Land Surface Temperature (LST), and Normalised Difference Water Index (NDWI).

Regarding the use of spatio-temporal models for drought analysis, Alito and Kerebih (2024) stated that these models play a crucial role in agricultural decision-making, particularly in visualising the distribution and trends of drought within a region. Mirzaee and Mirzakhani Nafchi (2023) also noted that spatio-temporal models are highly effective in identifying variations in vegetation indices across a region and temporal trends. Details regarding the differences between previous research and the current study are presented in **Table 2**. Based on **Table 2**, it is evident that several studies have utilised satellite imagery to analyse drought using various vegetation indices such as NDVI, NDWI, LST, and VHI. Almouctar et al. (2024) and Bashit et al. (2022) combined several indices and validated their results with meteorological data; however, they did not apply spatio-temporal modelling or directly link the results to impacts on agricultural production.

Table 2.

Comparison with Previous Research.

Researcher	Index	Spatio-Temporal Approach	Analysis of Impact on Rice Production	Validation Method	Description
Almouctar et al., (2024)	NDVI and LST	No	No	Correlation validation with weather data & field observations	Focus on detecting vegetative drought and soil temperature
Bashit et al., (2022)	NDVI, NDWI, and LST	No	No	Cross-validation with meteorological data	Focus on vegetation index analysis only
Wolteji et al., (2022)	NDVI, VHI, LST, and NDWI	No	No	Statistical validation against historical data	Utilisation of various types of vegetation indices but no spatio-temporal analysis
Alito & Kerebih, (2024)	NDVI, LST, VCI, TCI	Yes	No	Spatio-temporal model validation with survey data	Emphasises the importance of spatio-temporal analysis in agriculture
Mirzaee & Mirzakhani Nafchi, (2023)	NDVI, NMDI	Yes	No	Temporal trend analysis and statistical validation	Analysing vegetation index trends based on spatio-temporal data
Santhyami, et al., (2024)	Sentinel-2A-based NDDI	Yes (2017–2024)	Yes (Rice production in the Upper Bengawan Solo River Basin)	Validation with statistical tests (correlation, regression, and non-parametric LOWESS analysis)	Combining multispectral imagery, spatio-temporal modelling, and real-world impacts on agricultural production

Wolteji et al. (2022) employed a more comprehensive combination of indices and statistical validation, but the integration of spatio-temporal modelling remained absent. Meanwhile, the studies by Alito and Kerebih (2024), as well as Mirzaee and Mirzakhani Nafchi (2023), are notable for their use of spatio-temporal modelling to observe drought trends and distribution over time, although neither explored the impact of drought on rice production.

In contrast to these previous studies, the present research integrates a multispectral approach using the NDDI with long-term spatio-temporal modelling and directly analyses the impact of drought on rice production. This is accomplished using various validation methods, including correlation analysis, regression analysis, and non-parametric LOWESS analysis. As such, this study offers a novel and comprehensive contribution to the field of drought and food security research. The study presents a robust observation-based drought monitoring model that not only delineates the spatial distribution and temporal dynamics of drought but also provides empirical evidence of the relationship between hydrological drought and declining rice production. The findings of this research can serve as a scientific basis for developing drought mitigation strategies and sustainable agricultural adaptation planning in drought- and flood-prone areas, such as the Upper Bengawan Solo River Basin.

2. STUDY AREA

The study area is the Upper Bengawan Solo Watershed, encompassing seven cities and regencies: Surakarta City, and the regencies of Sukoharjo, Boyolali, Klaten, Wonogiri, Karanganyar, and Sragen. The total area of the watershed spans 3,773.99 km^2. Astronomically, it lies between 110° 13'7.16"E and 110°26'57.10"E longitude, and between 7°26'33.15"S and 8°6'13.81"S latitude. The detailed location and boundaries of the study area are illustrated in **Figure 1**.

According to the Schmidt and Ferguson climate classification, the region falls under the moderate climate category, with an average annual rainfall of 119.45 mm in 2024, an average temperature of 27.4° C, and a mean relative humidity of 76%. The soil types identified in the region include alluvial, andosol, complex soils, grumusol, latosol, lithosol, mediterranean, and regosol. Lithosol is the most dominant soil type, covering 1,465.3 km^2, followed by regosol, which spans 951.3 km^2.

Land use within the watershed is diverse, comprising residential areas, commercial buildings and offices, rice fields, drylands, plantations, vacant land, and water bodies. The topography varies from flat and undulating plains to hilly and volcanic terrain. The majority of the area is relatively flat (with slopes of 0-<5%), covering 2,506.10 km^2.

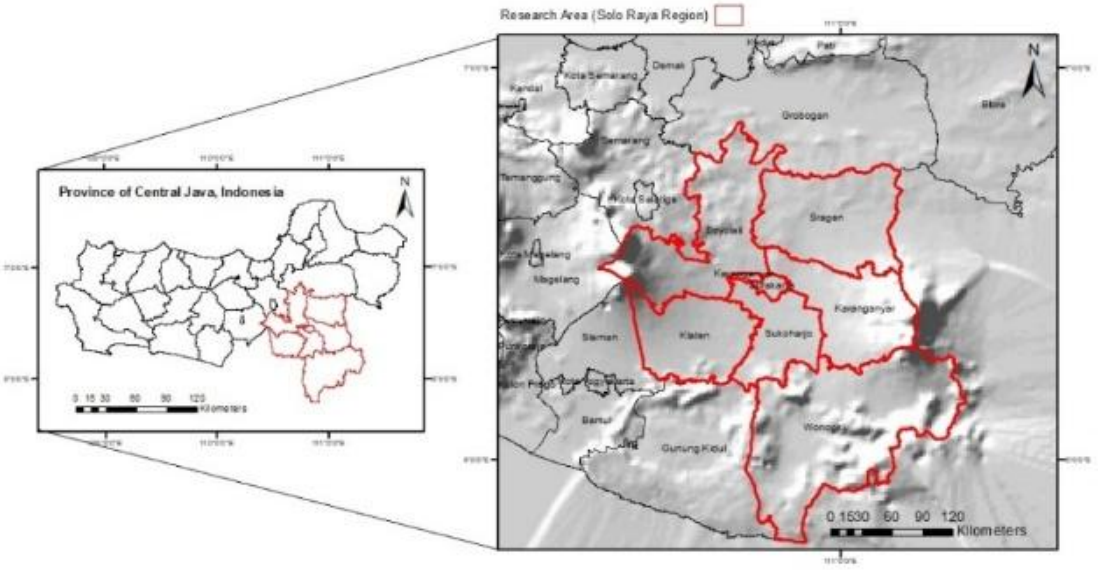

Fig. 1. Administrative Areas of the Upper Bengawan Solo River Basin.

Areas with slopes of 10-<30% account for 931.15 km², while the remainder consists of slopes between 5-<10% and above 30%. As of 2024, the population of the Upper Bengawan Solo Watershed reached 6,883,160, with an average population density of 2,689.29 inhabitants per km² and an annual population growth rate of 0.68%. The average sex ratio was recorded at 99.34. In the same year, total rice production in the study area amounted to 2,264,832 tonnes.

3. DATA AND METHODS

3.1. Sentinel-2A Satellite Imagery

Sentinel-2A satellite imagery is sourced from the Copernicus Open Access Hub, managed by the European Space Agency (ESA). This imagery is multispectral with high spatial resolution and encompasses 13 spectral bands, including: Band 1 (Coastal Aerosol), Band 2 (Blue), Band 3 (Green), Band 4 (Red), Band 5, 6, and 7 (Vegetation Red Edge), Band 8 (Near Infrared/NIR), Band 8A (Vegetation Red Edge), Band 9 (Water Vapour), Band 10 (Short-Wave Infrared/Cirrus), and Bands 11 and 12 (Short-Wave Infrared/SWIR). The spatial resolution of Sentinel-2A imagery varies by band, with resolutions of 10 m, 20 m, and 60 m (European Space Agency, 2025).

3.2. Image Preprocessing

Sentinel-2A imagery underwent atmospheric correction using the Sen2Cor Level-2A method, followed by geometric correction to align with the local UTM Zone 49S projection system. Annual composites were generated using the median composite approach to minimise the impact of residual cloud cover. Furthermore, spatial resolution enhancement was applied to the 20-metre bands through bilinear interpolation to improve image clarity.

3.3. Image Processing

At this stage, the following activities were carried out: atmospheric correction, geometric correction, image compositing, and image sharpening. Image processing was performed using a Geographic Information System (ArcGIS 10.3). Drought indices including NDVI, NDWI, and NDDI were calculated based on spectral band combinations, serving as indicators of vegetation condition and water availability. NDVI was employed to assess vegetation health, while NDWI was used to detect water content in both soil and vegetation. The NDDI index, combining NDVI and NDWI, served as a more integrated indicator of hydrological drought conditions. The specific formulae used for calculating each index are presented in **Table 3**.

Table 3.

Formulae for Calculating the NDVI, NDWI, and NDDI.

Spectral Vegetation Indices	Formulae	References
Normalised Difference Vegetation Index (NDVI)	$\frac{(\text{NIR} - \text{Red})}{(\text{NIR} + \text{Red})}$	(Ren et al., 2023)
Normalised Difference Water Index (NDWI)	$\frac{(\text{Green} - \text{NIR})}{(\text{Green} + \text{NIR})}$	(Shashikant et al., 2021)
Normalised Difference Drought Index (NDDI)	$\frac{(\text{NDVI} - \text{NDWI})}{(\text{NDVI} + \text{NDWI})}$	(Salas-Martínez et al., 2023)

3.4. NDDI Value Classification

The NDDI drought classification thresholds were adopted from relevant literature (Salas-Martínez et al., 2023) and locally adjusted based on the annual histogram distribution to ensure accurate representation of local conditions. The drought severity classification in the study area is based on NDDI values ranging from -1 to a maximum of 1. In this study, NDDI values are divided into five classes: water body, normal condition, mild, moderate, and severe drought. Further details are presented in **Table 4**.

Table 4.

Drought Severity Classification Based on NDDI Values.

NDDI Value Range	Drought Level
>0.46	Severe
0.4 – 0.6	Moderate
0.2 – 0.4	Mild
0 – 0.2	Normal Condition
≤ 0	Water Body

3.5. Spatio-Temporal Modelling of Hydrological Drought

Spatial modelling was conducted by overlaying annual NDDI maps with administrative boundaries of districts and cities within the Upper Bengawan Solo River Basin, resulting in a drought severity zoning map for each area. Meanwhile, temporal modelling involved analysing annual changes in drought index values over the period 2017–2024. This modelling process utilises Geographic Information System (GIS) technology, which facilitates the simultaneous integration and analysis of spatial and temporal data

3.6. Model Validation

Validation of the spatial-temporal model of hydrological drought in this study was performed using correlation and regression analyses between drought area, NDDI values, and rainfall. Data on drought area and NDDI values were derived from the spatial-temporal modelling results, while rainfall data were obtained from the Central Java Provincial Statistics Agency. Three primary relationships were analysed: (a) the correlation between drought area and NDDI values, (b) the correlation between drought area and rainfall, and (c) the correlation between NDDI values and rainfall. The Pearson correlation formulae applied is as follows:

$$r = \frac{\sum(x_i - \bar{x})(y_i - \bar{y})}{\sqrt{\sum(x_i - \bar{x})^2 \cdot \sum(y_i - \bar{y})^2}} \quad (1)$$

Description:

r: Pearson correlation coefficient (between -1 and 1)

x_i,y_i: Observation values for each variable

$\bar{x}$,$\bar{y}$: Average value of variables x and y

Interpretation of r values:

r>0.7: Indicates a strong relationship

0.3<r≤0.7: Indicates a moderate relationship

r≤0.3: Indicates a weak relationship

Significance tests were performed to assess whether the observed relationships were statistically significant at confidence levels of 95% ($p < 0.05$) or 99% ($p < 0.01$). Additionally, simple linear regression was utilised to examine the effect of the independent variable (NDDI) on the dependent variables (rainfall or drought area). The formulae used is as follows:

$$Y = \alpha + bX + \varepsilon \quad (2)$$

Description:

Y: Rainfall (mm/year) and drought area (ha)

X: NDDI index value

α: Intercept (Y value when X= 0)

b: Slope or regression coefficient (average change in Y for every 1 unit increase in X)

ε: Error or residual (difference between observed and predicted values)

3.7. Analysis of Drought Impact on Agricultural Production

This analysis of the impact of drought on agricultural production employs the Locally Weighted Regression (LOWESS) method. The parameters used to assess this impact are NDDI values and rice production data. There are several advantages to using this model, including: (a) the relationship between NDDI values and rice production is non-linear, so a linear regression approach cannot accurately describe the pattern of this relationship; (b) LOWESS is highly flexible because it does not assume a specific functional form such as linear or quadratic, but rather adjusts the curve shape based on local data; and (c) this method is suitable for small datasets. Mathematically, the formulae for this method are as follows:

$$\hat{y}_i = \sum_{j=1}^{n} w_{ij} y_j \tag{3}$$

Description:

$\hat{y}_i$: Estimated value at point xi

w_{ij}: Weight for data point j relative to xi, calculated based on the distance xj to xi,

y_j: Actual value at point j

The weight w_{ij}, is calculated using the tri-cube kernel function:

$$w_{ij} = \left(1 - \left(\frac{|x_j - x_i|}{d_i}\right)^3\right)^3 \quad \text{for } |x_j - x_i| \leq d_i \tag{4}$$

where d_i s the distance to the n-th point from x_i, used as the local neighbourhood range (determined by the parameter frac, which represents the percentage of nearest neighbours).

4. RESULTS

4.1. Spatio-temporal Analysis of Drought within the Study Area

Spatial and temporal approaches are essential for identifying the distribution and trends of drought within the study area. The spatial analysis in this study focuses on classifying drought severity based on its spatial distribution (**Table 5**). Meanwhile, the temporal analysis aims to identify recurring drought trends over multiple years (**Table 6**). This spatial-temporal approach facilitates a more detailed examination of drought dynamics and provides valuable insights into the contributing factors and their impacts on agricultural productivity. Furthermore, the results of the spatial-temporal drought analysis in the Upper Bengawan Solo River Basin are illustrated in **Figure 2**.

Table 5.

Drought Area by Region in the Upper Bengawan Solo River Basin.

No	Region	Area by Drought Category				
		Severe	Moderate	Mild	Normal Condition	Water Body
1	Boyolali	669,649.90	79,661.80	68,319.90	51,063.20	3,998.20
2	Klaten	458,779.50	47,182.50	30,484.20	21,311.50	537
3	Karanganyar	445,737.20	61,256	59,625.20	76,244.80	286.2
4	Sragen	640,449.70	48,066.90	43,640.30	52,473.60	9,659.40
5	Wonogiri	1,203,014.20	127,679.70	94,406.80	89,375.40	16,493.90
6	Sukoharjo	321,648.80	18,956.20	20,489.10	30,918.10	1,005.10
7	Surakarta	4,604.40	33.9	33.7	0	0

Based on **Table 5**, it is evident that Wonogiri Regency experiences the most extensive severe drought, covering an area of 1,203,014.20 hectares, followed by Boyolali, Sragen, Klaten, Karanganyar, Sukoharjo, with Surakarta City having the smallest area of 4,604.40 hectares. Similarly, in the categories of moderate, mild, and non-drought (normal conditions), Wonogiri Regency consistently has the largest area. The distribution of drought severity across the study area corresponds closely to its geographical size.

Table 6.

Drought Area by Years in the Upper Bengawan Solo River Basin.

Year	Area by Drought Category				
	Severe (Ha)	Moderate (Ha)	Mild (Ha)	Normal Condition (Ha)	Water Bodies (Ha)
2017	492,440.60	42,983.50	32,334.20	33,380.90	2,494.60
2018	571,438.60	14,025.50	7,176.80	10,690.60	216.7
2019	184,943.70	1,740.60	267.6	203	15.3
2020	162,143.60	8,718.20	10,720.50	4,358.20	493.5
2021	159,050.10	15,177.90	8,738.00	6,485.40	2,017.20
2022	75,842.50	39,278.30	37,303.50	37,070.50	1,972.50
2023	176,373.50	6,174.80	3,186.10	4,032.80	1,711.50
2024	159,050.10	15,177.90	8,738.00	6,485.40	2,017.20

Based on **Table 6**, the area classified as severely dry fluctuates annually, peaking in 2018 at 571,438.60 ha, before decreasing significantly to 75,842.50 ha in 2022. The area under normal conditions also varies, showing an increase in 2022 (37,070.50 ha) after lower levels in preceding years. Additionally, the extent of water bodies changes each year, reaching its highest in 2017 (2,494.60 ha) and its lowest in 2019 (15.3 ha). A detailed spatial-temporal analysis of hydrological drought in the Upper Bengawan Solo River Basin is illustrated in **Figure 2**. Based on **Figure 2**, the spatial distribution shows that the southeastern part of the watershed, particularly Wonogiri and Sragen, consistently experiences severe drought throughout the year. This pattern is closely related to the hilly topography, which hinders water drainage, and the lower rainfall in these areas compared to the central regions such as Klaten and Sukoharjo.

4.2. Drought Model Validation

The validation of the spatial-temporal modelling results of hydrological drought in this study was conducted using statistical methods, specifically correlation and regression analyses. The variables involved were drought extent, NDDI values, and rainfall (**Table 7**). Data on drought extent and NDDI values were obtained from the spatial-temporal modelling results, while rainfall data were sourced from the Central Java Provincial Statistics Agency. Three primary relationships were examined: (a) the correlation between drought extent and NDDI values, (b) the correlation between drought extent and rainfall, and (c) the correlation between NDDI values and rainfall. The results of the correlation analysis are presented in **Table 8** and **Figure 3**, while the regression results are shown in **Table 9** and **Figure 4**. Based on **Table 7**, it can be observed that this study employs three main variables in the statistical tests (correlation and regression): the area affected by drought (in hectares), the drought index value (NDDI), and the average annual rainfall (mm/year) within the Upper Bengawan Solo River Basin (DAS) for the period 2017‑2024. These three variables exhibit significant fluctuations from year to year. In 2018, the drought-affected area reached its peak, coinciding with a spike in the NDDI value. Conversely, 2022 recorded the highest rainfall and the lowest drought extent. The patterns identified in this dataset provide a critical foundation for statistical testing, both in terms of correlation and regression, to better understand the interrelationship between drought dynamics and the climatic factors that influence them.

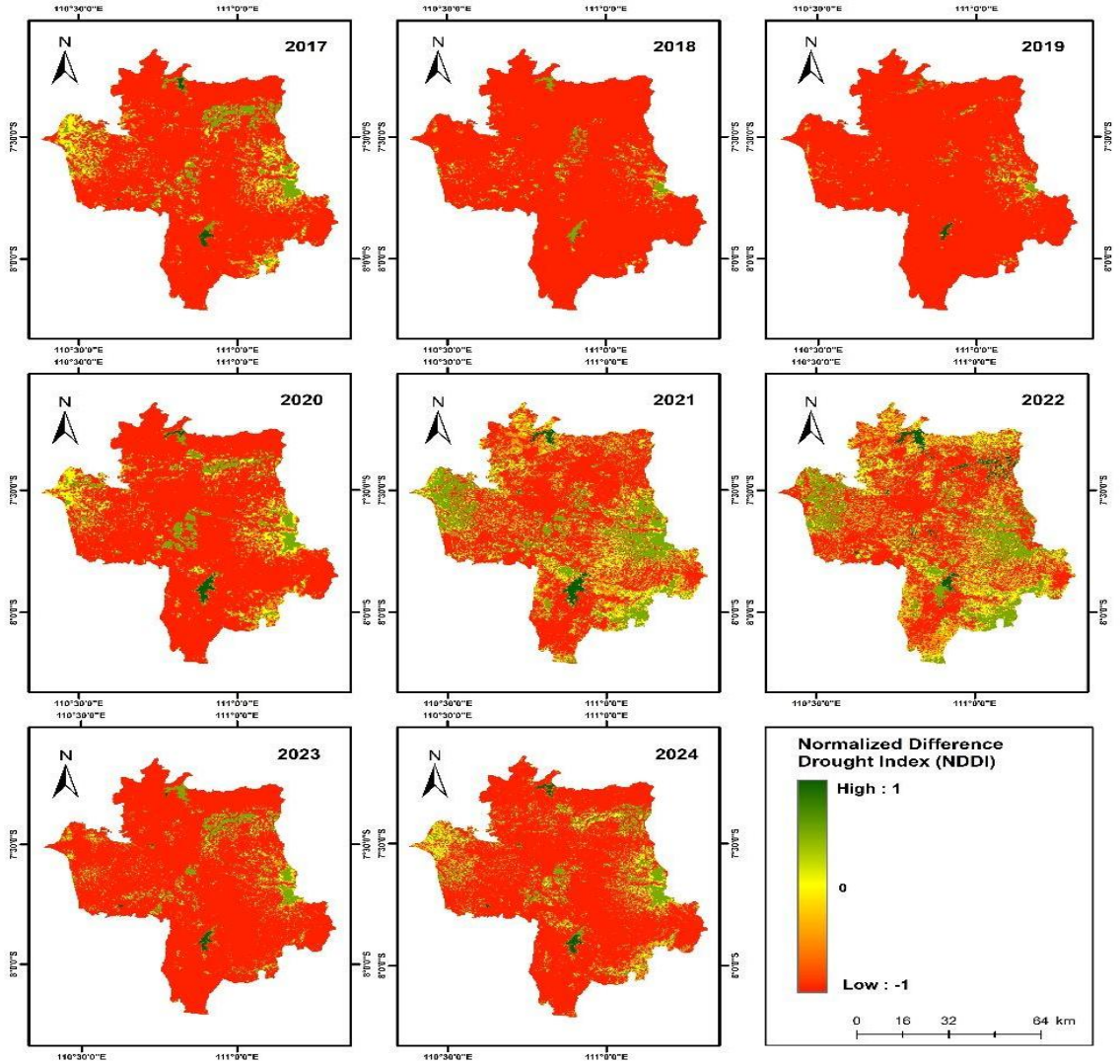

Fig. 2. Spatial-Temporal Map of Drought in the Upper Bengawan Solo River Basin.

Table 7.

Statistical Variables: Drought Area, NDDI Value, and Rainfall (2017–2024).

No	Year	Drought Area (Ha)	NDDI Value	Average Annual Rainfall (mm/year)
1	2017	567,758.30	0.82	65.81
2	2018	592,640.90	0.91	51.52
3	2019	186,951.90	0.76	82.04
4	2020	181,582.30	0.63	71.3
5	2021	182,966.00	0.64	117.13
6	2022	152,424.30	0.52	199.36
7	2023	185,734.40	0.71	165.39
8	2024	182,966.00	0.64	119.45

Table 8.

Pearson Correlation Results Between Research Variables.

Relationship	Correlation Coefficient (r)	p-value	Interpretation
Drought Area vs NDDI Value	0.840	0.009	Strong and statistically significant (positive)
Drought Area vs Rainfall	-0.633	0.092	Moderate and not statistically significant (negative)
NDDI Value vs Rainfall	-0.738	0.037	Strong and statistically significant (negative)

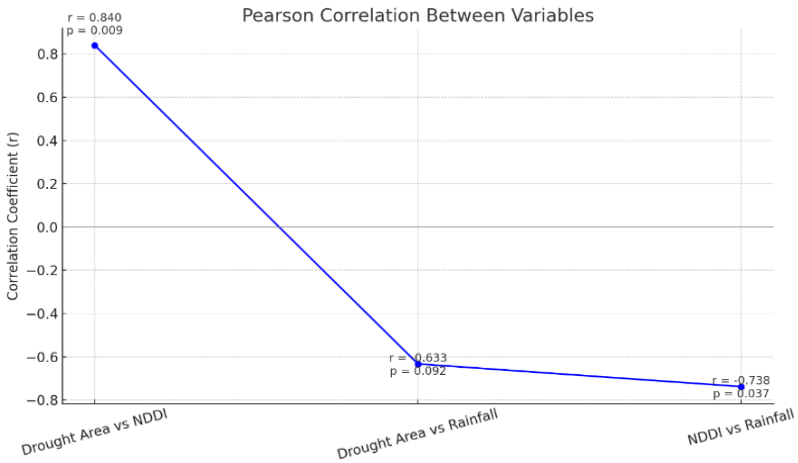

Fig. 3. Graph of Pearson Correlation Test Results between Research Variables.

The results of the Pearson correlation test indicate a strong and statistically significant positive relationship between the drought-affected area and the NDDI value, with a correlation coefficient of 0.840 and a p-value of 0.009. In contrast, the relationship between drought extent and rainfall shows a moderate negative correlation (-0.633), but it is not statistically significant (p-value = 0.092). Meanwhile, the correlation between NDDI and rainfall is strong and negative (-0.738) and statistically significant, with a p-value of 0.037. These findings reinforce that the NDDI is a relatively sensitive indicator in describing drought severity, as it is positively correlated with the expansion of drought-affected areas and negatively correlated with rainfall. On the other hand, the insignificant relationship between rainfall and drought extent suggests that rainfall alone is insufficient to explain the severity of drought impacts. Therefore, the use of composite indices such as the NDDI, which incorporate aspects of vegetation cover and soil moisture is essential for more comprehensive and accurate drought monitoring.

Table 9.

Simple Linear Regression Results Between Research Variables.

Relationship	Regression Equation	R^2	p-value	Interpretation
NDDI Value vs Rainfall	Rainfall = -310.05 × NDDI + 327.20	0.544	0.037	Significant, moderate negative relationship
Drought Area VS NDDI Value	Drought Area = -2,273.45 × Rainfall + 526,934.45	0.401	0.092	Not significant, weak negative relationship
NDDI Value VS Drought Area	Drought Area = 1,268,283.31 × NDDI - 613,426.37	0.706	0.009	Significant, strong positive relationship

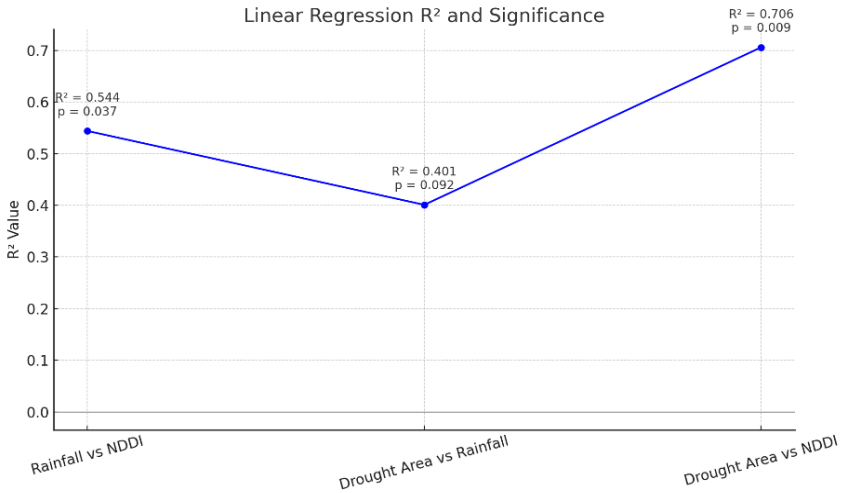

Fig. 4. Graph of Regression Test Results Between Research Variables.

Based on **Table 9** and **Figure 4**, the relationship between NDDI and rainfall has an R^2 value of 0.544 and a p-value of 0.037, indicating a moderate negative relationship that is statistically significant. The relationship between rainfall and drought area shows an R^2 of 0.401 and a p-value of 0.092, suggesting a weak negative relationship that is not statistically significant. Meanwhile, the relationship between NDDI and drought area yields an R^2 of 0.706 and a p-value of 0.009, reflecting a strong and statistically significant positive relationship.

These findings indicate that NDDI is a fairly reliable indicator for predicting hydrological drought conditions, given its strong and significant relationship with the extent of drought. In contrast, rainfall does not significantly influence the drought area, which may be due to other factors such as infiltration efficiency, irrigation water use, or soil response time to precipitation. The negative relationship between NDDI and rainfall further confirms that NDDI values tend to increase when rainfall decreases, signaling drought conditions. These results emphasize the importance of using image-based indices such as NDDI for comprehensive spatial and temporal drought monitoring.

4.3. The Impact of Drought on Agricultural Productivity

The analysis of the impact of modelled drought on agricultural production in this study was carried out using the Locally Weighted Regression (LOWESS) method. The parameters used to assess this impact were NDDI values and rice production data (**Table 10**). The complete results of the calculations using this method are presented in **Table 11** and **Figure 5**.

Table 10.

Statistical Variables: Drought Area, and Rice Production (2017–2024).

No	Year	Drought Area (Ha)	Rice Production (Tons)
1	**2017**	567,758.30	2,265,487
2	**2018**	592,640.90	2,353,781
3	**2019**	186,951.90	2,310,156
4	**2020**	181,582.30	2,439,558
5	**2021**	182,966.00	2,196,267
6	**2022**	152,424.30	2,422,889
7	**2023**	185,734.40	2,219,016
8	**2024**	182,966.00	2,264,832

Based on **Table 10**, this study utilises two statistical variables to assess the relationship between drought severity and agricultural productivity: the area affected by drought (in hectares) and annual rice production (in tonnes) within the Upper Bengawan Solo River Basin from 2017 to 2024. Throughout the observation period, both variables exhibit significant year-to-year fluctuations. The most extensive drought area was recorded in 2018, yet rice production remained relatively high. Conversely, the smallest drought-affected area occurred in 2022, which coincided with the peak in rice production. Interestingly, rice yields did not consistently decline during years of more severe drought, indicating that the correlation between these variables is not strictly linear.

Table 11.

Comparison of Actual and Estimated Rice Production Based on LOWESS Against NDDI Values (2017–2024).

No	Year	NDDI Value	Rice Production (Tonnes)	Estimated Production (LOWESS), (Tonnes)
1	**2017**	0.82	2,265,487	2,297,082
2	**2018**	0.91	2,353,781	2,345,025
3	**2019**	0.76	2,310,156	2,265,821
4	**2020**	0.63	2,439,558	2,239,768
5	**2021**	0.64	2,196,267	2,237,174
6	**2022**	0.52	2,422,889	2,422,889
7	**2023**	0.71	2,219,016	2,231,535
8	**2024**	0.64	2,264,832	2,237,174

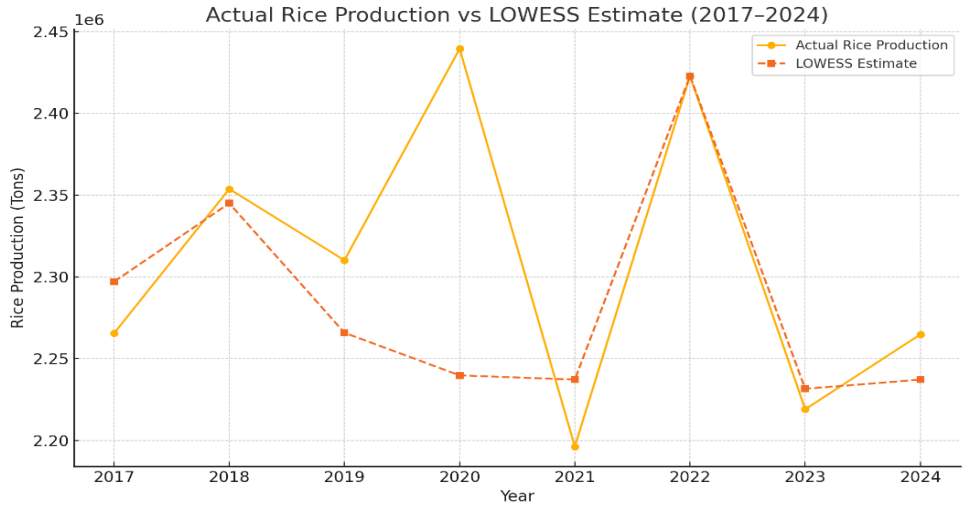

Fig. 5. Comparison Graph of Actual and Estimated Rice Production using the LOWESS Method.

Based on **Table 11** and **Figure 5**, the data points show a non-linear distribution. At lower NDDI values (approximately 0.52–0.63), rice production is relatively high (2.42–2.44 million tonnes). Production then decreases to its lowest point (2.20 million tonnes) at moderate NDDI levels (0.64–0.71), before increasing again at high NDDI values (0.91), with a production of 2.35 million tonnes. The LOWESS curve (red line) follows this pattern: it declines sharply from an NDDI of 0.52 to around 0.70, then rises again towards an NDDI of 0.91. This pattern indicates a non-linear relationship: rice production does not respond monotonically to NDDI values, but instead reaches its lowest point at moderate NDDI levels and is relatively higher at both low and high extremes.

5. DISCUSSION

The spatio-temporal model has proven effective in analysing trends and the distribution of hydrological drought in the Upper Bengawan Solo River Basin. This approach enables the visualisation of drought dynamics both temporally, through annual trend graphs, and spatially, through drought distribution maps across districts and cities. Validation results via statistical tests indicate a very strong positive correlation between drought-affected areas and the drought index (NDDI), with a coefficient ($r = 0.84$; $p < 0.01$), suggesting that increases in NDDI are aligned with the expansion of drought-affected areas. A significant negative correlation was also found between NDDI and annual rainfall ($r = -0.73$; $p < 0.05$), indicating that increased rainfall tends to reduce drought intensity. Meanwhile, a moderate yet statistically insignificant negative correlation was observed between rainfall and drought extent ($r = -0.63$; $p > 0.05$), implying that annual rainfall is not the sole determining factor. These findings are consistent with previous studies (Arias et al., 2024; Bolan et al., 2024; Harini et al., 2022), which have similarly concluded that rainfall is not the primary cause of drought. This supports the application of composite indices such as NDDI in more comprehensively representing drought conditions.

The choice of approach and satellite imagery is critical to determining the accuracy of drought models. This study employed the NDDI method due to its ability to integrate vegetation information (NDVI), soil moisture (NDWI), and water availability, thereby offering more representative drought estimates than conventional methods. These findings align with Salas-Martínez et al. (2023), who affirmed NDDI's effectiveness in identifying hydrological drought. Furthermore, the use of Sentinel-2A imagery supports detailed monitoring of vegetation and soil moisture owing to its high spatial and temporal resolution. This is reinforced by studies by Alonzo et al. (2023) and Staszel et al. (2024), which confirm Sentinel-2A as one of the most suitable multispectral datasets for ecological and agricultural analysis. Nonetheless, satellite imagery interpretation remains constrained by atmospheric disturbances, which may affect data accuracy.

As a vegetation and drought monitoring tool, NDDI offers advantages by integrating various biophysical parameters for rapid and effective identification of hydrological drought. The use of this index enables near real-time field condition estimation and provides reliable information for decision-making. Studies by Del-Toro-Guerrero et al. (2022) and Gelata et al. (2023) also demonstrate that NDDI-based spatio-temporal modelling can accurately assess drought conditions in specific regions. The effectiveness of this method makes it a key component of early warning systems and risk assessments for agriculture and water resources.

The model developed in this study was also applied to analyse the impact of drought on rice production in the study area. The analysis revealed that the relationship between drought extent and rice production is non-linear, necessitating the use of non-linear regression approaches (Cahyono et al., 2023). The LOWESS regression model was adopted to capture this pattern and showed that in several years with severe drought, rice production remained stable or even increased. This suggests the presence of other interventions such as efficient irrigation systems, the adoption of drought-tolerant varieties, and adaptive land management practices. These findings are in line with Del-Toro-Guerrero et al. (2022), who emphasised the critical role of socio-technical factors in maintaining food production resilience under drought stress.

This study provides a significant contribution to the development of remote sensing-based drought monitoring models in Indonesia, particularly for the agricultural sector, which is highly vulnerable to climate change. The integration of spatio-temporal modelling, the selection of appropriate vegetation indices, and rigorous statistical validation result in an analytical framework that is not only accurate but also practical. This model can serve as a foundation for agricultural adaptation planning and drought risk mitigation policy, both at local and national levels.

Future research is recommended to incorporate long-term climatic indices such as the Standardised Precipitation Index (SPI) and the Standardised Precipitation Evapotranspiration Index (SPEI) to enable broader climatological drought analysis. The application of machine learning methods also holds the potential to enhance drought prediction accuracy by integrating multiple data

sources. Moreover, integration with field data such as actual harvest yields, irrigation conditions, and local farming practices is crucial to refining the model and producing more precise policy recommendations for addressing climate change challenges in the agricultural sector.

6. CONCLUSIONS

This study successfully mapped the spatial and temporal dynamics of drought in the Upper Bengawan Solo River Basin from 2017 to 2024 using the NDDI index derived from Sentinel-2A imagery. Wonogiri, Boyolali, and Sragen were identified as the most severely affected areas, while urban regions such as Surakarta remained relatively unaffected. This distribution was influenced by topographical conditions, low rainfall levels, and the size of the regions. Temporally, drought exhibited sharp annual fluctuations, peaking in 2018 and decreasing significantly in 2022.

The NDDI index demonstrated a strong correlation with both the extent of drought-affected areas and rainfall, and it proved to be a more reliable predictor than rainfall alone in the linear regression model. This affirms the effectiveness of NDDI as a tool for drought monitoring and early warning systems. Furthermore, the LOWESS model used to estimate rice production based on NDDI values closely approximated actual yields, despite some limitations in years where NDDI values were identical. These findings underscore the potential of remote sensing integration to support food security and sustainable drought management. Future research is recommended to incorporate additional climatic variables and machine learning approaches to improve the accuracy of drought and agricultural yield predictions.

ACKNOWLEDGMENT

This research was supported by Universitas Muhammadiyah Surakarta through the International Research Collaboration Grant (Riset Kerjasama Internasional – RKI Scheme), and was conducted in collaboration with the Institute for Environment and Development (LESTARI), Universiti Kebangsaan Malaysia.

REFERENCES

Alito, K. T., & Kerebih, M. S. (2024). Spatio-temporal assessment of agricultural drought using remote sensing and ground-based data indices in the Northern Ethiopian Highland. Journal of Hydrology: Regional Studies. https://doi.org/10.1016/j.ejrh.2024.101700

Almouctar, M. A. S., Wu, Y., Zhao, F., & Qin, C. (2024). Drought analysis using normalized difference vegetation index and land surface temperature over Niamey region, the southwestern of the Niger between 2013 and 2019. In Journal of Hydrology: Regional Studies. https://doi.org/10.1016/j.ejrh.2024.101689

Alonzo, C. A., Galabay, J. M., Macatangay, M. N., Magpayo, M. B., & Ramirez, R. (2023). Drought Risk Assessment and Monitoring of Ilocos Norte Province in the Philippines Using Satellite Remote Sensing and Meteorological Data. AgriEngineering. https://doi.org/10.3390/agriengineering5020045

Anna, A. N., Sari, D. N., Sofwan, N. M., Rudiyanto, R., & Fikriyah, V. N. (2024). GIS-based Spatial Modelling of Shallow Groundwater Quality: an Evaluation in High Populated Area of Sukoharjo, Indonesia. International Journal of Environmental Science and Development, 15(5), 233–239. https://doi.org/10.18178/ijesd.2024.15.5.1491

Arias, P. A., Rivera, J. A., Sörensson, A. A., Zachariah, M., Barnes, C., Philip, S., Kew, S., Vautard, R., Koren, G., Pinto, I., Vahlberg, M., Singh, R., Raju, E., Li, S., Yang, W., Vecchi, G. A., & Otto, F. E. L. (2024). Interplay between climate change and climate variability: the 2022 drought in Central South America. Climatic Change. https://doi.org/10.1007/s10584-023-03664-4

Arifin, A., Sumange, L., Biba, M. A., Natsir, M., Mardiyati, S., & Fattah, M. A. (2023). Faktor dan Risiko Produksi Usahatani Padi Sawah Tadah Hujan Sulawesi Selatan. AGRIMOR. https://doi.org/10.32938/ag.v8i2.1933

Artikanur, S. D., Widiatmaka, Setiawan, Y., & Marimin. (2022). Normalized Difference Drought Index (NDDI) computation for mapping drought severity in Bojonegoro Regency, East Java, Indonesia. IOP Conference Series: Earth and Environmental Science. https://doi.org/10.1088/1755-1315/1109/1/012027

Badan Nasional Penanggulangan Bencana. (2025). Data dan Informasi Bencana Indonesia: Kekeringan. BNPB. https://dibi.bnpb.go.id/

Bashit, N., Ristianti, N. S., & Ulfiana, D. (2022). Drought Assessment Using Remote Sensing and Geographic Information Systems (GIS) Techniques (Case Study: Klaten District). International Journal of Geoinformatics. https://doi.org/10.52939/ijg.v18i5.2393

Bibi, F., & Rahman, A. (2023). An Overview of Climate Change Impacts on Agriculture and Their Mitigation Strategies. In Agriculture (Switzerland). https://doi.org/10.3390/agriculture13081508

BMKG. (2025). Fakta Perubahan Iklim September 2024. 1–54.

Bolan, S., Padhye, L. P., Jasemizad, T., Govarthanan, M., Karmegam, N., Wijesekara, H., Amarasiri, D., Hou, D., Zhou, P., Biswal, B. K., Balasubramanian, R., Wang, H., Siddique, K. H. M., Rinklebe, J., Kirkham, M. B., & Bolan, N. (2024). Impacts of climate change on the fate of contaminants through extreme weather events. Science of The Total Environment, 909, 168388. https://doi.org/10.1016/j.scitotenv.2023.168388

Boori, M. S., Choudhary, K., Paringer, R., & Kupriyanov, A. (2022). Using RS/GIS for spatiotemporal ecological vulnerability analysis based on DPSIR framework in the Republic of Tatarstan, Russia. Ecological Informatics. https://doi.org/10.1016/j.ecoinf.2021.101490

BPS Provinsi Jawa Tengah. (2024). Indikator Utama Pertanian Provinsi Jawa Tengah 2023. BPS Provinsi Jawa Tengah. https://jateng.bps.go.id/id/publication/2024/11/18/abddf5bea3c19291abc754d9/indikator-utama-pertanian-provinsi-jawa-tengah-2023.html

Cahyono, B. E., Rahagian, R., & Nugroho, A. T. (2023). Analisis Produktivitas Padi berdasarkan Indeks Kekeringan (NDWI dan NDDI) Lahan Sawah menggunakan Data Citra Sentinel-2A di Kecamatan Ambulu. *Indonesian Journal of Applied Physics*, *13*(1), 88. https://doi.org/10.13057/ijap.v13i1.70682

Christian, J. I., Martin, E. R., Basara, J. B., Furtado, J. C., Otkin, J. A., Lowman, L. E. L., Hunt, E. D., Mishra, V., & Xiao, X. (2023). Global projections of flash drought show increased risk in a warming climate. Communications Earth and Environment. https://doi.org/10.1038/s43247-023-00826-1

Del-Toro-guerrero, F. J., Daesslé, L. W., Méndez-Alonzo, R., & Kretzschmar, T. (2022). Surface Reflectance–Derived Spectral Indices for Drought Detection: Application to the Guadalupe Valley Basin, Baja California, Mexico. Land. https://doi.org/10.3390/land11060783

European Space Agency (ESA). (2025). Sentinel Data. Copernicus Open Access Hub. https://dataspace.copernicus.eu/explore-data/data-collections/sentinel-data

Gelata, F. T., Jiqin, H., Gemeda, S. C., & Asefa, B. W. (2023). Application of GIS using NDVI and LST estimation to measure climate variability-induced drought risk assessment in Ethiopia. Journal of Water and Climate Change. https://doi.org/10.2166/wcc.2023.154

Hadibasyir, H. Z., Firdaus, N. S., Fikriyah, V. N., & Sari, D. N. (2023). Assessing Performance of Modified Spectral Indices as Land Surface Temperature Indicators in Tropical Urban Areas. IOP Conference Series: Earth and Environmental Science. https://doi.org/10.1088/1755-1315/1190/1/012005

Harini, R. H., Ariani, R. D., & Yulianda, Y. (2022). Strategi adaptasi ketahanan pangan terhadap perubahan iklim di pinggiran Kota Yogyakarta. Majalah Geografi Indonesia. https://doi.org/10.22146/mgi.60245

Hussain, A., Jadoon, K. Z., Rahman, K. U., Shang, S., Shahid, M., Ejaz, N., & Khan, H. (2023). Analyzing the impact of drought on agriculture: evidence from Pakistan using standardized precipitation evapotranspiration index. Natural Hazards. https://doi.org/10.1007/s11069-022-

05559-6
Kumar, S., Sarthi, P. P., Barat, A., & Sinha, A. K. (2022). Variability in meteorological droughts as pivotal mechanism for rice production over the middle gangetic plains. Paddy and Water Environment. https://doi.org/10.1007/s10333-022-00907-5
Laksono, S. S., & Nurgiyatna, N. (2020). Sistem Pengukur Curah Hujan sebagai Deteksi Dini Kekeringan pada Pertanian Berbasis Internet of Things (IoT). Emitor: Jurnal Teknik Elektro. https://doi.org/10.23917/emitor.v20i02.8493
Mirzaee, S., & Mirzakhani Nafchi, A. (2023). Monitoring Spatiotemporal Vegetation Response to Drought Using Remote Sensing Data. Sensors. https://doi.org/10.3390/s23042134
Mohammed, S., Alkhereibi, A. H., Abulibdeh, A., Jawarneh, R. N., & Balakrishnan, P. (2023). GIS-based spatiotemporal analysis for road traffic crashes; in support of sustainable transportation Planning. Transportation Research Interdisciplinary Perspectives. https://doi.org/10.1016/j.trip.2023.100836
Mujiyo, M., Nurdianti, R., Komariah, & Sutarno. (2023). Agricultural Land Dryness Distribution Using the Normalized Difference Drought Index (NDDI) Algorithm on Landsat 8 Imagery in Eromoko, Indonesia. Environment and Natural Resources Journal. https://doi.org/10.32526/ennrj/21/202200157
Mustikaningrum, M., Widhatama, A. F., Widantara, K. W., Ibrohim, M., Hibatullah, M. F., Larasati, R. A. P., Utami, S., & Hadmoko, D. S. (2023). Multi-Hazard Analysis in Gunungkidul Regency Using Spatial Multi-Criteria Evaluation. Forum Geografi. https://doi.org/10.23917/forgeo.v37i1.19041
Ren, Y., Zhang, F., Zhao, C., & Cheng, Z. (2023). Attribution of climate change and human activities to vegetation NDVI in Jilin Province, China during 1998–2020. Ecological Indicators, 153, 110415. https://doi.org/10.1016/j.ecolind.2023.110415
Safura, A. H., & Sekaranom, A. B. (2024). PROJECTIONS OF FUTURE METEOROLOGICAL DROUGHT IN JAVA–NUSA TENGGARA REGION BASED ON CMIP6 SCENARIO. Geographia Technica, 11(2), 39–50. https://doi.org/10.21163/GT
Salas-Martínez, F., Valdés-Rodríguez, O. A., Palacios-Wassenaar, O. M., Márquez-Grajales, A., & Rodríguez-Hernández, L. D. (2023). Methodological estimation to quantify drought intensity based on the NDDI index with Landsat 8 multispectral images in the central zone of the Gulf of Mexico. Frontiers in Earth Science, 11. https://doi.org/10.3389/feart.2023.1027483
Shashikant, V., Shariff, A. R. M., Wayayok, A., Kamal, R., Lee, Y. P., & Takeuchi, W. (2021). Utilizing TVDI and NDWI to classify severity of agricultural drought in Chuping, Malaysia. Agronomy. https://doi.org/10.3390/agronomy11061243
Sigit, A. A., & Anna, alif N. (2023). Deteksi Kesehatan Mangrove berbasis Citra Satelit Landsat 8 OLI di Kecamatan Temon, Kulonprogo. In Laporan Hasil Riset.
Staszel, J., Lupa, M., Adamek, K., Wilkosz, M., Marcinkowska-Ochtyra, A., & Ochtyra, A. (2024). Spatial Insights into Drought Severity: Multi-Index Assessment in Małopolska, Poland, via Satellite Observations. Remote Sensing. https://doi.org/10.3390/rs16050836
Varghese, D., Radulović, M., Stojković, S., & Crnojević, V. (2021). Reviewing the potential of sentinel-2 in assessing the drought. In Remote Sensing. https://doi.org/10.3390/rs13173355
Wolteji, B. N., Bedhadha, S. T., Gebre, S. L., Alemayehu, E., & Gemeda, D. O. (2022). Multiple Indices-Based Agricultural Drought Assessment in the Rift Valley Region of Ethiopia. Environmental Challenges. https://doi.org/10.1016/j.envc.2022.100488
Zhang, Q., Yu, H., Li, J., Clothier, B., Singh, V. P., & Shen, Z. (2023). Divergent effectiveness of irrigation in enhancing food security in droughts under future climates with various emission scenarios. Npj Climate and Atmospheric Science. https://doi.org/10.1038/s41612-023-00362-x

LINKING TROPHIC STATE INDEX TO HIGH RESOLUTION SATELLITE IMAGERY DATA OF MRICA RESERVOIR, BANJARNEGARA – CENTRAL JAVA

***Yoga Candra DITYA*[1,5], *Muhammad RAMDHAN*[2*], *Siswanta KABAN*[1], *Gema WAHYUDEWANTORO*[3], *Suryo KUSUMO*[4], *Agus Djoko UTOMO*[1], *Sigid HARIYADI*[5], *Majariana KRISANTI*[5], *Luky ADRIANTO*[5]**

DOI: 10.21163/GT_2025.202.17

ABSTRACT

The increasing eutrophication of inland water bodies necessitates efficient, spatially extensive, and timely monitoring methods. This study investigates the utility of high-resolution PlanetScope satellite imagery for assessing the trophic state of the Mrica Reservoir in Banjarnegara, Central Java, Indonesia. Field measurements of Secchi Disk Depth (SDD), Total Phosphate (TP), and Chlorophyll-a (Chl-a) were collected at six observation stations and used to calculate Carlson's Trophic State Index (CTSI). These values were then correlated with satellite-derived vegetation indices−Normalized Difference Vegetation Index (NDVI) and Red Edge NDVI (RdEdNDVI). Polynomial regression analysis showed strong correlations between NDVI and TP ($R^2 = 0.975$) as well as between RdEdNDVI and Chl-a ($R^2 = 0.959$), confirming the potential of these indices to estimate key trophic indicators. Spatial mapping of CTSI indicated that the reservoir ranged from eutrophic to hypereutrophic, with the most degraded conditions observed near the outlet area. The findings underscore the effectiveness of remote sensing for detecting spatial variability in water quality, particularly when field sampling is limited. While challenges such as cloud cover, spectral limitations, and sampling resolution persist, this integrated approach offers a scalable and cost-efficient framework for reservoir monitoring. The study highlights the potential for replicating this method across similar freshwater systems in Indonesia to support sustainable water resource management.

Key-words: *Trophic State Index (TSI), PlanetScope, Remote Sensing, Water Quality Monitoring, Mrica Reservoir*

1. INTRODUCTION

Mrica Reservoir, formed by the Panglima Besar Soedirman (PB Soedirman) Dam on the Serayu River in Banjarnegara, Central Java, is a vital multipurpose water infrastructure in southern Java. Commissioned in 1988, the reservoir supports a wide range of services, including hydroelectric power generation, irrigation for agricultural lands, flood control, and raw water supply for surrounding communities. Over the decades, however, increased anthropogenic pressures such as agricultural runoff, sedimentation, and domestic waste have raised concerns about water quality deterioration in the reservoir (Anggraini et al., 2019). One of the most pressing environmental issues faced by reservoirs in tropical regions is eutrophication, a process driven by nutrient enrichment that leads to excessive algal growth and potential ecological imbalance (Barbosa et al., 2022).

[1] *Research Center for Conservation of Marine and Inland Water Resources, National Research and Innovation Agency, Cibinong, Bogor, Indonesia. (YCD) yogacditya@apps.ipb.ac.id, (ADU) agus172@brin.go.id*

[2] *Research Center for Geoinformatics, National Research and Innovation Agency, Bandung, West Java, Indonesia. (MR) muha307@brin.go.id, (SK) sisw016@brin.go.id*

[3] *Research Center for Biosystematics and Evolution, National Research and Innovation Agency, Cibinong, Bogor, Indonesia. (GW) gema001@brin.go.id*

[4] *Yayasan Karang Lestari Indonesia, Bekasi, Indonesia. (SK) suryo.admin@gmail.com*

[5] *Department of Aquatic Resources Management, Faculty of Fisheries and Marine Science, IPB University, Dramaga, Bogor, Indonesia. (SH) sigidhariyadi@gmail.com, (MK) majariana.krisanti@apps.ipb.ac.id, (LA) lukyadrianto@apps.ipb.ac.id*

[*] *Corresponding author: muha307@brin.go.id*

In reservoirs like Mrica, eutrophication not only degrades water quality but also threatens aquatic biodiversity, reduces reservoir capacity through sedimentation, and impairs the operation of hydroelectric systems. Similar challenges have been documented in other Indonesian reservoirs, such as Gajah Mungkur, where Carlson's Trophic State Index has been effectively used to evaluate eutrophication levels (Shaleh et al., 2014).

The Trophic State Index (TSI), particularly Carlson's TSI, has been widely used to classify the trophic status of inland waters based on parameters such as chlorophyll-a concentration, Secchi disk depth, and total phosphorus content (Carlson, 1977; Carlson & Simpson, 1996). However, in-situ monitoring of these parameters can be time-consuming, expensive, and spatially limited.

In recent years, satellite remote sensing has emerged as a cost-effective and scalable tool to monitor water quality, including eutrophication levels, in lakes and reservoirs. High-resolution satellite imagery, such as that from PlanetScope, allows the extraction of biophysical indicators like chlorophyll-a and turbidity through spectral reflectance values and band ratios. Numerous studies have demonstrated significant correlations between satellite-derived indices and water quality parameters, enabling the development of predictive models for TSI assessment (Alikas & Kratzer, 2017; Kutser, 2009; Tyler et al., 2006). Despite these advancements, there is limited research applying this approach to medium-sized reservoirs in Indonesia, including Mrica. This study aims to bridge that gap by linking in-situ Trophic State Index measurements with spectral data from high-resolution satellite imagery, providing a spatially comprehensive method for assessing and monitoring the trophic status of the Mrica Reservoir. This study presents a novel approach by integrating high-resolution PlanetScope satellite imagery with in-situ Trophic State Index (TSI) measurements to assess eutrophication in the medium-sized Mrica Reservoir—an application rarely explored in Indonesian inland waters. By developing a spatially comprehensive and cost-effective remote sensing-based model for trophic state monitoring, this research addresses existing gaps in local water quality assessment and offers a scalable tool for sustainable reservoir management in tropical regions.

2. METHODS

2.1. Study Area

The study was conducted in the Mrica Reservoir, located in Banjarnegara Regency, Central Java, Indonesia, at approximately 7° 20′ - 7° 25′ S latitude and 109° 34′ - 109° 38′ E longitude (**Fig. 1**).

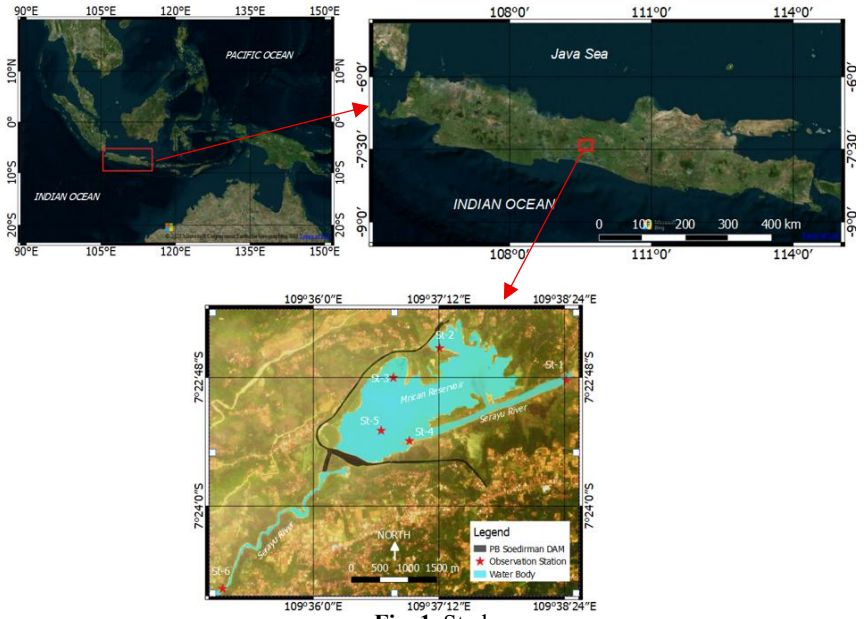

Fig. 1. Study area.

The reservoir was formed by the construction of the PB Soedirman Dam on the Serayu River, one of the major river systems in Central Java. Situated at an elevation of around 150–200 meters above sea level, the reservoir lies within a humid tropical climate zone characterized by distinct wet and dry seasons influenced by the monsoonal cycle.

Geographically, the surrounding area is dominated by a mixture of hilly terrain, agricultural lands, and forested slopes, contributing to a dynamic watershed environment. The topography features moderate to steep slopes in the upstream catchment, which significantly influence surface runoff, erosion, and sediment transport into the reservoir. These geomorphological conditions contribute to high sedimentation rates, a persistent challenge that reduces the reservoir's storage capacity and affects its operational efficiency.

2.2. Research Flowchart

As shown in **Fig. 2**., this study begins by defining the Area of Interest (AOI) of the Mrica Reservoir and acquiring high-resolution PlanetScope imagery with less than 10% cloud cover. The selected imagery is processed by masking the water body and deriving NDVI and Red Edge NDVI. Simultaneously, field data on Secchi Disk Depth (SDD), Total Phosphate (TP), and Chlorophyll-a (Chl-a) are collected from inlet, outlet, and reservoir points. These data are used for validation and statistical correlation with satellite indices. The results produce spatial distributions of SDD, TP, and Chl-a, which are then used to calculate the Trophic State Index (TSI) to assess the water quality of the Mrica Reservoir.

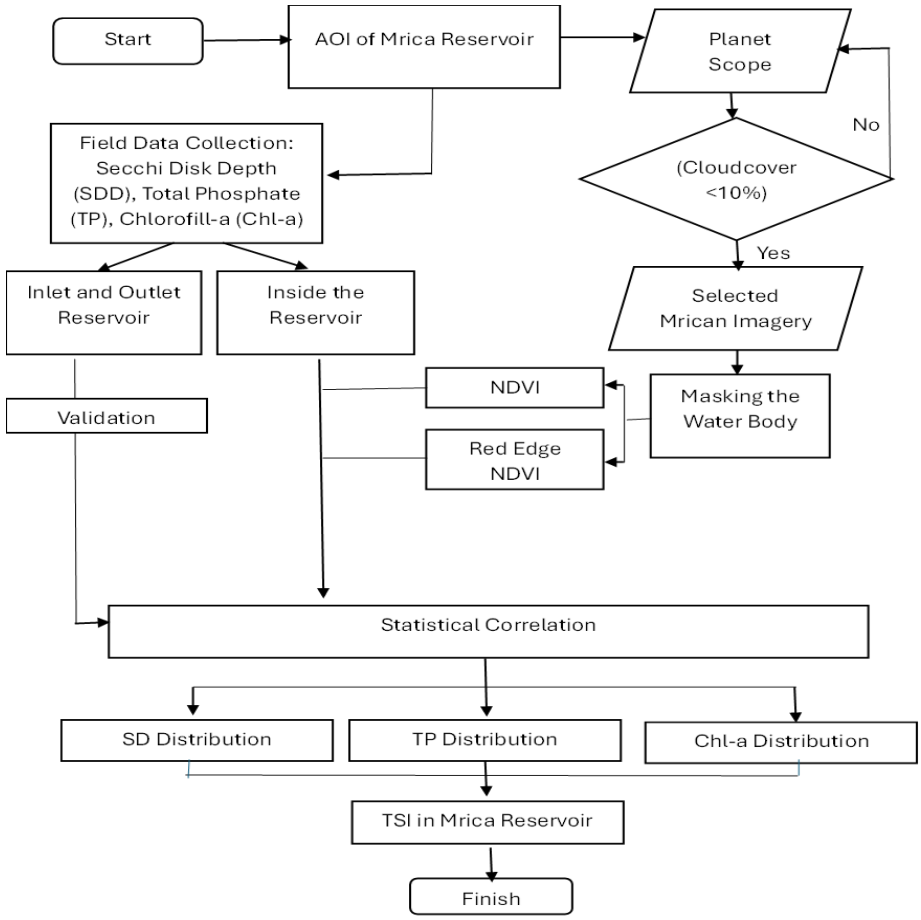

Fig. 2. Workflow of the research.

2.3. Satellite Data and Image Processing

High-resolution satellite imagery from PlanetScope was utilized for this study. The imagery was acquired during the dry season to minimize atmospheric disturbances and cloud cover. PlanetScope imagery provides daily images with a spatial resolution of approximately 3 meters and includes the following spectral bands used in this analysis:

Red band (R) with the wavelength of 665 μm

Red Edge band (RE) with the wavelength of 705 μm

Near Infrared band (NIR) with the wavelength of 865 μm

Two vegetation-related indices were computed to assess water quality proxies:

1. Normalized Difference Vegetation Index (NDVI):

$$NDVI = (NIR-R) / (NIR+R) \quad (1)$$

2. Red Edge NDVI (RdEd-NDVI):

$$RdEdNDVI = (NIR-RE)/(NIR+RE) \quad (2)$$

These indices were derived using cloud-free PlanetScope imagery clipped to the outline of Mrica Reservoir, obtained through Object Identification processing. Pre-processing steps included radiometric and geometric correction, atmospheric correction using surface reflectance products, and masking of non-water areas.

2.4. Field Sampling and Laboratory Analysis

Field observations were conducted at 6 sampling stations distributed across the reservoir to capture spatial variability. The stations were selected based on accessibility, representativeness of water bodies, and proximity to potential nutrient inflow sources.

At each station, Secchi Disk Depth (SDD) was measured in situ to assess water clarity. Water samples were collected from the surface layer using a bottle sampler. The collected water was then preserved and transported to the laboratory for chemical analysis.

The laboratory procedures followed the APHA Standard Methods for the Examination of Water and Wastewater, 24th Edition (APHA, 2017), which included: Chlorophyll-a (Chl-a) concentration analysis using spectrophotometry after pigment extraction. Total Phosphate (TP) determination using the ascorbic acid method after persulfate digestion.

2.5. Trophic State Index (TSI) Calculation and Classification

Carlson's TSI was computed based on three parameters: SDD, Chl-a, and TP. The following formulas were used (Carlson, 1977; Carlson & Simpson, 1996):

$$TSISD = 60 - 14.4\ln(SD) \quad (3)$$

$$TSIChl-a = 9.81\ln(Chl-a) + 30.6 \quad (4)$$

$$TSITP = 14.2\ln(TP) + 4.15 \quad (5)$$

$$CTSI = [TSI(SD) + TSI(Chl\text{-}a) + TSI(TP)] / 3 \quad (6)$$

where:

CTSI: Carlson Trophic State Index.

TSISD: Trophic state index for Secchi disk depth (SDD/m);

TSIChl-1: Trophic state index for chlorophyll-a (Chl-a/mgL^{-1});

TSITP: Trophic state index for total phosphorous (TP/mgL^{-1}).

Table 1 presents the classification of the Carlson Trophic State Index (CTSI) and its interpretation for lakes and reservoirs, which has been modified from the Indonesian Ministry of State for the Environment (MOSE, 2009). The CTSI categorizes water bodies based on nutrient levels, particularly nitrogen (N) and phosphorus (P), which influence water clarity and algal growth. Oligotrophic waters (CTSI 0‑20) are characterized by low nutrient concentrations and minimal signs of pollution. As nutrient levels increase, the water transitions to mesotrophic (20‑40) and eutrophic (40‑60) conditions, indicating moderate to high enrichment. High eutrophic (60‑70) and hypereutrophic (70‑100) classifications reflect severe nutrient pollution, often resulting in algal blooms and ecological degradation. This classification provides a useful framework for assessing the trophic state and ecological health of the Mrica Reservoir.

Table 1.

Classification of CTSI.

CTSI Class	State		Information
0-20	Oligotrophic		Trophic status of lake and/or reservoir water containing low levels of nutrients. This status indicates that the water quality is still natural and has not been polluted by sources of N and P nutrients.
20-40	Mesotrophic		Trophic status of lake and reservoir water containing moderate levels of nutrients. This status indicates an increase in N and P levels, but is still within tolerance limits because it has not shown any indication of water pollution.
40-60	Eutrophics	Meso-eutrophics	Trophic status of lake and reservoir water containing high levels of nutrients. This status indicates that the water has been polluted by increased levels of N and P.
60-70		High eutrophics	
70-100	Hyper-eutrophic		Trophic status of lake and reservoir water containing very high levels of nutrients. This status indicates that the water has been heavily polluted by increased levels of N and P.

2.6. Data Analysis

To quantify the relationship between satellite-derived vegetation indices and field-measured water quality parameters, a statistical correlation analysis was performed using second-order polynomial regression. The analysis aimed to evaluate how well NDVI and Red Edge NDVI (RdEdNDVI) derived from PlanetScope imagery−can predict key trophic state indicators, including SDD, Chl-a concentration, and TP. Vegetation index values were extracted at each of the six field sampling locations within Mrica Reservoir using spatial overlay methods in a GIS environment. For each index‑parameter pair, a second-degree polynomial trendline was fitted using the following general model:

$$Y = aX2 + bX + c \quad (7)$$

where:

Y is the field-measured water quality parameter (SD, Chl-a, or TP),

X is the NDVI or RdEdNDVI value,

a,b and c are polynomial coefficients.

The coefficient of determination (R^2) was used to assess the goodness-of-fit for each polynomial model. The index that yielded the highest R^2 value for each parameter was identified as the most effective predictor. This method enables the selection of the optimal remote sensing indicator to estimate water quality conditions and infer the Trophic State Index (TSI) distribution across the reservoir. All statistical modeling and visualization were performed using Microsoft Excel.

3. RESULTS AND DISCUSSION

3.1. Overview of Satellite Imagery and Field Observations

High-resolution PlanetScope imagery was online downloaded from the website https://www.planet.com/explorer (Planet Labs PBC, 2025) (**Fig. 3**). Image data was acquired on April 15, 2025, at 03:30:33 UTC, during the dry season to minimize cloud contamination and ensure optimal atmospheric conditions. The selected image exhibited less than 10% cloud cover and underwent standard preprocessing steps, including radiometric calibration, geometric correction, atmospheric correction using surface reflectance products, and masking of non-water areas. The final imagery was clipped to the delineated boundary of the Mrica Reservoir to extract relevant water quality indices, specifically the Normalized Difference Vegetation Index (NDVI) and Red Edge NDVI (RdEdNDVI).

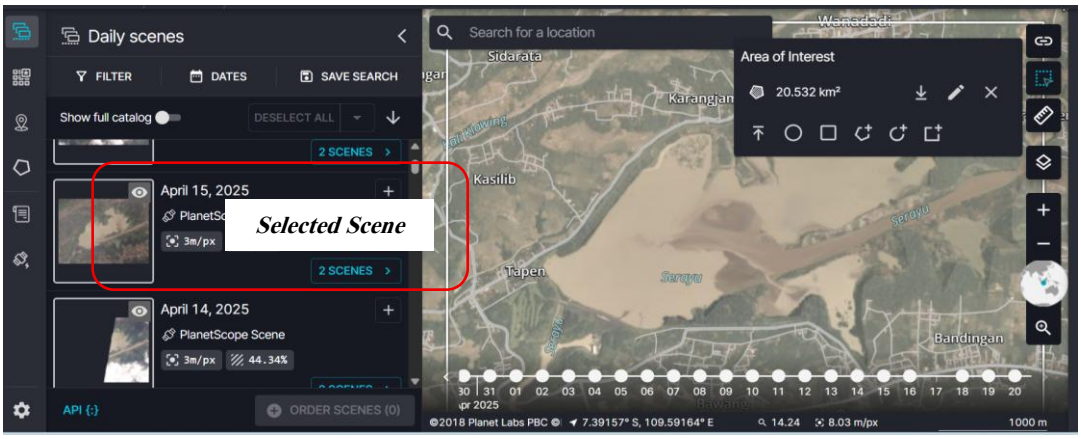

Fig. 3. Process of downloading the satellite imagery data on https://www.planet.com/ .

PlanetScope imagery was chosen for this study due to its high spatial resolution (~3 meters) and daily revisit frequency, which are essential for capturing fine-scale and timely changes in a medium-sized reservoir like Mrica, especially under frequent cloud cover in tropical regions. While Sentinel-2 offers a wider spectral range, its coarser resolution (10‑60 meters) and lower revisit rate (5 days) limit its suitability for detailed water quality assessments in smaller inland waters. PlanetScope also provides sufficient spectral bands (Red, Red Edge, NIR) to calculate key indices like NDVI and RdEd-NDVI, making it a practical and effective choice for this application. Field observations (**Fig. 4**) were conducted on April 22‑23, 2025, at six strategically selected sampling stations across the reservoir, covering the inlet, outlet, and central zones. These stations were chosen based on accessibility, hydrological significance, and representativeness of spatial variability.

The Secchi Disk Depth (SDD) values ranged from 0.10 to 0.29 meters, indicating high turbidity levels throughout the reservoir, particularly near the inlet zone, which is likely affected by sediment and nutrient inflow from upstream. Total Phosphate (TP) concentrations ranged from 0.042 to 0.301 mg/L, with the highest value detected in the southern part of the reservoir, suggesting external loading from agricultural or domestic sources.

Chlorophyll-a (Chl-a) concentrations varied between 3.461 and 11.471 mg/L, with peak values observed in shallow and poorly circulated regions, indicating elevated phytoplankton biomass and potential eutrophication. These in situ observations reveal significant spatial variation in water quality parameters and suggest the influence of both hydrological inputs and morphological characteristics of the reservoir. The collected field data serve as a basis for validating satellite-derived indices and for calculating the Carlson Trophic State Index (TSI) to assess the overall trophic condition of the Mrica Reservoir.

Fig. 4. Field survey activity for collecting data in observation station.

3.2. Spatial Distribution of Water Quality Parameters

Water quality parameters exhibited notable spatial variation across the six observation points within the Mrica Reservoir (**Table 2**). The Secchi Disk Depth (SDD) values, indicative of water transparency, ranged from 10 cm (St-6) to 29 cm (St-3). The shallowest SDD observed at Station 6, located in the southwestern part of the reservoir, suggests high turbidity likely due to suspended sediments and possible inflow of particulates. Conversely, the highest water clarity was recorded at Station 3, situated in the central area of the reservoir, indicating relatively low turbidity.

Total Phosphate (TP) concentrations varied significantly, ranging from 0.042 mg/L (St-3) to 0.301 mg/L (St-6). The elevated TP levels in Station 6 suggest a potential point-source nutrient input or accumulation of phosphorus-rich sediments in this region. Stations closer to the central and eastern reservoir (e.g., St-1 to St-3) recorded lower TP values, generally below 0.06 mg/L, suggesting comparatively less nutrient enrichment in those areas.

Chlorophyll-a (Chl-a) concentrations, which indicate phytoplankton biomass and serve as a proxy for algal productivity, ranged from 3.461 mg/L (St-4) to 11.471 mg/L (St-2). The highest Chl-a level at Station 2 corresponds with a relatively moderate TP level (0.054 mg/L), suggesting that local conditions such as light availability or water retention time may favor algal growth. Meanwhile, Station 4, despite having a relatively high TP concentration (0.117 mg/L), recorded the lowest Chl-a value, possibly due to light limitation from high turbidity or water column instability. These spatial patterns indicate that nutrient enrichment and algal productivity do not always correlate linearly, as they are also influenced by physical parameters such as turbidity, depth, and water circulation. Station 6 consistently recorded the most degraded water quality conditions−low SDD, high TP, and moderate Chl-a−pointing to this area as a potential hotspot of eutrophication within the Mrica Reservoir.

Tabel 2.

Observation points in Mrica Reservoir.

Observation Point	Date	Hour *	Longitude (E) **	Latitude (S)**	SDD (cm)	TP (mg/l)	Chl-a (mg/l)
St-1	23-Apr-25	11.32	109,64031	7,38041	21	0,058	3,893
St-2	23-Apr-25	12.58	109,62009	7,37542	22	0,054	11,471
St-3	23-Apr-25	09.30	109,61272	7,38003	29	0,042	5,072
St-4	23-Apr-25	10.36	109,61528	7,38989	17	0,117	3,461
St-5	23-Apr-25	10.07	109,61076	7,38828	20	0,077	8,481
St-6	22-Apr-25	16.32	109,58548	7,41294	10	0,301	6,346

**Western Indonesian Time Zone (UTC+7),*
*** Datum EPSG: 3857 (WGS 84/Pseudo Mercator)*

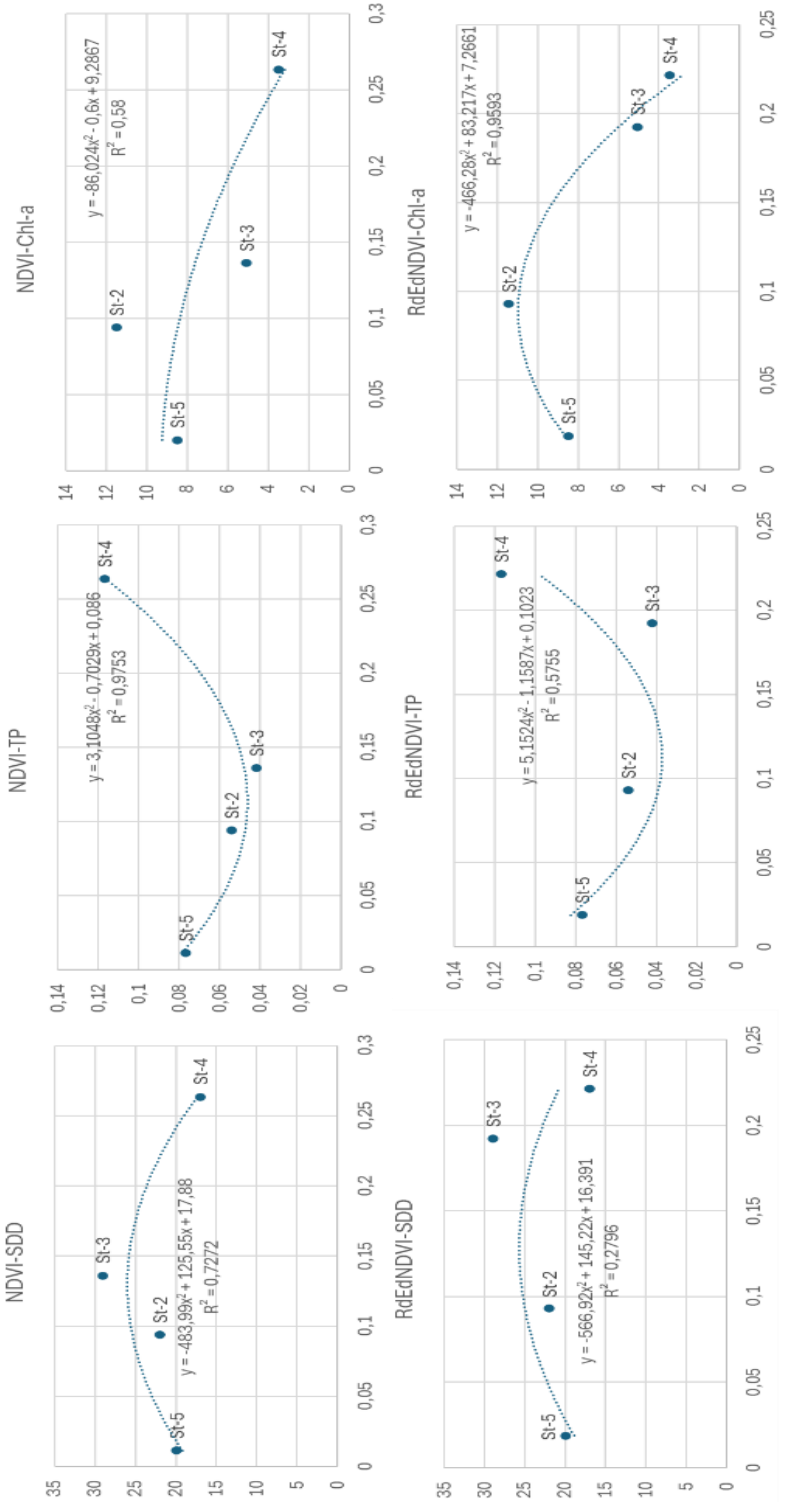

Fig. 5. Polynomial regression graph for each parameter and Satellite-Derived Indices.

3.3. Relationship Between Satellite-Derived Indices and Field Parameters

Polynomial regression analysis (**Fig. 5**) was conducted to examine the relationship between satellite-derived indices (NDVI and RdEdNDVI) and field-measured water quality parameters (SDD, TP, and Chl-a). Results showed that NDVI correlated most strongly with Total Phosphate (TP), yielding a high R^2 of 0.975, followed by SDD (R^2 = 0.727) and Chlorophyll-a (R^2 = 0.579). In contrast, RdEdNDVI showed the strongest correlation with Chl-a (R^2 = 0.959), while its relationships with TP (R^2 = 0.575) and SDD (R^2 = 0.280) were moderate to weak.

The best-fitting equations for NDVI were:

$$TP = -0.703(NDVI) + 3.105(NDVI^2) + 0.086 \quad (8)$$

$$SDD = 125.55(NDVI) - 483.99(NDVI^2) + 17.88 \quad (9)$$

Meanwhile, RdEdNDVI produced the most reliable model for estimating Chl-a:

$$Chl\text{-}a = 83.217(RdEdNDVI) - 466.276(RdEdNDVI^2) + 7.266 \quad (10)$$

These results indicate that NDVI (**Fig. 6a**) is a reliable indicator of nutrient levels (TP), possibly reflecting nutrient-induced changes in water color or algal presence. Conversely, RdEdNDVI (**Fig. 6b**) sensitivity to Chl-a is attributed to its red-edge band, which is more responsive to variations in algal pigments, especially in shallow or productive waters.

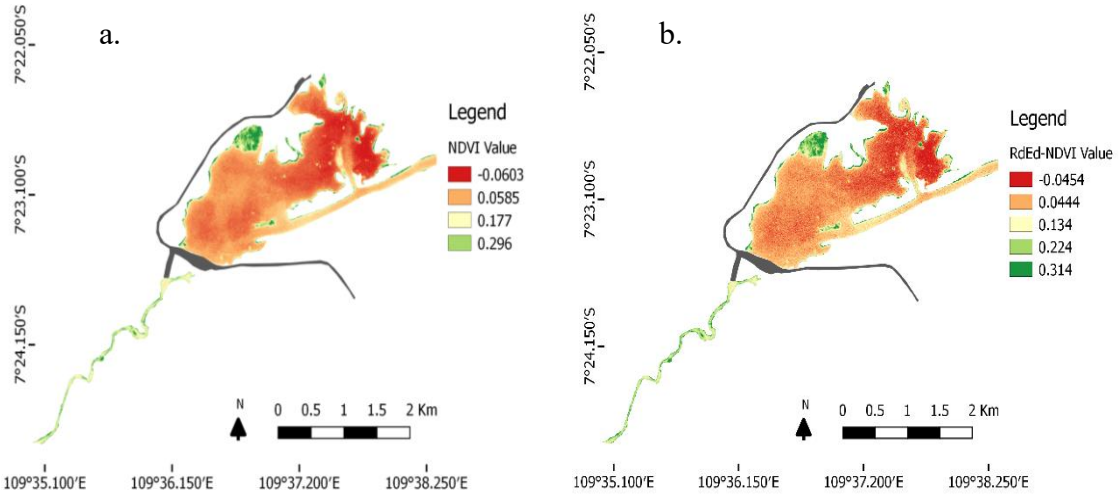

Fig. 6. Distribution map of Satellite-Derived Indice in Mrica Reservoir

Overall, the analysis confirms that both NDVI and RdEdNDVI can be used to estimate key water quality parameters, although their effectiveness varies depending on the parameter. NDVI is better suited for detecting nutrient-related signals such as TP, while RdEdNDVI is preferable for algal biomass (Chl-a) estimation. The relatively lower correlation with SDD suggests that water clarity is influenced by multiple factors, including inorganic particles, which are less detectable via spectral indices. **Fig. 7** shows the spatial distribution of Secchi Disk Depth (SDD), Total Phosphorus (TP), and Chlorophyll-a (Chl-a) in Mrica Reservoir derived from satellite imagery.

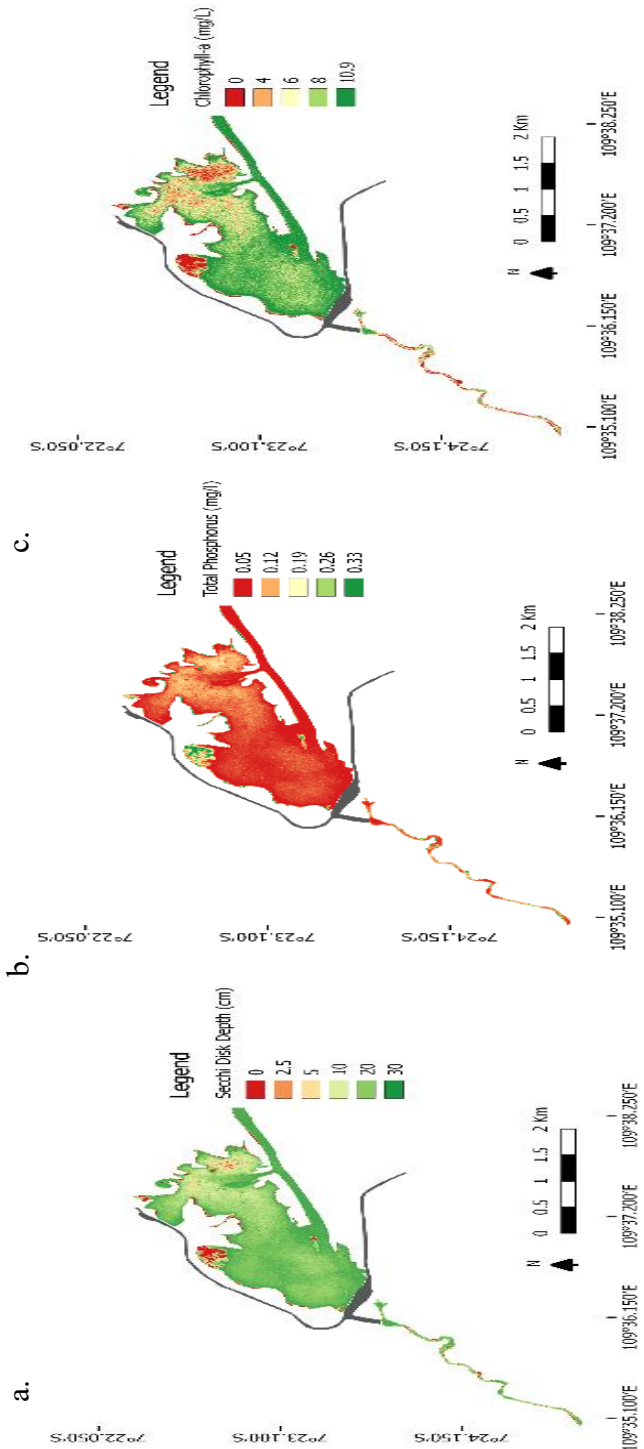

Fig. 7. Distribution map of Satellite-Derived parameters: a. SDD, b.TP and c. Chlorophyll-a.

Water clarity (SDD) is highest in the northern and central areas, while the southern region appears more turbid. TP and Chl-a concentrations are elevated in the southern and southwestern parts of the reservoir, indicating higher nutrient input and algal productivity near inflow areas. These patterns suggest a more eutrophic condition in the southern section, effectively captured through remote sensing analysis.

3.4. Trophic State Index (TSI) Analysis

The spatial distribution of the Carlson Trophic State Index (CTSI) across Mrica Reservoir is illustrated in **Figure 8**. The map reveals clear spatial variability in trophic conditions, with values ranging from moderately eutrophic to hypereutrophic.

Higher CTSI values are predominantly concentrated in the northern and inlet regions of the reservoir, which correspond to areas receiving direct nutrient inflow from upstream catchments.

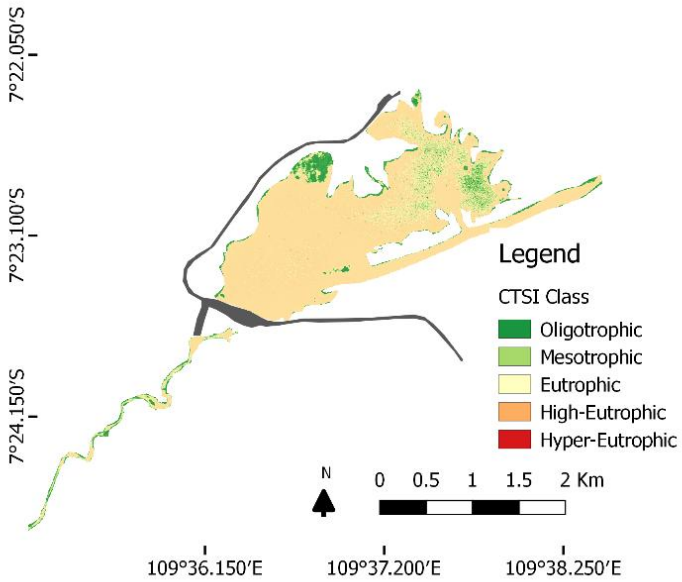

Fig. 8. Distribution of CTSI in Mrica Reservoir at April 15th 2025.

Station 6, located at the southern outlet, recorded the highest CTSI value of 76.4, classifying it as hypereutrophic. This suggests severe nutrient enrichment and likely frequent algal blooms. Other stations, such as St-2 and St-5, also fall within the eutrophic range (CTSI > 60), indicating considerable biological productivity and reduced water clarity. In contrast, the central and northern portions of the reservoir, represented by St-3 and St-1, showed comparatively lower CTSI values (59.8 and 63.4), though still within the eutrophic range.

The spatial interpolation highlights a degradation gradient from the inlet toward the outlet, implying that nutrient inputs are not well-distributed and may accumulate in stagnant or shallow zones. These findings align with earlier studies in other Indonesian reservoirs where land use pressures—particularly agriculture and settlements—contribute to elevated trophic conditions. Moreover, the variability in TSI values observed within Mrica Reservoir reflects the known challenges of applying standardized trophic indices in tropical systems, as highlighted by Cunha et al. (2021), who reported that traditional TSI interpretations may deviate significantly in tropical/subtropical contexts due to regional ecological and climatic factors.

This trophic state mapping underscores the importance of targeted management efforts in the upstream watershed to mitigate nutrient loading. Without intervention, areas such as the northern reservoir may experience further ecological stress, including reduced oxygen levels, harmful algal blooms, and impaired water usability.

The trophic status patterns and the correlation between NDVI-based indices and chlorophyll-a in Mrica Reservoir are consistent with findings from tropical reservoirs in Vietnam. For example, in Tri An and Dau Tieng reservoirs, NDVI derived from satellite imagery also showed strong correlations with chlorophyll-a concentrations, particularly during the dry season when algal blooms are more prominent (Hoang & Thi, 2025). This similarity underscores the broader applicability of vegetation indices for eutrophication assessment in Southeast Asia's tropical freshwater systems.

3.5. Implications of Remote Sensing for Water Quality Monitoring

This study demonstrates that vegetation indices derived from PlanetScope imagery—particularly NDVI and RdEdNDVI—can effectively estimate key eutrophication indicators. NDVI showed strong correlations with Total Phosphate ($R^2 = 0.975$) and Secchi Disk Depth ($R^2 = 0.727$), while RdEdNDVI had a slightly better relationship with Chlorophyll-a ($R^2 = 0.959$), likely due to its sensitivity to shallow water turbidity. These findings suggest that high-resolution remote sensing provides a viable alternative for spatially comprehensive monitoring, especially where field data are limited.

PlanetScope's 3-meter resolution and daily revisit capability offer significant advantages for detecting rapid or localized changes in small reservoirs like Mrica. Remote sensing reduces fieldwork dependence and enables monitoring of inaccessible zones. The effectiveness of red-edge indices in tropical aquatic environments has also been highlighted in recent studies (Liu et al., 2024), supporting their broader applicability.

However, limitations include cloud cover, mixed-pixel effects, and the inability to capture vertical water column variability. Calibration with field measurements remains essential. Despite these constraints, this approach aligns with similar research in Vietnam (Hoang & Thi, 2025) and holds potential for integration into Indonesia's national water quality monitoring framework. To enhance the practical use of remote sensing for water quality monitoring, we recommend a monthly satellite observation schedule, particularly during dry and post-rainy seasons when eutrophication risk is highest. Satellite-derived indices (e.g., NDVI, RdEdNDVI) should be integrated into local government GIS systems to support real-time visualization and spatial analysis for reservoir management. For accuracy, quarterly field validation is advised, with 12–20 sampling points measured for key parameters (e.g., Chlorophyll-a, SDD, TP) timed closely with satellite overpasses. This combined approach ensures consistent, scalable, and policy-relevant monitoring of reservoir health.

3.6. Limitations and Recommendations

This study acknowledges several limitations that may affect the accuracy and generalizability of the results. While PlanetScope offers high spatial resolution, its limited spectral range—particularly the absence of blue and shortwave infrared bands—reduces its sensitivity to water quality parameters such as turbidity and chlorophyll-a. Additionally, residual cloud cover (even below 10%) can introduce atmospheric noise, necessitating careful image pre-processing. The use of a single-date image restricts the ability to capture temporal variability in eutrophication dynamics, which can fluctuate significantly over days or weeks due to rainfall, runoff, or biological activity. As a result, the model may only reflect short-term water quality conditions, limiting its predictive robustness.

Field data collection posed additional challenges. Sampling was conducted over two consecutive days, potentially leading to temporal mismatches with the satellite overpass. Moreover, the limited number of sampling stations ($n = 6$) reduces the statistical power of the regression model and increases uncertainty in model coefficients. With such a small sample size, the coefficient of determination (R^2) may be unstable due to overfitting or the influence of outliers.

For spatial interpolation, techniques like IDW or Kriging become less reliable in areas far from sampling locations, with potential interpolation errors exceeding 20–30%, particularly in zones of rapid change such as inlets and outlets (Sferlazza et al., 2022). The importance of adequate spatial coverage has also been emphasized in coastal and wetland mapping applications, where undersampling can significantly distort feature representation (Wang et al., 2024; Costantino et al., 2020).

To address these limitations, future research should incorporate multi-temporal imagery across different seasons or hydrological events to better capture dynamic eutrophication trends. Integrating Sentinel-2, with its broader spectral capabilities, can enhance the sensitivity of spectral indices to water quality variations (Pahlevan et al., 2017; Wang et al., 2024). The use of machine learning algorithms, such as Random Forest or Support Vector Regression, may also improve model robustness, especially when field data are sparse. Finally, increasing the number of in-situ sampling stations (ideally >15–20) and synchronizing them with satellite overpass times would significantly improve the accuracy of validation efforts and reduce interpolation uncertainty.

4. CONCLUSIONS

The application of high-resolution PlanetScope satellite imagery in assessing the trophic state of Mrica Reservoir through the integration of remote sensing indices and field-based measurements has been discussed in this paper. By analyzing NDVI and RdEdNDVI alongside key water quality parameters−SDD, TP, and Chl-a, we identified strong correlations between satellite-derived indices and trophic indicators. NDVI was found to be particularly effective in estimating TP concentrations, while RdEdNDVI showed high sensitivity to Chl-a, highlighting their complementary utility for monitoring eutrophication.

The spatial distribution of CTSI revealed significant variation within the reservoir, with several zones−particularly near the outlet and southern sections−classified as eutrophic to hypereutrophic. These areas are likely influenced by anthropogenic nutrient loading and hydrological stagnation. Remote sensing provided valuable insight into spatial patterns that might be missed through limited field sampling alone, emphasizing its role in complementing traditional monitoring approaches.

Despite inherent limitations such as spectral constraints and cloud interference, the use of PlanetScope data proved beneficial for detecting spatial heterogeneity in water quality conditions. The integration of satellite imagery with in-situ data offers a cost-effective, scalable, and timely approach for supporting water resource management, especially in data-scarce regions.

Future efforts should focus on expanding temporal analysis, incorporating machine learning for predictive modeling, and enhancing field validation to improve the reliability of remote-sensing-based trophic state assessments. This approach has strong potential to be replicated in similar reservoirs across Indonesia, aiding in the development of sustainable freshwater management strategies.

REFERENCES

Alikas. K., & Kratzer. S. (2017). Improved retrieval of Secchi depth for optically-complex waters using remote sensing data. *Ecological Indicators*, 77. 218‑227. https://doi.org/10.1016/j.ecolind.2017.02.007

Anggraini, D., Pranoto, S.A., Wulandari, D.A. (2019). Economic Analysis of Mrica Reservoir Sedimentation Control. BRILIANT: Jurnal Riset dan Konseptual, 4(4), 567‑586. DOI: 10.28926/briliant.v4i4.378

APHA. (2017). Standard methods for the examination of water and wastewater (24th ed.). American Public Health Association.

Barbosa, C. C., Calijuri, M. d. C., Anjinho, P. d. S., Alves, A. C. (2022). An integrated modeling approach to predict trophic state changes in a large Brazilian reservoir. *Ecological Modelling*, 476: 110227. DOI: 10.1016/j.ecolmodel.2022.110227

Carlson. R. E. (1977). A trophic state index for lakes. *Limnology and Oceanography*, 22(2). 361‑369. http://dx.doi.org/10.4319/lo.1977.22.2.0361

Carlson. R.E. and Simpson. J. A. (1996). Coordinator's Guide to Volunteer Lake Monitoring Methods. North American Lake Management Society, 96 p. https://files.knowyourh2o.com/pdfs/CGVLMM.pdf

Cunha, D. G. F., Finkler, N. R., Lamparelli, M. C., Kalijuri , M. C., Dodds, W.K., & Carlson, R. E. (2021). Characterizing Trophic State in Tropical/Subtropical Reservoirs: Deviations among Indexes in the Lower Latitudes. *Environmental Management*, 68(3), 491‑504. DOI: 10.1007/s00267-021-01521-7

Costantino, D., Pepe, M., Dardanelli, G., & Baiocchi, V. (2020). Using optical satellite and aerial imagery for automatic coastline mapping. *Geographia Technica*, 15(2), 171‑190. DOI: 10.21163/GT_2020.152.17

Hoang, N. T., & Thi, T.V. (2025). Spatial Estimation of Trophic State for Reservoir Using Ground Monitoring and Remote Sensing Data. *Applied Environmental Research*, 47(1). https://orcid.org/0009-0008-6023-3240

Kutser. T. (2009). Passive optical remote sensing of cyanobacteria and other intense phytoplankton blooms in coastal and inland waters. *International Journal of Remote Sensing*, 30(17). 4401‑4425. DOI: 10.1080/01431160802562305

Liu, M., Zhan, Y., Li, J., Kang, Y., Sun, X., Gu, X., Wei, X., Wang, C., Li, L., Gao, H., & Yang, J. (2024). Validation of Red-Edge Vegetation Indices in Vegetation Classification in Tropical Monsoon Region−A Case Study in Wenchang, Hainan, China. *Remote Sensing*, 16(11), 1865. https://doi.org/10.3390/rs16111865

MOSE. (2009). Regulation of the Minister of State for the Environment Number 28 of 2009 concerning the Capacity to Carry Water Pollution Loads of Lakes and/or Reservoirs. Peraturan Menteri Negara Lingkungan Hidup Nomor 28 Tahun 2009 (5 august 2009), „Tentang Daya Tampung Beban Pencemaran Air Danau dan/atau Waduk", Republic Indonesia.

Pahlevan, N., Sarkar, S., Franz, B.A., Balasubramanian, S.V., He, J. (2017). Sentinel-2 MultiSpectral Instrument (MSI) data processing for aquatic science applications: Demonstrations and validations. *Remote Sensing of Environment*, 201, 47-56. https://doi.org/10.1016/j.rse.2017.08.033

Planet Labs PBC. (2025). PlanetScope satellite imagery. https://www.planet.com/products-v2b/.

Sagan, V., Peterson, K. T., Maimaitijiang, M., Sidike, P., Sloan, J., Greeling, B.A., Maalouf, S., Adams, C. (2020). Monitoring inland water quality using remote sensing: potential and limitations of spectral indices, bio-optical simulations, machine learning, and cloud computing. *Earth-Science Reviews*, 205, 103187. https://doi.org/10.1016/j.earscirev.2020.103187

Sferlazza, S., Maltese, A., Dardanelli, G., & La Mela Veca, D. S. (2022). Optimizing the sampling area across an old-growth forest via UAV-borne laser scanning, GNSS, and radial surveying. *ISPRS International Journal of Geo-Information*, 11(3), 168. https://doi.org/10.3390/ijgi11030168

Shaleh, F. R., Soewardi, K., & Hariyadi, S. (2014) Trophic State Evaluation in Inland Water Using Carlson's Index (Case Study: Gajah Mungkur Reservoir, Central Java). (Kualitas Air dan Status Kesuburan Perairan Waduk Sempor, Kebumen), *Jurnal Ilmu Pertanian Indonesia*, 19(3), 169‑173. https://journal.ipb.ac.id/index.php/JIPI/article/view/9152

Tyler. A. N., Hunter. P. D., Spyrakos. E., Groom. S., Constantinescu. A. M., & Kitchen. J. (2006). Developments in Earth observation for the assessment and monitoring of inland. transitional. coastal and shelf-sea waters. *Science of The Total Environment*, 572. 1307‑1321. https://doi.org/10.1016/j.scitotenv.2016.01.020

Wang, Y., Jin, S., & Dardanelli, G. (2024). Vegetation classification and evaluation of Yancheng coastal wetlands based on random forest algorithm from Sentinel-2 images. *Remote Sensing*, 16(7), 1124. https://doi.org/10.3390/rs16071124

PREDICTION OF SPATIAL LAND USE LAND COVER CHANGES IN BOVEN DIGOEL, SOUTH PAPUA IN 2031 AND 2041 USING LCM AND CA-MARKOV MODELS

Dewi Novita SARI[1], Muhammad Hafizh Fadhl MUTASHIM[2], Frichelia Varadhita RESTUVICA[2], Kusuma Prayoga Basuki PUTRA[3], Aziz Akbar MUKASYAF[4], Nirma Lila ANGGANI[4], Ayodya Rido NUGRAGA[2]

DOI: 10.21163/GT_2025.202.18

ABSTRACT

Boven Digoel Regency, located in South Papua Province, is one of the eastern regions of Indonesia targeted by the government for the development of a food estate project. However, massive land use and land cover (LULC) change require careful prediction over the coming decades to balance development with environmental sustainability. This study integrates advanced spatial modeling techniques to analyze recent trends and predict future LULC changes for 2031 and 2041. The objectives of this study are (1) to analyze the trend of forest to non-forest land use change in Boven Digoel Regency in 2024 using Land Change Modeler (LCM) and (2) to analyze the prediction of forest to non-forest land use change in 2031 and 2041 using Cellular Automata Markov (CA-Markov). The data used in this study include the administrative boundary of Boven Digoel, SPOT 6/7 imagery from 2016 and 2021, Digital Elevation Model (DEM), road network, government centers, river network, and settlements. The methods used in this study are a deep learning approach based on the LCM and a CA-Markov model, which combines CA-Markov land cover prediction methods. Results show that forest areas increased by 27.58% from 2016 to 2021 but are predicted to decline by 18.73% in 2031 and 51.49% in 2041, mainly due to ongoing plantation expansion in southern and northern Boven Digoel. This plantation expansion is predicted to spread from the southern and northern parts of Boven Digoel. Future studies should incorporate updated boundary information and integrate socio-economic, policy, and environmental drivers, such as soil and rainfall, to improve spatial accuracy and enhance the relevance of land use and land cover analysis.

Key-words: *LULC change, Multi-Criteria, LCM, CA-Markov, GIS.*

1. INTRODUCTION

South Papua is distinguished by its characteristic tropical rainforest climate and biodiversity, which is distinct from other regions of eastern Indonesia. Boven Digoel is one of the districts in South Papua that still faces significant challenges related to land use and land cover change. The Boven Digoel Forest is part of the lowland tropical rainforest landscape in Boven Digoel, Southern Papua, characterized by unique ecological features and relatively minimal large-scale anthropogenic disturbances. In the classification of natural forest ecosystems, this area is dominated by lowland tropical rainforest with high humidity, annual rainfall exceeding 2,500 mm, and extremely high biodiversity in terms of both flora and fauna. The dominant vegetation consists of tall, closed-canopy tree species such as *Pometia pinnata*, *Intsia bijuga*, *Palaquium* spp., as well as species from the *Dipterocarpaceae* family, which are found only in the Indo-Malayan and Papuan regions (Barri et al., 2019).

[1]*Department of Geographic Information Science, Faculty Geography Universitas Muhammadiyah Surakarta. Corresponding author* (DNS)* dns104@ums.ac.id

[2]*Laboratory of Remote Sensing and GIS, Faculty Geography Universitas Muhammadiyah Surakarta. (MHFM)* hafizhfadhl39@gmail.com *, (FVR)* varadhitapcd@gmail.com *, (ARN)* ayodya.rido@gmail.com

[3]*Department of Disaster Management, Faculty of Mineral Technology, Universitas Pembangunan Nasional "Veteran" Yogyakarta. (KPBP)* gisprayoga@gmail.com

[4]*Department of Geography, Faculty Geography Universitas Muhammadiyah Surakarta. (AAM)* aam617@ums.ac.id *, (NLA)* nla624@ums.ac.id

The stratified forest structure and dense canopy make this forest a highly effective natural carbon sink, with substantial stand biomass and a high rate of carbon accumulation (Hendri et al., 2022). Beyond its vegetation cover, the Boven Digoel Forest also holds crucial macro-ecological functions. The region forms part of the broader regional hydrological system, sustaining the stability of major river flows in Papua, such as the Digul River and its tributaries. In forestry science, the role of forests as catchment areas is vital for regulating water systems, preventing seasonal floods, and facilitating groundwater recharge (Wambrauw, 2015). In addition, the swamp and peat forest areas in the southern part of Boven Digoel serve as significant soil carbon stocks, with quantities reaching hundreds of tons per hectare. However, this potential also carries high vulnerability (Dommain et al., 2016). When swamp and peat forest areas are drained or cleared for food estate projects or large-scale plantations, the carbon stored over thousands of years can be released in a short period, triggering greenhouse gas emissions far greater than those caused by conventional land-use conversion (Gandhi, 2013). From a socio-ecological perspective, the forests of Boven Digoel cannot be separated from the presence of indigenous communities who have lived in and with the forest for generations (Putrie et al., 2025). Ethnic groups such as the Awyu, Korowai, Kombai, and others maintain an unwritten yet highly structured system of spatial management. Within the framework of forestry science, the practices of these indigenous communities reflect a form of traditional silvicultural system based on functional zonation (Kristin et al., 2025).

Unfortunately, the ecological and social values of the Boven Digoel forest are now under severe pressure, primarily due to national development policies that have yet to fully incorporate landscape-based approaches and the rights of indigenous peoples. Since the early 2000s, thousands of hectares of forest in this region have been allocated for large-scale plantation concessions, including the establishment of food estate areas (Parsch, 2024). The expansion of food estates as part of the National Strategic Projects (PSN) has further intensified this pressure. Spatial analyses and Land Use Land Cover (LULC) simulations indicate that much of the land being converted lies within primary forests, peatland areas, and customary territories (Putrie et al., 2025). Within the framework of sustainable forest management, such development contradicts the precautionary principle, as it disregards the forest's ecological carrying capacity, its carbon sequestration potential, and its socio-cultural values.

Food Estate is an Indonesian government program to increase national food security through integrated agricultural development (Direktorat Pengukuhan dan Penatagunaan Kawasan Hutan Direktorat Jenderal Planologi Kehutanan dan Tata Lingkungan, 2020). This program is part of the National Strategic Program (PSN) and the National Food Barn Program (LPN) for the period 2020-2024 (Widiastuti et al., 2023). This program is prioritized in several provinces, including North Sumatra, Central Kalimantan, East Nusa Tenggara, and Papua. This is reinforced by Regulation of the Minister of Environment and Forestry Number P.24/Menlhk/Setjen/Kum.1/10/2020 concerning the Provision of Forest Areas for Food Estate Development, referred to as P.24 (Walhi, 2021).

The province of South Papua will be one of the priority areas for the food estate plan in the coming year. The development will require at least 1.3 million hectares of forest land, part of which is in Boven Digoel Regency (Econusa, 2021). Boven Digoel Regency has an area of 2,710,829 ha (BPS, 2025). This area is certainly considered to have potential for converting peatlands into food estates in the future.

According to the initial report on the food estate project, carbon reserves estimated at 2.7 million hectares of forest and peatland in Merauke, Mappi, and Boven Digoel will be converted into food barns by 2024 (Lantipo, 2022). It is estimated that 2.7 million hectares of land in South Papua can absorb around 268 million tons of carbon (Simamora et al., 2021; Widiastuti et al., 2023; Swindles et al., 2024). This is not the first time this project has been carried out. Previously, there have been several stages of development on several islands in Indonesia (Rasman et al., 2023; Neilson & Wright, 2017). Based on data from several NGOs, approximately 200,000 hectares of peatland capable of absorbing ±50 million tons of carbon will be threatened with destruction as a result of this project (Walhi Kalimantan Tengah, 2021). This amount is only a small part of other land cover areas in Papua. This certainly contradicts Indonesia's agreement to the COP 26 international agreement in Glasgow

in 2021. Indonesia is being encouraged by the international community to reduce carbon emissions by 26% by 2030 (Redaksi Hijauku, 2021).

A novel methodology is imperative to forecast the long-term ramifications of developmental initiatives in Boven Digoel by using combination GIS (remote sensing) and deep learning). Remote sensing technologies, such as satellite imagery, LiDAR, and radar, enable large-scale and frequent monitoring of forested areas including remote zones thus, allowing accurate detection of land-use and land-cover changes, biomass, canopy structure, and forest health (FAO, 2019). When combined with GIS and advanced machine learning models (e.g., LCM, CA-Markov), these systems support accurate classification, predictive land-cover simulations, and evidence-based forest management (Gadal & Mozgeris, 2025). Moreover, long-term sensors like Landsat ensure continuity for temporal trend analysis. These remote methods are not only cost-effective compared to traditional ground surveys but also pivotal for early alerting, decision-making, and sustainable land governance (Wulder et al., 2019). In addition to land change data, spatial information is required to identify the location, distribution, and extent of forests that will be converted into agricultural land (Fikriyah et al., 2024).

Deep learning is a method that facilitates the expeditious and automated classification of extensive land use, and it can be integrated with spatiotemporal satellite imagery data (Masolele et al., 2021; Benjamin et al., 2020). The sophistication of this approach lies in its ability to classify data quantitatively, effectively, and cost-efficiently (Masolele et al., 2021; Sari et al., 2024). The Land Change Modeler (LCM) is a tool employed for the analysis of land use and land cover changes. It is most commonly used to detect, understand, and predict landscape changes, particularly in the context of environmental management and regional planning. It is integrated into software such as IDRISI TerrSet (Sànchez-Marrè, 2022). The LCM is capable of analyzing change patterns based on satellite imagery, identifying the drivers of change (e.g., human activities or environmental conditions), and predicting future changes using techniques such as Markov Chain and Cellular Automata (Mokarram & Minh, 2022).

The properties of the Markov CA model are contingent on past, present, and future conditions. This model incorporates specific binding rules for future pixel changes (Mokarram & Minh, 2022). Consequently, these models necessitate a high degree of accuracy. One applicable model is the CA-Markov model (Mishra et al., 2014). The software's advanced visualization capabilities and Kappa value model validation ensure the accuracy of the results, which support decision-making related to land use planning and sustainable environmental management.

Research on forest to non-forest land use change using LCM and CA-Markov is still rare, as the majority of studies focus on overall land use change. For instance, Akdeniz, (2022) examined alterations in land use in Belek, Turkey, employing Landsat imagery from 1985, 2000, and 2021, and projected future changes up to the year 2040 using LCM. The findings indicated an augmentation in residential areas, forests, and water bodies, accompanied by a diminution in barren land and agricultural land. The 2040 prediction indicates a 5.46% expansion of residential areas and a 4.21% decrease in agricultural land. Another study by Khan et al., (2021) detected land use changes in Quetta, Pakistan, between 1998 and 2018 and predicted changes up to 2028 using CA-Markov. Their findings include an increase in built-up areas by 6.56 km^2 and a decrease in green areas and open spaces.

Concurrently, Asra et al., (2020) employed the CA-Markov model to forecast land-use alterations in the Bila Sub-Watershed up to the year 2036. The results indicated a substantial decline in primary dryland forests and shrublands, accompanied by an increase in mixed dryland agriculture and secondary dryland forests. The scientific validity of this model is supported by a Kappa value of 0.9. The integration of these two methodologies has been demonstrated to yield precise outcomes for applications in land use forecasting and predictive studies.

Based on this background, the specific objectives of this study are as follows: (1) to analyze trends in the extent of forest to non-forest land use change in Boven Digoel Regency from 2016 to 2021 using LCM and (2) to analyze predictions of the extent of forest to non-forest land use in 2031 and 2041 using CA-Markov. The present study focuses on LULC modeling with driving factors such as distance to roads, government, settlements, rivers, and slope.

2. STUDY AREA

Boven Digoel Regency was formerly part of Merauke Regency in Papua Province and was established as a separate regency in 2002. Prior to the administrative restructuring and provincial changes, in 2000 the Merauke Regency Government allocated 460,000 ha for plantations, mostly forest areas, designated for 12 companies (Andrianto et al., 2014). Boven Digoel Regency is one of four regencies that share a direct border with Papua New Guinea. From an astronomical perspective, the Boven Digoel Regency is situated within the following coordinates: 4°58'–7°00' south latitude and 139°90'–141°00' east longitude. In the formation of the administrative region of Boven Digoel Regency up to 2023, Boven Digoel Regency has 20 districts with a population of 71,997 as of 2024 (Pemerintah Kabupaten boven Digoel, 2023). Boven Digoel exhibits the capacity to expedite the cultivation of food crops in Papua, with a total of 610,990 ha of rice field land designated as S3 land suitability class (Wulanningtyas et al., 2025). Approximately 1,531 ha of agricultural land are utilized by 2,044 indigenous farmers, primarily engaged in hunting, vegetable farming, fruit cultivation, bio-pharmaceuticals, oil palm, cocoa, and rubber. According to BPS data from 2025, over 90% of the indigenous or traditional communities of Boven Digoel reside in rural villages. This district is also one of the areas with the highest stunting rates in South Papua in 2023, at 42%, with a poverty rate of 20%. On the other hand, it has experienced an expansion of oil palm plantations exceeding 23,275.18 ha (Savitri et al., 2023). **Fig. 1.** illustrates the administrative location of the study area.

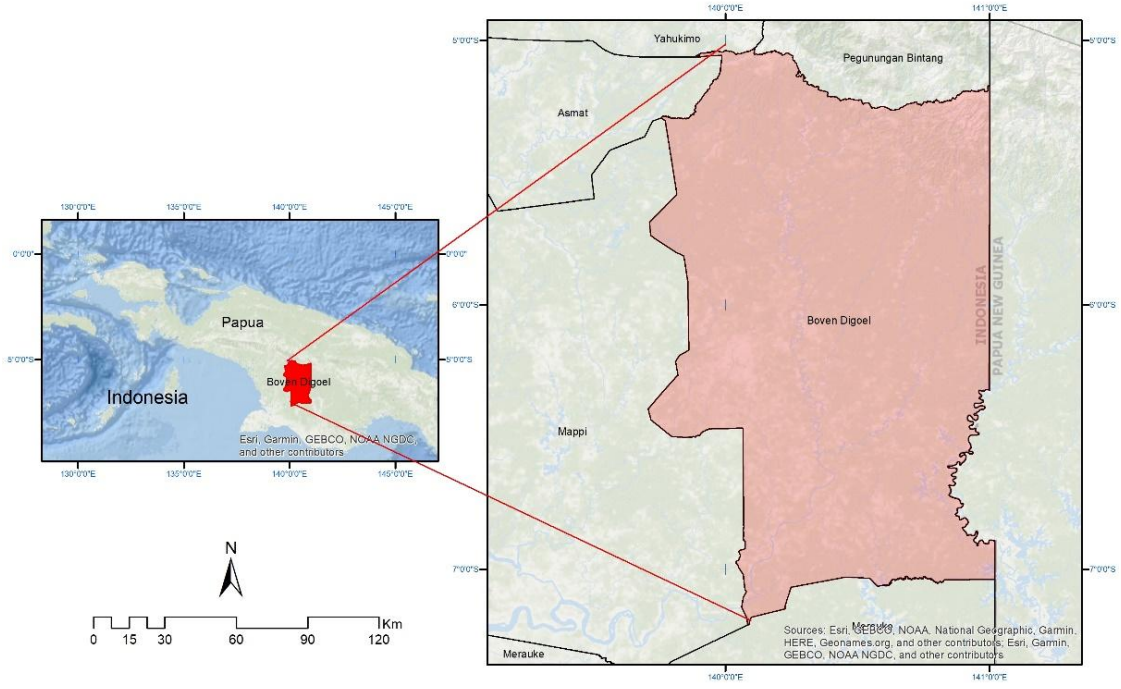

Fig. 1. Location of study in Boven Digoel, West Papua.

3. DATA AND METHODS

3.1. Pre-processing

The research process is divided into six stages: preparation, data processing, data analysis, data validation, and completion. The initial processing stage is comprised of three primary components: satellite image download, layer stacking, and radiometric correction of images. Its primary function is to amalgamate disparate scenes, comprising distinct bands, into a unified entity. Image correction

is a process that aims to enhance the visual clarity of images that have been compromised. This phenomenon is attributable to the elevated cloud cover observed around the equator. The correction implemented in this study is radiometric correction. **Table 1** shows the data utilized in this study following a geodatabase model (Nicoară & Haidu, 2011).

Table 1.

Data and sources used in the study.

Nr	Data	Source	Purpose
1	*Shapefile* data on the administrative boundaries of Boven Digoel Regency in 2016	Geospatial Information Agency	Research area boundaries
2	SPOT remote sensing images from 2016 and 2021.	USGS	LULC identification
3	Large-scale land cover classification regulations	Geospatial Information Agency	LULC identification
4	Digital Elevation Model (DEM) with a spatial resolution of 8–30 m.	Geospatial Information Agency (DEMNAS)	Analysis of driving factors slope
5	*Shapefile* data on road networks	Geospatial Information Agency	Analysis of driving factors to accessibility
6	*Shapefile* data on government centers	Geospatial Information Agency	Analysis of driving factors to government centers
7	*Shapefile* data on river networks	Geospatial Information Agency	Analysis of driving factors to rivers
8	*Shapefile* data on settlements	Geospatial Information Agency	Analysis of driving factors to LULC

3.2. Processing

In the digital image processing stage with deep learning, maximum likelihood classification (MCL) is used to identify differences in land use changes, mainly conservation forest land in Boven Digoel. MLC is a statistical-based guided model used to group image pixels into the most likely classes. This method is more complex in calculating probabilities (Malczewski, 1998). Based on the LULC classification of Boven Digoel from Geospatial Information Agency, there are eight land use/land cover types as follows in **Table 2.**

Table 2.

LULC classes Considered in this study.

Nr	LULC	Description
1	Agriculture	Areas utilized for agricultural purposes, with or without water management
2	Forest	Land covered with various types of trees or vegetation that are not managed by humans
3	Openland	Land that is neither cultivated nor inhabited
4	Plantation	Planned cultivation aimed at achieving optimal commodity yields
5	River	A substantial watercourse, typically formed naturally
6	Settlement	Areas specifically used for residential purposes
7	Shrubland	Land dominated by shrubs or low woody vegetation, typically less than 5 meters in height, with sparse or no large trees
8	Wetland	Low-lying land that is flooded and typically contains aquatic vegetation

Source: Geospatial Information Agency (2024).

The land use map generated from the supervised method is still an estimate (tentative). Accuracy testing of land use modeling with actual conditions in the field is required. In machine learning, there is a term called a confusion matrix that can be used for accuracy testing of land use modeling. A confusion matrix is a table that describes errors in land use obtained from the image classification process **(Table 3).** The table contains rows and columns representing the number of correctly and

incorrectly classified data points. The classification was based on 30 randomly selected samples generated using the Create Random Points tool in ArcGIS. All 30 samples were validated using Google Earth imagery from the same year as the input data to minimize validation errors. Among the eight-land use/land cover (LULC) classes, forest is the most dominant. Therefore, the sampling process generally yielded the highest number of samples from the forest class compared to other LULC classes. The following is an example of creating a confusion matrix. The matrix calculation consists of the overall proportion of the number of correct pixels (Congalton & Green, 2019). The Kappa coefficient is calculated based on the formula (Stehman, 1997) with interpretation (Landis & Koch, 1977):

$$Overall\ acuracy\ (OA) = \frac{\Sigma_i n_{ii}}{N} \quad (1)$$

$$Producer's\ accuracy\ for\ class\ i\ (PAi) = \frac{n_{ii}}{r_i} \quad (2)$$

$$User's\ accuracy\ for\ class\ i\ (UAi) = \frac{n_{ii}}{c_i} \quad (3)$$

$$Kappa = \frac{n\sum_{i=1}^{q}(nii) - \sum_{i=1}^{q}(riCi)}{n^2 - \sum_{i=1}^{q} riCi} \quad (4)$$

Table 3.

Confusion matrix used to compute OA, PA, and UA.

Validation / Model				Row Total (r_i)
	LCu	LCa	LCw	
LCu	nuu	nua	nuw	ru
LCa	nau	naa	naw	ra
LCw	nwu	nwa	nww	rw
Column total (C_i)	Cu	Ca	Cw	N

where:
nii = Number of correctly classified samples (pixels) in class i (diagonal of the confusion matrix)
N = Total sample for accuracy test
r_i = Total number of reference samples in class i (row total)
c_i = Total number of samples classified as class i (column total)
k = kappa coefficient
q = number of land classes

The accuracy of land use was assessed by calculating the Kappa coefficient, as outlined by Landis & Koch (1977). An acceptable accuracy value (substantial) when using the Kappa method is >0.6 for land use classification mapping. **Table 4.** presents the standard interpretation of Kappa results used in this study.

Table 4.

Interpretive standard for the kappa Index.

Kappa Index	Interpretation
>0.8	Almost Perfect
>0.6	Substantial
>0.4	Moderate
>0.2	Fair
0-0.2	Slight
<0	*Poor*

Source: Landis & Koch (1977).

3.3. Post-Processing

This study employed TerrSet LiberaGIS (version 20.0.2), utilizing the Land Change Modeler module. The mandatory stages were changing analysis and transition potential. In the first stage, the LCM Session Parameters were set using land cover data from two different years along with road and slope (elevation) data. Change Analysis was then conducted to identify land cover changes between the two years, followed by the creation of Change Maps to specify which land cover classes would be predicted in this case focusing on transitions toward plantation areas.

The Spatial Trend of Change module was applied to examine human-induced patterns of change, particularly the conversion of forest to plantations, using a polynomial trend function to capture dominant directions of change (Kurniawan & Roychansyah, 2023). The Transition Sub-model was then used to identify and model forest-to-plantation transitions, incorporating driving factors such as roads, settlements, government facilities, slope, and rivers. Finally, the Multi-Layer Perceptron (MLP) algorithm was applied to generate a transition potential map (ranging from 0 to 1), where values close to 0 indicate very low likelihood of change, and values close to 1 indicate very high likelihood of change (Clark Labs, 2017).

CA-Markov is a method for projecting land use changes by assuming that future land change patterns will be similar to those that occurred in the past (Deng et al., 2009; Asra et al., 2020). This projection takes into account land use classes in the previous period as well as the influence of surrounding land use (*neighborhood*) (Hadibasyir et al., 2023).

The Markov Chain module generates a transition matrix or probability matrix, which shows the transition of land use from the initial period to the predicted period. Markov equations are constructed by referring to the distribution of land use at the beginning and end of the observation period, which is represented in the form of a vector (single-column matrix), and a transition matrix that describes the probability of change between land classes. The relationship between the three matrices can be illustrated mathematically:

$$MLC.Mt = Mt+1 \tag{5}$$

$$\begin{vmatrix} LCuu & LCua & LCuw \\ LCau & LCaa & LCaw \\ LCwu & LCwa & LCww \end{vmatrix} \begin{vmatrix} Ut \\ At \\ Wt \end{vmatrix} = \begin{vmatrix} Ut+1 \\ At+1 \\ Wt+1 \end{vmatrix} \tag{6}$$

where:

Ut, *At*, and *Wt* represent the proportion (probability) of each land cover class (urban, agriculture, and woodland/water) at time *t*.

The transition probabilities are denoted by *LCij*, where *i* is class at time *t* and *j* is the class at time *t+1*.

For example, *LCcua* indicates the probability of land cover changing from urban *(u)* at time *t* to agriculture *(a)* at *t+1* (Asra et al., 2020).

The following **Table 5**. directly corresponds to the Markov transition probability matrix presented in Equation 4. The table represent the number of pixels in each land cover class at year *i* that are projected to year *i+n*.

Table 5.

Predicted land use calculations in CA-Markov.

LULC year i	LULC year i+n		
	Pit2	Pit2	Pzt2
Pit1	Xii	……	……
Pit1	……	Xii	……
Pzt1	……	……	Xii

Description:

Mt = Map at time *t*
Mt+1 = Map at time *t+1*
MLC.Mt = Markov Land Cover model applied to map *Mt*
LC = *LULC* changes
u = Urban
a = Agriculture
w = Woodland/water
Pit1 = Pixels of land use type *1* in year *t1*
Pit2 = Pixels in land use type *2* in year *t2*
i = year-1
n = prediction year
z = number of land use types
Xii = probability of pixels remaining in the same classin period *t1-t2*

3.4. Projection using driving factors

Forest land projections for 2031 and 2041 can be made using the CA-Markov algorithm (please see the research methodology in **Fig. 2**).

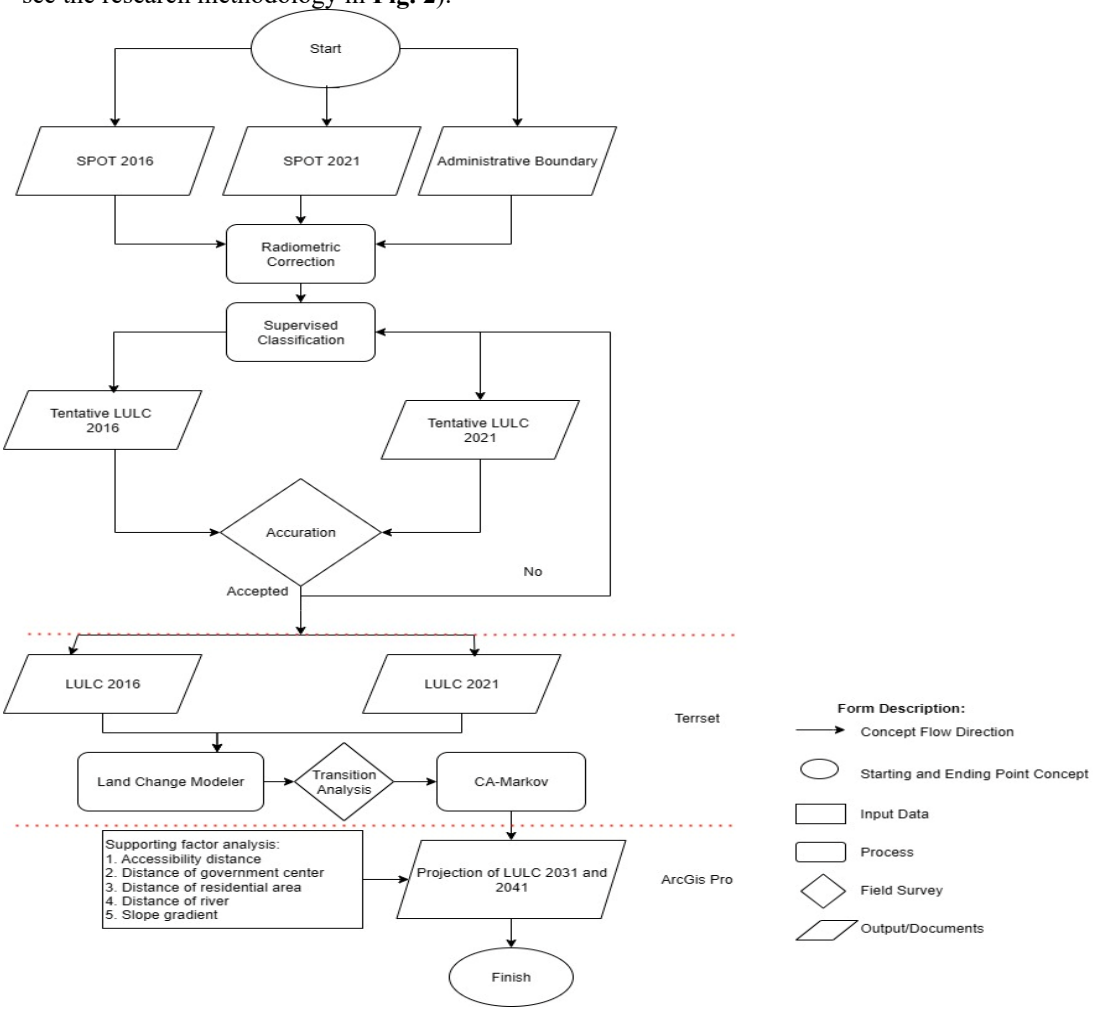

Fig. 2. Flowchart of research methodology.

The predictions are made using transition analysis with the most recent year being 2021. The selection of driving factors was based on observed land cover changes over the two-year period, reflecting human activities in the study area. Distance to roads represents accessibility and the influence of transportation networks on land development, while distance to government centers indicates concentrations of human activity, such as sub-district offices. Distance to settlements reflects population expansion, and proximity to rivers shows human utilization of water resources. Slope affects land use suitability, with steep areas generally avoided for settlements or other human activities, whereas flat areas are more likely to be developed.

The satellite data used are SPOT-6/7 (*Satellite Pour l'Observation de la Terre*) with spectral bands of Panchromatic (1.5 m), Blue (450–520 nm, 6 m), Green (530–590 nm, 6 m), Red (625–695 nm, 6 m), and NIR (760–890 nm, 6 m). The spatial resolution is 1.5 m (pan-sharpened) and 6 m (multispectral), with a temporal revisit of 1–3 days when both satellites operate in constellation (European Space Agency (ESA), 2024). The acquisition time was 2016 and 2021. These images can record appearances better than medium-resolution images, especially for areas around the equator with high cloud cover. The method used to create LULC maps is maximum likelihood classification. This method allows for maximum classification of land use based on criteria that have been exemplified at the time of classification (Mosleh, 2025). These datasets were processed and analyzed to generate land use/land cover maps, which were then used as inputs for the Land Change Modeler to project future scenarios. The results will be in the form of algorithm values from software that can distinguish land cover from predicted to unpredictable. Furthermore, the results can be analyzed using several supporting factors such as accessibility, distance from government centers, residential areas, river flows, and slope gradients. An example of prediction using driving factors was also conducted by Sow et al., (2016), who used satellite data from the Global Solar Atlas (GSA) and the Global Wind Atlas (GWA) to assess the potential of green hydrogen derived from two renewable energy sources, solar and wind.

4. RESULTS

4.1. Past LULC Classification and Classification Accuracy

Based on the results of LULC changes from 2016 to 2021 **(Fig. 3**), a confusion matrix was created to determine the overall accuracy and kappa index.

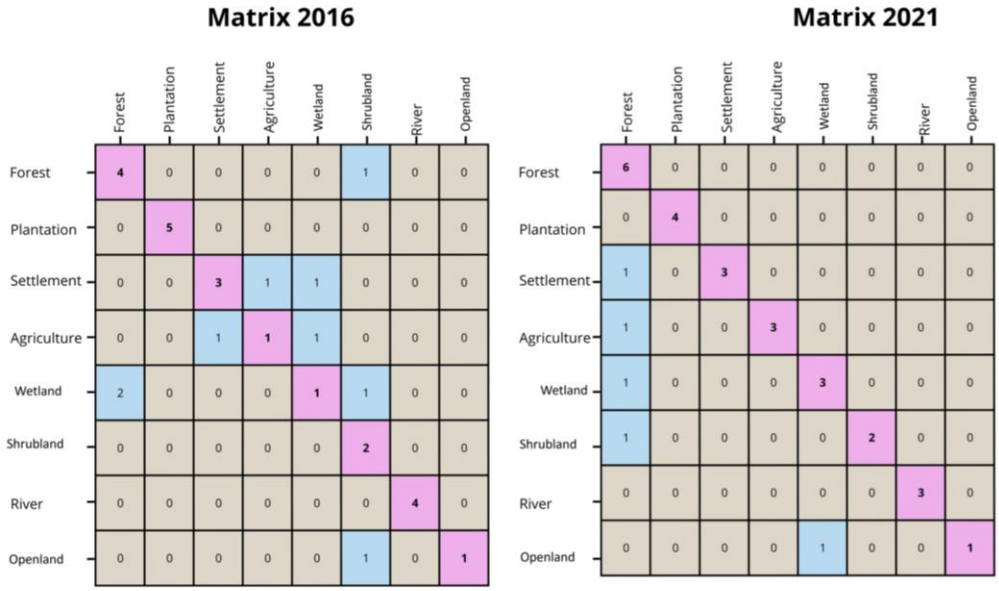

Fig. 3. Confussion matrix 2016 and 2021.

This became the basis for validating the prediction model to ensure its suitability for use (Congalton & Green, 2019). Based on the LULC modeling results, the matrix in 2016 had 21 correct values out of a total of 30 samples. The overall accuracy was 70% with a kappa index value indicating substantial agreement (0.652). Meanwhile, the matrix in 2021 had 25 correct values out of a total of 30 samples. The overall accuracy was 83.33%, with a kappa index indicating high agreement (0.804) between the classification and reference data. The confusion matrix results were then used to develop models for the years 2031 and 2041 using the TerrSet software.

4.2. Mapping and projection of LULC in Boven Digoel

Based on land cover change data from 2016 to 2021 (**Fig. 4** and **Table 6**), the most striking change occurred in the forest category, which increased by 329,765.53 ha (13.07%), from 1,992,569.58 ha (79.19%) to 2,322,335.11 ha (92.26%). This increase is a strong indication of rehabilitation or reforestation efforts, as well as the possibility of shrub or swamp land being reclassified as forest. This is reinforced by data showing that shrubland decreased dramatically by 148,426.51 ha (-5.90%) and swamp land decreased by 107,297.52 ha (-4.27%). Additionally, open land has significantly decreased by 17,222.55 ha (-0.68%), indicating substantial land conversion over the past five years. On the other hand, agricultural land has declined sharply to almost disappear, from 56,794.47 ha to only 149.82 ha (-2.25%), most likely due to conversion into forests, plantations, or other forms of land use. Conversely, plantation land increased by 6,279.56 ha (0.25%), indicating an expansion of areas for the cultivation of perennial crops. These changes reflect intensive land use dynamics, with a dominant conversion to forest and plantations, although further study is needed to determine whether the increase in forest cover is natural, the result of rehabilitation, or merely a change in classification.

According to data from the Indigenous Territory Registration Agency (BRWA) in 2024, Papua has approximately 13.4 million hectares of indigenous territory, with 92% of it, or 12.35 million hectares, having the potential to become indigenous forests (World Resource Institute (WRI) Indonesia, 2025). The indigenous community in Boven Digoel has a spatial management system based on “customary rights” (Ungirwalu et al., 2025), where customary areas are used communally and with full local wisdom. Traditional activities such as hunting, farming, fishing, and non-timber forest product collection are carried out without damaging the ecological structure of the forest. Therefore, the 2016-2021 LULC change showing an increase in forest area may reflect the sustainability of indigenous peoples' management practices or changes in land cover classification due to natural vegetation recovery in indigenous territories.

However, it cannot be ignored that during the same period there was a large-scale conversion of swamp and agricultural land to other forms of land cover (Savitri et al., 2023). This indicates external pressures, such as plantation expansion or development interventions, that have the potential to marginalize indigenous peoples’ management systems. In some cases (Amin et al., 2025) (Wulanningtyas et al., 2006), land conflicts arise due to overlaps between large-scale concessions and customary territories that have not been legally recognized.

Predictions of LULC changes for 2031 and 2041 (**Fig. 4**) indicate relatively moderate but consistent shifts, particularly between the two primary categories of forest and plantation. Forests, although still dominating land cover (more than 90% of the total area), are expected to undergo a gradual decline: by 20,020.36 ha (-0.75%) between 2021 and 2031, and by 16,481.52 ha (-0.66%) between 2031 and 2041. This decline suggests that pressure on forest areas persists, albeit not to the same extent as in previous periods. This phenomenon may be attributed to various factors, including plantation expansion and infrastructure development, which have led to a gradual shift in the boundaries of natural forests.

Conversely, the area dedicated to plantations is projected to rise steadily, from 68,963.04 ha in 2021 to 104,469.12 ha in 2041, representing an increase of 35,506.08 ha (1.42%) over the span of two decades.

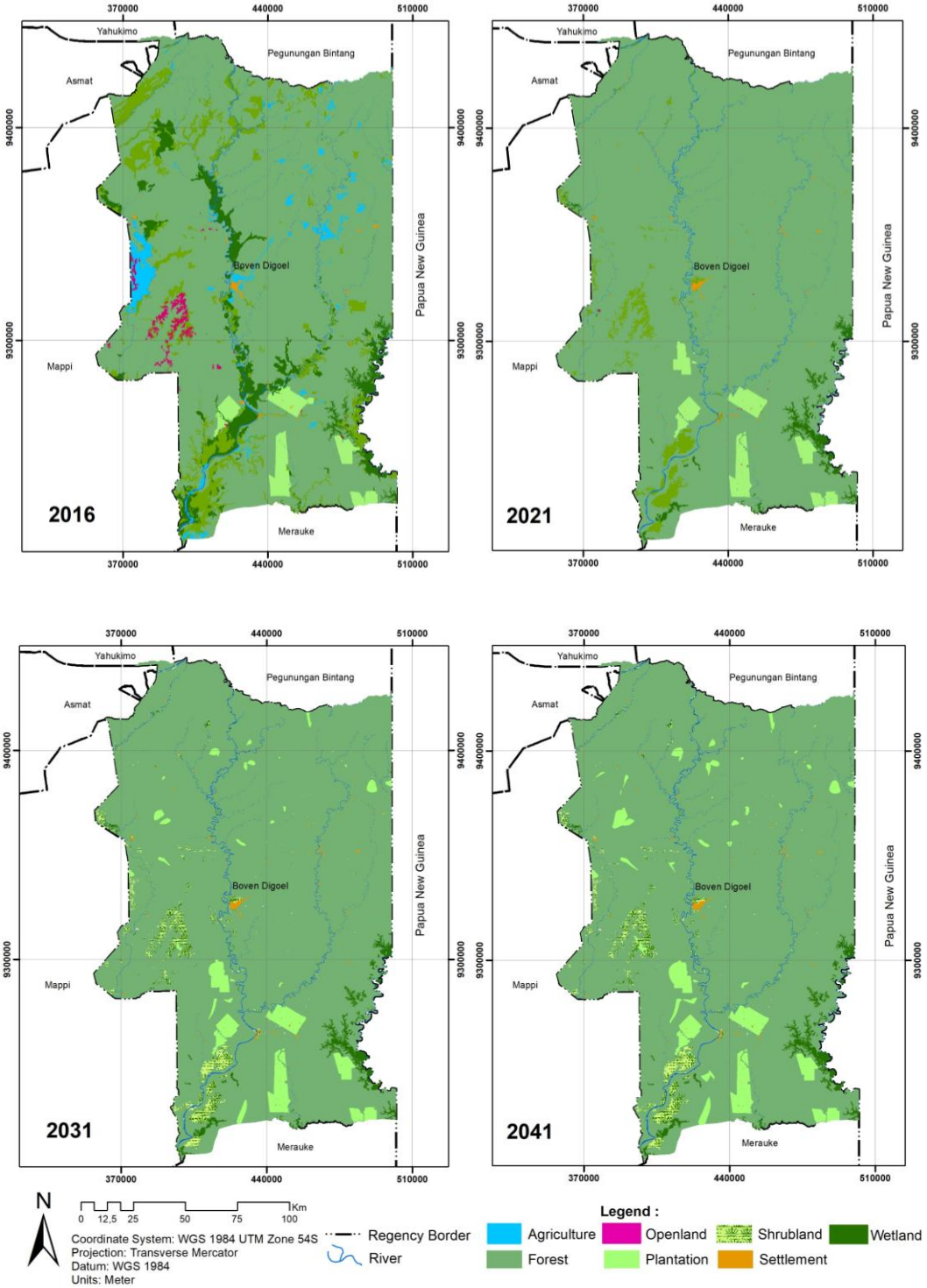

Fig. 4. Projection of LULC changes in Boven Digoel from 2016, 2021, 2031, and 2041.

Table 6.

Calculation of predicted LULC areas in 2016, 2021, 2031, and 2041.

LULC	Area 2016 (ha)	(%)	Area 2021 (ha)	(%)	LULC changes from 2016 to 2021 (ha)	(%)	Area 2031 (ha)	(%)	LULC Prediction 2021 to 2031 (ha)	(%)	Area 2041 (ha)	(%)	LULC Prediction 2031 to 2041 (ha)	(%)
Forest	1,992,569.58	79.19	2,322,335.11	92.26	329,765.53	13.07	2,302,314.75	91.51	-20,020.36	-0,75	2,285,833.23	90.86	-16,481.52	-0.66
Plantation	62,683.48	2.49	68,963.04	2.74	6,279.56	0.25	87,987.60	3.50	19,024.56	0.76	104,469.12	4.15	16,481.52	0.66
Settlement	7,560.84	0.30	6,477.69	0.26	-1,083.15	-0.04	6,472.53	0.26	-5.16	0.001	6,472.53	0.26	0	0
Agriculture	56,794.47	2.26	149.82	0.01	-56,644.65	-2.25	150.12	0.01	0.30	0.001	150.12	0.01	0	0
Wetland	143,388.09	5.70	36,090.57	1.43	-107,297.52	-4.27	36,072.18	1.43	-18.39	0.001	36,072.18	1.43	0	0
Shrubland	205,753.63	8.18	57,327.12	2.28	-148,426.51	-5.90	57,208.32	2.27	-118.80	0.004	57,208.32	2.27	0	0
River	29,672.07	1.18	25,352.07	1.01	-4,320.01	-0.17	25,246.44	1.00	-105.63	0.004	25,246.4	1.00	0	0
Openland	17,680.88	0.70	458.33	0.02	-17,222.55	-0.68	460.71	0.02	2.38	0.001	460.71	0.02	0	0
Total	2,516,103.04	100	2,517,153.75	100			2,515,912.65	100			2,515,912.65	100		

Source: Analysis, 2025.

This phenomenon signifies a shift toward the intensification of commodity-based economic activities, such as oil palm plantations (Obidzinski et al., 2025), which is often the main driver of land use change in Papua. This growth is likely to take space from natural forests or other land that is not intensively utilized. Meanwhile, other categories such as settlements, swamps, scrubland, and open land show a stagnant trend with no significant change. This may reflect physical space constraints, protection of specific ecosystems, or land-use policies that restrict the expansion of such land types. However, this stability could also indicate that future pressure will be more focused on forests as a reserve space for economic expansion.

4.3. Driving factors for LULC changes

Driving factors in LULC prediction modeling serve to determine the impact of land use changes and directly influence the accuracy and success of predictions (Congalton & Green, 2019). In this study, the main focus is on the conversion of forest land to plantations in the next 20 and 30 years. Driving factors can be derived from the causes of land conversion, such as distance from roads, distance from government offices, distance from settlements, distance from rivers, and slope (**Fig. 5**).

Road availability is one of the most influential factors affecting land change (Chen et al., 2022). Land proximate to major road networks is more susceptible to conversion, particularly to plantations and settlements. The high accessibility of these regions has been demonstrated to encourage investment and accelerate the mobilization of heavy equipment and construction logistics. The augmentation in plantation area from 2016 to the 2041 forecast is expected to be concentrated in areas proximate to major roads or recently constructed roads, suggesting a pattern of linear deforestation following transportation networks.

Areas in close proximity to government centers have been observed to experience heightened intensity in land cover changes (Allan et al., 2022). This phenomenon can be attributed to several factors, including heightened development activity, streamlined access to bureaucratic processes, and the strategic utilization of space for infrastructure, public services, or economic zones. Land use in Boven Digoel such as settlements, plantations, and open land is more likely to undergo changes in function in these zones, due to the attractiveness for investment and concentration of human activities. Conversely, land far from government centers tends to exhibit greater stability, particularly if it lacks adequate accessibility.

It has been demonstrated that areas adjacent to settlements are subject to elevated pressures with regard to land change (Allan et al., 2022), This phenomenon is especially evident in the transformation of scrubland, open land, or swamps into urban areas or plantations. Community activities in Boven Digoel, including the expansion of cultivated land and the construction of residential and public facilities, have contributed to these changes. Conversely, land situated in remote areas, distant from major population centers, exhibits greater stability. These areas frequently persist as natural forests or scrubland due to their inaccessibility to the day-to-day activities of the community.

Rivers function as customary activity corridors for indigenous communities and natural transportation routes in Boven Digoel. Consequently, land adjacent to rivers is subject to alterations in use, including traditional agriculture, water resource extraction, and the construction of basic facilities. However, these areas are also vulnerable to conversion into plantations, especially if companies utilize rivers as logistics routes. Nevertheless, in certain instances (Andrianto et al., 2014)(Wulanningtyas et al., 2025), the land around the river remains protected due to its status as a flood-prone area or conservation zone. Boven Digoel is characterized by the presence of several major rivers that extend in a uniform pattern from north to south.

The topography is also an important factor (Plateau et al., 2023). Land with low to moderate slopes (0‑15%) is more accessible and cultivable, rendering it more vulnerable to changes such as conversion to plantations, agriculture, or settlements. Conversely, regions characterized by precipitous slopes (>25%) are often preserved as woodlands, a practice influenced by factors including challenging accessibility, the potential for erosion, and their elevated ecological value. This phenomenon elucidates the predominance of forest fragmentation in hilly regions and steep slopes, while changes are more prevalent in relatively flat lowlands. Boven Digoel, as observed through the

DEM, exhibits low to moderate slope gradients across the majority of the region. A limited number of regions in the northern area are characterized by high slope gradients that border the Papua Mountains.

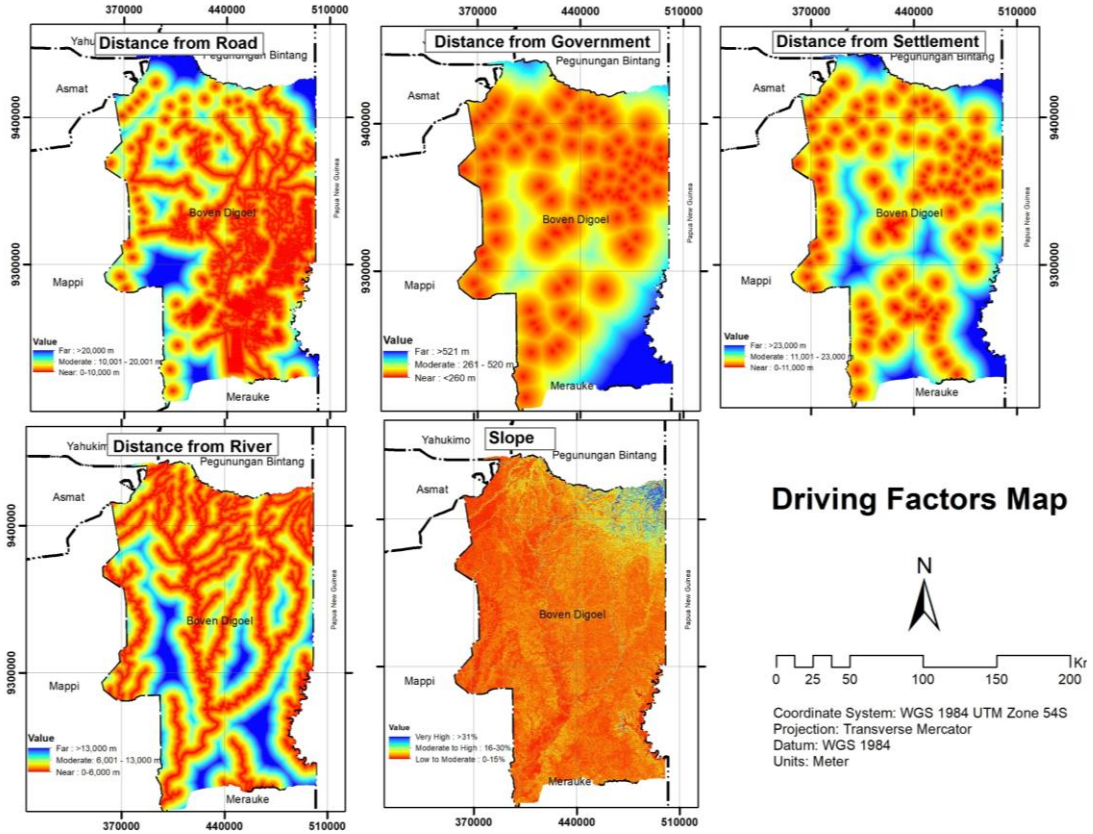

Fig. 5. Predictors of LULC include distance from roads, distance from government, distance from settlements, distance from rivers, and slope.

4.4. Model Validation

Model validation is used to test the results of our modeling. Model validation for 2031 and 2041 (**Fig. 6)** explains the statistical test results for the CA-Markov model, which can be seen in the Terrset software.

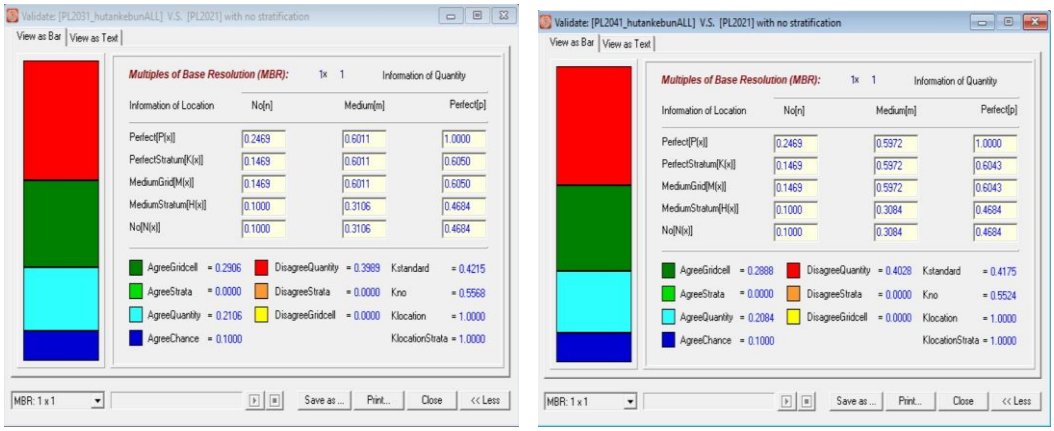

Fig. 6. Validation model results for 2031 (left) and 2041 (right).

The results of spatial validation between land cover predictions for 2031 and 2041 (**Fig. 6**) and actual conditions show varying levels of agreement in terms of location and quantity. The standard Kappa index (Kstandard) for 2031 is 0.4215, higher than that for 2041 at 0.4175, indicating moderate accuracy. The AgreeGridcell values for both years are nearly identical, approximately 0.29, indicating that only about 29% of the total pixels are spatially consistent. Meanwhile, the Klocation and Klocation Strata values are both 1, indicating that the prediction model has very high location accuracy, even perfect, both overall and based on stratification.

On the other hand, Kno values for 2031 and 2041 of 0.5568 and 0.5524 indicate that the agreement in terms of quantity is still moderate, so more attention needs to be paid to the distribution of predicted land use classes. The agreement proportion at the grid cell level (Agree Grid cell) is 0.29806 and 0.2888, and the agreement based on quantity (Agree Quantity) is 0.2106 and 0.2084, supporting these results. Conversely, the quantitative mismatch is quite high, at 0.3999 and 0.4028. These results indicate that although the prediction of land change locations is fairly accurate, the model still has limitations in balancing the distribution of area between land use classes precisely.

5. DISCUSSION

Based on the results of this study, the integration of LCM and CA-Markov can be used to predict spatial expansion of agricultural land while evaluating its potential environmental impacts, such as carbon stock calculations. Advanced spatial modeling can be used for the implementation of REDD+ (Reducing Emissions from Deforestation and Forest Degradation) schemes. By analyzing the dynamics of land cover changes over time and projecting future change patterns, spatial estimates of forest cover loss and land conversion with potential carbon emissions can be made. By integrating carbon stock data per land cover class, TerrSet can be used to calculate carbon stock changes and identify areas with high emissions risk due to deforestation.

From a forestry perspective, the conversion of forest land into non-forest uses, particularly plantations as projected to occur in Boven Digoel Regency until 2041 carries complex ecological and social implications. Deforestation not only reduces above and below ground carbon stocks but also disrupts critical functions of tropical forest ecosystems, such as hydrological cycle regulation, soil conservation, and habitat provision for Papua's endemic biodiversity (Simamora et al., 2021; Swindles et al., 2024). The significant forest loss of 36,501 ha from 2016–2041 is a clear indicator of land-use pressures that are inconsistent with the principles of sustainable forest management. Within the framework of the Forest Landscape Integrity Index (FLII), the decline of primary forest without clear silvicultural systems can diminish landscape integrity and trigger further degradation, even when such changes appear spatially small (Potapov et al., 2017).

In general, predictions from the CA-Markov model demonstrate a consistent expansion of plantations in lowland areas that were once natural forests. In forestry science, this illustrates the edge effect, where forest fragmentation creates transitional zones that are highly vulnerable to disturbances. These zones may eventually become the starting points of structural and functional degradation, reducing the forest's ability to store carbon and sustain biodiversity. From a management perspective, such trends must be mitigated through landscape-based forest governance, which integrates spatial predictions with adaptive forest zoning policies. For example, the implementation of protected functions in areas with the highest predicted change (deforestation hotspots) should be prioritized through social forestry schemes or the recognition of customary forests (Ungirwalu et al., 2025; World Resource Institute (WRI) Indonesia, 2025). This aligns with the principle of Free, Prior and Informed Consent (FPIC) in equitable tropical forestry (Giupponi, 2018).

The spatial estimations such as those presented in this study, the value of carbon stock loss and emissions can be mapped precisely and serve as the basis for conservation-based incentive schemes for indigenous peoples or carbon credit offset mechanisms (Swindles et al., 2024; Mokarram & Minh, 2022). In the context of food estate development, a land-sparing forestry approach preserving primary forest zones while intensifying agriculture on degraded lands should be prioritized to avoid trade-offs between food security and environmental conservation (Neilson & Wright, 2017). This approach is

more consistent with Indonesia's commitments to the SDGs (particularly SDG 13: Climate Action and SDG 15: Life on Land) as well as the 2015 Paris Agreement.

This study has some limitations related to data accuracy and the scope of LULC modeling. The availability of high-resolution, update boundary spatial data remains a challenge, which may affect the precision of LULC classification and change detection. We acknowledge that additional parameters could improve the model's accuracy in future studies. Studying LULC changes requires more complex parameters beyond distance to government centers, roads, settlements, rivers, and slope. Other driving factors, such as soil type and rainfall, can also influence LULC changes (Entahabu et al., 2023). For example, soil type provides information on mineral content, which can serve as a basis for land transformation. Rainfall affects not only soil strength but also water absorption capacity. Population size or density can also drive LULC changes, particularly in urban or semi-urban areas. However, in large areas with low population density, the effect of population as a driving factor may be insignificant, resulting in a lower impact on land use change.

The increase in plantation areas, as shown in **Fig. 4.** and **Table 6.** indicates intensified agricultural activity and human-induced land conversion in Boven Digoel. In contrast, settlement areas remain relatively stagnant, which may be attributed to low population growth, limited suitable land for new settlements, and local development policies that constrain residential expansion. The population growth rate in Boven Digoel Regency is relatively low, approximately 1.9% per year based on the latest data from the Central Statistics Agency, 2025. Total Fertility Rate (TFR) since 2020 is constant at 2.1 according to the population projection of 2015-2045 Intercensal Population Survey (SUPAS) (BPS, 2025). This contrast suggests that while agricultural expansion is actively transforming the landscape, urban or residential growth is more restricted, highlighting the different dynamics and drivers affecting land use change in the region. Therefore, the massive land changes occurring in this region are not driven by natural population growth but are instead structured and managed by government policies and industrial activities.

6. CONCLUSIONS

The results obtained indicate a significant increase in forest cover from 2016 to 2021, followed by a gradual decline until 2041, resulting in a total loss of 36,501 hectares. Conversely, the plantation area exhibited a consistent increase, rising from 2.49% to 4.15% of the total area, suggesting an expansion of cultivated land that has the potential to supplant natural cover. The categories of swamp, scrub, and open land underwent a precipitous decline, suggesting a transition to more intensive land use. Settlements and agriculture exhibited a marked tendency toward stagnation, with minimal to no observable change. The transition from forest to plantation is evident in the southern to northern expansion of Boven Digoel.

The application of LCM and Markov CA to model LULC change yielded an overall accuracy of 70% with a kappa index of 0.652 in 2016 and an overall accuracy of 83.33% with a kappa index of 0.804 for 2021. Consequently, the model for 2031 and 2041 is deemed acceptable, contingent upon the five driving factors that influence the model, namely distance to roads, government, settlements, rivers, and slope. The present study centered on the investigation of changes in land use and land cover (LULC) from forest land to plantations. The observed decrease in forest area is primarily associated with the expansion of plantation land, which increased from 68,963.04 ha, or 27.58% (2016‑2021), to 87,987.60 ha, or 18.73% (2021‑2031), and 104,469.12 ha, or 51.49% (2031‑2041). This finding suggests that forest conversion to non-forest (primarily plantations) is the dominant trend, with potential impacts on carbon stocks, biodiversity, and ecosystem stability.

ACKNOWLEDGMENTS

The author would like to express sincere gratitude to the Research and Innovation Institute (LRI) of Muhammadiyah University Surakarta for the 2025 Tridharma Integration Grant (HIT) scheme. The author would also like to thank the reviewers who provided input and suggestions during the publication process of this article, as well as all parties involved in data processing and writing.

REFERENCES

Akdeniz, H. B. (2022). Analysis of Land Use /Land Cover Changes and Prediction of Future Changes With Land Change Modeler : Case of Belek, Turkey. *Research Square*, *2*(2), 1–28.

Allan, A., Soltani, A., & Abdi, M. H. (2022). *Driving Forces behind Land Use and Land Cover Change : A Systematic and Bibliometric Review*.

Amin, C., Tyas, W., Jumadi, J., Novita, D., & Samson, M. G. M. (2025). Social Sciences & Humanities Open Navigating urban poverty : The role of livelihood capital in the livelihood strategies of urban beggars in Indonesia. *Social Sciences & Humanities Open*, *11*(January), 101298. https://doi.org/10.1016/j.ssaho.2025.101298

Andrianto, A., Sedik, B. F., Waridjo, H., Komarudin, H., & Obidzinski, K. (2014). The impacts of oil palm plantations on forests and people in Papua: a case study from Boven Digoel District. *CIFOR Working Paper*, *163*, 24-pp. http://www.cifor.org/library/5349/the-impacts-of-oil-palm-plantations-on-forests-and-people-in-papua-a-case-study-from-boven-digoel-district/

Asra, R., Mappiasse, M. F., & Nurnawati, A. A. (2020). Penerapan Model CA-Markov Untuk Prediksi Perubahan Penggunaan Lahan Penerapan Model CA-Markov Untuk Prediksi Perubahan Penggunaan Lahan Di Sub-DAS Bila Tahun 2036. *Agrovital : Jurnal Ilmu Pertanian*, *5*(May). https://doi.org/10.35329/agrovital.v5i1.630

Barri, M. F., Condro, A. A., Apriani, I., Cahyono, E., Hamdani, A., Prawardani, D. D., Syam, M., Albert Junior Ngingi, Habibie, A., Oktaviani, A. R., Jaya, A. F., Prasojo, F. A., Erwanto, A., & Situmorang, N. (2019). Papua Bioregion: The Forest and Its People. In *Forest Watch Indonesia (FWI) and Sajogo Institute*. https://terbitan.sajogyo-institute.org/wp-content/uploads/2020/08/FWI-2019-Papua-Bioregion-The-Forest-and-Its-People.pdf

Benjamin, B., Joachim, M., B, P. M., Fernando, S., Davide, G., Pavel, S., Leena, K., Roman, Ł. D., Jan, A., Małgorzata, S., Benjamin, B., Joachim, M., B, P. M., Fernando, S., Davide, G., Pavel, S., Leena, K., Mihai, A. C., Blal, E., … Santos-martín, F. (2020). Mapping and assessing ecosystem services in the EU - Lessons learned from the ESMERALDA approach of integration. *One Ecosystem*, *3*, 1–20. https://doi.org/10.3897/oneeco.3.e29153

BPS. (2025). *Kabupaten Boven Digoel dalam Angka*. https://bovendigoelkab.bps.go.id/id/publication/2024/02/28/2b8653eb40f15d687669d532/kabupaten-boven-digoel-dalam-angka-2024.html

Chen, X., He, X., & Wang, S. (2022). *Simulated Validation and Prediction of Land Use under Multiple Scenarios in Daxing District , Beijing , China , Based on GeoSOS-FLUS Model*.

Clark Labs. (2017). *TerrSet* (pp. 1–8). Clark University.

Congalton, R. G., & Green, K. (2019). *Assesing the Accuracy of Remotely Sensed Data : Principles and Practices* (The 3rd ed). CRC Press. https://doi.org/https://doi.org/10.1201/9780429052729

Deng, J. S., Wang, K., Hong, Y., & Qi, J. G. (2009). Landscape and Urban Planning Spatio-temporal dynamics and evolution of land use change and landscape pattern in response to rapid urbanization. *Landscape and Urban Planning Journal*, *92*, 187–198. https://doi.org/10.1016/j.landurbplan.2009.05.001

Direktorat Pengukuhan dan Penatagunaan Kawasan Hutan Direktorat Jenderal Planologi Kehutanan dan Tata Lingkungan. (2020). *Pemulihan Ekonomi Nasional (PEN) Food Estate*.

Dommain, R., Dittrich, I., Giesen, W., Joosten, H., Rais, D. S., Silvius, M., & Wibisono, I. (2016). Ecosystem services, degradation and restoration of peat swamps in the south east asian tropics. In *Peatland Restoration and Ecosystem Services: Science, Policy and Practice* (pp. 253–288). https://doi.org/10.1017/CBO9781139177788.014

Econusa. (2021). *Food Estate dan Nasib Keanekaragaman Hayati di Tanah Papua*. https://econusa.id/id/ecoblog/food-estate-dan-nasib-keanekaragaman-hayati-di-tanah-papua/

Entahabu, H. H., Minale, A. S., & Birhane, E. (2023). Modeling and Predicting Land Use/Land Cover Change Using the Land Change Modeler in the Suluh River Basin, Northern Highlands of Ethiopia. *Sustainability (Switzerland)*, *15*(10), 21–25. https://doi.org/10.3390/su15108202

European Space Agency (ESA). (2024). *SPOT*. Online Website. https://earth.esa.int/eogateway/missions/spot

FAO. (2019). *Satellite imagery key to monitoring changes in forest cover and land use. Food and Agriculture Organization of the United Nations*. https://www.fao.org/indonesia/news/detail/Satellite-imagery-key-to-monitoring-changes-in-forest-cover-and-land-use/en

Fikriyah, V. N., Darvishzadeh, R., Laborte, A., & Nelson, A. (2024). Sentinel-1 Backscatter Analysis of Ratoon Rice Crops: Example from Ratooning Practice in the Philippines. *4th International Symposium on Applied Geoinformatics (ISAG)*, 14923.

Gadal, S., & Mozgeris, G. (2025). Advances of Remote Sensing in Land Cover and Land Use Mapping. *Remote Sensing*, *17*(12), 1–7. https://doi.org/10.3390/rs17121980

Gandhi, Y. (2013). *Structure and Dynamics of Forests under Logging Concession in Papua, Indonesia* (Vol. 2100).

Giupponi, B. O. (2018). Free, Prior and Informed Consent (fpic) of Indigenous Peoples before Human Rights Courts and International Investment Tribunals. *International Journal on Minority and Group Rights*, *25*(4), 485–529. https://www.jstor.org/stable/27072156

Hadibasyir, H. Z., Firdaus, N. S., Fikriyah, V. N., & Sari, D. N. (2023). Assessing Performance of Modified Spectral Indices as Land Surface Temperature Indicators in Tropical Urban Areas. *IOP Conf. Series: Earth and Environmental Science 1190*. https://doi.org/10.1088/1755-1315/1190/1/012005

Hendri, Raharjo, S., Suarga, E., Faruk Rosyaridho, M., & Kalmirah, J. (2022). Towards low carbon development strategies from forestry sector in West Papua. *IOP Conference Series: Earth and Environmental Science*, *989*(1). https://doi.org/10.1088/1755-1315/989/1/012007

Khan, Z., Saeed, A., & Bazai, M. H. (2021). Land Use/Land Cover Change Detection and Prediction using The CA-Markov Model : A case Study of Quetta City, Pakistan. *Journal of Geography and Social Sciences*, *2*(October), 164–182.

Kristin, N. K. G., Dwi Pratiwi Markus, & Hadi Tuasikal. (2025). Legal Protection of Customary Forests of the Awyu Tribe in South Papua From a National and International Law Perspective. *Jurnal Ius Constituendum*, *10*(2), 296–315. https://doi.org/10.26623/jic.v10i2.12042

Kurniawan, H. B., & Roychansyah, M. S. (2023). The Social Equity of Public Green Open Space Accessibility: the Case of South Tangerang, Indonesia. *Geography, Environment, Sustainability*, *16*(1), 45–54. https://doi.org/10.24057/2071-9388-2022-124

Landis, J. R., & Koch, G. G. (1977). Kappa-type An Application of Hierarchical among Agreement of Majority in the Assessment Statistics Multiple Observers. *Biometrics*, *33*(2), 363–374.

Lantipo, Y. (2022). Melepas ratusan juta emisi karbon demi 2,7 juta Ha Food Estate di selatan Papua. *Jubi.Id*. https://arsip.jubi.id/melepas-ratusan-juta-emisi-karbon-di-selatan-papua/

Malczewski, J. (1998). *GIS and Multicriteria Decision Analysis*. John Wiley & Sons, Inc.

Masolele, R. N., Sy, V. De, Herold, M., Marcos, D., Verbesselt, J., Gieseke, F., Mullissa, A. G., & Martius, C. (2021). Remote Sensing of Environment Spatial and temporal deep learning methods for deriving land-use following deforestation : A pan-tropical case study using Landsat time series. *Remote Sensing of Environment*, *264*(May), 112600. https://doi.org/10.1016/j.rse.2021.112600

Mishra, V. N., Rai, P. K., & Mohan, K. (2014). *Original scientific paper*. *64*(1), 111–127. https://doi.org/10.2298/IJGI1401111M

Mokarram, M., & Minh, T. (2022). CA-Markov model application to predict crop yield using remote sensing indices. *Ecological Indicators*, *139*(May), 108952. https://doi.org/10.1016/j.ecolind.2022.108952

Mosleh, M. K. (2025). Integrating the CA–Markov model and geospatial techniques for spatiotemporal prediction of land use/land cover dynamics in Qus District, Egypt. *Modeling Earth Systems and Environment*, *11*(5), 315. https://doi.org/10.1007/s40808-025-02479-9

Neilson, J., & Wright, J. (2017). The state and food security discourses of Indonesia: feeding the bangsa. *Geographical Research*, *55*(2), 131–143. https://doi.org/https://doi.org/10.1111/1745-5871.12210

Nicoară, M. E., & Haidu, I. (2011). Creation of the Roads Network As a Network Dataset. *Geographia Technica*, *2*, 81–86.

Obidzinski, K., Andriani, R., Komarudin, H., & Andrianto, A. (2025). *Environmental and Social Impacts of Oil Palm Plantations and their Implications for Biofuel Production in Indonesia*. *17*(1).

Parsch, C. (2024). *Land-Use Change in Papua , Indonesia – Assessing Deforestation Patterns and Predicting Future Hotspots of Habitat Loss to Inform Spatial Conservation Planning*. Universität Göttingen.

Pemerintah Kabupaten boven Digoel. (2023). *Kajian Lingkungan Hidup Strategis (KLHS) Rencana Pembangunan Jangka Panjang Daerah (RPJPD) Kabupaten Boven Digoel*.

Plateau, Q., Ma, R., Zhou, W., Ren, J., Huang, Y., & Wang, H. (2023). Multi-scenario simulation and optimization control of ecological security based on GeoSOS-FLUS model in ecological fragile area in northeast. *Ecological Indicators*, *151*(December 2022), 110324. https://doi.org/10.1016/j.ecolind.2023.110324

Potapov, P., Hansen, M. C., Laestadius, L., Turubanova, S., Yaroshenko, A., Thies, C., Smith, W., Zhuravleva, I., Komarova, A., Minnemeyer, S., & Esipova, E. (2017). The last frontiers of wilderness: Tracking loss of intact forest landscapes from 2000 to 2013. *Science Advances*, *3*(1), 1–13. https://doi.org/10.1126/sciadv.1600821

Putrie, V. D., Putri, F. A., Hamka, M. H., Lumbantoruan, M. D. H., Novika, K. E., Wardiyah, A. A., & Yusuf, M. (2025). The role of planning document in managing land conversion: the case of indigenous forest conversion in boven digoel regency. *IOP Conference Series: Earth and Environmental Science*, *1498*(1). https://doi.org/10.1088/1755-1315/1498/1/012013

Rasman, A., Theresia, E. S., & Aginda, M. F. (2023). Analisis implementasi program food estate sebagai solusi ketahanan pangan Indonesia. *Holistic: Journal of Tropical Agriculture Sciences*, *1*(1), 33–65.

Redaksi Hijauku. (2021). *12 'Kesepakatan Lemah' dari COP26 Glasgow*. Hijauku.Com. https://hijauku.com/2021/11/14/12-kesepakatan-lemah-dari-cop26-glasgow/#google_vignette

Sànchez-Marrè, M. (2022). *Intelligent Decision Support Systems*. Springer. https://doi.org/https://doi.org/10.1007/978-3-030-87790-3_1

Sari, D. N., Anna, A. N., Taryono, T., Maulana, M. F., & Khumaeroh, D. N. F. (2024). Detection of Flood Hazard Potential Zones By Using Analytical Hierarchy Process in Tuntang Watershed Area, Indonesia. *Geographia Technica*, *19*(1), 61–78. https://doi.org/10.21163/GT_2024.191.05

Savitri, L. A., Dhanwani, N. D., & Amin, S. (2023). *Biopolitik Food Estate dan Kerusakan Metabolik Alam-Manusia Papua*. Fian Indonesia.

Simamora, B., Lubis, K., & Arini, H. (2021). Analisis Asumsi-Asumsi pada Program Food Estate di Papua. *Perspektif*, *10*(2), 293–300. https://doi.org/10.31289/perspektif.v10i2.4267

SOW, E. A., Vall, M. M., Abidine, M. M., Babah, H., Hamoud, A., Faye, G., & Semega, B. (2016). Assessment of Green Hydrogen Production Potential from Solar and Wind Energy in Mauritania. *Geographia Technica*, *11*(2), 39–50. https://doi.org/10.21163/GT

Stehman, S. V. (1997). Estimating standard errors of accuracy assessment statistics under cluster sampling. *Remote Sensing of Environment*, *60*(3), 258–269. https://doi.org/10.1016/S0034-4257(96)00176-9

Swindles, G. T., Mullan, D. J., Brannigan, N. T., Sim, T. G., Gallego-sala, A., Blaauw, M., Lamentowicz, M. L., Green, S. M., & Roland, T. P. (2024). *Climate and hydrology control apparent rates of peat accumulation across Europe*.

Ungirwalu, A., Mansoben, J. R., Runtuboi, Y. Y., Fatem, S. M., Peday, M. H., Marwa, J., & Maryudi, A. (2025). The fall of the kings: Power relations and dynamics in Papua's indigenous community in forest resource management. *Forest Policy and Economics*, *172*, 103424. https://doi.org/https://doi.org/10.1016/j.forpol.2025.103424

Walhi. (2021). *Kertas Posisi: Food Estate di Papua Perampasan Ruang Berkedok Ketahanan Pangan?*

Walhi Kalimantan Tengah. (2021). *Food Estate Kalimantan Tengah, Kebijakan Instan Sarat Kontroversi*. https://foodestate.pantaugambut.id/

Wambrauw, E. V. (2015). *Water Management in the Lowlands of Southern Papua Indonesia Using a Decision Support System and Integrating Traditional Ecological Knowledge* [UGM]. https://igsci.pasca.ugm.ac.id/file/water-management-in-the-lowlands-of-southern-papua-indonesia-using-a-decision-support-system-and-integrating-traditional-ecological-knowledge/

Widiastuti, M. M. D., Syaukat, Y., Falatehan, A. F., & Hakim, D. B. (2023). Tinjauan Implementasi Program Food Estate dan Prospeknya di Merauke Papua. *Forum Penelitian Agro Ekonomi*, *40*(2), 119–133. https://doi.org/http://dx.doi.org/10.21082/fae.v40n2.2022.

World Resource Institute (WRI) Indonesia. (2025). *Memperkuat Posisi Masyarakat Adat di Papua dengan Kejelasan Proses Perizinan dalam sektor Kehutanan*. https://wri-indonesia.org/id/wawasan/memperkuat-posisi-masyarakat-adat-di-papua-dengan-kejelasan-proses-perizinan-dalam-sektor

Wulanningtyas, H. S., Kasim, A., & Adnan. (2025). The potential of Inceptisol soil for rice development in Boven Digoel, Papua. *IOP Conference Series: Earth and Environmental Science*, *1463*(1). https://doi.org/10.1088/1755-1315/1463/1/012008

Wulanningtyas, H. S., Soplanit, A., Baliadi, Y., & Sulaeman, Y. (2006). Peatlands development potency for sago cultivation in Papua. *IOP Conf. Series: Earth and Environmental Science*. https://doi.org/10.1088/1755-1315/1463/1/012006

Wulder, M. A., Loveland, T. R., Roy, D. P., Crawford, C. J., Masek, J. G., Woodcock, C. E., Allen, R. G., Anderson, M. C., Belward, A. S., Cohen, W. B., Dwyer, J., Erb, A., Gao, F., Griffiths, P., Helder, D., Hermosilla, T., Hipple, J. D., Hostert, P., Hughes, M. J., … Zhu, Z. (2019). Current status of Landsat program, science, and applications. *Remote Sensing of Environment*, *225*(March), 127–147. https://doi.org/10.1016/j.rse.2019.02.015

GIS-BASED PREDICTION OF WATER QUALITY INDEX USING MACHINE LEARNING: A CASE STUDY OF THE THA CHIN RIVER, THAILAND

Pasin PROMHAN [1]*, ***Sitang PILAILAR*** [2]

DOI: 10.21163/GT_2025.202.19

ABSTRACT

This study integrates field data, machine learning (ML), and Geographic Information System (GIS) techniques to compute and predict the Water Quality Index (WQI) along the Tha Chin River Basin, Thailand. Five key water quality parameters—DO, BOD, COD, pH, and Salinity—were collected from monitoring stations between 2019 and 2022. These were normalized into Q-values and used to compute WQI through weighted aggregation. Six supervised ML algorithms were tested, with the Random Forest model yielding the highest predictive performance ($R^2 = 0.664$, MAE = 0.855) at a 10-hour lead time. Incorporating spatial indicators such as urban land cover and population density significantly enhanced model accuracy. Computed WQI values were visualized using Inverse Distance Weighted (IDW) interpolation to assess spatial and temporal trends. Results indicated a consistent decline in water quality from upstream to downstream, with all zones classified as "moderately degraded" or "degraded." The lowest WQI values were observed in Banglen District, ranging from 39 to 42, linked to high urban density and pollutant accumulation. In contrast, upstream areas such as Mueang Suphan Buri slightly improved over time. The study confirms that urban expansion is a major contributor to river water degradation. The proposed ML-GIS framework supports proactive monitoring, spatial prioritization, and evidence-based water resource management in rapidly urbanizing river basins.

Key-words: *Tha Chin River; Water Quality Index (WQI); Machine Learning; GIS; Spatial Interpolation. Environmental Monitoring; Random Forest.*

1.INTRODUCTION

Water quality deterioration is a growing concern in many regions across the globe, particularly in areas undergoing rapid development (Abbasi & Abbasi, 2012; Horton R.K, 1965) Increased agricultural production, unregulated industrial discharge, and expanding urban settlements contribute to elevated pollution loads in river systems, which serve as primary conduits for surface runoff and point-source wastewater. Monitoring and managing these dynamic water systems is critical for protecting public health, maintaining biodiversity, and ensuring water security.

The Water Quality Index (WQI) has long served as a composite metric that condenses multiple water quality parameters—such as Dissolved Oxygen (DO), Biochemical Oxygen Demand (BOD), chemical oxygen demand (COD) (Belete & Huchaiah, 2021), total suspended solids (TSS), Salinity, and pH—into a single value representing overall water quality status (Lumb, Halliwell, & Sharma, 2006). While effective for summarizing complex data, conventional WQI assessments are limited by their retrospective nature. To support real-time decision-making (Liu, Wang, Sangaiah, Xie, & Yin, 2019), predictive modeling approaches are increasingly required.

However, in practice, environmental datasets frequently contain gaps and noise due to missing measurements, equipment malfunctions, or human error (Magyari-Sáska, Haidu, & Magyari-Sáska, 2025). Machine learning (ML) techniques are gaining traction for their ability to capture non-linear relationships and generate accurate forecasts from complex datasets (Chen et al., 2020; Najah Ahmed et al., 2019).

[1] *Department of Water Resources Engineering, Kasetsart University, 10900 Bangkok, Thailand, (PP)* pasin.pro@ku.th *,(SP) fengstpl@ku.ac.th

For instance, (Ahmed et al., 2019) introduced a Wavelet De-noised Adaptive Neuro-Fuzzy Inference System (WDT-ANFIS) for predicting key water quality parameters, significantly outperforming traditional models through effective preprocessing and input optimization. Similarly, (Magyari-Sáska et al., 2025) demonstrated self-imputation techniques for handling incomplete hydrological time series, improving model robustness under data scarcity.

In addition, (Kouadri, Elbeltagi, Islam, & Kateb, 2021) compared multiple ML algorithms—including multilayer regression (MLR), random forest (RF), and support vector regression (SVR)—for WQI estimation in data-scarce regions, highlighting the benefits of sensitivity analyses in reducing input uncertainty while maintaining high predictive accuracy.

When combined with Geographic Information Systems (GIS), which add spatial dimensions such as land use, population density, and urbanization patterns (Ly et al., 2021). ML models can deliver more context-aware predictions. Integrating GIS-derived variables into ML workflows enhances spatial interpretability, enabling forecasts of site-specific WQI, mapping of pollution hotspots, and visualization of basin-wide trends (Kouadri et al., 2021; Magyari-Sáska et al., 2025; Wang, Kim, & Li, 2021).

The Tha Chin River basin in central Thailand presents an ideal setting to apply such an integrated ML–GIS framework. Stretching over 300 kilometers through diverse agricultural and urban landscapes, the basin exhibits a pronounced gradient of anthropogenic pressures affecting water quality. This study aims to: (i) evaluate the performance of six machine learning algorithms in forecasting WQI, (ii) incorporate GIS-derived spatial indicators into model development, and (iii) produce spatial visualizations of predicted WQI to support targeted water resource management.

2. STUDY AREA

The Tha Chin River is a major distributary of the Chao Phraya River, originating in Chainat Province in central Thailand. It flows southward for approximately 325 kilometers through Suphan Buri, Nakhon Pathom, and Samut Sakhon Provinces before discharging into the Gulf of Thailand. The river traverses a diverse range of landscapes, including agricultural zones, urban centers, and industrial areas, making it a representative basin for examining the interplay between land use and water quality dynamics (Pollution Control Department. PCD, 2020).

The upper and middle reaches of the basin are dominated by rice cultivation, aquaculture, and livestock farming, which contribute significant non-point source pollution through runoff containing nutrients and organic waste. In contrast, the lower basin−particularly around Nakhon Pathom and Samut Sakhon−is highly urbanized and industrialized, with dense residential populations and a concentration of agro-industrial facilities. These characteristics result in a complex pollution profile influenced by diffuse and point sources.

Water quality in the Tha Chin River has shown persistent degradation over the past two decades. According to the Pollution Control Department (PCD), downstream segments frequently fall into the "poor" or "very poor" categories of the national WQI classification, with elevated levels of BOD, COD, and reduced DO. Seasonal variation further complicates the basin's condition, as pollutant concentrations typically rise during the dry season due to reduced flow and dilution capacity (Pollution Control Department PCD, 2022).

To capture this variability, the study utilizes water quality monitoring data from five key PCD stations located along the river: Chainat (upper reach), Suphan Buri (mid-upper reach), Song Phi Nong (midstream), Nakhon Chai Si (mid-lower reach), and Mahachai (river mouth), as shown in **Fig. 1.** These sites provide consistent seasonal data across multiple years, forming the empirical foundation for model training and validation. Supplementary spatial datasets−including land use classifications, population density, and administrative boundaries−were integrated to enhance the spatial representation of anthropogenic pressures within the modeling framework.

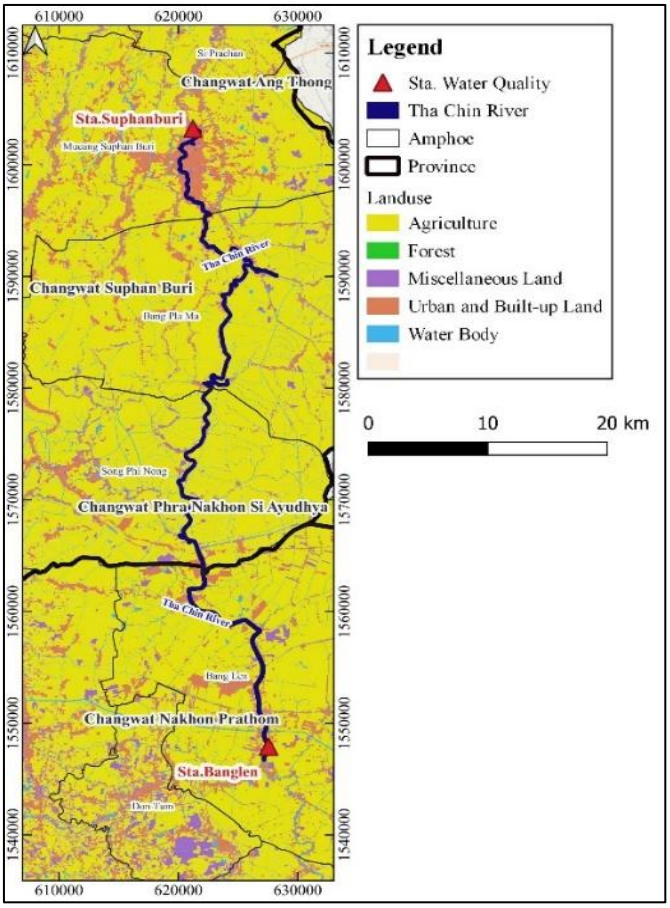

Fig. 1. The Chin River Basin and locations of water quality monitoring stations used in the study.

3. METHODOLOGY

This study employed an integrated approach combining water quality assessment, machine learning (ML) prediction, and Geographic Information System (GIS)-based spatial analysis. The methodology consisted of four main steps: (i) data collection and preprocessing, (ii) Water Quality Index (WQI) computation, (iii) machine learning model development, and (iv) spatial visualization of predicted WQI values, as shown in **Fig. 2.**

3.1. Data Collection and Preprocessing

In this study, five key parameters were selected in accordance with the Pollution Control Department (PCD) of Thailand's WQI framework: BOD, DO, COD, pH, and Salinity. These parameters represent both organic and inorganic pollution pressures, and their inclusion follows national reporting standards for surface water quality. The hourly water quality data from five PCD monitoring stations along the Tha Chin River were collected for 2019–2022. To ensure data reliability, outliers were removed using the interquartile range (IQR) method (Gazzaz, Yusoff, Aris, Juahir, & Ramli, 2012), and missing values were handled using linear interpolation. Z-score normalization was applied to standardize the dataset (Al-Faiz, Ibrahim, & Hadi, 2019).

Additional spatial data were compiled to represent anthropogenic influences within a 5 km buffer around each station. These included (i) population density, derived from official census records (2019–2022), and (ii) land use classifications from the Land Development Department (LDD) for the years 2019 and 2021. Land cover types were extracted using supervised classification in QGIS.

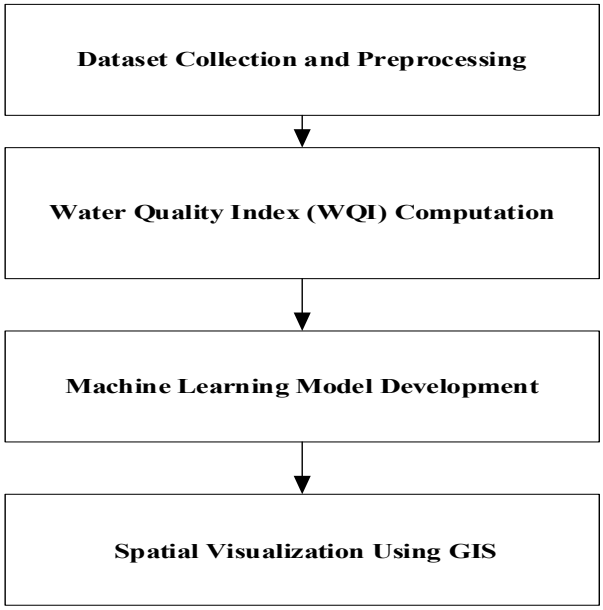

Fig. 2. Steps of work.

3.2. Water Quality Index (WQI) Computation

The Water Quality Index (WQI) was computed to integrate multiple physicochemical parameters into a single composite score that reflects the overall status of water quality in the Tha Chin River. This approach enables a consistent and comparable assessment across different sites and seasons (Abbasi & Abbasi, 2012; Ahmed et al., 2019). The computation of WQI involved two main stages:

(i) Q-value normalization, where raw parameter values were transformed into a dimensionless 0–100 scale based on PCD's rating curves; and

(ii) weighting factor application, where each parameter's Q-value was multiplied by its assigned weight to reflect its relative importance in the overall index. The final WQI score was obtained by summing the weighted Q-values and dividing by the sum of the weights.

The parameter ranges, classification thresholds, and corresponding weighting factors used in this study are presented in **Table 1**. Detailed descriptions of the normalization process and weighting scheme are provided in Sections 3.2.1 and 3.2.2.

3.2.1. Q-Value Normalization

Raw measurements of each water quality parameter were transformed into a standardized 0–100 scale, referred to as the Q-value, using parameter-specific rating curves developed by the PCD of Thailand. The Q-value represents the degree to which the measured parameter meets the desired water quality condition, with higher values indicating better quality. For each parameter, the transformation was carried out by matching the observed value to its corresponding score on the PCD's rating curve. These curves are non-linear and account for the unique response of each parameter to environmental conditions. For example, DO values close to saturation receive higher Q-values, while elevated BOD and COD—indicating greater organic pollution—receive lower scores. Similarly, pH values outside the optimal range (6.5–8.5) are penalized, and salinity values above freshwater tolerance levels result in reduced Q-values. This method aligns with previous applications of parameter normalization for WQI computation (Marzieh Mokarram & Zarei, 2021)and ensures comparability between parameters with different units and environmental implications. Alternative normalization methods, such as z-score or min–max scaling, were not assessed in this study in order to maintain consistency with the national water quality assessment framework.

3.2.2 Weighting Factors

In the composite WQI calculation, each normalized Q-value was multiplied by a weighting factor that reflects its relative importance in determining overall water quality. The weighting factors for DO, BOD, COD, pH, and Salinity were adapted from the PCD guidelines (PCD, 2021) and are supported by prior WQI studies in Thailand (PCD, 2017). The weighting factors applied in this study were: DO (0.28), BOD (0.24), COD (0.20), pH (0.14), and Salinity (0.14). These values sum to unity, ensuring that the resulting index remains bounded within the 0–100 scale. The overall WQI for each sampling site was computed using the weighted arithmetic mean method as expressed in Eq. (1):

$$\mathrm{WQI} = \sum(W_i \times Q_i) \tag{1}$$

where

Q_i = the water quality parameter s' index i

W_i = the associated weighing factor for each parameter

No sensitivity or uncertainty analysis was conducted in this study to test the impact of alternative weighting schemes, although such assessments have been recommended in recent literature. The chosen factors align with those used in previous WQI studies in Southeast Asia (Najah Ahmed et al., 2019), supporting methodological consistency and comparability with earlier work.

Table 1.

Equations for calculating Q-values for selected water quality parameters (adapted from PCD standards).

Variables	Range	Sub-index Function
DO	0.0≤x≤4.0	y=15.25x+1.667
	4.1≤x≤6.0	y=5x+41
	6.1≤x≤8.4	y=12.083x-1.5
	8.5≤x≤8.9	y=-78x+755.2
	9.0≤x≤11.2	y=-13.043x+177.09
	x≥11.3	y=7.561x+115.68
BOD	0.0≤x≤1.5	y=-19.333x+100
	1.6≤x≤2.0	y=-20x+101
	2.1≤x≤4.0	y=-15x+91
	x≥4.1	y=-6.4583x+56.833
Temperature	x<0	y=100
	0≤x≤30	$y=-0.0325x^2-1.8851x+96.236$
	x>30	y=0
COD	x≤20	-1.33x+99.1
	x>20	$103e^{-0.537x}$-0.04x
pH	x<2	y=0
	2≤x<4	$y=1.13x^2-3.66x+5.04$
	4.1≤x≤7.5	$y=-1.7479x^2+44.845x-144.25$
	7.5<x<10	$y=-3.1167x^2+23.279x+92.915$
	10≤x≤13	$y=1.157x^2-31.088x+210.06$
	x>13	y=0
Salinity		$y=14.341x^2-69.274x+86.549$

3.3. Machine Learning Model Development

Six supervised ML algorithms were applied to predict WQI values: Random Forest (RF), Support Vector Machine (SVM), k-Nearest Neighbors (KNN), Decision Tree (DT), Logistic Regression (LR), and AdaBoost (AB). Input features included the five water quality parameters and spatial variables (population and land use). The dataset was split into training (80%) and testing (20%) subsets. Features were normalized using Z-score normalization (Jha et al., 2015) (Eq. (2)):

$$Z = \frac{(x-\mu)}{\sigma} \tag{2}$$

where:

x = the raw value

μ = the mean of the feature

σ = the standard deviation

A 10-fold cross-validation was applied to each model to assess generalizability. The performance of each model was evaluated using the Coefficient of determination (R^2), Mean Squared Error (MSE), and Mean Absolute Error (MAE) (Fathi et al., 2022).

3.4. Spatial Visualization Using GIS

The predicted WQI values were spatially visualized using the Inverse Distance Weighting (IDW) interpolation method in QGIS 666(Mueller et al., 2004). This method estimates WQI at unsampled locations based on the spatial proximity and magnitude of known values. The interpolation was conducted separately for wet and dry seasons to capture seasonal variations in water quality(Magesh, Krishnakumar, Chandrasekar, & Soundranayagam, 2012).

$$Z(x_0) = \frac{\Sigma(\frac{Z_i}{d_i^p})}{(\frac{1}{d_i^p})} \tag{3}$$

where:

$Z(x_0)$ = the estimated WQI

Zi = the known value

di = the distance between points

p = the power parameter (set 2)

The output maps provided spatial insights into water quality patterns and supported the identification of potential pollution hotspots.

4. RESULT AND DISCUSSION

This section presents the results of the water quality assessment, machine learning model predictions, and spatial analysis, followed by a discussion of key findings. The analysis is based on data from five monitoring stations along the Tha Chin River, spanning dry and wet seasons from 2019 to 2022. Results are structured to highlight the transformation and classification of raw water quality data, the predictive performance of machine learning algorithms, and the spatial patterns of WQI concerning land use and population pressures.

Integrating Q-value normalization, spatial indicators, and machine learning allowed for a comprehensive understanding of how physicochemical and anthropogenic factors interact to influence river water quality. The following subsections discuss (i) Q-value normalization and WQI classification, (ii) predictive performance of ML models, (iii) influence of spatial indicators, and (iv) spatial interpolation of WQI for decision support.

4.1. Field Survey Results and Spatial Correlation with Anthropogenic Activities

From the total of 55 Pollution Control Department (PCD) monitoring locations within the Tha Chin River Basin, 26 field survey sites were selected through a stratified, criteria-based approach to ensure representativeness and practicality.

Fig. 3. Spatial distribution of EC, pH, DO, BOD, and TDS values across 26 sampling stations within the Tha Chin River study area.

The selection process involved three key steps:

1. Stratification by river reach and hydrological conditions – The river was divided into five longitudinal zones: upper, mid-upper, midstream, mid-lower, and lower reaches. This ensured that each section's distinct hydrological regime was captured, including variations in flow velocity, tidal influence, and upstream–downstream pollution dynamics.

2. Classification by dominant land use and pollution sources – Using recent land-use GIS layers, historical PCD WQI records (2013–2022), and point-source pollution data, candidate sites were categorized according to dominant influences: intensive agriculture, livestock farming, aquaculture, mixed urban–rural settlements, and industrial zones. Priority was given to sites exhibiting contrasting pollution profiles (e.g., "good" vs. "poor" historical WQI ratings) to enhance model sensitivity to varying water quality conditions.

3. Evaluation of accessibility, safety, and logistical feasibility – Sites with restricted access, overlapping influence zones with other stations, or safety risks (e.g., hazardous navigation, unstable banks) were excluded. This ensured that selected sites could be sampled consistently under both dry and wet season conditions.

The final 26 sites thus provided balanced coverage of the basin's geographic extent, anthropogenic pressures, and hydrological diversity, while remaining feasible for repeated seasonal sampling. This strategic selection aimed to capture the full spatial variability of water quality conditions within the Tha Chin River Basin, thereby enhancing the robustness of the subsequent GIS-based machine learning analyses. Water quality measurements focused on five key parameters: Electrical Conductivity (EC), pH, DO, BOD, and Total Dissolved Solids (TDS). **Fig. 3** shows a clear spatial degradation pattern that emerges as the river flows downstream. BOD concentrations steadily increase, especially around Banglen District, indicating rising levels of organic pollution. Meanwhile, DO levels decline, reflecting oxygen depletion associated with microbial activity. EC and TDS values also fluctuate, with notable peaks near Mueang Suphan Buri, where rice mill effluents contribute high-ion discharges, and downstream communities with intensive land use. Occasional spikes in BOD at specific stations were linked to high-density zones, such as temples or clustered residential areas.

These pollution patterns are closely associated with increasing human settlement and land use changes. Between 2019 and 2021, the study area experienced a notable expansion in urban and built-up areas. According to land classification results, urban land increased by 1.54% in Chai Nat, 11.89% in Nakhon Pathom, and 14.91% in Suphan Buri. These changes are visualized in **Fig. 4.**

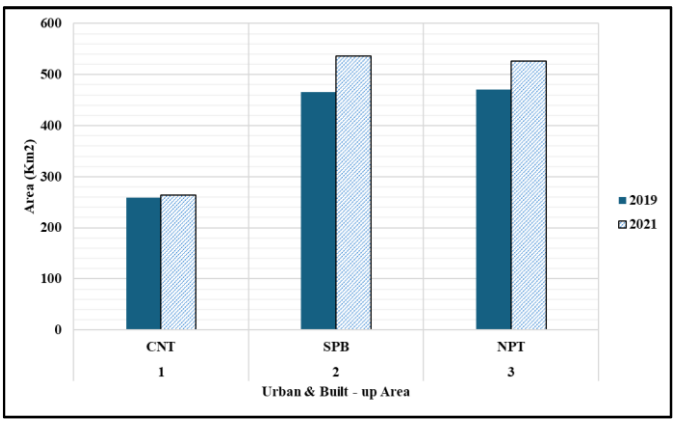

Fig. 4. Urban & Built-up Area expansion in Chai Nat (CNT), Nakhon Pathom (NPT), and Suphan Buri (SPB) from 2019 to 2021.

The correlation between these land use changes and the observed water quality deterioration underscores the significant impact of anthropogenic activities on river ecosystems. Increased urbanization, population density, and unregulated wastewater discharge contribute to higher pollutant loads, particularly in downstream segments. These field findings reinforce the rationale for integrating spatial indicators such as population density and urban land use into machine learning models discussed in later sections of this study.

4.2. Q-Value Normalization and WQI Classification

To enable standardized analysis across parameters with different units and scales, raw values of the five selected water quality indicators−DO, BOD, COD, pH, and Salinity−were first transformed into sub-indices using Q-value normalization. This approach scaled the parameters onto a standard 0‑100 range, facilitating the computation of the Water Quality Index (WQI) using the weighted arithmetic method (D. Satish Chandra, 2017). The transformation followed guidelines from the Pollution Control Department (PCD) of Thailand and aligned with WHO standards for water quality classification.

Fig. 5 provides an overview of Q-values across all parameters and stations, highlighting spatial and seasonal variation. Among the five indicators, DO and BOD showed the highest variability, consistent with seasonal hydrology and pollutant loading patterns. These indicators are susceptible to organic pollution and oxygen demand, making them reliable indicators of environmental stress.

A closer examination of Q-value behavior for DO and BOD is shown in **Fig. 6**.

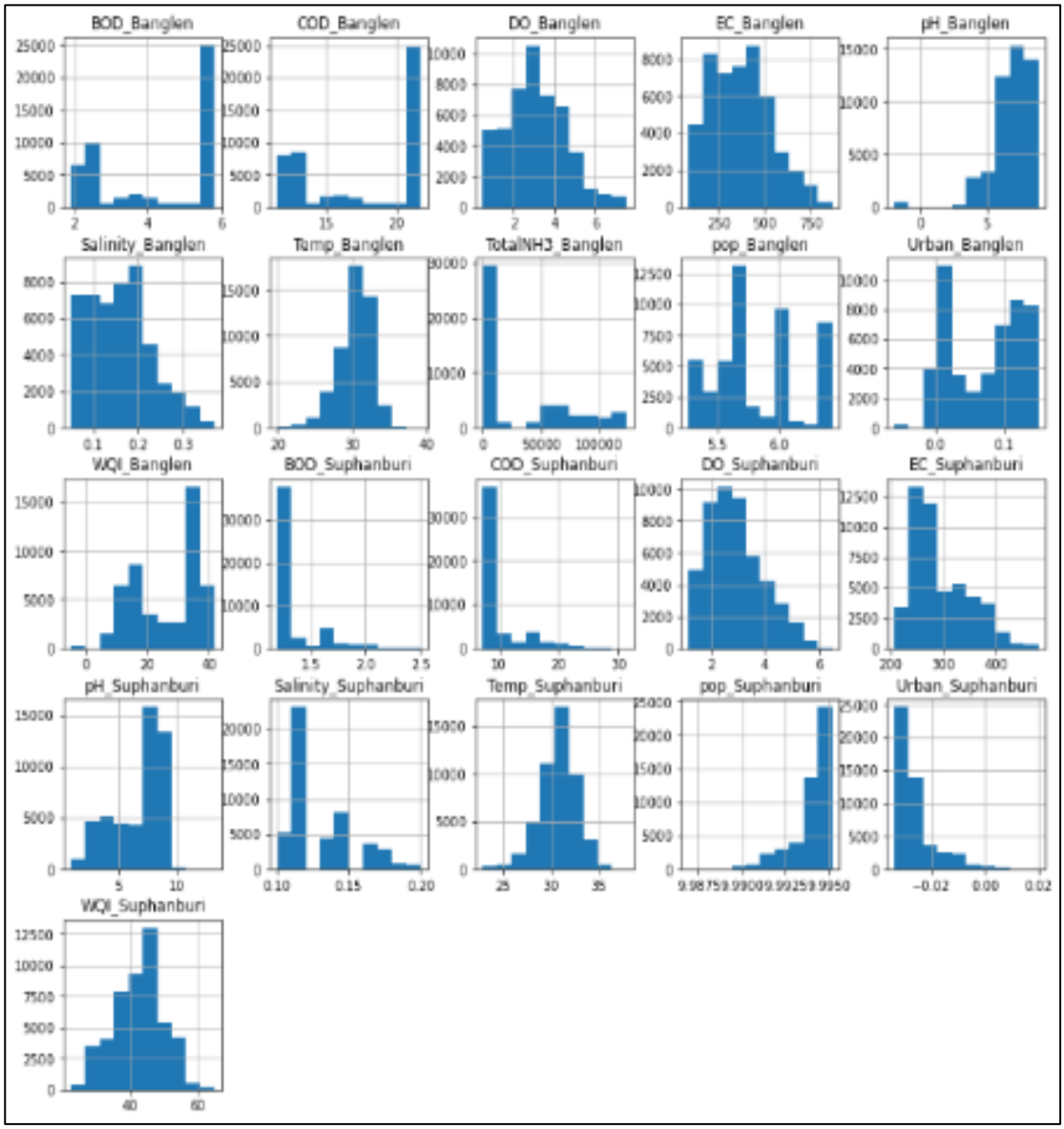

Fig. 5. Normalized Q-values of five water quality parameters across monitoring stations.

Fig. 6 demonstrates the successful normalization of these parameters across all monitoring stations and time periods. The transformation ensures that both extreme and moderate values are accurately represented in the index computation. Stations located in the downstream segment, particularly Mahachai and Nakhon Chai Si, displayed lower DO Q-values and elevated BOD Q-values, indicating higher organic pollution loads and reduced oxygen availability.

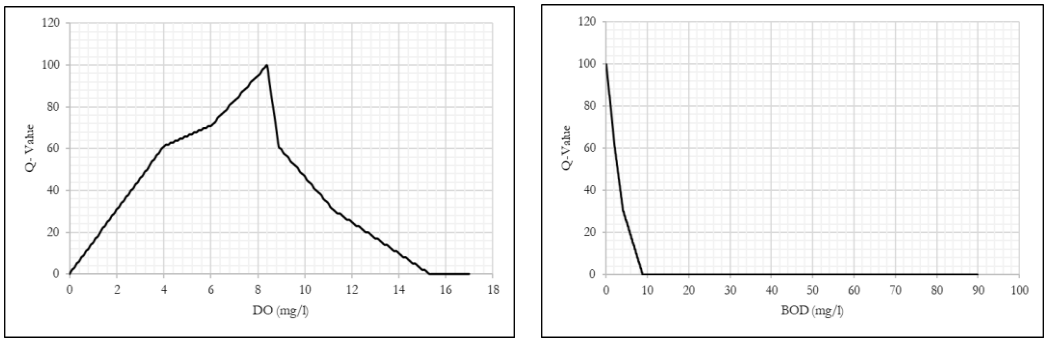

Fig. 6. Example of normalized Q-values for BOD and DO.

Following normalization, WQI scores were calculated by aggregating the Q-values using assigned weights. The resulting WQI values ranged from 23.5 to 81.6, covering classifications from "poor" to "good." A clear spatial trend emerged: upstream stations (e.g., Chainat, Suphan Buri) consistently showed higher WQI values, while downstream stations (e.g., Mahachai) exhibited significantly degraded conditions, especially during the dry season when river flow and dilution capacity were reduced. These results confirm that Q-value normalization not only standardizes data for WQI computation but also captures meaningful environmental gradients. The observed downstream decline aligns with land use pressures and pollution sources, supporting the case for integrating spatial indicators—such as population density and urban land use—into the modeling framework.

4.3. Correlation Analysis of Water Quality Parameters

To understand the interrelationships among water quality parameters and support the selection of input variables for predictive modeling, a Pearson correlation analysis (Senthilnathan, 2019) was conducted on the normalized dataset. This analysis revealed significant associations that reflect the underlying chemical and biological processes influencing river water quality, as shown in **Fig.7.**

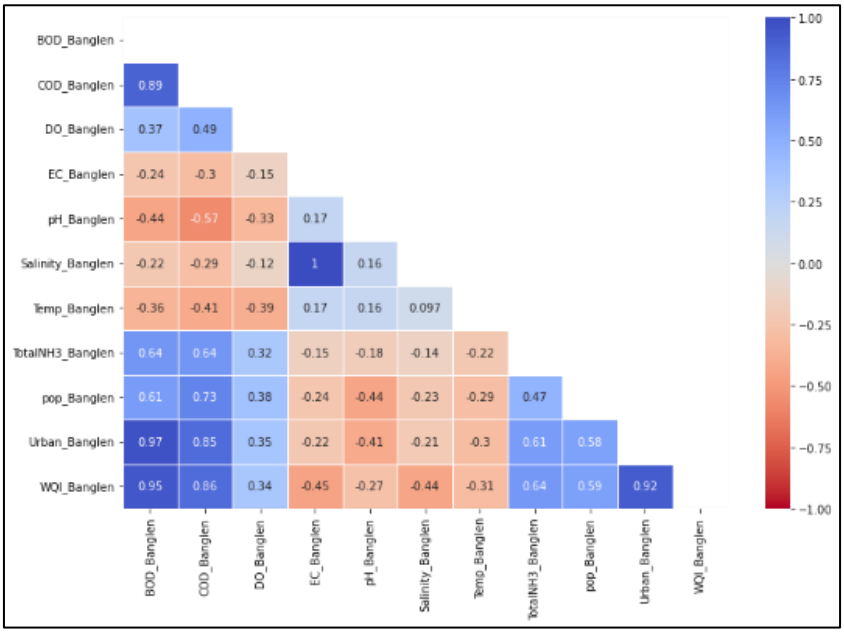

Fig. 7. Pearson correlation matrix of water quality parameters (DO, BOD, COD, pH, and Salinity) at Banglen Station.

Visually represents the degree of correlation for each parameter. The color coding in **Fig. 7.** visually indicates the degree of correlation for each parameter, where a strong correlation is represented by a value of 1 (the blue shade). As the correlation value decreases towards 0 (the red shade), the color shade darkens, indicating weaker or no correlation. Darker shades also represent inverse correlations, showing a negative relationship between parameters. This visualization helps quickly identify which parameters are strongly correlated, both positively and negatively, which is crucial for understanding how these parameters interact and impact WQI.

The Pearson correlation analysis revealed the following key relationships:

- **At the Same Station:**
  - BOD negatively correlates with EC, Salinity, populations, and pH. It is loosely associated with Temperature WQI and negatively correlated with DO.
  - DO is weakly y correlated with all parameters.
  - EC is highly correlated with Salinity and loosely associated with BOD and DO. It is weakly correlated with pH and Temperature.
  - pH and Temperature are highly and positively correlated with Salinity. They are loosely associated with BOD and DO and negatively correlated with EC.
  - The population is highly negatively correlated with BOD, DO, and COD. It is weakly associated with pH, EC, Temperature, and Salinity.
  - Urban & Built-up Areas are highly positively correlated with BOD and DO. It is loosely associated with pH, EC, Temperature, and Salinity.
- **Between Banglen Station and Suphanburi Station:**
  - BOD at Banglen Station weakly correlates with BOD at Suphanburi Station. It is loosely associated with DO and Temperature and negatively correlated with EC, Salinity, and pH.
  - At Banglen Station, it is weakly correlated with DO at Suphanburi Station, BOD, and pH. It is loosely negatively correlated with EC, Salinity, and Temperature
  - pH, Salinity, and Temperature at Banglen Station are highly and positively correlated with pH, Salinity, and Temperature at Suphanburi Station. They are loosely negatively correlated with DO and BOD.
  - WQI at Banglen Station weakly correlates with DO, EC, pH, Salinity, and WQI at Suphanburi Station. It is lightly associated with BOD and Temperature.
  - The population and Urban & Built-up Area at both stations are highly negatively correlated with BOD, DO, and COD and negatively correlated with EC, Salinity, and pH.

These correlation patterns are critical for two reasons. First, they validate the inclusion of these parameters in the WQI formulation by highlighting their distinct yet interconnected roles. Second, they indicate which variables are likely to carry more predictive weight in the machine learning models discussed in the next section.

4.4. Correlation Analysis of Water Quality Parameters

To understand the interrelationships among water quality parameters and support the selection of input variables for predictive modeling, a Pearson correlation analysis was conducted on the normalized dataset. This analysis revealed significant associations that reflect the underlying chemical and biological processes influencing river water quality, as shown in **Fig. 7.**

Due to the limited availability of high-frequency water quality monitoring data, this study adopted a predictive modeling approach that utilizes upstream water quality information to forecast downstream conditions. The input dataset comprised five key physicochemical parameters−Temperature, BOD, DO, pH, and Salinity−along with spatial variables such as population density and urban built-up area coverage. The goal was to anticipate pollution severity downstream and provide timely data for management intervention.

To evaluate the robustness of model forecasts over different horizons, the Random Forest (RF) algorithm−identified as the best-performing model−was tested across three lead times: 5 hours, 10

hours, and 17 hours. As shown in **Table 2**, all lead times produced consistently high predictive performance. The 10-hour lead time yielded the best overall results with the highest R^2 and lowest MAE, suggesting it provides the most balanced and stable forecast window.

Table 2.

Performance of Random Forest model at different lead times.

Lead Time	R^2	RMSE	MAE
5 Hours	0.663	6.593	0.841
10 Hours	0.664	7.096	0.855
17 Hours	0.657	6.398	0.824

Further comparison of machine learning models at the 10-hour lead time revealed that Random Forest (RF) outperformed all other algorithms, including k-Nearest Neighbors (KNN), Logistic Regression (LR), Decision Tree (DT), Support Vector Machine (SVM), and AdaBoost (AB). As shown in **Table 3**, RF achieved the highest R^2 value and the lowest prediction errors, confirming its suitability for modeling complex environmental data.

Table 3.

Performance comparison of machine learning models at 10-hour lead time.

Model	R^2	RMSE	MAE
Random Forest	0.664	7.096	0.855
KNN	0.593	11.532	1.197
Logistic Regression	0.588	14.685	1.353
Decision Tree	0.405	26.237	2.217
SVM	0.114	102.788	2.217
AdaBoost Classifier	0.158	107.419	6.327

Prediction error analysis showed that the RF model performed well in upstream locations such as Chainat and Suphan Buri, where water quality was more stable. In contrast, greater deviations occurred in Mahachai and Nakhon Chai Si, where urbanization and discharge variability introduced more complex conditions. Seasonally, WQI values were slightly overpredicted in the wet season (likely due to dilution from runoff) and underpredicted in the dry season, when pollutant concentrations peak due to low flow volumes. These insights highlight the importance of incorporating seasonal and site-specific variability into future model refinements.

4.5 Temporal and Spatial Change of WQI of the Tha Chin River

4.5.1. Relationship between WQI and accumulated Population along the River

To examine the long-term trends in surface water quality across the Tha Chin River Basin, the Water Quality Index (WQI), as illustrated in **Fig. 8**, was analyzed refering km.0 at Wat Sing District as the starting point. A comparative assessment of annual WQI values from 2020 to 2022 against the Pollution Control Department (PCD) 's standard classification for surface water quality revealed a consistent downward trend. The average WQI values were 39.9 in 2020, 39.0 in 2021, and further declined to 38.5 in 2022—each year, falling below the national standard.

Comparing these WQI values with the cumulative population along the river corridor from Wat Sing District downstream, a clear inverse relationship emerges. As the cumulative population increases, WQI values show a corresponding decline. This degradation is primarily attributed to elevated levels of BOD and COD, which rise with population density and accumulate downstream, contributing to deteriorating water quality.

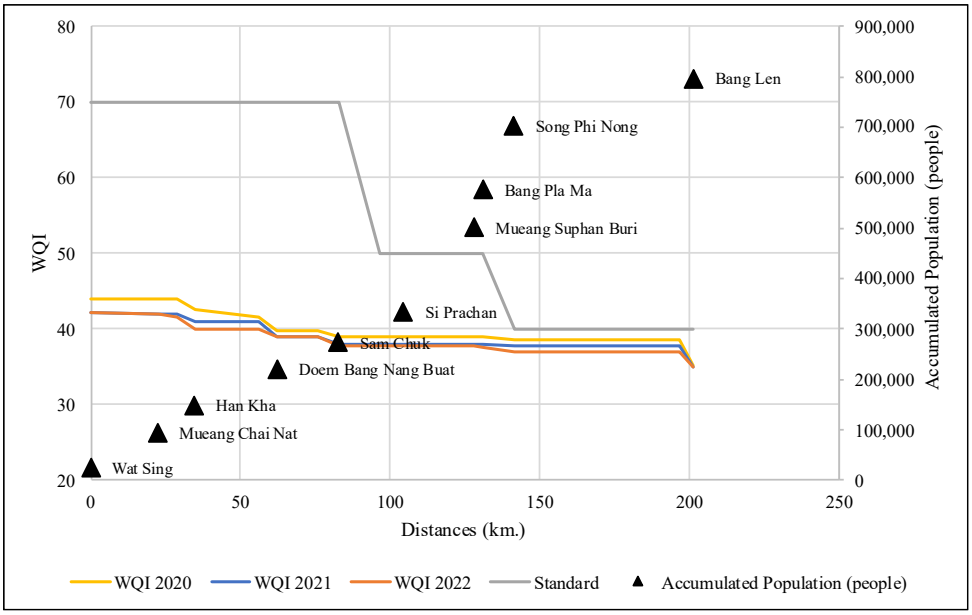

Fig. 8. The WQI values for the years 2020, 2021, and 2022 were compared against the national standard threshold established by the Pollution Control Department (PCD).

4.5.2. Spatial Visualization

To examine long-term patterns of surface water quality across the Tha Chin River Basin, Inverse Distance Weighted (IDW) interpolation was applied using QGIS 3.28 to generate annual spatial distribution maps of the Water Quality Index (WQI).

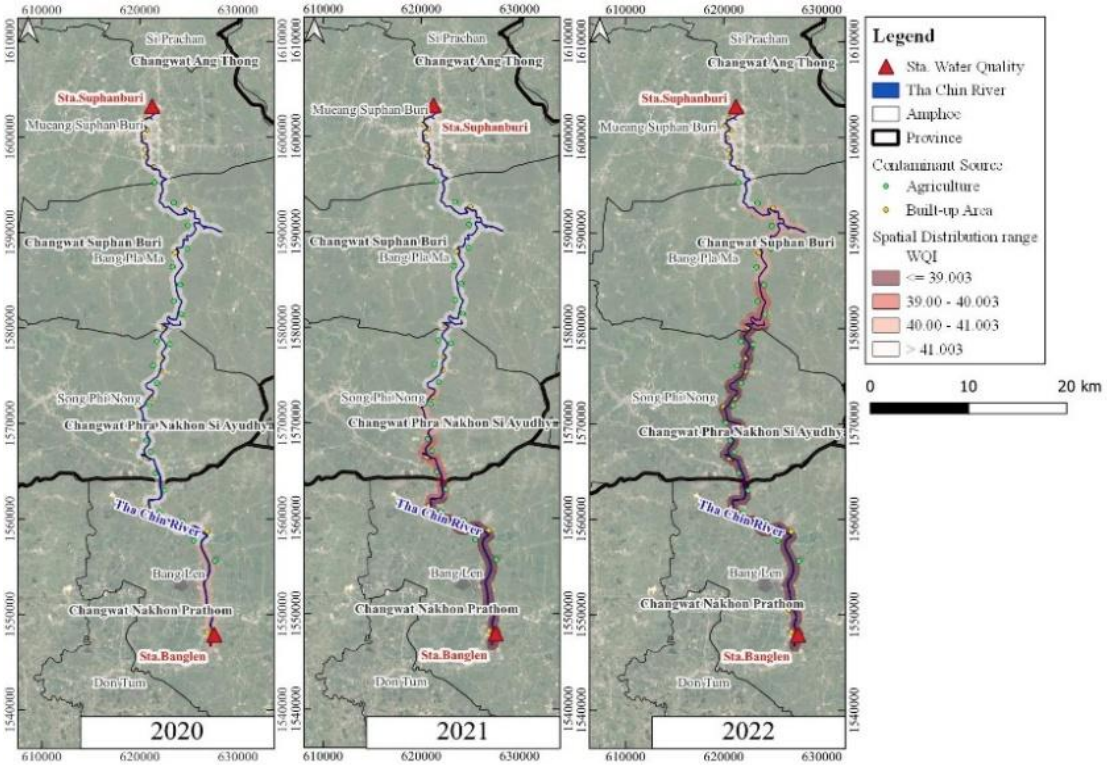

Fig. 9. Spatial distribution of WQI for 2020, 2021, and 2022, generated using IDW interpolation.

This geostatistical technique estimates unsampled values based on the weighted average of nearby measured points, offering a clear visual representation of spatial WQI variation (Tabios & Salas, 1985).

As shown in **Fig. 9**, the entire study area experienced persistent water quality degradation over the three years. All zones were categorized as either "moderately degraded" or "degraded," with no locations falling into the "good" or "excellent" categories. The deterioration trend is most pronounced in 2022, indicating a sustained decline in surface water quality across the basin.

When analyzed by district, Banglen consistently reported the lowest WQI values, ranging from 39 to 42, across all three years. This was attributed to high urban density and the accumulation of pollutants from upstream. Bang Pla Ma and Song Phi Nong displayed slightly higher and relatively stable WQI values within the "degraded" category. Mueang Suphan Buri District, located upstream, maintained moderately degraded water quality and showed a slight improvement trend from 2020 to 2022.

This decline in WQI aligns with spatial land use changes during the same period. Between 2020 and 2022, urban and built-up areas increased noticeably, particularly in Suphan Buri and Nakhon Pathom provinces. Although detailed agricultural land trends were not assessed, the documented expansion of the urbanized regions points to growing human pressure on the river system.

In summary, the IDW-interpolated maps provide strong visual and quantitative evidence of a long-term deterioration in water quality driven by increasing urban development. The spatial insight gained from this analysis highlights priority zones for policy intervention, wastewater control, and land use planning within the Tha Chin Basin.

5. CONCLUSION

This study demonstrates the effectiveness of combining field observations, machine learning (ML), and Geographic Information System (GIS) techniques to assess and predict water quality trends in the Tha Chin River Basin, Thailand. The approach analyzed key physicochemical parameters and spatial variables, including urban land expansion and population density, to generate a multidimensional understanding of river water quality between 2020 and 2022.

Spatial and temporal analysis of the Water Quality Index (WQI) revealed a clear degradation pattern throughout the study area. IDW-interpolated maps showed that all monitoring locations were classified as either "moderately degraded" or "degraded," with no sites reaching "good" or "excellent" quality. The temporal decline was most pronounced in 2022, with the poorest water quality consistently recorded in downstream districts such as Banglen. Conversely, Mueang Suphan Buri, located in the upstream portion of the basin, maintained a moderately degraded status and showed slight improvement over the three years.

In parallel, land use analysis confirmed a notable increase in urban and built-up areas between 2020 and 2022, especially in Suphan Buri and Nakhon Pathom provinces. This urban expansion corresponded with the declining WQI values in affected districts, reinforcing the impact of human-induced pressures on surface water quality.

To support predictive decision-making, six supervised ML algorithms were tested. The Random Forest model achieved the best performance ($R^2 = 0.664$, MAE = 0.855) at a 10-hour lead time and showed consistent accuracy across other forecast intervals. The inclusion of spatial indicators—such as population density and urban land cover—substantially enhanced model performance.

In conclusion, this study provides compelling evidence of spatially uneven and temporally worsening water quality conditions along the Tha Chin River. The ML-GIS integrated framework offers a scalable tool for identifying pollution hotspots, evaluating long-term degradation, and guiding targeted interventions in rapidly urbanizing river basins.

REFERENCES

Abbasi, T., & Abbasi, S. A. (2012). Water-Quality Indices. In *Water Quality Indices* (pp. 353-356).

Ahmed, U., Mumtaz, R., Anwar, H., Shah, A. A., Irfan, R., & García-Nieto, J. (2019). Efficient Water Quality Prediction Using Supervised Machine Learning. *Water, 11*(11). doi:10.3390/w11112210

Al-Faiz, M. Z., Ibrahim, A. A., & Hadi, S. M. (2019). The effect of Z-Score standardization (normalization) on binary input due the speed of learning in back-propagation neural network. *Iraqi Journal of Information & Communications Technology, 1*(3), 42-48. doi:10.31987/ijict.1.3.41

Belete, D. M., & Huchaiah, M. D. (2021). Grid search in hyperparameter optimization of machine learning models for prediction of HIV/AIDS test results. *International Journal of Computers and Applications, 44*(9), 875-886. doi:10.1080/1206212x.2021.1974663

Chen, K., Chen, H., Zhou, C., Huang, Y., Qi, X., Shen, R., . . . Ren, H. (2020). Comparative analysis of surface water quality prediction performance and identification of key water parameters using different machine learning models based on big data. *Water Res, 171*, 115454. doi:10.1016/j.watres.2019.115454

D. Satish Chandra, S. A., M.V.S. Raju. (2017). ESTIMATION OF WATER QUALITY INDEX BY WEIGHTED ARITHMETIC WATER QUALITY INDEX METHOD A MODEL STUDY. *International Journal of Civil Engineering and Technology (IJCIET) 8*(4), 8.

Fathi, P., Ebrahimi Dorche, E., Zare Shahraki, M., Stribling, J., Beyraghdar Kashkooli, O., Esmaeili Ofogh, A., & Bruder, A. (2022). Revised Iranian Water Quality Index (RIWQI): a tool for the assessment and management of water quality in Iran. *Environ Monit Assess, 194*(7), 504. doi:10.1007/s10661-022-10121-9

Gazzaz, N. M., Yusoff, M. K., Aris, A. Z., Juahir, H., & Ramli, M. F. (2012). Artificial neural network modeling of the water quality index for Kinta River (Malaysia) using water quality variables as predictors. *Mar Pollut Bull, 64*(11), 2409-2420. doi:10.1016/j.marpolbul.2012.08.005

Horton R.K. (1965). An index number for rating water quality. Journal of Water Pollution Control Federation. *37*(3), 300-306.

Jha, D. K., Devi, M. P., Vidyalakshmi, R., Brindha, B., Vinithkumar, N. V., & Kirubagaran, R. (2015). Water quality assessment using water quality index and geographical information system methods in the coastal waters of Andaman Sea, India. *Mar Pollut Bull, 100*(1), 555-561. doi:10.1016/j.marpolbul.2015.08.032

Kouadri, S., Elbeltagi, A., Islam, A. R. M. T., & Kateb, S. (2021). Performance of machine learning methods in predicting water quality index based on irregular data set: application on Illizi region (Algerian southeast). *Applied Water Science, 11*(12). doi:10.1007/s13201-021-01528-9

Liu, P., Wang, J., Sangaiah, A., Xie, Y., & Yin, X. (2019). Analysis and Prediction of Water Quality Using LSTM Deep Neural Networks in IoT Environment. *Sustainability, 11*(7). doi:10.3390/su11072058

Lumb, A., Halliwell, D., & Sharma, T. (2006). Application of CCME Water Quality Index to monitor water quality: a case study of the Mackenzie River Basin, Canada. *Environ Monit Assess, 113*(1-3), 411-429. doi:10.1007/s10661-005-9092-6

Ly, Q. V., Nguyen, X. C., Le, N. C., Truong, T. D., Hoang, T. T., Park, T. J., . . . Hur, J. (2021). Application of Machine Learning for eutrophication analysis and algal bloom prediction in an urban river: A 10-year study of the Han River, South Korea. *Sci Total Environ, 797*, 149040. doi:10.1016/j.scitotenv.2021.149040

Magesh, N. S., Krishnakumar, S., Chandrasekar, N., & Soundranayagam, J. P. (2012). Groundwater quality assessment using WQI and GIS techniques, Dindigul district, Tamil Nadu, India. *Arabian Journal of Geosciences, 6*(11), 4179-4189. doi:10.1007/s12517-012-0673-8

Magyari-Sáska, Z., Haidu, I., & Magyari-Sáska, A. (2025). Experimental Comparative Study on Self-Imputation Methods and Their Quality Assessment for Monthly River Flow Data with Gaps: Case Study to Mures River. *Applied Sciences, 15*(3). doi:10.3390/app15031242

Marzieh Mokarram , & Zarei, A. R. (2021). Determining prone areas to gully erosion and the impact of land use change on it by using multiple-criteria decision-making algorithm in arid and semi-arid regions. *Geoderma, 403*.

Mueller, T. G., Pusuluri, N. B., Mathias, K. K., Cornelius, P. L., Barnhisel, R. I., & Shearer, S. A. (2004). Map Quality for Ordinary Kriging and Inverse Distance Weighted Interpolation. *soil science Society of America Journal, 68*(6).

Najah Ahmed, A., Binti Othman, F., Abdulmohsin Afan, H., Khaleel Ibrahim, R., Ming Fai, C., Shabbir Hossain, M., . . . Elshafie, A. (2019). Machine learning methods for better water quality prediction. *Journal of Hydrology, 578*. doi:10.1016/j.jhydrol.2019.124084

PCD. (2017). *Total Water Quality Score for 5 Parameters. (New WQI Calculation)*. Pollution Control Department: Pollution Control Department

PCD, P. C. D. (2020). *A Decade of Water Quality Monitoring in Thailand's FourMajor Rivers The Result and the Implications for Management*. Pollution Control Department

PCD, P. C. D. (2022). *Water quality report for the year 2022*. Pollution Control Department: Pollution Control Department

Senthilnathan, S. (2019). Usefulness of Correlation Analysis. *SSRN Electronic Journal*. doi:10.2139/ssrn.3416918

Tabios, G. Q., & Salas, J. D. (1985). Geographic Spatial Distribution Map. *American Water Resouces Association, 21*(3), 16.

Wang, R., Kim, J. H., & Li, M. H. (2021). Predicting stream water quality under different urban development pattern scenarios with an interpretable machine learning approach. *Sci Total Environ, 761*, 144057. doi:10.1016/j.scitotenv.2020.144057

COMPARISON OF Triple-Dip LA NIÑA IN 2020-2023 WITH STRONG AND WEAK LA NIÑA EVENTS ON INDONESIAN RAINFALL AND SST

Gangga Dara DESTYANO [1], ***Anindya WIRASATRIYA*** [1,2*], ***Muhammad ZAINURI*** [1,2], ***Yusuf Jati WIJAYA*** [1], ***Bayu MUNANDAR*** [1], ***Muhammad HELMI*** [1,2]

DOI: 10.21163/GT_2025.202.20

ABSTRACT

The Triple-Dip La Niña event that occurred from 2020 to 2023 was a rare phenomenon characterized by enhanced convection and extreme rainfall. This study aims to quantify and compare rainfall and SST during different La Niña conditions, and to analyze the factors driving rainfall variability over these events. This research examines three La Niña events: Triple-Dip (2020-2023), strong (2010-2011), and weak La Niña (2017-2018), within Indonesia, located between 6°N-11°S and 95°E-141°E. In this study, satellite-based rainfall, SST and surface wind data served as primary data sources, which were analyzed using anomaly map. Triple-Dip and strong La Niña events exhibit similar spatial patterns of anomalies in rainfall and sea surface temperature (SST). During the JJASON period, these phenomena led to increased rainfall across much of Indonesia, including regions such as Sumatra, Western and Central Kalimantan, Sulawesi, parts of Maluku, Papua, Western Java, the waters off western Sumatra, the Natuna Sea, Java Sea, Banda Sea, and Arafura Sea. This season also saw a rise in SST throughout most of Indonesia. Conversely, during the December to May period, Triple-Dip and strong La Niña resulted in reduced rainfall in areas like Sumatra, Java, Kalimantan, Sulawesi, Maluku, and Papua, along with a decrease in SST in the Natuna Sea, Java Sea, Flores Sea, and the Indian Ocean, from the western waters of Sumatra to the southern waters of Java. In contrast, weak La Niña events displayed a more scattered pattern of rainfall anomalies, though the SST anomaly distribution was largely similar to that of Triple-Dip and strong events, except during June-August. During June-August, weak events showed a decline in SST in the Southern Java Sea. The increase in rainfall during La Niña events was particularly notable during June-November, attributed to the elevated SST across most of Indonesia.

Key-words: *Triple-Dip La Niña; Rainfall; Sea Surface Temperature, Indonesia.*

1. INTRODUCTION

Indonesia is located in the tropical region between two continents, i.e., Asia and Australia; and two oceans i.e., Pacific and Indian Oceans. This makes Indonesia become a country with high rainfall (Ramadhan *et al*., 2020). Rainfall in Indonesia is strongly affected by monsoon wind which is known as Asian-Australian Monsoon System. The Asian (Australian) monsoon is defined by northwesterly (southeasterly) winds that move from Asia (Australia) to Australia (Asia), carrying moist (dry) air and resulting in a rainy (dry) season across much of Indonesia (Griffiths *et al*., 2009; Chang *et al*., 2005; Chang *et al*., 2006; Alifdini *et al*., 2021; Ferijal and Fauzi, 2024). This wind pattern is also referred to as the northwest monsoon or simply west monsoon (WM), which reaches its peak between December and February (DJF), and the southeast monsoon or simply east monsoon (EM), which is most intense from June to August (JJA). From March to May (MAM) and from September to November (SON) are known as the transition I and transition II seasons, respectively. In the longer timescale, El Niño Southern Oscillation (ENSO) that occurs in the Pacific Ocean becomes the main

[1]*Diponegoro University, Department of Oceanography, Faculty of Fisheries and Marine Science, Indonesia. ganggadaradestyano@gmail.com (GDD), anindyawirasatriya@lecturer.undip.ac.id (AW), muhammadzainuri1962@gmail.com (MZ), yusufjatiwijaya@lecturer.undip.ac.id (YJW), bymunandar@gmail.com (BM), muhammadhelmi69@gmail.com (MH)*

[2]*Diponegoro University, Center for Coastal Rehabilitation and Disaster Mitigation Studies, Indonesia*

**Corresponding author: anindyawirasatriya@lecturer.undip.ac.id*

driver for interannual climate variability within the Indonesian Region including rainfall (Simanjuntak *et al*. 2022). ENSO have two main phases, i.e. La Niña and El Niño. La Niña (El Niño) happens when sea surface temperature (SST) in the middle and east equatorial Pacific cooler (warmer) than usual. Ocean Nino Index (ONI) have been widely used to identify the ENSO phase (Haile *et al*., 2021). ONI is obtained by measuring SST in Nino 3.4 (120-170°W, 5°N-5°S). When the SST anomaly ≥0,5°C indicating El Nino phase, anomaly between (-0.5) to 0.5°C: neutral, dan anomaly ≤ (-0,5°C) indicating La Niña. These phenomena cause increasing/decreasing rainfall in Indonesia (Yustiana *et al*., 2023). During La Niña, strong easterly winds moves warm water masses to Indonesia. This condition cause boots the convection, which lead to increasing precipitation and causing extreme rainfall (Rodysill *et al*., 2019).

Study about the impact of La Niña to the rainfall in the Indonesian Region have been conducted by many researchers (e.g., Prasetyo *et al*., 2017; Hidayat *et al*., 2018; Firmansyah *et al*., 2022; Zaini *et al*., 2024). However, La Niña that happened in 2020-2022 is special case since it happened consecutively for 3-years which is called Triple-Dip La Niña. Historically, Triple-Dip La Niña happened in 1973-1976 and 1998-2001, then happened again in 2020-2023. Although some of study about Triple-Dip La Niña in 2020-2023 have been conducted (e.g., Shi *et al*., 2023; Zhang *et al*., 2024), the impact of this phenomena on Indonesian rainfall is not extensively studied. Alhadid and Nugroho (2024), have found that there were increasing on zonal wind strength, relative humidity, and rainfall in Indonesia during the Triple-Dip La Niña. This condition significantly happened in north and east Indonesia during JJA and SON. However, the comparison between these phenomena with previous La Niña events has not been explained yet. In this study, we aim to show a comparison of the impact of Triple-Dip La Niña in 2020-2023 with strong La Niña (2010-2011) and weak La Niña (2017-2018) on Indonesian rainfall and SST. Then, the factors that cause the rainfall and SST variability during those periods is analyzed. This study used remote sensing techniques to collect data for wide area coverage. The data is constructed from multiple satellites to obtain gap-free data. Then, this data is analyzed seasonally, i.e. west (DJF), transition I (MAM), east (JJA), and transition II (SON).

2. STUDY AREA

Our study area is Indonesian archipelago which is located between the coordinate 95-141°E and 11°S-6°N (**Fig. 1**). Indonesia has five major islands, such as Sumatra, Kalimantan, Java, Sulawesi, and Papua. Positioned between the continents of Asia and Australia and near the Pacific Ocean, Indonesia's climate is significantly influenced by monsoon winds and the ENSO phenomenon, which are crucial in shaping the country's rainfall patterns. According to Aldrian and Susanto (2003), regions in Indonesia have been categorized based on their rainfall characteristics. In particular, southern Indonesia, Maluku, and northern Sulawesi are heavily impacted by ENSO. Additionally, monsoon wind patterns affect various parts of Indonesia, with the eastern season typically being dry and the western season generally experiencing more rain.

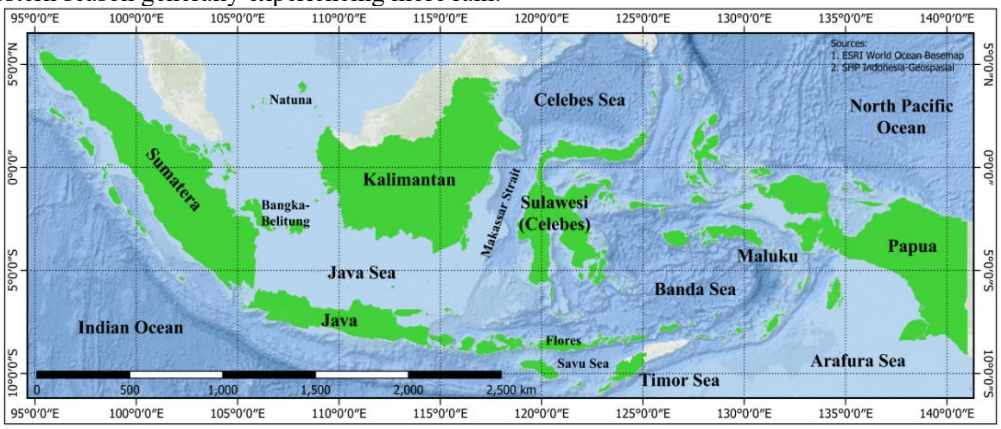

Fig. 1. Study area.

3. DATA AND METHODS

3.1. Data

The La Niña periods were identified using Nino 3.4 Index, which derived from https://www.cpc.ncep.noaa.gov/ when the index value is lower equal than -0.5°C (Rohmat *et al*., 2023; Nurafifah *et al*., 2022). We used period of Triple-Dip La Niña during 2020-2023, which was compared to the strong La Niña (2010-2011) and weak La Niña (2017-2018) periods (**Fig. 2**). For the rainfall data, we used CPC Morphing Technique (CMORPH) daily rainfall, with the spatial resolution up to 0.25°. The SST data derived from Operational Sea Surface Temperature and Sea Ice Analysis (OSTIA) with the spatial resolution of 0.05°. OSTIA uses infrared and microwave, also in-situ measurement for collecting the SST data. This data would be filtered based on wind speed for representing fundamental SST (Cuervo *et al*., 2022). The wind data used Cross-Calibrated Multiplatform (CCMP) with the spatial resolution up to 0.25° and interval up to 6 hours (Mears *et al*., 2022). This data represents wind speed for 10 m above sea surface. The CMORPH, OSTIA, and CCMP data were downloaded for period of 2007-2023.

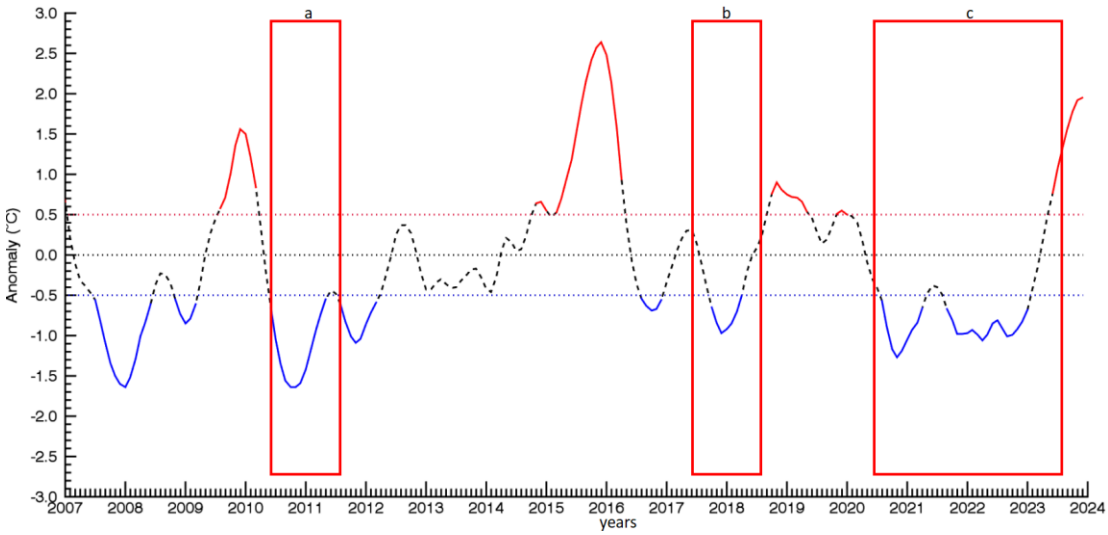

Fig. 2. Historical ONI index shows El Nino (red), La Niña (blue), and Neutral (dashes) phases from 2007 to 2023. The red boxes are the period of a) strong, b) weak and c) triple dip La Niña analyzed in this study.

3.2. Climate Data Calculation

This study used a quantitative method. The quantitative method is a systematical study method that uses numbers and statistical analysis (Millenia *et al*., 2022). This method is used to identify the correlation between rainfall and La Niña phenomena. We extracted the rainfall, SST, and wind data, then compiled monthly and seasonally. The seasonally-compiled data would be compiled into climatology using equation (1) (Wirasatriya *et al*., 2017). The

The formula is expressed as follows:

$$\bar{X}(x,y) = \frac{1}{n}\sum_{i=1}^{n} xi\,(x,y,t) \qquad (1)$$

where: $\bar{X}(x,y)$ is monthly mean value or monthly climatology value at position (x,y), $xi(x,y,t)$ is i^{th} value of the data at (x,y) position and time t. Furthermore, n is number of data in *1* month and number of monthly data in *1* period of climatology (i.e., from 2007 to 2023 = 17 data) for monthly calculation and monthly climatology calculation respectively. Next we calculated anomaly of triple-dip, strong and week La Niña periods seasonally from their climatology (2007-2023).

3.3. Statistical and Spatial Analysis

The Rainfall, SST, and wind data were analyzed seasonally. Triple-Dip La Niña data was compared with strong and weak La Niña. Precipitation was diagnosed spatially based on Aldrian and Susanto (2003), where climatic regions classified as southern Indonesia (from south Sumatra to Timor Island, southern Kalimantan, Sulawesi, and part of Irian Jaya), northwest Indonesia (from northern Sumatra to northwestern Kalimantan), and including Maluku also the northern part of Sulawesi. Statically, rainfall and SST data would be correlated with the Nino 3.4 Index using Pearson Correlation (2) (Nurafifah *et al*., 2022). The formula is expressed as follows:

$$r = \frac{n\sum XY - \sum X \sum Y}{\sqrt{\{n\sum X^2 - (\sum X)^2\}\{n\sum Y^2 - (\sum Y)^2\}}} \quad (2)$$

where: *r, X, Y* and *n* are correlation coefficient value, independent variable, dependent variable and amount of data, respectively.

4. RESULTS AND DISCUSSIONS

4.1. Rainfall Variability During La Niña Periods

During La Niña periods, the average rainfall calculated for the Indonesia Region (6°U-11°S dan 95°E-111°E). Triple-Dip La Niña during JJA(DJF) shows rainfall up to 6.22 (8.70) mm/day, strong La Niña shows rainfall up to 7.01 (8.46) mm/day, and weak La Niña shows rainfall up to 6.39 (7.87) mm/day (**Table 1**). This condition indicates a dry (wet) season during JJA (DJF), which has been mentioned by previous research (Mulsandi *et al*., 2024). From the anomaly data, that triple-Dip indicates increasing rainfall during JJA (0.84 mm/day), SON (1.46 mm/day), and DJF (0.71 mm/day) while decreasing rainfall during MAM (-0.21 mm/day). Strong La Niña shows an increase in rainfall during JJA (1.63 mmm/hari), SON (1.78 mm/day), DJF (0.47 mm/day), and MAM (0.83 mm/day). Weak La Niña indicates increased rainfall during JJA(SON) up to 1.01(1.20) mm/day and decreased rainfall during DJF(MAM) up to -0.12(-0.18) mm/day. This study reveals that La Niña's impact is more conspicuous during JJASON than DJFMAM. Kurniadi *et al*. (2021) reported that ENSO influence on Indonesia's rainfall is more significant during the dry season (JJA). Alhadid dan Nugroho (2024) also found that the increase in Indonesia's rainfall during Triple-Dip Niña is more pronounced during JJASON, which is supported by previous research (Nur'utami and Hayasaka, 2022; Aldrian and Susanto, 2003).

Table 1.
Average and Anomaly of Rainfall, SST, and Wind Speed during different La Niña Conditions.

Periods	Season	Rainfall (mm/day)	Anomaly (mm/day)	SST (°C)	Anomaly (°C)	Wind Speed (m/s)	Anomaly (m/s)
Triple-Dip La Niña (2020-2023)	JJA	6.22	0.84	28.97	0.38	3.88	-0.22
	SON	7.16	1.46	29.19	0.39	1.36	-0.17
	DJF	8.70	0.71	29.14	0.07	2.55	0.34
	MAM	6.49	-0.21	29.53	0.05	2.73	-0.08
Strong La Niña (2010-2011)	JJA	7.01	1.63	29.10	0.51	3.36	-0.73
	SON	7.47	1.78	29.44	0.64	1.55	0.03
	DJF	8.46	0.47	29.06	-0.01	2.85	0.63
	MAM	7.53	0.83	29.18	-0.30	2.60	-0.22
Weak La Niña (2017-2018)	JJA	6.39	1.01	28.67	0.09	4.35	0.25
	SON	6.90	1.20	29.04	0.24	1.73	0.25
	DJF	7.87	-0.12	29.15	0.07	2.57	0.36
	MAM	6.51	-0.18	29.45	-0.03	3.68	0.84

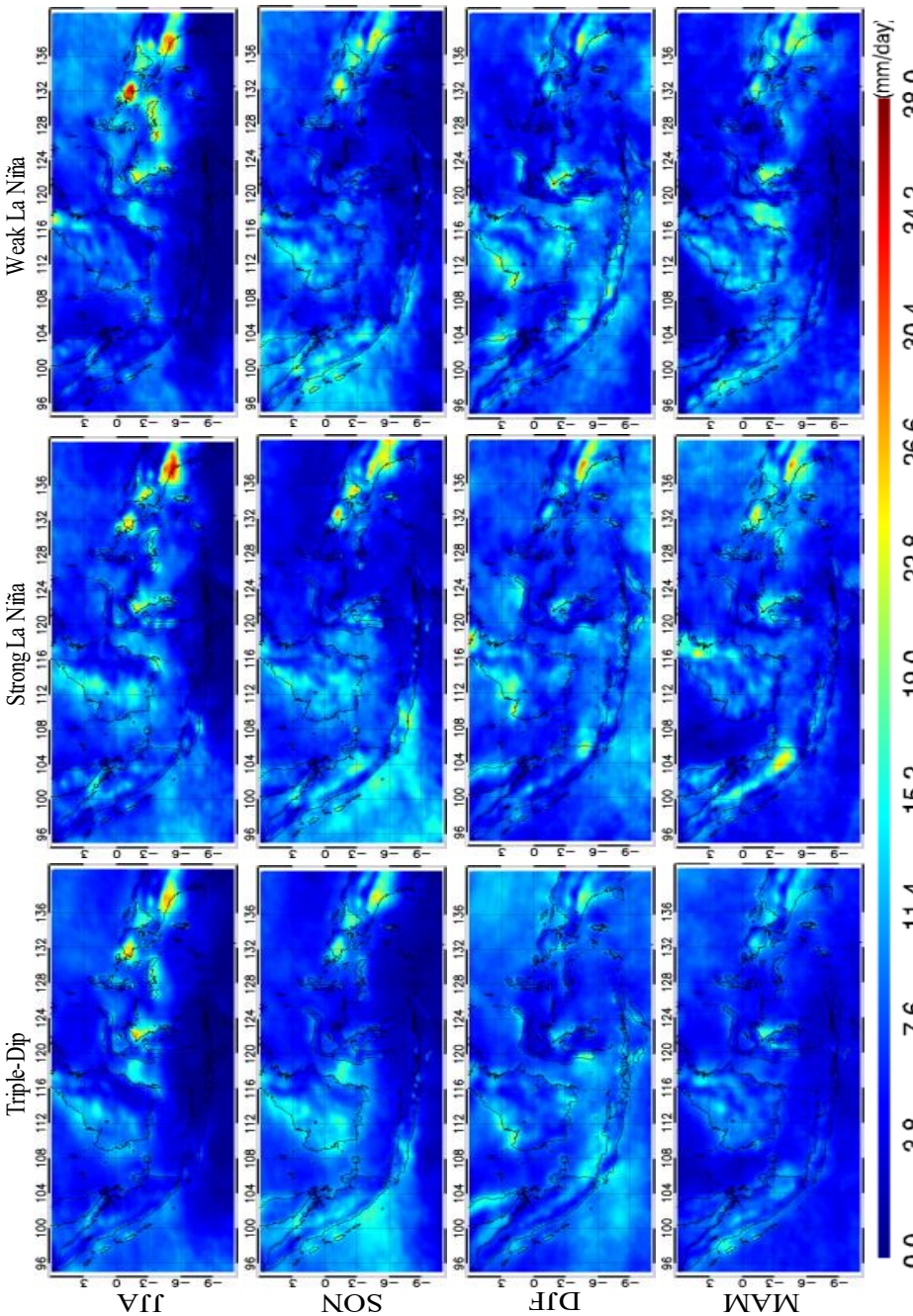

Fig. 3. Rainfall distribution during La Niña Periods in east season (JJA), transition II (SON), west season (DJF), and transition I (MAM).

La Niña periods indicate light rain up to 19.0 mm/day in Sumatra, Kalimantan, Western Java, Sulawesi, Maluku, and Papua. Those periods also indicated moderate rainfall, around 22.8-34.2 mm/day in Central Sumatra, Maluku, Western Papua, and Papua during JJASON. Triple-Dip and Strong La Niña show negligible rainfall around Central and Western Java, Bali, and Nusa Tenggara. Most of Java Island experienced insignificant rainfall during weak La Niña. Those conditions indicate a dry season in Indonesia during this season. Siswanto *et al*. (2022) have mentioned that the peak of the dry season in Indonesia occurred during July-August (JJA), while the wet season was during December-February (DJF). The three periods of La Niña during SON show Java, Bali, and Nusa Tenggara experiencing light rainfall. Strong La Niña shows rainfall up to 22.8 mm/day in Sumatra, Central Kalimantan, Central Java, Southern Sulawesi, Makassar Strait, and the Western waters of Sumatra. On the other hand, Triple-Dip and weak La Niña show the Banda Sea, Timor Sea, and parts of the Arafura Seas experiencing insignificant rainfall (**Fig. 3**).

During DJFMAM, most parts of Indonesia experienced light rainfall of up to 7.6 mm/day in the La Niña periods. Triple-Dip during DJF indicates rainfall of up to 15.2 mm/day in Southern Sumatra, Central Java, parts of Southern Kalimantan, parts of Southern Sulawesi, parts of Nusa Tenggara, and parts of the Southern waters of Java. Strong La Niña shows similar conditions in Southern Sumatra (up to 22.8 mm/day), Western and Southern Sulawesi, parts of Nusa Tenggara, parts of Papua (up to 30.4 mm/day), and parts of Arafura to Timor Sea. Weak La Niña during DJF shows similar conditions in Southern Sumatra, Central and Eastern Java, Southern Kalimantan, Western and Southern Sulawesi (up to 22.8 mm/day), and Papua (up to 22.8 mm/day). During MAM, Triple-Dip shows rainfall up to 15.2 mm/day in Northern Sumatra, Northern Kalimantan, Western Sulawesi, and Papua.

Strong La Niña shows rainfall of up to 22.8 mm/day in Sumatra, Northern Kalimantan, Western Sulawesi (up to 15.2 mm/day), and Papua (up to 26.6 mm/day). Weak La Niña during MAM indicates parts of Bali Nusa Tenggara, Timor, Southern waters of Java, Savu Sea, and Natuna Sea experience negligible rainfall. Rainfall of up to 22.8 mm/day can also be found in Northern Sumatra, Makassar Strait, Western Sulawesi, and Papua (**Fig. 3**). In this case, DJF indicates the wet season in Indonesia.

Triple-Dip and strong La Niña periods during JJA indicate an increase in rainfall of up to 3.0-6.0 mm/day in Sumatra, Western and Central Kalimantan, Sulawesi, parts of Maluku, Papua (up to 12.0 mm/day during strong La Niña), Western Java, western Sumatra waters, Natuna Sea, Java Sea, Banda Sea, and Arafura Sea. Triple-Dip also shows similar conditions in Makassar Strati dan Maluku Sea. During strong La Niña, this condition also occurred in the Flores and Sulawesi Sea. Weak La Niña shows an increase in rainfall of up to 3.0 mm/day around Southern Sumatra, Western Kalimantan, Sulawesi, Maluku (up to 9.0 mm/day), Western Papua (up to 9.0 mm/day), and Papua. Triple-Dip and strong La Niña during this season indicate a decrease in rainfall of up to 3.0 mm/day in Northern Kalimantan, Western Papua, the northern part of Papua, and parts of Sumatra (except Triple-Dip). Decreasing rainfall also occurred during weak La Niña in Western and Central Java, Timor Island, Southern Papua, the Indian Ocean, and parts of the Timor Sea and the Arafura Sea. During SON, Triple-Dip and weak La Niña caused rainfall increase in Sumatra (except the Northern), Kalimantan (except the Northern), Sulawesi, Maluku, Papua (except the Northern), Java to Nusa Tenggara, Indian Ocean, Natuna Sea, Java to Banda Sea, Sulawesi Sea, Timor Sea, and Arafura Sea. Strong La Niña also shows rainfall increase of up to 12 mm/day in the parts of Papua and Indian Ocean. During DJFMAM, Triple-Dip and strong La Niña caused a rainfall decrease in Sumatra, Java, Kalimantan, Sulawesi, Maluku, and Papua.

During DJF, weak La Niña caused rainfall to increase by up to 3.0-9.0 mm/day in Central Java to Eastern Nusa Tenggara, which did not occur in other periods. Strong La Niña also showed similar conditions during MAM in Central Java to Nusa Tenggara, including Timor Island, while causing a rainfall increase of up to 15.0 mm/day in Southern Sumatra (**Fig. 4**). This study reveals that the Triple-Dip La Niña caused an increase in rainfall in most of Indonesia which is in line with previous studies (Alhadid and Nugroho, 2024; Aldrian and Susanto, 2003). Ariska *et al*. (2024) also mentioned that La Niña caused rainfall increases in most of Indonesia during August-October (ASO).

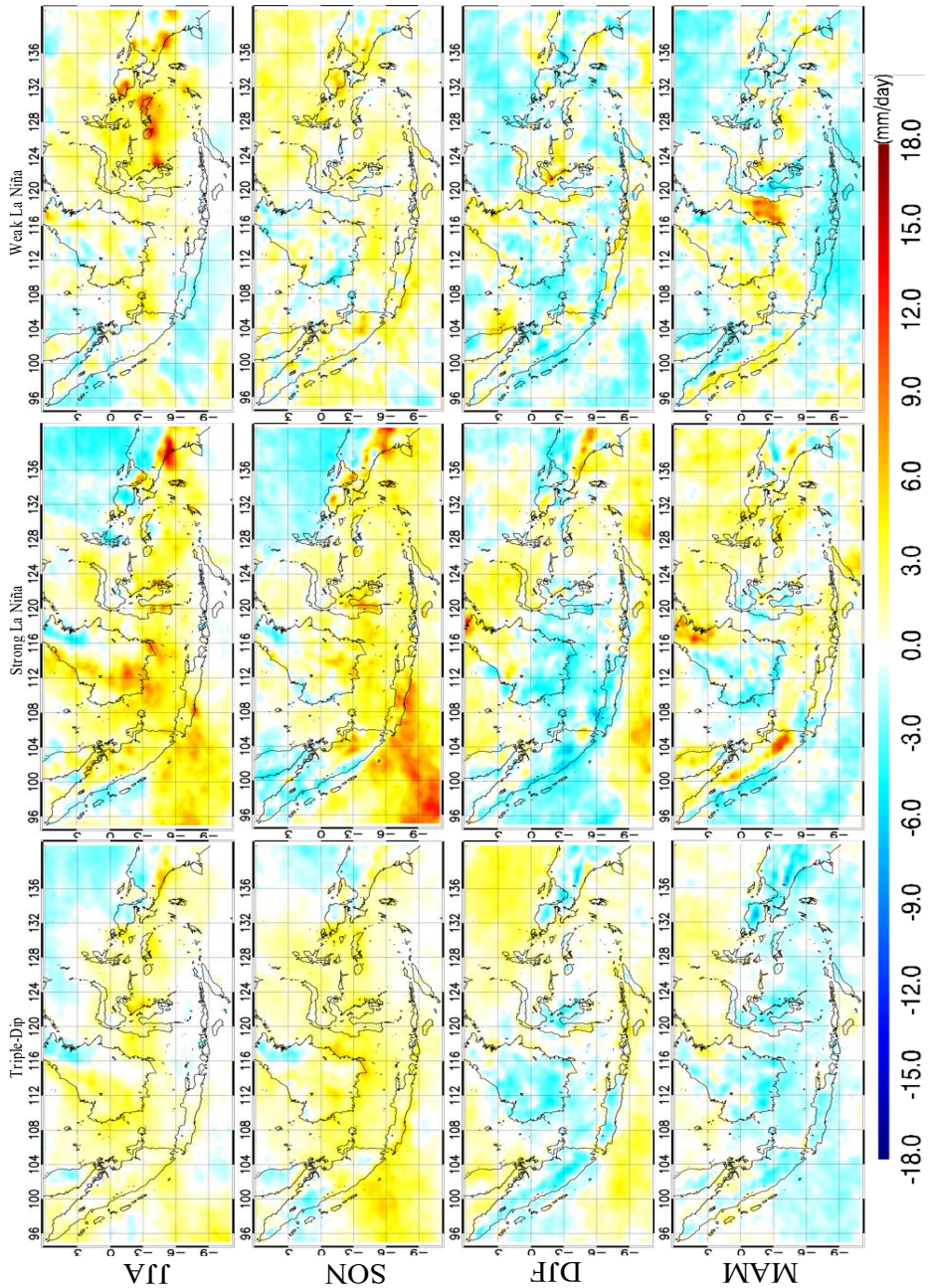

Fig. 4. Rainfall Anomaly during La Niña periods in east season (JJA), transition II (SON), w However, weak La Niña experiences a decline in SST up to 0.3°C around the Natuna Sea, Java Sea,

4.2. SST and Wind Variability During La Niña Periods

The three La Niña periods during JJASON indicate SST up to 30°C in Northern Indonesia, including the Malacca Strait, the Pacific Ocean, Natuna, Sulawesi, and Maluku Sea, due to lower wind speeds around 1.7-3.3 m/s (**Fig. 5**). The southern parts of Indonesia indicate lower SST around 26.0-29.0°C in the Southern waters of Indonesia, including Southern Java, Savu, Timor, and the Arafura Sea due to higher wind speed, around 6.7-9.2 m/s (**Fig. 6**). During JJA, Weak La Niña shows SST in the Java Sea at 28.0°C, lower than Triple-Dip (29.0°C) and Strong La Niña (29.5°C). During this period, the Southern Java Sea, Savu, and the Arafura Sea indicated similar conditions, where the SST was around 25.0-27.5°C. The wind in the Southern Java Sea during La Niña blows up to 8.3-10.0 m/s and is relatively parallel along the coastline. This condition triggers the occurrence of Ekman Transport and upwelling in that area (Wirasatriya *et al*. 2020; Rachman *et al*., 2024).

Triple-Dip, strong, and weak La Niña shows lower SST around 26.5°C in the Natuna Sea during DJF. The wind speed was up to 5.8 m/s from the north, which supports low SST water input in this area. Research by Zandika *et al*. (2024) mentioned that strong winds during DJF blew from the north to the south, supporting cool water from the northern Natuna Sea. On the other hand, most of Indonesia's eastern waters, including the Pacific Ocean, Sulawesi, Maluku, Banda, Arafura, and the Timor Seas, indicate higher SST around 28.5-30.0°C. During this season, strong La Niña also indicates SST around 28.0-28.5°C in the Indian Ocean (the Western water of Sumatra to the southern waters of Java), shown by a weak period with lower intensity.

Triple-Dip and strong La Niña caused SST to increase to 0.3-0.7°C during JJA in most of Indonesia, including the Indian Ocean, Natuna Sea, Java Sea, Sulawesi Sea, Maluku Sea, Flores Sea, Banda Sea, Savu Sea, the Western Pacific Ocean, Arafura Sea, and Timor Sea. Strong La Niña indicates an increase in SST of up to 1.7-1.3°C in the Maluku Sea, which makes it different from Triple-Dip. On the other hand, Strong La Niña experienced a decrease in SST up to 0.3°C in the Southern Java Sea and Natuna. This is due to the reduction of wind speed to around 0.8-5.0 m/s in some areas, especially the western waters of Sumatra, Natuna to Java Sea, and Makassar Strait. During SON, strong La Niña causes a decline in SST up to 2.0°C in the Southern Java Sea. This area experiences an increase in SST during weak La Niña, which is indicated by a decline in the negative anomaly. However, Triple-Dip events during SON are relatively similar to the previous season. The three La Niña periods cause SST to increase to 0.3-0.7°C in Sulawesi waters, the Maluku Sea, the Makassar Sea, and the Pacific Ocean, indicated by the positive anomaly.

Negative anomalies occurred in the Natuna Sea, Java Sea, the Indian Ocean, Savu Sea, Timor Sea (except weak La Niña), parts of the Arafura Sea (except Triple-Dip), Banda Sea (except Triple-Dip), and Flores Sea. In this case, Arafura and the Banda Sea indicate a 0°C anomaly during Triple-Dip, and the Timor Sea experiences a positive anomaly during weak La Niña. A different condition occurred during MAM, where Triple-Dip caused an increase in Arafura and the Banda Sea up to 0.3°C. Strong La Niña experienced an increase in SST to 0.3-0.7°C in the Hindia Ocean, Java Sea, Flores Sea, Banda Sea, Maluku Sea, Arafura Sea, and Timor Sea. This period also shows a decrease in SST up to 1.3°C in the Natuna Sea. However, weak La Niña experiences a decline in SST up to 0.3°C around the Natuna Sea, Java Sea, Flores Sea, Banda Sea, and Maluku Sea, which makes this period different from others (**Fig. 7**). This condition occurs due to an increase in wind speed to 2.5-3.3 m/s in that area. In this study, most of Indonesia's waters experienced an increase in SST during JJASON in Triple-Dip and strong La Niña. This is in line with Asyam *et al*. (2024), which shows an increase in SST and Rainfall in Indonesia during La Niña. In MAM, stronger wind speed during Strong La Niña causes SST to be cooler than triple dip La Niña.

However, an inconsistency found in MAM when the coolest SST during strong La Niña did not correspond to the maximum wind speed in the area of southern Indonesia. The maximum wind speed is found during weak La Niña. We assume that there is another mechanism that prevents the strong wind speed cools SST during weak La Niña which may related to the surface radiation flux, or intra-seasonal disturbance. This is left for the future study.

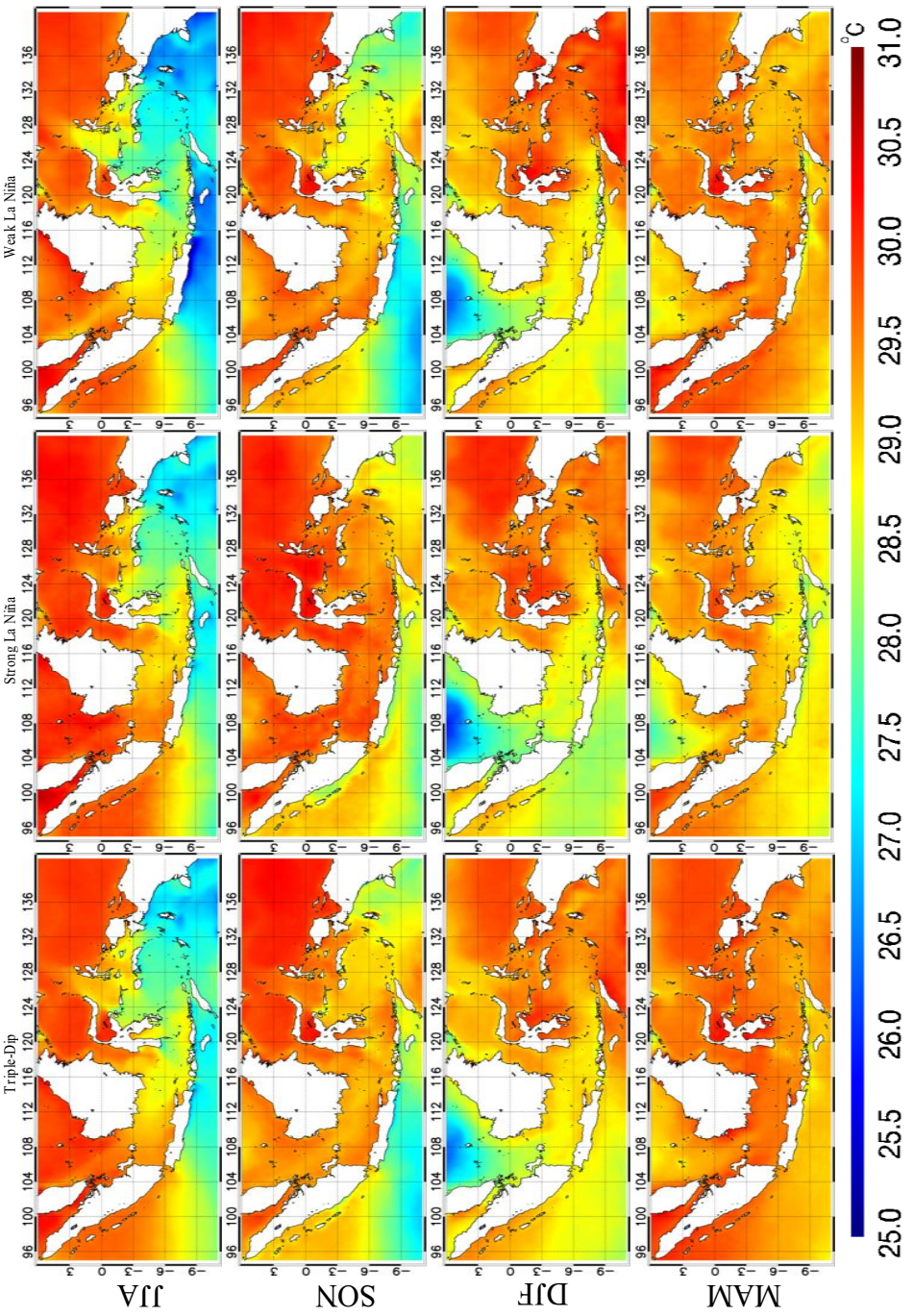

Fig. 5. SST distribution during La Niña periods in east season (JJA), transition II (SON), west season (DJF), and transition I (MAM).

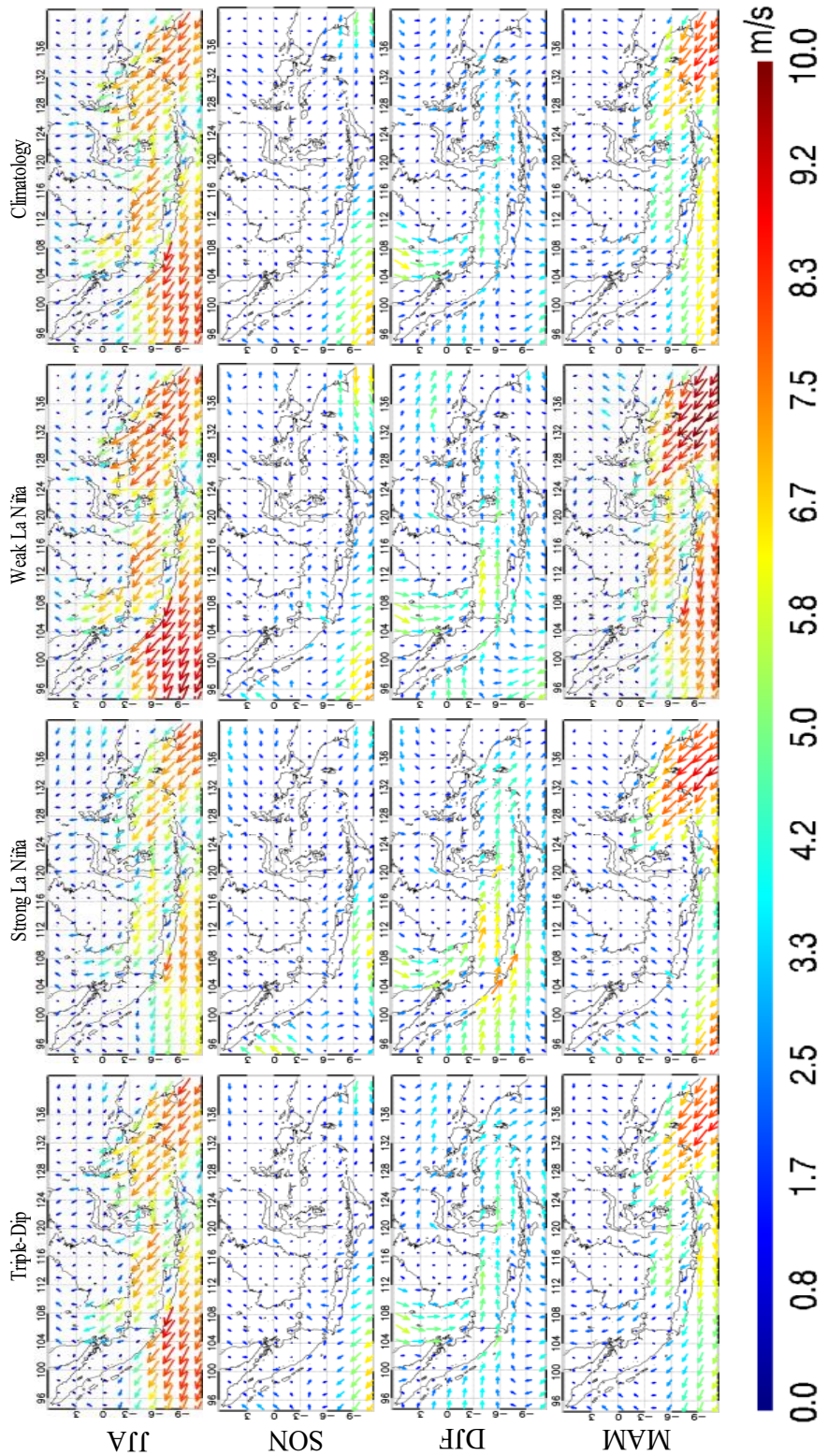

Fig. 6. Surface wind distribution during La Niña periods and climatology in east season (JJA), transition II (SON), west season (DJF), and transition I (MAM).

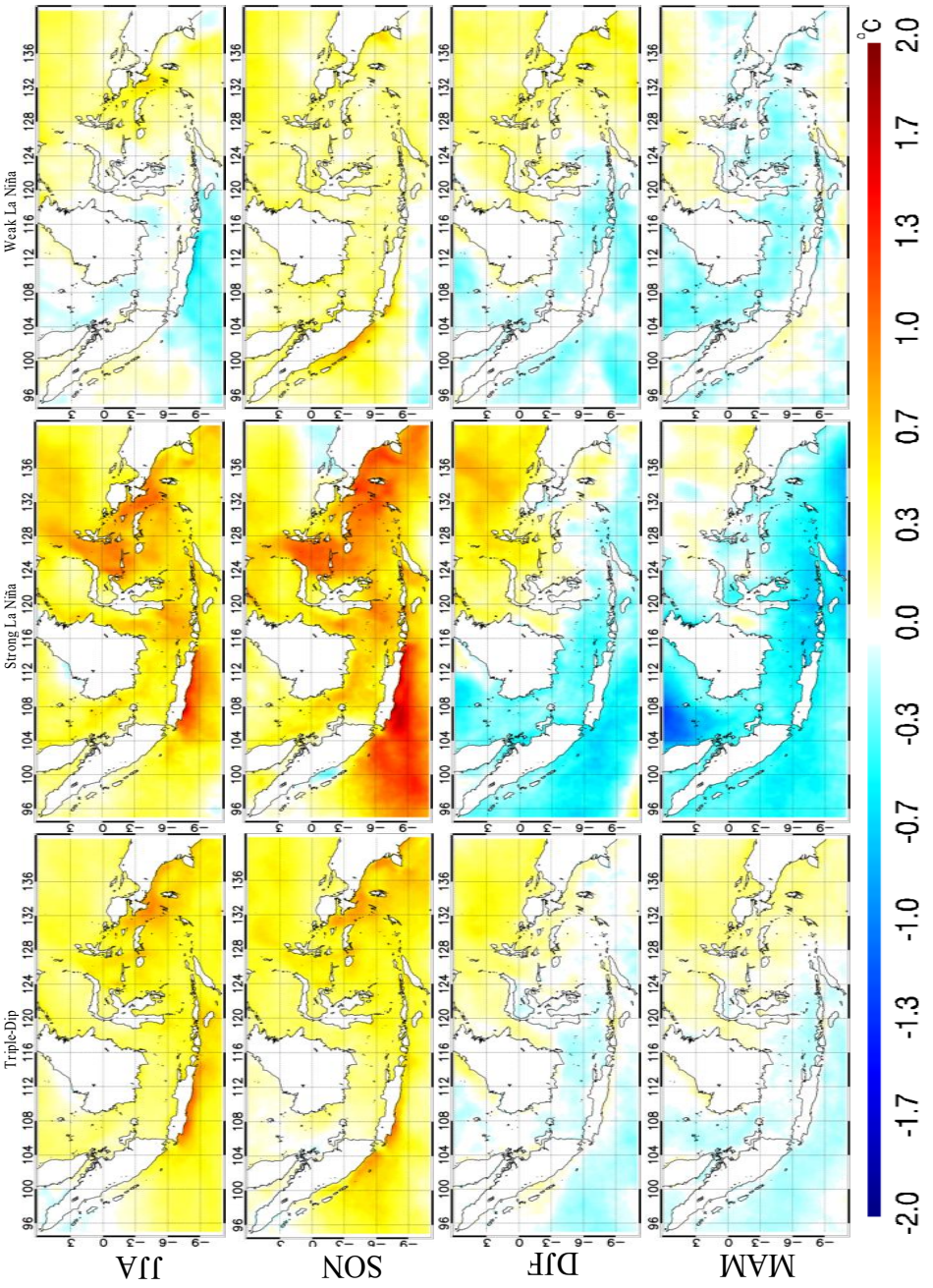

Fig. 7. SST anomaly during La Niña periods in east season (JJA), transition II (SON), west season (DJF), and transition I (MAM)

4.3. Spatial correlation analysis

To quantify the relation among ENSO, rainfall and SST, spatial correlation analysis is provided in **Fig. 8**. Most of Indonesia indicates a correlation value up to -0.8 during JJASON, except for the northern part of Sumatra and the northern part of Papua. ENSO during DFJ shows a positive correlation in Northern Sumatra, Central Java, parts of Nusa Tenggara, parts of Kalimantan, parts of Kalimantan, parts of Sulawesi, and parts of Papua in the range 0.2-0.4. During this season, Central and Southern Sumatra, parts of Kalimantan, Sulawesi, Timor Island, and Maluku show negative correlation values up to 0.2-0.4. MAM shows different conditions, where most of the Islands in Indonesia, including the western coast of Sumatra, Kalimantan (except the Nothern), Sulawesi, Maluku, Papua, and Java to Nusa Tenggara have a positive correlation up to 6.0. Ariska *et al*. (2024) found that rainfall in Indonesia is sensitive to the change in SST in the Pacific and Indian Oceans. Aldrian and Susanto (2003) found that Southern Indonesia, Southern Kalimantan, Sulawesi, parts of Papua, Maluku, and Northern Sulawesi have significant responses of a rainfall pattern to ENSO during JJASON. Hidayat *et al*. (2018) found that Nino 3.4 exhibits an inverse correlation during every season, except MAM. This study reveals that ENSO's influence on Indonesia's rainfall was more pronounced during JJASON (Kurniadi *et al*. 2021). ENSO and SST show similar conditions, where an average correlation during JJA(SON) was around -0.43(-0.49).

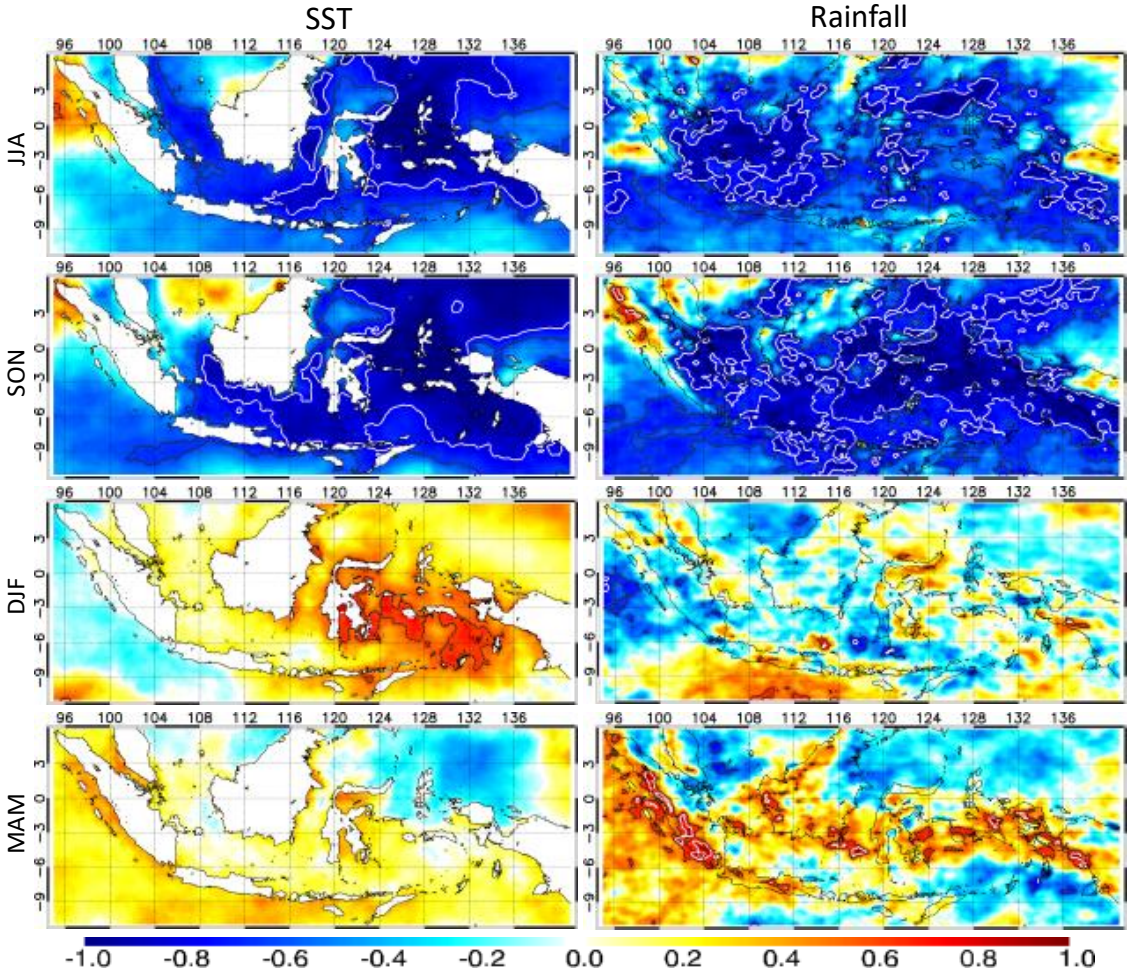

Fig. 8. ENSO correlation to Rainfall and SST where black and white contours show p-values of 0.05 and 0.01, respectively.

Most of Indonesia's waters indicate a strong negative correlation of up to -0.8. The western water of Northern Sumatra shows a strong positive relation up to 0.4 during JJA and in the Natuna Sea during SON. During DJFMAM, most of Indonesia's water shows a positive correlation up to 0.6. During DJF, a negative correlation of up to 0.3 was found in some areas, like the western waters of Sumatra and the southern water of Western Java. This condition also occurs in parts of the Natuna Sea (up to 0.3), the Sulawesi Sea, the Maluku Sea, and the Western Pacific Ocean (up to 0.6). Hendon (2003) reported a strong negative correlation between ENSO and SST around Indonesia. This study reveals that the correlation of ENSO and SST varies in season.

The occurrence of La Niña (El Nino) was indicated by a decline (incline) of the SST in the Pacific. In this case, a negative correlation between ENSO and Indonesia's SST represents the occurrence of La Niña caused an increase in Indonesia's SST. Research by Dewi *et al*. (2020) found that during the La Niña (El Nino), the SST in the Java Sea tends to be cooler (warmer) in the northwest monsoon and tends to be warmer (cooler) in the southwest monsoon, which is representing a negative correlation in Java Seas.

4.4. Discussion

Triple-Dip La Niña is a rare phenomenon, which happened in 1973-1976, 1998-2001, and occurred again in 2020-2023. According to Shi *et al*. (2024), this Triple-Dip La Niña (2020-2023) occurs after the neutral phase, which makes it different from previous Triple-Dip events. This study found that Triple-Dip La Niña in 2020-2023 was influenced by the North Pacific Meridional Mode (NPMM) and South Pacific Meridional Mode (SPMM) through tropical and extra-tropical interaction. This interaction causes negative SST anomalies and strengthens easterly wind anomalies in the equatorial Pacific.

Zhang *et al*. (2024) found that robust cross-equatorial southern wind anomalies contribute to cooling the SST in the Central and Eastern Pacific due to westward zonal flow anomalies in the upper ocean and upwelling anomalies along the eastern coast. This condition shifted the SST cooling pattern to the southeastern tropical Pacific and Sustained the La Niña state. Fadhilah *et al*. (2024) mentioned that this Triple-Dip phenomenon influenced SST anomalies and controlled rainfall around the Pacific Area, including Indonesia. Alhadid and Nugroho (2024) reported that the Triple-Dip La Niña caused most of Indonesia's region to experience zonal wind strengthening, relative humidity, and rainfall increase. Triple-Dip and strong La Niña periods in all seasons reveal relatively similar anomaly patterns of rainfall, SST, and wind. During JJASON, Triple-Dip and Strong La Niña caused an increase in rainfall in most of Indonesia, including Sumatra, Western and Central Kalimantan, Sulawesi, parts of Maluku, Papua, Western Java, western Sumatra waters, Natuna Sea, Java Sea, Banda Sea, and Arafura Sea. Alhadid and Nugroho (2024) also reported an increase in those areas during Triple-Dip La Niña. During this season, the increase in SST occurs in most of the Indonesia region. Warmer SST enhances evaporation, which contributes to increasing the air humidity. This condition leads to the development of a convective cloud, leading to inclined rainfall. Lu *et al*. (2023) found that an area with warmer SST has abundant participation. The wind also influenced the increase in precipitation and SST. In this case, the wind blew from the east to the west in the Western Pacific Ocean, containing more moisture due to the warmer SST in that area. In this case, the decreasing wind speed in most of Indonesia caused SST increase, contributing to the development of convective clouds and increasing the rainfall in Indonesia.

Alhadid and Nugroho (2024) explained that the strengthening of eastward trade winds increased air humidity in the Indonesian region and caused rainfall to increase. During DJFMAM, Triple-Dip and strong La Niña caused a decrease in rainfall in Sumatra, Java, Kalimantan, Sulawesi, Maluku, and Papua, as reported by Alhadid and Nugroho (2024). The SST declined during this season in the Natuna Sea, Java Sea, Flores Sea, and the Indian Ocean (the western water of Sumatra to the southern water of Java). This condition occurred due to the incline of wind to 0.8-5.8 m/s across the Java, Flores, Banda, Arafura, and Timor Seas.

On the other hand, weak La Niña shows an increase in rainfall in Southern Sumatra, Western Kalimantan, Sulawesi, Maluku, Western Papua, and Papua. This event also caused an inclination of SST in most of Eastern Indonesia, including Sulawesi, Maluku, Arafura, Timor Seas, and the Western Pacific Ocean during JJA. This season also shows negative anomalies up to 0.3°C in Southern Java, which indicates a decline in the SST. This condition occurred due to the monsoon wind. The wind blew from the southeast to the northwest at 8.3-10.0 m/s and parallel to the coastline. Nurlatifah *et al*. (2021) found that high-speed monsoonal wind in Southern Java during JJA develops Eddy currents, leads to the occurrence of upwelling, and contributes to cooling the SST. This condition occurred during DJF in Natuna, Java, Southern Java, and Flores Seas, including the Banda and Arafura Seas during MAM. Puryajati *et al*. (2021) found that SST in the Natuna Sea declined during this season due to the peak speed of the monsoonal wind. Yulihasti *et al*. (2021) also found that the South China Sea during DFJ experienced a decline in SST due to the monsoon wind containing cool air from Asia. Wangdiarta *et al*. (2024) found that SST in Masalembo declined because of cold water input induced by the west monsoon during La Niña.

The increase in rainfall and SST during the La Niña events occurs more significantly during JJASON than DJFMAM. This condition occurred due to the SST increase in almost all regions of Indonesia during JJASON. This condition leads to inclined evaporation, which contributes to enhanced air humidity. On the other hand, warmer air led to an updraft, which increased rainfall in most of Indonesia. The cooler SST in the Pacific Ocean during the La Niña events reduces the air temperature and increases the air density. This condition develops updraft in Indonesia and downdraft in the Pacific Ocean. The occurrence of this mechanism indicates the strengthening of the Walker cycle, as explained by Zaini *et al*. (2024). This study also reveals that Triple-Dip and strong La Niña show relatively identical rainfall, SST, and wind spatial anomaly patterns, even with different intensities. The weak La Niña events show a more scattered rainfall anomaly spatial pattern. During the Triple-Dip and strong La Niña, a strengthening of wind anomaly in the Western Pacific contributed to the inclined air humidity and strengthening of Walker Circulation in Indonesia, as reported by several previous studies (Alhadid and Nugroho, 2024; Hidyat *et al*., 2018; Mulsandi *et al*., 2024; Nur'Utami and Hayasaka, 2022).

5. CONCLUSIONS

Using satellite-based rainfall, SST and surface wind data, we compare the condition of Triple-Dip and strong La Niña in different seasons within the Indonesian region. Triple-Dip and strong La Niña reveal similar spatial anomaly patterns of rainfall, and SST. Triple-Dip and Strong La Niña during JJASON caused an increase in rainfall in most of Indonesia, including Sumatra, Western and Central Kalimantan, Sulawesi, parts of Maluku, Papua, Western Java, western Sumatra waters, Natuna Sea, Java Sea, Banda Sea, and Arafura Sea. The increase in SST during this season occurred in most of the Indonesian region. During DJFMAM, Triple-Dip and strong La Niña caused a decrease in rainfall in Sumatra, Java, Kalimantan, Sulawesi, Maluku, and Papua. This season also shows a declined SST in the Natuna Sea, Java Sea, Flores Sea, and the Indian Ocean (the western water of Sumatra to the southern water of Java). Weak La Niña shows a scattered spatial pattern of rainfall anomaly. However, the spatial distribution of SST anomaly was relatively similar to Triple-Dip and Strong Events, except during JJA. During JJA, Weak events indicate a declined SST in the Southern Java Sea. The increased rainfall during La Niña events was more pronounced during JJASON due to the inclined SST in most of Indonesia's region.

A C K N O W L E D G E M E N T

This research is funded by Universitas Diponegoro under Professor Research Scheme with contract number: 222-282/UN7.D2/PP/IV/2025.

REFERENCES

Aldrian, E., & Susanto, R.D. (2003). Identification of three dominant rainfall regions within Indonesia and their relationship to sea surface temperature. *International Journal of Climatology*. 23 (12), 1435-1452. doi: 10.1002/joc.950.

Alhadid, B., & Budi Nugroho, A. (2024) The Study of Triple-Dip La Niña Phenomenon (2020-2023) and Its Impact on Atmospheric Dynamics and Rainfall in The Indonesian Region. In: Beck, M.C., Khamilji, A., Abdullah, A.M., Istiningsih (eds.) *ICRSE 2024: the Proceeding International Conference on Religion, Science and Education, 15 November 2023*. Yogyakarta, Universitas Islam Negri Sunan Kalijaga. pp. 707-716. Available from: https://sunankalijaga.org/prosiding/index.php/icrse/article/view/1135

Alifdini, I., Shimada, T, A. & Wirasatriya, A. (2021) Seasonal Distribution and Variability of Surface Winds in the Indonesian Seas using Scatterometer and Reanalysis Data. *International Journal of Climatology,* 1-19. https://doi.org/10.1002/joc.7101

Ariska, M., Suhadi, Supari, Irfan, M., & Iskandar, I. (2024). Spatio-Temporal Variations of Indonesian Rainfall and Their Links to Indo-Pacific Modes. *Atmosphere*. 15 (9), 1036. Available from: Available from: doi: 10.3390/atmos15091036

Asyam, A.M.D., Rochaddi, B., & Widiaratih, R. (2024). The Relationship between ENSO and IOD on Sea Surface Temperature and Rainfall in South Central Java. *Indonesian Journal of Oceanography*. 06 (02), 165-172. Available from: Available from: doi: 10.14710/ijoce.v6i2.17274 (in Bahasa)

Chang, C-P., Wang, Z., McBride, J., & Liu, C-H. (2005). Annual Cycle of Southeast Asia—Maritime Continent Rainfall and the Asymmetric Monsoon Transition. *Journal of Climate* 18: 287-301. https://doi.org/10.1175/JCLI-3257.1.

Chang, C.P., Wang, Z., & Hendon, H. (2006) The Asian winter monsoon. *The Asian Monsoon*. Springer Praxis Books. Springer, Berlin, Heidelberg, pp 89-127.

Cuervo, J.V., Castro, S. L., Steele, M., Gentemann, C., Gomez-Valdes, J., & Tang, W. (2022). Comparison of GHRSST SST Analysis in the Arctic Ocean and Alaskan Coastal Waters Using Saildrones. *Remote Sensing*, 14 (3), 692. Available from: doi: 10.3390/rs14030692

Dewi, Y.W., Wirasatriya, A., Sugianto, D.N., Helmi, M., Marwoto, J., & Maslukah L. (2020). Effect of ENSO and IOD on the Variability of Sea Surface Temperature (SST) in Java Sea. In: IOP Conference Series: Earth and Environmental Science *The 5th International Conference on Tropical and Coastal Region Eco Development, 17-18 September 2019, Semarang, Indonesia*. Semarang, IOP Publishing. p. 012007. Available from: doi: 10.1088/1755-1315/530/1/012007

Fadhilah, R., Faid, G.M., Ekananda, G.A., Lestari, L., Faizal, I., Martasuganda, M.K., & Purba, N.P. (2024). Near-Surface Oceanic Condition During a Triple Dip La Nina in the Pacific Ocean. In: Springer Proceedings in Physics *Proceedings of the International Conference on Radioscience, Equatorial Atmospheric Science and Environment and Humanosphere Science, INCREASE 2023, 21-22 November 2023, Indonesia*. Bandung, Springer Nature Singapore Pte Ltd. pp. 123-136. Available from: doi: 10.1007/978-981-97-0740-9_12

Ferijal, T., & Fauzi, A. (2024). Analysis of Local Climate Change Impacts on the Rainfall Patterns and Dry Spells in Banda Aceh and Aceh Besar, Indonesia. *International Journal of Design and Nature and Ecodynamics*. 19(3): 947–954. Available from: doi: 10.18280/ijdne.190324

Firmansyah, A. J., Nurjani, E., & Sekaranom, A. B. (2022). Effects of the El Niño-Southern Oscillation (ENSO) on rainfall anomalies in Central Java, Indonesia. *Arabian Journal of Geosciences*. 15 (24), 1746. Available from: doi: 10.1007/s12517-022-11016-2

Griffiths, M.L., Drysdale, R.N., Gagan, M.K., Zhao, J-X., Ayliffe, L.K., Hellstrom, J.C., Hantoro, W.S., Frisia, S., Feng, Y-X., Cartwright, I., Pierre, E.S., Fischer, M.J., & Suwargadi, B.W. 2009. Increasing Australian–Indonesian monsoon rainfall linked to early Holocene sea-level rise. *Nature Geoscience* 2: 636–639. https://doi.org/10.1038/ngeo605.

Haile, B. T., Zeleke, T. T., Beketie, K. T., Ayal, D. Y., & Feyisa, G. L. (2021). Analysis of El Niño Southern Oscillation and its impact on rainfall distribution and productivity of selected cereal crops in Kembata Alaba Tembaro zone. *Climate Services*. 23, 100254. Available from: doi: 10.1016/j.cliser.2021.100254

Hendon, H.H. (2003). Indonesian Rainfall Variability: Impacts of ENSO and Local Air–Sea Interaction. *Journal of Climate*. 16 (11), 1775-1790. Available from: doi: 10.1175/1520-0442(2003)016<1775: IRVIOE>2.0.CO;2

Hidayat, R., Juniarti, M. D., & Ma'Rufah, U. (2018). Impact of La Niña and La Niña Modoki on Indonesia rainfall variability. In: IOP Conference Series: Earth and Environmental Science *The 4th International Symposium on LAPAN-IPB Satellite for Food Security and Environmental Monitoring 9–11 October 2017, Bogor, Indonesia*. Bogor, IOP Publishing. p. 012046. Available from: doi: 10.1088/1755-1315/149/1/012046

Kurniadi, A., Weller, E., Min, S.K., & Seong, M.G. (2021). Independent ENSO and IOD Impacts on Rainfall Extremes Over Indonesia. *International Journal of Climatology*. 41, 3640-3656. Available from: doi: 10.1002/joc.7040

Lu, M.M., Tsai, W.Y.H., Huang, S.F., Cho, Y.M., Sui, C.H., Solis, A.L.S., & Chen, M.S. The Philippine Springtime (February–April) Sub-Seasonal Rainfall Extremes and Extended-Range Forecast Skill Assessment Using the S2S Database. *Weather and Climate Extremes*, 41, 100582. Available from: doi: 10.1016/j.wace.2023.100582

Mears, C., Lee, T., Ricciardulli, L., Wang, X., & Wentz, F. (2022). Improving the Accuracy of the Cross-Calibrated Multi-Platform (CCMP) Ocean Vector Winds. Remote Sensing. 14 (17), 4230. Available from: doi: 10.3390/rs14174230

Millenia, Y.W., Helmi, M., & Maslukah, L. (2022). Analysis of the Mechanism of the Influence of IOD, ENSO and Monsoon on Sea Surface Temperature and Rainfall in the Waters of the Mentawai Islands, West Sumatra. *Indonesian Journal of Oceanography*. 4 (4), 87-98. Available from: doi: 10.14710/ijoce.v4i4.14414 (in Bahasa)

Mulsandi, A., Koesmaryono, Y., Hidayat, R., Faqih, A., & Sopaheluwakan, A. (2023). On the Interannual Variability of Indonesian Monsoon Rainfall (IMR): a Literature Review of The Role of its External Forcing. Jurnal Meteorologi dan Geofisika. 24 (2), 115-127. Available from: https://www.researchgate.net/publication/379068533_On_The_Interannual_Variability_of_Indonesian_Monsoon_Rainfall_IMR_A_Literature_Review_of_The_Role_of_its_External_Forcing

Nurafifah, U. O., Zainuri, M., & Wirasatriya, A. (2022). The Effect of ENSO and IOD on the Distribution of Sea Surface Temperature and Chlorophyll-a During the Upwelling Period in the Banda Sea. *Indonesia Journal of Oceanography*. 04 (24), 74 - 85. Available from: doi: 10.14710/ijoce.v4i3.14971 (in Bahasa)

Nurlatifah, A., Martono, Susanti, I., & Suhermat, M. Variability and trend of sea level in southern waters of Java, Indonesia. *Journal of Southern Hemisphere Earth System and Science*. 71 (3), 272-283. Available from: doi: 10.1071/ES21004

Nur'utami, M.N., & Hayasaka, T. (2022). Interannual Variability of the Indonesian Rainfall and Air-Sea Interaction over the Indo–Pacific Associated with Interdecadal Pacific Oscillation Phases in the Dry Season. *Journal of the Meteorological Society of Japan*. 100 (1), 77-97, Available from: doi: 10.2151/jmsj.2022-004

Prasetyo, Y., & Nabilah, F. (2017). Pattern Analysis of El Nino and La Niña Phenomenon Based on Sea Surface Temperature (SST) and Rainfall Intensity using Oceanic Nino Index (ONI) in West Java Area. IOP Conference Series: Earth and Environmental Science *The 5th Geoinformation Science Symposium 2017 (GSS 2017), 27–28 September 2017, Yogyakarta, Indonesia*. Yogyakarta, IOP Publishing. p. 01204, Available from: doi: 10.1088/1755-1315/98/1/012041

Puryajati, A. D., Wirasatriya, A., Maslukah, L., Sugianto, D. N., Ramdani, F., Jalil, A. R., & Andrawina, Y. O. (2021). The Effect of ENSO and IOD on the Variability of Sea Surface Temperature and Rainfall in the Natuna Sea. IOP Conference Series: Earth and Environmental Science *6th International Conference on Tropical Coastal Region Eco-Development 2020, 27-28 October 2020, Indonesia*. Semarang, IOP Publishing. p. 012020. Available from: doi: 10.1088/1755-1315/750/1/012020

Rachman, H.A., Setiawan, M.D., Hidayah, Z., Syah, A.F., Nandika, M.R., Gaol, J.L, Asy-Syakur, A.R., & Syamsudin, F. (2024). Dynamic of upwelling variability in southern Indonesia region revealed from satellite data: Role of ENSO and IOD. *Journal of Sea Research*. 202, 102543. Available from: doi: 10.1016/j.seares.2024.102543

Ramadhan, R., Marzuki, M., Suryanto, W., Sholihun, S., Yusnaini, H., Muharsyah, R., & Hanif, M. (2022). Trends in rainfall and hydrometeorological disasters in new capital city of Indonesia from long-term satellite-based precipitation products. *Remote Sensing Applications: Society and Environment*. 28, 100827. Available from: doi: 10.1016/j.rsase.2022.100827

Rodysill, J. R., Russell, J. M., Vuille, M., Dee, S., Lunghino, B., & Bijaksana, S. (2019). La Niña-driven flooding in the Indo-Pacific warm pool during the past millennium. *Quaternary Science Reviews*. 225, 106020. Available from: doi: 10.1016/j.quascirev.2019.106020

Rohmat, F. I. W., Harjupa, W., Rohmat, D., & Rohmat, F. I. W. (2023). The impacts of global atmospheric circulations on the water supply in select watersheds in the Indonesian Maritime Continent using SPI. *Heliyon*. 9 (5), e15604. Available from: doi: 10.1016/j.heliyon.2023.e15604

Shi, L., Ding, R., Hu, S., Li, X., & Li, J. (2023). Extratropical impacts on the 2020–2023 Triple-Dip La Niña event. *Atmospheric Research*. 294, 107412. Available from: doi: 10.1016/j.atmosres.2023.106937

Simanjuntak, P., & Klimatologi Bangka Belitung, S. (2022). Zonal and Meridional Wind Components as Precursors Determining the Start of the Season and the Influence of ENSO on Their Variations. *Prisma Fisika*. 10 (3), 371-376. Available from: doi: 10.26418/pf.v10i3.59057 (in Bahasa)

Siswanto, S., Wardani, K.K., Purbantoro, B., Rustanto, A., Zulkarnain, F., Anggraheni, E., Dewanti, R., Nurlambang, T., & Dimyati, M. (2022). Satellite-based meteorological drought indicator to support food security in Java Island. *PLoS ONE*. 17 (6), e0260982. Available from: doi: 10.1371/journal.pone.0260982

Wangdiarta, F.P., Wirasatriya, A., & Harsono, G. (2024). Sea Surface Temperature (SST) Response to ENSO in Masalembo Waters for the Period 2010-2019. *Indonesian Journal of Oceanography*, 06 (01), 57-71. Available from: doi: 10.14710/ijoce.v6i1.17944 (in Bahasa)

Wirasatriya, A., Setiawan, R. Y., & Subardjo, P. (2017). The Effect of ENSO on the Variability of Chlorophyll-a and Sea Surface Temperature in the Maluku Sea. *IEEE Journal of Selected Topics in Applied Earth Observations and Remote Sensing*. 10 (12), 5513-5518. Available from: doi: 10.1109/JSTARS.2017.2745207

Wirasatriya, A., Setiawan, J.D., & Sugianto, D.N. (2020). Ekman Dynamics Variability along the Southern Coast of Java Revealed by Satellite Data. *International Journal of Remote Sensing*. 41 (21), 8475-8496. Available from: doi:https://doi.org/10.1080/01431161.2020.1797215

Yulihasti, E., Hadi, T.W., & Syahputra M.R. 2021. Mode of Wind and Sea Surface Temperature Over the South China Sea During Rainy Season in Indonesia. In: IOP Conference Series: Earth and Environmental Science *International Conference on the Ocean and Earth Science, 18-20 November 2020, Southern Jakarta, Indonesia*. Southern Jakarta, IOP Publishing. p. 012003. Available from: doi: 10.1088/1755-1315/789/1/012003

Yustiana, M., Zainuri, M., Sugianto, D. N., Batubara, M. P. N., & Hidayat, A. M. (2023). The Impact of Inter-Annual Climate Variability (El Niño, La Niña) on Rainfall and Sea Level Anomalies on the North Coast of Central Java. *Buletin Oseanografi Marina*. 12 (1), 109-124. Available from: doi: 10.14710/buloma.v12i1.48377 (in Bahasa)

Zaini, A. Z. A., Vonnisa, M., & Marzuki, M. (2024). Impact of different ENSO positions and Indian Ocean Dipole events on Indonesian rainfall. *Vietnam Journal of Earth Sciences*. 46 (1), 100-119. Available from: doi: 10.15625/2615-9783/19926

Zandika, R., Ismunarti, D.H., Kunarso, Hatmaja, R.B., Al Ayubi, M.A. (2024). Thermal Front Variability and its Relationship with Chlorophyll-a in the Fisheries Management Area of the Republic of Indonesia 711. *Buletin Oseanografi Marina*. 13 (2): 250-260. Available from: doi: 10.14710/buloma.v13i2.60304. (in Bahasa)

Zhang, S., Fan, H., Hu, X., & Lin, S. (2024). Unprecedented cross-equatorial southerly wind anomalies during the 2020–2023 Triple-Dip La Niña: Impacts and mechanisms. *Atmospheric Research*. 304, 107412. Available from: doi: 10.1016/j.atmosres.2024.107412

GIS-BASED ANALYSIS OF SLOPE, LANDSLIDE AND FLOOD HAZARDS, AND LAND USE INTEGRATED WITH INDIGENOUS KNOWLEDGE IN *NAGARI* SIJUNJUNG, INDONESIA

HARYANI [1*], ***Eri BARLIAN*** [2], ***I Nengah TELA*** [1], ***Ezra ADITIA*** [1], ***Aprizon PUTRA*** [3]

DOI: 10.21163/GT_2025.202.21

ABSTRACT

This study aims to examine how the traditional settlement of *Nagari* Sijunjung, guided by the Minangkabau philosophy of *Alam Takambang Jadi Guru*, aligns with the area's physical characteristics and functions as an inherent disaster risk reduction system. Specifically, it analyzes the relationship between slope conditions, land use, and hazard potential by integrating indigenous spatial planning with Geographic Information System (GIS)–based risk analysis. The study was conducted in *Nagari* Sijunjung, a 157.1 ha cultural heritage site in West Sumatra, Indonesia, containing 77 traditional *Rumah Gadang*, sacred sites, and diverse clan settlements. Spatial datasets from satellite imagery, Digital Elevation Model (DEM), and official maps were overlaid with indigenous zoning to assess congruence between cultural principles and hazard avoidance strategies. Results show that flat and gentle slopes (0–8%) serve as the core zones for settlements and agriculture, while steeper slopes (8–15%) are preserved as protected forest or rubber plantations, functioning as ecological buffers against landslides. Flood-prone River plains are allocated for seasonal agriculture, while settlements are located on slightly elevated terrain. In conclusion, indigenous zoning closely aligns with physical hazard assessments based on slope, soil, geology, rainfall, and land use analysis, demonstrating that traditional planning offers a culturally grounded and hazard-aware model for community-based disaster risk reduction.

Key-words: *Disaster risk reduction; GIS; Indigenous knowledge; Land use planning; Nagari Sijunjung.*

1. INTRODUCTION

Indonesia ranks among the nations most vulnerable to a wide range of natural hazards, including earthquakes, volcanic eruptions, floods, and landslides. Data from the Indonesian National Board for Disaster Management (BNPB) 2022 indicate a consistent rise in disaster frequency, particularly in areas where land-use changes are misaligned with the physical and ecological characteristics of the landscape (Kegel et al., 2025). While modern, technology-driven mitigation strategies have been widely promoted, they often demand substantial financial, technical, and institutional resources, making them less applicable in communities with limited capacity. In contrast, numerous Indigenous communities across Indonesia have long relied on sophisticated systems of local knowledge as adaptive strategies to manage environmental risks (Asrawijaya, 2024; Karnoto et al., 2025). One prominent example is the customary spatial planning system, which not only regulates the arrangement of settlements, agricultural areas, and conservation zones but also inherently reduces disaster risks through nature-based and culturally embedded mechanisms (Lestari et al., 2025). These systems have evolved over generations, shaped by accumulated experience, continuous observation of environmental cues, and philosophical principles passed down orally or through customary law (Wiersum, 2004; Hiwasaki et al., 2014).

---

[1]*Department of Urban and Regional Planning, Universitas Bung Hatta, Padang Indonesia. (Hy)* irharyanimtp@bunghatta.ac.id*; (INT)* nengahtela@bunghatta.ac.id*; (EA)* adi@bunghatta.ac.id
[2]*Department of Coaching, Universitas Negeri Padang, Padang, Indonesia. (EB)* e.barlian@fik.unp.ac.id
[3]*National Research and Innovation Agency (BRIN), Cibinong - Bogor, Indonesia. (AP)* apri024@brin.go.id
[*]*Corresponding author email:* irharyanimtp@bunghatta.ac.id

Administratively, the study focuses on the traditional settlement of *Nagari* (Indonesian: *Nagari*, abbreviated Village) Sijunjung, located in Sijunjung Regency, West Sumatra Province, and traversed by the Batang Kuantan River. The Regency consists of 11 *Nagari*, including Sijunjung, Muaro, Paru, Pematang Panjang, Silokek, and Aie Amo. Topographically, most of the area comprises gentle slopes (2–8%), which are optimal for settlement and agriculture, while steeper slopes (8–15%) are designated as protected forest. This topographical information was obtained from the slope classification generated through the Digital Elevation Model (DEM)/Shuttle Radar Topography Mission (SRTM) analysis conducted in this study.

The traditional settlement of *Nagari* Sijunjung embodies the Minangkabau socio-ecological philosophy of *Alam Takambang Jadi Guru*, literally "Nature Unfolds to Be a Teacher" which guides the community in selecting settlement areas, determining farmland allocation, and designating conservation areas (Heider, 2011; Nasri et al., 2022; Lah et al., 2024). Empirical observations have shown that these settlements are often located on ridge lines or elevated terrain to avoid flooding, with building orientations adapted to prevailing winds and water flow. Traditional *Rumah Gadang* (Indonesian: *Rumah Gadang* abbreviated Big House) houses are built on stilts, providing structural resilience against both inundation and seismic activity.

However, rapid modernization, expanding infrastructure projects, and insufficient legal recognition of customary land rights have gradually altered these spatial configurations. Such shifts risk undermining the embedded disaster-mitigation functions of the traditional system (Sutanta et al., 2013). Consequently, this study integrates spatial slope analysis, indigenous settlement typology, and the Community-Based Disaster Risk Reduction (CB-DRR) framework to examine how the *Nagari* Sijunjung spatial system remains functional, adaptive, and relevant within the context of contemporary, risk-based spatial planning.

This study aims to examine how the traditional settlement of *Nagari* Sijunjung, guided by the Minangkabau philosophy of *Alam Takambang Jadi Guru*, aligns with the area's physical characteristics and functions as an inherent disaster risk reduction system. Specifically, it seeks to analyze the relationship between slope conditions, land use, and hazard potential, integrating indigenous spatial planning principles with modern risk-based spatial analysis using the Geographic Information System (GIS). This study offers a novel integration of GIS–based spatial hazard assessment with indigenous knowledge systems in the context of the traditional settlement of *Nagari* Sijunjung. By directly comparing scientifically mapped hazard zones with customary zoning patterns, the study demonstrates that traditional spatial arrangements can serve as an effective, culturally grounded model for contemporary disaster risk-sensitive land use planning.

2. STUDY AREA

The study was conducted in the traditional settlement of *Nagari* Sijunjung, a designated cultural heritage area that represents a well-preserved example of the traditional Minangkabau spatial arrangement. According to the West Sumatra Cultural Heritage Preservation Office (BPCB), the site covers approximately 157.1 ha and is home to nine major clans, namely Chaniago, Piliang, Malayu, Tobo, Bodi, Panai, Patopang, Bendang, and Malayu Tak Timbago. Within the area, 77 traditional *Rumah Gadang* remain in active use as centers of social, cultural, and customary activities, along with important heritage sites such as *Batu Tabonek* and *Tempat Berkaul Adat*, both of which hold significant spiritual value for the community. The heritage designation follows Law No. 11/2010 on Cultural Heritage, which mandates protection through rescue, security, zoning, maintenance, and restoration.

Nagari Sijunjung is situated in Sijunjung Sub-district, Sijunjung Regency, West Sumatra Province, Indonesia, at coordinates 100°55′30″–101°00′30″ E and 0°42′30″–0°38′30″ S, with elevations ranging from 120 to 930 meters above sea level (MASL). Its strategic location along a network of collector and local roads ensures high accessibility to the Sub-district center and neighboring *Nagari* such as Koto VII, Kamang Baru, and Tanjung Gadang. The Batang Kuantan River flows through the area, serving both as a natural boundary and the primary water source for the community (Prambudi et al., 2023).

Beyond its ecological and economic functions, the river also holds deep cosmological significance in local cultural narratives, influencing settlement placement and land-use decisions. The combination of cultural heritage value, adaptive topography, and abundant natural resources makes *Nagari* Sijunjung an exemplary case for examining how indigenous knowledge systems can be integrated with spatial analysis in the context of disaster risk mitigation and risk-based spatial planning. For more details, see the map in **Figure 1** below.

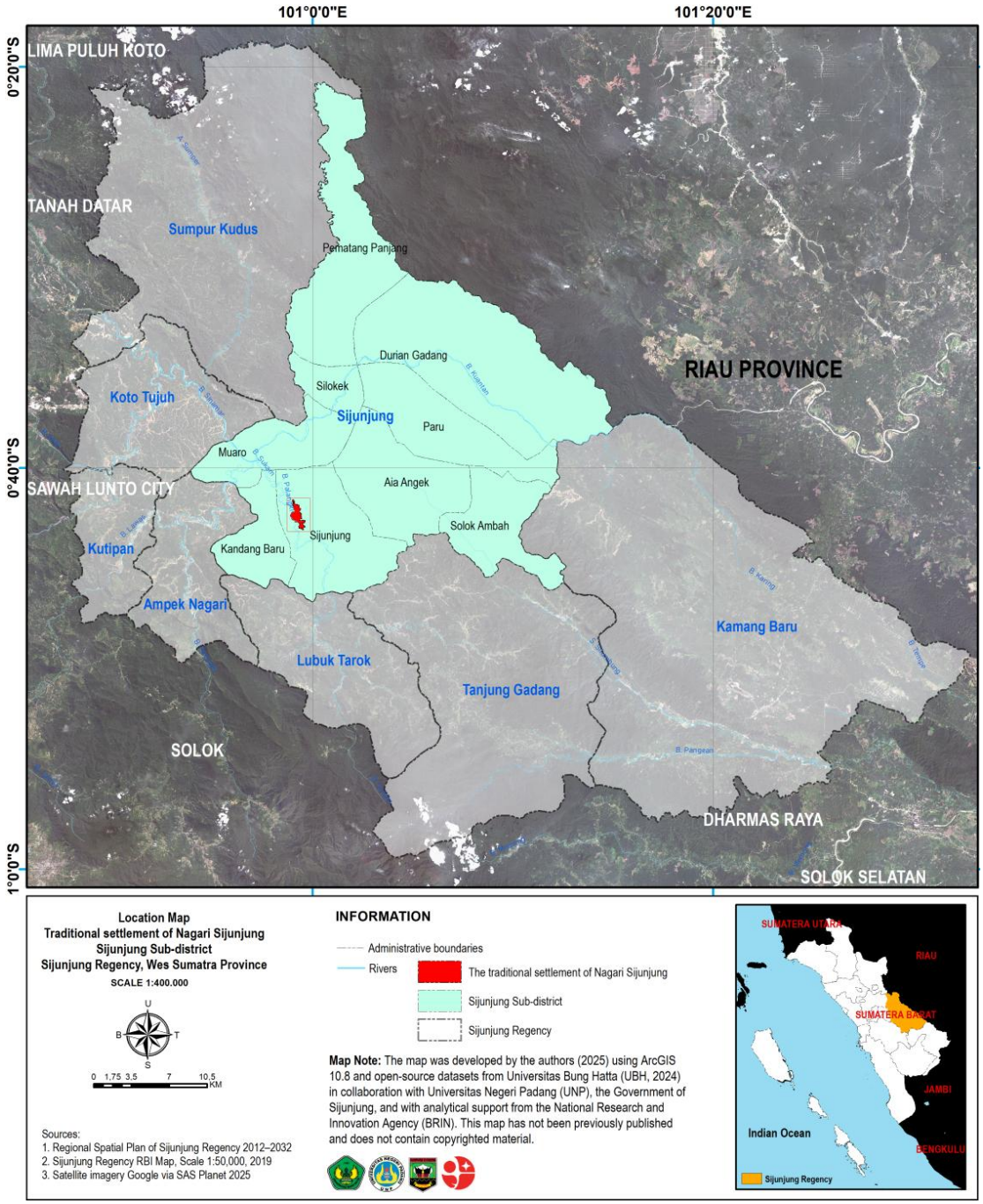

Fig. 1. Location Map of the traditional settlement of *Nagari* Sijunjung.

3. METHODS

3.1. Spatial analysis approach

To ensure analytical accuracy, multiple spatial datasets were obtained from both authoritative and field-based sources. These included 1) High-resolution recent satellite imagery from Google, downloaded via SAS Planet 2025, for land cover mapping and settlement identification; 2) DEM/SRTM data for slope analysis; 3) Land use maps from the Geospatial Information Agency (BIG), used as a baseline for detecting land-use changes and complemented with field verification; 4) Hydrography data from the *Rupa Bumi Indonesia* (RBI) maps by BIG, detailing rivers, streams, and water bodies; 5) Rainfall statistics from the Meteorology, Climatology, and Geophysics Agency (BMKG) for hazard classification; and 6) Administrative boundary maps at the *Nagari*, Sub-district, and Regency levels, sourced from the Regional Spatial Planning (RSP) Sijunjung Regency. Data processing was performed using ArcGIS software. Considering the integration of multiple raster and vector datasets, the use of a GEODATABASE structure is essential to ensure coherent data management and relational analysis (Nicoară & Haidu, 2011).

Data processing was performed using ArcGIS software. Slope classification was generated from DEM/SRTM data, while land use classification was derived from satellite imagery and refined through ground validation. The slope analysis applied a 30 m resolution DEM/SRTM dataset. Overlay analysis was then conducted to assess the spatial relationship between land use and hazard-prone zones, and buffer analysis was applied to delineate protective zones around critical natural features such as rivers, steep slopes, and natural evacuation corridors. Ground checks were carried out at 25 GPS points across settlement, agriculture, forest, and river zones to confirm land use classification. The classification accuracy reached 87%, with a Kappa coefficient of 0.82 (Chahkar et al., 2020), indicating strong agreement between the satellite-derived map and field conditions. Slope data derived from DEM/SRTM were compared with three ground-control transects, showing less than 5% deviation in slope class assignment. These validations ensure that the overlay and buffer analyses are methodologically robust.

For landslide assessment, areas dominated by alluvial and latosol soils with loose texture showed higher susceptibility when combined with steep slopes and high rainfall, while zones underlain by volcanic and igneous formations demonstrated greater stability. For flood assessment, alluvial soils in river plains retained high water content and prolonged inundation, whereas andosol and lithosol soils in elevated zones allowed higher infiltration and reduced ponding. These factors strongly influenced the final hazard maps, explaining why some zones with similar slopes exhibited different hazard levels. Landslide hazard assessment followed the parameter and weighting framework proposed by Paimin et al. (2009). The resulting hazard classifications were then compared with traditional Minangkabau zoning principles to determine the extent to which indigenous. The resulting hazard classifications were then compared with traditional Minangkabau zoning to determine the extent to which indigenous spatial arrangements align with scientific hazard assessments as outlined in **Tables 1 and 2** below.

Table 1

Landslide hazard assessment parameters.

Parameter	Class/Category	Value	Weight
Soil type	Alluvial, Latosol, Grumosol (1); Mediterranean, Podsolic, Glei Humus (2); Regosol, Andosol (3)	1–3	1
Land use	Lake/Pond, River, Fishpond, Brackish Pond (0); Shrubland (2); Rice Field, Dry Field, Plantation, Mixed Garden (4); Settlement, Mining, Open Field (5); Swimming Pool (3)	0–5	2
Rainfall (mm)	2001–2500 (3); 2501–3000 (4); ≥3001 (5)	3–5	3
Slope (%)	0–2% (1); 2–8% (2); 8–15% (3)	1–3	4
Geology	Sedimentary, easily weathered (3); Volcanic, medium strength (2); Igneous/metamorphic, strong (1)	1–3	3

Source: Paimin et al. (2009).

Table 2

Landslide hazard classifications.

Hazard Level	Score Range	Description
Low	1.5–2.3	Requires monitoring during the rainy season
Moderate	>2.3–3.1	Potential hazard during high rainfall or slope disturbance
High	>3.1–3.7	Very prone; requires mitigation and special handling

Source: Paimin et al. (2009).

Following the classification of landslide hazard levels presented in **Table 2** above, the analysis was extended to assess flood hazard potential. This assessment applied a set of parameters that capture the influence of land use, rainfall intensity, elevation, slope, and soil type on flood risk. The criteria and scoring system, adapted from Şen (2018); Nguyen (2019) in **Tables 3 and 4** below.

Table 3

Flood hazard assessment parameters.

Parameter	Class/Category	Value	Weight
Land use	Lake/Pond, River, Mining, Open Land, Settlement, Swamp (5); Swimming Pool, Irrigated/Rain-fed Rice Field, Shrubland (4); Forest Plantation, Primary/Secondary Dryland Forest (3); Mixed Garden, Rubber/Oil Palm (2); Sandbar (1)	1–5	5
Rainfall (mm)	>3500 (5); 3001–3500 (4); 2501–3000 (3); 2001–2500 (2); <2000 (1)	1–5	4
Elevation (m)	0–25 (5); 26–50 (4); 51–100 (3); 101–250 (2); >250 (1)	1–5	3
Slope (%)	0–2% (1); 2–8% (2); 8–15% (3)	1–3	4
Soil type	Alluvial, Latosol, Grumosol (5); Regosol, Andosol (3); Mediterranean, Podsolic, Glei Humus (2); Lithosol (1)	1–5	4

Sources: Şen (2018); Nguyen (2019).

Table 4

Flood hazard classifications.

Hazard Level	Score Range	Description
Very Low	2.4–3.0	Not significant
Low	>3.0–3.6	Light inundation potential
Moderate	>3.6–4.2	Moderate risk during heavy rain
High	>4.2–4.8	Very prone; requires mitigation

Sources: Şen (2018); Nguyen (2019).

3.2. Indigenous knowledge–spatial integration approach

This approach aimed to document, interpret, and integrate local wisdom that guides settlement planning and disaster mitigation in the Minangkabau tradition, with spatial analysis results. The emphasis is on how the philosophy of *Alam Takambang Jadi Guru* is embedded in settlement spatial arrangements and how these customary principles align with scientific hazard mitigation strategies. More details can be seen in **Table 5** below.

By triangulating indigenous narratives, field observations, and mapping, this method not only validates the cultural logic of settlement patterns but also demonstrates their functional role in mitigating risks such as floods and landslides. The outputs, ranging from GIS-based models, offer a framework for integrating cultural heritage into sustainable CB-DRR planning.

Table 5

Description of the indigenous knowledge–spatial integration approach.

Stages	Activities	Purposes
Data collection – indigenous knowledge	Conduct in-depth interviews with *Ninik Mamak* (Indonesian: abbreviated Customary Leaders), *Nan Tuo di Kampuang* (Indonesian: abbreviated Village Elders), Rumah Gadang, and community members to capture traditional norms, decision-making processes, and lived experiences.	Capture and document traditional norms, governance structures, and lived experiences related to settlement planning.
	Carry out participatory observation of building orientation, site selection for houses *Rangkiang* (Indonesian: abbreviated Rice Barns), ommunal facilities, and zoning based on customary land functions.	Document ecological adaptation patterns and local disaster risk mitigation strategies.
	Tambo (Indonesian: abbreviated Customary Manuscripts), historical, and traditional maps to identify the ecological, spiritual, and social values embedded.	Identify the cultural principles guiding spatial arrangements and resource use.
Spatial data analysis	Slope, land use, and hazard maps to assess the physical constraints and hazard exposure of the settlement area.	Understand topographical limitations and hazard.
	Overlay hazard maps with customary zoning patterns to assess spatial congruence with hazard-prone areas.	Compare zoning decisions with mapped hazards.
Integration process	Perform data triangulation between indigenous narratives, field observations, and spatial analysis outputs to validate findings.	Accuracy of insights for both local and scientific.
	Identify effective customary zones for hazard mitigation, such as avoiding settlements at the foot of steep slopes or close to large rivers.	Highlight functional aspects of indigenous knowledge in disaster risk reduction.
	Develop narrative–spatial mapping to the relationship between indigenous principles and physical conditions.	Present integrated evidence of cultural–spatial alignment.
Expected outputs	Produce a spatial model of *Nagari* Sijunjung's traditional settlement functioning as a natural disaster mitigation system	Provide a culturally grounded planning framework.
	Create an integrated model combining local wisdom and spatial data for risk-based planning.	Strengthen evidence-based policy-making.
	Formulate policy recommendations for preserving spatial arrangements within the CB-DRR strategies.	Support sustainable disaster risk reduction.

4. RESULTS

4.1. Slope analysis based on the concept of *Nagari* formation

The slope analysis was conducted to examine how topographical gradients influence the spatial organization of the traditional settlement of *Nagari* Sijunjung. This analysis directly aligns with the Spatial Data Analysis stage outlined in the Indigenous Knowledge–Spatial Integration Approach, where slope data are processed and overlaid with customary zoning maps. Data were derived from a DEM with a resolution of 30 meters. This spatial dataset was then integrated with qualitative insights obtained from in-depth interviews and participatory observation, ensuring that the functional meaning of each slope class was interpreted through the lens of the philosophy of *Alam Takambang Jadi Guru*. More details can be seen in **Table 6** below.

Table 6

Slope classification of the Traditional settlement of *Nagari* Sijunjung area.

Class (%)	Area (Ha)	General function
0–2%	0.7	Fertile lowlands, suitable for wet rice cultivation and core settlement
2–8%	117.5	Gentle: traditional settlement areas, social activities, and agriculture
8–15%	38.67	Steep: protected forest, conservation, water sources, and reserve space

Source: Data analysis, 2025.

Based on **Table 6** above, approximately 118.2 ha (0–8% slope) form the primary settlement and agricultural core of the *Nagari*. These zones host *Rumah Gadang*, *Balai Adat*, and irrigated rice fields, reflecting their suitability for stable structures and intensive farming. In contrast, steeper slopes (8–15%) covering 38.67 ha are reserved for protected forest or shifting cultivation, ensuring watershed protection and preventing erosion. According to interviews with *Ninik Mamak* and *Tuo Kampuang*, settlements are intentionally located away from steep slopes to avoid landslide risk. These practices align with the philosophy *Alam Takambang Jadi Guru*, which dictates that land use should harmonize with natural conditions and maintain the balance of upstream–midstream–downstream spaces.

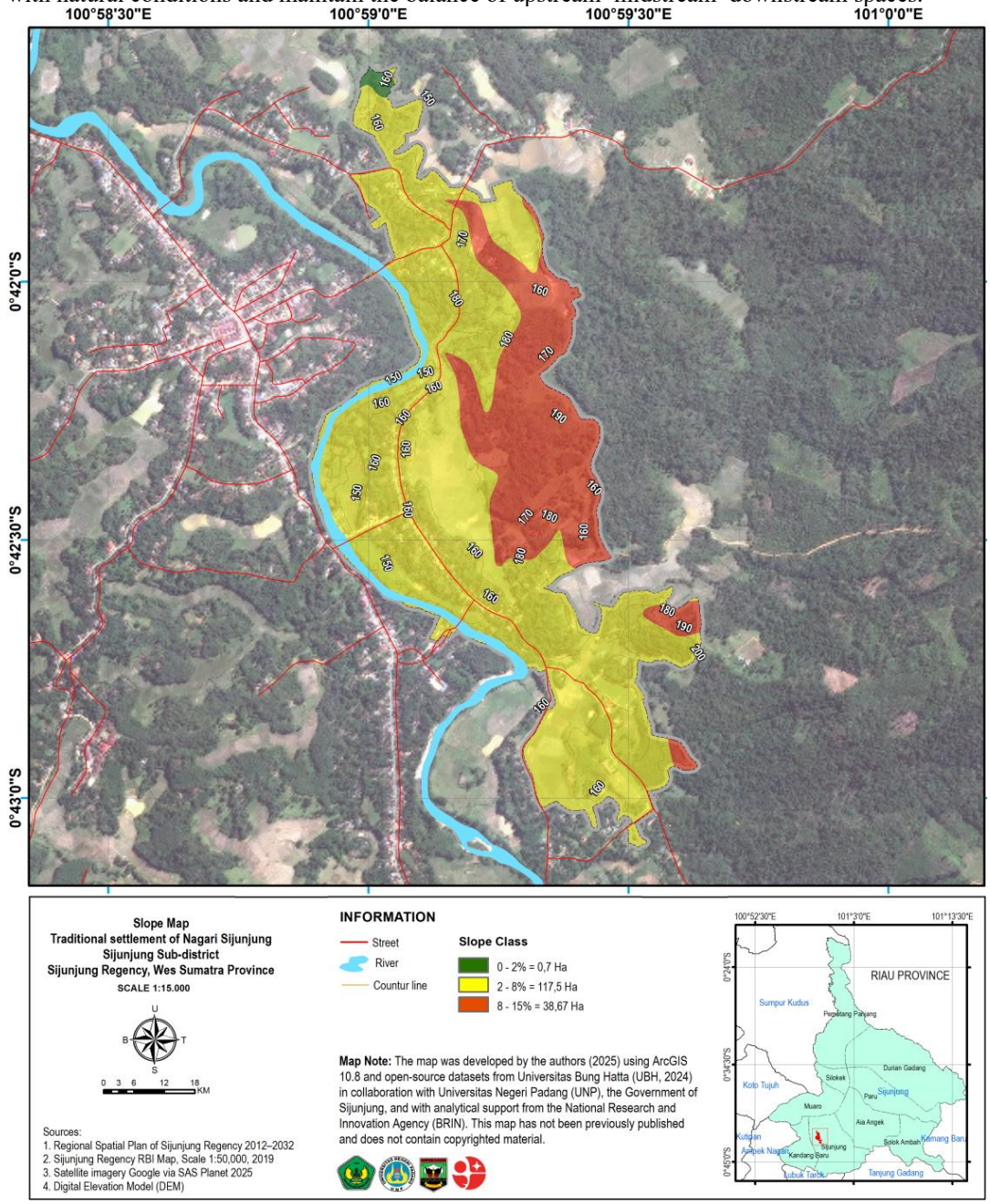

Fig. 2. Slope Map of the traditional settlement of *Nagari* Sijunjung area.

The designation of land functions also reflects a long-standing social consensus, in which customary leaders regulate land allocation to ensure intergenerational resource security and mitigate environmental degradation. For more details, see the map in **Figure 2.**

The analysis results indicate that traditional Minangkabau settlement patterns inherently incorporate disaster risk reduction strategies. The integration of scientific mapping with customary wisdom provides a replicable model for risk-sensitive land use planning in other cultural landscapes. Physically, gentle slopes of 0–8% reduce surface runoff velocity and provide more stable ground for buildings and rice fields, while steeper slopes of 8–15% increase gravitational force and erosion risk (Osman, 2018). This explains why settlements are concentrated in flat to gentle terrain, while forest vegetation is maintained on steeper slopes to prevent landslides and protect water sources.

4.2. Hazard potential analysis for landslides and floods

The hazard potential analysis for the traditional settlement of *Nagari* Sijunjung area was conducted by integrating physical terrain characteristics with indigenous spatial planning principles. The methodology followed Paimin et al. (2009) for landslide hazard assessment, and Şen (2018); Nguyen (2019) for flood hazard assessment. This approach enabled the comparison between scientific hazard mapping and traditional settlement layouts, supporting the research objective of integrating local wisdom into DRR planning.

4.2.1. Landslide hazard potential

Landslide hazard analysis was performed using a weighted method (Paimin et al., 2009). Each parameter was assigned a score based on its class/category, and the cumulative value determined the hazard level classification. More details can be seen in **Table 7** below.

Table 7

Landslide hazard potential and indigenous mitigation strategies.

Hazard levels	Spatial zone	Area (Ha)	Total area %	Indigenous mitigation strategy
High (>8% slope; unstable geology)	Eastern and southern steep slope zones	150.8	24.2%	No permanent settlement; preserved as protected forest to maintain slope stability and water sources
Moderate (2–8% slope, transitional land)	Peripheral mid-slopes near mixed gardens	6.36	4.0%	Seasonal cultivation and erosion-control vegetation planting
Low (0–2% slope, stable soils)	Core settlement and paddy fields	-	71.8%	Settlement use and wet rice agriculture supported by traditional drainage systems
Total		**157.1**	**100%**	

Source: Data analysis, 2025.

The high hazard zones are concentrated in the eastern and southern uplands with steep slopes and weaker geological formations, as identified through GIS-based slope and geology layers. Soil and geological conditions played a significant role in delineating hazard levels. Areas underlain by sedimentary rocks that are easily weathered showed higher susceptibility to mass movement, especially when combined with steep slope gradients (Permana et al., 2020; Triyatno et al., 2020). Similarly, soil types such as alluvial and latosol with relatively loose texture increased surface instability during high rainfall. Conversely, volcanic and igneous formations with stronger structural properties reduced susceptibility, explaining why certain upland zones with similar slopes exhibited different hazard levels (Rahmani et al., 2020). During high rainfall, loose-textured soils such as alluvial and latosol easily absorb water, become saturated, and lose stability, increasing the chance of slope movement (Sjamsiah et al., 2019). Sedimentary rocks that weather quickly also reduce slope strength, while volcanic or igneous rocks remain more stable.

Vegetation, especially rubber plantations, plays an important role by binding the soil with deep roots and reducing runoff, which naturally lowers the risk of landslides. Indigenous practice avoids these zones for settlement, designating them as protected forest, which acts as a natural landslide barrier. The moderate zones are used for mixed agriculture with erosion control measures, while low zones coincide with the core settlement and paddy fields. This alignment confirms that local wisdom inherently incorporates slope stability considerations into spatial planning. For more details, see the map in **Figure 3** below.

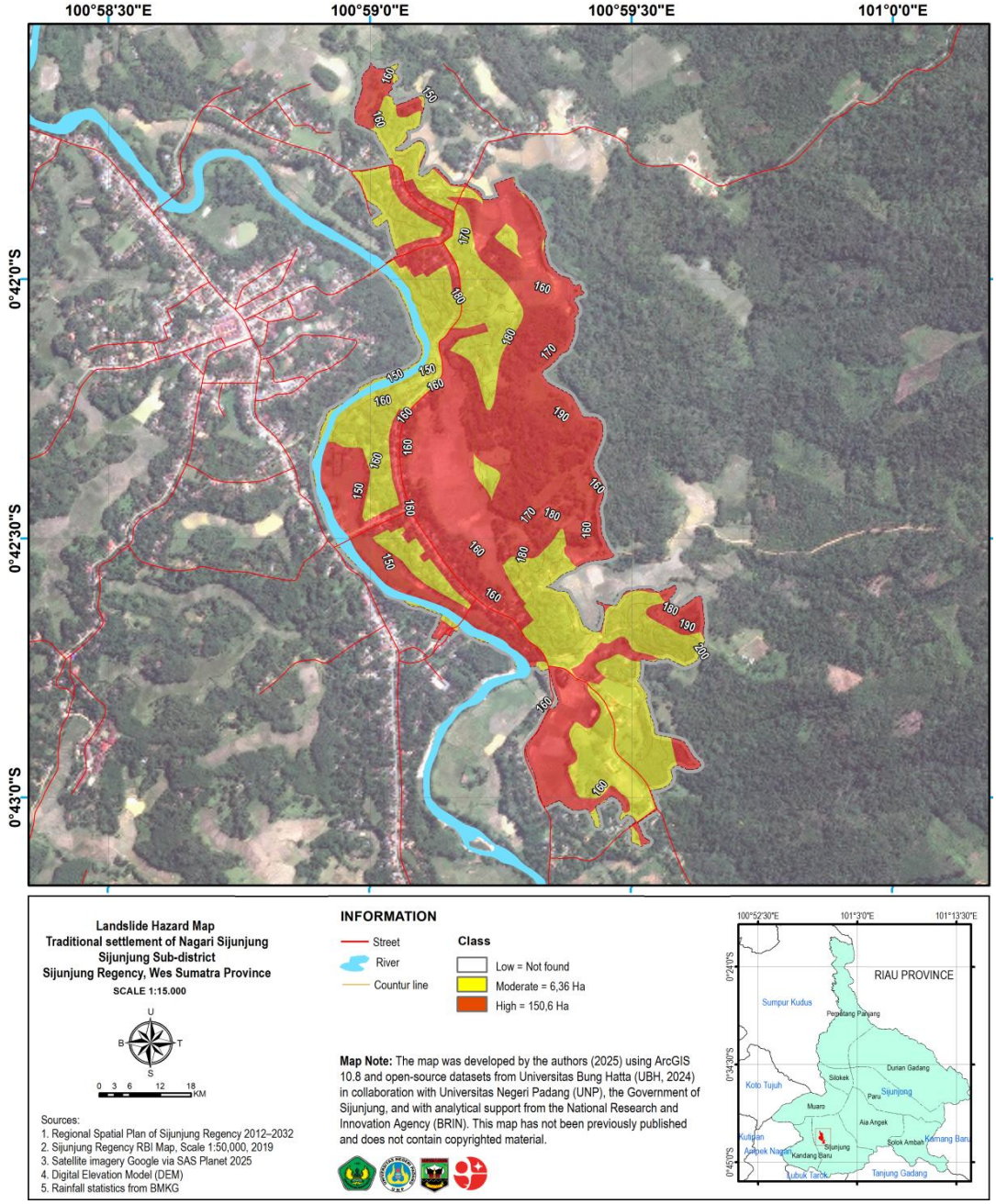

Fig. 3. Landslide hazard map of the traditional settlement of *Nagari* Sijunjung area.

4.2.2. Flood hazard potential

The flood hazard analysis followed the scoring by Şen (2018); Nguyen (2019). Each factor was weighted to generate the flood susceptibility data. More details can be seen in **Table 8** below.

Table 8

Flood hazard potential and indigenous mitigation strategies.

Hazard levels	Spatial zone	Area (Ha)	Total area %	Indigenous mitigation strategy
Very High (<250 m)	River floodplain in northern and central	117.4	74.8%	Avoid permanent housing; use for seasonal farming; preserve vegetation
High (within hydrological catchment)	Transitional areas between river and settlement	39.5	25.2%	Traditional stilt housing (*Rumah Gadang*), community-managed drainage channels
Low–Moderate (>250 m)	Elevated settlement areas	-	<0.5%	Maintain upstream water retention areas (*nan di hulu ditahan*)
Total		**157.1**	**100%**	

Source: Data analysis, 2025.

In higher elevation zones with andosol or lithosol soils, infiltration capacity was greater, reducing flood accumulation despite heavy rainfall (Hermon et al., 2019; Hermon et al., 2024). Heavy rainfall on alluvial plains with low slope (<2%) causes water to accumulate because of low permeability, leading to prolonged inundation. In contrast, areas with andosol or lithosol soils at higher elevation allow faster infiltration, so flooding is less severe (Sjamsiah et al., 2019). Land use, like rainfed rice fields function as temporary water storage during peak rainfall to reduce the spread of floods toward settlements. For more details, see the map in **Figure 4**.

Indigenous settlement patterns avoid this floodplain for permanent housing, instead allocating it for rice cultivation and grazing during the dry season. The high-hazard zones are occupied by traditional elevated housing that reduces flood impact. This approach demonstrates a preventive spatial arrangement embedded in cultural norms. Overlaying the landslide and flood hazard maps reveals that 1) High landslide hazard zones are primarily located in elevated forested areas, while very high flood hazard zones are confined to low-lying river floodplains; 2) Indigenous spatial zoning ensures that core settlements are located in low landslide risk and low–moderate flood risk areas; and 3) The combined hazard-avoidance strategy aligns to integrate indigenous knowledge into CB-DRR frameworks. This spatial congruence between traditional planning and hazard mapping confirms that the philosophy of *Alam Takambang Jadi Guru* has practical risk reduction value and should be preserved in formal planning policies.

4.3. Land Use Analysis of the Traditional settlement of *Nagari* Sijunjung based on Slope Map

An overlay analysis between the land use map and the slope classification map of the Sijunjung Traditional Settlement reveals a strong alignment between spatial utilization and the area's physical characteristics. This pattern reflects the Minangkabau philosophy of *Alam Takambang Jadi Guru*, in which each spatial function is adapted to geographical conditions, resource potential, and disaster risks, such as floods and landslides. The indigenous community has long applied ecological adaptation principles in their spatial planning, ensuring that settlements occupy safe zones, seasonal agriculture is concentrated in lowlands, and steep slopes are preserved with vegetation to prevent soil degradation. More details can be seen in **Table 9.**

Based on **Table 5** above, a spatial configuration of land use in Nagari Sijunjung that closely follows slope contours embodies disaster risk reduction principles rooted in local wisdom. This arrangement reflects a long-standing cultural understanding of how topography, hydrology, and soil stability interact to determine the most suitable allocation of land for settlements, agriculture, and conservation. He et al. (2017) found that communities in mountainous regions of China strategically adapt cropping and vegetation patterns to slope gradients to mitigate erosion and maintain soil productivity.

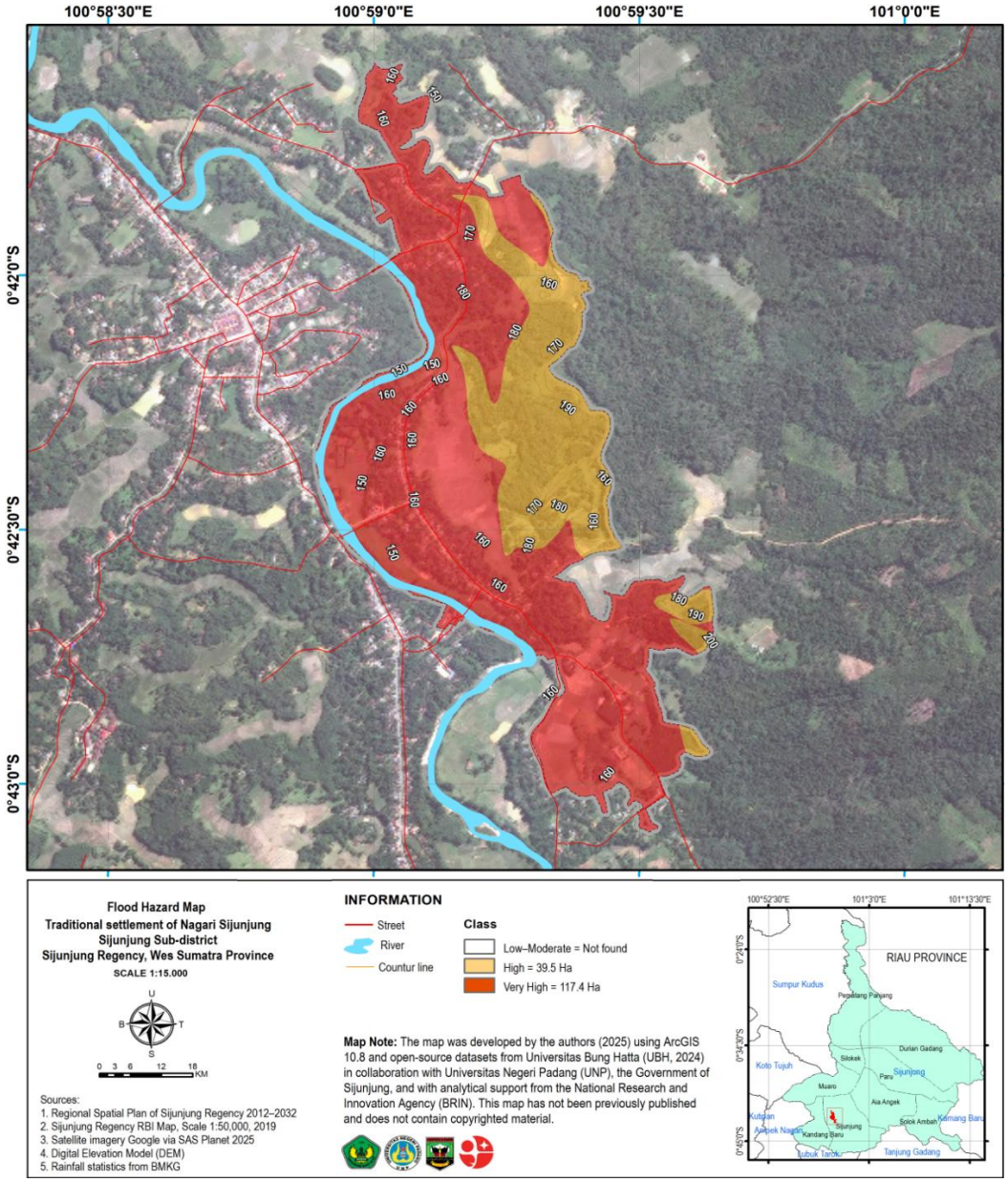

Fig. 4. Flood hazard map of the traditional settlement of *Nagari* Sijunjung area.

Table 9

Flood hazard potential and indigenous mitigation strategies.

Land Use types	Area (Ha)	Notes
Settlement	13.69	Concentrated in central lowland areas and along riverbanks
Rubber Plantation	75.73	Dominates gentle to moderate slope zones
Rainfed Rice Field	46.30	Located in lowland areas adjacent to rivers
Mixed Garden	14.68	Distributed across the midland zones
Swamp	0.92	Situated near river channels
River	5.29	Primary hydrological feature of the landscape
Dry Field/Cropland	0.20	Minor extent, found in small open flat areas
Shrubland	0.14	Minor extent, functioning as natural vegetative cover

Source: Data analysis, 2025.

Putra et al. (2025) similarly noted that agricultural development on gentle slopes is less vulnerable to erosion when combined with basic soil conservation measures.These findings align with Hermon et al. (2019), who demonstrated that perennial vegetation significantly improves slope stability in tropical regions, where perennial cover functions as a bioengineering measure for slope protection. Overall, the land use pattern shows how each element works physically, like rubber plantations on steep slopes stabilize the soil, rice fields in the floodplain act as retention areas to hold excess water, and *Rumah Gadang* on stilts in transitional zones allow communities to adapt to residual flood risk.

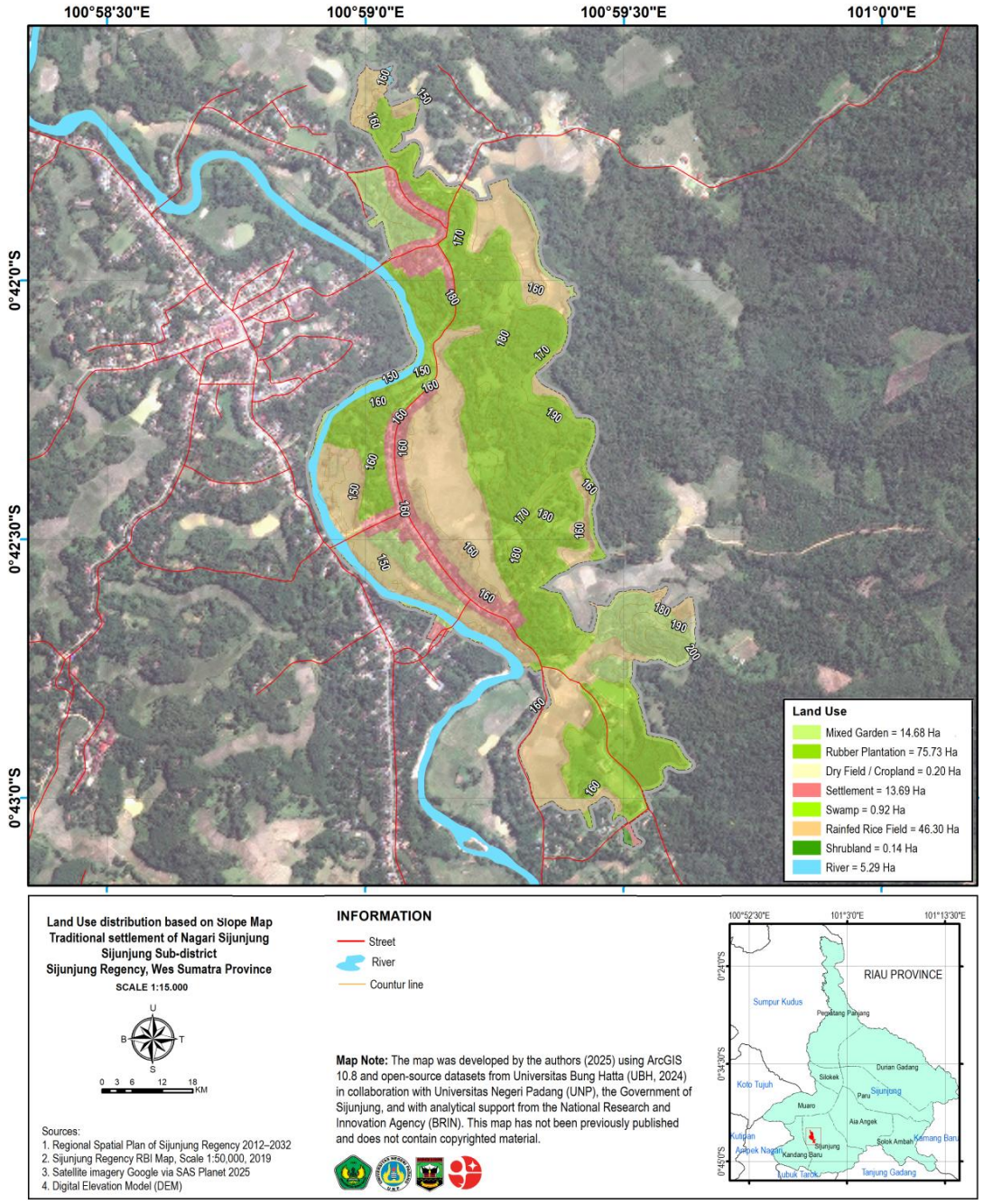

Fig. 5. Land use distribution based on slope map of the traditional settlement of *Nagari* Sijunjung area.

This strategy is consistent with the Minangkabau proverb *"Nan tanah tinggi dipakai rimbo, bukan untuk alun-alun kampuang"*. Flood-prone areas are managed through a combination of zoning and ecological buffers. Settlements and croplands are generally located close to river channels but are set back from the immediate riverbank to reduce inundation risk during peak rainfall events. Swamps (0.92 ha) and low-lying open fields serve as natural buffer zones, absorbing excess surface water and attenuating flood peaks. In the lower plains, rainfed rice fields function as seasonal water retention areas, temporarily storing runoff and preventing prolonged flooding of settlement zones. For more details, see the map in **Figure 5**.

This approach reflects the Minangkabau principle "*Nan di hilia ndak ditabam, nan di hulu ditahan*", which emphasizes source-based water management to safeguard downstream settlements. Barlian et al. (2024) demonstrated that hazard-based zoning and agricultural retention areas effectively reduce flood peaks, while Arora (2023) reported that Himalayan indigenous communities similarly align farmland with hydrological flow paths to retain water and protect villages. Overlay analysis between the land use map and slope map confirms that Sijunjung's indigenous spatial planning is closely aligned with natural conditions. This reflects the Minangkabau philosophy of *Alam Takambang Jadi Guru* as a practical framework guiding: 1) Placement of settlements in safe, stable zones; 2) Allocation of steep slopes for vegetative conservation; 3) Use of lowlands for seasonal agriculture and water storage; and 4) Preservation of rivers, swamps, and riparian vegetation as ecological infrastructure. This spatial logic is reinforced by another local saying, *"Bumi dipijak, langik dijunjuang; alam dibaco, Nagari dibangun"*. The resulting land use pattern represents a socio-ecological equilibrium where environmental processes and cultural norms converge to sustain both community resilience and landscape integrity.

4.4. Analysis of slope, land use, disaster potential, and local wisdom

This study analyzes the relationship between slope conditions, land use patterns, disaster potential, and the application of local wisdom in the traditional settlement of *Nagari* Sijunjung.

Table 10

Results of integrating slope analysis, land use, disaster potential, and local wisdom.

Analysis stage	Field findings	Ecological & social functions	Relation to local wisdom
Slope and land use	The 0–8% slope zone is utilized for settlements and agriculture (rainfed rice fields); the 8–15% slope zone is used for rubber plantations and mixed vegetation.	Optimizes fertile land and accessibility, reduces landslide risk in flat zones.	Principle of land use according to stable slope contours.
Vegetation-based landslide mitigation	Rubber plantations covering approximately 75.73 ha are located on steep slopes.	Deep root systems bind the soil, reduce erosion, and slow surface runoff.	Traditional proverb "*Nan tanah tinggi dipakai rimbo, bukan untuk alun-alun kampuang*".
Flood adaptation	Rice fields and wetlands are located in floodplains; settlements are set back to gentle slope zones.	Provides water absorption areas, reduces inundation risk in settlements.	Traditional proverb "*Nan di hilia ndak ditabam, nan di hulu ditahan*"
Philosophical reflection	Spatial function placement refers to the philosophy of *Alam Takambang Jadi Guru*.	Ensures ecological–social balance, maintains resource sustainability.	Placement of settlements, forests, and agricultural areas follows ecosystem logic.
Integration of modern and local data	Overlaying slope, land, and disaster risk maps with customary zoning.	Strengthens socio-ecological resilience and cultural identity.	Risk-based planning model rooted in local cultural values.

Source: Data analysis, 2025.

The analysis was conducted by overlaying slope maps, land use maps, and disaster risk maps, then comparing them with indigenous knowledge documented through interviews, participant observation, and the review of traditional manuscripts (*Tambo*). The results of the analysis are presented in **Table 10**, formulated based on the indigenous knowledge–spatial integration approach, modified from the framework in **Table 5** (see method).

The synthesis of information shown in **Table 6** reveals that the Sijunjung indigenous community has gradually shaped a land-use system that is both environmentally attuned and hazard-aware. Over time, settlement placement, agricultural zoning, and conservation areas have been organized in a manner that directly corresponds to the area's geomorphology. Flat and gently inclined lands are prioritized for housing and crop cultivation, while steeper slopes are purposefully maintained under protective vegetation cover. This approach supports the view of McDonald (1984) that contour-sensitive land allocation not only reduces ecological degradation but also sustains agricultural yield potential. The decision to utilize rubber plantations within high-susceptibility landslide areas demonstrates a deliberate application of natural slope-stabilization methods. Osman (2018) highlights that deep-rooted perennial crops can enhance slope stability and diminish runoff intensity, thereby lowering landslide risks. Similarly, Lele (2009) describes the dual role of perennial vegetation in watershed management, combining economic value with ecosystem services, which mirrors the function of rubber trees in Sijunjung.

In managing flood hazards, the community adopts a zoning pattern that designates floodplain zones for paddy fields and wetlands, while positioning settlements on slightly elevated ground. This method preserves natural flood absorption capacity and reduces structural vulnerability during peak rainfall. Comparable adaptive zoning practices are documented by Gurung (2024) in rural Nepal, where settlement relocation combined with water flow-aligned agriculture significantly mitigated flood losses. Long et al. (2020) further emphasize that integrating natural buffer zones into spatial plans is a critical element of flood-resilient settlement design. The embedding of the philosophy of *Alam Takambang Jadi Guru* into these spatial decisions reflects the deep interdependence between cultural identity and environmental stewardship. Rani et al. (2025) argue that blending traditional ecological knowledge with modern ecosystem-based planning produces context-specific adaptation strategies that are both sustainable and socially legitimate. The case of Sijunjung also resonates with the CB-DRR framework described by King et al. (2016), wherein community wisdom becomes the cornerstone for hazard-informed land-use policy.

4.5. Hazard potential, land use, and local wisdom in the formation of *Nagari*

This study examines the application of the philosophy *Alam Takambang Jadi Guru* in the spatial planning of *Nagari* Sijunjung, with a particular focus on managing landslide and flood risks. The analysis draws upon slope maps, land-use maps, and field observations, which are then compared with the principles of Minangkabau local wisdom. A summary of the findings is presented in **Table 11**, which is structured based on the indigenous knowledge–spatial integration framework outlined in **Table 5**, but modified to reflect field-based results.

Information shown in **Table 6** above indicates that, despite the accelerating influence of contemporary development, the guiding principles of *Alam Takambang Jadi Guru* still underpin how land is allocated in *Nagari* Sijunjung. Land-use zoning in the area demonstrates a deliberate relationship between terrain characteristics and functional land designation. Steeper slopes are retained under vegetation with protective value, while flatter land is prioritized for settlements and crop production, an arrangement consistent with the ecosystem-based disaster risk reduction model described by Estrella & Saalismaa (2012), where spatial choices are made to reduce hazard exposure while maintaining livelihoods. The use of rubber plantations on slopes classified as highly susceptible to landslides reflects a proactive bioengineering approach to slope stabilization. As noted by Asbjornsen et al. (2014), deep-rooted perennial crops play a vital role in reinforcing soil structure and mitigating erosion in tropical environments. However, where vegetation buffers are reduced or cleared, the stability benefits diminish, increasing vulnerability.

Table 11

Integration of hazard potential analysis, land use, and local wisdom in *Nagari* Sijunjung.

Analysis stage	Field findings	Ecological & social functions	Link to local wisdom
Application of *Alam Takambang Jadi Guru*	Settlements placed on gentle slopes; agriculture follows slope gradient; forest preserved in hazard-prone areas.	Maintains ecosystem balance, minimizes disaster risks.	Proverb "*Alam Takambang Jadi Guru*" as spatial guideline.
Landslide Analysis – Steep Slopes (8–15%)	Dominated by rubber plantations; some areas near settlements; risk increases if vegetation cover is removed.	Rubber roots stabilize soil; vegetation loss heightens landslide susceptibility.	Proverb"Nan tanah tinggi dipakai rimbo".
Flood Analysis – Flat/Gentle Slopes (0–8%)	Main settlements near rivers; high flood risk due to sedimentation and reduced infiltration zones.	Natural floodplains absorb runoff; natural drainage must be maintained.	Proverb "Nan di hilia ndak ditabam, nan di hulu ditahan".
Spatial Suitability	Mostly consistent with customary principles; some modern interventions, such as roads and housing, encroach into hazard zones.	Reduces effectiveness of natural protection if expansion is uncontrolled.	Partial alignment with *Alam Takambang Jadi Guru*.
Spatial Planning Recommendations	Riparian conservation, steep-slope rehabilitation, conservative farming, restriction of expansion into hazard zones.	Enhances disaster resilience and environmental sustainability.	Restores land-use patterns to customary philosophy.

Source: Data analysis, 2025.

In low-lying floodplain areas, settlement placement and agricultural zoning aim to preserve hydrological function. Paddy fields and wetland zones serve as natural retention areas, slowing and absorbing runoff before it reaches settlement areas. This mirrors the floodplain conservation strategies discussed by Hartanto & Rachmawati (2017), who argue that maintaining undeveloped flood storage capacity is critical for both disaster prevention and ecological health. While the prevailing land-use pattern generally aligns with Minangkabau spatial ethics, the encroachment of infrastructure and plantation activities into high-risk zones signals the need for targeted policy control. King et al. (2016) emphasize that such interventions are crucial for ensuring that community-based hazard knowledge is effectively translated into enforceable land-use regulation. The proposed measures, namely riparian zone preservation, reforestation of steep slopes, and adoption of soil-conserving agricultural practices, offer dual benefits of ecological sustainability and cultural continuity. Geetha et al. (2025) underscore that combining indigenous environmental knowledge with appropriate modern tools enhances adaptive capacity, creating spatial systems that are both risk-informed and locally grounded.

5. CONCLUSIONS

The spatial organization of *Nagari* Sijunjung reflects a deep integration of geomorphological realities, ecological functions, and Minangkabau local wisdom, particularly the philosophy of *Alam Takambang Jadi Guru*. Slope analysis shows that flat and gently sloping areas (0–8%) are primarily used for settlements, social infrastructure, and intensive agriculture, while steeper slopes (8–15%) are preserved under vegetation, mainly rubber plantations and customary protected forest. This configuration minimizes landslide risks, optimizes fertile land use, and safeguards upstream water resources. Hazard mapping confirms that indigenous land allocation inherently avoids high-risk zones.

Landslide-prone areas with unstable geology are excluded from permanent settlements, serving instead as ecological buffers. Rubber plantations on these slopes function as natural bioengineering systems, stabilizing soil and reducing runoff. In flood management, river floodplains are reserved for seasonal agriculture and grazing, while settlements are strategically placed on slightly elevated terrain. These arrangements preserve natural flood absorption capacity, reduce structural vulnerability, and maintain hydrological balance. Overlaying slope, land use, and hazard maps demonstrates a high degree of spatial congruence between indigenous zoning and scientific disaster risk assessments. Such alignment indicates that traditional planning is not only culturally rooted but also hazard-aware, offering a practical framework for CB-DRR.

Despite this resilience, modern development pressures such as road construction and plantation expansion into hazard-prone zones pose emerging threats to ecological stability and cultural integrity. Targeted interventions, including riparian conservation, steep-slope rehabilitation, and soil-conserving agricultural practices, are essential to maintain both environmental sustainability and socio-cultural identity. The *Nagari* Sijunjung case illustrates how integrating indigenous knowledge with modern spatial analysis can produce adaptive, risk-sensitive land use models. Preserving and formalizing these practices within planning policy can strengthen resilience, protect ecosystems, and ensure that cultural values remain central to sustainable landscape management.

ACKNOWLEDGMENTS

The authors acknowledge the Institute for Study and Community Service (LPPM) Universitas Bung Hatta (UBH) for academic and institutional support. Appreciation is also extended to Universitas Negeri Padang (UNP) as a partner institution, and to the Government of Sijunjung Regency, West Sumatra Province, for providing data access and field facilitation. The authors also thank the *Kerapatan Adat Nagari* (KAN) of *Nagari* Sijunjung for sharing their indigenous knowledge and local wisdom, which contributed significantly to this study.

REFERENCES

Arora, S., Bhatt, R., Sharma, V., & Hadda, M. S. (2023). Indigenous practices of soil and water conservation for sustainable hill agriculture and improving livelihood security. *Environmental Management, 72*(2), 321–332. DOI: 10.1007/s00267-022-01602-1

Asbjornsen, H., Hernandez-Santana, V., Liebman, M., Bayala, J., Chen, J., Helmers, M., Ong, C. K., & Schulte, L. A. (2014). Targeting perennial vegetation in agricultural landscapes for enhancing ecosystem services. *Renewable Agriculture and Food Systems, 29*(2), 101–125. DOI: 10.1017/S1742170512000385

Asrawijaya, E. (2024). Traditional ecological wisdom for the resilience of indigenous peoples in Indonesia. *Besari: Journal of Social and Cultural Studies, 1*(2), 59–77. DOI: 10.71155/besari.v1i2.29

Barlian, E., Umar, I., Anwar, S., Lanin, D., & Putra, A. (2024). Mitigation of flood hazard areas in Antokan watershed. *AIP Conference Proceedings, 3255*(1), 0192510. DOI: 10.1063/5.0192510

Chahkar, A., Ortega-Terol, D., Hernández-López, D., Ballesteros, R., Ortega, J. F., & Moreno, M. A. (2020). Assessing the accuracy of multiple classification algorithms for crop classification using Landsat-8 and Sentinel-2 data. *Remote Sensing, 12*(11), 1735. DOI: 10.3390/rs12111735

Estrella, M., & Saalismaa, N. (2012). The role of ecosystems management for disaster risk reduction. *Ecosystem Approach to Disaster Risk Reduction*, 5.

Geetha, V. (2025). Environmental hazards, vulnerability, and disaster research for development: A review. In B. Auddiya (Ed.), *Multidisciplinary research area in arts, science & commerce*. 2. 18–32.

Gurung, H. B. (2024). Flood hazard in Bardiya, Nepal: Causes, consequences and effective mitigation strategies (Thesis), Tribhuvan University.

Hartanto, I. S., & Rachmawati, R. (2017). Assessing the spatial-temporal land use change and encroachment activities due to flood hazard in North Coast of Central Java, Indonesia. *Indonesian Journal of Geography, 49*(2), 165–176. DOI: 10.22146/ijg.28402

He, S., Wang, D., Fang, Y., & Lan, H. (2017). Guidelines for integrating ecological and biological engineering technologies for control of severe erosion in mountainous areas – A case study of the Xiaojiang River Basin, China. *International Soil and Water Conservation Research, 5*(4), 335–344. DOI: 10.1016/j.iswcr.2017.05.001

Heider, K. G. (2011). Minangkabau folk psychology. *The cultural context of emotion: Culture, mind, and society*. Palgrave Macmillan. DOI: 10.1057/9780230337596_3

Hermon, D., Ganefri., Putra, A., & Oktorie, O. (2019). Characteristics of melanic epipedon based on biosequence in the physiography of Marapi - Singgalang, West Sumatra. *IOP Conference Series: Earth and Environmental Science, 314*(1), 012010. DOI: 10.1088/1755-1315/314/1/012010

Hermon, D., Hamzah, T. A. A. T., Febriandi., Ramadhan, R., Putra, A., Rahmi, L., Sihaini, E., & Sari, N. (2024). Characteristics of community adaptive resilience in overcoming the hazards of flood disaster in Kampar Regency-Indonesia. *International Journal of GEOMATE, 26*(122), 71–78. DOI: 10.21660/2024.122.4646

Hiwasaki, L., Luna, E., & Shaw, R. (2014). Local and indigenous knowledge for community resilience: Hydro-meteorological disaster risk reduction and climate change adaptation in coastal and small island communities. UNESCO. https://coilink.org/20.500.12592/cjps6r

Karnoto, B. K., Purwanto, A., & Budiaman, B. (2025). Integrating indigenous knowledge with modern disaster risk reduction systems for enhanced community resilience. *International Journal of Environmental Sciences, 11*(1), 1–15. DOI: 10.64252/jf3bj759

Kegel, J. F., MacAfee, E., & de Jong, E. (2025). Desensitised flood risk perception to extensive disasters in a marginalised urban kampong in Indonesia. *Environmental Hazards, 24*(1), 91–112. DOI: 10.1080/17477891.2024.2343404

King, D., Gurtner, Y., Firdaus, A., Harwood, S., & Cottrell, A. (2016). Land use planning for disaster risk reduction and climate change adaptation. *International Journal of Disaster Resilience in the Built Environment, 7*(2), 158–172. DOI: 10.1108/IJDRBE-03-2015-0009

Lah, N. A. A., Mohamed Khaidir, K. A., Abdul Wahab, M. H., & Couto, N. (2024). "*Alam Takambang Jadi Guru*" philosophy in Minang-Malay vernacular ornamentation wisdom. *Asian Journal of Environment-Behaviour Studies, 9*(29), 1–23. DOI: 10.21834/ajebs.v9i29.455

Lele, S. (2009). Watershed services of tropical forests: From hydrology to economic valuation to integrated analysis. *Current Opinion in Environmental Sustainability, 1*(2), 148–155. DOI: 10.1016/j.cosust.2009.10.007

Lestari, Z. A., Syafutra, R., & Rina, S. D. (2025). Sacred forests and sustainable practices: The role of the Lom Tribe's local wisdom in disaster resilience. *Global Review of Tourism and Social Sciences, 1*(3), 1–12. DOI: 10.53893/grtss.v1i3.347

Long, N.V., Cheng, Y., & Le, T. D. N. (2020). Flood-resilient urban design based on the indigenous landscape in the city of Can Tho, Vietnam. *Urban Ecosystems, 23*(4), 675–687. DOI: 10.1007/s11252-020-00941-3

Mayasari, M., Antariksa, & Wulandari, L. D. (2023). Cultural Landscape of Minangkabau Traditional Settlement in Nagari Sijunjung Traditional Settlement. *International Journal of Architecture, Arts and Applications, 9*(1), 6–13. DOI: 10.11648/j.ijaaa.20230901.12

McDonald, G. T. (1984). Planning rural land development: Forestry and agriculture in northeastern Australia. *Geographical Research, 22*(1), 100–121. DOI: 10.1111/j.1467-8470.1984.tb00464.x

Nasri, D., Mulyadi, Juliastuty, D., Awwali, M., & Danerek, S. (2022). The legacy of ecological insights in Minangkabau kieh. *Heritage of Nusantara: International Journal of Religious Literature and Heritage, 11*(2), 206–237. DOI: 10.31291/hn.v11i1.665

Nguyen, H. T. (2019). Spatial planning in flood-prone areas (Dissertation), Technische Universität Darmstadt.

Nicoară, M. E., & Haidu, I. (2011). Creation of the roads network as a network dataset within a geodatabase. *Geographia Technica, 6*(2), 81–86.

Osman, K. T. (2018). Soils on steep slopes. *Management of soil problems*. DOI: 10.1007/978-3-319-75527-4_8

Paimin, Sukresno, & Pramono, I. B. (2009). *Teknik mitigasi: Banjir dan tanah longsor*. Tropenbos International Indonesia Programme.

Permana, R. S., Buana, A. P., Akmam, A., Amir, H., & Putra, A. (2020, May 6). Using the Schlumberger configuration resistivity geoelectric method to estimate the rock structure at landslide zone in Malalak agam. *Journal of Physics: Conference Series, 1481*(1), 012034. DOI: 10.1088/1742-6596/1481/1/012034

Prambudi, Y., Widiyastuti, D., & Fandeli, C. (2023). Study of sustainable tourism development in Silokek Geopark, Sijunjung Regency, West Sumatra. *BARISTA: Journal of Language and Tourism Studies, 10*(1), 1–15. DOI: 10.34013/barista.v10i1.1209

Putra, A., Hermon, D., Dewata, I., Barlian, E., & Triyanto. (2025). USLE method for erosion prediction and conservation measures at the Air Dingin Watershed of the upstream part in Padang City, Indonesia. In *Erosion measurement, modeling, and management: Challenges and solutions* (1st ed). 26.

Rahmani, T. R., Sari, D. P., Akmam, A., Amir, H., & Putra, A. (2020, May 6). Using the Schlumberger configuration resistivity geoelectric method to analyze the characteristics of slip surface at Solok. *Journal of Physics: Conference Series, 1481*(1), 012030. DOI: 10.1088/1742-6596/1481/1/012030

Rani, J., Gulia, V., Sangwan, A., Dhull, S. S., & Mandzhieva, S. (2025). Synergies of traditional ecological knowledge in biodiversity conservation: A paradigm for sustainable food security. *Ecologically mediated development: Sustainable development and biodiversity*. 41. DOI: 10.1007/978-981-96-2413-3_2

Sjamsiah., Sappewali., Jannah, M. M., & Hamrullah, H. (2019). Determination of the physical and chemical properties of the complex latosol soil, Mediterranean, alluvial and its inhibitory effect on dog saliva bacteria. *Proceedings of the 1st International Conference on Science and Technology*. 132–139.

Şen, Z. (2018). *Flood modeling, prediction and mitigation*. Springer. DOI: 10.1007/978-3-319-52356-9

Sutanta, H., Rajabifard, A., & Bishop, I. D. (2010). Integrating spatial planning and disaster risk reduction at the local level in the context of spatially enabled government. *Spatially Enabling Society*. 1. 56–68.

Triyatno., Bert, I., Idris., Hermon, D., & Putra, A. (2020). Hazards and morphometry to predict the population loss due of landslide disasters in Koto XI Tarusan - Pesisir Selatan. *International Journal of GEOMATE, 19*(76), 161–167. DOI: 10.21660/2020.76.ICGeo12

Wiersum, K. F. (2003). Use and conservation of biodiversity in East African forested landscapes. *Tropical forests in multi-functional landscapes*. Prince Bernhard Centre, Utrecht University.

Aims and Scope

Geographia Technica is a journal devoted to the publication of all papers on all aspects of the use of technical and quantitative methods in geographical research. It aims at presenting its readers with the latest developments in G.I.S technology, mathematical methods applicable to any field of geography, territorial micro-scalar and laboratory experiments, and the latest developments induced by the measurement techniques to the geographical research.

Geographia Technica is dedicated to all those who understand that nowadays every field of geography can only be described by specific numerical values, variables both oftime and space which require the sort of numerical analysis only possible with the aid of technical and quantitative methods offered by powerful computers and dedicated software.

Our understanding of ***Geographia Technica*** expands the concept of technical methods applied to geography to its broadest sense and for that, papers of different interests such as: G.I.S, Spatial Analysis, Remote Sensing, Cartography or Geostatistics as well as papers which, by promoting the above mentioned directions bring a technical approach in the fields of hydrology, climatology, geomorphology, human geography territorial planning are more than welcomed provided they are of sufficient wide interest and relevance.

Targeted readers:

The publication intends to serve workers in academia, industry and government.
Students, teachers, researchers and practitioners should benefit from the ideas in the journal.

Guide for Authors

Submission

Articles and proposals for articles are accepted for consideration on the understanding that they are not being submitted elsewhere.

The publication proposals that satisfy the conditions for originality, relevance for the new technical geography domain and editorial requirements, will be sent by email to the address editorial-secretary@technicalgeography.org.

This page can be accessed to see the requirements for editing an article, and also the articles from the journal archive found on www.technicalgeography.org can be used as a guide.

Content

In addition to full-length research contributions, the journal also publishes Short Notes, Book reviews, Software Reviews, Letters of the Editor. However the editors wish to point out that the views expressed in the book reviews are the personal opinion of the reviewer and do not necessarily reflect the views of the publishers.

Each year two volumes are scheduled for publication. Papers in English or French are accepted. The articles are printed in full color. A part of the articles are available as full text on the www.technicalgeography.org website. The link between the author and reviewers is mediated by the Editor.

Peer Review Process

The papers submitted for publication to the Editor undergo an anonymous peer review process, necessary for assessing the quality of scientific information, the relevance to the technical geography field and the publishing requirements of our journal.

The contents are reviewed by two members of the Editorial Board or other reviewers on a simple blind review system. The reviewer's comments for the improvement of the paper will be sent to the corresponding author by the editor. After the author changes the paper according to the comments, the article is published in the next number of the journal.

Eventual paper rejections will have solid arguments, but sending the paper only to receive the comments of the reviewers is discouraged. Authors are notified by e-mail about the status of the submitted articles and the whole process takes about 3-4 months from the date of the article submission.

Indexed by: **CLARIVATE ANALYTICS**
SCOPUS
GEOBASE
EBSCO
SJR
CABELL

ISSN: 1842 - 5135 (Print)
ISSN: 2065 - 4421 (Online)